HAL open science

The impact of climatic events and drought on the shrinkage and swelling phenomenon of clayey soils interacting with constructions

Hossein Assadollahi Tejaragh

▶ To cite this version:

Hossein Assadollahi Tejaragh. The impact of climatic events and drought on the shrinkage and swelling phenomenon of clayey soils interacting with constructions. Géotechnique. Université de Strasbourg, 2019. English. ⟨NNT : 2019STRAD011⟩. ⟨tel-02331567⟩

HAL Id: tel-02331567

https://theses.hal.science/tel-02331567v1

Submitted on 24 Oct 2019

HAL is a multi-disciplinary open access archive for the deposit and dissemination of scientific research documents, whether they are published or not. The documents may come from teaching and research institutions in France or abroad, or from public or private research centers.

L'archive ouverte pluridisciplinaire **HAL**, est destinée au dépôt et à la diffusion de documents scientifiques de niveau recherche, publiés ou non, émanant des établissements d'enseignement et de recherche français ou étrangers, des laboratoires publics ou privés.

Autorisation HAL

HAL Authorization

UNIVERSITÉ DE STRASBOURG

ÉCOLE DOCTORALE MSII (ED n°269)

Laboratoire ICUBE - UMR 7357

Département Génie Civil Énergétique (GCE) - INSA

THÈSE présentée par :

Hossein ASSADOLLAHI

préparée à **l'Institut National des Sciences Appliquées de Strasbourg (INSA)**

soutenue le : **17 Juin 2019**

pour obtenir le grade de : **Docteur de l'Université de Strasbourg**

Discipline/ Spécialité : Génie Civil & Environnemental - Géotechnique

L'impact des événements climatiques et de la sécheresse sur le phénomène du retrait gonflement des argiles en interaction avec les constructions

THÈSE dirigée par :

M. NOWAMOOZ Hossein	Maître de conférence, INSA de Strasbourg

RAPPORTEURS :

Mme MASROURI Farimah	Professeur, Université de Lorraine - ENSG
M. CUI Yu-jun	Professeur, Ecole des Ponts ParisTech

EXAMINATEURS :

Mme HATTAB Mahdia	Professeur, Université de Lorraine
M. FLEUREAU Jean-Marie	Professeur, Centrale Supélec (ECP)

The impact of climatic events and drought on the shrinkage and swelling phenomenon of clayey soils interacting with constructions

By

Hossein Assadollahi

A DISSERTATION
submitted to the National Institute of Applied Sciences (INSA) at the
University of Strasbourg

In Partial Fulfillment of Requirements
For the Degree of **Doctor of Philosophy**

Major: Civil and Environmental Engineering
(Geotechnical Engineering)

Strasbourg, France
June 17, 2019

Approved:

Farimah Masrouri	Reviewer	Professor	University of Lorraine - ENSG
Mahdia Hattab	Examiner	Professor	University of Lorraine
Yu-jun Cui	Reviewer	Professor	Ecole des Ponts ParisTech
Jean-Marie Fleureau	President	Professor	Centrale Supélec (ECP)
Hossein Nowamooz	Thesis supervisor	Associate professor	INSA of Strasbourg

Dedicated to
My father and my mother

Dédié à
Mon père et à ma mère

"When people ask me if a god created the universe, I tell them that the question itself makes no sense. Time didn't exist before the big bang, so there is no time for god to make the universe in. It's like asking directions to the edge of the earth; The Earth is a sphere; it doesn't have an edge; so looking for it is a futile exercise. We are each free to believe what we want, and it's my view that the simplest explanation is; there is no god. No one created our universe, and no one directs our fate. This leads me to a profound realization; There is probably no heaven, and no afterlife either. We have this one life to appreciate the grand design of the universe, and for that I am extremely grateful."

Stephen Hawking
(1942 - 2018)
Brief Answers to the Big Questions

Acknowledgments

This research work was carried out within the framework of a CIFRE program in collaboration with the ICUBE laboratory at the National Institute of Applied Sciences of Strasbourg and the R&D department of DETERMINANT group. I would like to thank all the collaborators for their support and their warm welcome during these 3 years of thesis.

First of all, my deep gratitude goes to the members of the jury, Prof. Jean-Marie Fleureau who accepted to chair the jury, Prof. Yu-Jun Cui and Prof. Farimah Masrouri who did me the honor of being my reviewers. I also would like to thank Prof. Mahdia Hattab for having accepted to be part of this thesis jury.

I would like to express my deepest gratitude and acknowledgments to my supervisor Dr. Hossein Nowamooz for his trust, his availability, his encouragement, his valuable scientific advices and the supervision of this work. I also would like to thank Mr. Alain Tabatabai, my industrial supervisor, for his availability, his kindness and his forbearance that he showed me during this thesis.

With regard to the DETERMINANT R&D department in which I carried out this thesis, I would like to thank Mr. Claude Perrodo, Dr. Blandine Tharaud, Mr. Didier Loiseau, Mr. Éric Petitpas (from the AQC) and especially Dr. Anh Quan Dinh for their help, availability and guidance during our technical discussions throughout this research work. A big thank you to all my colleagues in the office for the unforgettable shared moments: Sindy, Bocar, Marième, Amélie, Aurélie, Cécile, Nihel, Yasmina, Imane, Lyes, Ahmed, Mohammed, Eric, Bruno, Patrice, Carla, Nathalie, Sofia, Johanna, Ytong, Paul Yvon, Mikael, Karine, Juliette, Delphine, Jeff, Gregoire, Julien, Stephanie, Ingrid, Jeremy, Alain, Charles, Olivier, Kévin, Stéphane, Loïc, Shazade and François.

I cannot ignore the constant support of all the other PhD students from the GCE department of INSA who have been encouraging me throughout this work and with whom I shared very good moments: Anicet Dansou, Fujiao Tang, Laura Gaillard, Guixian Liu, Calypso Chadfeau, Peng Jing. Thank you to all of you.

I would particularly like to thank Alain Franck Béchade, Prof. Alain Denis and Jean-François Lataste from I2M Bordeaux, Sébastien Gourdier from BRGM and David Mathon from CEREMA, for their help in restoring data on the instrumented site of Roaillan. I thank them for their vast knowledge in the field of clayey soils and for taking the time to answer all my questions.

My warmest thanks to Dr. Siavash Ghabezloo from the ENPC who guided me from the first day of my arrival in France and at the Ecole des Ponts in 2014.

I would like to thank all my friends who contributed in one way or another to the accomplishment of this work during this period. Thanks to Manuel, Sirine, Olivier, Marine, Rawaz, Youssef, Luis, Rouba, Gabriele, Amir, Pauline, Mehrdad, Alireza, Raheleh, Hassan, Ava, Bahador, Ali, Anna, Homa, Mahsa, Faezeh, Mina, Pierre, Samuel, Moahmmad, Saeed and Behrang, for their encouragement, their presence and all the pleasant moments that we shared together.

I will not be able to finish my acknowledgments without thinking of my beloved family, my wonderful parents and my brother Yacine whose support and constant encouragement contributed to the success of this work. Without them all this would not have been possible. A big thank you to them who have been with me despite the distance and have supported me unconditionally in all the projects that I have undertaken from the beginning to the present day.

Remerciments

Ce travail de recherche a été réalisé dans le cadre d'une convention CIFRE entre le laboratoire ICUBE de l'INSA de Strasbourg et le département R&D de la société DETERMINANT. Je tiens à remercier tous les collaborateurs pour leur soutien et leur accueil pendent ces 3 années de thèse.

J'adresse tout d'abord mes remerciements aux membres du jury, M. Jean-Marie FLEUREAU qui a accepté de présider le jury, M. Yu-Jun CUI et Mme Farimah MASROURI qui m'ont fait l'honneur d'être rapporteurs. Je remercie également Mme Mahdia HATTAB d'avoir accepté de faire partie de ce jury de thèse.

Je tiens à adresser ma profonde reconnaissance et mes vifs remerciements à mon directeur de thèse M. Hossein NOWAMOOZ pour sa confiance, sa disponibilité, ses encouragements, ses précieux conseils scientifiques et le suivi de ce travail. Je remercie également M. Alain TABATABAI, le responsable industriel de thèse, pour sa disponibilité, sa gentillesse et sa patience qu'il a manifesté à mon égard durant cette thèse.

En ce qui concerne le département R&D de DETERMINANT dans lequel j'ai réalisé cette thèse, je tiens à remercier M. Claude PERRODO, Mme. Blandine THARAUD, M. Didier LOISEAU, M. Éric PETITPAS (de l'AQC) et surtout M. Anh Quan DINH pour leur aide, leur disponibilité et leurs conseils durant nos discutions techniques tout au long de ce travail de recherche. Un grand merci à tous mes collègues du bureau pour les moments inoubliables partagés : Sindy, Bocar, Marième, Amélie, Aurélie, Cécile, Nihel, Yasmina, Imane, Lyes, Ahmed, Mohammed, Éric, Bruno, Patrice, Carla, Nathalie, Sofia, Johanna, Ytong, Paul Yvon, Mikael, Karine, Juliette, Delphine, Jeff, Grégoire, Julien, Stéphanie, Ingrid, Jérémy, Alain, Charles, Olivier, Kévin, Stéphane, Loïc, Shazade et François.

Je ne saurais passer sous silence l'appui constant de tous les autres doctorant(e)s du département GCE de l'INSA qui n'ont cessé de m'encourager tout au long de ce travail et avec qui j'ai partagé de très bons moments : Anicet DANSOU, Fujiao TANG, Laura GAILLARD, Guixian LIU, Calypso CHADFEAU, Peng JING. Merci à vous tous.

Je tiens tout particulièrement à remercier Alain Franck BECHADE, Alain DENIS et Jean-François LATASTE de l'I2M de Bordeaux, Sébastien GOURDIER du BRGM et David MATHON du CEREMA, pour leur aide à la restitution des données sur le site instrumenté de Roaillan. Je les remercie pour leurs vastes connaissances dans le domaine des sols argileux et pour avoir pris le temps de répondre à toutes mes interrogations.

Mes vifs remerciements à M. Siavash GHABEZLOO de l'ENPC qui m'a guidé dès le premier jour de mon arrivé en France et à l'Ecole des Ponts en 2014.

Je tiens à remercier tous mes amis qui ont contribué d'une façon à l'autre à l'achèvement de ce travail au cours de cette période. Merci à Manuel, Sirine, Olivier, Marine, Rawaz, Youssef, Luis, Rouba, Gabriele, Amir, Pauline, Mehrdad, Alireza, Raheleh, Hassan, Ava, Bahador, Ali, Anna, Homa, Mahsa, Faezeh, Mina, Pierre, Samuel, Moahmmad, Saeed et Behrang, pour leur encouragement, leur présence et tous les moments agréables qu'on a partagé ensemble.

Je ne pourrai finir ces remerciements sans penser à ma famille, mes merveilleux parents et mon frère Yacine dont le soutien et l'encouragement permanent ont contribué à l'aboutissement de ce travail. Sans eux tout cela n'aurait pas été possible. Un grand merci à eux qui ont été à mes côtés malgré la distance et qui m'ont épaulé sans condition dans tous les projets que j'ai entrepris dès le début jusqu'à ce jour.

List of publications

Journal papers:

1. **Assadollahi H.**, Nowamooz, H. (2018). Investigation of in situ soil-atmosphere interaction with a hydro-thermal simulation approach: Application to an instrumented site. *European Journal of Environmental and Civil Engineering* [Under review]
2. **Assadollahi H.**, Nowamooz, H. (2019). Long term behavior of natural clays in a building foundation under climate change scenarios. *Environmental Geotechnics* [Under review]
3. **Assadollahi H.**, Nowamooz, H. (2019). Long term analysis of the shrinkage and swelling of clayey soils in a climate change context by numerical modelling and field monitoring. *Computers and Geotechnics* [Under review]

Conference papers with peer review:

4. **Assadollahi H.**, Nowamooz, H. (2017). Clay-Atmosphere Interaction in a high risk of shrinkage and swelling zone. Scientific research abstracts, *XVI International Clay Conference / ICC 2017 Vol. 7, p. 46.*
5. **Assadollahi H.**, Nowamooz, H. (2018). In-situ shrinkage and swelling in expansive clays induced by climatic conditions. *Proceedings of the 7th international conference on unsaturated soils.* Hong Kong, *Vol. 2, p. 1043-1048.*
6. **Assadollahi H.**, Nowamooz, H. (2018). Characterizing drought in the south of France using the standardized precipitation-evapotranspiration index SPEI. *Proceedings of the 7th international conference on unsaturated soils.* Hong Kong, *Vol. 2, p. 1237-1242.*
7. **Assadollahi H.**, Nowamooz, H. (2018). Using a Complementary Evapotranspiration Relationship to Estimate Surface Suction for Soil-Atmosphere Interaction Analysis: Wu W., Yu HS. (eds) *Proceedings of China-Europe Conference on Geotechnical Engineering.*
8. **Assadollahi H.**, Nowamooz, H. (2018). Modeling Root Water Uptake, Climate and Unsaturated Vegetated Clays Interactions in the Context of Shallow Foundation Soils. In: Hoyos L., McCartney J. (eds) Novel Issues on Unsaturated Soil Mechanics and Rock Engineering. GeoMEast 2018. *Sustainable Civil Infrastructures.* Springer, Cham
9. **Assadollahi H.**, Nowamooz, H. (2018). The effect of environmental factors on the stability of residential buildings built on expansive clays. In: Hoyos L., McCartney J. (eds) Recent advancements on expansive soils. GeoMEast 2018. *Sustainable Civil Infrastructures.* Springer, Cham
10. **Assadollahi H.**, Nowamooz, H. (2018). Predicting Swelling Potential and Soil-Water Retention Curves of Some Characterized Expansive Clays Based on Geotechnical Properties. In: Hoyos L., McCartney J. (eds) Novel Issues on Unsaturated Soil Mechanics and Rock Engineering. GeoMEast 2018. *Sustainable Civil Infrastructures.* Springer, Cham

Abstract

Climate change and severe climatic events such as long drought/rehydration periods are at the origin of the shrinkage and swelling phenomenon in expansive soils. This phenomenon is affected by Soil-Vegetation-Atmosphere (SVA) interactions and can cause severe structural damage to lightly loaded constructions such as residential buildings. The objective of this research work is to simulate the in-situ behavior of the shrinkage-swelling in expansive soils in a SVA context using numerical tools.

A soil-atmosphere interaction method is primarily presented along with a coupled hydro-thermal soil model. This approach was established in order to determine primarily, the natural time variable boundary conditions at the considered soil surface based on the mass and energy balance concept, and secondly to determine the spatial-temporal changes of the soil suction, water content and temperature. This approach was validated using in situ observations of monitored sites. Thereafter, the influence of the water uptake by vegetation was incorporated in the source term of the unsaturated water flow theory, using an existing root water uptake model.

Subsequently, the temporal variations of the soil suction were related to the volume change behavior using a simple approach developed based on the experimental results of drying/wetting tests performed in the literature. The associated volumetric indices in the void ratio-log suction plan, along with the complementary parameters of the linear model were correlated with basic geotechnical parameters.

The proposed approach was validated with in situ data provided from an experimental site. The Roaillan experimental site was instrumented in order to monitor the soil's physical changes along with the structural behavior of the building. Comparisons between the simulated and observed soil suction, soil water content, temperature and soil movements in time and depth showed an acceptable performance of the predictions. The approach was then extended to study the influence of future climate projections (2050) on the soil's physical variables and movements. Three RCP climate change scenarios were considered in this analysis which revealed different possible behavior in both short term and long term.

Finally, the developed approach was applied to the French territory by dividing it to six different climatic regions. Different soil parameters were attributed to each of these climatic regions in order to set the reference condition. Thereafter, the influence of different external factors was analyzed on the soil movements over a chosen period. The study finally suggests the adequate actions to take for minimizing the amplitude of the shrinkage and swelling phenomenon in a SVA context.

Key Words:

Drought, Shrinkage-Swelling of clayey soils, Soil-Vegetation-Atmosphere interactions, climate change, suction, unsaturated expansive soils, Geotechnical modelling, Geotechnical monitoring

Résumé

Le changement climatique et les événements climatiques sévères tels que les périodes de sécheresse/humidification prolongées sont à l'origine du phénomène de retrait-gonflement dans les sols argileux. Ce phénomène est affecté par les interactions sol-végétation-atmosphère (SVA) et peut causer d'importants dommages structurels aux constructions légères telles que les bâtiments résidentiels. L'objectif de ce travail de recherche est de modéliser le comportement in situ du retrait-gonflement des sols gonflants dans un contexte SVA en se basent sur des outils numériques.

Une méthode d'interaction sol-atmosphère est initialement présentée accompagnée d'un modèle couplé hydro-thermique du sol. Cette approche a été principalement mise en place afin de déterminer les conditions aux limites temporelles à la surface du sol en se basent sur la notion du bilan de masse et d'énergie pour déterminer a posteriori, les modifications spatio-temporelles de la succion du sol, de la teneur en eau et de la température. Cette approche a été validée à l'aide des observations in situ des sites instrumentés. Par la suite, l'influence de l'absorption d'eau par les végétations a été intégrée dans le terme source de l'écoulement de l'eau dans un milieu non saturé, à l'aide d'un modèle d'absorption d'eau de racine existant.

Les variations temporelles de succion ont été postérieurement reliées au comportement volumique du sol en appliquant une approche simple développée à partir des résultats expérimentaux des essais de séchage/humidification réalisés dans la littérature. Les indices associés dans le plan indice des vides-log succion, ainsi que les paramètres complémentaires du modèle linéaire ont été corrélés aux paramètres géotechniques de base.

L'approche proposée a été ultérieurement validée avec des données in situ fournies par la surveillance d'un site expérimental. Le site expérimental de Roaillan a été instrumenté afin de surveiller les modifications physiques du sol ainsi que le comportement structurel du bâtiment. Les comparaisons entre les résultats de la modélisation et les observations in situ de la succion du sol, la teneur en eau, la température et les mouvements du sol dans le temps ont montré une performance acceptable du modèle. L'approche a ensuite été appliquée pour étudier l'influence des projections climatiques futures (2050) sur les variables physiques et les mouvements du sol sur ce site. Trois scénarios RCP relatifs aux changements climatiques ont été examinés dans cette étude, qui ont révélé des différents comportements possibles à court terme et à long terme.

Finalement, l'approche développée a été appliquée au territoire français en le divisant en six régions climatiques. Différents paramètres de sol ont été attribués à chacune de ces régions climatiques afin de définir les conditions de référence. En conséquence, l'influence de différents facteurs externes sur les mouvements du sol a été analysée sur une période donnée. Enfin, l'étude suggère les mesures adéquates à prendre pour minimiser l'amplitude du phénomène de retrait et de gonflement dans un contexte SVA.

Mots clés :

Sécheresse, retrait-gonflement des sols argileux, interactions sol-végétation-atmosphère, changement climatique, succion, sols gonflants non saturés, modélisation géotechnique, instrumentation géotechnique

Table of contents

General Introduction **1**

Chapter 1. Literature review **4**

1.1 Clays shrinkage and swelling 4

1.1.1 The phenomenon and influencing factors 4

1.1.2 Clays shrinkage swelling hazard in France 7

1.1.3 Economic issues of Geotechnical drought in France 9

1.1.4 Climate change impact in France and drought indexes 11

1.2 Soil-Vegetation-Atmosphere interactions 14

1.2.1 Water balance 15

1.2.2 Energy balance 27

1.2.3 Water uptake by vegetation 35

1.3 Volume change behavior of unsaturated expansive soils 41

1.3.1 Experimental investigations on volume change behavior of expansive clays 41

1.3.2 Modelling approaches of the volume change behavior 49

1.4 Conclusion 72

Chapter 2. Modelling shrinkage and swelling of unsaturated natural soils in a Soil-Vegetation-Atmosphere context **73**

2.1 Introduction 73

2.2 Adapted Soil-Atmosphere Interaction analysis 73

2.2.1 Simplified Mass balance approach 73

2.2.2 Thermal based energy balance approach 74

2.2.3 Investigation of surface temperature estimation 78

2.2.4 Validation of the thermal based energy balance approach 81

2.3 Hydro-Thermal modelling approach 84

2.3.1 Water flow simulation approach in unsaturated soils 84

2.3.2 Heat transport simulation approach in unsaturated soils 94

2.4 Vegetation effect 96

2.4.1 Root Water Uptake modelling approach (RWU) 96

2.4.2 Root distribution function 97

2.4.3 Potential transpiration and crop coefficient 99

2.5 Modelling shrinkage and swelling of soils 102

2.5.1 Adapted physical concept 102

2.5.2 Correlation of the volumetric indices with basic geotechnical parameters 107

2.5.3 Performance evaluation 111

2.5.4 Parametric analysis 113

2.6 Complementary parameters and validation 115

2.6.1 Correlation of model's suction parameters with basic geotechnical parameters 115
2.6.2 The effect of the applied stress on the volumetric indices 117
2.7 Conclusion 123
Chapter 3. Application and validation 125
3.1 Application to Roaillan experimental site 125
3.2 Monitoring of the Roaillan site 126
3.2.1 Geotechnical Investigations 127
3.2.2 Structural and Geotechnical monitoring sensors 130
3.3 Model setup for simulating the site 134
3.3.1 Model dimensions and adapted profiles 134
3.3.2 Soil input parameters 140
3.3.3 Climatic parameters 145
3.3.4 Vegetation parameters 146
3.3.5 Boundary condition and FE Mesh geometry 147
3.3.6 Initial Conditions 150
3.4 Comparison and Validation with field measurements 152
3.4.1 North angle measurements 152
3.4.2 South angle measurements 159
3.5 Conclusion 162
Chapter 4. Further investigations on soil movements 163
4.1 Differential movements at Roaillan experimental site 163
4.1.1 Loading conditions at each angle 163
4.1.2 Soil movements at each angle 165
4.1.3 Differential soil movements 176
4.2 Climate change impact on soil movements 177
4.2.1 Short term soil movements 181
4.2.2 Long term soil movements 188
4.3 Applicable approach towards France 194
4.3.1 Introduction 194
4.3.2 Reference condition and soil parameters 195
4.3.3 Parametric analysis 197
4.4 Conclusion 201
General conclusion 203
References 206
Appendix 1: Resin injection for controlling expansive soils 221
A1.1 Introduction 221
A1.2 Site investigation 222

A1.3 Monitoring procedure 222
A1.4 Results and discussion 223
A1.5 Conclusions 225
Appendix 2: HYDRUS 2D/3D 226
A2.1 Introduction 226
A2.2 Simulation process 226
Appendix 3: Validation of the shrink-swell approach with a laboratory cyclic suction-controlled test 227
A3.1 Studied material 227
A3.2 Methodology 228
A3.3 Results 229
Appendix 4: Stress distribution in a soil mass 230
A4.1 Theory: 230
A4.2 Determination of the soil stress 231

List of Tables

Table 1.1 - The list of the preventive solutions classified by different themes (INERIS) 9

Table 1.2 - Existing evapotranspiration models 18

Table 1.3 - Formulation of the actual and the potential evapotranspiration..... 23

Table 1.4. Energy balance components in positive and negative state. 28

Table 1.5 - Different net radiation models..... 31

Table 1.6 - Albedo values for different surface types (Dobos, 2003)..... 32

Table 1.7 - Different air emissivity models 32

Table 1.8 - Soil emissivity values for different surface conditions..... 33

Table 1.9 - Different equations for calculating the sensible heat (H). 33

Table 1.10 - Different equations for calculating the latent heat of vaporization (Le)..... 34

Table 1.11 - Different equations used for the calculation of the soil heat flux..... 35

Table 1.12 - Different root water uptake models 37

Table 1.13 - Two ETc calculation methods. 40

Table 1.14 - Different models for partitioning ETc into soil evaporation and transpiration. 40

Table 2.1 - Studied soil samples parameters..... 87

Table 2.2 - Evaluation of the swelling potential using different methods. 90

Table 2.3 - Regression statistics for the two predicted variables (PI and W) 92

Table 2.4 - Predicted variables and coefficients for the calculation of SWRC. 93

Table 2.5 - Root water uptake distribution parameters 98

Table 2.6 - Soil data used for the correlation of the volumetric indices with basic geotechnical parameters.....109

Table 2.7 - Regression statistics of the volumetric indices.....112

Table 2.8 - Literature data of the volumetric indices at different loading condition under drying wetting cycles....118

Table 2.9 - Fitted A and B parameters for k_s and λ_s along with the plasticity index, the liquid limit and the volumetric indices at zero stress conditions. 121

Table 3.1 - Soil identification parameters of the Roaillan experimental site (Mathon and Godefroy, 2015) 129

Table 3.2 - Hydro thermal input soil parameters 143

Table 3.3 - Volume change parameters of the soil at 1, 2 and 3m depth (North angle).....144

Table 4.1 - Loading actions on each angle of the building 165

Table 4.2 - Shrink-Swell parameters at the north angle of the building. 165

Table 4.3 - Shrink-Swell parameters at the south angle of the building. 172

Table 4.4 - Reference condition parameters in the divided regions 195

Table A.1 - Geotechnical properties of the studied material in Le Deffend experimental site. 227

Table A.2 - Input and output parameters of the shrink-swell model for the Deffend clayey soil. 228

List of Figures

Figure 1.1 - shrinkage and swelling phenomenon (BRGM) 5

Figure 1.2 - Some examples of cracked residential buildings due to shrink-swell of clays. 6

Figure 1.3 - Typical behavior of a masonry structure exposed to a curvature of the foundation soil (Page, 2001): a) Typical reaction to a concave curvature (compression zone) and b) Typical reaction to a convex curvature (traction zone) 6

Figure 1.4 - Geotechnical drought hazard mapping (Source BRGM, MRN 2018) 7

Figure 1.5 - Ranking of the costliest climatic events in France since 1988 (Source FFA, MRN, 2018) 10

Figure 1.6 - Mapping the average costs of "drought" claims by municipality from 1995 to 2014 (CCR, MRN, 2018)11

Figure 1.7 - Representative Concentration Pathway scenarios (RCP) in: a) radiative forcing and b) global surface warming (IPCC, 2019) 12

Figure 1.8 - Definition of local characteristics of Geotechnical drought events. Example of the evolution of SSWI3 over the period of 1998 to 2008 on a site located close to Toulouse with a threshold of 5% (Soubeyroux et al., 2011) 14

Figure 1.9 - Hydrological cycle and water balance components (after Blight, 1977) 16

Figure 1.10 - Typical drying curves for sand and clay showing actual evaporation, AE, as a percentage of potential evaporation, PE, relative to water availability (Holmes, 1961). 17

Figure 1.11 - Schematic of the water flow during evaporation (Mahfouf and Noilhan 1991) 20

Figure 1.12 - Comparison of the aerodynamic methods for the calculation of the evapotranspiration rate using monthly climatic data. 23

Figure 1.13 - AE/PE ratio as a function of a) water content and b) soil surface suction (Wilson et al., 1997) cited by Ta (2009), Hemmati (2009) and Song (2014) 24

Figure 1.14 - Comparison of the results obtained on the evapotranspiration rate, a) for thick samples, and b) for thin samples. (Data used by Wilson et al., 1997, Wilson et al., 1994, Kondo et al., 1990, Ta, 2009) 25

Figure 1.15 - AE/PE variation based on the experimental results obtained by the existing data in the literature. (Data from Wilson et al., 1997, Kondo et al., 1990) 26

Figure 1.16 - The schematic representation of the relationship between AE/PE and the water potential of the soil at the surface (Aydin et al., 2005) 27

Figure 1.17 - Typical measurement of energy balance components during the day and night. (Blight, 1997) 28

Figure 1.18 - Schematic representation of the components of the energy balance. (Tanner, 1968 cited by Hillel, 2004) 28

Figure 1.19 - Principle of sun radiation and its associated components (after FAO 56) 29

Figure 1.20 - Schematic representation of the influence of trees on the differential soil movements of constructions. (Béchade, 2015) 36

Figure 1.21 - Different root distribution functions. 38

Figure 1.22 - Schematic representation of the reference evapotranspiration (ET0) and the crop evapotranspiration (ETc). 39

Figure 1.23 - Void ratio changes versus suction for Boom clay sample under a constant vertical stress of 5.5 MPa (Robinet et al., 1997) 42

Figure 1.24 - Variation of the volumetric strain during drying-wetting cycles under different vertical stresses. (Alonso et al., 2005) 42

Figure 1.25 - Shrink-swell patterns involving full shrinkage and partial shrinkage cycles (s = suction; w = water content) (Tripathy and Subba Rao, 2009). 43

Figure 1.26 - Drying-wetting tests on natural clayey soils: a) Champenoux Clay b) Deffend Clay (Nowamooz, 2007). 44

Figure 1.27 - Variation of the void ratio in cyclic controlled-suction paths and versus the number of records at different vertical stresses for both loose and dense clayey soils of the Deffend experimental site (Nowamooz and Masrouri, 2009) 45

Figure 1.28 - Variation of the cumulated strain with cyclic variations of suction under a vertical stress of 100 kPa for three initial dry densities of the GMZ bentonite. (Zhao et al., 2019) 46

Figure 1.29 - Soil movements measured at 1, 3 and 10 m depth using a TELEMAC extensometer (Fernandes et al., 2015) 47

Figure 1.30 - Measured soil movements between 1 and 3m depth and along with the daily hydric condition over the period of September 2008 to February 2014 (Fernandes et al., 2015). 48

Figure 1.31 - ERT profile between May and June 2009 in the Pessac site in Bordeaux, France (Chrétien et al., 2014) 49

Figure 1.32 - Typical soil-water characteristic curve illustrating different desaturation zones (after Vanapalli and Fredlund, 2000) 50

Figure 1.33 - Constitutive surfaces for an unsaturated soil (a) the solid skeleton phase, (b) the water phase (Fredlund and Rahardjo, 1993) 53

Figure 1.34 - a) State surfaces proposed by Vu and Fredlund, (2004) and fitted for Regina clay, and b) the concept of the hydro-mechanical coupling (Jahangir et al., 2013). 55

Figure 1.35 - The 3D geometry of the Arlington site modelled in ABAQUS (Zhang & Briaud, 2015) 56

Figure 1.36 - Comparisons between the observation and simulation results of the Arlington site (Zhang & Briaud, 2015; Zhang, 2004) 56

Figure 1.37 - Yield surface of the Barcelona basic model (BBM) (Alonso et al., 1990) 58

Figure 1.38 - State surface of the BExM model (Alonso et al., 1999). 59

Figure 1.39 - Vertical displacement versus time in different points of the studied swelling soil (Nowamooz et al., 2009). 60

Figure 1.40 - Schematic view of soil-vegetation-atmosphere interaction modelling using the ϴ-STOCK model (Hemmati, 2009; Hemmati et al., 2012) 61

Figure 1.41 - Comparison of the modelled and measurement soil movements in the Mormoiron site from January 2007 to May 2008. (Hemmati, 2009; Hemmati et al., 2012) 62

Figure 1.42 - Soil water content versus volumetric strain obtained from the shrink test (Briaud et al., 2003). 63

Figure 1.43 - Determination of heave index (Nelson et al., 2007) cited by Adem and Vanapalli, (2015). 64

Figure 1.44 - Finite element mesh and area of the time variable atmospheric boundary condition, for a) case study 1, Maryland, Near Newcastle, Australia and for b) case study 2, Amarillo site, in Texas (Shams et al., 2018). 65

Figure 1.45 - Comparison of the simulated soil movements with in-situ observations for a) the first case study and b) for the second case study (modified after Shams et al., 2018). 66

Figure 1.46 - 1D model of the Braybrook site in Vadose/w (Rajeev et al., 2012). 67

Figure 1.47 - Comparison of the simulated soil surface movements with the measured data at the Braybrook site (modified after Karunarathne et al., 2018). 67

Figure 1.48 - Predicted and measured monthly surface movements at 1.8 m outside slab edge along longitudinal axis at Amarillo site (modified after Wray et al., 2005). 69

Figure 1.49 - Flowchart for the step-by-step procedure of the MEBM (Adem and Vanapalli, 2013) 70

Figure 1.50 - Predicted cumulated vertical soil movements under the center point a vegetation cover close to a pavement using the MEBM (Adem and Vanapalli, 2013). 71

Figure 2.1 - The variation of G/Rn ratio for different types of soils with: a) 40% water content; b) 25% water content; c) 5% water content. (Santanello and Friedl 2003) 75

Figure 2.2 - Climatic parameters of the Toulouse site. 78

Figure 2.3 - Calculated a) air emissivity coefficient and b) vapor pressures using climatic parameters of the Toulouse site. 79

Figure 2.4 - Calculated soil surface temperature along with the air temperature of the Toulouse site. 80

Figure 2.5 - Half hourly recorded meteorological data along with a) the soil surface temperature for July 2011 at the Héricourt region in Franche Compté 81

Figure 2.6 - Comparison of the measured data (An et al. 2017b) and the simulated soil surface temperature using the energy balance approach. 82

Figure 2.7 - Comparison of the derived net solar radiation from the soil surface temperature to seven net radiation models (Héricourt site) 83

Figure 2.8 - Damaged residential buildings due to the shrink-swell phenomenon in France (Assadollahi & Nowamooz, 2018a) 85

Figure 2.9 - Plasticity range of 78 soil samples collected from the supporting soil of damaged buildings. 86

Figure 2.10 - Swelling potential of 78 soil samples 86

Figure 2.11 - Soil water retention curves for a) very high swelling potential soils (20.11<W.PI<63.66), b) high swelling potential soils (16.38<W.PI<30.1), c) medium swelling potential soils (4.68<W.PI<22.94), d) Low swelling potential soils (2.78<W.PI<8.7). 89

Figure 2.12 - Regression analysis on the predicted and measured a) PI and b) W 92

Figure 2.13 - Comparison of the predicted and the measured PI and W% relationship with the natural water content, the Liquid limit and the percent passing from 2mm. 93

Figure 2.14 - Comparison between the calculated SWRC with measured W.PI and predicted W.PI 94

Figure 2.15 - Generated TCF function for different soils using HYDRUS 2D 95

Figure 2.16 - The water stress reduction function versus the soil water pressure head (Feddes et al. 1976). 96

Figure 2.17 - Schematic representation of the potential water uptake distribution function based on Vrught et al. (2002) model. 97

Figure 2.18 - Different configuration of root density distribution into the soil 98

Figure 2.19 - Leaf Area Index plots a) for validation in a grass cover field b) for typical vegetation types. 100

Figure 2.20 - Typical Kc curve along with different crop development stages (Allen et al. 1998) 101

Figure 2.21 - Physical modelling approach of the volume change behavior of an unsaturated soil subjected to wetting drying cycles at a) loose state and b) dense state 102

Figure 2.22 - Possible drying paths for a loose soil 104

Figure 2.23 - Possible wetting paths for a dense soil 105

Figure 2.24 - Possible drying paths for a dense soil and possible wetting paths for a loose soil. 106

Figure 2.25 - Correlation of k_s with basic geotechnical parameters: a) Plasticity index; b) void ratio; c) Saturation water content; d) dry density. 108

Figure 2.26 - Correlation of λ_s with basic geotechnical parameters: a) Plasticity index; b) void ratio; c) Saturation water content; d) dry density. 111

Figure 2.27 - Linear regression of the predicted and the observed a) k_s and b) λ_s. 112

Figure 2.28 - Comparison of the proposed equation for k_s with each geotechnical parameter; a) for PI by maintaining e, w and γ_d constant; b) for e by maintaining PI, w and γ_d constant; c) for w% by maintaining PI, e and γ_d constant; d) for γ_d by maintaining PI, e and w% constant 114

Figure 2.29 - Comparison of the proposed equation for λ_s with each geotechnical parameter; a) for PI by maintaining e, w and γ_d constant; b) for e by maintaining PI, w and γ_d constant; c) for w% by maintaining PI, e and γ_d constant; d) for γ_d by maintaining PI, e and w% constant 115

Figure 2.30 - a) the variation of the transition suction with the dry density b) the variation of the shrinkage limit suction with the shrinkage limit. 116

Figure 2.31 - Relationship between measured shrinkage index SI and plasticity index PI based on the presented data. 117

Figure 2.32 - Variation of the volumetric indices; a) k_s and b) λ_s with the applied stress for the Al Qatif clay. 118

Figure 2.33 - Variation of the volumetric indices; a) k_s and b) λ_s with the applied stress for the Macau silty sand. 119

Figure 2.34 - Variation of the volumetric indices; a) k_s and b) λ_s with the applied stress for the low plasticity clay. 119

Figure 2.36 - Variation of the volumetric indices; a) k_s and b) λ_s with the applied stress for the London clay. 120

Figure 2.37 - Variation of the volumetric indices; a) k_s and b) λ_s with the applied stress for the clayey soil. 120

Figure 2.38 - Variation of the volumetric indices; a) k_s and b) λ_s with the applied stress for the Deffend clay. 120

Figure 2.35 - Variation of the volumetric indices; a) k_s and b) λ_s with the applied stress for the Madrid clay. 121

Figure 2.39 - Variation of fitting parameter A a) for k_s with the plasticity index; b) for k_s with the Liquid limit; c) for λ_s with the plasticity index and d) for λ_s with the liquid limit. 122

Figure 2.40 - Variation of fitting parameter B a) with k_s under zero stress condition; b) with λ_s under zero stress condition. 123

Figure 2.41. Flowchart of the adapted modelling approach 124

Figure 3.1 - Studied site location with the associated shrink-swell hazard map. 125

Figure 3.2 - The schematic representation of the monitored building with probes and the cracked monitored walls. 127

Figure 3.3 - Core samples at different locations surrounding the building (CEREMA). 128

Figure 3.4 - Plasticity range of studied samples by the Casagrande plasticity chart 130

Figure 3.5 - Calibration of the soil matrix suction sensors with the water content for three collected samples (CEREMA, 2015) 131

Figure 3.6 - Some instruments used in for monitoring: a) displacement sensor, measuring crack closing/openings (F10TN); b) Soil matrix suction sensor (Watermark); c) Soil volumetric water content/moisture sensor (Theta Probe) 132

Figure 3.7 - Different data loggers used in the monitoring operations 133

Figure 3.8 - 2D profile of the geological formation at the north angle (A-A' cross section). 134

Figure 3.9 - 2D profile of the geological formation at the south angle (B-B' cross section) 135

Figure 3.10 - Results of the monitoring at the north angle of the building: a) water content variations near the building vs variations near the tree; b) soil suction variation at different depth near the tree – sensors installed in the same depth have a 0.25 to 0.5 137

Figure 3.11 - Results of the monitoring at the south angle of the building: a) water content variations near the building; b) water content variations near the tree at three different depths; c) crack closing/openings on the south side of the building; d) crack clos 139

Figure 3.12 - SWRC of the soil layers in a) the north angle and b) the south angle of the building. 140

Figure 3.13 - Unsaturated Hydraulic Conductivity functions of the soils in a) the north angle and b) the south angle of the building. 141

Figure 3.14 - Thermal conductivity functions fitted to typical soils data. 142

Figure 3.15 - Shrink-Swell curve [w,e] of three soil samples collected from the Roaillan experimental site. 145

Figure 3.16 - Climatic parameters of the Roaillan experimental site: a) Rainfall (mm/day) b) Air temperature (°C) c) Relative humidity (-) d) Wind speed at 10 m height (m/s) e) Global solar radiation (W/m2) 146

Figure 3.17 - Vegetation parameters of the experimental site. 147

Figure 3.18 - Calculated evapotranspiration of the experimental site: a) Reference evapotranspiration (ET0) b) Crop evapotranspiration (ETc) 148

Figure 3.19 - Partitioning of the evapotranspiration rate into potential transpiration (Tpot) and potential evaporation (Epot): a) For the north angle b) For the south angle 148

Figure 3.20 - Calculated time variable boundary condition of the experimental site for the hydro-thermal simulation: a) Infiltration rate (P-ET0) b) Soil surface temperature 149

Figure 3.21 - The adapted geometry and triangular meshing of the north angle geological formation of the site along with the applied boundary conditions 149

Figure 3.22 - The adapted geometry and triangular meshing of the south angle geological formation of the site along with the boundary conditions. 150

Figure 3.23 - Initial condition plots of water content and temperature: a) and b) at the north angle respectively c) and d) at the south angle respectively. 151

Figure 3.24 - Initial root distribution pattern at: a) the north angle and b) the south angle 152

Figure 3.25 - Comparison of the measured and the simulated soil suction in the north angle of the building - close to the tree (TR1 to TR7) 153

Figure 3.26 - Comparison of the measured and the simulated soil suction in the north angle of the building - close to the building (BU1 to BUS7) 154

Figure 3.27 - Comparison of the simulated volumetric water content with field measurements at the north angle 155

Figure 3.28 - Comparison of the simulated soil temperature with field measurements. 156

Figure 3.29 - Comparison of the simulated water content and temperature profiles with field measurements by H5 and H6 probe. 157

Figure 3.30 - Comparison of the simulated soil movements with field measurements, a) 1m; b) at 2m; c) at 3m depth. 158

Figure 3.31 - Comparison of the measured and the simulated water content at 1, 2 and 3m depth in the south angle. 159

Figure 3.32 - Comparison of the simulated water content profiles with field measurements by H1 probe close to the tree. 161

Figure 4.1 - Detailed floor plan of the building 163

Figure 4.2 - Cross section at the right side of the plan 164

Figure 4.3 - North side elevation of the building 164

Figure 4.4 - South side elevation of the building 164

Figure 4.5 - Comparison of the soil physical variables close to the tree and the building at 1m depth (point 1 and 1b). 166

Figure 4.6 - Comparison of the soil physical variables close to the tree and the building at 1.7m depth (point 2 and 2b). 167

Figure 4.7 - Comparison of the soil physical variables close to the tree and the building at 2.3m depth (point 3 and 3b). 168

Figure 4.8 - Comparison of the soil physical variables close to the tree and the building at 3.75m depth (point 4 and 4b). 169

Figure 4.9 - Comparison of the soil physical variables close to the tree and the building at 5m depth (point 5 and 5b). 170

Figure 4.10 - Water content plots at four different times illustrating the influence of root water uptake at the north angle of the building. 171

Figure 4.11 - Comparison of the soil physical variables close to the tree and the building at 1m depth (point 1 and 1b). 172

Figure 4.12 - Comparison of the soil physical variables close to the tree and the building at 2m depth (point 2 and 2b). 173

Figure 4.13 - Comparison of the soil physical variables close to the tree and the building at 3m depth (point 3 and 3b). 174

Figure 4.14 - Water content plots at four different times illustrating the influence of root water uptake at the south angle of the building. 175

Figure 4.15 - Differential soil surface movements at the north and the south angle. 176

Figure 4.16 - Differential soil movements under the foundation in the north and south angle a) of the building b) close to the trees 177

Figure 4.17 - Calculated evapotranspiration of the experimental site with the projected climatic parameters: a) Reference evapotranspiration (ET0) b) Crop evapotranspiration (ETc) 178

Figure 4.18 - Partitioning of the evapotranspiration rate into potential transpiration (Tpot) and potential evaporation (Epot) in the north side of the building: a) with RCP 2.6 model b) with RCP 4.5 model and c) with RCP 8.5 model. 179

Figure 4.19 - Partitioning of the evapotranspiration rate into potential transpiration (Tpot) and potential evaporation (Epot) in the south side of the building: a) with RCP 2.6 model b) with RCP 4.5 model and c) with RCP 8.5 model. 180

Figure 4.20 - Calculated time variable boundary condition of the experimental site for the hydro-thermal simulation with the RCP models: a) Infiltration rate (P-ET0) b) Soil surface temperature 181

Figure 4.21 - Cumulative soil surface movements using the RCP models (short term) at a) the north side and b) at the south side of the building. 182

Figure 4.22 - Calculated variables using RCP models (short term) at 1m depth, under the foundation (1m depth) at the north angle of the building, a) soil suction; b) soil temperature; c) soil water content; d) void ratio; e) daily soil movements; f) cumulative soil 183

Figure 4.23 - Calculated variables using RCP models (short term) at 2.3m depth, close to the tree at the north angle, a) soil suction; b) soil temperature; c) soil water content; d) void ratio; e) daily soil movements; f) cumulative soil movement 184

Figure 4.24 - Calculated variables using RCP models (short term) at 1m depth, under the foundation at the south angle of the building, a) soil suction; b) soil temperature; c) soil water content; d) void ratio; e) daily soil movements; f) cumulative soil movements 185

Figure 4.25 - Calculated variables using RCP models (short term) at 2m depth, close to the tree at the south angle of the building, a) soil suction; b) soil temperature; c) soil water content; d) void ratio; e) daily soil movements; f) cumulative soil movements 186

Figure 4.26 - Short term differential soil movements under the foundation (1m depth) and close to the tree (2 and 2.3m depth) using the a) RCP 2.6 scenario; b) RCP 4.5 scenario; and c) RCP 8.5 scenario 187

Figure 4.27 - Cumulative soil surface movements using the RCP models (long term) at a) the north side and b) at the south side of the building. 188

Figure 4.28 - Calculated variables using RCP models (long term) at 1m depth, under the foundation at the north angle of the building, a) soil suction; b) soil temperature; c) soil water content; d) void ratio; e) daily soil movements; f) cumulative soil movements 189

Figure 4.29 - Calculated variables using RCP models (long term) at 2.3m depth, close to the tree at the north angle of the building, a) soil suction; b) soil temperature; c) soil water content; d) void ratio; e) daily soil movements; f) cumulative soil movements 190

Figure 4.30 - Calculated variables using RCP models (long term) at 1m depth, under the foundation at the south angle of the building, a) soil suction; b) soil temperature; c) soil water content; d) void ratio; e) daily soil movements; f) cumulative soil movements 191

Figure 4.31 - Calculated variables using RCP models (long term) at 2m depth, close to the tree at the south angle of the building, a) soil suction; b) soil temperature; c) soil water content; d) void ratio; e) daily soil movements; f) cumulative soil movements 192

Figure 4.32 - Long term differential soil movements under the foundation (1m depth) and close to the tree (2m and 2.3m depth) using the a) RCP 2.6 scenario; b) RCP 4.5 scenario; and c) RCP 8.5 scenario 193

Figure 4.33 - Six climate regions in France 194

Figure 4.34 - Reference soil movements in six different regions in France 196

Figure 4.35 - Influencing parameters along with the reference condition calculated for six regions. 196

Figure 4.36 - Calculated soil movements at different vegetation (tree) distances from the foundation in six different regions in France. 198

Figure 4.37 - Calculated soil movements at different foundation depth in six regions of France. 199

Figure 4.38 - Calculated soil movements for different foundation width in six regions of France. 200

Figure 4.39 - Calculated soil movements at different applied stresses, in six regions of France. 201

Figure A.1 - The general monitoring process and foundation soil treatment of damaged buildings by polyurethane injection repair technique (Assadollahi et al. 2018a). 221

Figure A.2 - Results obtained from the optical fiber sensors at 4 different position of the building along with the results of in-situ PANDA tests before and after the injection process (Assadollahi et al., 2018a). 223

Figure A.3 - Schematic of the suction-controlled odometer device using osmotic solutions reported in Nowamooz et al. (2009). 227

Figure A.4 - Shrinkage curve of the studied material in the Deffend site (6.44 - 6.48m) determined by Nowamooz (2007) 228

Figure A.5 - Comparison between the simulated and the measured volumetric deformations under 20 kPa vertical stress in a cyclic suction control test: a) applied suction b) volumetric deformations 229

Figure A.6 - Vertical stress caused by a flexible strip load (M. Das and Sobhan, 2012) 230

Figure A.7 - Contours of $\Delta\sigma z/$q below a strip load (M. Das and Sobhan, 2012) 231

General Introduction

Concerns continue to grow around the world on the impact of climatic events that cause huge economic and human losses to the society. Current available projections show that France will experience wetter winters with more intense rainfalls, especially in the north and drier summers associated with higher temperatures at the end of the 21st century. In France, global warming and environmental factors have caused a great deal of structural damage, particularly on light-weight constructions (residential building, industrial building, pavement structures, pipelines, etc.) built on swelling soils, because of the significant changes in the physical and mechanical properties of the ground which is associated with differential movements due to the shrinkage and swelling phenomenon. This phenomenon also called the "geotechnical drought" is at the origin of numerous damages on these types of constructions. Damage to lightly loaded structures founded on expansive soils has been widely reported in many countries such as Australia, China, India, Israel, South Africa, the United Kingdom and the United States of America. In the United States alone, total damage due to expansive soil is estimated to cost $US15 billion per year, more than twice the damage from floods, hurricanes, tornadoes, and earthquakes combined. The American Society of Civil Engineers (ASCE) estimates that one in four homes have some damage caused by expansive soils. The annual cost of expansive soil damage in China is estimated to be approximately $US15 billion. The Association of British Insurers has estimated that the average cost associated with damage due to expansive soil is over £400 million a year, making it the most damaging geo-hazard in the UK today.

In France, this kind of natural disaster is known as the second costliest natural hazard after the floods (5 billion euros between 1988 and 2007) and must be taken into account in the climate change adaptation plans (ARGIC ANR Projects). To date, there is no reliable database associated with a predictive method capable of informing the concerned stakeholders: insurance companies, public authorities and private sectors. In this context, there is the necessity to set up a methodology taking into account all the factors that play a role in triggering and aggravating this phenomenon.

The occurrence of this phenomenon requires two types of factors, the predisposition factors (nature of the soil, hydrogeological context, surrounding vegetation) and the triggering factors (evaporation, precipitation). Wetting and drying cycles cause significant variations in the soil suction both at the surface and the depth and consequently, a considerable variation in the volume of the voids, which results in differential movements in the soil. Therefore, it is of paramount importance to study the impact of these factors on the coupled behavior of soils through numerical tools to predict the intensity of shrinkage-swelling over time. Several models exist in the literature for describing the hydro-mechanical behavior of unsaturated swelling clay materials. The combination of these models with the actual in situ behavior while considering the Soil-Vegetation-Atmosphere (SVA) interaction is a complex task. In the **first chapter** of this thesis a state of the art of different methods for the determination of the soil movements over time in SVA context, was given.

In the **second chapter** of this thesis, a numerical method for the Soil-Vegetation-Atmosphere (SVA) continuum was primarily set up in order to determine the natural time variable boundary conditions based on meteorological data. A coupled hydro-thermal soil model is used with the

help of the HYDRUS software to determine the spatial-temporal variations in the soil suction, the moisture content and the temperature. The influence of environmental stresses such as the presence of vegetation is also taken into account through root water uptake models. The SVA interaction analysis is based on the water flow and heat transfer theory in unsaturated soils. In the second part, in order to determine the soil volume change behavior or more precisely the shrinkage-swelling over time, the temporal variations of the soil suction are related to the soil void ratio by proposing a linear model based on the results of the experimental tests carried out in the literature. A simple approach has been proposed to determine the volumetric indices of the soils subjected to drying wetting cycles. These indices correspond to the slopes of the linear model in the void ratio-suction plane and are correlated with the basic geotechnical parameters such as the plasticity index, the dry density, the liquid limit, the saturation water content and the void ratio at saturation.

In the **third chapter** of this thesis, the validation of the proposed approach was performed by comparing the results of the numerical modeling with the measurements collected on an instrumented site in southwestern France. The site concerns a damaged building affected by environmental factors including climatic conditions and the presence of trees in its proximity. The observed damages are composed of structural cracks on the walls due to the differential settlement of the foundations (strip footing). The geotechnical investigation confirmed the presence of sensitive clay layers, up to 5m depth below the structure. An instrumentation campaign was launched to monitor the variations in the physical properties of these clayey soils at different depths. Soil water content, temperature and suction sensors were installed in the two most damaged angles of the building. Crack meter probes were installed on almost all cracks to monitor their openings/closing during the instrumentation period. A multipoint borehole extensometer was installed on one angle of the building (north) to monitor the shrinkage-swelling of clays at different depths. The comparison between the numerical simulations and experimental measurements showed an acceptable coherence which allowed to study the influence of the trees on the shrinkage-swelling of the soil, in their influence zone. This analysis revealed the influence of the water uptake by tree roots on the volume change behavior of the soil and consequently its differential movements in the two angles of the building.

In the **fourth chapter** of this thesis, the method was then extended to study the impact of different climate change scenarios on the clay shrinkage and swelling in the short term and long term. Three RCP (Representative Concentration Pathway) scenarios were considered in this analysis: a mitigation scenario (RCP 2.6), a second stabilization scenario (RCP 4.5) and a last severe scenario (RCP 8.5). Meteorological data were projected up to 2050 for each of these scenarios, considering the influence of vegetation in the calculation of the evapotranspiration. The simulation results showed an increase in differential movements in the soil, particularly close to the trees. RCP 4.5 and 8.5 scenarios have been identified as cyclic scenarios in which the hydro-thermal variables and consequently the soil shrinkage-swelling, vary in a regularly cyclic manner over time and give rise to larger differential movements.

In the last part of this thesis, the developed approach has been applied on a national scale. To do so, France is divided into six climatic regions. One specific soil type is attributed to each of these climatic regions based on the available maps for the soil distribution in France. These soils (reference soils) are defined using the input parameters of the method (PI, w%, e_0 and γ_d). The reference condition also includes the vegetation and building (foundation) parameters. This

reference condition in each region is used to provide the temporal variations of soil suction under the building foundation, obtained using the SVA interaction analysis. These temporal variations are then used in the calculations of the soil movements over the 2016 – 2018 period. A parametric study is also conducted to study the influence of these factors on the soil movements. The results are potentially useful for relevant stakeholders of the domain, including insurers and reinsurers in terms of severity and amplitude of the shrinkage-swelling phenomenon throughout the French territory. Finally, the concluding remarks of this work were presented.

Chapter 1. Literature review

1.1 Clays shrinkage and swelling

The concept of shrinkage-swelling of clays (or RGA in French) refers to the repeated movements of shrinkage and swelling of the soil respectively associated with the drought and rehydration phases of so-called "swelling" or "expansive" soils. The differential ground movements induced by this shrinkage-swelling can influence and damage Civil Engineering structures or infrastructures that are vulnerable to this solicitation in the soil. In this section, the triggering factors of the shrinkage and swelling phenomenon are primarily presented and different issues associated with the phenomenon are explained.

1.1.1 The phenomenon and influencing factors

This phenomenon affects lightweight constructions and their foundations in a cyclic way due to the physical and mechanical changes of the supporting soil's (clay, in most cases) characteristics by being exposed to different environmental factors. It can also cause damages on other types of structures (bridges, roads, tunnels, etc.) and all underground networks (including drainage or water distribution networks).

Unlike other types of soils, clays are more likely to be affected by hydraulic variations due to atmospheric conditions or climatic changes. Its nature and microstructure are such that it is more vulnerable than other types of soils. A variation in water content affects the initial volume and conditions of clays. Capillary phenomena, and especially suction generation, are at the origin of the volume change behavior of clays and in consequence the shrink-swell phenomenon. The occurrence of shrinkage-swelling in nature requires two types of factors:

- Predisposing factors (nature of the soil, hydrogeological context, vegetation);
- Triggering factors (evapotranspiration, precipitation and climate change).

The predisposing factors are known as the factors that induce the shrinkage-swelling phenomenon, but are not enough to trigger it. There are some internal factors that are related to the nature of the soil, and environmental factors that characterize the site (E. Jahangir, 2011). The most important predisposing factors are:

- The nature of the soil: The nature of soil, its microstructure, its water content, and all its mechanical properties play a very important role in triggering the shrink-swell phenomenon. Even though, clayey soils are the most common predisposing factor in generating the shrink-swell phenomenon, but the existence of external environmental factors makes the soil more vulnerable to it.

- **The hydrogeology of the site:** The presence of a water table at a shallow depth may eventually affect the physical and mechanical properties of the superficial soils. This highlights the importance of geological formations and their influences on the soil surface.

- **Vegetation:** Vegetation plays a fairly important role in the volume change behavior of clayey soils. The tree roots and vegetation covers can apply a strong suction during drought

periods, however lower suction values are generated during humid periods. Vegetation is a common cause of second-generation claims. When a damaged construction has been properly repaired and new damages reappear after a while, a second-generation claim is declared. The new damages of the construction are often explained by incident factors that have not been identified and treated. The influence of vegetation and suction generated by roots is one of the costliest incident factors for second-generation claims.

On the other hand, triggering factors are characterized as the factors that cause a shrinkage-swelling phenomenon which have a significant effect only if there are predisposing factors (Vincent et al., 2009). These factors can be classified into two general categories:

- **Climatic phenomena:** Clayey soils do not behave in the same way in an arid climate, as in a semi-arid and temperate climate. Thus, they are likely to experience large volume changes in rainy seasons after a long drought period. It is during the drought period that the soil can show a significant decrease in volume (shrinkage). The meteorological phenomena are the main cause of the clay's shrinkage-swelling by directly influencing the soil moisture content (climate change, evaporation, precipitation, etc.). When the evaporation rate is higher than the precipitation, the soil can be in water deficit state which is followed by soil shrinkage.

- **Anthropogenic factors:** On the other hand, anthropogenic factors affect the natural hydrological evolution of the soil, by modifying the distribution of superficial and underground flows. In general, they result from engineering works such as drainage in the immediate vicinity of the considered structure or the failure of a buried pipe.

To summarize, the shrinkage swelling phenomenon takes place in the presence of a swelling soil as a predisposition factor and a soil water content variation as a triggering factor.

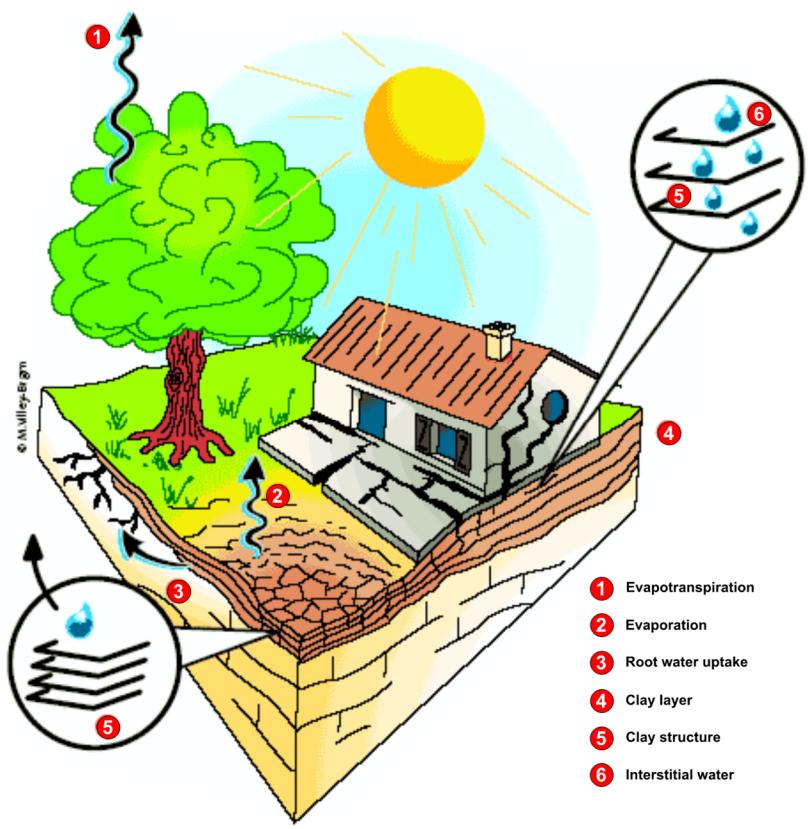

Figure 1.1 - shrinkage and swelling phenomenon (BRGM)

As shown in Figure 1.1, during drought-humidification cycles, the supporting soil of light-weight constructions (in this case, buildings), is subjected to shrinkage and swelling phases respectively. The repeated differential soil movements can result in structural damages which are usually characterized as visible cracks in both sides of the structural elements. These cracks are mainly classified as stair-like cracks, horizontal cracks and vertical cracks in some cases. Figure 1.2 shows some common examples of cracks on residential buildings due to the shrink-swell phenomenon.

Figure 1.2 - Some examples of cracked residential buildings due to shrink-swell of clays.

Considering the curvature of the ground, which can typically take a concave or a convex form depending on the climatic conditions of the site, it potentially leads to compression or traction forces in the structure. This depends on the position of the structures in the affected area and the interaction between the soil and the exposed structure. Figure 1.3 shows schematically the different types of cracks and damages that can be expected on a masonry structure located in a concave curvature zone (compression zone) or in a convex curvature zone (traction zone) due to the shrinkage and swelling of its supporting soil, respectively. It should be mentioned that each case can have different failure modes (flexure, shear, etc.).

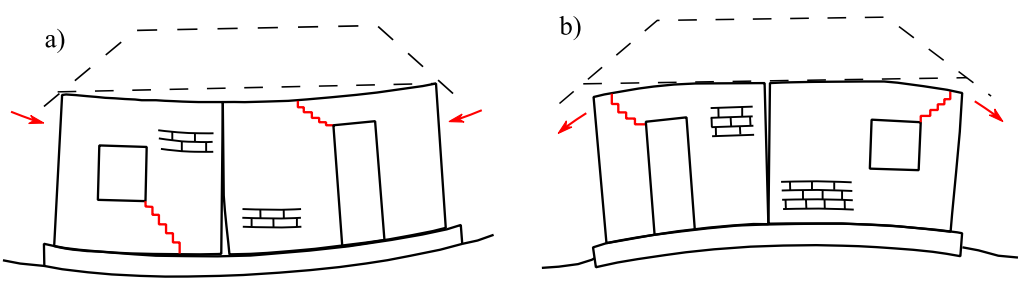

Figure 1.3 - Typical behavior of a masonry structure exposed to a curvature of the foundation soil (Page, 2001): a) Typical reaction to a concave curvature (compression zone) and b) Typical reaction to a convex curvature (traction zone)

In France, the occurrence of this phenomenon were observed especially during the drought of 1976 which was at the origin of numerous damages concerning particularly individual buildings located in the Parisian region. Between 1989 and 1992, many French municipalities were affected by this loss, which led the government to integrate it into the natural disaster system introduced by the law of 13 July 1982. During the summer of 2003, several thousands of individual houses built on clayey soils were cracked and damaged as a result of differential settlements due to this phenomenon. This issue obligated more than one French town out of five to apply for the recognition of the natural disaster state in this period.

1.1.2 Clays shrinkage swelling hazard in France

This section focuses on the clay shrinkage-swelling (Retrait Gonflement des Argiles in French) hazard or the geotechnical drought (drought). It is not therefore the damage caused to agricultural crops, nor the consequences of the deficit in water resources, but of those resulting from the predisposing and triggering factors. According to the General Directorate for Risk Prevention (DGPR), while a dynamic knowledge production and deployment of Risk Prevention Plans (PPR) is now well established concerning the risk of flood, but the balance sheet is much more mitigated for the Geotechnical drought so that more than the half of the regions of metropolitan France are concerned by this risk. Up to this date, nearly 10,500 municipalities have already applied for recognition of the natural disaster state (CatNat) for Geotechnical drought.

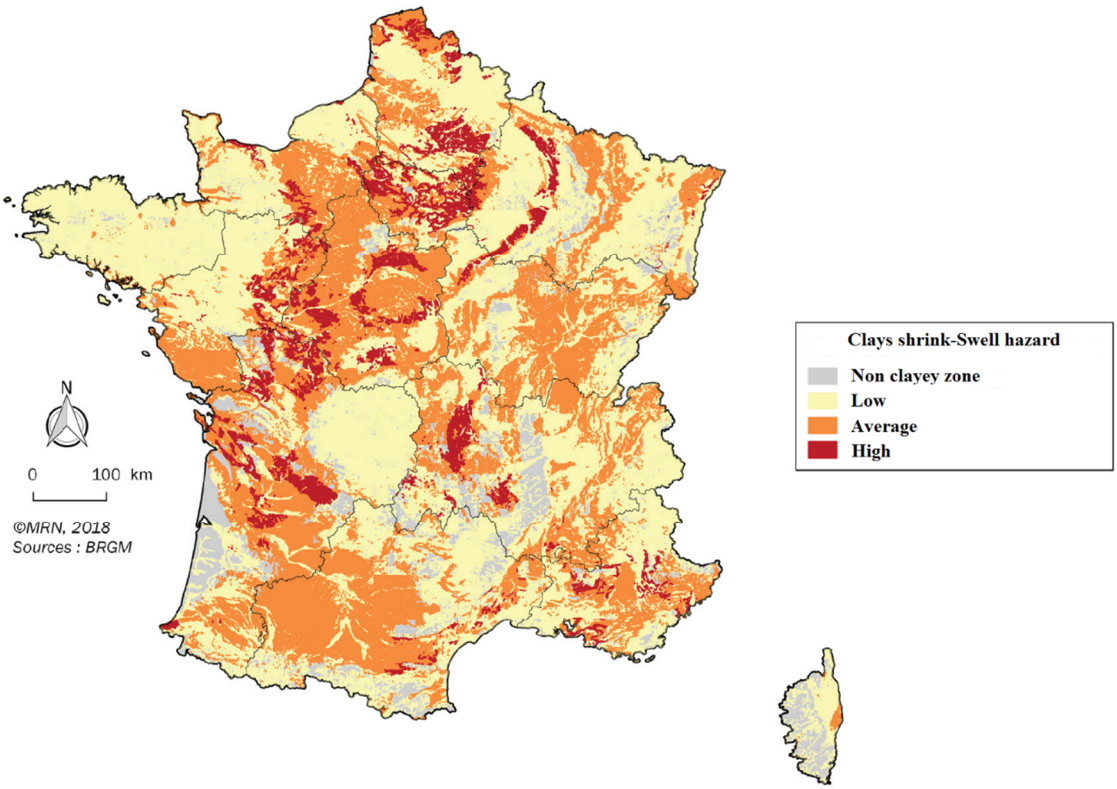

Figure 1.4 - Geotechnical drought hazard mapping (Source BRGM, MRN 2018)

According to the General Commissariat for Sustainable Development of France (CGDD), one-fifth of the surface of the metropolitan area is affected by a risk of shrinkage and swelling of "strong or medium", i.e. about 114,500 km². Figure 1.4 shows the hazard mapping of the shrink-

swell phenomenon or the Geotechnical drought in France which was updated by the Natural Risk Mission association (MRN) based on the French Geological Survey's (BRGM) data.

Since most of the associated damages with this phenomenon could probably be avoided by respecting some preventive rules of construction, the Ministry of Ecology, Energy, Sustainable Development and Regional Planning of France (MEEDDAT) entrusted the French Geological Survey (BRGM) with a program for mapping the risk of this phenomenon in order to locate areas in which the probability of occurrence of the phenomenon is high and to develop, in the most affected municipalities, Natural Risk Prevention Plans (PPRn) to impose preventive constructive rules.

After a quick review of the main factors conditioning the phenomenon, the current state of progress of the national hazard mapping program is presented here and the hazard was, extrapolated to the entire metropolitan France. Based on the French Geological Survey's (BRGM) hazard mapping for metropolitan France, the statistical studies department of the CGDD has recently conducted a study on the exposure to shrinkage and swelling phenomenon. The study indicates that one town out of ten has more than 75% of its territory in high or medium hazard and 400 towns have all their territory in high or medium hazard. In terms of building exposure, a study carried out by MRN identifies around 4.3 million single-detached houses built in high or medium hazard risk areas (i.e. 23% of individual housing). Approximately a third of these houses are located in Nouvelle Aquitaine and Île-de-France region within departments such as Essonne (91) where urbanization is concentrated in exposed areas with nearly 60% of individual houses located in the 40% of the department in high or medium hazard risk. Thanks to the combined progress of the geoscientists and the climatologists, this risk is theoretically more and more predictable and thus, mappable in general or specialized risk prevention plans (PPR). Preventive ways can therefore be prescribed theoretically to avoid construction in the most at-risk areas, or to adapt planning and construction techniques particularly for the foundations of individual buildings. Except in areas of steep slope or in special cases that are exposed to a high risk of shrinkage-swelling can remain constructible, if regulatory measures are respected.

In order to bring efficient solutions to the management of this phenomenon, the ARGIC project (Analysis of the shrinkage and swelling of clays and its Impact on Constructions) was elaborated following a call for projects launched in 2005 by the French National Agency of Research (ANR) as part of the RGCU (Civil and Urban Engineering Network) program. It took place over three years from February 2006, under the coordination of the BRGM and in collaboration with twelve other organizations. Following the ARGIC project, the ARGIC 2 project, managed by the French Institute of Science and Technology for Transport, Development and Networks (IFFSTTAR), was launched at the end of 2010. Its overall objective was to finalize the work of the original ARGIC project, to improve the construction practice, and to complete scientific knowledge on clays and their interactions with climate, vegetation and buildings.

Based on these national projects, it is thus possible to structure the preventive solutions of the phenomenon according to four themes, each having a particular objective:

- Theme 1: Investigate and characterize the foundation soil;
- Theme 2: to limit/reduce the amplitude of the shrinkage/swelling in the soil;
- Theme 3: to limit/reduce the transmission of shrinkage/swelling towards the structure, in the context of soil/structure interaction;
- Theme 4: increase/improve the resistance of the structures to oppose the different mechanisms of collapse influencing the structure.

Table 1.1 summarizes the main prevention methods according to the ARGIC project report, which can be associated with each other to maximize efficiency. As mentioned previously, the type of structural damages of the constructions on clayey soils during drought period are most often cracks on different structural and non-structural elements of the construction. These damages are the response of the construction to settlement or heave of its foundations. Their location and opening correspond to the localized movements of shrinkage or swelling of the soil beneath these foundations. Repair or reinforcement techniques are adapted in response to these deformations, whether they have been observed or predicted to occur. The repair techniques generally applied to lightweight constructions damaged by this phenomenon during drought and rehydration periods, can be attributed to four families:

Table 1.1 - The list of the preventive solutions classified by different themes (INERIS)

Preventive solutions	**Theme 1**	**Theme 2**	**Theme 3**	**Theme 4**
Investigate and characterize the foundation soil	×			
Manage tree plantations		×		
Manage the soil water content		×		
To control the underground water flow		×		
Choose the location			×	
Define the overall architecture			×	
Defining the dimensions of structures			×	
Increase the depth of the foundations via a full basement or deeper strip footings			×	
Use deep or semi-deep foundations			×	
Making vertical joints			×	
Choose the type of structure				×
Common actions on all foundations			×	×
Improve shallow foundations			×	×

a) Underpinning the construction, with intervention on the foundation system and/or on the slab (piles, micro piles, soil reinforcements, resin injections, concrete beams, etc.), (Appendix 1);

b) Action on the structure (stiffening or making joints to locate the deformations);

c) Action on the environment to limit the amplitude of the variations of the soil moisture under the foundations (root barriers, geotextiles, etc.);

d) No reinforcement, but a simple filling of the cracks when one considers that the movements are stabilized (special mortars for crack sealing);

The cost of the repair solution due to the shrink-swell hazard is a huge concern for insurance companies and thus there is a need for the economical evaluation of the costs by concerned organizations.

1.1.3 Economic issues of Geotechnical drought in France

Compensation for damages caused by the Geotechnical drought is often costly for owners, public authorities and especially insurers. This phenomenon is "the second range of compensations for natural disasters" in France and has to be taken into account by individuals and public authorities in the concerning programs for climate change adaptation. The global cost in relation to the drought (Geotechnical drought) is close to 11 billion euros, at mid-2018 (revalued by the index of the French Building Federation - FFB). At the national level, over the period of 1989-

2015, the average cost of a "Geotechnical drought" is estimated around €16,300 according to the French Federation of Insurance (FFA) and appears to be the highest of the "damage" guarantees. The exceptional drought of 2003, the fifth most expensive weather event in metropolitan France since 1988 (FFA, 2018) alone costed nearly 2 billion euros. Figure 1.5 shows twenty of the costliest climatic events since 1988 in which floods have costed about 6.3 billion euros and the Geotechnical droughts costed around 5.5 billion euros.

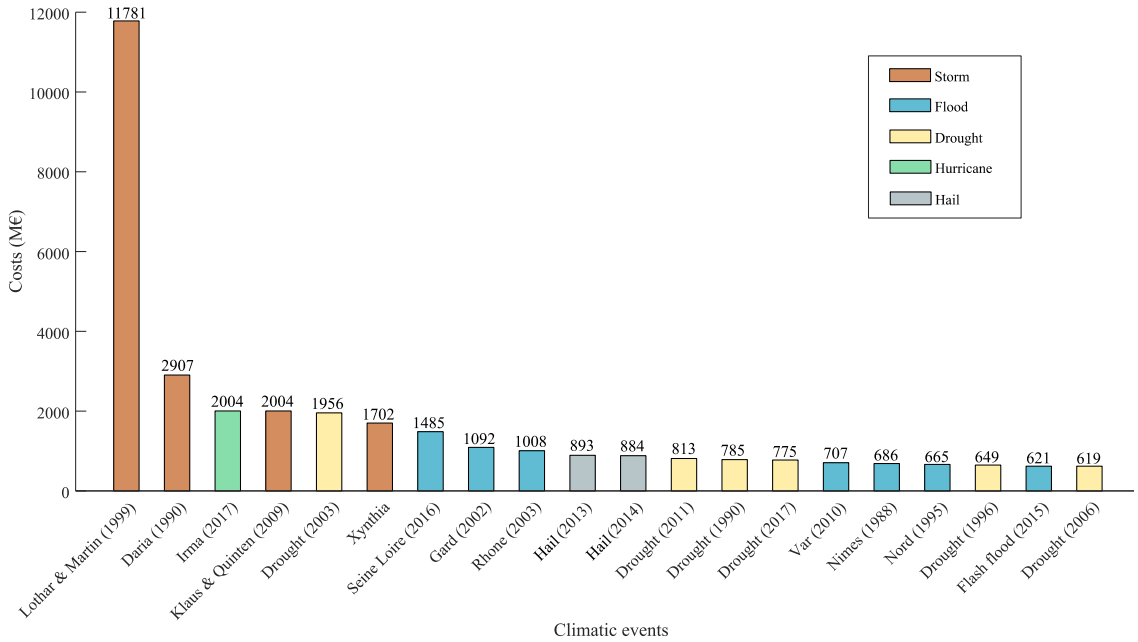

Figure 1.5 - Ranking of the costliest climatic events in France since 1988 (Source FFA, MRN, 2018)

Among these most expensive events, six are related to Geotechnical drought. This natural hazard appears therefore in the second position based on the number of events, just after the floods. It should be mentioned that the Geotechnical drought events are very recent because among the six events, three took place after 2010. According to the BRGM study of 2018 and the FFA study in 2015 on the increase of the costs related to climate change, the costs of the damages will be multiplied by 1.5 or 2.5 because of climate change. Consequently, according to the FFA, the Geotechnical drought, over the period 2014-2039, would cost around 21 billion euros, which is to triple the annual average costs of today.

The Geotechnical drought affects almost all regions of metropolitan France. In fact, they have all already, at least once, undergone a CatNat drought recognition. More than half of the towns (communes) that are concerned have an average cost of damage greater than €10,000 (mainly individual buildings). These towns are distributed in a relatively homogeneous manner across all the concerned territories as shown in Figure 1.6. The 68 towns in the largest average cost category (more than €20,000) are concentrated in Ile de France, Nouvelle-Aquitaine and Occitanie regions. The regions which have the most towns with more than €10,000 average cost are, in descending order: New Aquitaine (29%); Occitanie (20%); Ile de France (11%); Loire Valley Center (9%); Burgundy Franche Comté (6%).

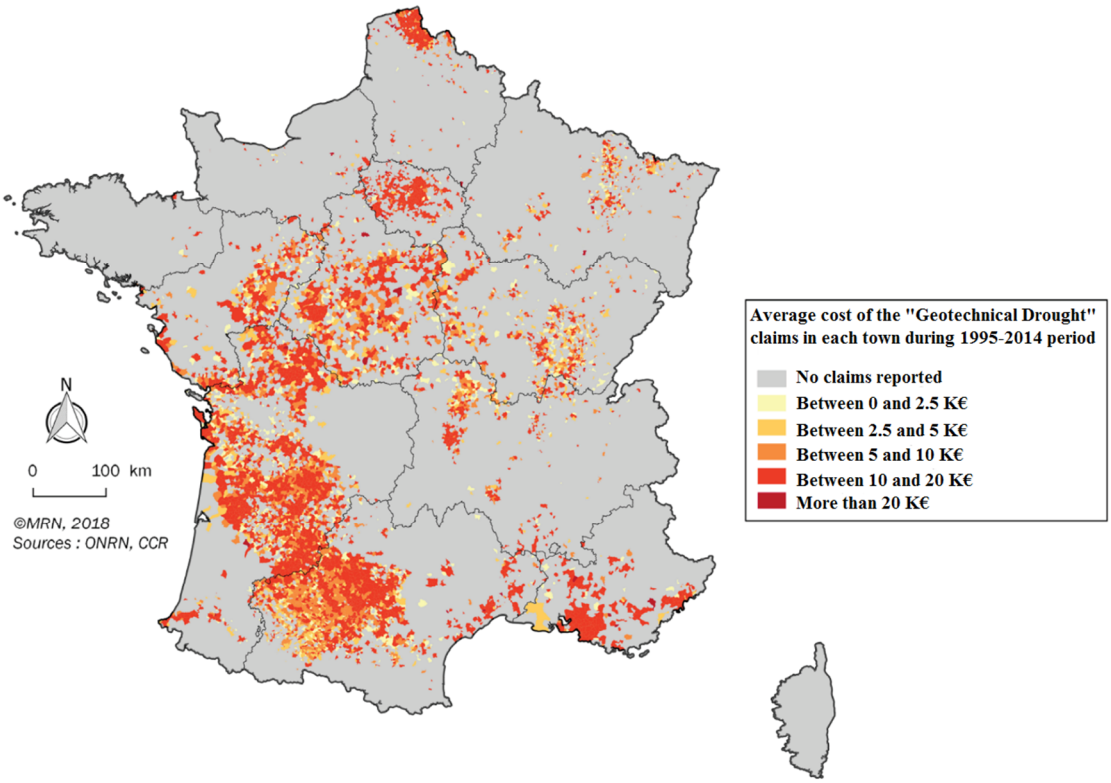

Figure 1.6 - Mapping the average costs of "drought" claims by municipality from 1995 to 2014 (CCR, MRN, 2018)

It is observed that the concentration of both damages and the associated average costs of the phenomenon in the south west of France are more accentuated compared to other regions. This is despite the fact that there is a medium shrink-swell hazard in the south west of France according to the hazard map in Figure 1.4. The reason can be the influence of climatic factors and mainly soil properties in this region in France and not only the risk factor.

The studies cited in this section highlight that the associated economic losses with the Geotechnical drought or the shrink-swell phenomenon of clayey soils during the past years are important and that deep understanding of its mechanism and its future impact is needed in order to propose preventive solutions.

1.1.4 Climate change impact in France and drought indexes

Climate change is the changes in statistical patterns of weather which may last for longer durations. Natural climate pattern doesn't remain constant all the time, but shows internal variability and fluctuates around certain values. Climate change is the change in the natural pattern i.e. mean, spread, trend etc. of atmospheric variables. If there is a change in climate due to external forcing, it doesn't correct itself to natural patterns. Intergovernmental Panel on Climate Change (IPCC) is the leading scientific intergovernmental body, which assess and review the latest information and knowledge of climate and provide guidelines to enable the scientific community to better understand and study the climate change. The Working Group on Coupled Modelling (WGCM) established the Coupled Model Inter comparison Project (CMIP) in 1995 to set the standards to study the general circulation models (GCMs). CMIP is developed in phases to foster the climate model improvements but also to support national and international assessments of climate change. In the third phase of CMIP (CMIP3) different emission scenarios

were suggested based on socioeconomic, technological and other factors (Solomon et al. 2007). According to the latest report of IPCC, Assessment Report 5 (AR5), four probable future emission scenarios (CMIP5) based on different total radiative forcing are suggested as shown in Figure 1.7. Four pathways have been selected for climate modeling and research, which describe different climate futures, all of which are considered possible depending on how much greenhouse gases are emitted in the years to come. These four RCPs (Representative Concentration Pathway) include one mitigation scenario leading to a very low forcing level (RCP 2.6), two stabilization scenarios (RCP 4.5 and RCP 6), and one scenario with very high greenhouse gas emissions RCP 8.5 (IPCC, 2013).

Despite all the uncertainties related to both the quality of the models and the adapted socio-economic assumptions, all the simulations currently available show that there is a high probability that France will experience wetter winters with more intense rainfall, especially in the north and drier summers associated with higher temperatures at the end of the 21st century. France will continue to warm up, with summer droughts more frequent, longer and more intense. During the summer of 2003, almost all the metropolitan territory had been affected by the shrinkage-swelling phenomenon since more than 8,800 French municipalities declared claims on their territory, including in the north-east of France. The 2003 drought event clearly showed that the regional climatic differences could be largely neglected during such an event and only the non-clayey zones could potentially be sheltered from this type of climatic event.

Recent works on climate change, especially the ClimSec project conducted by Météo-France (Vidal et al., 2010, Soubeyroux et al., 2011), showed that the frequency and intensity of heat waves and drought periods were inevitably increased during the century on the French territory. Thus, the main results of the simulations, based on the climate projections of the Fourth Assessment Report (AR4) of the IPCC, show that during the first third of the century, the probability of agricultural drought increased; in the middle of the century and there are unusual droughts in terms of spatial distribution or intensity which affect regions that did not undergo these phenomena before. Consequently, at the end of the century, soil drought could become extreme (compared to the current climate) over most of the territory so that one summer out of three, or even one summer out of two, would be at least as hot as the 2003 summer in France.

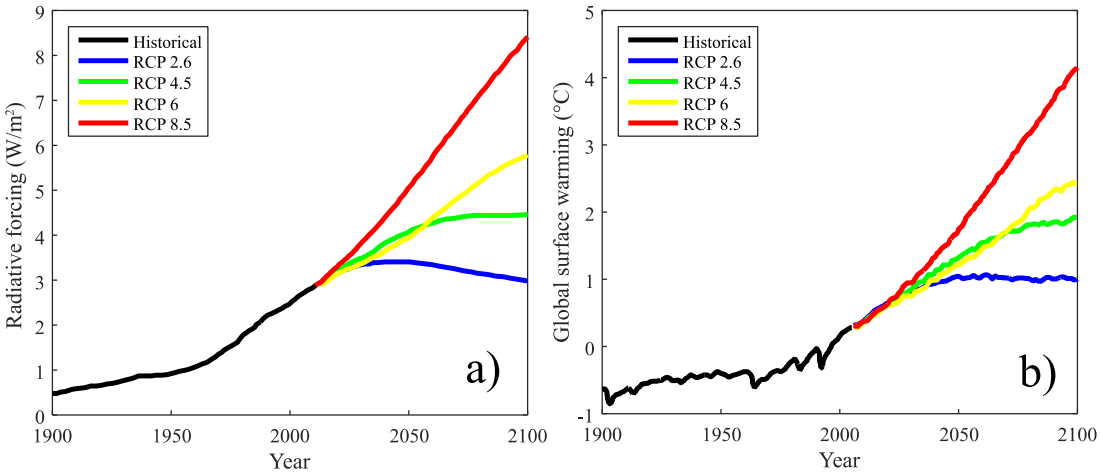

Figure 1.7 - Representative Concentration Pathway scenarios (RCP) in: a) radiative forcing and b) global surface warming (IPCC, 2019)

The French Insurance Association estimates that by 2040, the insurance cost of geotechnical drought is expected to nearly triple based on the RCP 8.5 scenario (AFA, 2015). 60% of this increase is due to climate change. The work carried out by the CCR and Météo-France shows that the annual damages resulting from the climatic events should double by 2050 in which the climate change alone would be 20% based on the climate projections of the RCP 4.5 scenario. More specifically, with regard to drought, the cost of the phenomenon should double: most of these changes would be due to the increase in vulnerability and less than 5% would be caused by climate change. The first estimates of the impact of climate change on the shrink-swell phenomenon, based on different assumptions, both in terms of climate projections and in terms of damage models, result in inconsistent results. This is the reason why the BRGM (Gourdier and Plat, 2018) conducted a recent study within the framework of the Natural Risks, Insurance and Climate Change working group, in order to build a model of damage costs associated to the Geotechnical drought that allows to evaluate the impact of climate change and its associated uncertainties. The model results are able to estimate the benefits of an adaptation policy resulting in an improvement in the quality of construction. The proposed model is based on a drought index, the real estate evolutions in France and the cost of the drought claims in France. The physical part of this model concerns the determination of the drought index which is presented in this section.

To describe the physical characteristics of a drought, several indices and indicators have been developed based on different variables such as duration, gravity (intensity) and spatial-temporal distribution. In the same way, the diversity of the fields of application does not allow to have a universal index for their characterization. However, the World Meteorological Organization (WMO) recommended in 2009 the use of the Standardized Precipitation Index (SPI), for the monitoring of meteorological droughts which is based on only on rainfall data (McKee et al. 1993, 1995). The SPI index is based on the probability of rainfall over a given time scale. The probability of precipitation is transformed into an index through statistical analysis. A probability distribution function is adjusted to this long series of data and is then transformed into a normal distribution so that the mean value of SPI for a location and for a specific time step becomes equal to zero.

Serrano et al. (2008) proposed the Standardized Precipitation Evapotranspiration Index based on precipitation and given temperatures that combine multi-scale characters with the ability to include the effects of temperature variability on the assessment of drought periods. The need for the development of this index is due to the fact that other drought indexes are not completely relevant in the cases of an abnormal increase in temperature and an associated decrease in precipitation. Climate change is not limited to a decrease in precipitation but also to a gradual increase in temperature during the studied period. This has been the subject of the development of this index which takes into account rainfall and temperature data (evapotranspiration). Like the SPI index, the SPEI is calculated based on the difference between precipitation and the potential evapotranspiration i.e. the water balance and a probability distribution function are adjusted on it. Studies indicate that the SPEI index is a more practical tool to recognize past drought events and even predict a drought period, if climate projection data are available.

Another type of drought index is based on the soil moisture content and is named the Soil Wetness Index (SWI), which is calculated from the actual soil moisture content, the moisture content at the wilting point and the moisture content at field capacity of the soil. This indicator is standardized by transforming the statistical distribution (using a distribution function) of this

variable on a reduced normalized normal distribution, to obtain the Standardized SWI or SSWI. During the ClimSec project (2008), the SPI and SSWI indices were calculated from the results obtained by the SIM model (SAFRAN-ISBA-MODCOU) with a monthly archive starting in 1958. The analysis of droughts from these standardized indices could identify locally independent events and determine their characteristics, as shown in Figure 1.8. This example was calculated over a 3-month period (SSWI3) of a site located close to Toulouse. The index shows 3 events reaching the 5% probability of occurrence threshold over the period of 1958-2008. Different local characteristics of the drought are defined: beginning of the event, duration, magnitude (absolute value of the sum the index values during the event, in months) and severity (absolute value of the minimum value reached). The identification of drought events can then be carried out on other sites in France in order to highlight their impact in a regional scale (Soubeyroux et al., 2011).

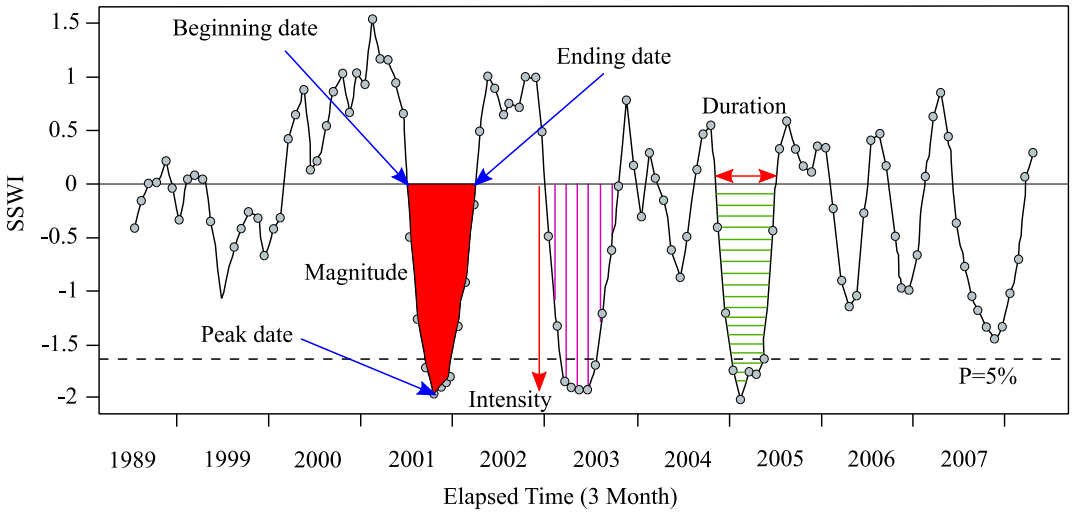

Figure 1.8 - Definition of local characteristics of Geotechnical drought events. Example of the evolution of SSWI3 over the period of 1998 to 2008 on a site located close to Toulouse with a threshold of 5% (Soubeyroux et al., 2011)

As discussed in this section, the shrink-swell phenomenon is widely spread in metropolitan France due to the climatic conditions, the variability in soil properties and external environmental solicitations. These interactions between different variables in the triggering mechanism of this phenomenon can be studied in a framework of Soil-Vegetation-Atmosphere interaction methods. The next section gives a detailed presentation of the relevant models for this kind of analysis.

1.2 Soil-Vegetation-Atmosphere interactions

The ground surface is constantly influenced by energy (heat), moisture, and gases that leave or enter the atmosphere. Soil-vegetation-atmosphere transfer models (SVATs) are used to link to global and regional climate models to more accurately describe how soil, vegetation, and water surfaces exchange fluxes with the atmosphere. The development of SVAT models has emerged from the convergence of both the works of climatologists that developed the concept of heat and

moisture flow in the atmosphere from the earth's surface and biophysicists/ecologists that developed the response of plant species to environmental conditions using the temperature, humidity levels, solar radiation, cloud cover, wind speed, precipitation, etc.

The knowledge of the associated parameters and variables are prior to the use of the SVA interaction models in the context of shrinkage and swelling phenomenon. Knowledge of hydrological science is required to grasp the details of the SVA interactions. Thus a brief introduction of the main controlling parameters and variables are presented in this section. The first part details the hydrological cycle by introducing the water balance and its components. The second part focuses on the energy balance and its associated components which lead to the building blocks of the soil-atmosphere interaction methods. The third and the last part, details the "vegetation" part of these interaction and different modelling ways of trees and plan species during SVA analysis.

1.2.1 Water balance

In hydrology, the water balance equation is used to describe the flow of water in and out of a closed system like the soil by using he principles of conservation of mass. The equation makes it possible to directly obtain the evaporation rate by knowing the precipitation (P), the runoff (R_{off}), the infiltration rate in the soil (I_{inf}) and the interception (I_{int}). Blight (1997), proposed the following expression for the water balance equation:

$$P - (I_{int} + R_{off}) = ET + I_{inf} \tag{1.1}$$

These elements are also presented in Figure 1.9. Among the components of the water balance, evaporation and infiltration are the most important from a geotechnical point of view. It should be noted that other parameters such as runoff are also important and even difficult to determine because they depend on several hydrological parameters. Ta (2009) pointed out that the use of the water balance is not suitable for large areas because the determination of the parameters becomes more and more difficult. According to Singh (1989) and Song (2014) the difficulty of monitoring dependent variables makes the use of this model very difficult which demand a very adequate installation.

1.2.1.1 Evapotranspiration process

The evapotranspiration is a process of the transfer of water contained in the soil, towards the atmosphere by a phenomenon called evaporation (which occurs on the surface of the soil) and by the transpiration of the plants. The following paragraphs help to better understand each of these phenomena.

Evaporation is a gradual transition from the liquid state to the gaseous state. Evaporation from the soil surface is a natural phenomenon and an important part of the hydrological cycle. Many authors have given definitions concerning this phenomenon (Freeze 1969, Wilson 1990, Wilson et al 1997). Freeze's definition takes into account the removal of ground water at the surface, with associated upward flow. On the other hand, according to Wilson (1990), this definition does not refer to the mechanism of the vapor flow. He considers that the term evaporation returns to open water and the surface of the soil. According to Lal and Shukla (2004); Musy and Higy (2004), evaporation at the soil surface occurs under the following conditions:

- A continuous power supply (Solar Radiation)
- An atmospheric condition (negative gradient of the area, close to and at the surface of the ground)
- Continuous supply of soil water (water content, suction, hydraulic conductivity)

The hydrological cycle for evaporation is shown in Figure 1.9:

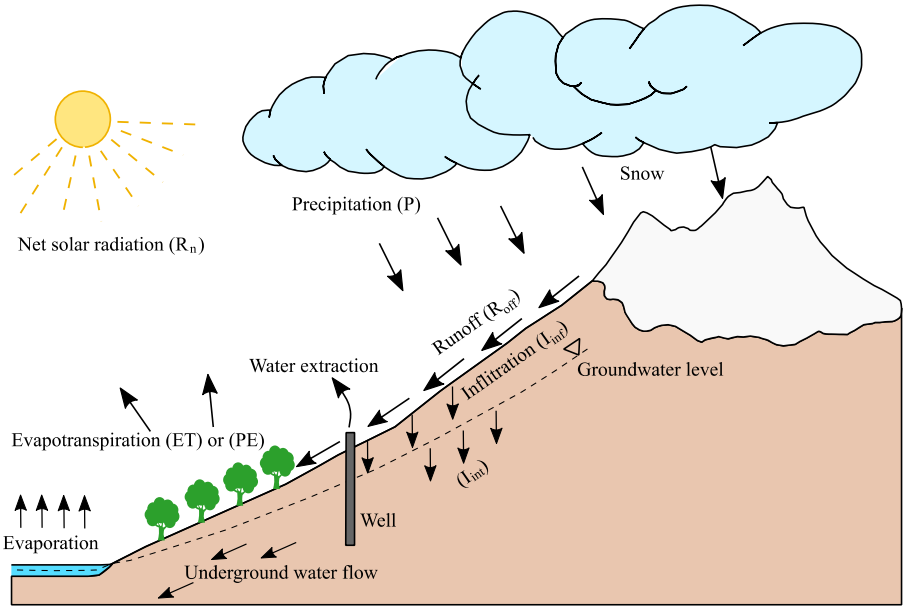

Figure 1.9 - Hydrological cycle and water balance components (after Blight, 1977)

Plant transpiration is the continuous process caused by evaporation of water by vegetation. The definition of transpiration given by Wilson (1990) is "The process by which water vapor is transferred into the atmosphere from water in plants". Burt et al. (2005) gave a definition of transpiration as a specific form of evaporation in which the water of plant tissue is vaporized and eliminated in the atmosphere mainly by plant stomata. Given the different definitions above, a simple term can be adopted as follows: transpiration is the evaporation of water from plants (Hillel, 2004).

Actual evapotranspiration (AE) refers to the exact amount of water evaporated by a real vegetation cover or bare soil. In contrast, potential evapotranspiration (PE) is a value calculated by mathematical formulas. ET (PE) is thus the subject of various definitions, depending on the authors and the calculation methods used. This notion of potential water consumption was introduced by Thornthwaite in 1948, and then taken up by Howard Penman in his formula for calculating (1948). According to the World Meteorological Organization (WMO, 1974), and International Glossary of Hydrology (WMO/UNESCO, 1992) potential evapotranspiration is the amount of water vapor that could be emitted from a surface of pure water per unit of water area and unit of time under existing atmospheric conditions. In other words, potential evapotranspiration is only a function of meteorological data and can be calculated based on these data, while actual evapotranspiration also depends on soil properties and its value is obtained by direct measurements.

Many methods are introduced to calculate PE (ET). These methods are classified in four different categories as mentioned in Table 1.2 which include the mass balance approached, the

resistance methods, the aerodynamic methods and the suction-based methods. The basic assumption used by most of these methods is that water is freely available at the evaporation surface. In other words, the surface is a water surface or a saturated soil surface (Wilson et al., 1994).

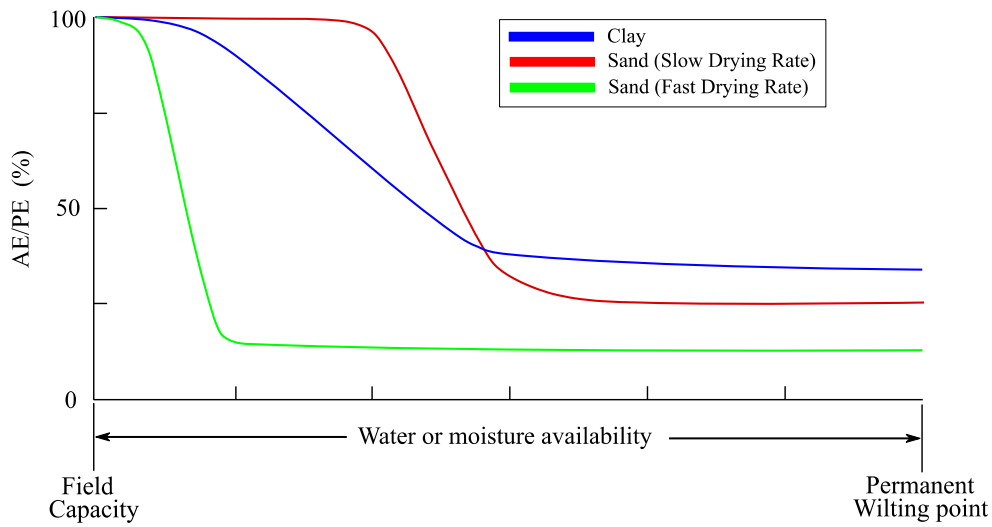

Figure 1.10 - Typical drying curves for sand and clay showing actual evaporation, AE, as a percentage of potential evaporation, PE, relative to water availability (Holmes, 1961).

Figure 1.10, shows the relationship between PE from a water-free surface and actual AE from a sand and a typical clayey surface that evaporate from an almost saturated state. Holmes (1961) showed that AE equals PE for both sand and clay soils when the moisture content is high or close to the field capacity (saturation). The ratio of AE/PE for each soil type begins to decrease as the availability of water decreases to the permanent wilting point of the soil. According to these authors, the limit of permanent wilting point implies that the soil has high negative interstitial pressures. It can also be deduced that as water becomes less available in the soil, the AE/PE ratio decreases considerably depending on the texture and the rate of soil drying. For example, the AE/PE ratio for fast-drying sand is significantly lower than that of slow-drying sand when water availability is at the midpoint between field capacity and permanent wilting point (Wilson et al. al., 1997). The clay curve indicates a higher actual evaporation rate than both types of sand (fast drying and slow drying) as water availability approaches the permanent wilting point. In summary this figure indicates that the actual rate of evaporation from the soil surface relative to the potential evaporation rate (AE/PE) depends both on the availability of water, the texture of the soil, and the rate of drying.

According to research conducted by Wilson et al., In 1994, water content, soil suction, temperature, are among the parameters that show significant variations (significant gradients) in the area near the surface of the soil at different rates of evaporation. The evaporation rate can also be affected by certain physical parameters. It is proportional to the speed of the incoming sun's radiation and the soil water content as well as the temperature of the area and the texture at the soil surface. These parameters will be detailed in the following sections. Therefore, by having these notions of this phenomenon, the models proposed in the literature can be evaluated. Here is a summary of these models as shown in Table 1.2.

Table 1.2 - Existing evapotranspiration models

Model type	Expression	References	Parameters
Mass balance	$ET = f(u)(e_s - e_a)$	Dalton (1802)	$f(u)$: Wind speed function e_s : Saturation vapor pressure at the soil surface e_a : Air vapor pressure close to the surface
Resistance α	$E = \frac{\rho_a[\alpha q_{sat}(T_s) - q_{ref}]}{r_a}$	Mahfouf and Noilhan (1991)	ρ_a : Air density α : Relative humidity at the soil surface $q_{sat}(T_s)$: Specific humidity at the soil temperature q_{ref} : Specific humidity at the refrence height r_a : Aerodynamic resistance (s/m).
Resistance β	$E = \frac{\rho_a \beta[q_{sat}(T_s) - q_{ref}]}{r_a}$ $\beta = \frac{r_a}{(r_a + r_s)}$	Mahfouf and Noilhan (1991)	r_s : Resistance to a flux from vegetation (s/m).
Aerodynamic	$ET = 1{,}6\left(\frac{L}{12}\right)\left(\frac{N}{30}\right)\left(\frac{10T_a}{I}\right)^{a_1}$	Thornthwaite (1948)	L: Length of the day (h) N: Number of days of the month T_a: Mean air temperature I: Somme of the i indexes of 12 months.
	$ET = \frac{P_m}{0{,}9 + \left(\frac{P_m}{T_m}\right)^2}$	Turc (1954-1955)	ET: Monthly evapotranspiration P_m: Monthly rainfall T_m: Mean temperature
	$ET = \frac{\Delta R_n + \rho_a c_p \frac{(e_s - e_a)}{r_a}}{\lambda_v(\Delta + \gamma)}$	Penman-1 (1948)	ET: Evapotranspiration (kg/m^2.s) Δ: slope of the vapor pressure curve [Pa °K^{-1}] R_n: Net solar radiation (W/m^2) ρ_a: density of air (kg m^{-3}) c_p: heat capacity of air (J kg^{-1} K^{-1}) λ_v: latent heat of vaporization (J kg^{-1}) γ: Psychrometric constant (66 Pa K^{-1}) $(e_s - e_a)$: Vapor pressure deficit (Pa)
	$ET = \frac{\Delta(R_n - G) + \rho_a c_p \frac{(e_s - e_a)}{r_a}}{L_v\left(\Delta + \gamma\left(1 + \frac{r_s}{r_a}\right)\right)}$	Penman-Monteith (1948)	ET: Evapotranspiration (mm/s) G: Ground heat flux (W m^{-2}), L_v: Volumetric latent heat of vaporization. Energy required per water volume vaporized. (L_v = 2453 MJ m^{-3})
	$ET = 0.0018(25 + T_a)^2(100 - hr)$	Romanenko (1961)	ET : Evapotranspiration (mm/day) hr : Relative humidity (%) T_a : Mean temperature (C°)
	$ET = 0.4(1 + 4.08\ u_2)(e_s - e_a)$	Rohwer (1931)	e_s ; e_a: (mm Hg) u_2 : Wind speed (miles/jour)
Suction based	$h_s = \exp\left(-\frac{\psi M g}{RT}\right)$ $\frac{AE}{PE} = \frac{\exp\left(\frac{gM}{RT_s}\psi\right) - h_a}{1 - h_a}$	Wilson et al. (1997)	AE: Actual evapotranspiration PE: Potential evapotranspiration (ET) $\frac{AE}{PE}$: Evapotranspiration rate h_a: Air relative humidity h_s: Soil relative humidity ψ: Total soil surface suction M: Molar mass of water (18.016 g/mol) g: Acceleration (9.81 m/s^2) R: Molar gas constant (8.3143 J/mol/K)

1.2.1.2 Masse balance model:

Evaporation from the water surface or water-saturated soil surface can be calculated by the Dalton equation (1802) as shown in Table 1.2. The mass transfer equation describes evaporation as a function of the difference in vapor pressure between the surface of water and the overlying air. The vapor pressure of the evaporation surface of water, e_s, is the saturation vapor pressure of water, which is a function of temperature (Brutsaert 1982). The vapor pressure in the air above water, e_a, is determined on the basis of saturation vapor pressure at the measured air temperature and the relative humidity (Wilson et al 1997). Determining the saturation vapor pressure at the soil surface is not easy because of the presence of large temperature gradient at the surface. Therefore, e_s is replaced by e_a, (instead of the surface temperature). This approach is often used in the work of Hemmati (2009) and Song (2014). Ta (2009) studied the phenomenon of evaporation through advanced experimental measurements, notably the Environmental chamber.

This model is rather applicable in the case of a surface of water or a soil surface saturated with water. It is not appropriate to use this model for unsaturated soils. Song (2014) points out that this model is the basis of several coupled models and is a solid foundation for the construction of new models. Ta (2009) summarizes that several modifications are made to this model in the literature but only to meteorological parameters. The soil parameters have been neglected, which is totally at odds with the literature that justifies the effect of soil parameters on evaporation.

1.2.1.3 Resistance models:

This method is based on the concept of electrical resistance. The flow of water vapor that evaporates from the soil surface is considered as the electric current (I) and the resistance to the vapor transfer in the atmosphere is considered as the ratio of the voltage to the current (R =V/I). This notion of resistance is applicable to the atmosphere, the soil, and the vegetation. A schematic representation of this model was presented by Mahfouf and Noilhan in 1991 as shown in Figure 1.11.

This concept has been accepted by several authors in the literature (Aluwihare and Watanabe 2003, Kondo et al., 1990, Mahfouf and Noilhan 1991). These authors agree that the water available between the solid soil grains diffuses to the surface through the pores space in the soil structure and then when the soil has become unsaturated, the water vapor is transferred from the evaporation surface to the soil surface by molecular diffusion. Then the water vapor is transferred from the soil surface to the atmosphere through a laminar or turbulent flow. It should be noted that if vegetation existed on the soil surface, water vapor would also be limited in terms of resistance at this level and this resistance should be added to the resistance of the soil and the atmosphere. Thus, following the concept of resistance model, the resistance imposed on the water vapor through the transfer from the evaporation surface to the soil surface is defined as r_s. The resistance imposed on the water vapor through the transfer from the soil surface to the atmosphere is defined as r_a.

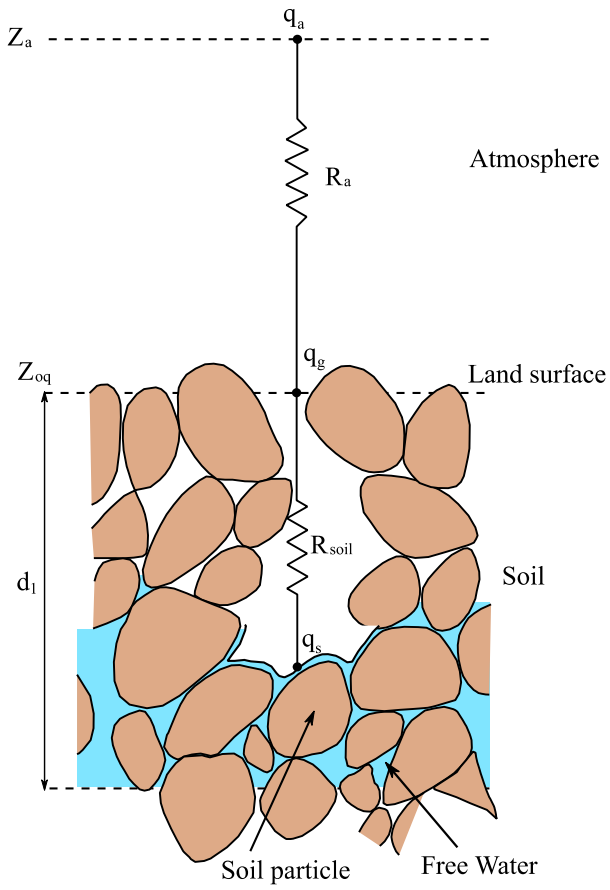

Figure 1.11 - Schematic of the water flow during evaporation (Mahfouf and Noilhan 1991)

Depending on the water vapor transfer mode, two typical models of resistance were constructed, the α model and the β model. According to the work of Mahfouf and Noilhan, 1991, the α model overestimates the rate of evaporation when there is a large gradient of water content at the soil surface. This overestimation has been underlined by several authors. The β model can produce reasonable estimates of evaporation during the day, but its performance is limited during the night (Mahfouf and Noilhan, 1991).

To conclude, the determination of resistance terms is essential in this model. There are numerous expressions describing both aerodynamic resistance (which depends on atmospheric parameters) and soil resistance which depend on the nature of the soil.

1.2.1.4 Aerodynamic models

These methods are able to give the evaporation value for different time periods (day, week, month). Methods based on meteorological data are among the most suitable methods in the Geotechnical Engineering field. This may be because these methods use only simple climate data such as mean temperature and relative humidity. Climatic methods for estimating evaporation or evapotranspiration produce a regional estimate, that is, they combine the effect of microclimates in a regional scale. There are several aerodynamic methods based on climatic data for estimating the rate of evaporation or evapotranspiration. Here are some models used in the literature:

- *Thornthwaite (1948) model:*

Thornthwaite (1948) developed a method for the estimation of potential evapotranspiration as an aid to the classification of climatic regions (Wilson, 1990). It is a method based on the air temperature that produces a monthly estimate of potential evapotranspiration. Thornthwaite considered climatic parameters such as, solar radiation, temperature, relative humidity, and wind speed, the most dominant factors that control evapotranspiration in comparison with vegetation and soil parameters. He concluded that parameters such as solar radiation, and relative humidity are unreliable and should not be included in the formulation. Therefore, the average monthly air temperature, is the most stable parameter because it is a function of both the net solar radiation and the water content (which is related to the relative humidity).

This method is simple and does not use sophisticated data. It has been used by several researchers and has proven to be very reliable for many applications. Nevertheless, this method also has some disadvantages and it can be very inaccurate over a short period of time. According to Wilson (1990), this method produces no predictions for stored or dispersed energy. In general, this method is limited to the estimation of potential evapotranspiration, on a large regional scale for a period of at least one month.

- *Turc (1954-1955) model:*

Turc proposes a formula that takes into account the water supply limit by taking into account the precipitation as mentioned in Table 1.2. According to Blight (1997) this model cannot be applied under certain conditions, because during a period of drought, the precipitation is zero, but that does not mean that the evaporation stops. Contrary to what is defined in this model which gives zero evapotranspiration if the precipitation is zero.

- *Penman (1948) model:*

The Penman equation describes evaporation from an open water surface, and was developed by Howard Penman in 1948. Penman's equation requires daily mean temperature, wind speed, air pressure, and solar radiation to calculate the rate of evaporation as shown in Table 1.2. The calculated evaporation will be in units of $kg/(m^2 \cdot s)$, kilograms of water evaporated every second for each square meter of area. The proposed equation is one of the modified Dalton equations because it uses the basis of mass transfer. The Penman method is the most used in estimating potential evapotranspiration (Wilson 1990). It is simple because it requires the usual climatic parameters such as temperature, relative humidity, wind speed which changes the parameters of the model. The model itself is the trigger for several developments in the literature such as the Penman-Monteith method. This method was developed for a water-free surface and was subsequently returned to bare ground. This model assumes a daily time step so that the net heat exchange with the ground is insignificant, and a unit area surrounded by similar open water or vegetation so that net heat and vapor exchange with the surrounding area cancels out. In some case the net solar radiation can be replaced by other factors to total net available energy in presence of additional heat fluxes.

The disadvantage of Penman's method could be its unreliability in areas with horizontal advection of sensible heat flux; the obligation to use a correction coefficient when applied to evapotranspiration conditions where water is not freely available; on estimating evapotranspiration when applied to arid regions and not taking into account the soil heat flux (Wilson, 1990).

- *Penman-Monteith model:*

Like the Penman equation, the Penman–Monteith equation (after Howard Penman and John Monteith) approximates net evapotranspiration (ET), which requires as input, daily mean temperature, wind speed, relative humidity and solar radiation. The United Nations Food and Agriculture Organization (FAO) standard method for modeling evapotranspiration is the Penman–Monteith equation. The standard method of the American Society of Civil Engineers (ASCE) modifies the Penman–Monteith equation for using it with an hourly time step. Evapotranspiration contributions are very significant in a watershed's water balance, yet are often not emphasized in results because the precision of this component is often weak relative to more directly measured phenomena, e.g. rain and stream flow. In addition to weather uncertainties, the Penman–Monteith equation is sensitive to vegetation specific parameters which can change the rate of evapotranspiration using adapted coefficients which will be discussed in next sections.

This method only takes into account the resistance to the diffusion of vapor in the atmosphere, nevertheless in the presence of vegetation, another term of resistance enters in the formulation of this model, more details on these parameters are available in the works of Hemmati (2009). Resistance to vegetation vapor diffusion is a function of solar radiation, vapor pressure deficit, and soil moisture content. As a general rule, solar radiation is used for the calculation of the net solar radiation (R_n); air temperature is used to determine ρ_a, e_s and Δ; relative air humidity is used to calculate e_a; and the wind speed is used for the calculation of r_a. The heat soil heat flux G is generally estimated as a function of R_n or by direct measurement. Like the Penman method, this method is only applicable for a free water surface or a saturated soil surface. This has been the subject of the developments of new models based on the soil suction.

- *Romanenko (1961) model:*

This method depends on the air temperature and relative humidity, which makes it quite simple to interpret. However, this model does not take into account the soil heat flux and the net solar radiation which is an important component of the energy balance. Also, the influence of the vegetation is not considered in this method. The use of this model can be appropriate for quick estimates of the evapotranspiration rate with limited climatic data.

- *Rohwer (1931) model:*

The Rowher model is one of the modified Dalton-type methods, based on the mass balance approach, which uses the wind speed as input parameter and makes the calculations simple. The disadvantage with this method is the fact that it underestimates evapotranspiration and does not take into account other influencing climatic factors. Also, the influence of the vegetation is not considered in this model.

The presented aerodynamic models are compared to each other using the climatic parameters of a site in the south of France (Figure 1.12). It can be observed that the Rohwer model shows lower ET values compared to other models and the Penman model shows the highest monthly ET values during the considered year. The Penman-Monteith model lies between these two models which could be a reasonable estimation of the potential evapotranspiration rate considering the soil and the vegetation parameters.

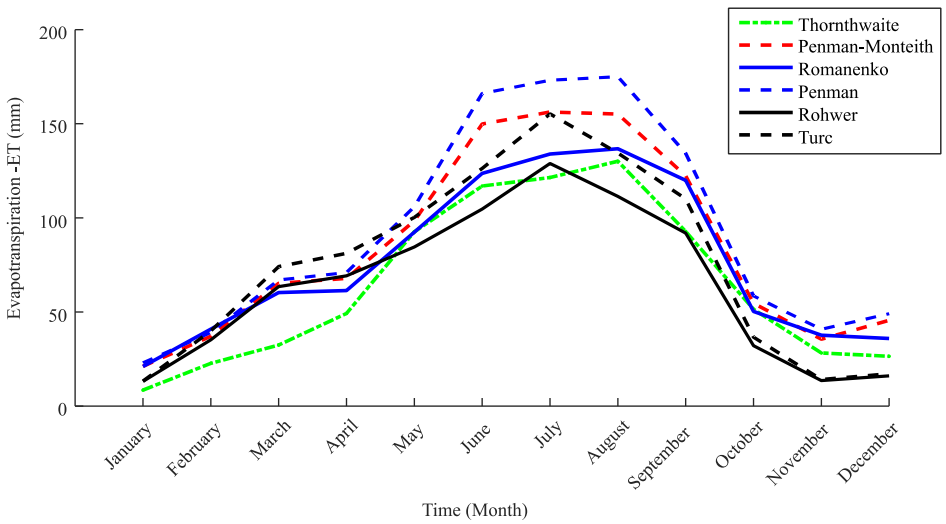

Figure 1.12 - Comparison of the aerodynamic methods for the calculation of the evapotranspiration rate using monthly climatic data.

1.2.1.5 Suction based models

The evaluation of the evapotranspiration rate from the surface of an unsaturated soil has been the subject of several investigations in the field of geotechnical engineering in the literature. Campbell (1985) proposed a relationship between the actual evapotranspiration (AE) and the relative humidity of the soil (h_s) and the air (h_a), by knowing the potential evapotranspiration (PE or ET) as mentioned in Table 1.3.

Wilson et al. (1997) introduced suction on the soil surface to estimate the rate of evapotranspiration. This approach was developed through laboratory testing on three different soil types (Limon, Clay, Sand). Soil surfaces have been saturated and evaporated to a state of complete drying. Actual evapotranspiration was measured for each soil type and potential evapotranspiration was determined on the water tank used in the tests. The AE/PE ratio was first analyzed versus the soil moisture content as shown in Figure 1.13 a). It can be observed that the AE/PE ratio is different for each soil type at a specific water content, thus the proposal of a unique relationship is not possible. This is why the water content is converted to suction through the water retention curves of each soil, and the AE/PE ratio is plotted against suction (Figure 1.13 b)). It can be observed that there is a unique relationship on all curves for all three soil types.

Table 1.3 - Formulation of the actual and the potential evapotranspiration

Formulation	Description	Parameters	Combination
$AE = f(u)(e_{soil} - e_a)$	Actual evapotranspiration from the soil surface	e_{soil} : Air vapor pressure at the soil surface	$\frac{AE}{PE} = \frac{\left(\frac{e_{soil}}{e_s} - \frac{e_a}{e_s}\right)}{1 - \left(\frac{e_a}{e_s}\right)} = \frac{h_s - h_a}{1 - h_a}$
$\mathrm{PE} = f(u)(e_s - e_a)$	Potential evapotranspiration	e_s : Saturation vapor pressure at the water surface	

Applying Dalton's method for two different cases, the AE/PE ratio can be deduced. It should be mentioned that for the sake of simplicity, the temperature at the surface of the soil, at the

surface of the water and in the air were taken all equal and therefore e_s is considered as the saturation vapor pressure in all three cases.

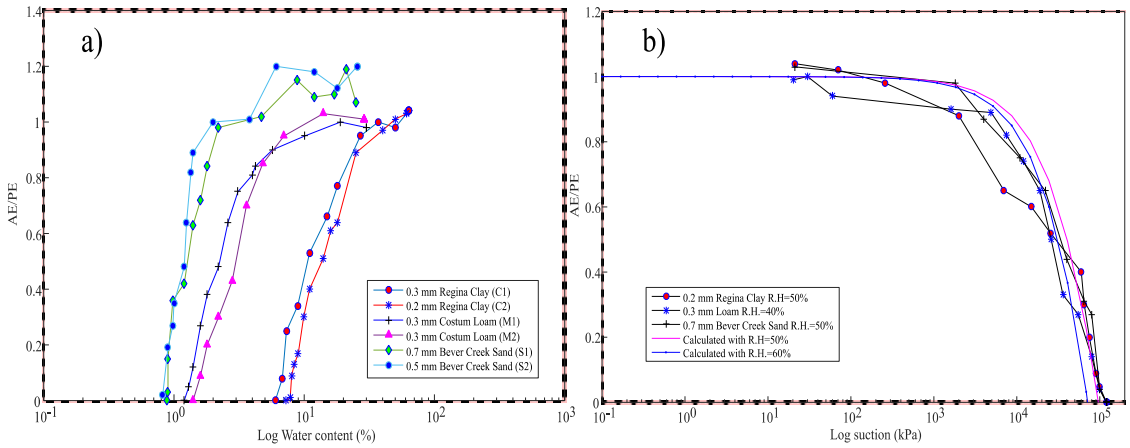

Figure 1.13 - AE/PE ratio as a function of a) water content and b) soil surface suction (Wilson et al., 1997) cited by Ta (2009), Hemmati (2009) and Song (2014)

Calculations are carried out on the AE/PE curve as a function of suction. Two calculations were performed with two different relative humidity values (50 and 60%). The experimental results are consistent with the calculation method used. Some points are to be discussed regarding this approach, Wilson et al. (1997) used very thin samples (less than one millimeter) in their work. Ta (2009) emphasizes that the use of a very thin soil layer to study an evaporation process is not very relevant, as such a process usually involves a long duration and interactions between different soil layers. In addition, the concept of storage of water in the soil is no longer valid, so the evaporation is not exactly what we can have in nature. He also points out later that this thin thickness is the cause of the disappearance of the third phase of the evaporation process. On the other hand, this model is not able to give an equation for the calculation of the potential evapotranspiration and thus, an expression of PE is necessary for the application of this approach.

That being said, it is essential to analyze the shape of the curves in presence of even thicker layers. Kondo et al. (1990) are also among the authors who evaluated this approach but with samples with different thicknesses. The tests carried out by Kondo et al. (1990) were performed on sand and loam samples ranging from 0 to 20 mm thick. The study highlights the effect of the position of measurement of the suction on the rate of evaporation. When approaching the surface (0 mm), the curves tend to rise upwards and behave in a unique manner. Indeed, the curves averaged over 20 mm are well below the curves with the suction measured at the surface (0 mm). Moreover, a superposition of the curves is observed when the suction is higher on the surface of the ground. To analyze these results, data from Kondo et al. (1990); Wilson et al. (1994) and Wilson et al. (1997) were plotted together in two diagrams, one having thick layers, the other having thin layers. In the first case, 5 soils are used, three of which are from the work of Wilson et al. (1997) and the other two are reported by the work done by Kondo et al. (1990). The layers are not superimposed and there is a large difference in the rate of evapotranspiration (AE/PE) at a constant suction value. On the other hand, one can observe a net superposition of the curves in the case of the thin layers (0.2 mm, 0.3 mm, 0.7 mm, 0 mm) for all types of soils studied by

these authors (Figure 1.14). This highlights the independence of the soil texture to the evapotranspiration rate (AE/PE).

Finally, these curves were reported on a single diagram (Figure 1.15). The evolution of the upward curves shows the effect of the thickness of the samples or in other words the measuring point (surface or depth). According to Ta (2009), it is observed that the thinner the soil layer in which the suction is measured, the higher the position of the corresponding curve. The work highlights the effect of the measurement carried out at different depths in the soil, on the rate of evapotranspiration (AE/PE). The curves are superimposed when the suction is averaged over a thinner soil thickness.

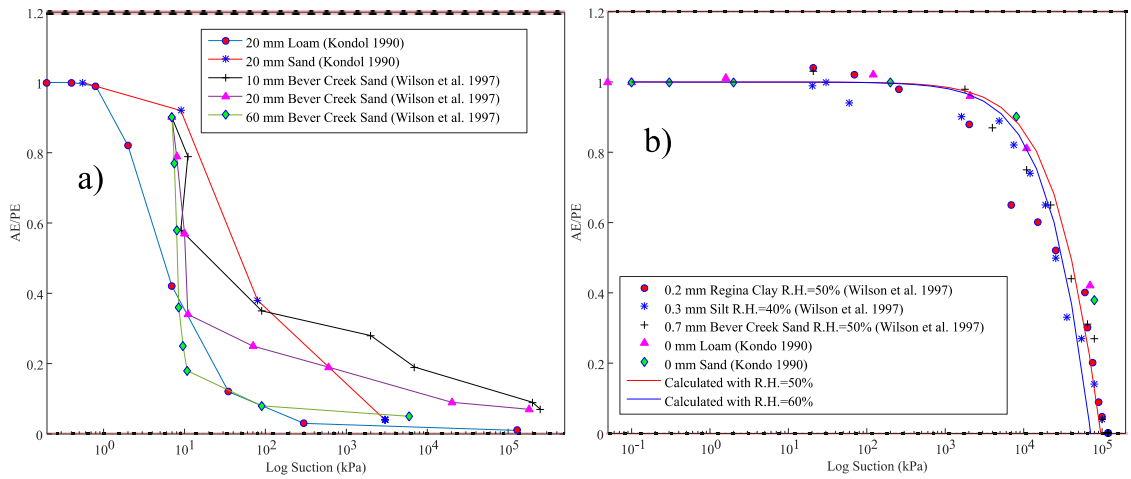

Figure 1.14 - Comparison of the results obtained on the evapotranspiration rate, a) for thick samples, and b) for thin samples. (Data used by Wilson et al., 1997, Wilson et al., 1994, Kondo et al., 1990, Ta, 2009)

Some points can be summarized by these studies:

a) The use of water content as key parameters is not relevant because each soil type gives a specific representation and does not give a unique representation for all the different types of soil.

b) On the other hand, the use of suction allows the evapotranspiration rate (AE/PE) to be independent of the type of soil.

c) A decrease in the thickness of the samples or the displacement of the measuring point at the surface of the soil, leads to a convergence and superposition of the curves.

d) At the same suction value, the closer the measuring point is to the soil surface, the higher the evapotranspiration rate (AE/PE).

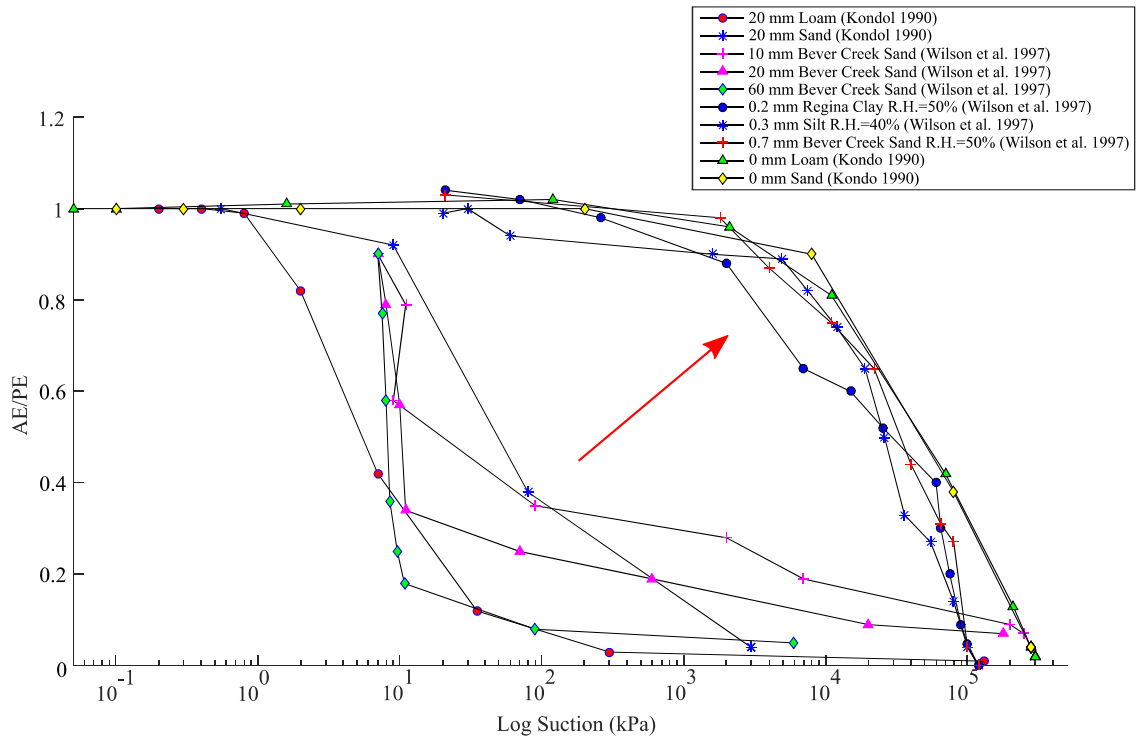

Figure 1.15 - AE/PE variation based on the experimental results obtained by the existing data in the literature. (Data from Wilson et al., 1997, Kondo et al., 1990)

There are also other suction models, such as the Aydin et al. (2005) model, cited by Song (2014) in his work. This model is based on the AE/PE ratio and the water potential at the surface. For the evaporation process in saturated soil, the authors estimated that the evaporation of the soil is on a potential rate until the soil exceeds the threshold of water potential. Therefore, the soil is saturated until the threshold water potential is reached (ϑ_{tp}). Then, the rate of evaporation decreases, until finally it reaches a very low threshold (negligible) called the air-dryness water potential (ϑ_{ad}). The relationship between AE/PE and the soil water potential is shown in Figure 1.16 and the model is expressed in the following form:

$$\mathrm{AE} = \frac{\log|\vartheta| - \log|\vartheta_{ad}|}{\log|\vartheta_{tp}| - \log|\vartheta_{ad}|}\mathrm{PE} \tag{1.2}$$

Where ϑ is the absolute soil water potential (cm of water). It should be noted that the in this model, the potential evapotranspiration (ET or PE) is calculated by the Penamn-Monteith method by considering no resistance terms. Thereafter, since the water potential of the dry soil at the surface is supposed to be in equilibrium with the atmosphere, therefore by using the relative humidity of the air, ϑ_{ad} is calculated with the Kelvin equation (Aydin et al., 2008).

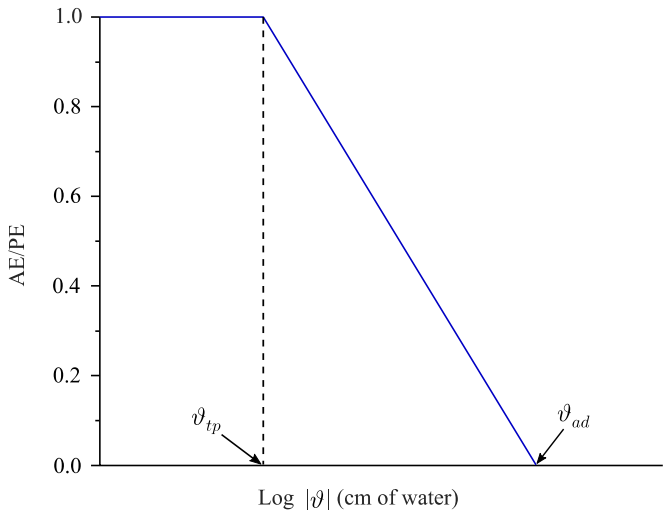

Figure 1.16 - The schematic representation of the relationship between AE/PE and the water potential of the soil at the surface (Aydin et al., 2005)

Some suction based models for evapotranspiration have been presented in this section. These models are able to take into account both soil and atmospheric/climatic parameters. Research carried out by Ta (2009); Song (2014) was based on these types of models in order to build a relationship with the soil cracking during the evapotranspiration process. Hemmati (2009) used these models to study the soil THM (Thermo-Hydro-Mechanical) behavior. Several authors have employed this new approach because the introduction of surface suction allows the evapotranspiration rate to be independent of the soil's nature, texture and its drying time. But the important point that should also be evaluated is the measurement of suction at the soil surface which can be a difficult task to perform and requires adequate equipment. It should be mentioned that some complementary evapotranspiration relationships (CR) can be used to determine the AE/PE ratio theoretically and consequently estimate the soil surface suction using the Kelvin's law.

1.2.2 Energy balance

The energy balance proposed by Blight (1997) is defined as follows:

$$R_n = G + H + L_e \tag{1.3}$$

where H (W/m^2) is the sensible heat flux; Le (J/kg) is the latent heat flux and R_n and G are the net solar radiation and the soil heat flux (W/m^2) respectively as described previously. Measurements by Blight (1997) highlight the distinction between day and night in terms of energy (Figure 1.17). During the night all the components are almost zero but the important part of the solar radiation is evapotranspiration (evaporation) during the day. According to Cui et al. (2010) energy balance components can have negative and positive values depending on the associated state. This concept is shown in Table 1.4.

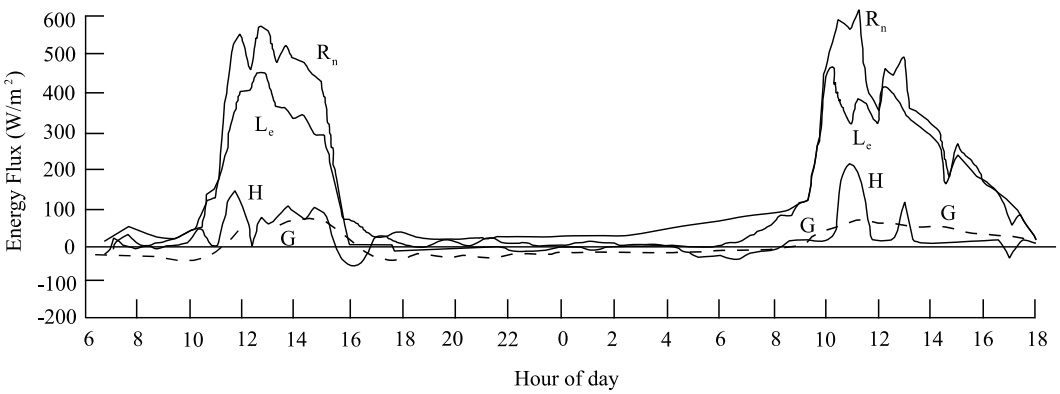

Figure 1.17 - Typical measurement of energy balance components during the day and night. (Blight, 1997)

This notion can also be deduced from Tanner's (1968) schema cited by Hillel (2004) in Figure 1.18. The first diagram (a) represents the radiation balance, the diagram (b) represents the energy balance components during the day and the diagram (c) represents the energy balance during the night.

Table 1.4. Energy balance components in positive and negative state.

Energy components	**Positive (+)**	**Negative (-)**
H	Energy is used to warm up the air	Air loses energy due to cold
L_e	Water evaporation	Vapor condensation
G	Energy is transferred into the soil	Energy is transferred into the atmosphere

Each of these components depend on several other parameters. In the following section, the determination of each component of the energy balance will be detailed.

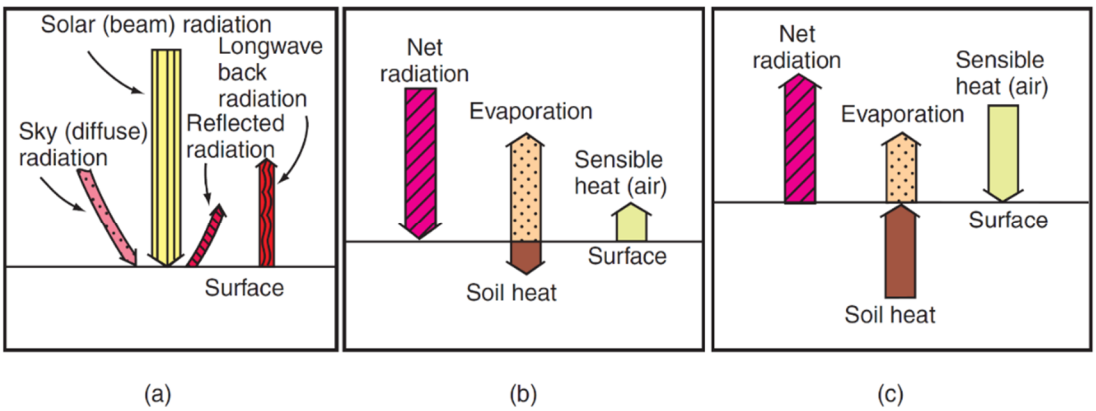

Figure 1.18 - Schematic representation of the components of the energy balance. (Tanner, 1968 cited by Hillel, 2004)

1.2.2.1 Net solar radiation (R_n)

Many authors have proposed empirical or semi empirical methods for the net radiation. We present here some of these models summarized in Table 1.5.

Model 0: The net solar radiation can be calculated using the Blight (1997) expression that relates the air temperature and the soil surface temperature to net solar radiation. Figure 1.19 shows the major components of the sun's radiation in the atmosphere:

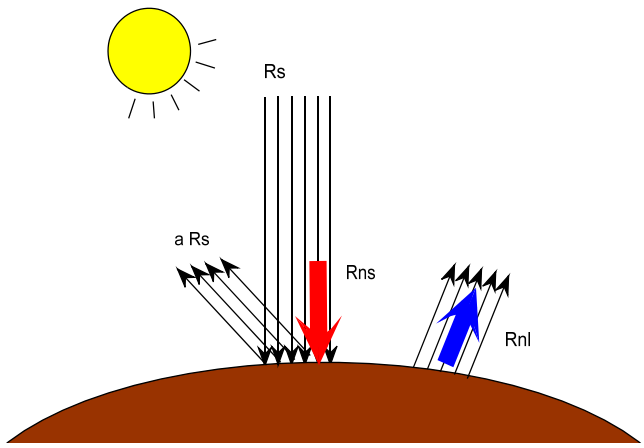

Figure 1.19 - Principle of sun radiation and its associated components (after FAO 56)

The relationship is established as follows:

$$R_n = R_{ns} - R_{nl} \tag{1.4}$$

whereR_{nl} is the long wave net radiation and R_{ns} is the short-wave net radiation which can be expressed as a function of the incoming solar radiation (R_s) as follows:

$$R_{ns} = (1-a)R_s \tag{1.5}$$

The long wave solar radiation is depended on the soil and the air emissivity coefficient, the air and the soil surface temperature and the soil surface albedo. The final form of the net radiation based on this model takes the form expressed in Table 1.5 where the first term $(1-a)R_s$ is the short-wave net radiation and the second term $\varepsilon_s\sigma\ (T_s)^4 + \varepsilon_a\sigma\ (T_s)^4$ is the long-wave net radiation. a is the soil surface albedo, σ is the Stefan-Boltzmann constant ($\sigma = 5.67 \times 10^{-8}\ \ (Wm^{-2}K^{-4})$), ε_s is the soil surface emissivity, T_a and T_s are the air temperature and the soil surface temperature respectively (°K), ε_a is the air emissivity.

Model 1: The Penman-Monteith Food and Agricultural Organization of the United Nations 56 standard model (FAO 56) is the most known and applied net radiation model, where a, R_s, σ are the same as cited before, $T_{(a\ max)}$ and $T_{(a\ min)}$ are the minimum and maximum daily air temperature (°K), b' and c' are the emissivity factors and are equal to 0.34 and -0.14 respectively, d' and e' are the cloud factors respectively equal to 1.35 and 0.35, e_d is the air pressure at the dew point temperature (kPa) in which T_d is the dew point temperature (°C), expressed as a function of the air temperature (°C). R_{so} is the clear sky solar radiation and R_a is the extraterrestrial solar radiation, where the term 24(60)/π is the inverse angle of rotation in daily time

scale, G_{sc} is the solar constant (0.0820 MJ/m2/min) and d_r is the invers relative distance of the earth-sun, where J is the number of the day in the year between 1 (1 January) and 365 or 366 (31 December). δ is the solar decimation and ω_s is the sunset hour angle, where φ is the latitude in (rad).

Model 2: Monteith and Szeicz (1961) demonstrated that there was a linear relationship between the net solar radiation (R_n) and the incoming global solar radiation (R_{si}). This model known as the Basic Regression Model (BRM) has been introduced for different climate types. In the equation a_3 and b_3 are constant parameters depending on the climate site. For plain sites, these constants are a_3=0.6 and b_3=-23.23 respectively. These constants are equal to a_3=0.61/0.57 and b_3=-30.31/-32.62 for hill/mountainous site respectively.

Model 3: Berliand et al. (1970) proposed a global Basic Regression Model as mentioned in Table 1.5.

Model 4: Linacre (1993) proposed a model that takes the averaging constant parameters into account.

Model 5: Wright (1982) proposed a nonlinear equation to calculate the net solar radiation. This equation is similar to the FAO56 equation in which a'_1 and b'_1 are the emissivity factors and a'_2 and b'_2 are the cloud factors.

Model 6: Monteith (1973) proposed an equation using air temperature, cloud cover, sunset time angle and latitude of the considered site.

Model 7: Irmak et al. (2003) proposed a new radiation model by using measured climatic data, in which R_{si} (the global solar radiation) is in MJ/m^2/day, and T is the temperature in (°C) and d_r is the same as in the FAO 56 equation.

Table 1.5 - Different net radiation models

N	Sources	Net radiation models	Complementary equations
0	Blight (1997)	$R_n = (1-a)R_s - \varepsilon_s \sigma\ (T_s)^4 + \varepsilon_a \sigma\ (T_a)^4$	-
1	FAO 56	$R_n = (1-a)R_s - \sigma \left[\frac{{T_{a\ max}}^4 + {T_{a\ min}}^4}{2}\right] \left(b' + c'\sqrt{e_d}\right) \left(d'^{\left(\frac{R_{si}}{R_{so}}\right)} - e'\right)$	$e_d = 0.6108 \exp\left(\frac{17.27\ T_d}{T_d + 237.3}\right)$ $R_{so} = (0.75 + 2 \times 10^{-5}\ z)R_a$ $R_a = \frac{24(60)}{\pi} G_{sc} d_r [\omega_s \sin(\varphi)\sin(\delta) + \cos(\delta)\sin(\omega_s)]$ $d_r = 1 + 0.033 \cos\ (\frac{2\pi}{365} J)\ ,\qquad \delta = 0.409 \sin\ (\frac{2\pi}{365} J - 1.39)$ $\omega_s = \arccos[-tan(\varphi)\, tan(\delta)]$
2	Monteith and Szeicz (1961)	$R_n = a_3 R_s + b_3$	
3	Berliland et al. (1970)	$R_n = 0.63\ R_s - 40$	
4	Linacre (1993)	$R_n = 0.593\ R_s - 28.72$	
5	Wright (1982)	$R_n = (1-a)R_s - \sigma \left[\frac{{T_{a\ max}}^4 + {T_{a\ min}}^4}{2}\right] (a'_1 - b'_1\sqrt{e_d}) \left(a'_2 \left(\frac{R_s}{R_{so}}\right) + b'_2\right)$	$\begin{cases} a'_1 = 0.26 + 0.1 \exp(-[0.0154(J-180)^2]) \\ b'1 = -0.139 \end{cases}$ $\begin{cases} a'_2 = 1.126\ , \quad b'_2 = -0.07 \quad \rightarrow \left(\frac{R_{si}}{R_{so}}\right) > 0.7 \\ a'_2 = 1.017\ , \quad b'_2 = -0.06 \quad \rightarrow \left(\frac{R_{si}}{R_{so}}\right) \leq 0.7 \end{cases}$
6	Monteith (1973)	$R_n = 0.89[(1-a)R_s + \varepsilon_a(1-d)\sigma(T_a)^4 + d\sigma(T_a)^4 - 0.98\ \sigma(T_a)^4]$	$\begin{cases} d = \left(1.33 - 1.33\left(\frac{R_{si}}{R_{so}}\right)\right)^{0.294} & c \geq 1 \\ d = 0, & c < 1 \end{cases}$
7	Irmak et al. (2003)	$R_n = -0.054\ T_{max} + 0.111 T_{min} + 0.462\ R_s - 49.243 d_r + 50.831$	-

Some of the key parameters of the net radiation models are described here. There are plenty of expressions and reference values for the model parameters in the literature. The surface albedo depends on the nature, texture and moisture of the soil. There are terms that connect Albedo soil to its water content. According to Bavel and Hillel (1976):

$$a = f(\theta_s) = \begin{cases} a = 0.25 & \theta_s < 0.1 \\ a = 0.10 & \theta_s \geq 0.25 \\ a = 0.35 - \theta_s & 0.1 \leq \theta_s < 0.25 \end{cases} \tag{1.6}$$

The Albedo also depends on the angle of sun radiation, so that value changes during the day. Table 1.6 summarizes Albedo's average values for different types of surface textures and roughness.

Table 1.6 - Albedo values for different surface types (Dobos, 2003)

Nature of the surface	**Albedo (a)**
Blackbody	0
Forest	0.05–0.2
Grassland and cropland	0.1–0.25
Dark-colored soil surfaces	0.1–0.2
Dry sandy soil	0.25–0.45
Dry clay soil	0.15–0.35
Sand	0.2–0.4
Mean albedo of the earth	0.36
Granite	0.3–0.35
Glacial ice	0.3–0.4
Light-colored soil surfaces	0.4–0.5
Dry salt cover	0.5
Fresh, deep snow	0.9
Water	0.1–1

There are wide range of models for calculating the air emissivity. Table 1.7 presents some common models.

Table 1.7 - Different air emissivity models

Expression	**Reference**	**Parameters & units**
$\varepsilon_a = 0.52 + 0.206\ {e_a}^{0.5}$	Brunt (1932)	e_a (kPa) is the vapor pressure of air; h_a (%) is the relative humidity of air; e_s (kPa) is the saturated vapor pressure at air temperature T_a (ºC).
$\varepsilon_a = 0.767\ {e_a}^{\frac{1}{7}}$	Brutsaert (1982)	
$\varepsilon_a = 1.24\ \left(\frac{e_a}{T_a}\right)^{\frac{1}{7}}$	Brutsaert (1988)	
$\varepsilon_a = 0.7 + 5.95 \times 10^{-4} e_a\, exp\left[\frac{1500}{T_a + 273.1}\right]$ $e_a = \frac{h_a}{100} e_s$ $e_s = 0.6107\, exp\left[\frac{17.269\ T_a}{T_a + 273.1}\right]$	Idso (1981)	

The soil surface emissivity is also a parameter that depends on different soil properties. The values of some soil surface emissivity are listed in Table 1.8.

Table 1.8 - Soil emissivity values for different surface conditions.

Nature of the surface	**Soil Emissivity (ε_s)**	**Reference**
Soils, dark, wet to light, dry	0.9-0.98	Oke (1987)
Sand, wet	0.98	Van Wijk and Ubing (1963)
Sand, dry	0.95	Van Wijk and Ubing (1963)
Dark clay, wet	0.97	Van Wijk and Ubing (1963)
Dark clay, dry	0.95	Van Wijk and Ubing (1963)
Grass, green	0.96-0.98	Van Wijk and Ubing (1963)
Bare soil (mineral)	0.95-0.97	Gao (2006)
Bare organic soil	0.97-0.98	Gao (2006)
Snow	0.97-0.99	Gao (2006)

1.2.2.2 Sensible Heat (H)

The sensible heat is the amount of heat that is exchanged, without physical phase transition, between multiple bodies forming an isolated system. Many expressions are provided in the litterer for calculating H. Some of these equations are listed in Table 1.9. It should be mentioned that all these models can be used in the soil-atmosphere interaction analysis. However, using the models that consider the resistance terms in the sensible heat are not recommended due to the time-consuming calculation process. On the other hand, it is also important to include the surface temperature in the model in order to take into account the thermal gradient.

Table 1.9 - Different equations for calculating the sensible heat (H).

Expression	**Reference**	**Parameters & unit**
$H = \lambda_a \dfrac{\partial T_a}{\partial y}$	Cui et al. (2005)	λ_a is the thermal conductivity of the air (0.025 W/m/K).
$H = \rho_a C_p \dfrac{(T_s - T_a)}{r_a}$	Chehbouni et al. (1997)	T_s is the the surface temperature (°C); r_a is the aerodynamic resistance (s/m)
$H = h_v\ (T_s - T_a)$	Staniec & Nowak (2016)	h_v is the heat transfer coefficent which depends on the wind speed.
$H = \rho_a c_p k_H \dfrac{\partial T_a}{\partial y}$ $\rho_a = \left(\dfrac{P}{RT_a}\right)\left(1 - \dfrac{0.378 P_v}{P}\right)$	Blight (1997)	P is the atmospheric pressure (kPa); P_v is the vapor pressure (kPa); R is the gas constant (0.287 KJ/Kg/°K); T_a is the air temperature in Kelvin (°K); c_p is the specific heat of air (1.1 KJ/kg/°K); k_H is the diffusivity of the air (m^2/s); y is the elevation (m).

1.2.2.3 Latent heat of vaporization (L_e)

The determination of the latent heat of evapotranspiration (Le) requires the development of theoretical approaches on the basis of the mass transfer equation. Several authors have proposed equations allowing the calculation of this energy balance term. Blight (1997) defines the latent heat flux using the presented equation in Table 1.10. Where L_v is the latent heat (J/Kg), this

parameter is solely a function of temperature. Some authors have proposed calculation methods for this parameter. Frelin (1998) proposed a simple expression for a temperature range between 0 and 180 °C. On the other hand, Priestly and Taylor (1972) proposed an equation based on the Penman's model which takes into account the net solar radiation and the soil heat flux. This can be useful in solving the energy balance equation. Additionally, the Bowen ratio can be used to described L_e in function of the sensible heat (H) which is also another alternative for solving the energy balance equation.

Table 1.10 - Different equations for calculating the latent heat of vaporization (Le)

Expression	**Reference**	**Parameters & unit**
$L_e = \frac{L_v \rho_a \varepsilon\ k_v}{P} \frac{\partial P_v}{\partial y}$ $L_v = 4.186 \times 10^{-3}(597.5 - 0.592\ T)$	Blight (1997) Frelin (1998)	L_v is the latent heat (J/Kg); T is the temperature (°C); ε is the ratio of the molecular mass of water to the molecular mass of air (0.622); k_v is the vapor diffusivity (m2/s).
$L_e = \propto f_{sw} \frac{\Delta}{\Delta + \gamma} (R_n - G)$	Priestly and Taylor (1972)	$\propto$ is a constant equal to 1,26; f_{sw} depends on the volumetric water content at the soil surface.
$L_e = \frac{H}{\beta}$	Bowen (1962)	β is the Bowen's ratio

1.2.2.4 Soil heat flux (G)

The soil heat flux is the energy received by the soil to heat it per unit of surface and time. The soil heat flux is positive when the soil receives energy (warms) and negative when the soil loses energy (cools). According to Cui et al. (2005) and Cui and Zornberg (2008), the soil heat flux can be measured through instrumentation methods or by measurements made directly on the temperature and the water content of the considered soil. They express G, as mentioned in Table 1.11, in function of the soil thermal conductivity. This parameter is the subject of several researches in the literature. Vries (1963) gives a method for determining this parameter based on the fraction of minerals in the soil and the mode of occupation of these minerals in the soil microstructure. Song (2014) points out that this parameter can be measured with specific soil sensors.

Apart from this method, the soil heat flux can also be deduced by the calorimetry method and the restored force method. More details on these methods are available in Ta (2009). There are also empirical relationships in the literature linking G to H or R_n. The latter has been used in the work of Hemmati (2009) as shown in Table 1.11. G is a fraction of R_n with a vegetation term that depends on the surface characteristics. Santanello and Friedl (2003) developed an equation which is a function of R_n and a cosine function. The equation was established based on the hourly simulation results of the energy balance components on different soils. This equation is more adapted for hourly time scale calculations. It should also be mentioned that G can be a constant fraction of R_n based on the provided information in the literature. According to Verhoff et al. (1999) G is 5 to 10% of R_n. Also, as cited by Hemmati (2009), the G/R_n ratio can vary

between 0.3-0.33 for a bare soil surface and vary between 0.03-0.15 in a hydraulic stress condition considering a daily time step.

Table 1.11 - Different equations used for the calculation of the soil heat flux.

Expression	**Reference**	**Parameters & unit**
$G = \lambda_s \frac{\partial T_a}{\partial y}$	Cui et al. (2005)	λ_s is the soil thermal conductivity (W/m/°K).
$G = \xi_s \; e^{-0.4\,LAI} \; R_n$	Hemmati (2009)	ξ_s is a parameter that depend on the type of vegetation cover; $e^{-0.4\,LAI}$ is the term that reduces heat flow due to the presence of vegetation.
$G = R_n . c. cos[\frac{2\pi}{b}(t + 10800)]$	Santanello and Friedl (2003)	b and c are empirical constants.

Recently, the soil-atmosphere interaction was investigated both experimentally and numerically by different authors using different combination of the presented mass and energy balance components (An, 2017; An et al., 2017a; An et al., 2018a; An et al., 2018b; Sedighi et al., 2018)

1.2.3 Water uptake by vegetation

Trees, and more generally vegetation, can be at the origin of a triggering factor or at least an aggravating factor of the shrink-swell phenomenon as mentioned previously. If the vegetation roots grow under the foundations of a construction, the generated soil suction and associated soil movements can cause considerable settlement and consequently structural damages. Some trees are more harmful than others for buildings, Cutler and Richardson (1989) investigated 11,000 claims in England, following the drought of 1976. They suggest that the most harmful plant species for buildings, in presence of expansive clays are oak, poplar, linden, ash and plane tree that are most frequently causing disasters. Poplars, willows, oaks and elms have significant influence distances. Other studies have shown that small trees also have a large radius of influence. Cherry, plum, mulberry, ash and hazel are also potentially dangerous if they are not planted at a sufficient distance from the houses. The GZI (Geotechnical Zone of Influence) which is the volume of the ground in which there is interaction between: the structure or the construction on the ground and the environment (soil), provides the necessary distances between a tree and a construction. In order to avoid any risk damage related to the interactions between vegetation and construction, the GZI should be respected. According to Béchade et al. (2015) the following parameters must be identified in order to determine the GZI of the considered vegetation:

- Number of trees and shrubs, age, height, distance to the construction,
- Slope of the ground, lithology, fineness and permeability of the different layers of soil,
- Possible percolations/water circulation due to the presence of sand in soil layers,
- Influence of root density and depth along with the root suction.

As shown in Figure 1.20, the root water uptake by trees can cause differential soil movements to the constructions if they interact in the GZI. Thus, there is a need for the evaluation of these interactions by experimental and numerical methods.

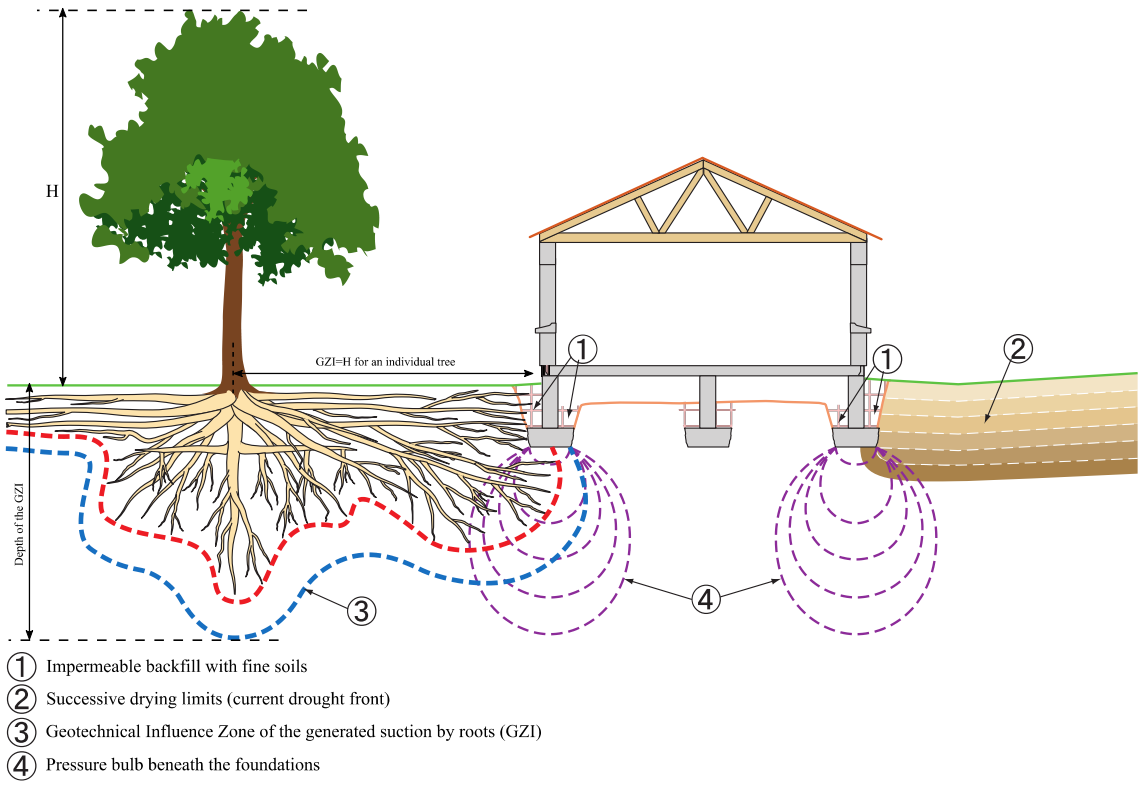

Figure 1.20 - Schematic representation of the influence of trees on the differential soil movements of constructions. (Béchade, 2015)

The influence of the vegetation on the ground movements were analyzed by different authors in the literature. Nyambayo and Potts (2010), developed a root water uptake model which has been coded into a finite element program that could perform coupled hydro-mechanical analyses. The input data of their model includes rainfall, potential evapotranspiration and maximum root depth. Hemmati (2009) investigated the Soil-Vegetation-Atmosphere interaction in a thermo-hydro-mechanical context using the ϴ-Stocks code. The input parameters of the model are the climatic data of the considered site and the soil physical and mechanical properties. Richards et al. (1983) based their calculations on volume change aspects of soils. To calculate the potential soil movement caused by vegetation, the extremes of total soil suction and a quantitative value of the volume change properties of the soil were required. The instability index, has been suggested by these authors as a measure of the soil property and was measured on two of the most expansive and widespread soil types in Adelaide to investigate the induced ground movements. Mathur (1999) used a finite element simulation method to calculate the induced ground movements by the changes in the extraction rate of soil moisture based on a validated root water uptake model and a homogeneous elastic soil domain. The important part of these modeling approaches concerned the determination of the root extraction term in the water flow simulation models which is the essential variable for the assessment of the water uptake by vegetation roots.

The estimation of the root water uptake and the water movement in plant species is crucial to quantify the transpiration rate and hence the water exchange between the ground surface and the atmosphere through the considered species. For understanding the soil-vegetation interactions, mathematical modelling can be used. The flow of water from the soil to roots was first evaluated experimentally by Kramer (1933), and has since been identified in a wide variety of plant species across a range of dry to wet climates.

1.2.3.1 Root water uptake models

There are a wide range of root water uptake models which can be used for estimation of water uptake by plants. The accuracy of the water uptake prediction by plants depends on the selection of the proper mathematical models. Root uptake models are available in different forms i.e. linear, nonlinear, and exponential. Molz and Remson (1981) classified these models into two categories. The first category follows a microscopic approach which has contributed significantly to the understanding of the root water uptake process (Gardner 1960; Hillel et al. 1975). The most common formulations, referred as category-I, are based on the work of Gardner (1964). In general, these equations take the form of the second major type of water uptake term. The second category follows a macroscopic approach, in which the entire root system is treated as a single unit to sum up the effects of all individual roots. In category-II approach, the root water uptake model is represented by a volumetric sink term, which is added to the Richards (1931) equation. There are several models with sink term that are reported in the literature (Feddes et al. 1976; Molz and Remson 1971; Van Genuchten 1987; Vrugt et al. 2001). In some conditions, when the available water in the soil is limited, the extraction term in models was reduced by a factor. This factor is a function of the soil–water pressure head, and the hydraulic conductivity in the root zone and is known as the water uptake stress reduction factor (a). Van Genuchten (1987) expanded the formulation of Feddes by including osmotic stress and proposed an alternative S-shaped function to describe the water uptake stress reduction function, and suggested that the influence of the osmotic head reduction can be either additive or multiplicative. It should be mentioned that in contrast to the Feddes et al. (1978) model, this formulation of the stress reduction factor, a (h,hϕ), does not consider a transpiration reduction near saturation. According to Van Genuchten (1987) such a simplification seems to be justified when saturation occurs for only relatively short periods of time. Table 1.12 shows some of these root water uptake models. In geotechnical engineering applications, the interest is given to the category-II models which has a macroscopic view on the root zone.

Table 1.12 - Different root water uptake models

Model's name	**Equation**	**Reference**	**Parameters**
Gradner	$S = O\ (\delta - \tau - z)kL$	Gardner (1964)	Water potential and soil suction
Molz and Remson	$S = \frac{TL(z)D_s(\theta)}{\int_0^v L(z)D(\theta)dz}$	Molz and Remson (1970)	Soil water diffusivity
Feddes	$S = -\frac{K(\theta)[h_r(z) - h(z)]}{b(z)}$	Feddes et al. (1974)	Pressure head
Feddes	$S(h) = \alpha(h)\ b_{(x,y,z)}\ S_t\ T_{pot}$	Feddes et al. (1978)	Soil suction, root distribution and potential transpiration
Hillel	$S = \frac{\phi_{soil} - \phi_{plant}}{R_{soil} - R_{roots}}$	Hillel and Talpaz (1976)	Total hydraulic head and hydraulic resistance
Van Genuchten	$S(h, h_\phi) = a(h, h_\phi)\frac{T_p}{L_R}$	Van Genuchten (1987)	Soil pressure head and the osmotic head, Potential transpiration

Prasad	$S(h) = a(h)S_{max}$	Prasad (1988)	Soil moisture pressure head, transpiration, and root depth
Li	$S(h) = \frac{K_{z1-z2}\ PT_j}{\lvert z_1 - z_2 \rvert}$	Li et al. (1999)	Potential transpiration and total root length
Vrugt	$S_m(z) = \frac{\beta(z)T_{pot}}{\int_0^{z_m} \beta(z)dz}$	Vrugt et al. (2001)	Root water distribution, maximum rooting depth, and potential transpiration

1.2.3.2 Root density functions

Vegetation roots connect the soil water reservoir to the atmosphere by providing a link between the water fluxes from the soil through the plant directly to the atmosphere. The plant root growth over a generation is comprised of four growth stages. The growth in the initial stage is represented by an exponential growth rate following a linear growth period with a relatively constant rate, and finally the growth becomes progressively less until a steady state is attained. According to Feddes and Raats (2004), the pattern of water uptake by roots is strongly related to root density both in space and in time. The category-II models (macroscopic root water models) consider root density distribution as uniform (Feddes et al. 1978; Prasad 1984) with depth. Later, based on the various linear and nonlinear root distribution patterns, functions that decrease with depth (Prasad 1988; Wu et al. 1999) has been proposed as an improvement to the existing functions. As mentioned by Prasad (Prasad 1988), a discrepancy still exists between the observed and simulated water depletion using the linear model of maximal root water extraction distribution. Thus, a nonlinear model would represent a more realistic root distribution pattern. Figure 1.21 shows different root distribution models adapted by these researchers. Even though nonlinear models could perform better than linear root distribution models, but they cannot completely represent the real root distribution on site. To cope with this issue Vrugt et al. (2001) and (2002) developed root distribution functions in 2D and 3D plans which allow to impose a non-linear root distribution pattern on the soil profile and gives more realistic results of the water extraction in the soil.

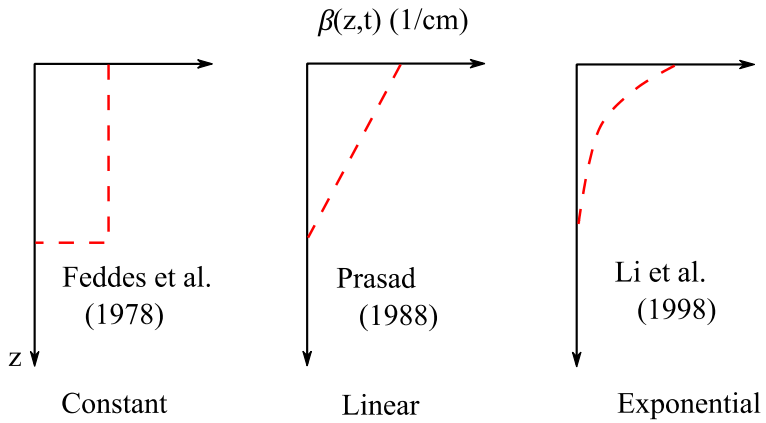

Figure 1.21 - Different root distribution functions.

1.2.3.3 Essential parameters of root uptake models:

The complex parameters of the root uptake models such as root length density and root water potential are chosen by trial and error to make the overall model fit the data. It is difficult to evaluate the performance of the root water uptake models in an unambiguous manner, because,

in most cases they are part of one- or two-dimensional soil water flow formulation. Such models at best are calibrated using field data such as soil moisture contents, rainfall rates or amounts, soil evaporation, and plant transpiration rate (Luo et al. 2003).

The evapotranspiration rate from a cropped (vegetative) surface can be derived from studies of the soil water balance determined from cropped fields or directly measured by lysimeters. This type of evapotranspiration is called the crop evapotranspiration denoted as ET_c and is calculated by multiplying the FAO grass reference evapotranspiration (ET_o), by a crop coefficient which could be in a single or dual form. According to Allen et al. (1998), in the single crop coefficient approach, the effect of transpiration and soil evaporation are combined into a single K_c coefficient. The coefficient integrates differences in the soil evaporation and transpiration rate between the considered vegetal species and the grass reference surface. In the dual crop coefficient approach, the effects of plant transpiration and soil evaporation are determined separately. Two coefficients are used: the basal crop coefficient (K_{cb}) to describe plant transpiration, and the soil water evaporation coefficient (K_e) to describe evaporation from the soil surface. Figure 1.22 shows the concept of the crop evapotranspiration (single crop coefficient) along with the reference evapotranspiration.

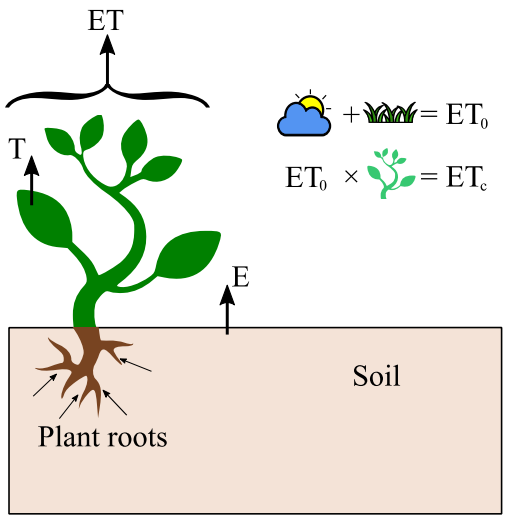

Figure 1.22 - Schematic representation of the reference evapotranspiration (ET0) and the crop evapotranspiration (ETc).

Most of the effects of the various weather conditions are incorporated into the ET_o estimate. Therefore, as ET_o represents an index of climatic demand, K_c varies predominately with the specific crop (plant) characteristics and only to a limited extent with climate. This enables the transfer of standard values for K_c between locations and between climates. This has been a primary reason for the global acceptance and usefulness of the crop coefficient approach and the K_c factors developed in past studies (Allen et al. 1998). The single crop coefficient, K_c, is basically the ratio of the crop ET_c to the reference ET_o, and it represents an integration of the effects of four primary characteristics that distinguish the crop (or plant species) from reference grass which are the surface albedo, the vegetation height, the flux resistance term and the evaporation from the soil. K_c is determined using the tables provided in the FAO 56 guide. It should be mentioned that it can also be modelled numerically based on the climatic data of the considered site in different stages of the vegetation growth. Table 1.13 summarizes these two calculation methods.

Table 1.13 - Two ETc calculation methods.

ET_c calculation	**K_c determination**	**Remarks**
1	Graphical	Based on the reference tables
2	Numerical	Based on tables & climatic data

ET_c needs to be partitioned into soil evaporation (E) and plant transpiration (T) during the different crop or vegetal species growth period. For modeling the distribution of the potential transpiration, which is a surface flux, into a potential root uptake profile throughout the active root zone, partitioning of the crop evapotranspiration into its components of evaporation and transpiration is important. During the growth of a crop, initially soil is bare; in development and end stage, soil is covered by plants partly; and during middle stage, soil is fully covered with plants. These three conditions play a very important role in partitioning the crop evapotranspiration into its components i.e. soil evaporation (E), plant transpiration (T) and interception (I_{int}), which is insignificant and can be neglected. The partitioning of ET_c into T and E can be carried-out using some of the existing models in the literature as listed in Table 1.14.

Table 1.14 - Different models for partitioning ETc into soil evaporation and transpiration.

Model's name	**Equation**	**Reference**	**Parameters**
ENWAT-BAL	$T = (\psi_s + \psi_{c-max} - \psi_c)10^3 \left(\frac{LAI}{r_{plant}}\right)$	Evett and Lascano (1993)	ψ_s is soil water potential; ψ_c and ψ_{c-max} are water potential and maximum water potential of the canopy, respectively (m); r_{plant} is a hydraulic resistance factor of the plant.
SWEAT	$T = \frac{(AH_l - AH_c)}{\lambda\ (r_{st} + r_{lbl})}$	Daamen and Simmonds (1994)	AH_l and AH_c are the absolute humidity of the leaf and the canopy (kg m^{-3}); r_{st} is canopy resistance for stomata r_{lbl} is the canopy resistance for leaf boundary layer
TSEB	$T = \alpha_{PT} f_g \frac{s}{\lambda(s+\gamma)} {R_n}^c$	Priestley and Taylor (1972)	α_{PT} is constant (1.3); f_g is the fraction of green vegetation in the canopy; ${R_n}^c$ is the net radiation at the canopy (Wm^{-2}).
Feddes	$T = ET_c\ [1 - \exp(-k.\,LAI)]$	Feddes et al. (1978)	LAI is the Leaf Area Index; k is a constant equal to 0.6.

The ENWATBAL model was applied by Evett and Lascano, (1993) for partitioning ET_c into evaporation and transpiration using the energy balance approach and vegetation parameters in the transpiration expression which is calculated numerically. In the SWEAT model the interaction between E and T is quantified via a simple two-layer approach without requiring detailed information concerning canopy structure. Unlike other models, SWEAT does not require a soil resistance parameter however, the determination of the canopy resistance parameters is quite a difficult task. The two-source energy balance (TSEB) model was developed to compute ET using

surface temperature data. The required inputs for the model include the net radiation at the canopy surface and another vegetation parameter.

In this section, the main parts of the SVA interaction analysis were presented. The models used in each part of these interactions can be employed based on the modelling purpose. In the next section the modelling approaches for the shrink-swell phenomenon are described along with incorporating SVA interaction analysis in the models.

1.3 Volume change behavior of unsaturated expansive soils

In Geotechnical Engineering and Environmental Geotechnics, the SVAT models were rarely used to evaluate the hydro-thermal, hydro-mechanical or thermo-hydro-mechanical behavior of unsaturated soils. However, some researchers have tried to fill in the gaps between the hydrologist and Geotechnical scientists. Expansive soils (clays) are the most known to be influenced by these environmental solicitations as discussed previously. In fact, the variations of the moisture content in expansive soils can potentially have an influence on the associated volume change and consequently on the soil movements. The understanding of the volume change behavior is crucial for the reliable design of foundations on expansive soils and for the assessment of the drought-hydration periods over time. In this section, a brief introduction of the volume change behavior of unsaturated clayey soils is primarily presented and secondly the experimental studies on the volume change are discussed. Finally, the modelling approaches of the volume change and the soil movements in time are reviewed.

1.3.1 Experimental investigations on volume change behavior of expansive clays

In this section, some advanced laboratory experiments on the volume change of expansive soils are primarily presented. The volume change behavior of clayey soils in these experiments are investigated under drying-wetting cycles. On the other hand, in situ measurements of soil shrinkage and swelling over time, could give insights of the volume change behavior of swelling soils under natural conditions in the environment. These field investigations are also presented in this section.

1.3.1.1 Laboratory experiments under suction cycles

Many studies carried out with the oedometer and controlled suction tests were devoted to the study of the volume change behavior of swelling soils under hydraulic and mechanical stress. Robinet et al., (1997) performed using the oedometer, cyclic sorption-desorption tests under constant vertical stress of 5.5 MPa, on a Boom clay sample obtained from a consolidated sludge. The results are shown in Figure 1.23 where 3 phases can be distinguished in the drying process. A first phase of small variation of the void ratio, associated with low values of suction which corresponds to an over consolidated type of behavior; a second phase where the soil behavior is normally consolidated, corresponding to considerable suction variations, for which the variation of the void ratio is more significant; a third phase, which corresponds to greater suction values, for which the variation of the void ratio is small and reversible. In this last phase, the deformations are elastic. On the other hand, during the wetting process, the slope of the humidification part corresponds approximately to the first drying phase.

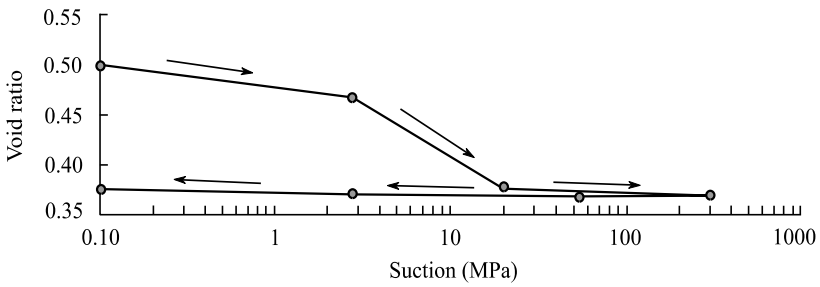

Figure 1.23 - Void ratio changes versus suction for Boom clay sample under a constant vertical stress of 5.5 MPa (Robinet et al., 1997)

Since soils in natural environments are subjected to numerous drying-wetting cycles in time, thus it is of common interest to investigate the fate of their volume change. During the past years, many researchers tried to experimentally investigate the volume change behavior of clayey soils during multiple drying-wetting cycles in order to propose adequate modelling approaches. In this context Dif and Bluemel (1991) and Al-Homoud et al. (1995) found accumulation of shrinkage on their studied samples. Some authors observed an opposite effect. Alonso et al., (2005) have observed both cumulative swelling increase and cumulative shrinkage increase with the number of cycles. They concluded that the cyclic behavior of unsaturated swelling soils depends highly on their initial state (initial moisture content and dry density). The cyclic behavior of swelling soils was also analyzed by different authors, all underlying the effect of initial conditions on the shrink-swell behavior (Basma et al., 1996, Delage et al., 1998, Yahia-Aïssa, 1999, Tripathy et al., 2002, Alonso et al., 2005, Airo Farulla et al., 2007 and 2010, Tripathy and Rao, 2009; Nowamooz and Masrouri, 2009, Nowamooz et al., 2009, Zemenu et al., 2009, Estabragh et al., 2015, Zhao et al., 2017).

Alonso et al. (2005) carried out drying-wetting tests on a mixture of bentonite-sand (80% bentonite), with a pre-consolidation pressure of 5 MPa. They conducted three series of cyclic tests with vertical net stresses equal to 96, 196 and 396 kPa. As shown in Figure 1.24, a cumulative shrinkage at the end of the drying-wetting cycles are observed. The volume change behavior of the material becomes reversible after multiple drying-wetting cycles. The amplitude of this shrinkage decreases with increasing the applied vertical stress.

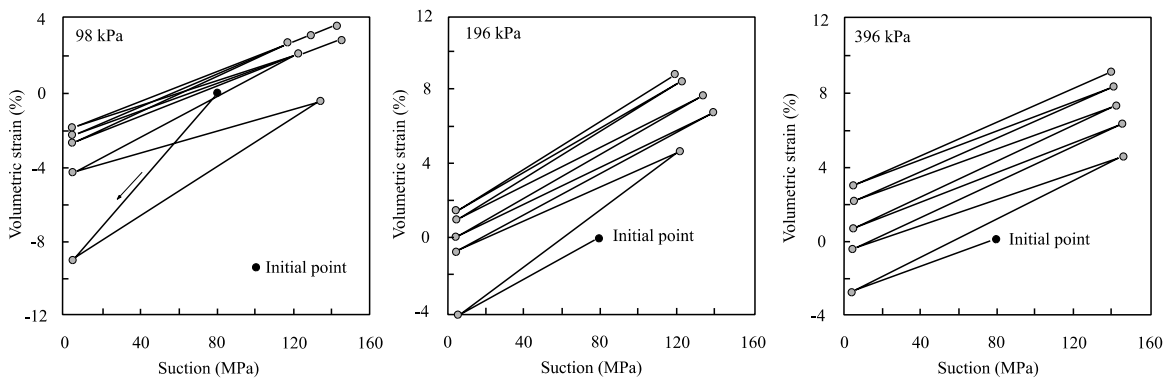

Figure 1.24 - Variation of the volumetric strain during drying-wetting cycles under different vertical stresses. (Alonso et al., 2005)

It should be mentioned that the studied material by Alonso et al., (2005) was in a loose state which is the reason why cumulated shrinkage is observed after several drying wetting cycles.

They concluded that this cumulative shrinkage is dependent on the initial state (density and internal structure) of the soil as well as the applied suction range, which is in a high range in their study (4-130 MPa).

Subsequently, when the number of cycles increases, the volumetric changes of the soil between two consecutive drying-wetting cycles decreases. This shows the tendency of the soil to reach an elastic state (reversible) after undergoing small number of drying wetting cycles. Tripathy and Rao (2009) investigated the effect of shrinkage pattern on the shrinkage -swelling behavior of compacted expansive soils by alternately soaked and dried wetting–drying tests using a fixed-ring oedometer cell. Figure 1.25 shows one of the test results for a sample subjected to wetting–drying cycles with full swelling/full shrinkage and full swelling/partial shrinkage cycles. In their study, the specimen's suction is not controlled, only the water contents of the samples at the reversal points of wetting–drying cycles were measured which allows the determination of a suction value using the retention curve of the studied sample. Shrinkage patterns based on several predetermined heights of the sample were found to provide similar conditions as that of controlled suction tests. For a given pattern of shrinkage, the water content at the end of shrinkage cycles was found to remain nearly unchanged with increasing number of shrink-swell cycles. According to the authors, complementary experiments indicated that there may be an immediate equilibrium state attained by the soil without showing either an increased or a decreased vertical swelling if suction at the shrinkage cycles is less than the past suction; otherwise, the equilibrium state is reached with the soil showing fatigue of swelling. The soil suction at the shrinkage cycles has been shown to affect the reversible volumetric and vertical deformations.

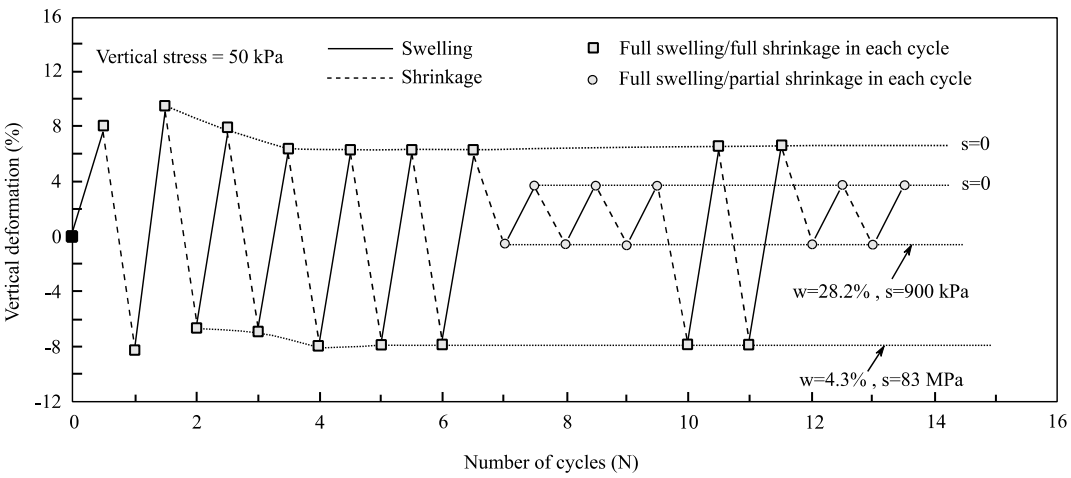

Figure 1.25 - Shrink-swell patterns involving full shrinkage and partial shrinkage cycles (s = suction; w = water content) (Tripathy and Subba Rao, 2009).

The volume change behavior of some natural clayey soils was also investigated in the context of the ARGIC project in Nowamooz (2007). In this research, two natural clayey soils from different sites in France (Deffend and Champenoux) were tested using suction controlled tests. The volume change was investigated by plotting the soil void ratio versus the applied soil suction. Figure 1.26 a) shows the changes in the void ratio of the Champenoux clay samples during a drying-wetting cycle. It can also be observed that the void ratio variations corresponding to each cycle, decrease as the studied samples are deeper (in the core sampling). This could potentially be due to the effect of density. Also, Figure 1.26 b) shows the void ratio changes for the Deffend

clay in two different core sampling depth and at two different locations. It is observed that the three phases in the drying process are present for both samples and the wetting phase slope is approximately the same as the first drying phase.

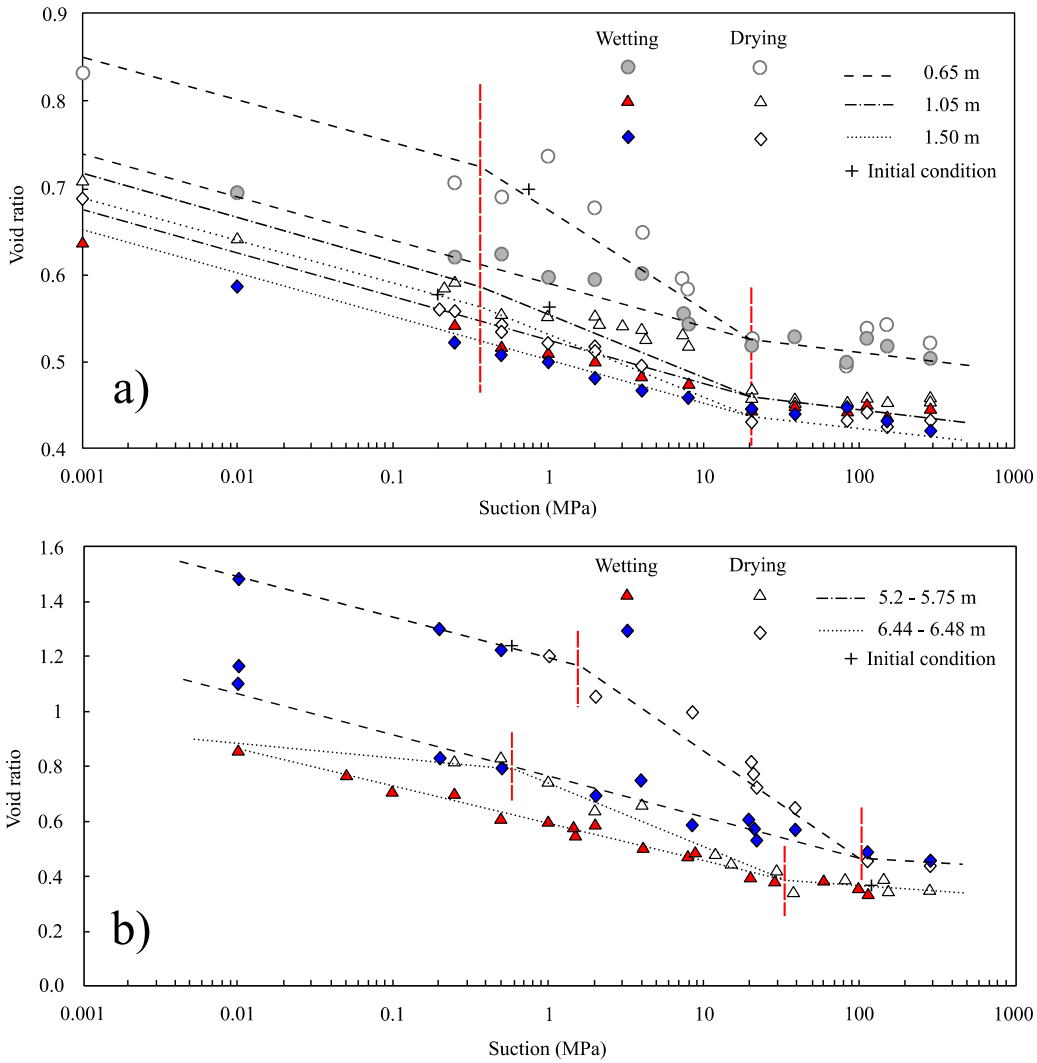

Figure 1.26 - Drying-wetting tests on natural clayey soils: a) Champenoux Clay b) Deffend Clay (Nowamooz, 2007).

The experiments carried out by Nowamooz and Masrouri (2009) on a natural clayey soil in two different dense and loose state show that wetting-drying cycles generates cumulative swelling and cumulative shrinkage respectively as shown in Figure 1.27. These experiments were carried out on the Deffend natural clay at two different initial densities under vertical stresses of 15, 30 and 60 kPa and were plotted in the e-log suction plan. The behavior of these samples (loose and dense) tends to a single and reversible state after several wetting-drying cycles in the imposed suction range (from 0 to 8 MPa). Subsequently any higher suction imposition than 8MPa, could generate larger volume changes and plasticity in the material. It can also be mentioned that the increase in the vertical stress decreases potentially the amplitude of the cumulated swelling of the soil and increases the cumulated shrinkage, regardless of the initial condition of the soil. The

impact can be shown in Figure 1.27 where the void ratio is plotted against the number of experimental records in this test.

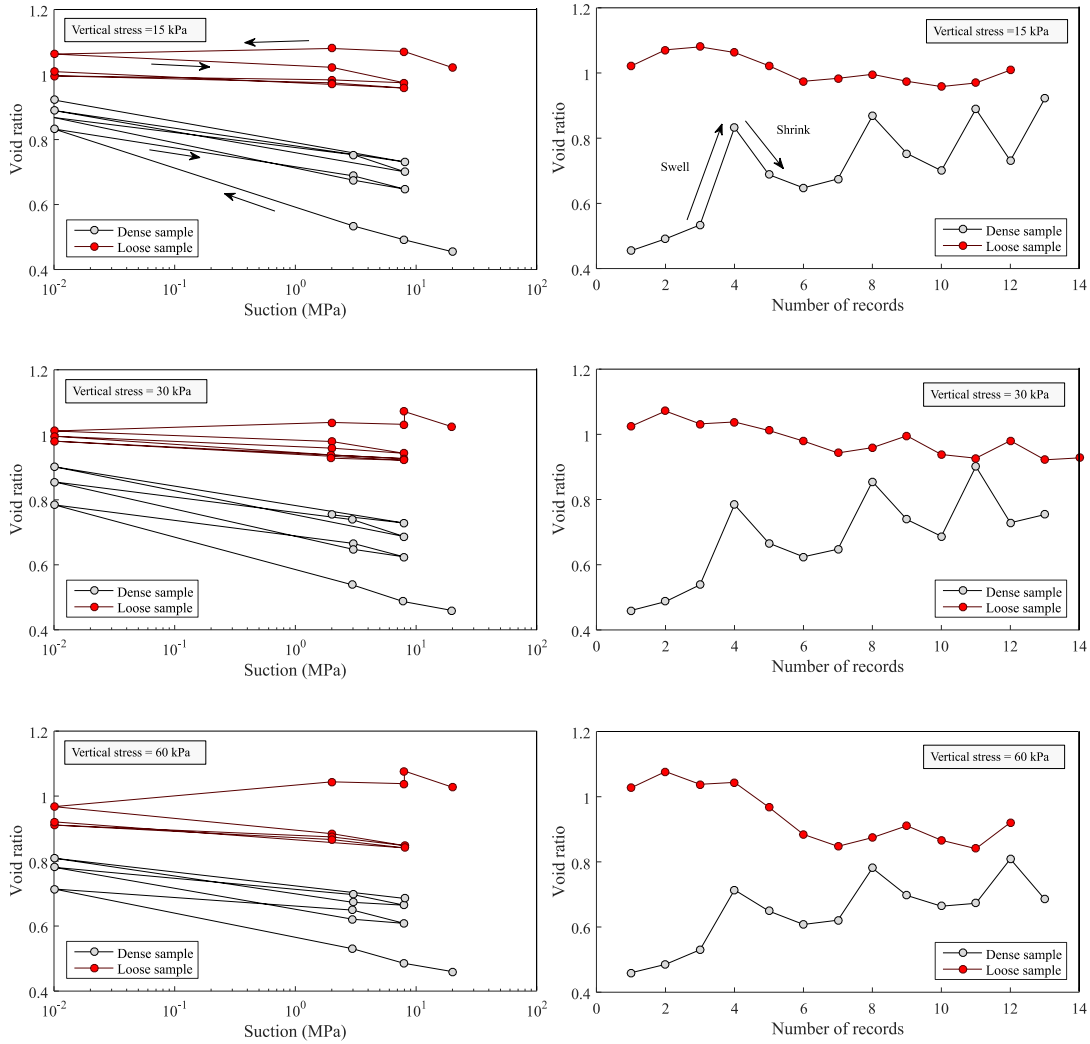

Figure 1.27 - Variation of the void ratio in cyclic controlled-suction paths and versus the number of records at different vertical stresses for both loose and dense clayey soils of the Deffend experimental site (Nowamooz and Masrouri, 2009)

As shown in Figure 1.27, the void ratio tends to lower values for the loose soil as both the number of cycles and the vertical stress increases in the experiment. As for the dense soil, the void ratio increases as the number of cycles increase. However, the cumulative swelling of the dense soil decreases as the vertical stress increases. It can also be observed that the amplitude of the swelling in the dense soil, decreases as the vertical stress increases. However, for the loose soil, the amplitude of the soil shrinkage increases as the vertical stress increases. This highlights the importance of both the loading and initial conditions on the hydro-mechanical response of natural clayey soils to drying-wetting cycles.

Other authors have also analyzed the hydro-mechanical response of some artificial materials in drying-wetting cycles. Zhao et al. (2019) investigated the shrink-swell behavior of a compacted GMZ bentonite on wetting-drying cycles at three initial dry densities under five vertical net stresses with a modified oedometer cell. The specimens were compacted to initial dry densities of 1.3 g/cm^3, 1.5 g/cm^3 and 1.7 g/cm^3 and 50-400 kPa vertical stress range during drying-wetting

cycles. Figure 1.28 shows the evolution of the cumulated strain for the specimens tested with 0 to 110 MPa suction range under a vertical stress of 100 kPa. For specimens with dry density of 1.7 g/cm^3, cumulated swelling strains are observed. For the specimen with dry densities of 1.5 g/cm^3, the cumulated strain is almost zero. However, for the specimen with dry densities of 1.3 g/cm^3, a cumulated shrinkage is observed. Similar results were also obtained by Nowamooz and Masrouri, (2010). It should be mentioned that the effect of the vertical stress on the cumulated shrinkage or swelling of the material shows similar results to Nowamooz and Masrouri, (2009) as reported previously. The loose specimens (1.3 g/cm^3) showed cumulated shrinkage with increasing the number of cycles and the vertical stresses. Approximately the same behavior is observed for the specimens with 1.5 g/cm^3 dry densities. However, for the dense specimens (1.7 g/cm^3), the cumulated swelling increases with the number of cycles and it decreases with the increase of the vertical stress, between the range of 100-400 kPa.

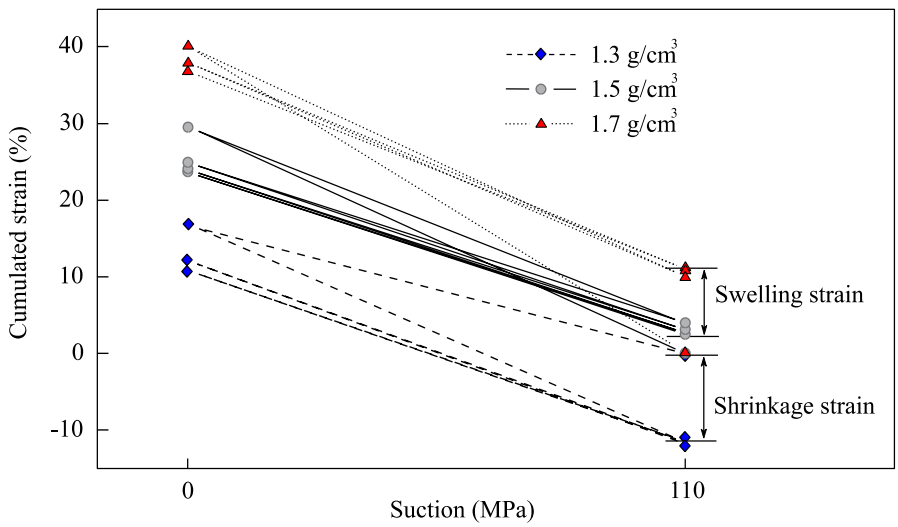

Figure 1.28 - Variation of the cumulated strain with cyclic variations of suction under a vertical stress of 100 kPa for three initial dry densities of the GMZ bentonite. (Zhao et al., 2019)

Based on the presented experimental results in the literature, the following points can be deduced:

- The amplitude of the shrinkage-swelling of a soil is a function of the initial state, particularly its density. Generally, an initially dense soil will tend to have accumulated swelling strains, whereas for an initially loose soil, cumulative shrinkage will tend to occur.
- Regardless of the initial conditions, by increasing the vertical stress on the soil, the amplitude of swelling strains decreases and the soil tends to show cumulative shrinkage. In case of large vertical stress, the generated strains by shrinkage and swelling are neglected due to the highly potential deformations.
- There is generally a tendency to reach an equilibrium stage where the generated strains in the soil become reversible after undergoing drying wetting cycles.

In nature, swelling soils have already undergone a large number of hydraulic stresses. Therefore, the variations of the soil volume are in a reversible domain and independent of the volume changes corresponding to larger suction range. The irreversible volume changes could potentially

happen if the soil is subjected to unusual environmental conditions (i.e. triggering and aggravating factors of the shrink-swell phenomenon) which can generate larger suction, like high intensity drought periods or the presence of other environmental factors such as vegetation.

1.3.1.2 In situ experiments on the volume change:

Although the behavior of clayey soils is well understood from advanced laboratory experiments, but few studies have investigated their in-situ behavior. Vincent et al. (2009) reported some in situ experimentations in different fields in France in the context of the ARGIC project which led to better understanding of the shrinkage-swelling phenomenon under environmental conditions. Andrieux et al., (2011) compared the in-situ observations to laboratory experiment, in a clayey geological formation. Li and Zhang, (2011) studied the in-situ desiccation cracking of clayey soils under natural drying-wetting conditions. Fernandes et al. (2015) studied the in-situ shrinkage and swelling of clayey soils in a geological formation close to the Bordeaux city in the south west of France during several drying-wetting cycles. Different types of sensors were used to continuously measure the movements of the clay bed-rock and the variations in the temperature and water content of the soil. These parameters were correlated with annual climatic variations as measured by the meteorological station. The results obtained thus far represent five drying-wetting cycles, thus enabling a medium-term study of the shrinkage-swelling of a clayey soil over time. As shown in Figure 1.29, shrinkage trends occurred over the first three years, and swelling phases were insufficient to compensate for this shrinkage. To confirm the reliability of the measurements, two different extensometers were used in this site. Similar results were obtained in both extensometers which were therefore, used in the evaluation process.

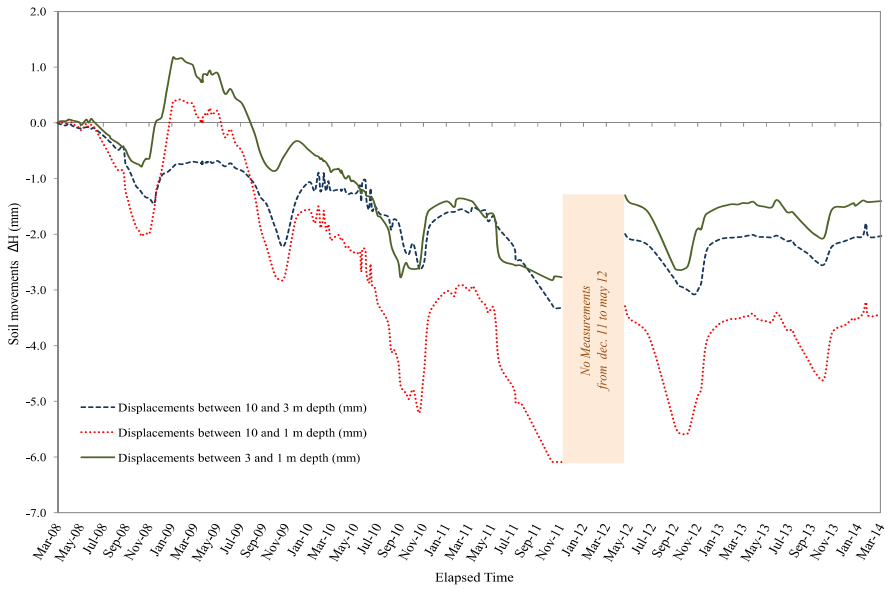

Figure 1.29 - Soil movements measured at 1, 3 and 10 m depth using a TELEMAC extensometer (Fernandes et al., 2015)

The authors also investigated the correlation between the natural climatic conditions of the site with the shrinkage and swelling phases. For this purpose, the infiltration rate or simply the difference between the precipitations and the evapotranspiration was considered as the correlated parameter. This parameter is named as “hydric condition (HC)” in their work. Figure 1.30 shows the hydric condition on each day. In this figure, a negative value for HC represents water loss,

and it can be observed that the swelling ceases as HC becomes negative but is reactivated when HC becomes positive, as observed between March and May 2009. In the same way, shrinkage ceases as HC becomes positive, showing that a water infiltration process has begun.

According to Fernandes et al., (2015), the behavior of the soil at depths between 1 and 3m depends highly on the quantity of effective rain (raw rainfall that is greater than potential evapotranspiration) or water loss (when potential evapotranspiration is greater than raw rainfall).

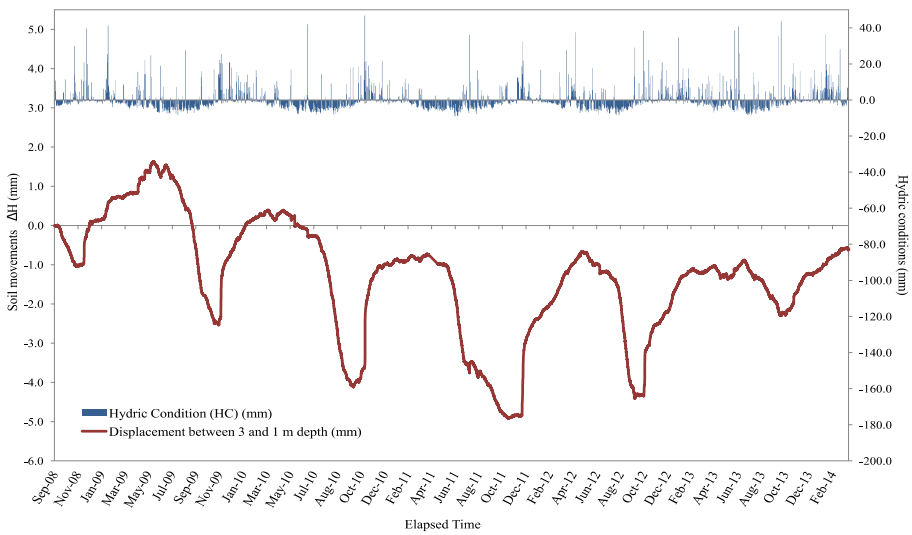

Figure 1.30 - Measured soil movements between 1 and 3m depth and along with the daily hydric condition over the period of September 2008 to February 2014 (Fernandes et al., 2015).

It should also be mentioned that the cumulative hydric conditions are in accordance with the shrinkage and swelling phases. These measurements also demonstrated a cumulative shrinkage over several years with non-negligible movements (of almost 1 cm). The potential trends for shrinkage were also observed during three consecutive cycles which were reversed at the beginning of a second swelling phase. To resume, the 5 year in-situ monitoring results provided reliable understanding of the shrinkage-swelling phenomenon in response to climatic conditions in clayey soils formation.

The in-situ behavior of clayey soils in response to seasonal water content changes were also investigated by geophysical prospection methods by Chrétien, (2010) and Chrétien et al., (2014). In their study, Electrical Resistivity Tomography (ERT) and time domain reflectometry (TDR) were used simultaneously to measure resistivity and soil moisture in an experimental field in order to primarily quantify the soil moisture content, and secondly to compare the resistivity variations obtained from ERT to the soil moisture variations. The obtained results in their study showed the potential of quantifying the seasonal soil moisture content, and especially of detecting a rapid increase in humidity based on soil spatial heterogeneity. Figure 1.31 presents an ERT profile carried out for investigating the seasonal moisture variations. The data showed that the beginning of the drying phase in the top layers started between May and June 2009, which is usually a period when the soil and vegetation cover undergoes considerable hydric stress (maximum evapotranspiration coupled with low effective rains). A relative resistivity profile at two different times (as indicated in Figure 1.31) were compared to water content profile variations at the same spot. Results indicate that only the first meter of the soil profile is influenced by climatic conditions and that there is a reliable correlation between these two parameters.

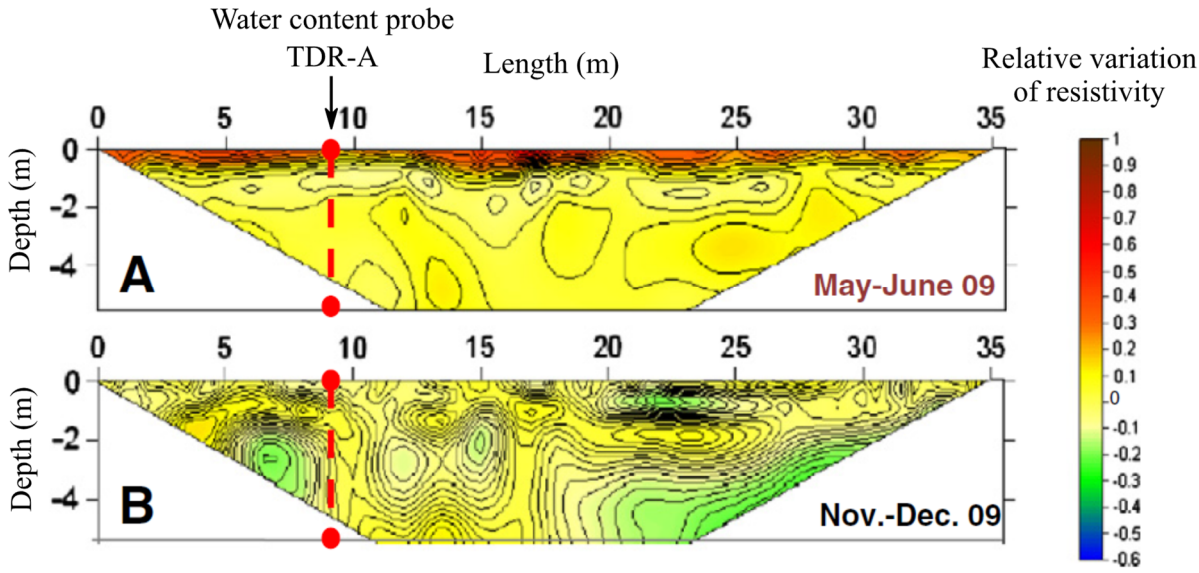

Figure 1.31 - ERT profile between May and June 2009 in the Pessac site in Bordeaux, France (Chrétien et al., 2014)

According to Chrétien et al., (2014), these results also allow to follow and visualize the evolution of the desiccation process in clayey soils. The process is different for wetting and drying, and this information is helpful in better understanding soil deformations on heterogeneous construction sites. In conclusion, ERT proved to be a useful tool for delimiting soil facies based on their drying and humidification behavior.

The presented studies were mostly focused on the monitoring of the soil behavior and the climatic parameters without considering the monitoring of an eventual structure interacting with these soils. However, better understanding of the shrink-swell phenomenon and its associated damages on lightweight constructions could be achieved by monitoring the climatic parameters, the soil physical properties and the structural behavior of the construction.

1.3.2 Modelling approaches of the volume change behavior

In order to model the mechanical behavior of saturated soils, the concept of effective stress $(\sigma - u_w)$ was introduced by Terzaghi in 1936. He stated that the stress at any point of a soil mass can be expressed by the total stress. However, if the voids in the soil are filled with water, the stress will be composed of two parts: the effective stress (σ') and the identical water pressure in all directions. This effective stress is explained by: $(\sigma' = \sigma - u_w)$ and governs all measurable effects of stress variation, such as compression, variation in shear strength, and volume change. To describe the behavior of unsaturated soils, the concept of soil suction, which is the negative pressure relative to atmospheric pressure, is involved. The soil suction is described as the difference between the air and water pressure $(u_a - u_w)$ in the pores. The gaseous phase (air) surrounds the soil when a saturated soil begins to dry from a precise pressure which is the air entry value on the water retention curve that connects the moisture content or the saturation degree to the soil suction as shown in Figure 1.32. It is conventionally accepted that the soil becomes unsaturated when the suction level exceeds that of the inflow value. In other words, a soil reaches an unsaturated water state as soon as air is present in the pores in addition to water.

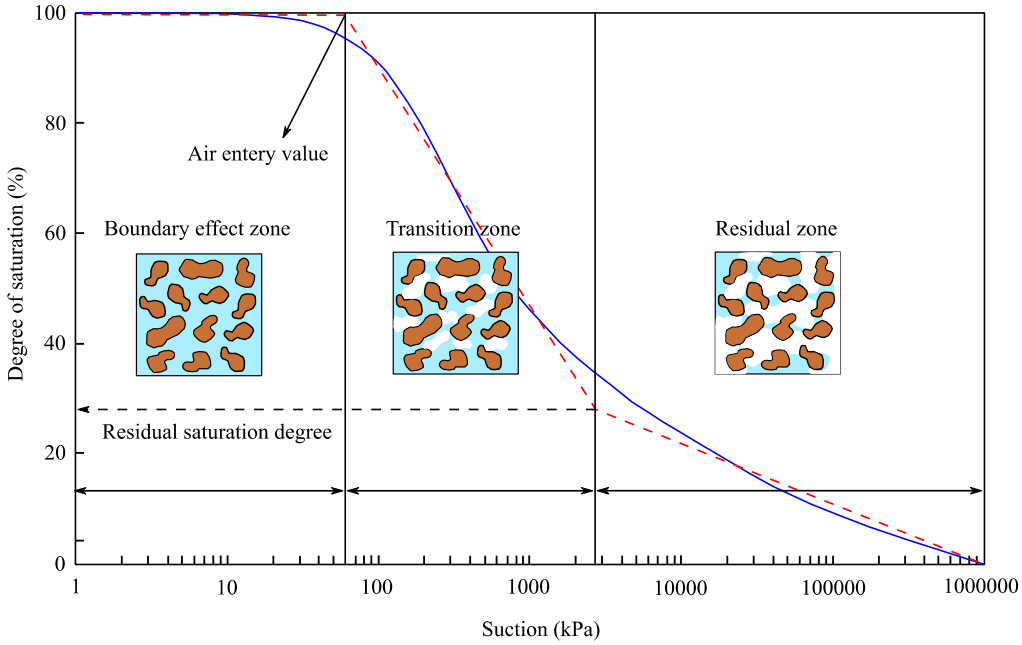

Figure 1.32 - Typical soil-water characteristic curve illustrating different desaturation zones (after Vanapalli and Fredlund, 2000)

This concept has been the subject of study in the unsaturated soil mechanics research community which consequently led to the development of constitutive soil models. The volume change behavior of expansive clayey soils is usually modelled using advanced modelling theories with the definition of additional parameters. In this section, some modelling approaches of clayey soils volume change (soil movements) in time are presented. The prediction of the soil movements over time has been widely investigated by different researchers in the past years (e.g. Alonso et al., 1999; Briaud et al., 2003; Vu and Fredlund, 2004, 2006; Zhang, 2004; Wray et al., 2005; Overton et al., 2006; Nelson et al., 2007; Hemmati, 2009; Adem & Vanapalli, 2013; Zhang & Briaud, 2015; Karunarathne et al., 2018). According to Briaud et al., 2003, all models for predicting the soil movements in time must include two components: The prediction of the seasonal water content and soil suction changes over time using unsaturated moisture flow equation; and the prediction of the volume change behavior by linking the seasonal suction/water content changes to it using constitutive soil models. The current models were classified in three categories by Adem & Vanapalli, (2014) in a review article and also by Briaud et al. (2003) in their modelling work: a) consolidation theory-based methods that use the matric suction and the net stress as state variables b) water content-based methods that use the soil water content as a state variable, and c) suction-based methods that use the matric suction as a state variable.

1.3.2.1 Consolidation theory-based methods:

The consolidation theory in unsaturated soils, links the coupled hydraulic and mechanical process during volume change behavior. The volume change constitutive models are characterized in two type of elastic and elastoplastic models. Fredlund and Morgenstern (1976) and Lloret et al (1987) have proposed elastic models relating the volume change increments to the increments of the net stress and the soil suction. On the other hand, one of the well known elastoplastic models developed by Alonso et al. (1990) for unsaturated soils is the Barcelona Basic

Model (BBM). This model allows the determination of the soil volume change in different conditions by taking into account a considerable number of parameters. The model is based on two independent stress variables (net stress and the soil suction) as for elastic models.

The volume change behavior of the soil was widely investigated in the literature by considering the soil as an elastic material. To describe the deformation state of an unsaturated soil in an elastic domain, two constitutive relationships have been suggested. One for the soil structure (void ratio, volumetric strain), and the other one for the water phase (in terms of water content or saturation degree). Assuming that the soil behavior is like an incrementally isotropic, linear elastic material, the constitutive relationship for the soil structure can be written as suggested by Fredlund and Rahadjaro, (1993) as below:

$$\begin{aligned} d\varepsilon_v = d\varepsilon_x + d\varepsilon_y + d\varepsilon_z &= \frac{3(1-2\mu)}{E}\ d(\sigma_m - u_a) + \frac{3}{H_s} d(u_a - u_w) \\ &= \frac{1}{B_s} d(\sigma_m - u_a) + \frac{3}{H_s} d(u_a - u_w) \end{aligned} \tag{1.7}$$

where ε_v is the volumetric soil strain; ε_x, ε_y and ε_z are the normal strains in the x, y, and z directions, respectively; σ_m is the mean total normal stress, and $\sigma_m = (\sigma_x + \sigma_y + \sigma_z)/3$, in which σ_x, σ_y, and σ_z are the normal stresses in the x, y, and z directions, respectively; μ is the Poisson's ratio; E is the modulus of elasticity for the soil structure with respect to a change in net normal stress; H_s is the modulus of elasticity for the soil structure with respect to a change in matric suction; and B_s is the bulk modulus of soil.

According to Fredlund and Morgenstern, (1976), the constitutive equation for the water phase defines the water volume change in the soil element for any change in the total stress and matric suction. By assuming that water is incompressible, the constitutive equation for the water phase can be formulated as a linear combination of the stress state variables changes as follows:

$$\begin{aligned} \frac{dV_w}{V_0} &= \frac{d(\sigma_x - u_a)}{E_w} + \frac{d(\sigma_y - u_a)}{E_w} + \frac{d(\sigma_z - u_a)}{E_w} + \frac{d(u_a - u_w)}{H_w} \\ &= \frac{3}{E_w} d(\sigma_m - u_a) + \frac{1}{H_w} d(u_a - u_w) \end{aligned} \tag{1.8}$$

where V_w is the volume of water in the soil; V_0 is the initial volume of the soil; E_w is the volumetric modulus of water associated with a change in net normal stress; and H_w is the water volumetric modulus associated with a change in matric suction. The constitutive relationships for volume change of soil structure and water phase in a compressible form can be decried as developed by Fredlund and Morgenstern (1976):

$$d\varepsilon_v = \frac{dV_v}{V_0} = m_1^s\ d(\sigma_m - u_a) + m_2^s\ d(u_a - u_w) \tag{1.9}$$

$$d\theta = \frac{dV_w}{V_0} = m_1^w\ d(\sigma_m - u_a) + m_2^w\ d(u_a - u_w) \tag{1.10}$$

where m_1^s and m_2^s are the coefficients of total volume change with respect to a change in net normal stress and a change in matric suction, respectively; m_1^w and m_2^w are the coefficients of

pore water volume change with respect to a change in net normal stress and a change in matric suction, respectively. The coefficients of total volume changes can be calculated from constitutive surfaces for void ratio and soil water content. The following complementary relationships can also be provided:

$$m_1^s = \frac{1}{B_s} \ , \ m_2^s = \frac{3}{H_s} \ , \ m_1^w = \frac{3}{E_w} \ , \ m_2^w = \frac{1}{H_w} \tag{1.11}$$

The five unknowns (soil displacement in x, y and z, water volume change and air volume change) can be obtained from three equilibrium equations for the soil structure and two continuity equations (water and air phase continuities). However, the pore air pressure is generally assumed to be atmospheric and remains unchanged during the consolidation process. Thus, only the stress equilibrium condition and the water flow continuity can be considered in the analysis. Based on the continuum mechanics theory, the stress state for an unsaturated soil should satisfy the equilibrium conditions (the sum of the net total stress and the body force vectors should be equal to zero). The differential equations for the soil skeleton phase in a 3D problem are expressed as below:

$$\begin{aligned}
&(\lambda + G_s)\frac{\partial \varepsilon_v}{\partial x} + G_s \nabla^2 u - (3\lambda + 2G_s)\frac{1}{H_s}\frac{\partial (u_a - u_w)}{\partial x} + b_x = 0 \\
&(\lambda + G_s)\frac{\partial \varepsilon_v}{\partial y} + G_s \nabla^2 v - (3\lambda + 2G_s)\frac{1}{H_s}\frac{\partial (u_a - u_w)}{\partial y} + b_y = 0 \\
&(\lambda + G_s)\frac{\partial \varepsilon_v}{\partial z} + G_s \nabla^2 w - (3\lambda + 2G_s)\frac{1}{H_s}\frac{\partial (u_a - u_w)}{\partial z} + b_z = 0
\end{aligned} \tag{1.12}$$

where G_s is the shear modulus $\left(G_s = \frac{E}{[2(1+\mu)]}\right)$; u, v, and w are the displacements in the x, y, and z directions, respectively; b_x, b_y, and b_z are the body forces in the x, y, and z directions, respectively; $\lambda = \frac{\mu E}{(1+\mu)(1-2\mu)}$; $\nabla^2 = \frac{\partial^2}{\partial x^2} + \frac{\partial^2}{\partial y^2} + \frac{\partial^2}{\partial z^2}$.
By considering the time derivative of the water phase constitutive equations, and the Darcy's law in the water phase continuity equation, the differential equations for the water phase developed by Fredlund and Hasan, (1979) are expressed as below:

$$\begin{aligned}
m_1^w \ \frac{d(\sigma_m - u_a)}{\partial t} + m_2^w \ \frac{d(u_a - u_w)}{\partial t} \\
= \frac{\partial}{\partial x}\left[k_w^x \frac{\partial}{\partial x}\left(\frac{u_w}{\rho_w g} + Y\right)\right] + \frac{\partial}{\partial y}\left[k_w^y \frac{\partial}{\partial y}\left(\frac{u_w}{\rho_w g} + Y\right)\right] \\
+ \frac{\partial}{\partial z}\left[k_w^z \frac{\partial}{\partial z}\left(\frac{u_w}{\rho_w g} + Y\right)\right]
\end{aligned} \tag{1.13}$$

where k_w^x, k_w^y, and k_w^z are the hydraulic conductivity functions in the x, y, and z directions, respectively. The extension of this equation was used by Fredlund and Rahardjo (1993) to express the differential equation for the water phase based on the water content changes ($d\theta$):

$$\left(\frac{m_1^w}{m_1^s}\right)\frac{\partial \varepsilon_v}{\partial t} + \left(m_2^w - \frac{m_1^w m_2^s}{m_1^s}\right)\frac{d(u_a - u_w)}{\partial t} = \frac{\partial}{\partial x}\left[k_w^x \frac{\partial}{\partial x}\left(\frac{u_w}{\rho_w g} + Y\right)\right] + \frac{\partial}{\partial y}\left[k_w^y \frac{\partial}{\partial y}\left(\frac{u_w}{\rho_w g} + Y\right)\right] + \frac{\partial}{\partial z}\left[k_w^z \frac{\partial}{\partial z}\left(\frac{u_w}{\rho_w g} + Y\right)\right] \tag{1.14}$$

According to the authors, Eq. (1.12) and (1.14) together are the differential equations for the coupled soil consolidation that can be used to predict the volume change behavior of unsaturated expansive soils.

- *Fredlund and Rahardjo (1993) model:*

Fredlund and Rahardjo (1993) developed a nonlinear elastic model, based on the concept of state surface, to model the hydro-mechanical behavior of unsaturated soils. The concept of state surface used in this model estimates the volume change of the soil from its initial state and its final state. Moreover, this model does not take into account the stress path, i.e. the state surface is unique regardless of the stress path. They indicated that the swelling phenomenon can be described as a nonlinear elastic behavior within the framework of the unsaturated soil consolidation theory. They assumed that the soil is isotropic, that the air phase is continuous, and that the soil particles as well as the water in the pores are incompressible. The authors consider that an unsaturated soil is composed of four phases, two of which, the skeleton and the adsorbed water, have zero volume variation. The other two phases (air and free water) are governed by the flow rules. The corresponding equations are expressed previously for the soil structure and the water phase. The constitutive laws of the solid phase (soil structure) and the water volume change of unsaturated soils are presented in Figure 1.33.

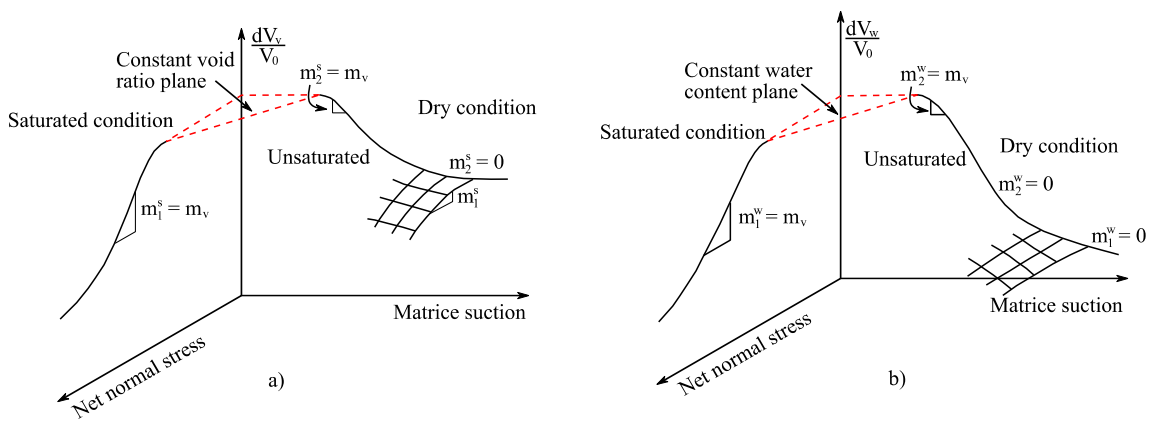

Figure 1.33 - Constitutive surfaces for an unsaturated soil (a) the solid skeleton phase, (b) the water phase (Fredlund and Rahardjo, 1993)

Using these two slopes m_1^s and m_2^ss, Fredlund and Rahardjo defined the mechanical elastic modulus (E) and the water elastic modulus (H) for uniaxial, biaxial or triaxial loading conditions by introducing soil compression indices. The model uses two elastic modules for the water and mechanical parts which are completely separated. In the definition of elastic modulus, the compression indices (slopes) are not related to each other. Therefore, this model is more suitable for an uncoupled calculation.

- *Vu and Fredlund (2004) method:*

Vu and Fredlund (2004) extended the general consolidation theory of unsaturated soils and proposed a method for the prediction of 1D, 2D, and 3D soil heave over time. Based on Fredlund and Rahardjo (1993) work, six mathematical functions for state surface of swelling soils were proposed. The governing equations for soil structure and for water phase were solved numerically using uncoupled and coupled analyses. The analysis results include soil heave and matric suction changes obtained during the transient process. The uncoupled solutions can be achieved relatively easier than the coupled solutions by considering independently, the non-linear functions of soil properties involved in water flow or stress deformation process. A case history of a floor slab of a light industrial building located in Regina, Saskatchewan, Canada, was used by Vu and Fredlund (2004) to test the validity of their prediction method. The total heave predicted under the steady state condition was in a good agreement with the measured heave.

Vu and Fredlund, (2006) investigated the challenges associated with the numerical modelling of unsaturated expansive soils. The challenges are primarily related to the quantification of the void ratio constitutive surface, the characterization of the void ratio constitutive surface at low stresses and (or) suction, and the solution of coupled equations with several nonlinear unsaturated soil property functions. These challenges were overcome by providing a continuous, smooth void ratio constitutive surface based on the soil swelling indices obtained from the conventional oedometer tests. Based on the authors' conclusions, it was suggested that an uncoupled analysis may be adequate for most heave prediction problems. The determination of the volume change coefficients requires the establishment of the void ratio and water content constitutive surfaces which were obtained from the consolidation tests or suction controlled triaxial tests. It should be mentioned that these kinds of tests are usually time consuming and require advance laboratory equipment which are mostly expensive. The advantage of this model is its simplicity and its ability to model the behavior of the swelling soil. Its disadvantage is that it does not distinguish the elastic domain from the plastic domain. Thus, the behavior on a single constitutive surface remains reversible. Therefore, this model is considered as nonlinear elastic even if the considered surface models the plastic deformation of the soil. Moreover, the dependence of the void ratio on the stress path is not taken into account in this model.

This model was employed by Jahangir (2011) and Jahangir et al., (2013) to develop an analytical framework for the soil-structure interaction during drought periods. The hydro-mechanical behavior of the swelling soil was modeled using the presented state surface approach and the behavior of the structure was investigated with the Euler–Bernoulli beam theory, and the ground behavior was investigated with a Winkler-derived model. Figure 1.34 a) shows the state surface used for the Regina clay (analyzed by Vu and Fredlund, 2004 and 2006). The mechanical and hydraulic coupled analysis was considered in this state surface through the compressibility of soil with respect to the applied load and the suction. Figure 1.34 b) shows the concept of the modelling approach in their study. The soil was considered to be a homogenous and isotropic medium, and its variability under the structure was not considered. The analytical model's results were compared with those obtained using a numerical model performed with an elastic-plastic model (BExM, which will be described in next sections) for unsaturated swelling soils. The results showed good agreement between the models. However, the results were not compared to actual in situ and real case field measurements. The analytical framework was then used to

investigate the deflection transmission ratio for different building types on three types of expansive soils undergoing different possible suction variations.

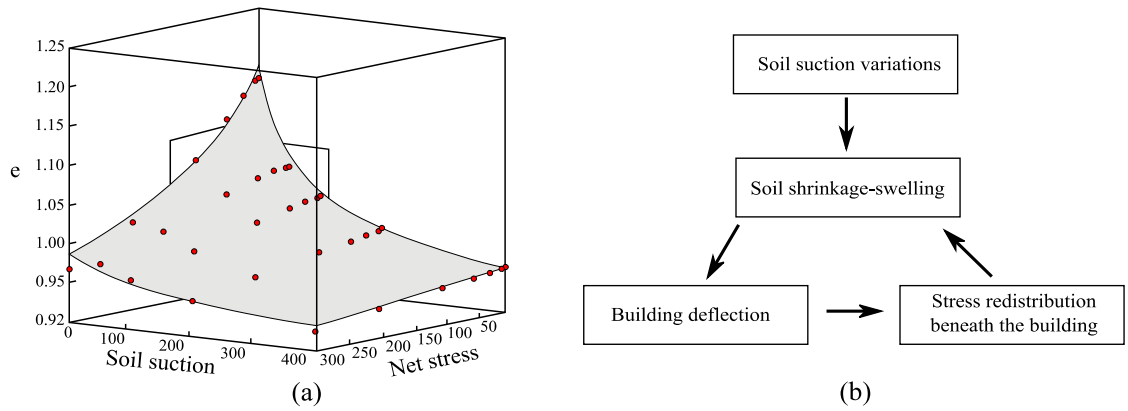

Figure 1.34 - a) State surfaces proposed by Vu and Fredlund, (2004) and fitted for Regina clay, and b) the concept of the hydro-mechanical coupling (Jahangir et al., 2013).

- *Zhang (2004) method:*

Zhang (2004) investigated the coupled consolidation for both saturated and unsaturated soils by simultaneously using the constitutive surfaces. A thermodynamic approach was used to explain the coupled consolidation process for saturated and unsaturated soils following Terzaghi's 1D consolidation theory for saturated soils. The coupled consolidation theory for saturated and unsaturated soils is included with the differential equations for soil structure and water phase. However, to derive the differential equation for water phase, Zhang assumed that the continuity equation for the water phase is similar to that for the heat transfer based on thermodynamics principles. Commercial software such as ABAQUS and ANSYS were used to solve the coupled consolidation theory.

The method was applied to the Arlington site in Texas, USA where four spread footings were simulated over a period of 2 years on expansive soils. The footings were influenced by different environmental factors such as climatic conditions and vegetation. The ABAQUS software was used to calculate the soil movements in time by introducing atmospheric boundary conditions in the software. The soil-structure interaction was also taken into account at the soil-slab interface.

The same site was also modeled by Briaud et al. (2003) to investigate the damage caused by expansive soils to both concrete and asphalt pavements and by Zhang and Briaud (2015) for modeling the 3D behavior of residential buildings on expansive soils under different environmental conditions. In this recent study, the differential equations for the soil structure were used along with the differential water phase based on Fredlund and Rahardjo (1993) model. The geometry of the model is presented in Figure 1.35. The method was validated based on the in-situ soil movements of the four footings. The most significant changes made in this research were the inclusion of climatic factors to determine boundary conditions and simulations of fully coupled volume change behavior for unsaturated expansive soils and fully coupled soil–structure interactions (Zhang & Briaud, 2015).

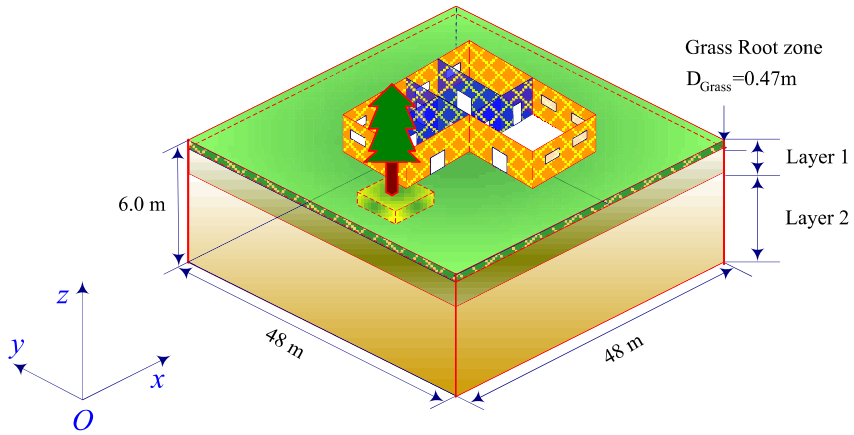

Figure 1.35 - The 3D geometry of the Arlington site modelled in ABAQUS (Zhang & Briaud, 2015)

Figure 1.36 shows the comparison of the average values of the predicted soil movements at four corners of the considered footing with the measured soil movements of the four footings. The comparison of the predicted movements with the measured movements of each footing did not lead to a good comparison particularly in the last year where there the soil tends to swell. However, considering the average values of the measured soil movements could lead to better comparison results. In the study performed by Zhang (2004), the average measured soil movements were considered in the comparison which led to better agreement with the predicted values.

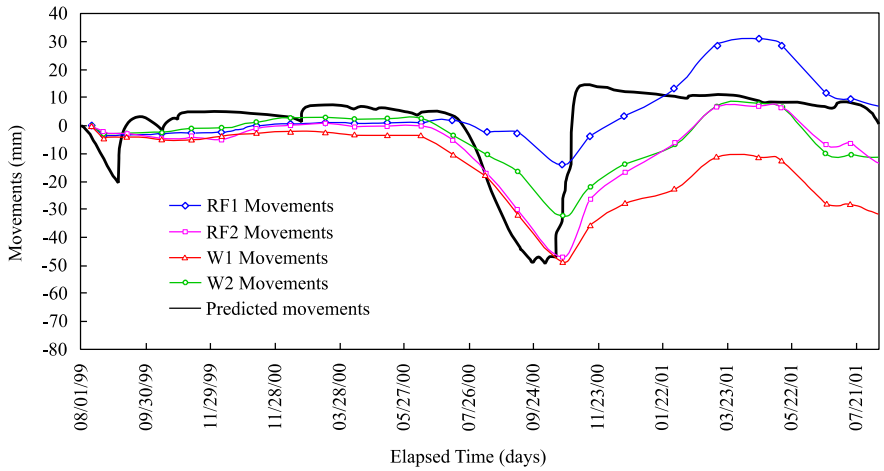

Figure 1.36 - Comparisons between the observation and simulation results of the Arlington site (Zhang & Briaud, 2015; Zhang, 2004)

This method is a comprehensive approach for modeling the water flow and the soil movement over time. However, finite element computer programs are required to solve the complex numerical solutions in this approach in order to address the analogy between the thermal and hydraulic problems. Using constitutive surfaces in this approach contributed to the use of a unified system to simulate the volume change behavior of expansive soils under both saturated and unsaturated conditions. However, the application of these 3D constitutive surfaces is faced with limitations in practice. It should also be mentioned that the tests used in this approach to construct the 3D constitutive surface of the soil are not conditioned as usually experienced on the field. In addition to that, conventional geotechnical laboratories are not equipped with the necessary equipment

and material to perform the required tests which are also time consuming and not cost effective at some point.

- *Barcelona Basic Model (BBM):*

Since elastic models does not take into account the distinction between reversible and irreversible strains, elastoplastic constitutive models were introduced. Lloret and Alonso (1980) concluded that the constitutive models based on the concept of elastoplasticity provide better understanding of expansive soil behavior particularly, the issues associated with the stress path dependency and soil collapse upon wetting. Alonso et al. (1990) are among the first researchers to propose an integrated elastoplastic model for the volume change behavior and shear strength of unsaturated soils based on two independent stress variables: suction and net stress. This model is called the BBM model (Barcelona Basic Model). The authors considered that the surface-state approach, with a single constitutive surface to describe the behavior of unsaturated soils, cannot be used to treat irreversible soil deformations due to unloading (or hydration) in the soil, since stress path dependence in unsaturated soil is not considered in the conventional state surface approach.

The BBM is characterized by two yield curves whose hardening laws are controlled by total plastic volumetric deformation (Figure 1.37). For isotropic stress conditions, the two yield surfaces F_1, F_2 are defined in terms of the net mean stress $p = (\sigma_1 + \sigma_2 + \sigma_3)/3 - u_a$, deviatoric stress $q = \sigma_1 - \sigma_3$, and the matric suction. The first yield surface, known as the loading collapse (LC) yield surface, is related to irreversible compression that can occur on an increase of load (loading strains) or decrease of suction (collapse strains) $F_1 = q^2 - M^2(p + p_s)(p_0 - p) = 0$. In this function, M is the slope of the critical state line as indicated in Figure 1.37, p_s is the parameter related to the effect of suction on the cohesion of the soil, and p_0 is the preconsolidation stress at the current value of suction and are described as follows:

$$p_s = k.s \quad ; \quad \frac{p_0}{p^c} = \left(\frac{p_0^*}{p^c}\right)^{\frac{[\lambda(0)-\kappa]}{[\lambda(s)-\kappa]}} \tag{1.15}$$

where k is a parameter describing the increase in cohesion with suction; p_0^* is the preconsolidation stress at zero suction (in saturated condition); p^c is the reference stress; κ is the normal swelling index; and $\lambda(s)$ and $\lambda(0)$ are the compression indices of the soil at the current value of suction and at the saturated condition (s = 0), respectively. $\lambda(s)$ is described as a function of the soil suction as below:

$$\lambda(s) = \lambda(0)[(1 - r)\exp(-\beta_s s) + r] \tag{1.16}$$

where β_s and r are soil parameters. The F_1 yield function describes a family of elliptical yield curves associated with different suction values by varying p_0 and p_s with suction.

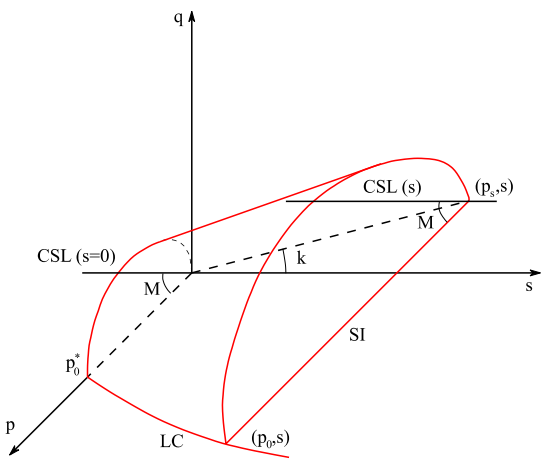

Figure 1.37 - Yield surface of the Barcelona basic model (BBM) (Alonso et al., 1990)

The second yield equation, known as the suction increase (SI) yield surface (shown in Figure 1.37), defines the irreversible compression that can occur on increasing suction (drying phase) as $F_2 = s - s_0 = 0$. In this function, s_0 is the maximum previously attained value of the suction. Since it is assumed in the model that the soil stays elastic and isotropic within the yield surfaces, the elastic volumetric strain is expressed as below:

$$d\varepsilon_v^e = \frac{\kappa}{1+e}\frac{dp}{p} + \frac{\kappa_s}{1+e}\frac{ds}{s+p_{atm}} \tag{1.17}$$

where κ_s is the suction swelling index, e is the void ratio, and p_{atm} is the atmospheric pressure (i.e. 101.3 kPa). Once the net mean stress p reaches the yield value p_0, the plastic component of volumetric strain caused by yielding on the LC yield surface can be expressed as:

$$d\varepsilon_{vp}^p = \frac{\lambda(0)-\kappa}{1+e}\frac{dp_0^*}{p_0^*} \tag{1.18}$$

The same way as the net mean stress, with an increase in suction, when the yield suction $s = s_0$ is reached, the plastic volumetric strain caused by yielding on the SI yield surface is expressed as follow:

$$d\varepsilon_{vs}^p = \frac{\lambda_s-\kappa_s}{1+e}\frac{ds_0}{s_0+p_{atm}} \tag{1.19}$$

Plastic or irreversible deformations, control the positioning of these two yield surfaces (LC, SI) using the $d\varepsilon_{vp}^p$ and $d\varepsilon_{vs}^p$. To couple both yield surfaces assuming that their position is controlled by the total volumetric strain could simply be the sum of the volumetric plastic strains in each yield surface ($d\varepsilon_v^p = d\varepsilon_{vp}^p + d\varepsilon_{vs}^p$). Each plastic strain equation is then used to describe the hardening laws. The BBM was widely used in the literature to study the coupled behavior of unsaturated expansive soils. Event thought the calculation of the soil movements in time is possible with the adequate constitutive laws but the disadvantages and the limitations should also be taken into account.

- *Barcelona Expansive Model (BExM):*

Alonso et al. (1990) and Gens and Alonso (1992) stated that the BBM provides a simple representation of swelling, but is unable to reproduce the large swelling strain exhibited by expansive soils. The model allows only for small reversible swelling in elastic zone. It is therefore intended for use with partially saturated soils of moderate to low plasticity, such as sandy clays, clayey sands and silts, and granular soils. Gens and Alonso (1992) extended the BBM for unsaturated highly expansive clays. Alonso et al. (1999) performed a series of modifications and developments on the framework proposed by Alonso et al. (1990) and Gens and Alonso (1992) to propose an enhanced model, called Barcelona Expansive Model (BExM). The originality of the BExM model is the appearance of two functions named SI and SD in the suction-net stress plane (Figure 1.38), which distinguish two structural levels: microstructure and macrostructure. The SI (Suction Increase) line explains the shrinkage phenomenon associated with an increase in suction. The SD line (Suction Decrease) stands for the swelling phenomenon associated with a decrease in suction. The evolution of these two lines can modify the state surface (LC). An increase of suction expands the state surface and vice versa. The influence of suction variation on the yield surface results in a hydro-mechanical coupling. In this model the microstructure is assumed to be saturated and elastic. Therefore, the increment of the microstructural deformation depends only on the effective stress.

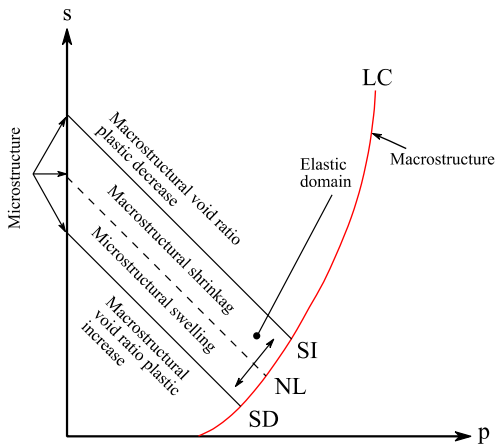

Figure 1.38 - State surface of the BExM model (Alonso et al., 1999).

Based on the definition of the two coupling functions, the model provides a good representation of the phenomena of stress-suction path dependency and swelling shrinkage fatigue during drying wetting cycles. Comparison with experimental tests performed in a suction-controlled oedometer apparatus confirms the ability of the model to capture well the qualitative trends of the data and to adjust them quantitatively in a satisfactory way (Alonso et al., 1999).

This model was applied in the literature for different application purposes especially, the shrink-swell phenomenon in expansive clays. Mrad (2005) implemented the BExM model in the Code_Bright finite element program to study the hydro-mechanical behavior of expansive clays in the context of different applications. The model was applied to a shallow strip footing on expansive soil by considering five drying-wetting phases which were constructed by applying suction on the soil surface. It should be mentioned that the suction values were not calculated through a soil-atmosphere analysis. The model was not validated with field measurements but

the results seemed to be coherent since a shrinkage of the soil is observed during drying phase and swelling trends during wetting phases.

Nowamooz (2007) and Nowamooz et al., (2009) investigated experimentally and numerically the behavior of natural expansive clays in different sites in France. The BExM model was employed in their work to study the behavior of a shallow foundation on expansive clays. The Code_Bright finite element program was used to incorporate the hydro-mechanical behavior of the expansive soil. A time variable suction range was imposed to the soil surface between 0 and 100 MPa, where 100 MPa is the suction corresponding to the soil shrinkage limit. The wide suction range was selected to observe the extreme shrinkage–swelling problems that could potentially be encountered. The results of the simulation are presented in Figure 1.39. Since the building and the foundation prevent the water flow under the building, the soil settles differently in each point because of the differential suction variation. The simulation allows to better understand the movements of shallow foundations on expansive soils and consequently to assess the influence of highly intensive drought periods on the shrinkage swelling phenomenon.

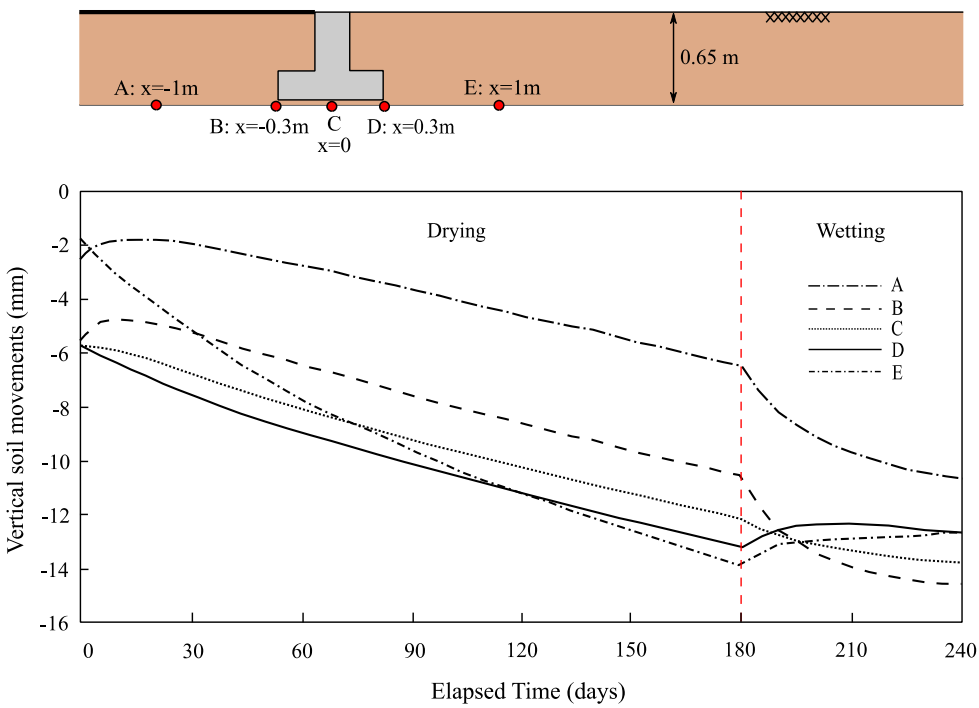

Figure 1.39 - Vertical displacement versus time in different points of the studied swelling soil (Nowamooz et al., 2009).

- *ϴ-STOCK code*

The ϴ-STOCK code developed by Gatmiri and Arson (2008) is a finite element program that is capable of modelling the Thermo-Hydro-Mechanical behavior of geomaterials in both saturated and unsaturated conditions. The considered loads in this approach are thermal, hydraulic and mechanical. The employed fields are thus the displacement of the skeleton, the gas and fluid pressure and the temperature of the porous medium which are treated as fully coupled phenomena. The independent variables used in this approach are: The net stress, the soil suction and the temperature. In order to calculate the volumetric deformation modulus, the volume change

behavior is formulated by means of a void ratio state surface, which is dependent on the net stress, the suction, and the temperature.

This model was extended by Hemmati (2009) to study the soil movements in time in a SVA context. The soil-vegetation-atmosphere interaction model, is implemented in ϴ-STOCK to calculate the hydraulic and thermal boundary conditions. The hydraulic boundary condition is defined by the liquid water mass flux (positive for water infiltration and negative for evapotranspiration) calculated from the mass balance and the heat boundary condition is defined by the soil heat flux calculated form the energy balance equations described in previous sections. Standard climatic parameters, soil characteristics and vegetation parameters were used in the numerical calculation which led to the determination of the soil water content, temperature and suction followed by the soil movements using the retention properties and the state surface on the unsaturated soils. The model was validated with the field measurements of the Mormoiron site instrumented by the BRGM which was located in the Vaucluse region in France and have a Mediterranean type of climate. The climatic data were provided from the nearest station and were used as input parameters in the numerical model. Laboratory measurements on the soil in the (e-log s) plan and the retention curve were used to assign the soil properties to the model. A schematic view of the modelling method is presented in Figure 1.40.

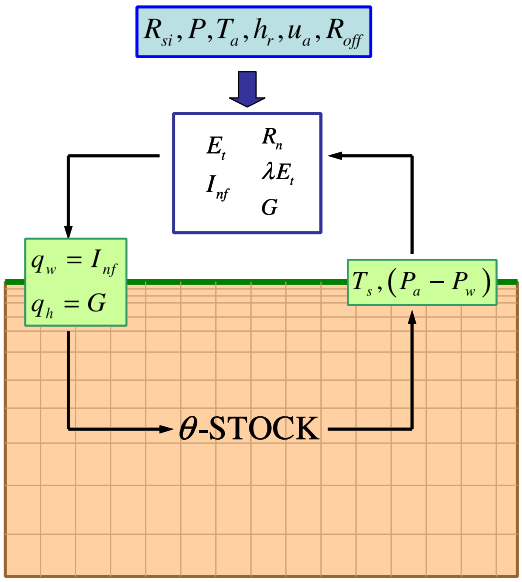

Figure 1.40 - Schematic view of soil-vegetation-atmosphere interaction modelling using the ϴ-STOCK model (Hemmati, 2009; Hemmati et al., 2012).

The application of the model to the Mormorion site provides the soil movements in time at different depth. Figure 1.41 shows the comparison between the simulation results and in-situ measurements of the soil movement using settlement gauges. According to Hemmati et al. (2012), a good agreement is observed between calculation and measurements. The days where a high swelling was observed, correlate well with the days with considerable rainfall.

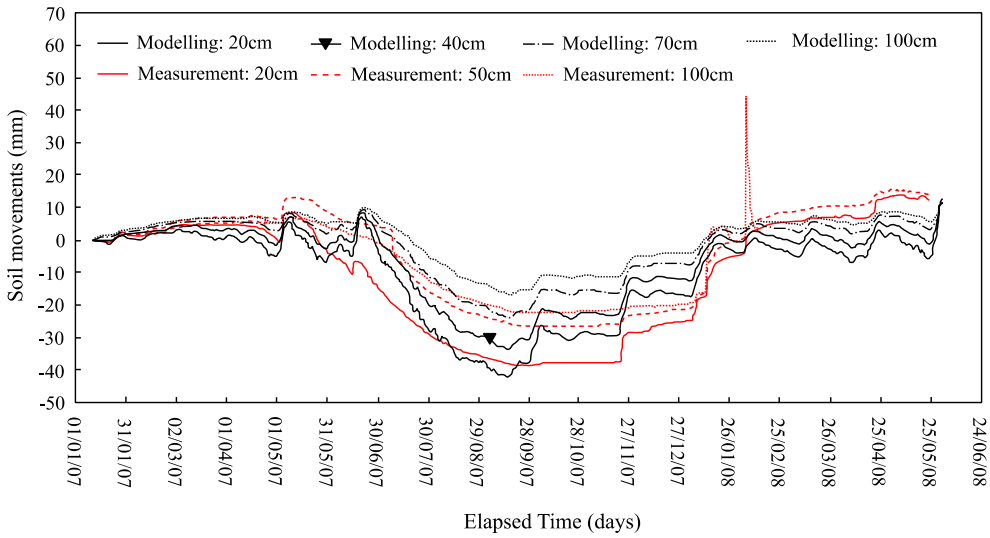

Figure 1.41 - Comparison of the modelled and measurement soil movements in the Mormoiron site from January 2007 to May 2008. (Hemmati, 2009; Hemmati et al., 2012)

The model was extended to study different scenarios in order to assess the cumulative soil movements during the considered period. It was observed that the maximum annual settlements are similar to obtained results by the short-term calculations for a considered year. The results globally show the pertinence of the developed soil-vegetation-atmosphere interaction model however, the numerous numbers of parameters in the model and the sophisticated experimental tests could be some of the disadvantages for using this method in engineering practice.

1.3.2.2 Water content-based methods

Rather than solving sophisticated numerical models based on the consolidation theory, the soil movements in time can also be evaluated based on the changes in water content over time. Since it is easier to measure than the soil suction, it could potentially be sufficient for the estimation of soil shrinkage or swelling. Some of these methods are presented in this section.

- *Briaud et al. (2003) method:*

Briaud et al. (2003) investigated the shrinkage and swelling of the Arlington site over time by proposing a water content-based method. The soil water content is used as a governing parameter since it can be either measured or calculated by already established methods in the literature. In order to obtain a relationship between the water content changes over time and the generated volumetric strains, the shrinkage test was suggested. Figure 1.42 shows the typical relationship of water content versus volumetric strain obtained from the shrink test. The shrink-swell modulus (E_w) was defined as the slope of the approximated straight line in the test. The soil surface movement for a given time (ΔH) can be calculated in terms of the shrink-swell modulus and the shrinkage ratio f (i.e. the ratio of the vertical strain to the volumetric strain) using the following equation:

$$\Delta H = \sum_{i=1}^{n} \Delta H_i = \sum_{i=1}^{n} \left(\frac{H_i f_i \Delta w_i}{E_{wi}} \right) \tag{1.20}$$

where n is the number of soil layers, H_i is the thickness of the ith soil layer, and Δw_i is the change in water content as a function of time for the ith layer. More details of this method are available in Briaud et al. (2003).

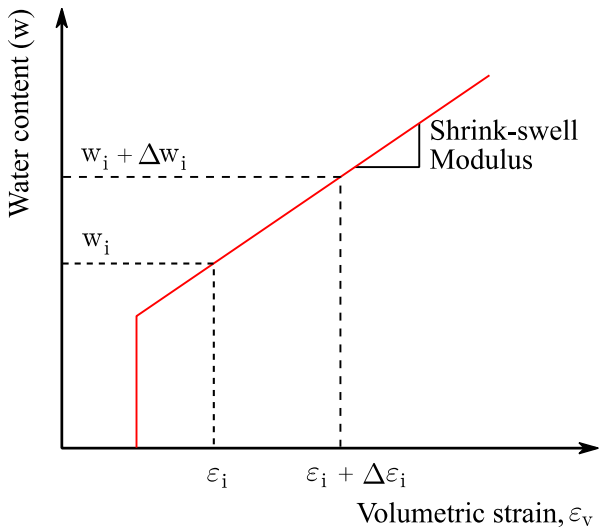

Figure 1.42 - Soil water content versus volumetric strain obtained from the shrink test (Briaud et al., 2003).

The Arlington site's measurements were used to evaluate the performance of the proposed approach. The results are comparable to the measurements; however better predictions were achieved by Zhang (2004). However, this method has its own advantages. This approach is based on the water content changes over time which are more reliable than suction values and much easier to measure. Only one experimental test is required in this method which is less than the previous models. As the limitations and disadvantages of the method, the use of an uncoupled analysis can be cited. According to Briaud et al. (2003), another drawback is that any theoretical consideration must make use of the soil-water characteristic curve (SWCC) to transform the governing equations from suction-based equations to water content-based equations.

- *Overton et al. (2006) method:*

Based on the migration of the wetting front through the soil profile, Overton et al. (2006) proposed a method for evaluating the free in-situ heave of expansive soils over time. For this purpose, the VADOSE/W (Geo-Slope, 2005) software was used in their work to perform transient water flow analysis in the soil. The soil-atmosphere interaction can be taken into account in this software by introducing input climatic parameters such as precipitation, evapotranspiration, temperature and runoff. According to Nelson and Miller (1992), the free-field heave can be calculated using the oedometer method using the following equation:

$$\rho = \sum_{i=1}^{n} C_H z_i \log_{10} \left(\frac{\sigma'_{cv}}{\sigma'_f} \right)_i \tag{1.21}$$

where ρ is the free-field heave, C_H is the heave index, z_i is the thickness of the ith soil layer, σ'_f is the in situ effective stress state at the midpoint of the soil layer for the conditions under which heave is being computed, and σ'_{cv} is the swelling pressure from the constant-volumetric

oedometer test. The consolidation swell test and the constant volume test is used in this approach to determine C_H (Figure 1.43). The accurate determination of C_H can be obtained by several consolidation-swell tests at different pressures and one constant volume oedometer test which is potentially time consuming and not applicable in engineering practice. In order to determine the model's parameters from a single oedometer test, simple relationships were developed by Nelson et al. (2006) between the swell pressure from consolidation-swell test σ'_{cs} and the swell pressure from constant volume oedometer test σ'_{cv}.

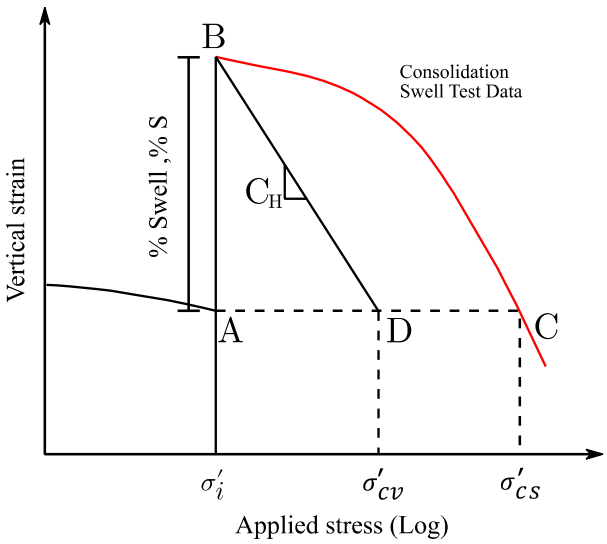

Figure 1.43 - Determination of heave index (Nelson et al., 2007) cited by Adem and Vanapalli, (2015).

It should be mentioned that coherent results can only be obtained in this method under certain conditions concerning site specific analysis. In addition, another disadvantage of this model is the use of the oedometer as the experimental technique for the calculation of the free-field heave which is time consuming to conduct. It should be added that this method does not provide the shrinkage of the soil over time and the calculations are only based on the soil heave.

- *Shams et al., (2018) method:*

Shams et al., (2018) investigated the 3D modelling of soil-structure interaction under climatic conditions. The method presents sophisticated three-dimensional (3D) hydro-mechanical finite element (FE) numerical models using coupled flow-deformation and stress analyses capable of simulating the complex behavior of reactive soils and slab foundations. The performance of the developed method is verified through three case studies. The ability of the method to simulate the moisture flow and suction variations in relation to climate changes is validated through two case studies involving field observations. The ABAQUS software was used to simulate the soil movements based on the moisture changes in their analysis. The moisture-swell model was used in ABAQUS which relates the volumetric swelling of porous soil materials to the degree of saturation of the wetting liquid in the partially saturated flow condition. The relationship between the volumetric shrinkage or swell strain and reduction in moisture content observed by Kodikara and Choi (2006) during shrinkage tests that followed a linear correlation, was used in their work ($\varepsilon_{vol,swell/shrink} = \delta.\Delta w$). The coefficient is determined based on either the free swell

oedometer test or triaxial test results. This approach is valid for slurry and compacted clayey soils. Thereafter, an idealized S-shape moisture-swell curve was developed for a highly plastic clayey soil by considering a maximum free swelling strain of 8%. This moisture-swell curve should be established for each specific site based on the soil's characteristics. In the first case study, a 3D FE model is developed and validated with field measurements of soil mound formation for a flexible cover membrane resting on an expansive soil in Maryland, Near Newcastle, Australia. In this case study, the soil movements were measured over 5 years. The modelled geometry for this site is presented in Figure 1.44 a). The area of precipitation is associated to the soil-atmosphere interaction phase and the time variable atmospheric boundary conditions based on climatic parameters. In the second case study, the soil moisture content and suction change with the soil depth in response to the surface suction changes is simulated in 3D analysis and verified against field observations for the Amarillo site, in Texas (Figure 1.44 b)).

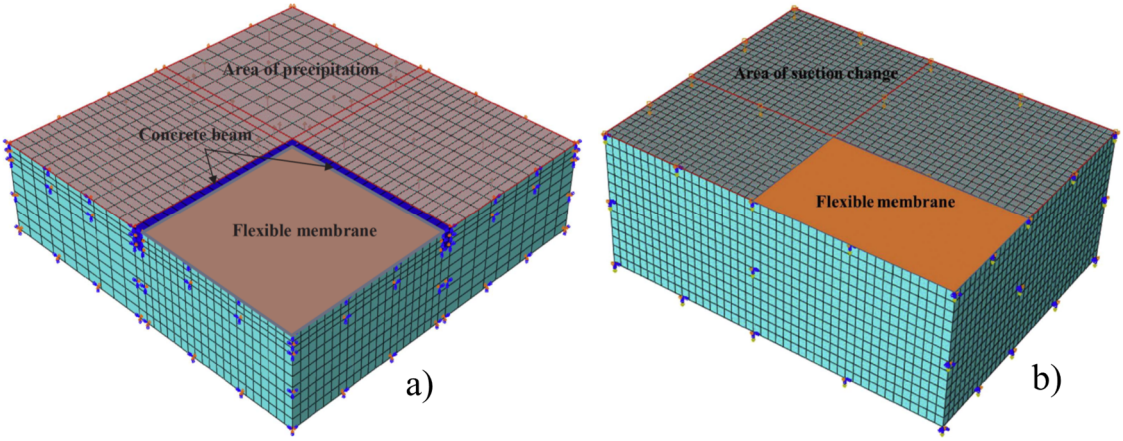

Figure 1.44 - Finite element mesh and area of the time variable atmospheric boundary condition, for a) case study 1, Maryland, Near Newcastle, Australia and for b) case study 2, Amarillo site, in Texas (Shams et al., 2018).

Figure 1.45 a) shows a comparison between the field observations and FE results, for the movement at the edge and the center in the first case study. Results shows that the numerical analysis is in a reasonable agreement with the data. The two points show continuous swelling over time, with lower shrinkage trends during the dry season. However, there is less tendency to heave towards the end of the observation period. It can also be seen that the point at the center, was less influenced by the climatic conditions which consequently generates lower moisture changes and soil movements. This is attributed to the fact that the water propagates with time towards the center of the membrane, and the heave at the center approaches that of the edge at the end of the 5 years. According to Shams et al., (2018), the difference in the heave values between the field observations and FE results may be due to the actual precipitation rates which may differs from the average rate used in the FE analysis. Figure 1.45 b) illustrates a comparison between the measured and FE predicted soil movement with time for points located at the surface, 1.8m outside the covered area along the short direction and a point located at 0.6m from the center of the covered area along the long axis. It can be seen that the predicted movements with time for both the point located outside the cover area and the point located inside the cover area agree fairly well with the measured data and the variation trends are well captured by the FE model, indicating a good modelling prediction capability (Shams et al., 2018).

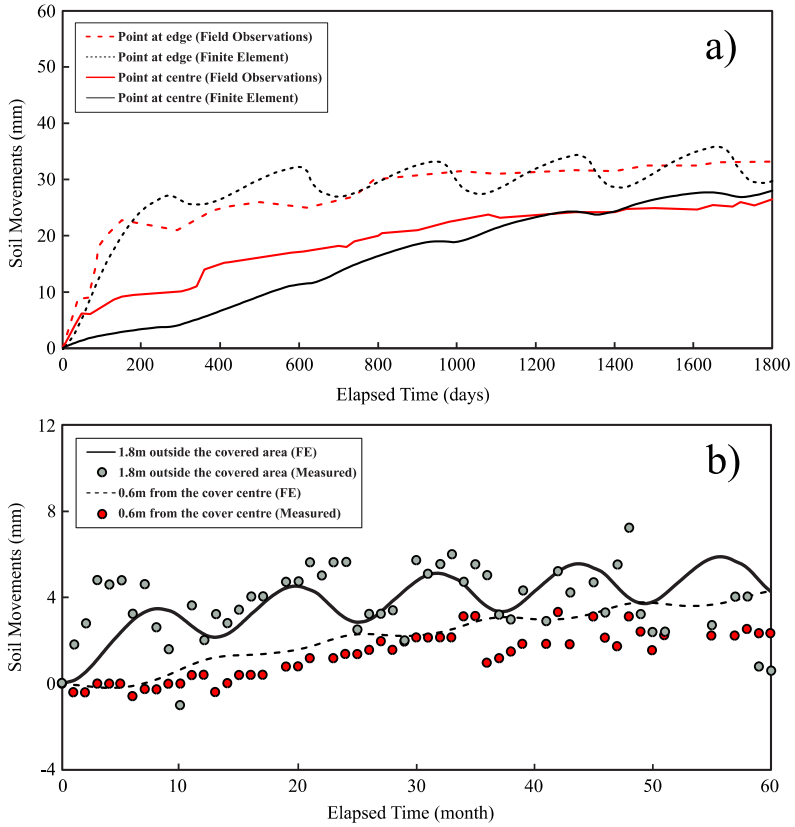

Figure 1.45 - Comparison of the simulated soil movements with in-situ observations for a) the first case study and b) for the second case study (modified after Shams et al., 2018).

The presented method provided insights into the capability of the proposed 3D coupled flow-deformation and stress analysis in realistically simulating the behavior of stiffened slab foundations on expansive soils. The use of this method allowed to overcome some major limitations in most existing methods. These include: (i) realistic formation of 3D soil mounds, based on coupled seepage and deformation analyses, rather 2D or uncoupled analysis and (ii) simultaneous stress analysis and transient seepage, by involving the effect of suction change on the soil stiffness and implementing representative contact elements in the soil-structure interaction phase. However, the volume change relationship is dependent of a moisture-swell test (conducted using an oedometer) which is not included in usual geotechnical laboratory tests. This kind of test could be time consuming and require advanced equipment and trained staff.

- *Karunarathne et al., (2018) method:*

Karunarathne et al., (2018), modelled the moisture induced ground movements in expansive soils using both transient hydro-thermal simulation and moisture dependent volume change simulation. The soil moisture variation due to climatic conditions was modelled using Vadose/w for two sites in Melbourne, Australia. The model was validated against the regular measurements from the Braybrook site. The predicted soil moistures from the Vadose/w model were used to predict the possible ground movement using FLAC3D software. The predicted ground movements were also validated using the field monitored ground movements at the Braybrook site. The Vadose/w software was also employed by Rajeev et al., (2012) to model the variation of the soil water content and suction in time using soil-atmosphere interaction analysis. In both studies,

a 1D soil column (Figure 1.46) was modelled in Vadose/w using both hydraulic and thermal properties and time variable climatic data as boundary conditions. It should be mentioned that the influence of vegetation was also taken into consideration in the transient analysis by defining a LAI function for the soil cover.

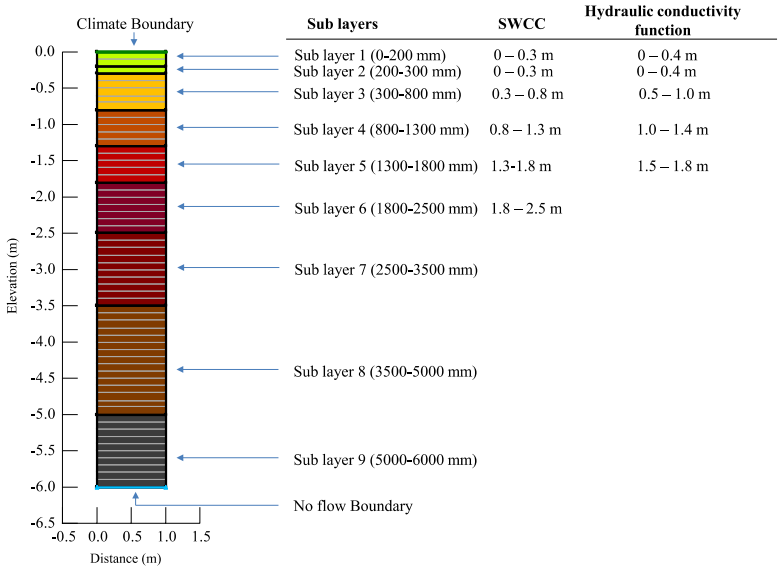

Figure 1.46 - 1D model of the Braybrook site in Vadose/w (Rajeev et al., 2012).

In this current method, (Karunarathne et al., 2018) the moisture induced ground movements in a soil column of a given depth were also simulated using a framework developed in the finite difference software FLAC3D. Formulations in the developed FLAC model were based on the assumption of isotropic free swelling behavior of soil in which the linear swelling strain is related to the change in moisture content through a linear expansion coefficient (as the previous method). Stress changes are calculated based on the soil elastic modulus change (stiffness) versus the moisture variations. Laboratory tests were conducted to determine the relationship of the soil elastic modulus with the moisture content which was implemented in the FLAC3D software. Figure 1.47 illustrates the comparison between the measured and the simulated surface ground movements. Results show a good agreement between the simulated and measured movements suggesting the verification of both moisture data and soil movement simulations.

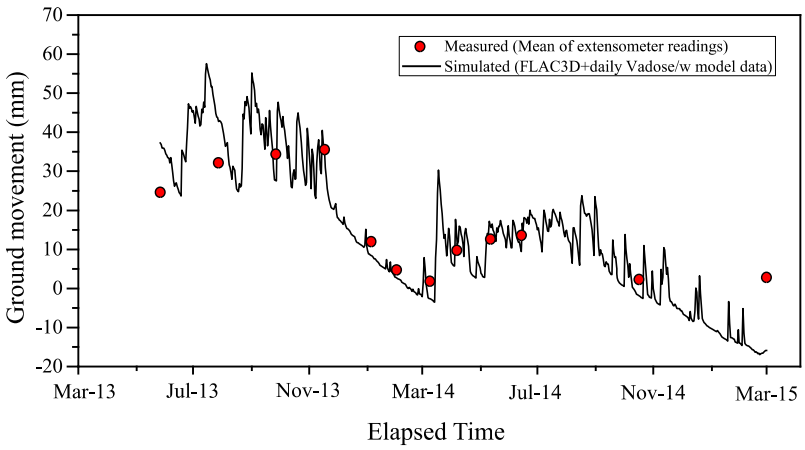

Figure 1.47 - Comparison of the simulated soil surface movements with the measured data at the Braybrook site (modified after Karunarathne et al., 2018).

In their study, a complementary analysis was performed to investigate the long-term soil moisture changes and soil movements over the past decades. Three arbitrary climate change scenarios were adapted to generate projected climatic parameters and thus, the expected future soil movements. Simulation results gave an insight on both the past and future soil movements at two different sites in Australia. However, it should be mentioned that these scenarios were selected based on typical assumptions on climatic parameters which implies a verification of the results by considering real climate change scenarios. According to the authors, the models are capable of reliably predicting soil moisture changes and ground movements, which are key parameters of designing shallow footings on expansive soils, and will therefore greatly assist the footing design for residential structures. Even though this method is applicable in engineering practice with the help of a commercial software, the required laboratory tests for the calculation of the soil volume change based on the changes of the soil stiffness and water content are time consuming and are not included in usual geotechnical laboratory test reports.

1.3.2.3 Suction-based methods

The moisture movement in unsaturated soils is often described in terms of soil suction in Geotechnical Engineering field. According to Richards (1974), the soil suction can be used to represent the state of the soil saturation state much more effectively than the water content firstly because, soil suction is primarily controlled by the soil environment and not by the soil itself, and it typically does not exhibit discontinuous trends. The soil suction profile tends towards an equilibrium value at a particular depth under a particular climatic condition while water content is highly sensitive to the soil material properties (e.g. soil type, clay content, soil density, and soil structure). Secondly because, the correlation of soil parameters (i.e. permeability or hydraulic conductivity, diffusivity, and shear strength) with water content is poor unless other soil properties such as density and clay content are considered, but these parameters can be conveniently correlated with the soil suction. The building block of the suction-based methods is based on the volume change of expansive soil which can be related to the soil suction through the changes in the void ratio or volumetric strain. Two available method in the literature are presented in this section.

- *Wray et al., (2005) method:*

Research carried out by Wray et al., (2005) led to the development of a computer program named SUCH which stands for SUCtion and Heave. This computer program is capable of predicting the soil moisture changes and the consequent soil surface movements (shrinkage/swelling) under covered surfaces over time. The program is based on two numerical models, a numerical model for the unsaturated water flow in the soil and a volume change model for estimating the vertical soil movements based on the changes in the soil suction (Wray, 1997). The developed program is written in FORTRAN language, which uses the finite difference technique to solve the transient suction diffusion equation. As expressed in Adem and Vanapalli, (2015), two main sets of information must be given in the program. Firstly, the initial suction values at each node and secondly the time variable suction changes as boundary conditions. Thereafter, the unsaturated flow can be used to determine the distribution of soil suction in the soil mass over time and the resulting soil movements using the suction-based model expressed as below:

$$\Delta H_{i,j,k} = \Delta_z \gamma h_{i,j,k} \left(\Delta pF_{i,j,k} - \Delta pP_{i,j,k}\right) \tag{1.22}$$

where $\Delta H_{i,j,k}$ is the incremental volume change (swell/shrink) at grid point (i, j, k) over the increment thickness Δ_z; $\gamma h_{i,j,k}$ is the suction compression index at grid point (i, j, k) which can be estimated by different methods (refer to Adem and Vanapalli, (2015) for more information); $\Delta pF_{i,j,k}$ is the change of total soil suction expressed in pF units at grid point (i, j, k), and $\Delta pP_{i,j,k}$ is the change of soil overburden over the increment thickness Δ_z at grid point (i, j, k). The vertical movement of each nodal point at the top surface of the soil mass was calculated by summation of the vertical movements of the nodal points on the vertical line passing through that surface point extending from the top to the bottom of the active zone of the soil mass (Wray et al., 2005). This method was validated using different sites with varying climatic and soil conditions SUCH model was used in these sites to estimate soil suction variations throughout the soil mass and the vertical soil movement at monthly intervals over a period of 5 years (from August, 1985 to July, 1990). Figure 1.48 shows the predicted and measured monthly soil surface movements at 1.8 m outside of a slab edge along longitudinal axis at the Amarillo site studied by Wray et al., (2015). The comparison of the simulated soil movements with the measured values shows reasonable agreement. However, an over estimation of the predicted values is observed during the simulation. The application of the developed model to real case studies depends highly on the adapted parameters and the initial and boundary conditions of the problem. Since the initial soil suction is required in this approach, reliable field measurements could be challenging especially in expansive clays. This could be one of the drawbacks of this model.

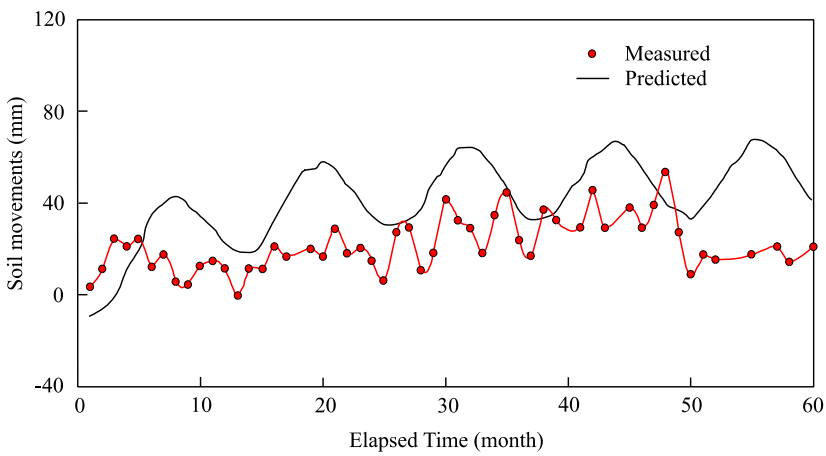

Figure 1.48 - Predicted and measured monthly surface movements at 1.8 m outside slab edge along longitudinal axis at Amarillo site (modified after Wray et al., 2005).

- *Adem and Vanapalli, (2013) method (MEBM):*

This method provides the soil movement changes over time and is referred to the modulus of elasticity-based method (MEBM). The model is based on the constitutive equation for the soil-structure along with the soil-atmosphere interaction model using the VADOSE/W (Geo-Slope, 2007) software. In this model, the soil was assumed to be an isotropic, linear elastic material and the influence of the mechanical stress on the soil volume change is assumed to be neglected which limits its application on lightly loaded structures. Based on the Fredlund and Morgenstern (1976)

constitutive equation the total vertical soil movement Δh at any depth can be calculated by the following expression developed by Adem and Vanapalli, (2013):

$$\Delta h = \sum_{i=1}^{n} \left\{ H_i \left[\frac{(1+\mu)(1-2\mu)}{E(1-\mu)} \Delta(u_a - u_w) \right]_i \right\} \tag{1.23}$$

Based on this equation, the Poisson's ratio should be defined which will allow the determination of the shrink/swell over time using the matric suction changes in the active zone depth and the corresponding modulus of elasticity as key parameters. The distribution of the soil suction into the active zone depth was determined using the soil-atmosphere interaction in VADOSE/W and a semi-empirical function which was recently proposed by proposed Adem and Vanapalli (2015) for estimating the elasticity modulus of unsaturated soils. The strength of this semi-empirical model lies in its use of conventional soil properties that include the SWCC and the soil modulus of elasticity under saturated condition E_{sat} (Adem and Vanapalli, 2013):

$$E_{unsat} = E_{sat} \left(1 + \alpha \frac{u_a - u_w}{\frac{P_{atm}}{101.3}} S^{\beta} \right) \tag{1.24}$$

where E_{unsat} is the elasticity modulus of the soil under unsaturated conditions; S is the degree of saturation; and α, β are the fitting parameters. According to Adem and Vanapalli, (2015), these two values where considered for the reasonable modelling of the volume change behavior in unsaturated soils ($\alpha = 0.05$; 0.15 and $\beta = 2$). The step by step flowchart of the modelling approach is presented in Figure 1.49.

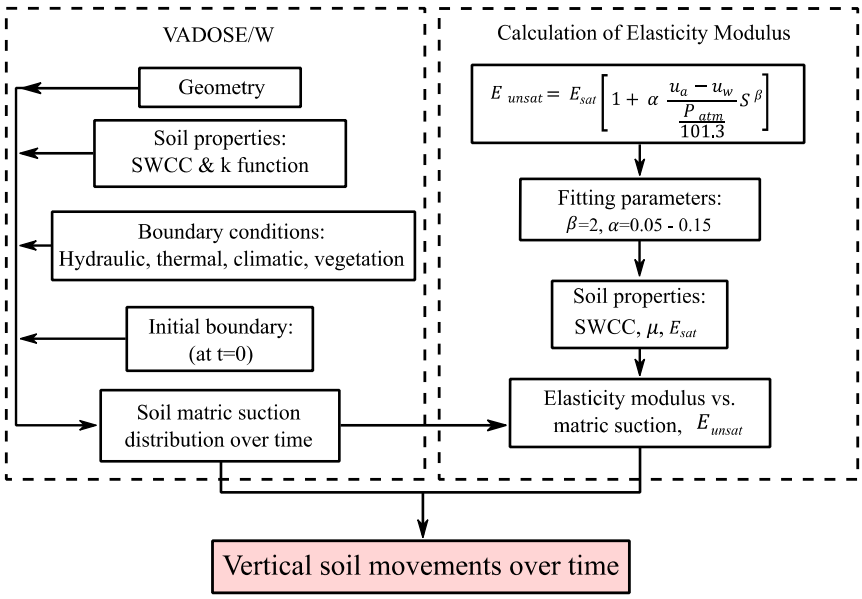

Figure 1.49 - Flowchart for the step-by-step procedure of the MEBM (Adem and Vanapalli, 2013)

The model was applied to numerous sites and the results were validated with the provided in-situ measurements. A primary validation was carried out with the investigated site by Vu and Fredlund (2004), (floor slab of a light industrial building in Regina) and the results were in good

agreement with the coupled modelling approach. A recent application of the MEBM model is reported in Adem and Vanapalli, (2015), where the vertical movements of an expansive soil close to a road pavement is modelled (Regina site). In this approach, the influence of loading conditions was not taken into account in the model and the free shrinkage and swelling of the soil is thus investigated (Figure 1.49).

The simulated suction time series were compared to the modelling results of Ito and Hu (2011). These authors, studied the same site as well and calculated the suction variations in time at different depth. The soil movements were also calculated by Ito and Hu (2011) using a similar approach. Results obtained by MEBM are presented in Figure 1.50. The total vertical soil movements at any depth for a given time were calculated by the accumulation of daily soil movements for all days prior to that given time. The fluctuations in the total vertical soil movements were relatively large close to the ground surface; however, they were completely stopped at 6 m depth. The maximum upward soil movement (soil swelling) and the maximum downward soil movement (soil shrinkage) were found to be close to those predicted by Ito and Hu (2011). In this model, not only the influence of matric suction variation on the soil volume change is considered, but also the influence of the mechanical stress is incorporated using the elastic modulus based on the hydraulic state, the compaction and the confinement level of the material. This could be a potential advantage of this model compared to the previous ones. As mentioned previously, the highlighted drawbacks of the MEBM could potentially be the use of the soil elasticity modulus as a key parameter (which is not always reliable) and the fact that the influence of the loading conditions are not directly considered in the proposed volume change method.

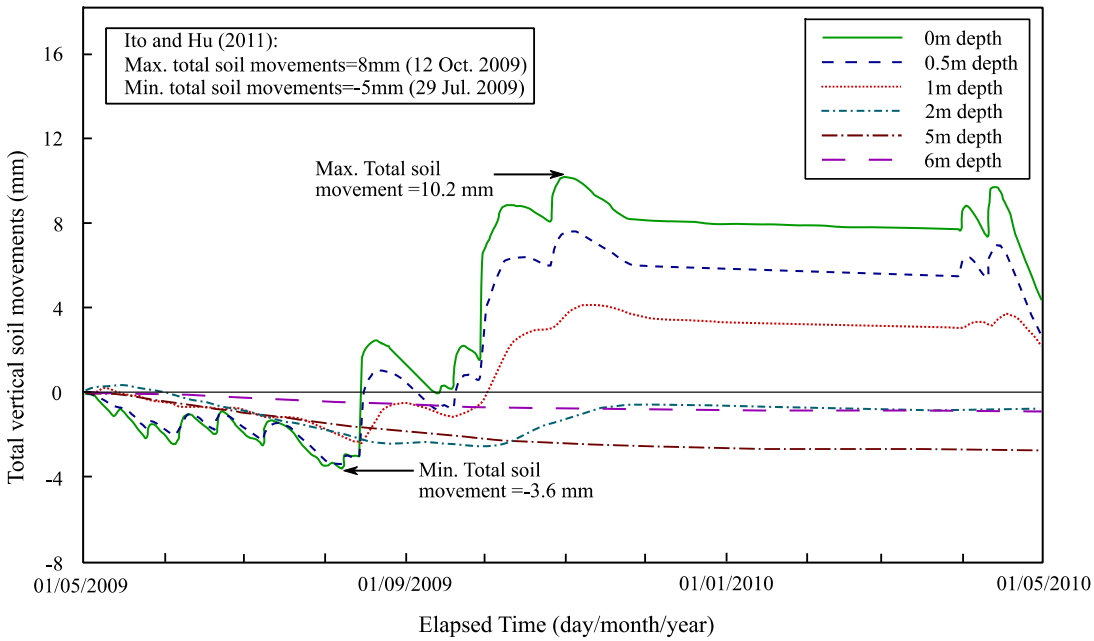

Figure 1.50 - Predicted cumulated vertical soil movements under the center point a vegetation cover close to a pavement using the MEBM (Adem and Vanapalli, 2013).

In this section, most of the well-known methods for predicting the volume change behavior of expansive soils over time were presented. The consolidation theory-based methods are numerically sophisticated to solve and some of these models require advanced laboratory experiments and equipment. These models are less employed in engineering practice due to the numerous

required parameters which are obtained by sophisticated experimental tests. For example, the BBM-BExM model requires about 10-22 parameters that are deduced by advanced laboratory experiments. The water-content based methods are the most proposed methods based on this literature review. This is potentially due to the fact that the measurement of this quantity is simpler and more reliable than the soil suction. Most of these methods were based on uncoupled analysis and thus less sophisticated numerical challenges should be overcome which is a potential advantage of this kind of methods. On the other hand, sophisticated laboratory tests are required in most of these methods for the establishment of the volume change relationship. Nevertheless, water content-based methods could be a reliable candidate for modelling the soil movements over time in engineering practice if adequate experimental equipment are provided. However, suction based methods are less proposed in the literature but can be adapted in engineering practice if correctly applied to the specific case. Latest developed models showed the ability of the suction-based methods in estimating the soil movements over time by conducting routine Geotechnical experimental tests. Also, reliable results are obtained if the volume change parameters are correctly related to the soil suction variations.

1.4 Conclusion

In this first chapter, the shrink-swell phenomenon and its associated problems in both physical and economical aspects were presented. The severity of this phenomenon in France due to climate change and different environmental factors, highlights the needs for the assessment and the development of numerical models that can incorporate properly the intensity of this phenomenon over the elapsed time. Soil-Vegetation-Atmosphere transfer models are the most adapted type of analysis for this kind of time dependent problems. The use of these models requires the proper determination of the soil parameters along with the time variable boundary conditions through interaction methods. Current presented models are able to provide the hydro-thermal variation of the soil's properties with respect to time at different depth. These variations can be used as boundary conditions in order to describe the volume change behavior of expansive soils. Presented models confirmed the capability of using this kind of relationship for the volume change analysis. Most of the volume change models showed coherent results while compared to field observations. This implies that the uncoupled version of these models can also be used to assess the shrink/swell phenomenon which can reduce the complexity of numerical calculations. The use of water content or suction as key variable in the volume change analysis is usually carried out along some laboratory tests which is in most cases time consuming and expensive. Therefore, there is still the need for the improvement of these models by proposing cost effective and practical methods. The use of basic geotechnical properties in this kind of models could be a major improvement in engineering practice.

Chapter 2. Modelling shrinkage and swelling of unsaturated natural soils in a Soil-Vegetation-Atmosphere context

2.1 Introduction

In this chapter, the adapted modelling approach for the SVA interaction analysis is primarily presented. A simplified soil-atmosphere interaction method is employed to determine the time variable atmospheric boundary conditions using routine meteorological data. Secondly, a hydro-thermal soil model is used to determine the spatial-temporal variations of the soil water content, suction and temperature in the considered soil profile using the soil retention and thermal properties. The determination of the retention properties is based on basic geotechnical parameters which lead to the estimation of the soil water retention curve. Thereafter, the effect of water uptake by vegetation is incorporated in the hydro-thermal soil model using the concept of the SVA interaction method in the source term of the unsaturated flow equations. Finally, the time series of the soil suction are used as boundary conditions to determine the soil shrinkage and swelling in time using a simple approach which is based on the experimental results obtained on the volume change behavior of clayey soils under drying wetting cycles, in the literature. A linear model is adapted in this phase to incorporate the volume change behavior under suction changes in the void ratio-suction plan. The essential parameters of the model i.e. the volumetric indices (the slopes of the linear model) are estimated using correlation and multiple regression analysis on basic geotechnical parameters. The performance of this correlation is also investigated in this chapter. The capacity of the proposed approach is verified by comparing the calculation results to that of a suction controlled test.

2.2 Adapted Soil-Atmosphere Interaction analysis

2.2.1 Simplified Mass balance approach

Climate induced solicitations are modelled using a soil-atmosphere interaction method which is based on the mass and energy balance equations. The mass balance approach is presented using the following equation by neglecting the effect of runoff and the interception in the calculation for the sake of simplicity:

$$P = ET + I_{inf} \tag{2.1}$$

where P is the precipitation rate (mm/day), I_{inf} is the infiltration rate into the soil (mm/day) and ET (mm/day) is the reference evapotranspiration (potential evapotranspiration) which is calculated by considering the FAO 56 (Penman 1948) as follows:

$$ET_0 = \frac{0.408\ \Delta\ (R_n - G) + \gamma \frac{900}{T+273}\ u_2\ (e_s - e_a)}{[\Delta + \gamma\ (1 + 0.34\ u_2)]} \tag{2.2}$$

where, R_n is the net radiation at the crop surface [MJ m^{-2} day^{-1}], G is the soil heat flux density [MJ m^{-2} day^{-1}], T is the mean daily air temperature at 2m height [°C], u_2 is the wind speed at 2m height [m s^{-1}], e_s and e_a are the saturation and actual vapor pressure respectively [kPa], Δ is the slope of the vapor pressure curve [kPa °C^{-1}] and γ is the psychometric constant, 66 (Pa/°C).

2.2.2 Thermal based energy balance approach

On the other hand, the energy balance approach is described based on the soil surface temperature. The energy balance ($R_n = G + H + L_e$) is considered as mentioned previously and R_n is defined using one of the presented models in chapter 1. The net solar radiation is described using the Blight (1997) expression which is a function of the soil surface temperature as mentioned in Table 1.5.

$$R_n = (1 - a)R_{si} - \varepsilon_s \sigma\ (T_s)^4 + \varepsilon_a \sigma\ (T_a)^4 \tag{2.3}$$

The air emissivity (ε_a) is calculated using the equation proposed by Brutsaert (1988):

$$\varepsilon_a = 1.24\ \left(\frac{e_a}{T_a}\right)^{\frac{1}{7}} \tag{2.4}$$

where T_a is in Kelvin and e_a is the air vapor pressure in mb which depends on the air temperature T_a and the saturated vapor pressure (e_s) expressed by Idso (1981) as follow:

$$e_0 = 0.6107 \exp\left(\frac{17.269\ T_a}{T_a + 237.1}\right) \tag{2.5}$$

$$e_a = e_s . h_a \tag{2.6}$$

By considering the soil surface temperature as the unknown, it is essential to describe two components of the energy balance (G and L_e) as a function of the net solar radiation (R_n). The soil heat flux (G) is related to the net solar radiation by using the proposed equation of Santanello and Friedl (2003). The authors used a soil-atmosphere-vegetation model by solving the heat and moisture flow simultaneously into the first 2 cm of the considered soil profile. Simulations were carried out for different type of soils (Clay, Clayey loam, Loam, Sand) with volumetric water contents varying from saturated to unsaturated state (0.4, 0.25 and 0.05). Figure 2.1 a), b) and c) show the effect of soil moisture (saturated or not) and its texture on the G/Rn ratio. Based on the simulation results, the following relationship was deduced by Santanello and Friedl (2003) and is used in this work:

$$G = R_n . c . \cos[\frac{2\pi}{b}(t + 10800)] \tag{2.7}$$

where t is the solar time angle (seconds), b and c are empirical constants.

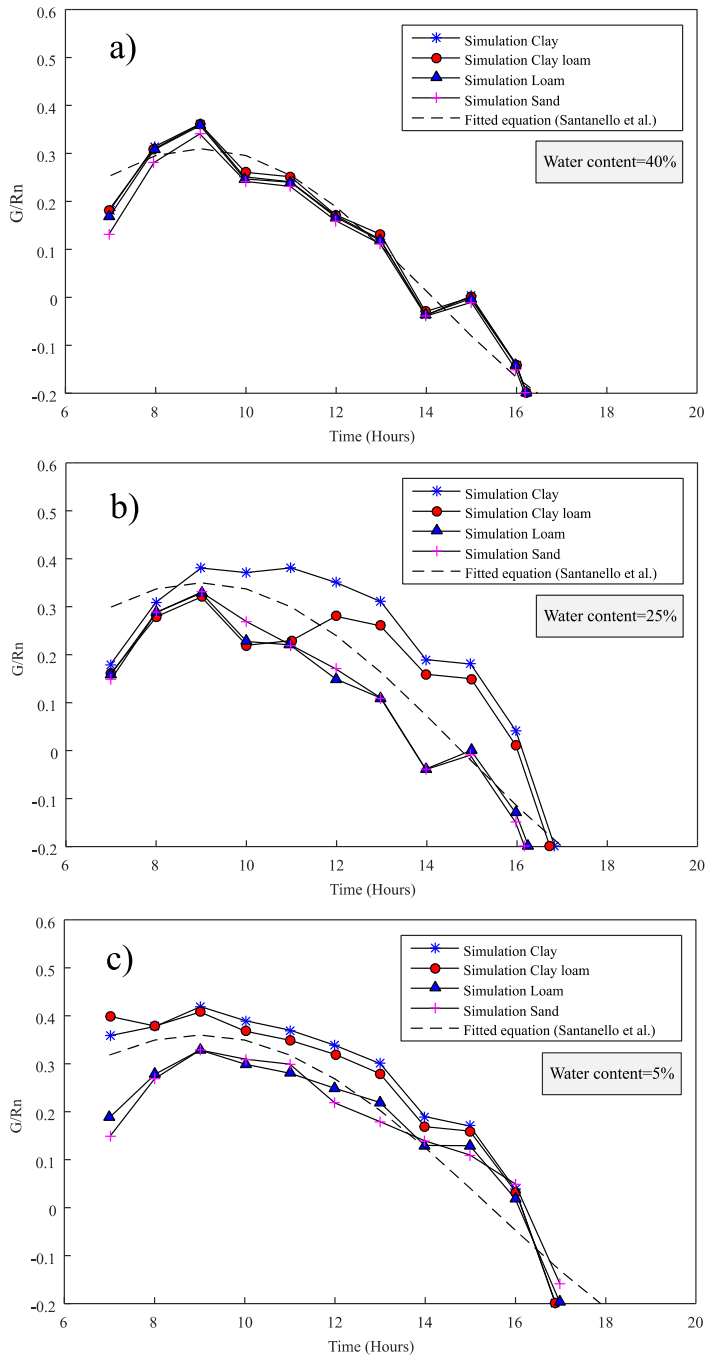

Figure 2.1 - The variation of G/Rn ratio for different types of soils with: a) 40% water content; b) 25% water content; c) 5% water content. (Santanello and Friedl 2003)

Based on the simulation results from this study, it can be observed that the general trends follow the proposed expression. It can be observed that all soils behave the same way in a saturated state. This reasoning is also valid for soils in an unsaturated and dry state. There is a slight difference between the saturated and dry state in the early hours of radiation for clayey soils, however, this difference is negligible as time passes during the day. For the sake of simplicity, b and c were respectively taken equal to 100000 and 0.35 which represents a unique fitting curve regardless of the soil texture but based on the simulation and measured results

reported in Santanello and Friedl (2003). As mentioned in chapter 1, this G/R_n expression is developed in hourly time scales, however constant G/R_n ratios were taken into account for daily time scale calculations.

The sensible heat (H) is the conductive heat flux from the Earth's surface to the atmosphere and is calculated using either surface resistance terms and aerodynamic approaches or by using classical newton formula with heat transfer coefficient (Staniec & Nowak 2016):

$$H = h_v(T_s - T_a) \tag{2.8}$$

In this equation, h_v represents the heat transfer coefficient at the soil surface and is expressed according to Notton et al. (2006) as follow:

$$h_v = \begin{cases} 5.6 + 3.9\ v\ , & v \leq 5\ \left(\frac{m}{s}\right) \\ 7.2\ v^{0.78}\ , & v > 5\ \left(\frac{m}{s}\right) \end{cases} \tag{2.9}$$

where v is the wind speed in m/s. Since the wind speed data are recorded at different heights in different meteorological stations, it is essential to apply changes to the wind speed values when the recorded data are far from the soil surface (2-4-10 m). The wind speed profile is expressed as the following equation to calculate the wind speed at any given height:

$$v = v_r \left(\frac{z}{z_r}\right)^{1/7} \tag{2.10}$$

The latent heat flux is the flux of heat from the ground surface to the atmosphere that is associated with evaporation or transpiration of water at the surface. Several authors have proposed equations allowing the calculation of this energy balance term (Penman 1948). The latent heat of evapotranspiration is deduced using the Priestley and Taylor (1972) equation:

$$L_e = \propto\ f_{sw} \frac{\Delta}{\Delta + \gamma}\ (R_n - G) \tag{2.11}$$

where α is assumed to be constant equal to 1.26. The coefficient f_{sw} depends on the volumetric water content at the soil surface. A complete saturated state represents a maximum value of 1 in the soil. Δ is the slope of saturation vapour pressure curve at the air temperature (kPa/°C) as mentioned previously and is calculated using the following equation:

$$\Delta = \frac{4098\ e_0}{(T_a + 237.3)^2} \tag{2.12}$$

With all the energy components described previously in this section, the thermal based energy balance equation can be presented as below by substituting Eq. (2.8) and (2.11) into Eq. (1.3):

$$T_s = T_a + \frac{1}{h_s}\left[\ (R_n - G)\ \left(1 - \propto\ f_{sw} \frac{\Delta}{\Delta + \gamma}\right)\right] \tag{2.13}$$

By replacing the net solar radiation and the soil heat flux by the previously mentioned equations ((2.3) and (2.7)) into Eq. (2.13), the following equation with a single unknown, the soil surface temperature (Ts):

$$T_a - T_s + \frac{1}{h_s}[(1 - c.\cos\left[\frac{2\pi}{b}(t + 10800)\right])\Big((1-a)R_{si} - \varepsilon_s\sigma\ (T_s)^4 + \varepsilon_a\sigma\ (T_s)^4\Big)\left(1 - \propto\ f_{sw}\frac{\Delta}{\Delta+\gamma}\right)] = 0 \tag{2.14}$$

By solving this equation, the soil surface temperature (T_s) can be now determined, based on the recorded metrological data. The thermal based energy balance approach which provides the variations of the soil surface temperature in time, can be compared to experimental measurements for validation purposes. It should be mentioned that in a daily time scale the part dedicated to the G/R_n ratio will be reduced to constant values (Assadollahi and Nowamooz, 2017; Assadollahi and Nowamooz, 2018f). The approach is primarily investigated using only the provided meteorological daily data of a site in the south of France close to Toulouse. However, measurements of surface temperature are needed, therefore, the soil surface temperature measurements (half-hourly) from another site in the Héricourt region of France were compared to the estimated values obtained from the thermal-based energy balance approach.

2.2.3 Investigation of surface temperature estimation

2.2.3.1 Toulouse site description

In order to investigate the soil surface temperature using the proposed thermal based energy balance approach along with the energy balance components, a site was chosen in the south of France close to Toulouse city. It should be mentioned that no measurements of the soil surface temperature are available in this site, however a set of meteorological data are available for evaluating the proposed energy balance approach. The data corresponds to the year 2000 right before the 2003 intense drought and are presented in Figure 2.2 which are the input parameters for the soil-atmosphere interaction analysis.

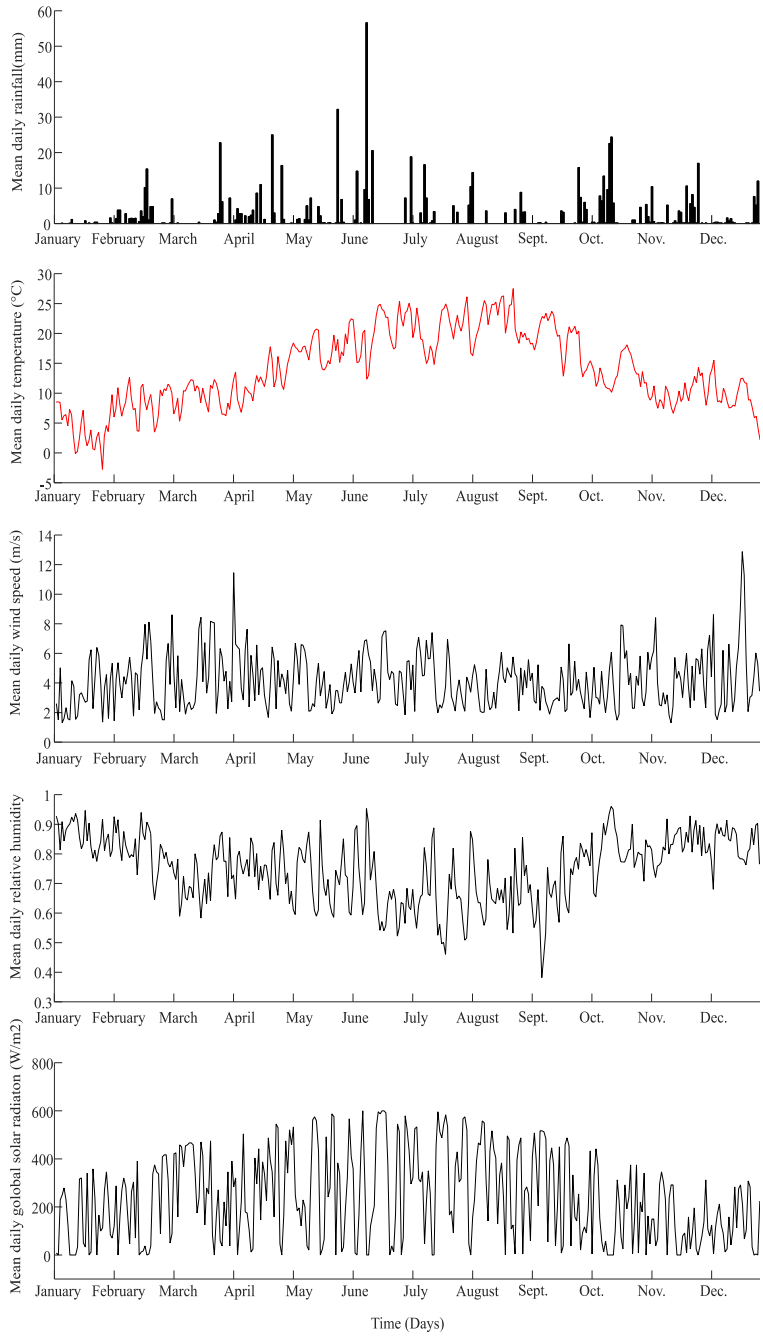

Figure 2.2 - Climatic parameters of the Toulouse site.

Based on the provided climatic parameters and by using the expressions presented in the previous section, the complementary parameters can be determined. In order to proceed, the soil Albedo and the air emissivity coefficient should be determined. The surface albedo is adapted based on the nature of the soil surface cover which is a clay in this site (0.25). The G/R_n ratio is taken equal to 0.35 as suggested for a bare soil surface. To calculate the emissivity coefficient of the air, it is first necessary to determine the vapor pressure at the air temperature (e_a) which is determined by the calculation of the saturation vapor pressure (e_s). Figure 2.3 a) shows the saturation vapor pressure and the air vapor pressure in kPa during the considered period. Therefore, the air emissivity coefficient can be calculated which is also presented in Figure 2.3 b). The heat transfer coefficient (h_s) is also calculated using the win speed data.

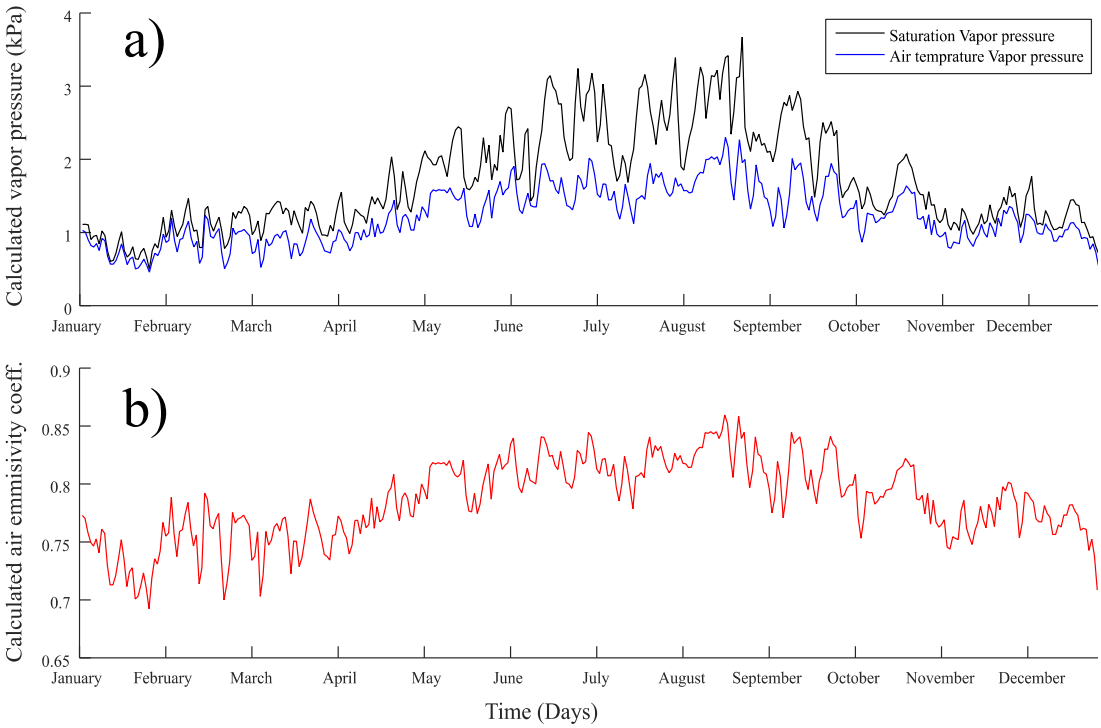

Figure 2.3 - Calculated a) air emissivity coefficient and b) vapor pressures using climatic parameters of the Toulouse site.

2.2.3.2 Surface temperature calculation

Using the thermal based energy balance concept, the soil surface temperature can be now determined. The air temperature along with the vapor pressure and the soil / air emissivity coefficients are used in Eq. (2.14) to calculate the surface temperature. Figure 2.4 shows the calculated soil surface temperature along with the air temperature. It can be observed that the difference in these two temperature time series are not always negligible. However, there are some points where the difference can be neglected. This appears mostly during cold periods or when the temperature tends to drop. Even though the difference is not considerable for this case, but the adapted approach will be taken into account in further analysis. This difference is related to the variation of the air thermal conductivity, which also depends on the wind speed. It is essential to consider the soil temperature in coupled analysis as temporal boundary condition instead of replacing it with the air temperature due to the influence that can have on the soil

water content. This first estimate with the proposed method must be compared to measurements carried out on site, for a primary validation. It should also be mentioned that the deviations of the surface temperature from the air temperature can be different in different time scale of measurements or calculations. This aspect is verified in the next section where the measurements and the calculations are in half hourly time scale.

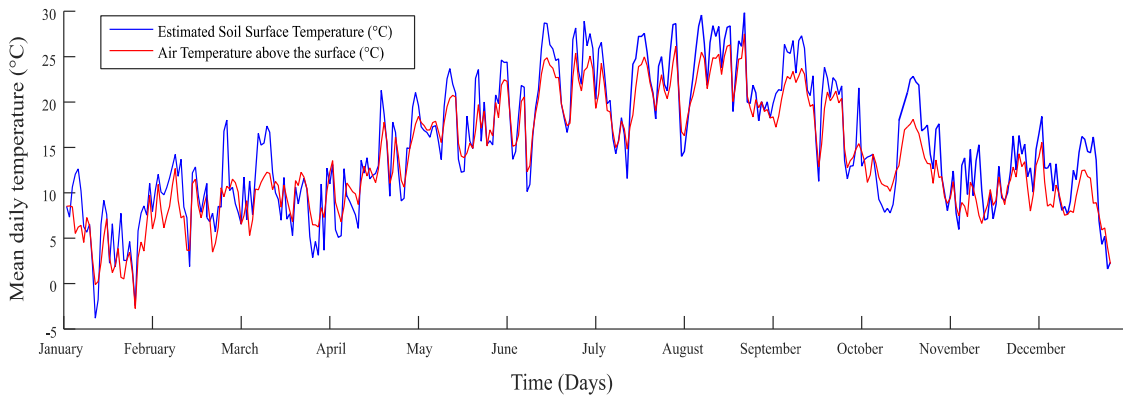

Figure 2.4 - Calculated soil surface temperature along with the air temperature of the Toulouse site.

As a complementary analysis, the different components of the energy balance approach can also be determined since the soil surface temperature is known which also allows the determination of the net solar radiation along with G, H, L_e. Nevertheless, it is also of paramount importance to perform a validation of the thermal based energy balance approach with field measurements. It should be mentioned that the validity of the simplified mass balance approach presented in previous sections is not verified here since the simple approach has been accepted and adapted on different cases. Thus, the attention is given to the proposed thermal based energy balance approach.

2.2.4 Validation of the thermal based energy balance approach

2.2.4.1 Héricourt site description

The Héricourt site was instrumented to study the soil-atmosphere interaction of an embankment during drought humidification cycles and was constructed with lime/cement treated silty soil. A microclimate monitoring system was installed in July 2011 on the embankment for measuring climatic parameters such as air temperature, relative humidity, wind speed and solar radiation which are reported in An et al. (2017b). The soil surface temperature was measured along this period with temperature probes (Figure 2.5).

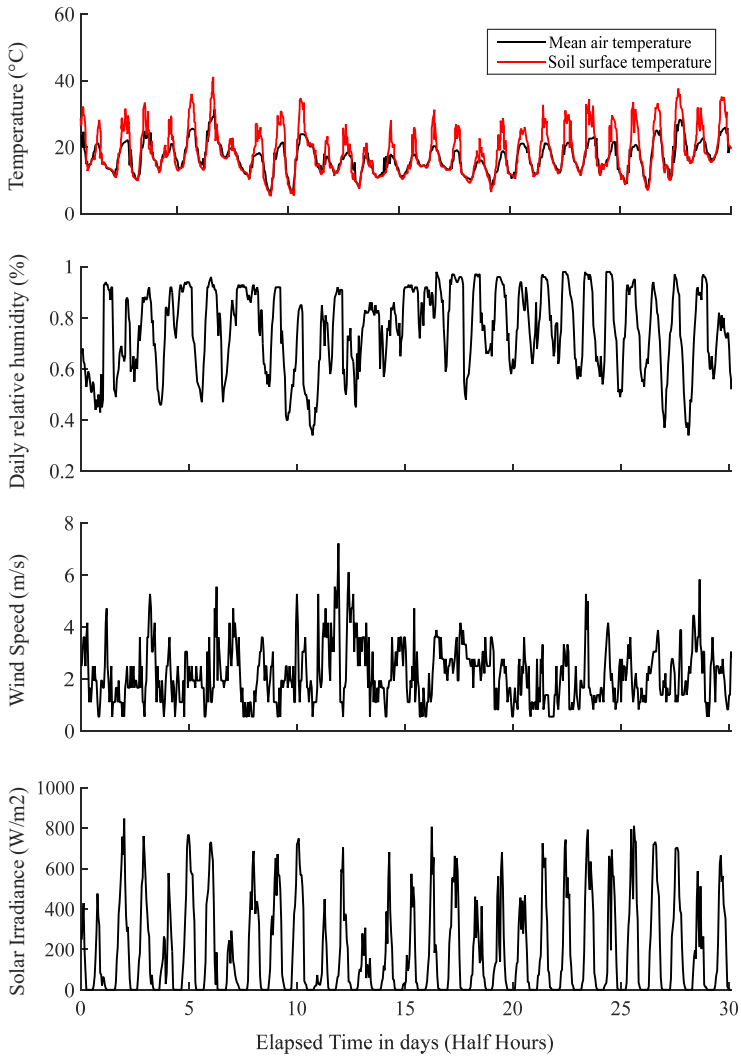

Figure 2.5 - Half hourly recorded meteorological data along with a) the soil surface temperature for July 2011 at the Héricourt region in Franche Compté

2.2.4.2 Comparison of the soil surface temperature

All input parameters (Air temperature, relative humidity, wind speed and the global solar irradiance) of the Héricourt site were used to calculate the soil surface temperature. Figure 2.5 presents all these parameters and shows the difference between the air temperature and the measured soil surface temperature with a half hourly time scale. The saturated and air vapor

pressure of water are calculated using the air temperature data. The air emissivity coefficient is then derived by using the air vapor pressure. The wind speed data are corrected and applied to Eq. (2.10) to find the air heat transfer coefficient in Eq. (2.9). Constant values of Albedo and soil surface emissivity coefficient are also deduced from Table 1.6 and Table 1.8. The soil surface emissivity coefficient varied between 0.9 and 0.98, therefore a constant value of 0.95 is considered in this study for this specific site. Figure 2.6 shows the calculated soil surface temperature and the measured soil surface temperature for the Héricourt region. It can be observed that, in situ measurements of soil surface temperatures are in coherence with the estimations derived from the thermal-based energy balance approach.

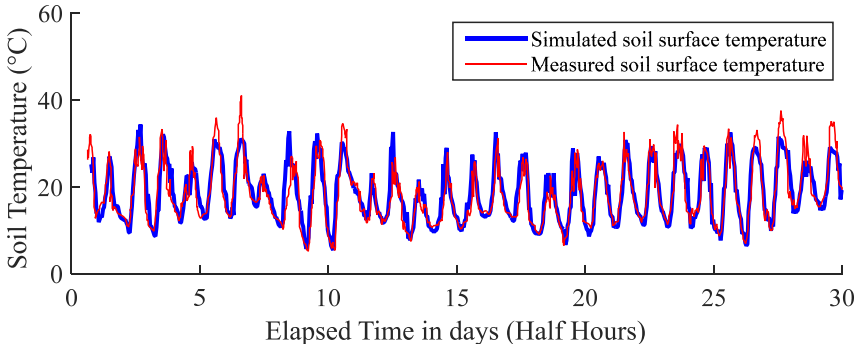

Figure 2.6 - Comparison of the measured data (An et al. 2017b) and the simulated soil surface temperature using the energy balance approach

2.2.4.3 Comparison of the derived net radiation to other net radiation models

In this context, the calculated soil surface temperature by Eq. (2.14) is primarily used to estimate the net solar radiation in the Héricourt site. The estimated net solar radiation is compared with the reported net radiation models. In this case, a half hourly time scale has been adapted because measurements were done on this time scale. Figure 2.7 shows the calculated net solar radiation of the proposed approach versus the net solar radiation derived from the mentioned models. The R^2 values are globally acceptable while the highest values are observed for the BRM models. Two sophisticated R_n models (FAO56 and Monteith) show lower R^2 values than the other models. It is worth mentioning that this correlation depends also on the time scale of the net radiation calculation.

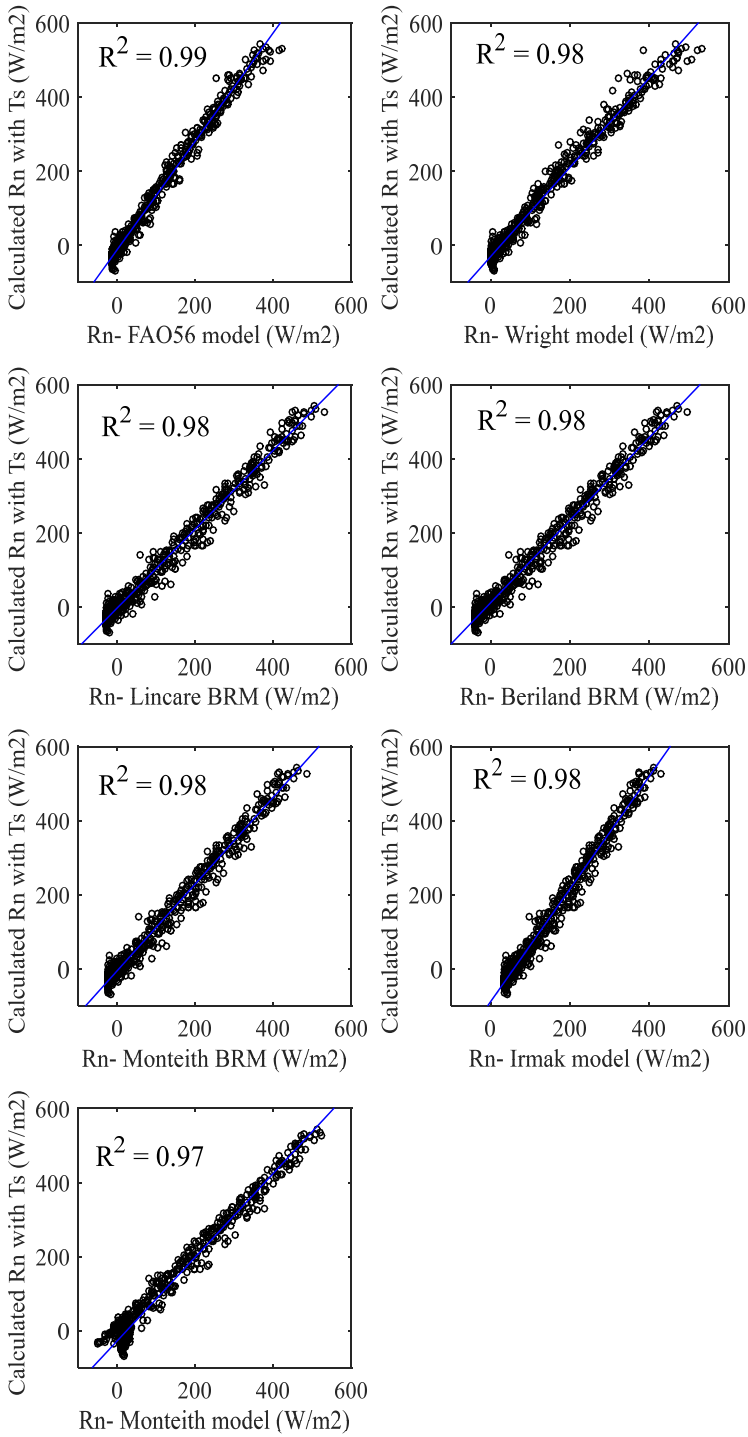

Figure 2.7 - Comparison of the derived net solar radiation from the soil surface temperature to seven net radiation models (Héricourt site)

These comparisons justify the use of the thermal based energy balance approach along with the simplified water balance approach in the adapted soil-atmosphere interaction analysis through a coupled hydro-thermal simulation approach in which the variations of the soil water content are related to the variations of the thermal conductivity.

2.3 Hydro-Thermal modelling approach

In order to analyze the hydraulic and thermal state of soil in depth, hydro-thermal soil models are used. The soil-atmosphere interaction analysis provides the necessary natural atmospheric conditions for coupled hydro-thermal analysis in unsaturated soils by using the mass balance which gives the infiltration rate by subtracting the rate of evapotranspiration from the amount of precipitations and the thermal based energy balance which provides the soil surface temperature by knowing the net solar radiation, the sensible and latent heat of evapotranspiration as described in the previous section. In this section the modelling theory is presented with the associated equations.

2.3.1 Water flow simulation approach in unsaturated soils

The HYDRUS 2D software package (Šimůnek et al., 2006) was used for the modeling purpose in this work (see Appendix 2). The unsaturated water flow equation in a porous media can be described using Richards equation as follow:

$$\frac{\partial \theta}{\partial t} = \frac{\partial}{\partial z}\left[K(\psi)\left(\frac{\partial \psi}{\partial z}+1\right)\right] - S(z,t) \tag{2.15}$$

where θ represents the volumetric water content [L^3L^{-3}]. ψ is the soil water pressure head or the soil suction in [L], $K(\psi)$ is the hydraulic conductivity function [LT^{-1}], t is the time, z is the elevation [L] and $S(z,t)$ is the sink term [$L^3L^{-3}T^{-1}$] which represents the water uptake be vegetation roots and will be presented in the next section. The soil hydraulic conductivity and the water retention functions, proposed by Mualem (1976) and van Genuchten (1980), are given by:

$$K(S_e) = K_s {S_e}^l \left[1 - \left(1 - {S_e}^{\frac{1}{m}}\right)^m\right]^2 \tag{2.16}$$

$$\theta(h) = \begin{cases} \theta_r + \dfrac{\theta_s - \theta_r}{[1+|\alpha\psi|^n]^m} & h < 0 \\ \theta_s & h \geq 0 \end{cases} \tag{2.17}$$

where K_s is the saturated hydraulic conductivity, θ_r and θ_s are the residual and saturated water contents respectively [L^3L^{-3}], and S_e is the relative saturation ($S_e = (\theta - \theta_r)/\ (\theta_s - \theta_r)$) and is dimensionless. α, n, m, and l are the shape parameters of the above functions and are usually obtained by fitting the retention model to experimental data.

As mentioned in the first chapter, the swelling potential of a soil is determined based on the geotechnical parameters, using the indirect methods (Atterberg's limits, clay content, oedometer test, etc.). Each swelling class of expansive soil can represent different retention properties. Therefore, the aim of this section is to perform simple and multi variate regression analysis on some soil's geotechnical properties in order to estimate the key parameters for developing the soil-water retention curves for each swelling categories of soils when direct measurements of the soil retention capacities are not available.

2.3.1.1 Characterizing some expansive soils

The data base provided by DETERMINANT on 100 managed shrink-swell claims was used in this analysis. Figure 2.8 shows some residential buildings which were damaged by the shrink-swell of expansive clays on the map of France. It can be observed that almost all parts of France are concerned about this phenomenon however, there is globally more concentration on the south of France due to the sensitive geological formations which are mainly composed of clays and also the climate which is mostly drier than other parts of France during summer. This highlights the extent of this phenomenon in France and the need for deeper comprehension of its mechanism.

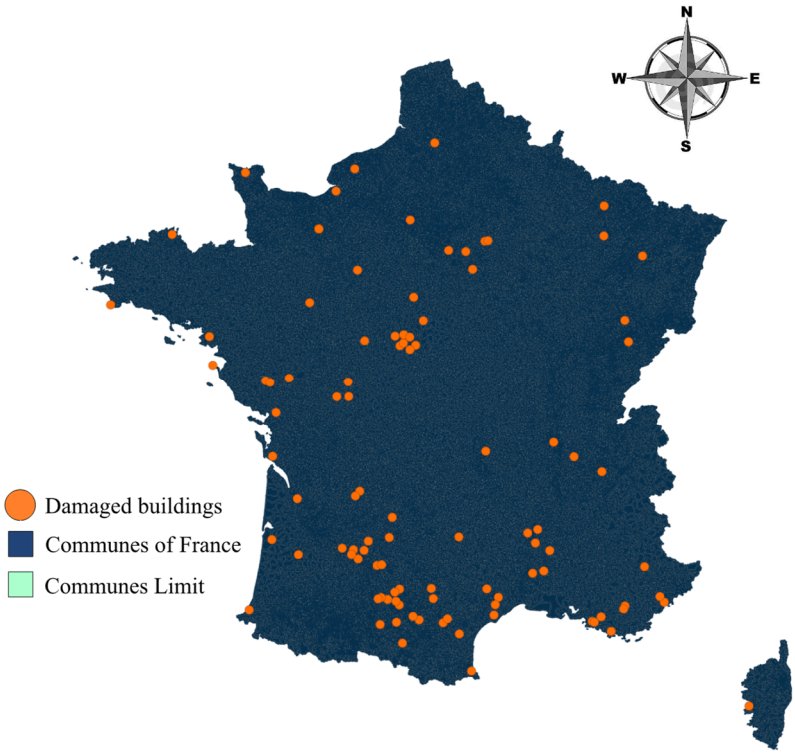

Figure 2.8 - Damaged residential buildings due to the shrink-swell phenomenon in France (Assadollahi & Nowamooz, 2018a)

In this section 78 soil samples tested from the supporting soil of these damaged buildings are analyzed. The measured parameters of these samples are presented in Table 2.1. The Plasticity index (PI), Liquide limit (LL), VBS (Blue Methylene value), Natural water content (w%), Consistency Index (CI), Percent Passing from 80µm (W<80µm) and Percent passing from 2mm (Θ<2mm) are presented. The plasticity range of these soils are presented in Figure 2.9 on the Casagrande plasticity chart. It can be seen that most of these samples are in the range of CI and CH soils. In order to characterize the swelling potential of these soils 7 different characterization methods were used based on the available measured parameters.

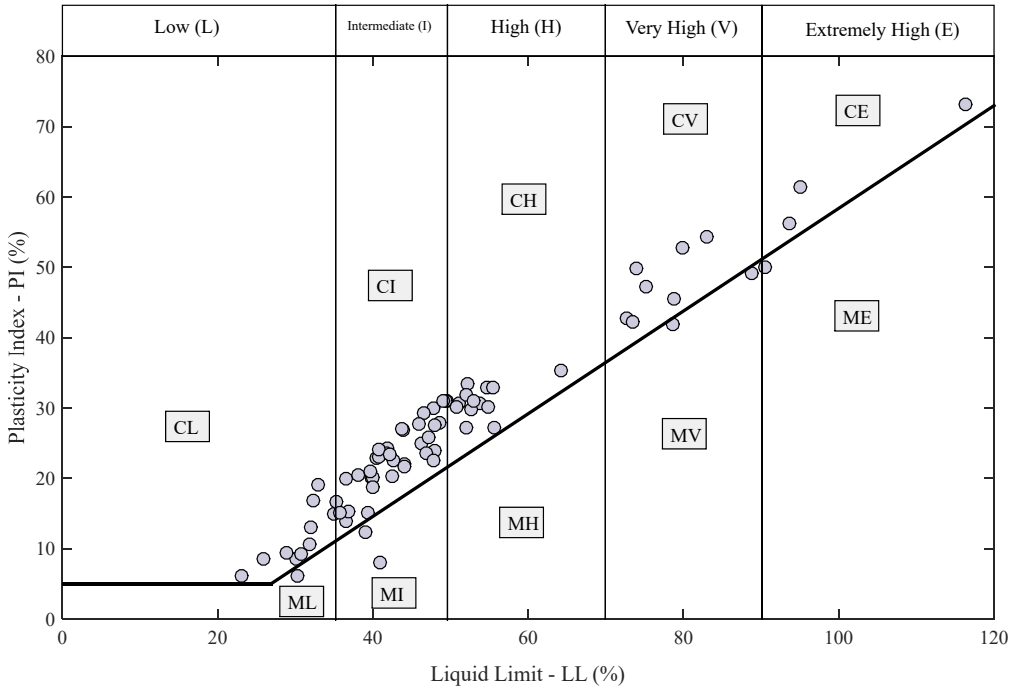

Figure 2.9 - Plasticity range of 78 soil samples collected from the supporting soil of damaged buildings.

The Seed et al. (1962) method which is based on the plasticity index and the heave potential which is calculated by $e_g=2.16^{-3}IP^{2.24}$. The proposed method by Dakshanamurthy and Raman (1973) and Chen (1975) is based only on the Liquide limit (LL). The method used by Chassagneux et al. (1996) is based on the VBS, and the plasticity index (PI). The method developed by Piran et al. (2000) is based only on the plasticity index (PI). The method applied by Jones and Holtz (1973) is based on the Plasticity index (PI), the shrinkage limit (SL) and the Liquid limit (LL) and finally the method developed by Ghen (1988) (cited by Derriche and Kebaili (1998)) is based on the Liquide limit (LL) and the percent passing from 74 µm.

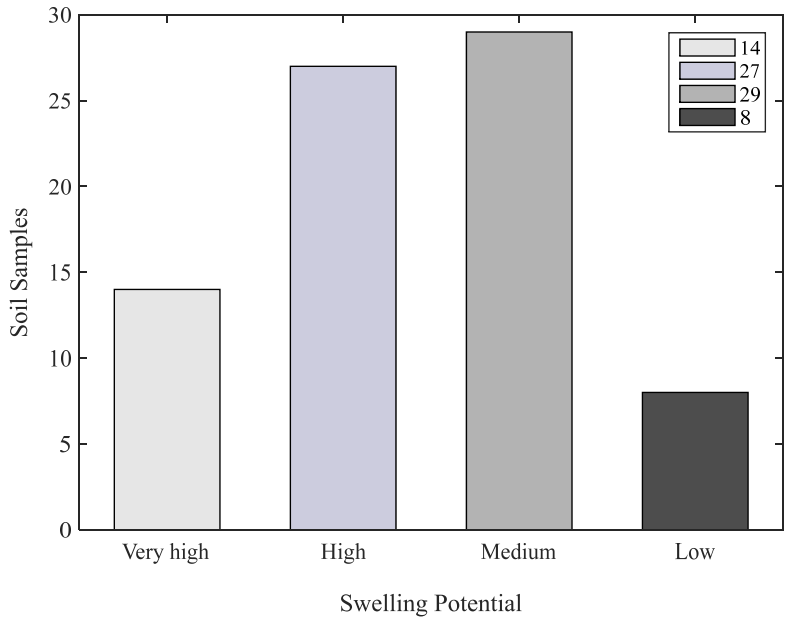

Figure 2.10 - Swelling potential of 78 soil samples

Table 2.1 - Studied soil samples parameters

N°	French soil classification	Liquide Limit (LL)	VBS	Plasticity index (PI)	Natural water content (w%)	Consistency index (CI)	%<80 µm	%<2 mm
1	A2	41.4	4.59	23.7	16.3	1.1	96.8	98.8
2	A3	54.7		33	19	1.1	70	99.4
3	A3	52		27.2	26.5	0.9	78.9	98.3
4	A2	44		22	29.7	0.7	84.5	98.2
5	A2	48	5.1	24	13.7	1.43	80.3	88.6
6	A2	35		15	19.4	1	79.2	88.9
7	A3	49.5		31	22.7	0.9	97.1	98.7
8	A3	47.8		29.9	22.1	0.9	93.9	98.3
9	A3	51.1		30.7	21.4	1	94.4	99.3
10	A4	116.3		73.2	53.6	0.9	85.9	99
11	A3	55.6		27.3	22.9	1.2	72.6	99.3
12	A3	53.7		30.6	21.1	1.1	92	98
13	A2	35.3	2.37	16.7	16.7	1.1	53.9	97.1
14	A3	49.3		31	18.8	1	63.7	98.9
15	A3/A2	46.2		25	23.7	0.9	72.4	94
16	A2	39.8		20.2	16.9	1.1	60.9	90.9
17	A2	39		12.3	32.2	0.6	66.8	99.7
18	A2	36.5		13.9	15.1	1.5	44.3	75.4
19	A3	48.6		27.9	20.4	1	93.8	99.9
20	A2/A3	41.8		24.2	19.9	0.9	53.6	69.9
21	A3	50.7		30.2	17.4	1.1	54.2	84.2
22	A2/A3	40.5		22.9	15.9	1.1	78.8	97.4
23	A3	46.5		29.3	24.4	0.8	94.4	99.7
24	A2/A3	46.9	6.65	23.6	26.2	0.9	95	99.3
25	A2	41.7		23.5	15.9	1.1	49.3	78.3
26	A3	52.2		33.4	19.2	1	73.2	99
27	A2	32.3		16.9	13.9	1.1	87.2	97.6
28	A3	64.2		35.3	29.4	1	66.9	99.4
29	A3	47.1		25.8	26.2	0.8	95.6	99.8
30	A3	52		31.8	19.4	1	72.4	99.6
31	A1	30.3		6.2	23.9	1	98.4	99.8
32	A4	75.2		47.3	32.9	0.9	94.9	99.2
33	A4	93.6		56.3	45.5	0.9	77.4	95.5
34	A1	40.7	0.59	23.1	12.3	1.2	28.9	96.2
35	A2/A3	42.7		22.6	17.7	1.1	72.8	99.4
36	A4	88.8		49.1	45.4	0.9	68.3	95.2
37	B5	31.8		10.7	16.7	1.4	29.8	75.9
38	A4	78.8		45.5	40.5	0.8	90.7	98.9
39	A2	39.8		20.1	15.7	1.2	55.5	84.9
40	A2	36.5		20	14.9	1.1	81.5	98.4
41	A3	52.7		29.8	18.8	1.1	89.6	95.7
42	A2	40		20.2	20.8	1	97.3	99.7
43	A3	43.9		26.8	21.2	0.8	88.8	96.9
44	A3	45.9		27.7	18.9	1	73.2	97
45	A4	132.5		74.9	95.1	0.5	85	98.7
46	A2	39.6		21	17.8	1	49.4	99.8
47	A1	23.1		6.2	13.1	1.6	54.5	93.4
48	A1	30.1		8.5	22.8	0.9	74.6	87.7
49	A4	83		54.4	28	1	96	100
50	A4	95		61.5	37.4	0.9	45.5	95.8
51	A2/B6	39.9		18.8	21.9	1	42	90.8
52	A3/A2	43.7		27.1	23.9	0.7	74.8	98.7
53	A4	73.9		49.9	73.9	0.9	80.9	98.5

54	A2	40.7		24.1	16.8	1	74.3	97
55	A4	72.6		42.7	28.6	1	79.9	99.1
56	A2	32		13	18	1.08	78.9	99.4
57	A4	73.4		42.3	38.4	0.8	99.2	99.8
58	A4	78.6	8.25	41.9	32.8	1.1	83.8	91.2
59	A1	40.9	0.65	8.1	32.2	1.1	46.8	92.3
60	A2	39.3		15.2	15.2	0.9	85.8	98.8
61	A3	53	5.2	31	20.6	1.05	95	99.7
62	A2	44		21.6	29.7	0.7	87.9	98.9
63	A2	42.5		20.3	27.1	0.8	87.5	93.9
64	A2	38.1		20.4	20.3	0.9	76.6	93.5
65	B6	36.9		15.3	23.2	0.9	32.2	88.3
66	A3	47.8		22.5	16.2	1.2	60.7	82.3
67	A3	55.5		32.9	21.3	1	69.7	98.3
68	A4	90.5		50.1	45.5	0.9	86	99
69	A3	48		27.5	20.6	1	91.2	99.9
70	A3	49		31	20.6	0.92	93.2	98.9
71	A1	25.9		8.6	17.4	1	62.7	97.7
72	B5	30.8	1.16	9.3	12.6	2	29.8	95
73	A4	79.9	0.9	52.8	30	0.9	38.1	82.2
74	A2	33		19.1	11.3	1.1	24.5	71.7
75	A3	54.8		30.2	31.2	0.8	95.7	99.8
76	A1	28.8		9.5	22.7	0.6	91.6	98.9
77	A2/A3	42.1		23.4	22.4	0.8	75.8	97.8
78	A2/B5	35.8		15.2	14.7	1.4	36.5	55.3

Table 2.2 shows the swelling potential of these soil samples characterized with these seven methods. It should be mentioned that C, V, H, M, L and N in Table 2.2 refer to Critical swelling potential, Very high swelling potential, High swelling potential, Medium swelling potential, Low swelling potential and Non-swelling soil respectively. For this study the characterization is based on only four categories (V, H, M and L) as mentioned in the last column of Table 2.2. Figure 2.10 shows the amount of soil samples in each of these categories. It can be seen that there is a higher number of soil samples that are characterized as high swelling potential (27 samples) and medium swelling potential (29 samples). Only 8 samples are in the low swelling potential range.

2.3.1.2 Soil water retention curves (SWRC) with predicted W.PI

Based on the method developed by Ganjian et al. (2007) the Soil-Water retention curves could be predicted using the soil index properties and the Van Genuchten (1980) equation. This method was validated with experimental measurements thus it is used in this study. Since the soil suction at equilibrium is expected to be proportional to the specific surface area at a given saturation degree, though the weighted PI, meaning the product of the percent passing from 80µm and PI, is considered as the key parameter which is correlated to the Van Genuchten parameters as follow:

$$\frac{1}{\alpha} = 0.0015(\mathrm{W.PI})^3 + 0.1028(\mathrm{W.PI})^2 + 0.5871(\mathrm{W.PI}) + 11.813 \tag{2.18}$$

$$n = 0.00011(\mathrm{W.PI})^2 - 0.01358(\mathrm{W.PI}) + 1.76987 \tag{2.19}$$

$$m = -5 \times 10^{-6}(\mathrm{W.PI})^2 - 0.00014(\mathrm{W.PI}) + 0.14745 \tag{2.20}$$

By calculating $\frac{1}{\alpha}$ and n and m for these 78 soil samples based on the W.PI parameter, the soil-water retention curves for each four categories (V, H, M and L) are deduced and presented in Figure 2.11. A mean retention curve was chosen to represent the SWRC of each four categories. These soils parameters will be used in further analysis.

The plasticity index (PI) of the soil and the percentage passing from 80 µm are the two main variables for the establishment of the soil water retention curve. In order to predict these values, regression analysis was carried out for developing a relationship between these variables and other measured geotechnical properties (Natural water content w%, percent passing from 2mm, φ, and the liquid limit, LL). The following expressions are deduced for PI and W by the regression analysis for these 78 soil samples:

$$\mathrm{PI} = -13.793 - 0.191(\mathrm{w\%}) + 0.782(\mathrm{LL}) + 0.068(\% < 2\mathrm{mm}) \tag{2.21}$$

$$\mathrm{W} = -72.62 + 0.105(\mathrm{w\%}) + 0.04(\mathrm{LL}) + 1.498(\% < 2\mathrm{mm}) \tag{2.22}$$

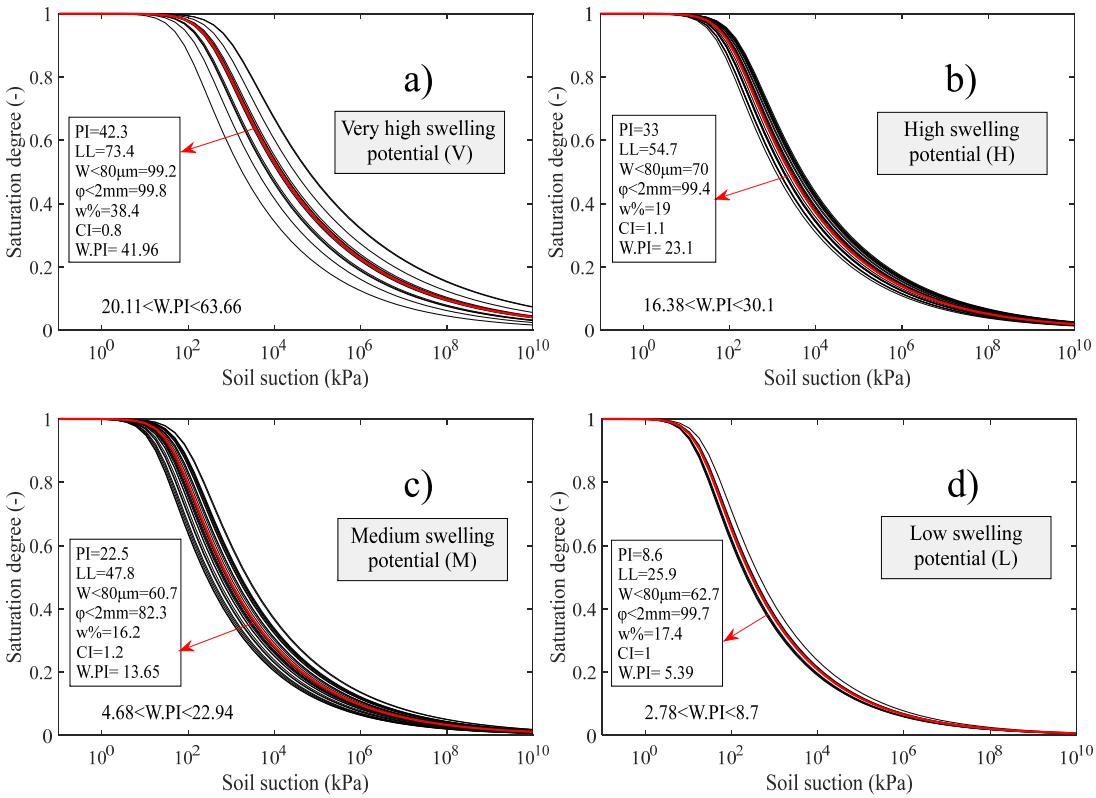

Figure 2.11 - Soil water retention curves for a) very high swelling potential soils (20.11<W.PI<63.66), b) high swelling potential soils (16.38<W.PI<30.1), c) medium swelling potential soils (4.68<W.PI<22.94), d) Low swelling potential soils (2.78<W.PI<8.7).

Table 2.2 - Evaluation of the swelling potential using different methods.

N°	Seed et al. (1962)				Dakshanamurthy and Raman (1973)						Chen (1975)				Chassagneux et al. (1996)				Piran et al. (2000)				Jones and Holtz (1973)			Ghen (1988)				Chosen for this study			
	V	H	M	L	C	V	H	M	L	N	V	H	M	L	V	H	M	L	V	H	M	L	H	M	L	V	H	M	L	V	H	M	L
1																																	
2																																	
3																																	
4																																	
5																																	
6																																	
7																																	
8																																	
9																																	
10																																	
11																																	
12																																	
13																																	
14																																	
15																																	
16																																	
17																																	
18																																	
19																																	
20																																	
21																																	
22																																	
23																																	
24																																	
25																																	
26																																	
27																																	
28																																	
29																																	
30																																	
31																																	
32																																	
33																																	
34																																	
35																																	
36																																	
37																																	
38																																	
39																																	
40																																	

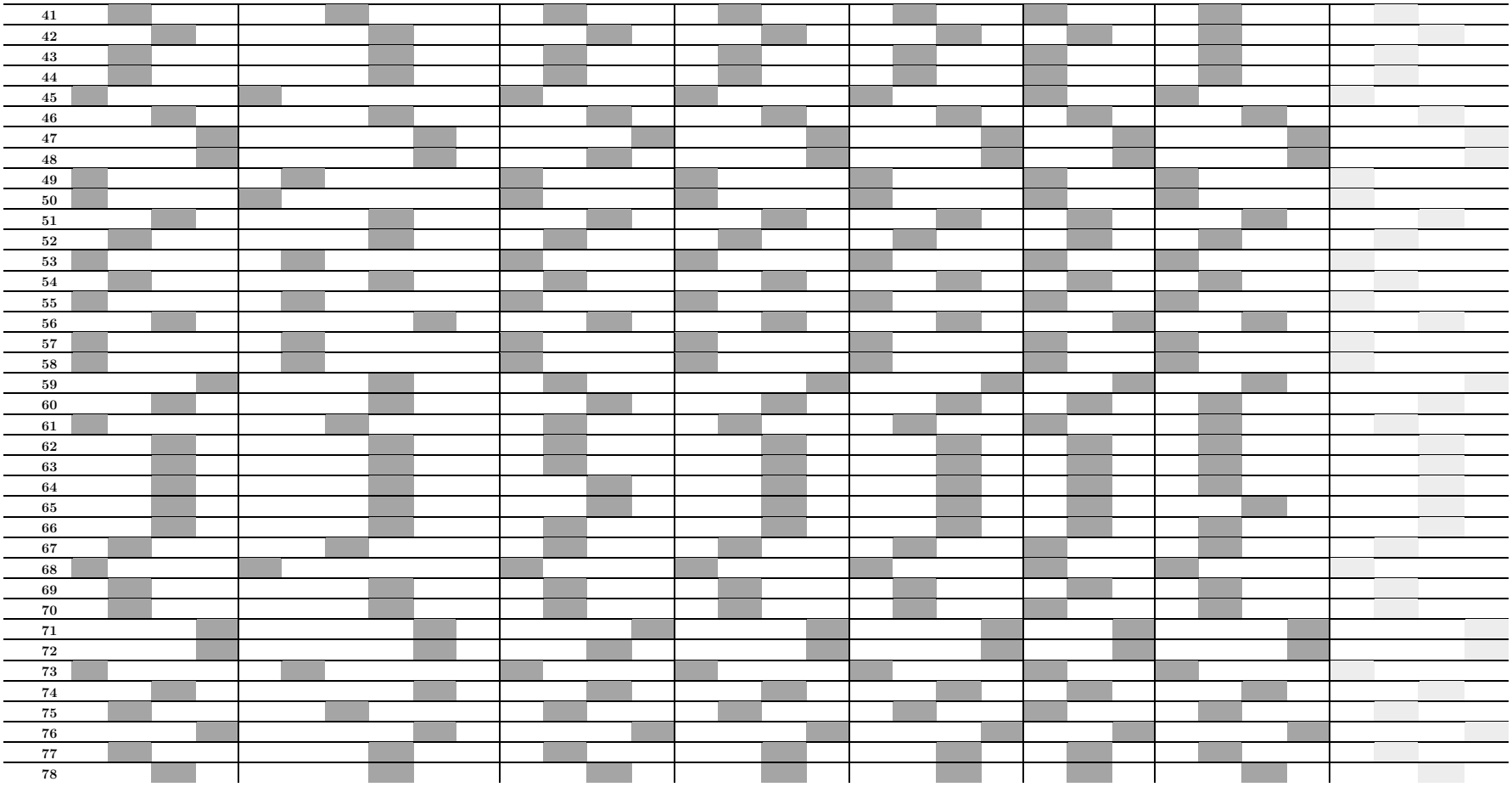
41
42
43
44
45
46
47
48
49
50
51
52
53
54
55
56
57
58
59
60
61
62
63
64
65
66
67
68
69
70
71
72
73
74
75
76
77
78

2.3.1.3 Analysis and comparisons

Table 2.3 shows the regression statistics for these two expressions (2.21) and (2.22) as it is shown graphically on Figure 2.12 a) and b). R^2 values for the PI regression shows that there is good coherence between the predicted and the measured PI values however the R^2 coefficient is smaller but acceptable in higher W values.

Table 2.3 - Regression statistics for the two predicted variables (PI and W)

Regression Statistics	PI	W<80 µm
Multiple R	0.974	0.654
R Square	0.949	0.427
Adjusted R Square	0.947	0.404
Standard Error	3.326	15.491
Observations	78	78

To establish the soil water retention curves based on W and PI, a comparison of the predicted and the measured W and PI with the natural water content, liquid limit and percent passing form 2mm, were carried out to validate and confirm the performance of the developed linear expressions (Eq. (2.21) and (2.22)). Figure 2.13 a) to c) shows the results of the comparison of the predicted and the measured PI with the cited geotechnical properties. It can be observed that there is generally good agreement with the measured data. Figure 2.13 d) to f) shows the results of this comparison with the measured and predicted W. The plots show that there is an acceptable agreement with the measured data (less correlations for W). Thus, the linear expressions can be employed in further analysis.

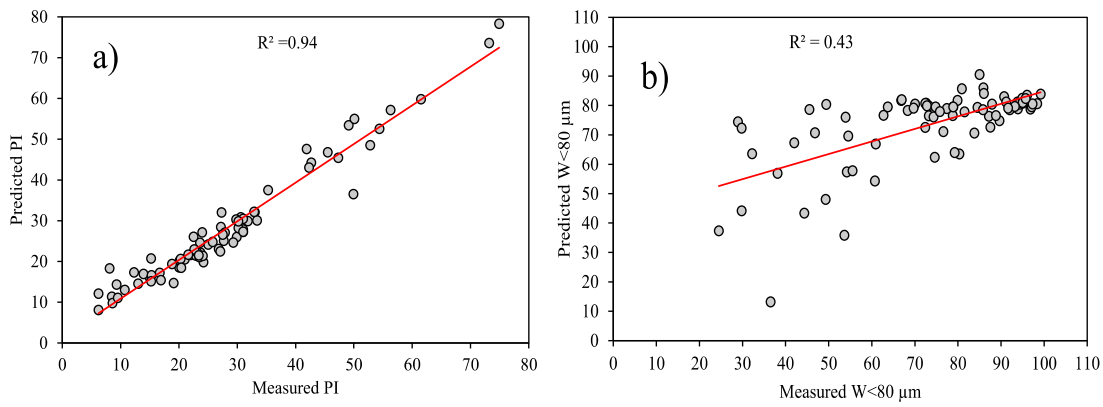

Figure 2.12 - Regression analysis on the predicted and measured a) PI and b) W

By analyzing the approach, the SWRC of different swelling categories (V, H, M, L) could be calculated using Eq. (2.21) and (2.22). To do so, the PI and the W of four soils in different categories (Figure 2.11) are primarily used as reference SWRC which are calculated using Eq. (2.18) to (2.20).

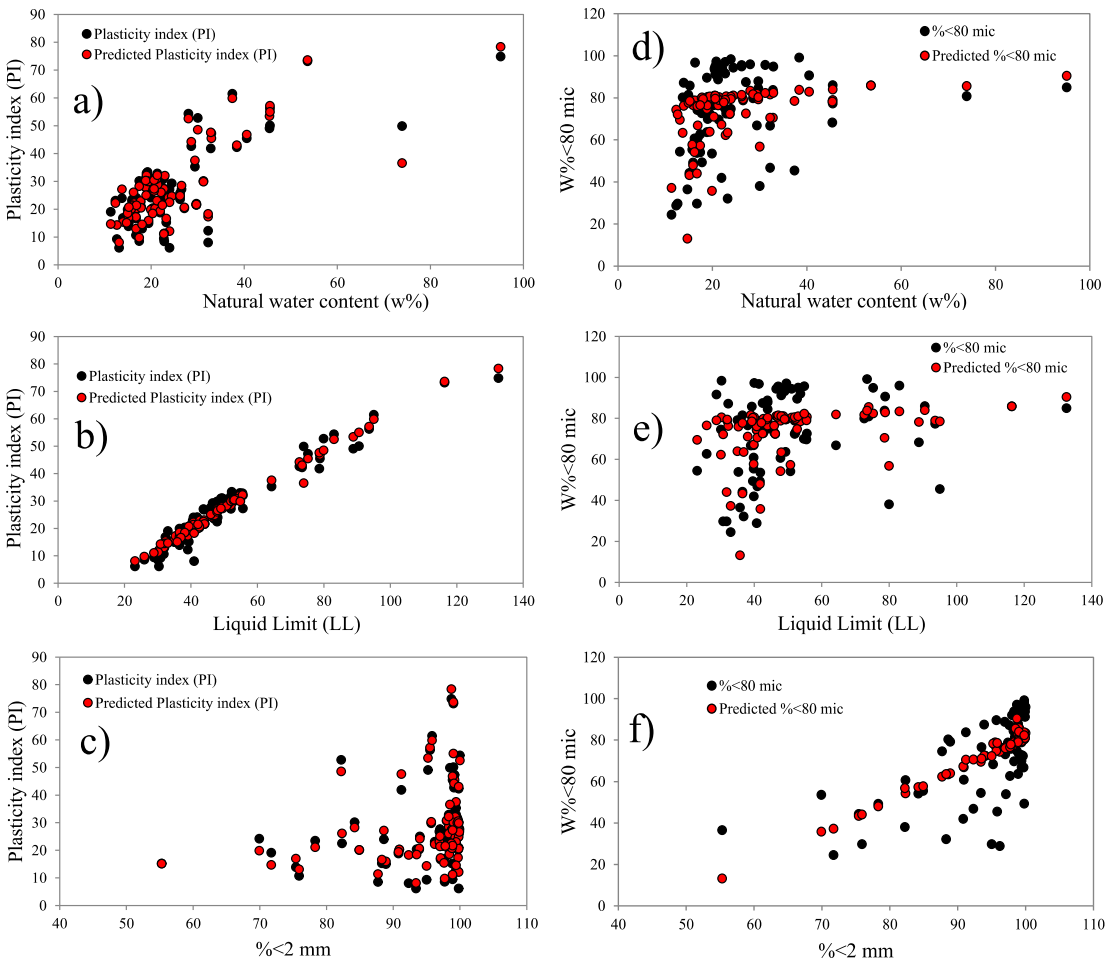

Figure 2.13 - Comparison of the predicted and the measured PI and W% relationship with the natural water content, the Liquid limit and the percent passing from 2mm.

Secondly, the water retention curves of these four soils are calculated using the predicted values and coefficients as indicated in Table 2.4. Finally, a comparison is made with the reference SWRCs which were established using measured values. Figure 2.14 shows the comparison for these four soils in four different swelling categories. It can be observed that there is a good agreement with the SWRC calculated by predicted W.PI values and the SWRCs calculated with measured W.PI values. The error could be related to the low regression coefficient of the percent passing from 80 µm (W%).

Table 2.4 - Predicted variables and coefficients for the calculation of SWRC.

Soil	**PI (%)**		**W (<80µm)**		**W.PI**		**a**		**b**		**c**	
	Pred.	Meas.	Pred.	Meas.	Pred.	Meas.	Pred.	Meas.	Pred.	Meas.	Pred.	Meas.
V	43.1	42.3	83.8	99.2	36.11	41.96	237.793	328.28	1.423	1.393	0.136	0.133
H	32.1	33	80.5	70	25.84	23.1	121.508	98.719	1.492	1.514	0.140	0.141
M	26.1	22.5	54.3	60.7	14.17	13.65	45.0512	42.827	1.599	1.605	0.144	0.144
L	9.8	8.6	76.6	62.7	7.50	5.39	22.6477	18.202	1.674	1.699	0.146	0.146

Globally, this approach allows to estimate the soil retention curve based on three laboratory measured parameters (LL, w%, φ <2mm) and consequently allows the determination of the key parameters (PI and W) for the estimation of the retention curves. This linear regression approach could be used in soil-vegetation-atmosphere analysis if direct measurements of the retention curve are not available. It was also shown that the modified approach is in good agreement with the original one even with considering soils with different swelling potentials.

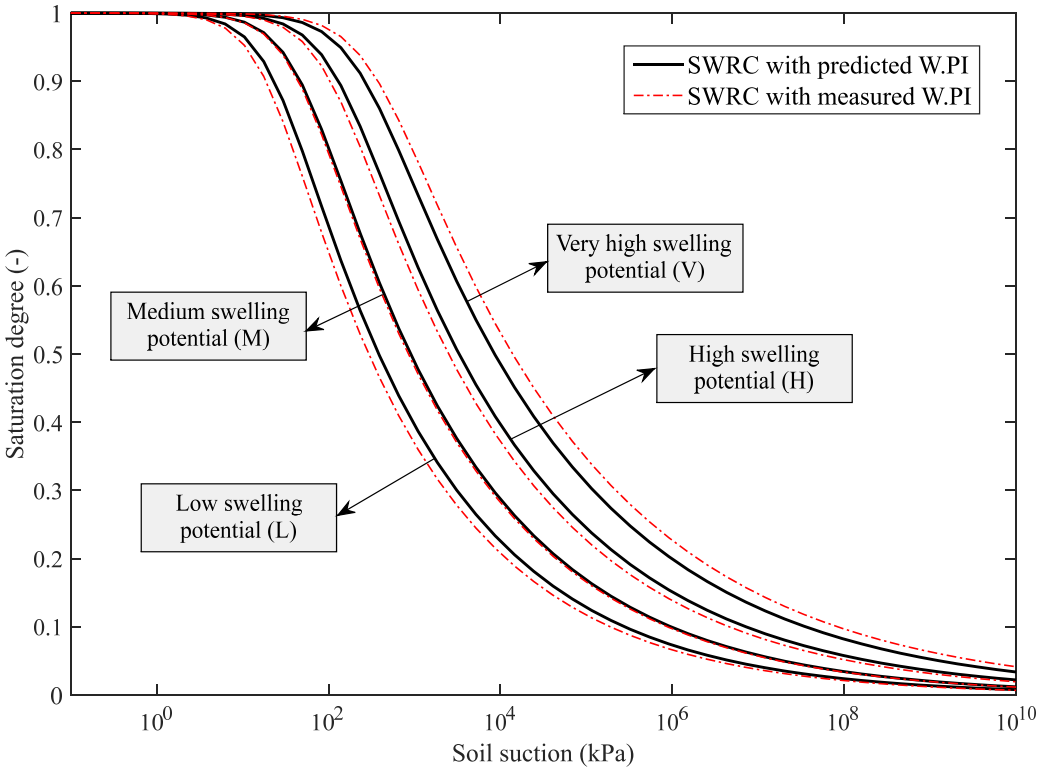

Figure 2.14 - Comparison between the calculated SWRC with measured W.PI and predicted W.PI

2.3.2 Heat transport simulation approach in unsaturated soils

The seasonal soil temperature distributions in depth, are modeled using a coupled approach which relates the seasonal water content variations to the soil thermal conductivity. The differential equation of the heat transfer proposed by Sophocleous (1979) can be described by neglecting the water vapor diffusion as follows:

$$C(\theta)\frac{\partial T}{\partial t} = \frac{\partial}{\partial x_i}\left(\lambda_{ij}(\theta)\frac{\partial T}{\partial x_j}\right) - C_w q_i \frac{\partial T}{\partial x_i} \tag{2.23}$$

where $C(\theta)$ and C_w are the volumetric heat capacities [$Jm^{-3}K^{-1}$] of the porous medium (soil) and the liquid phase, respectively. $\lambda_{ij}(\theta)$ is the apparent thermal conductivity of the soil [$Wm^{-1}K^{-1}$]. The porous medium volumetric heat capacity $C(\theta)$ is composed of the solid phase (C_n), organic phase (C_0) and liquid phase (C_w) volumetric heat capacities which can be described using the following equation (De Vries 1963):

$$C(\theta) = C_n\theta_n + C_0\theta_0 + C_w\theta_w \tag{2.24}$$

where θ refers to a volumetric fraction [L^3L^{-3}], and subscripts n, o, w represent solid phase, organic matter and liquid phase, respectively. In this study the volume fraction dedicated to organic matter is neglect for the sake of simplicity. Thus, the volumetric heat capacity is the combination of the solid and liquid fraction. The heat transported by the flow of water is presented in the second term of the right side of the Eq. (2.23) and the first term describes the heat flow due to conduction phenomenon into the soil.

In this study, the thermal conductivity is expressed using the Chung and Horton, (1987) equation as a function of the soil volumetric water content with empirical parameters b_1, b_2 and b_3 [$MLT^{-3}K^{-1}$].

$$\lambda_0(\theta) = b_1 + b_2\theta + b_3\theta^{\,0.5} \tag{2.25}$$

This simple empirical function can be used to estimate the soil thermal conductivity based on the soil texture and represents in most cases good coherence with the thermal conductivities derived by experiments. It should be mentioned that $\lambda_{ij}(\theta)$ is a function of the fluid flux density and longitudinal-transvers thermal dispersivities along with the thermal conductivity $\lambda_0(\theta)$. Figure 2.15 shows some calculation results of the thermal conductivity functions of different soils, using the HYDRUS 2D thermal library.

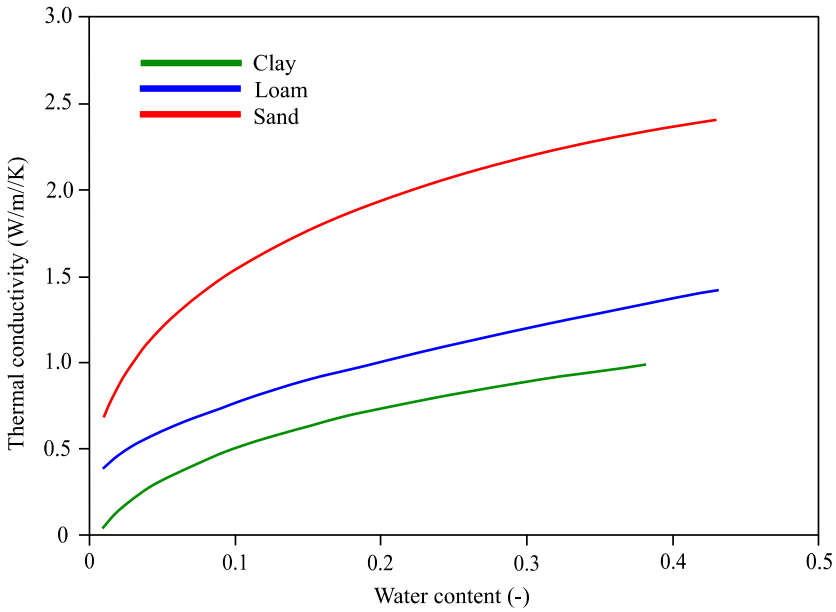

Figure 2.15 - Generated TCF function for different soils using HYDRUS 2D

In addition to the thermal conductivity function, a scaling technique similar to one used to describe spatial variability of soil hydraulic properties (Vogel et al., 1991) is used in HYDRUS to express the temperature dependence of the soil hydraulic conductivity. More details on this approach can be found in the HYDRUS 2D manual.

2.4 Vegetation effect

The effect of vegetation root on the hydraulic state of the soil can be studied in a framework of SVA analysis. As the behavior of the unsaturated crop root zone is unpredictable, researchers point out the needs for development of numerical models to simulate this behavior. As mentioned previously the root water uptake is largely affected by root system distribution, soil hydraulic properties, and climatic conditions over time.

2.4.1 Root Water Uptake modelling approach (RWU)

The main goal of the water uptake simulation models is to track different components of the field water balance and to simulate the water content or the soil matrix potential distribution within the soil profile at different times. Since 1960, the unsaturated water flow in different models is calculated using analytical solution of the Richards' equation. The root water uptake models fall into two groups based on how the uptake term is handled. Most of the developed models are classified into two categories, microscopic and macroscopic models. Microscopic models consider the detailed information and the dynamics of the root system which is very difficult and time consuming to determine. On the other hand, macroscopic models are based on a static root depth or a simplified water extraction term (constant, uniform, linear and exponential) in the root zone. In this study the root water uptake (RWU) is expressed using the Feddes model (Feddes et al. 1978) which uses a constant water extraction distribution term.

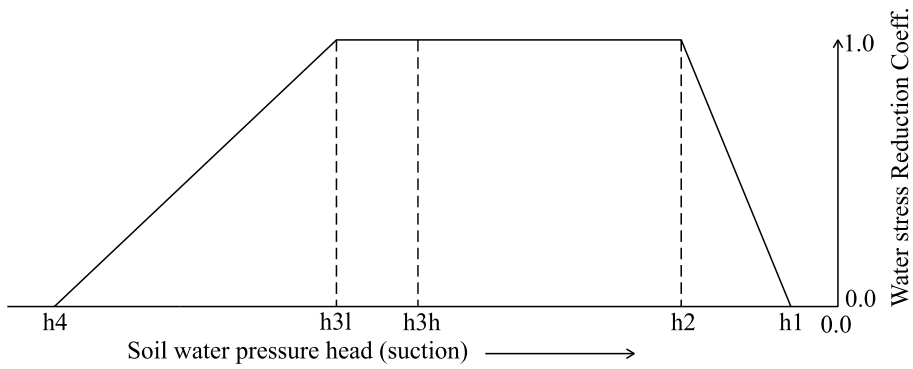

Figure 2.16 - The water stress reduction function versus the soil water pressure head (Feddes et al. 1976).

The sink term in the Richards equation is a function of potential transpiration, the root distribution pattern and the soil suction (pressure head) which is expressed as $S(h) = \alpha(h)\ b_{(x,y,z)}\ S_t\ T_{pot}$; where the water stress response function $\alpha(h)$ is a prescribed dimensionless function of the soil water pressure head and is shown in Figure 2.16. The second term $b_{(x,y,z)}\ S_t\ T_{pot}$ is the potential water uptake rate denoted as S_p [T^{-1}] (Vogel, 1987). S_t is the width [L] of the soil surface associated with the transpiration process, T_{pot} is the potential transpiration rate [LT^{-1}], and $b_{(x,y,z)}$ is the normalized water uptake distribution function [L^{-2} or L^{-3}] which describes the spatial variation of the potential uptake term, S_p, over the root zone. The water uptake is considered to be equal to zero close to saturation state as shown in Figure 2.16 (point h1). When the soil is close to a dry state or is in its wilting point the root water uptake is also equal to zero (h4). An optimal state of water uptake is observed between h2 and h3

pressure heads while the pressure head decreases or increases linearly between h3 and h4 or h1 and h2. The value of h3 varies with the potential transpiration rate between h3l and h3h.

2.4.2 Root distribution function

The normalized water uptake distribution function can be attributed by introducing an arbitrary shape or by using the following expression proposed by Vrugt et al. (2002) for a 2D root distribution pattern:

$$b_{(x,z)} = \left(1 - \frac{z}{Z_m}\right)\left(1 - \frac{x}{X_m}\right)\exp\left(-\left(\frac{p_z}{Z_m}|z^* - z| + \frac{p_x}{X_m}|x^* - x|\right)\right) \tag{2.26}$$

where X_m and Z_m are the maximum rooting lengths in the x-, and z- directions [L], respectively; x and z are distances from the origin of the vegetation species (tree) in the x- and z- directions [L], respectively. p_x [-] and p_z [-], x^* [L] and z^* [L] are empirical parameters, and $b_{(x,z)}$ denote the two-dimensional spatial distribution of the potential root water uptake which is a dimensionless quantity [-]. As verified by Vrugt et al. (2002), the root water uptake can be flexible and can allow the spatial variations of the water uptake as influenced by root density patterns and non-uniform water infiltration or extractions.
Different components of the presented root water uptake model are shown in Figure 2.17 where Ω_R is the region occupied by the root zone. The area over the root zone is an arbitrarily prescribed distribution function. Normalizing the uptake distribution ensures that $b_{(x,z)}$ integrates to unity over the flow domain (soil domain). More information on the integration methods could be found in Vrugt et al. (2002).

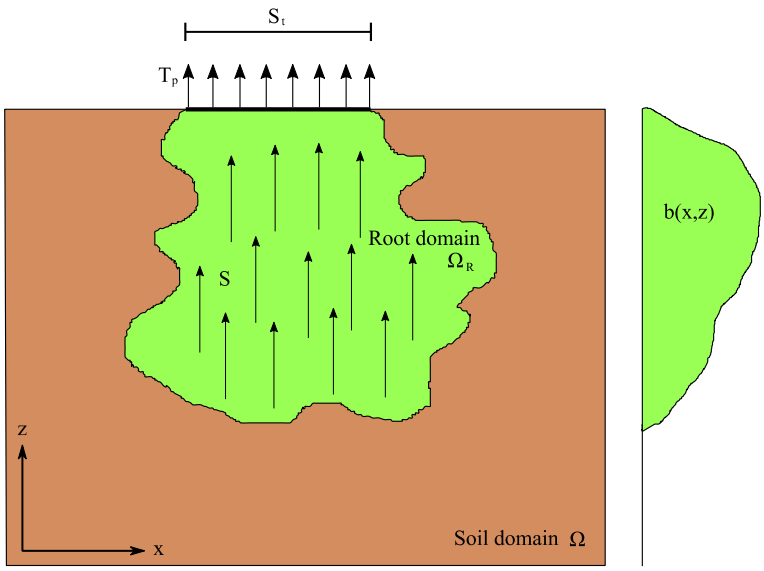

Figure 2.17 - Schematic representation of the potential water uptake distribution function based on Vrught et al. (2002) model.

The root distribution pattern can be specified by adjusting the parameters of the root distribution function. Table 2.5 shows the parameters of the root distribution function for four different configurations. These configurations can be shown in Figure 2.18 a) to d). A square 3*3m soil

domain is considered and the vegetation species (tree) is located in the upper left corner of the soil domain.

Table 2.5 - Root water uptake distribution parameters

Figure	Z_m (m)	z^*	p_z	X_m (m)	x^*	p_x
Figure 2.18 a)	2	0	1	2	0	1
Figure 2.18 b)	2	0	0.5	3	3	0.5
Figure 2.18 c)	3	0	0.5	1.5	5	0.5
Figure 2.18 d)	2	0.1	1.5	3	3	2

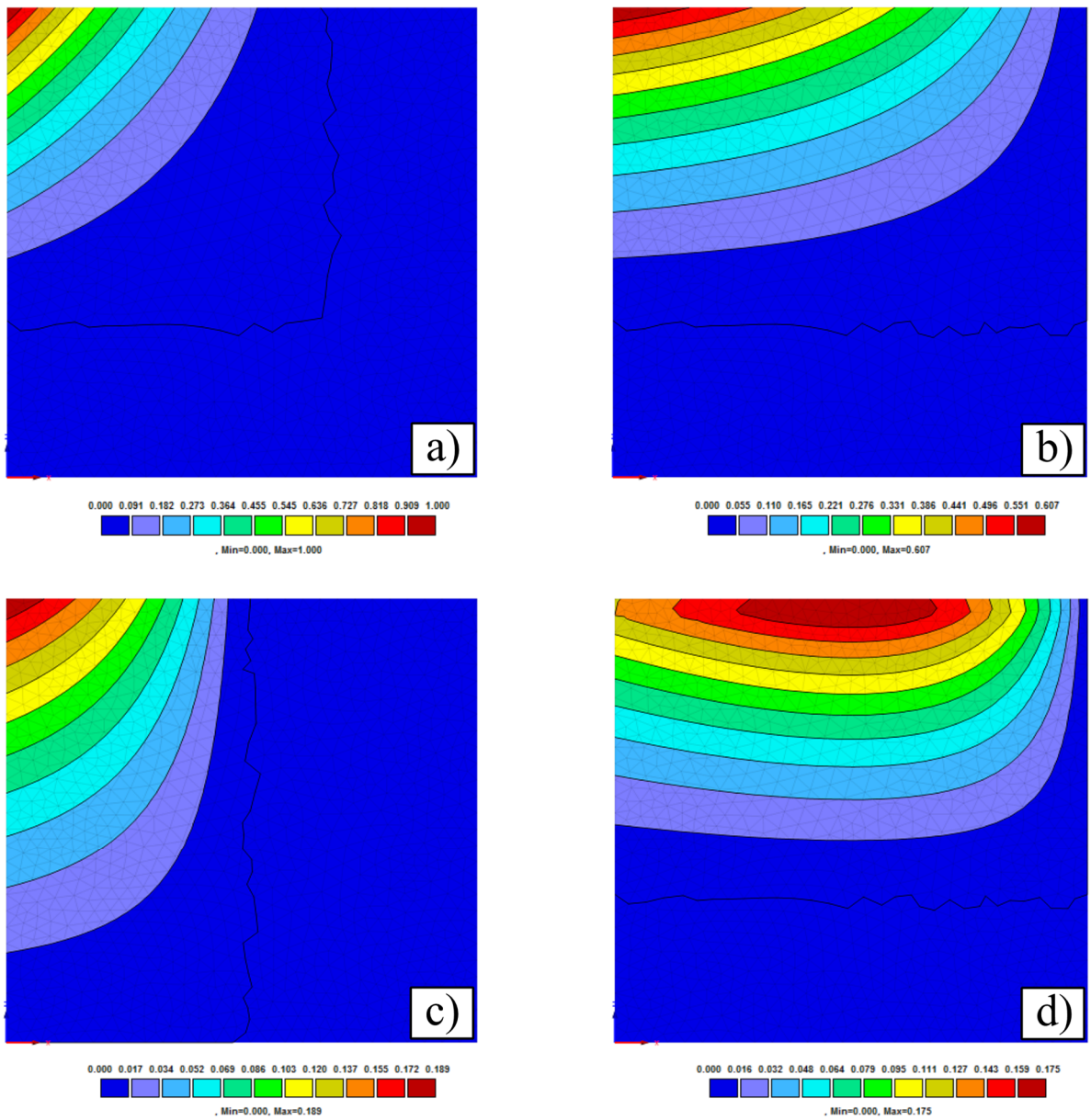

Figure 2.18 - Different configuration of root density distribution into the soil

2.4.3 Potential transpiration and crop coefficient

The potential transpiration due to the presence of vegetation can be calculated using the expression presented in the previous chapter ($T_{pot} = ET_c\ [1 - \exp(-k.\,LAI)]$) where, LAI is the leaf area index which is a dimensionless quantity and is described as the leaf area (upper side only) per unit area of the soil below it. It is expressed as m^2 leaf area per m^2 ground area (Allen et al. 1998). This parameter is usually measured by hygrometric sensors. The general trend of the measured data follows almost a cosine type function and can be expressed using the following expression:

$$LAI = LAI_g\,.\cos\left[(t_n + 120)\frac{\pi}{365}\right]^2 \tag{2.27}$$

where, LAI_g is the maximum value of the observed leaf area indexes in the growing stage of a given species. This value can be determined using the provided tables in Anser et al. (2003) for different grass and vegetation types. t_n is the number of the cumulative days during the considered period. To test the applicability of the proposed equation, a set of measured LAI data from a grassland are reported in this section. Figure 2.19 a) shows the minimum and the maximum LAI for a grassland based on the provided Tables in Anser et al. (2003) along with the fitted LAI on the experimental data reported by Qu et al. (2016) in a grass type cover during a year. As shown in the fitted curves it can be observed that the beginning of the growing phase is fixed to March and there is an acceptable agreement between the fitted model and the provided data. Different LAI plots for some typical vegetation are also presented in Figure 2.19 b). It can be observed that the LAI at maturity (LAI_g) for the grasslands varies between 0.3 and 5. However, the LAI for the most of the crops and the forest trees vary between 0.2 and 8.7 and 0.01 and 15, respectively. The LAI values for different species could vary based on the species height and quality. For typical crop and tree species, these values could be found in Chojnicki et al. (2010). For example, the mean LAI value at maturity for an oak tree is about 2 based on the reported measurements in Chojnicki et al. (2010).

In the T_{pot} equation, k is a constant representing the extinction coefficient per unit leaf area (0.6) and ET_c is the crop evapotranspiration (potential evapotranspiration) which is calculated by multiplying the crop coefficient (K_c) to the reference evapotranspiration (ET_0) ($ET_c = K_c ET_0$). The procedure for calculating the crop evapotranspiration based on Allen et al. (1998) begins primarily by identifying the crop growth stages, determining their lengths, and selecting the corresponding K_c coefficients; then adjusting the selected K_c coefficients for frequency of wetting/drying or climatic conditions during the different stages and finally constructing the crop coefficient curve.

The growing stages of the crops are determined using the tables provided in Allen et al. (1998). Changes in vegetation and ground cover mean that the crop coefficient K_c varies during the growing phase. The trends in K_c during the growing period are represented in the crop coefficient curve. Three values of K_c are required to describe and construct the crop coefficient curve: those during the initial stage ($K_{c\ ini}$), the mid-season stage ($K_{c\ mid}$) and at the end of the late season stage ($K_{c\ end}$). Typical values of these coefficients are provided in Allen et al. (1998). However, these coefficients can be influenced by the wetting drying cycles and the climatic conditions of the site.

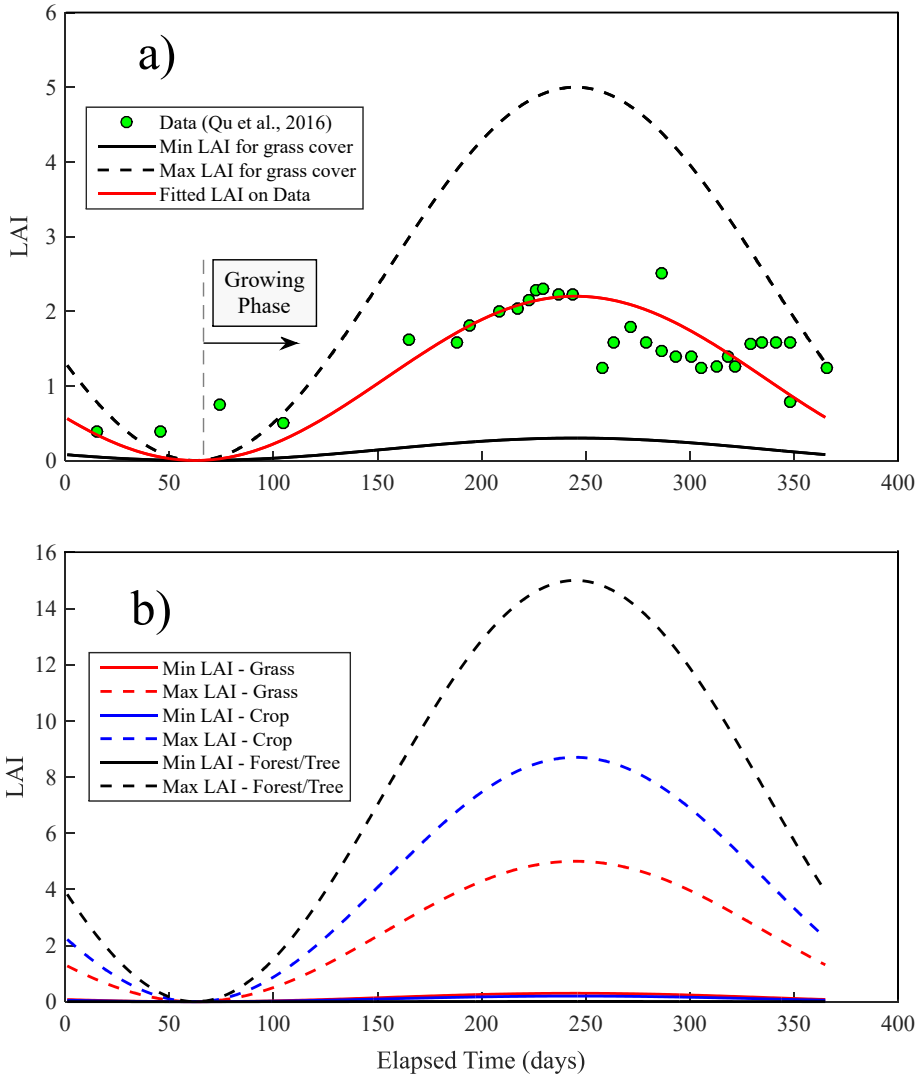

Figure 2.19 - Leaf Area Index plots a) for validation in a grass cover field b) for typical vegetation types.

In this research work, the initial stage crop coefficient ($K_{c\ ini}$) is assumed to be constant based on the provided values, however the mid-season ($K_{c\ mid}$) and the late season stage ($K_{c\ end}$) crop coefficients are adjusted by using the following expressions suggested in Allen et al. (1998):

$$K_{c\ mid} = K_{c\ mid\ (Tab)} + [0.04\ (u_2 - 2) - 0.004(h_{a\ min} - 45)] \left(\frac{h}{3}\right)^{0.3} \tag{2.28}$$

$$K_{c\ end} = K_{c\ end\ (Tab)} + [0.04\ (u_2 - 2) - 0.004(h_{a\ min} - 45)] \left(\frac{h}{3}\right)^{0.3} \tag{2.29}$$

where $K_{c\ mid\ (Tab)}$ and $Kc_{\ end\ (Tab)}$ are reference values taken from the provided tables, u_2 is the mean value of daily wind speed at 2 m height over grass during the mid-season growth stage [m s^{-1}], $h_{a\ min}$ is the mean value for daily minimum relative humidity during the mid-season growth stage [%] and h is the mean plant height during the mid-season stage [m] for 0.1 m < h < 10 m. A typical K_c curve is presented in Figure 2.20.

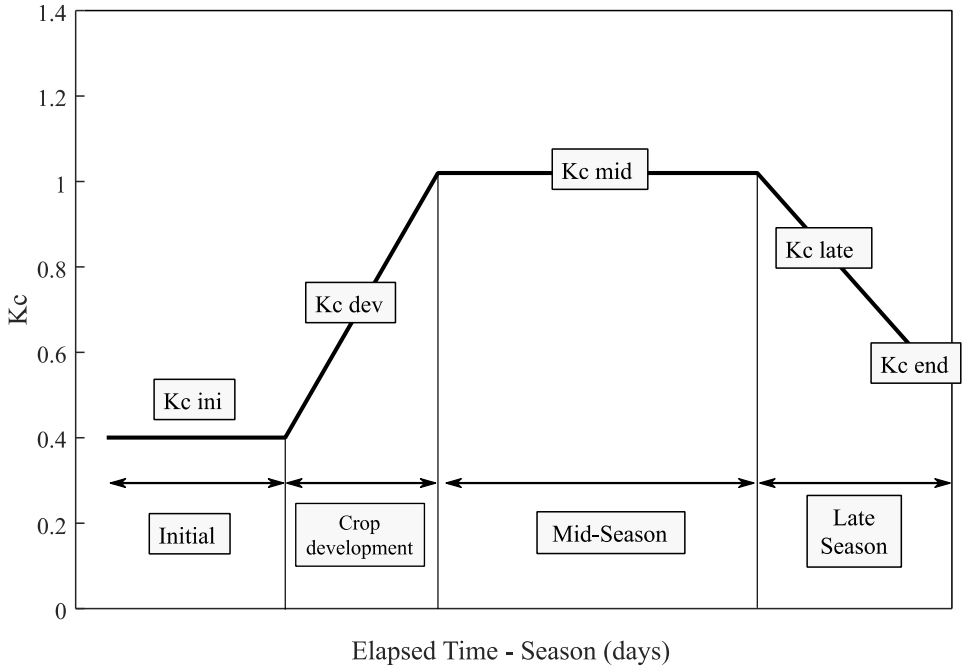

Figure 2.20 - Typical Kc curve along with different crop development stages (Allen et al. 1998)

The potential evaporation from the soil surface (E_{pot}) is the parameter that allows to deduce the surface hydraulic condition and is calculated by the partitioning of the crop evapotranspiration (potential evapotranspiration) into the potential transpiration (T_{pot}) and potential evaporation (E_{pot}) using the T_{pot} expression by subtracting T_{pot} from ET_c ($E_{pot} = ET_c - T_{pot}$).

2.5 Modelling shrinkage and swelling of soils

2.5.1 Adapted physical concept

The trainset hydro-thermal analysis of the soil-vegetation-atmosphere interaction leads to the calculation of the seasonal soil water content, temperature and suction in the soil medium. The volume change behavior of an unsaturated soil is related to the variation of the soil suction as well as the loading conditions (net stress). The soil void ratio is influenced by wetting drying cycles which changes the soil suction state. Experiments carried out by Nowamooz et al. (2013, 2016) pointed out that a soil in a loose state tends to decrease in volume and a soil in a dense state tends to increase in volume after several drying wetting cycles. The physical modelling is based on the drying-wetting tests on the (e-log S) plan of different soils. The general concept of the modelling approach can be shown in Figure 2.21 a) and b).

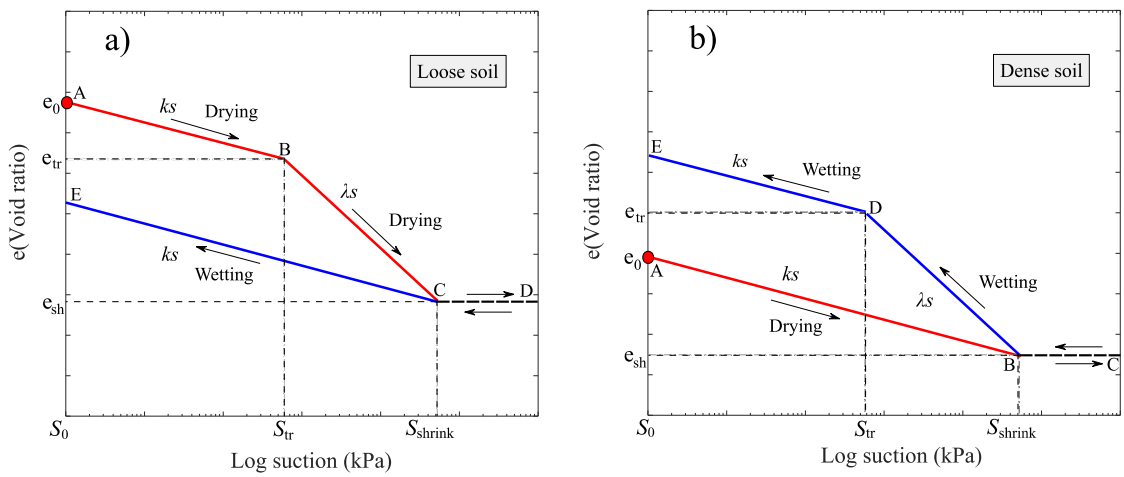

Figure 2.21 - Physical modelling approach of the volume change behavior of an unsaturated soil subjected to wetting drying cycles at a) loose state and b) dense state

The drying wetting paths are controlled by two volumetric indices denoted as k_s and λ_s. For the loose soil, the A-B drying path corresponds to a small variation in the void ratio and is consequently characterized as an elastic over consolidated behavior. The B-C drying path corresponds to a larger void ratio variation with respect to suction which defines a normally consolidated plastic domain. The transition between these two paths happens at a suction state (point B) named the transition suction (S_{tr}) with its associated void ratio (e_{tr}). On the las drying path (C-D), very small and almost negligible variation of the void ratio is observed which corresponds to an elastic behavior. The volumetric changes are considered negligible beyond point C which is represented by the shrinkage limit suction (S_{Shrink}) and its associated void ratio (e_{sh}). On the other hand, the slope of the wetting path (D-E-C) corresponds approximately to that of (A-B) with an elastic behavior. The same comments can be made on the dense soil with point D for the transition suction and point B for the shrinkage limit suction. The slopes can be calculated as below for both density state of the soil:

$$k_s = \frac{e_0 - e_{tr}}{\log\left(\frac{S_0}{S_{tr}}\right)} \tag{2.30}$$

$$\lambda_s = \frac{e_{tr} - e_{sh}}{\log\left(\frac{S_{tr}}{S_{shrink}}\right)} \tag{2.31}$$

In order to grasp the volumetric changes of the soil, the cumulative volumetric deformation at each drying/wetting cycle are calculated as below:

$$\Delta H = \sum_{j=1}^{t_{end}} \frac{e_{j+1} - e_j}{1 + e_j}\ dz \tag{2.32}$$

where j denotes each time step (days), t_{end} is the considered ending time of the calculation, dz is the considered length of the soil profile and e is the void ratio. The volumetric changes of the soil, depends on the possible drying and wetting paths on the (e-Log S) plot. Figure 2.22 shows different possible paths during the drying process of the soil in a loose state. S_j and S_{j+1} denote the applied suctions in two steps in time. Each path can produce different amount of volume change. While S_j and S_{j+1} are less than the shrinkage limit suction, the three paths showed in Figure 2.22 a), b) and c) can be considered. The volumetric changes are controlled by k_s in Figure 2.22 a) while both S_j and S_{j+1} are less than S_{tr}. However, if the soil suction at the second time step (S_{j+1}) is greater than S_{tr}, the volumetric changes are calculated based on the combination of k_s and λ_s as shown in Figure 2.22 b). Additionally, if both S_j and S_{j+1} are greater than S_{tr} the volume change is calculated based on λ_s as shown in Figure 2.22 c). On the other hand, if S_{j+1} is greater than S_{shrink}, three different conditions can be considered. If S_j is less than S_{tr} as shown in Figure 2.22 d), the volumetric changes are calculated using both k_s and λ_s and considering e_{sh} in the calculations. However, if S_j is greater than S_{tr}, only λ_s is considered in the calculations as shown in Figure 2.22 e). Finally, if both S_j and S_{j+1} are greater than S_{tr}, no volumetric changes take place in the model as shown in Figure 2.22 f).

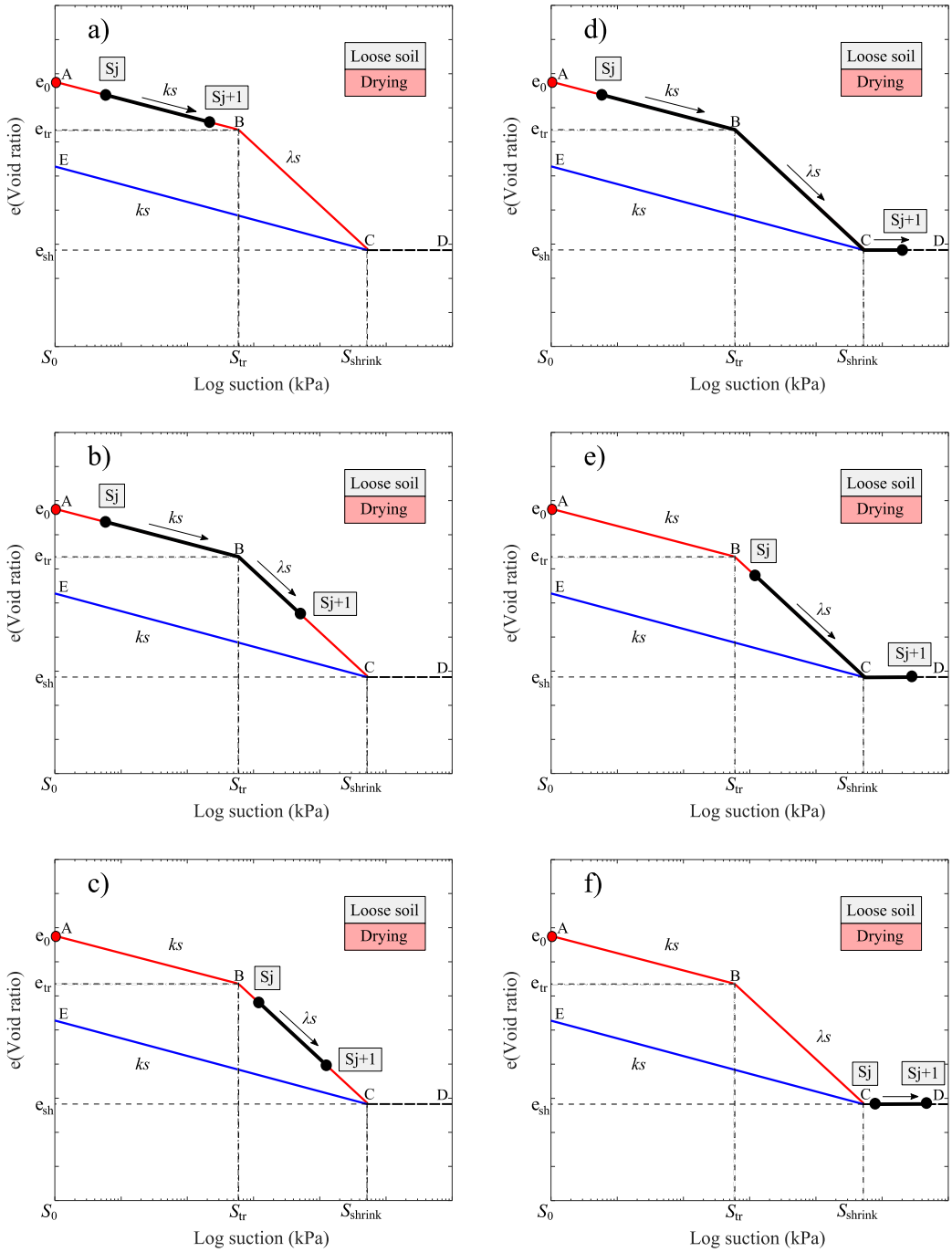

Figure 2.22 - Possible drying paths for a loose soil

The possible paths could also be verified for a dense soil in the wetting phase as shown in Figure 2.23. While S_j and S_{j+1} are less than the shrinkage limit suction, the three paths showed in Figure 2.23 a), b) and c) are considered. Figure 2.23 a) shows the volume change behavior of a dense soil during a wetting path while S_j and S_{j+1} are both greater than S_{tr}. If S_{j+1} is less than S_{tr} the volume changes are calculated based on k_s and λ_s as shown in Figure 2.23 b). However, if both S_j and S_{j+1} are less than S_{tr}, the volume change is only controlled by k_s as shown in Figure 2.23

c). Three additional conditions can be considered while S_j is greater than S_{shrink} as shown in Figure 2.23 d), e) and f). The volume changes are controlled by λ_s if S_{j+1} is greater than S_{tr} as shown in Figure 2.23 d) and by both k_s and λ_s if S_{j+1} is less than S_{tr} as shown in Figure 2.23 e). It should be mentioned that no volumetric changes are observed in Figure 2.23 f) if both S_j and S_{j+1} are greater than S_{shrink}.

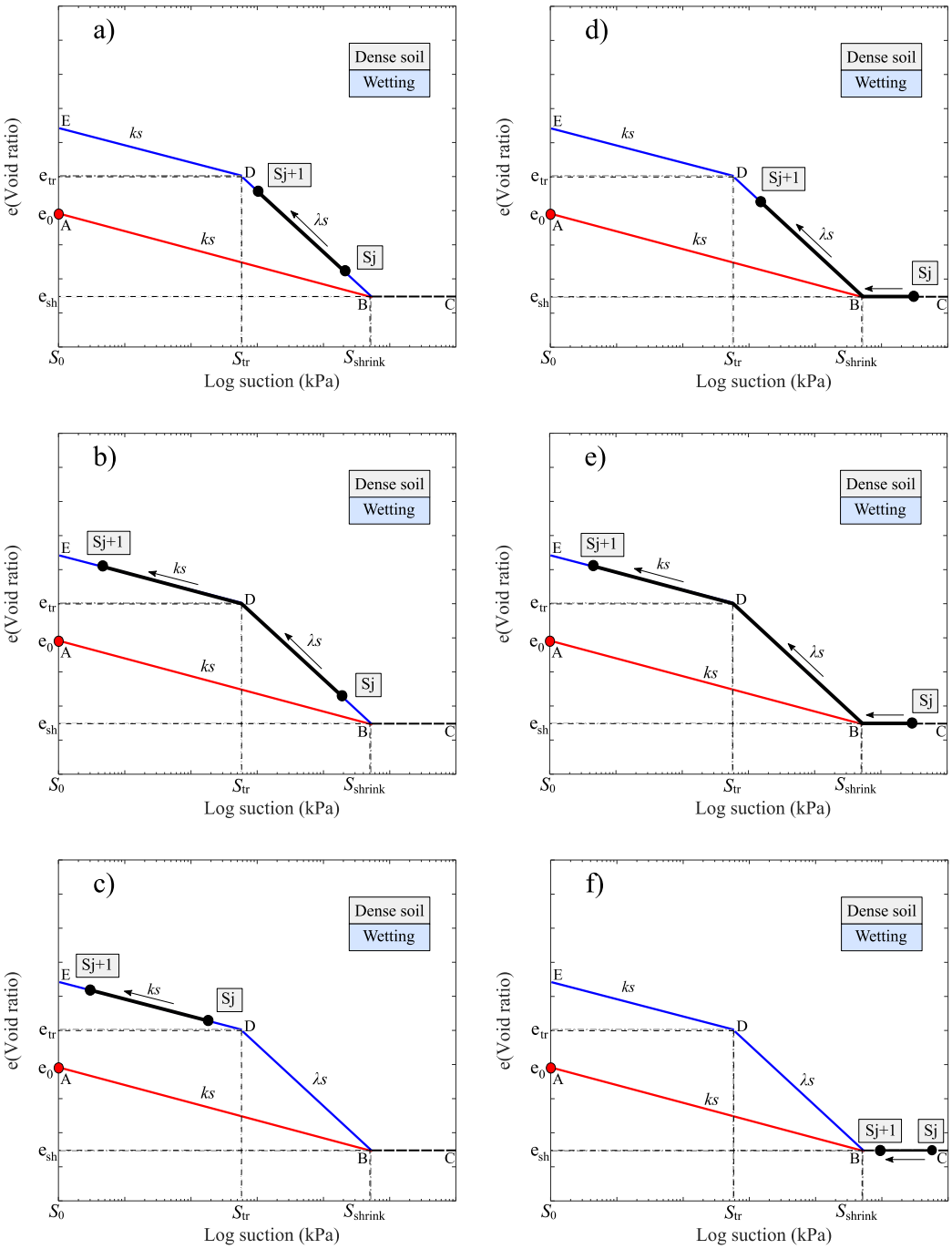

Figure 2.23 - Possible wetting paths for a dense soil

Figure 2.24 shows the possible wetting paths for a loose soil along with the possible drying paths for a dense soil based on the adapted shrink-swell model. As shown in Figure 2.24 a) while both S_j and S_{j+1} are less than S_{shrink} the volume changes are controlled by k_s in the wetting path of a

loose soil. If S_j is greater than S_{shrink} the volume changes are still controlled by k_s since there is no volume change while the applied suction is greater than S_{shrink}. Based on Figure 2.24 c) there is no volume change if both S_j and S_{j+1} are greater than S_{shrink}.

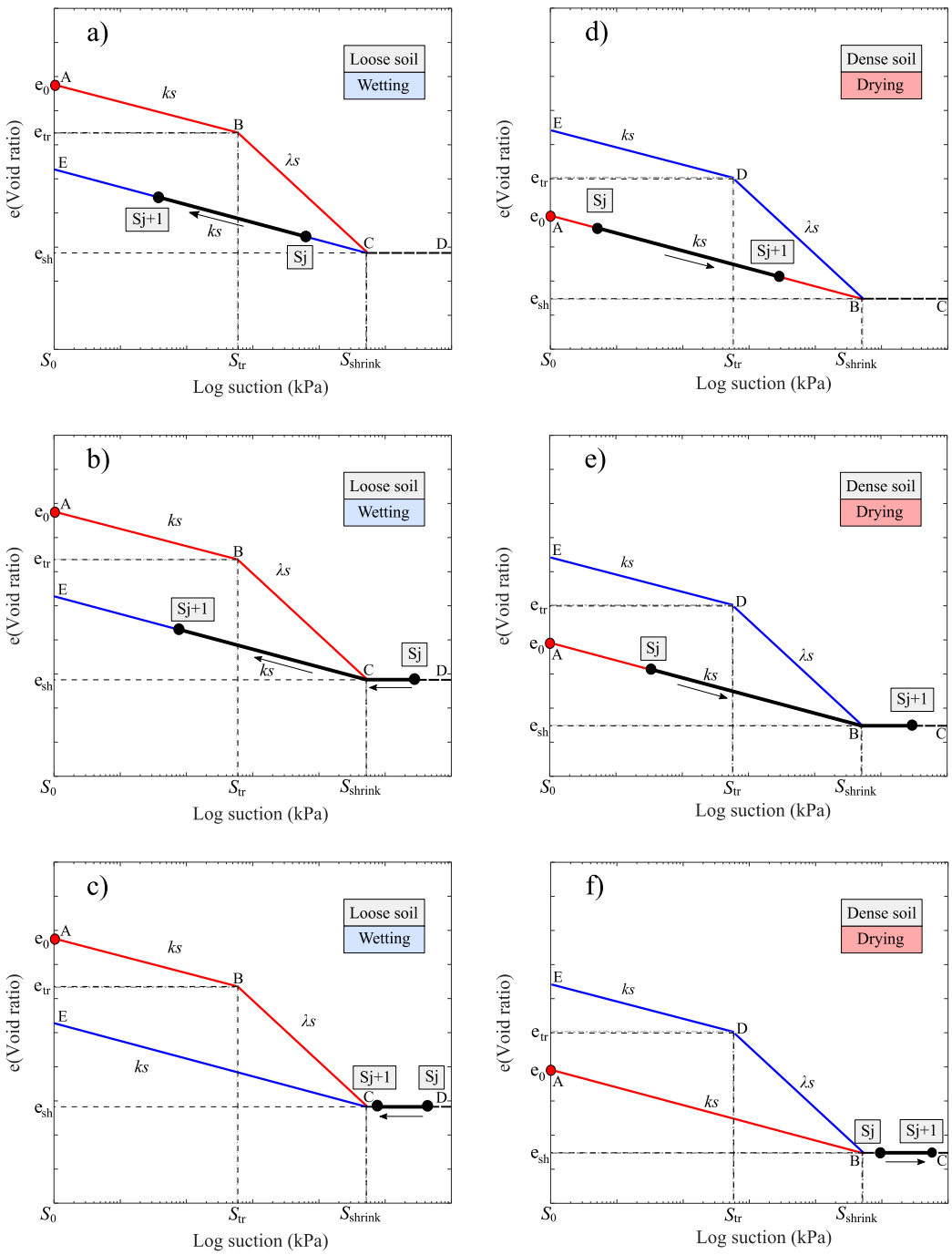

Figure 2.24 - Possible drying paths for a dense soil and possible wetting paths for a loose soil.

On the other hand, Figure 2.24 d) shows the volume change of a dense soil in a wetting path when both S_j and S_{j+1} are less than S_{shrink}. If S_{j+1} is greater than S_{shrink} the volume changes are controlled by k_s as well since there is no volume change after S_{shrink} as shown in Figure 2.24 e). However, the calculations of the volume change are based on S_{shrink} unlike Figure 2.24 d). Finally,

there is no volume change and consequently no volumetric deformation if both S_j and S_{j+1} are greater than S_{shrink} while a drying path in a dense soil.

In order to determine the void ratio changes over time the two volumetric indices (k_s and λ_s) should be always known. A suction controlled drying wetting test on a soil sample can lead to the calculation of the indices and their associated suction and void ratio values. However, performing these kinds of drying/wetting tests in the (e-Log S) plan is a quite difficult and time-consuming task. Alternative approaches can be adapted to estimate the volumetric indices based on basic geotechnical properties of the soil.

2.5.2 Correlation of the volumetric indices with basic geotechnical parameters

To establish a relationship between the volumetric indices and the basic geotechnical parameters, different drying/wetting tests performed in the literature were analyzed. The establishment of these relationships was proposed by different authors (Ho et al. 1992, Fleureau et al. 2002, Li et al. 2017, Li et al. 2018). However, the database used in these studies were limited to a small number of soils. The study carried out by li et al. (2017) considered the correlation of the swelling index with respect to void ratio which is the equivalent of λ_s in this study and the correlation of the swelling index with respect to water content which is not considered here. No correlations were performed on the k_s index which represents the elastic behavior of the soil. It should be also mentioned that all correlations were performed only with the soil liquid limit which is a very simple parameter to obtain as a basic geotechnical parameter. However, these indices could also be influenced by other basic parameters. More than 55 soils were investigated in this study, the considered geotechnical parameters and the calculated volumetric indices by the drying wetting tests (or only drying tests) on different soils are presented in Table 2.6.
Considering the effect of each of these parameters on k_s and λ_s, a multivariate regression analysis was performed on the data. Figure 2.25 and Figure 2.26 show respectively the correlation of k_s and λ_s with the plasticity index, the saturation void ratio, the saturation water content and the dry density of the soil. It should be mentioned that the shrinkage limit and the liquid limit showed less correlation with k_s and λ_s and thus were not considered in the multivariate regression analysis. As shown in Figure 2.25 a) the k_s volumetric index is a 2-degree polynomial function of the plasticity index of the soil. By increasing the plasticity index, the absolute value of k_s tends to increase. The same comment could be made for Figure 2.25 b) and c) where k_s is a linear function of the void ratio and saturated water content respectively. However, as shown in Figure 2.25 d), k_s is a logarithmic function of the soil dry density and tends to increase with the increase of the soil's dry density.

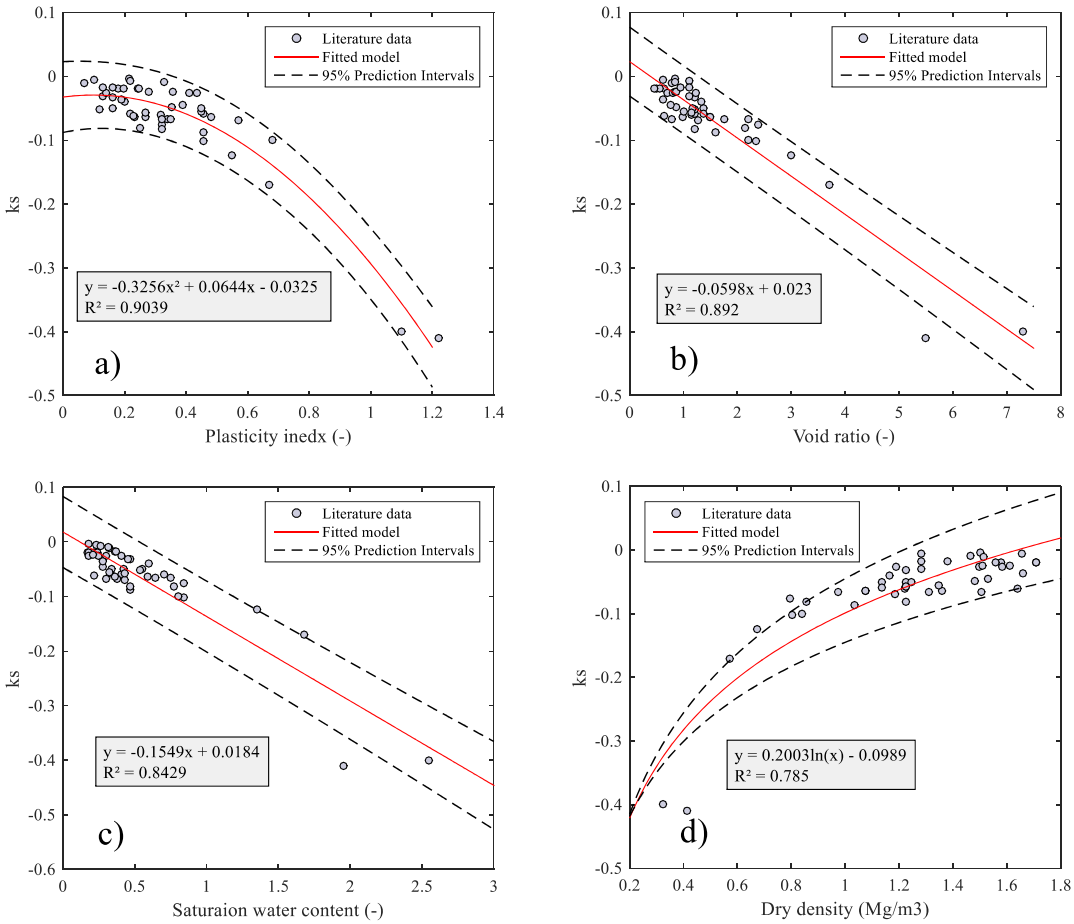

Figure 2.25 - Correlation of k_s with basic geotechnical parameters: a) Plasticity index; b) void ratio; c) Saturation water content; d) dry density.

On the other hand, Figure 2.26 a) shows the variation of λ_s with the plasticity index. The absolute value of the index increases as the plasticity index increases as well. For both Figure 2.26 b) and c), λ_s increases linearly with the increase of the void ratio and the saturation water content respectively. Finally, a logarithmic curve relates the changes of λ_s with the soil dry density. As the dry density increases, λ_s decreases as shown in Figure 2.26 d).

Table 2.6 - Soil data used for the correlation of the volumetric indices with basic geotechnical parameters.

References	Materials	k_s	λ_s	Plasticity index (%)	Liquide limit – LL (%)	Saturation void ratio	Saturation water content (%)	Dry density (Mg/m³)	Shrinkage Limit SL (%)	S_{tr} (kPa)	S_{shrink} (kPa)
Nowamooz (2007)	Champenoux clay	-0.02	-0.05	24.5	61	0.63	0.22	1.58	9.1	400	20000
Nowamooz (2007)	Champenoux clay	-0.02	-0.035	18.1	49	0.5	0.17	1.71	9.1	400	20000
Nowamooz (2007)	Champenoux clay	-0.02	-0.035	19.6	51	0.56	0.18	1.71	9.1	400	20000
Nowamooz (2007)	Deffend Clay	-0.06	-0.17	31.9	85.6	1.14	0.41	1.22	12	1800	100000
Nowamooz (2007)	Deffend Clay	-0.02	-0.1	24.6	64.6	0.45	0.24	1.56	12	560	30000
Estabragh et al. (2015)	Clay	-0.03051	-0.11	57	88	1.15	0.17	1.6	13	80	10000
Zhang et al. (2015)	Nanyang Clay	-0.004	-0.033	21.6	38.8	0.84	0.182	1.5	10.5	90	200000
Fleureau et al. (1993)	Jossigny Loam	-0.05	-0.107	16	37	1.38	0.555	1.131	15	2.7	1800
Fleureau et al. (1993)	Montmorillonite	-0.4	-0.752	110	170	7.3	2.55	0.324	25	1	1000
Fleureau et al. (1993)	Yellow clay	-0.04	-0.082	20	40	1.32	0.6	1.16	22	10	1000
Ng et al. (2016)	Low plasticity clay	-0.0135	-0.05	17	36	1.18	0.109	1.124	11	190	23000
Fleureau et al. (2002)	Interstratified clay	-0.1236	-0.361	55	90	3	1.35	0.67	23	10	10000
Fleureau et al. (2002)	La Verne Clay	-0.0323	-0.052	16	35	1.2	0.47	1.22	28.5	3	1300
Biarez et al. (1987)	Sterrebeek Loam	-0.01037	-0.0323	7	27	0.78	0.324	1.51	16	1.8	100
Biarez et al. (1987)	Marne	-0.0306	-0.0884	13	38	1.1	0.456	1.28	14	5	3000
Liu et al. (2015)	Redbank Clay	-0.087	-0.1548	45.6	73.2	1.6	0.471	1.035	20	30	10000
Liu et al. (2015)	Maryland Clay	-0.05786	-0.176	45.7	69.8	1.2	0.335	1.223	14	100	4000
Liu et al. (2015)	Warner Clay	-0.0257	-0.0399	43.6	66	0.7	0.244	1.583	11	50	10000
Liu et al. (2015)	Wilsonton Clay	-0.026	-0.0723	41	71.3	0.8	0.411	1.495	17	100	100000
Krisdani et al. (2008)	Sandy Silt	-0.026	-0.0549	14	41	1.23	0.18	1.19	9	1	3000
Yigzaw (2009)	Est Romainville clay	-0.0249	-0.0868	35.6	75.2	0.85	0.3	1.51	14	600	60000
Yigzaw (2009)	West Romainville clay	-0.0485	-0.0831	35.5	68.2	0.87	0.34	1.48	18.5	320	15000
Yigzaw (2009)	Argenteuil marne	-0.0199	-0.066	47.4	89.5	0.92	0.3	1.42	23	150	30000
Benchouk et al. (2013)	Sikkak Clay	-0.0645	-0.17	27	50	1.5	0.75	1.076	18	48	5500
Benchouk et al. (2013)	Bouhennak marl	-0.05859	-0.1788	22	47	1.37	0.705	1.135	14	100	5000
Benchouk et al. (2013)	Maghnia clay	-0.17	-0.434	67	112	3.7	1.68	0.572	20	30	7000
Benchouk et al. (2013)	Bentonite deposit	-0.09408	-0.297	88	130	2.7	1.95	0.727	24	70	2500
Zhang et al. (2015)	Regina clay	-0.04685	-0.2897	50	75	2.75	0.95	0.717	16	6	5000
Elkady et al. (2013)	Al Qatif clay	-0.0217	-0.1924	77	137	2	0.7	0.897	10	100	18000
Li et al. (2018)	Châtaignier Clay	-0.0667	-0.1302	34	71	2.2	0.375	1.31	24	2	40000
Li et al. (2018)	Boughrara Clay	-0.02425	-0.093	28	54	0.86	0.21	1.61	13	380	5000
Li et al. (2017)	Camargue Silt	-0.051	-0.0657	12	36	1.2	0.54	1.223	19.5	5	10000
Zhou and Xu (2016)	Macau silty sand	-0.0036	-0.03663	10	38	0.624	0.233	1.657	20	35	400
Baille et al. (2014)	Calcigel bentonite	-0.41	-0.7408	121.9	178	5.5	1.95	0.414	11.8	40	2000
Baille et al. (2014)	NX illite	-0.1015	-0.1987	45.5	77.8	2.35	0.84	0.803	25.7	20	6500

Baille et al. (2014)	Spergau kaolin	-0.0634	-0.0518	23.3	53.4	1.5	0.59	1.076	25.8	20	6500
Ito & Azam (2013)	High plasticity clay	-0.0157	-0.0898	52.7	82.8	1.1	0.312	1.34	15	300	50000
Mbonimpa et al. (2006)	Soil 6042	-0.00643	-0.0833	52	78	0.89	0.3333	1.424	17	50	1000
Mbonimpa et al. (2006)	Soil 6044	-0.00943	-0.0485	33	60	0.84	0.3169	1.462	22	20	1000
Mbonimpa et al. (2006)	Soil 6061	-0.01776	-0.1316	13	40	0.95	0.3598	1.38	17.5	150	1000
Mbonimpa et al. (2006)	Soil 6066	-0.07232	-0.2689	47	80	2.69	0.95	0.73	20	5.5	4000
Mbonimpa et al. (2006)	Soil 6068	-0.06641	-0.1886	35	51	1.76	0.6446	0.97	13	5	4000
Mbonimpa et al. (2006)	Soil 6069	-0.0488	-0.355	66	92	3	1.071	0.67	16	6	2000
Mbonimpa et al. (2006)	Soil 6072	-0.05898	-0.2598	47	71	2.49	0.9256	0.77	16	2.5	1800
Mbonimpa et al. (2006)	Soil 6079	-0.07595	-0.2322	32	70	2.39	0.8415	0.794	16	10	2100
Mbonimpa et al. (2006)	Soil 6080	-0.08067	-0.1845	25	58	2.15	0.7761	0.854	26	2	450
Sun et al. (2007)	Pearl clay	-0.00645	-0.0152	22	49	1.099	0.26	1.282	22.16	19	500
Marinho (1994)	London clay	-0.06338	-0.1489	48	77	0.98	0.36	1.359	20	1000	7000
Marinho (1994)	Clay/sand=90/10	-0.05577	-0.1736	45	69	1	0.32	1.345	15	300	2000
Marinho (1994)	Clay/sand=70/30	-0.04461	-0.108	39	65	0.76	0.28	1.529	12	300	5500
Marinho (1994)	Clay/sand=50/50	-0.06135	-0.0973	23	40	0.64	0.22	1.641	9.5	300	1400
Marinho (1994)	Carsington clay	-0.06667	-0.06	32	63	0.79	0.3	1.503	17	200	4000
Marinho (1994)	London clay Chattenden	-0.0689	-0.1514	57	89	1.27	0.43	1.185	21	500	7000
Marinho (1994)	Janga Clay	-0.05	-0.1513	45	73	1.16	0.42	1.246	17	190	10000
Marinho (1994)	Boom Clay	-0.0576	-0.1482	27	56	1.15	0.43	1.252	16	270	6000
Marinho (1994)	LC500 clay	-0.01736	-0.047	16	50	1.1	0.37	1.281	30	100	3000
Marinho (1994)	Kaolin	-0.08186	-0.2594	32	64	1.2	0.47	1.223	33	300	700
Marinho (1994)	80% Kaolin 20% Silt	-0.036	-0.0654	19	36	0.62	0.28	1.661	20	400	1000
Marinho (1994)	Queensborough Clay	-0.09989	-0.2284	68	102	2.2	0.8	0.841	20	30	1000

It can be observed from Figure 2.25 and Figure 2.26 that the proposed fitted models have an acceptable agreement with the data presented in Table 2.6. Most of the dispersed data stay between the upper and lower 95% prediction interval of the fitted linear and nonlinear models. Based on this analysis, each volumetric index can be defined by these four parameters using the following expressions:

$$k_s = 0.03858\ PI - 0.1052\ PI^2 - 0.0158\ e - 0.012\ w - 0.1795\ \gamma_d + 0.24085 \ln(\gamma_d) + 0.15227 \tag{2.33}$$

$$\lambda_s = -0.011291\ PI - 0.02547\ PI^2 - 0.0233\ e - 0.0227\ w - 0.2944\ \gamma_d + 0.483 \ln(\gamma_d) + 0.23108 \tag{2.34}$$

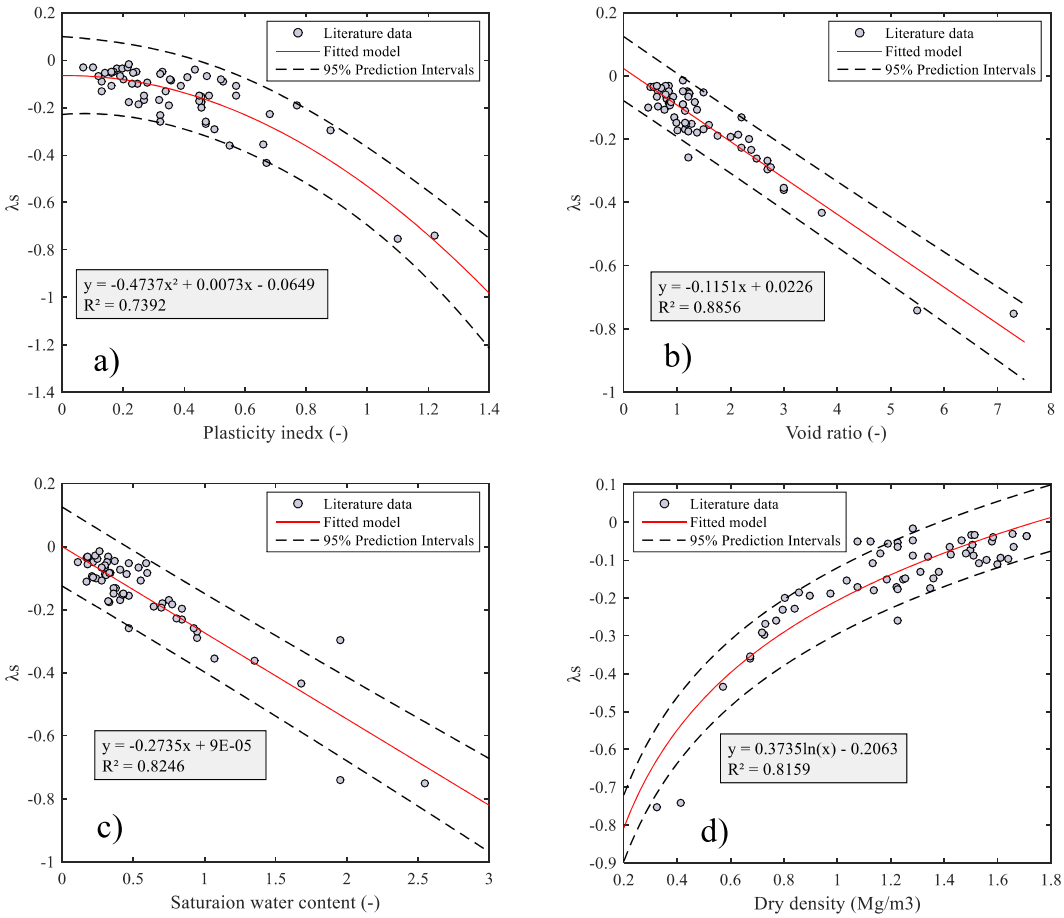

Figure 2.26 - Correlation of λ_s with basic geotechnical parameters: a) Plasticity index; b) void ratio; c) Saturation water content; d) dry density.

2.5.3 Performance evaluation

The performance of these proposed equations could be evaluated by comparing the predicted values to the measured values available in Table 2.6. The mean absolute deviation (MAD), the mean squared error (MSE) and the root mean squared error (RMSE) expressed as below were used to evaluate the error of the predicted values:

$$MAD = \frac{\sum_{i=1}^{n} |y_i - p_i|}{n} \tag{2.35}$$

$$MSE = \frac{\sum_{i=1}^{n} (y_i - p_i)^2}{n} \tag{2.36}$$

$$RMSE = \sqrt{\frac{\sum_{i=1}^{n} (y_i - p_i)^2}{n}} \tag{2.37}$$

where y_i is the observed value, p_i is the predicted value and n represents the total number of observations. The mean absolute deviation (MAD) is the sum of absolute differences between the observed value and the predicted value divided by the number of observations. The mean squared error (MSE) as the most common error metric, penalizes larger errors as it is the sum of the squared errors divided by the number of observations. The RMSE is the square root of MSE which represents the mean deviation of predicted values with respect to the observed ones, in the same units as the model variable under evaluation. Table 2.7 summarizes these errors along with the coefficient of determination for both k_s and λ_s indices.

Table 2.7 - Regression statistics of the volumetric indices.

Error metrics	k_s	λ_s
Mean absolute deviation (MAD)	0.000283	9.79E-18
Mean squared error (MSE)	5.82E-6	1.67E-5
Root mean squared error (RMSE)	0.00241	0.00408
Coefficient of determination (R^2)	0.902	0.92

The calculated error metrics indicates that there is an acceptable prediction capacity of the proposed approach. Figure 2.27 a) and b) show the linear regression of predicted k_s and λ_s with the observed ones, respectively. It can be observed that the coefficient of determination is 0.90 for k_s and 0.92 for λ_s which shows a good agreement with the observed values.

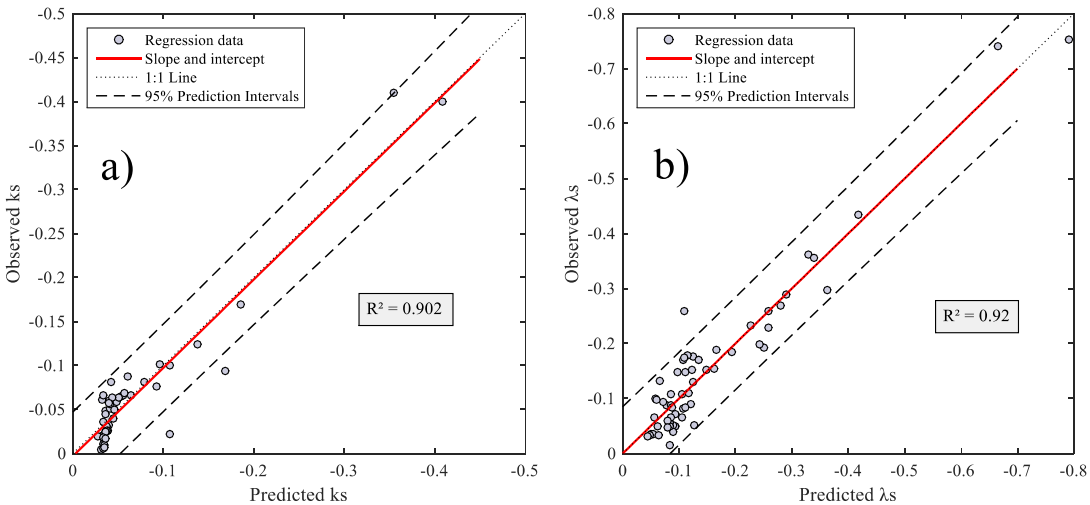

Figure 2.27 - Linear regression of the predicted and the observed a) k_s and b) λ_s.

2.5.4 Parametric analysis

The performance of the proposed equations (Eq. (2.33) and (2.34)) can also be evaluated by a parametric analysis which compares each parameter in the equation to the measured ones by maintaining other parameters constant. For this purpose, a set of data in Table 2.6 was chosen so that only one parameter of the main 4 parameters (PI, e, w, γ_d) varies with the volumetric indices and the other three parameters stay constant. Figure 2.28 and Figure 2.29 show the comparison carried out with the proposed equations and the data set used in this analysis with the three constant parameters, shown in each figure. It is generally observed that the proposed equation is able to predict almost correctly the variation of the volumetric indices with basic geotechnical properties. It should be mentioned that the data used in this correlation approach is gathered from the literature and the considered constant set of parameters are not exactly constant but they have small variation from each other which is probably the reason for these small deviations from the model in some cases like in Figure 2.28 c) and d) and in Figure 2.29 b). However, the performance of this analysis can also be evaluated by additional experimental measurements by studying the effect of each geotechnical parameter on the volumetric indices separately.

Figure 2.28 a) shows the comparison between the simulated and the measured variations of the plasticity index with k_s by maintaining the other parameters constant. It can be observed that there is a good agreement between the two. The same comments could be made for the variation of the void ratio as shown in Figure 2.28 b). The small number of points considered in the analysis is because of the fact that the tested materials with three equal parameters and one varying parameter, are rare in the literature. The variation of the water content with constant PI, e and the dry density is shown in Figure 2.28 c). It can be observed that the changes of k_s with the water content can be considered negligible for small range of water content variations based on the measured and the fitted model. Finally, the variation of k_s with the dry density is shown in Figure 2.28 d) by maintaining PI, e and γ_d constant. The variation of k_s within the large range of dry density variations can also be considered negligible based on the fitted model results and observations.

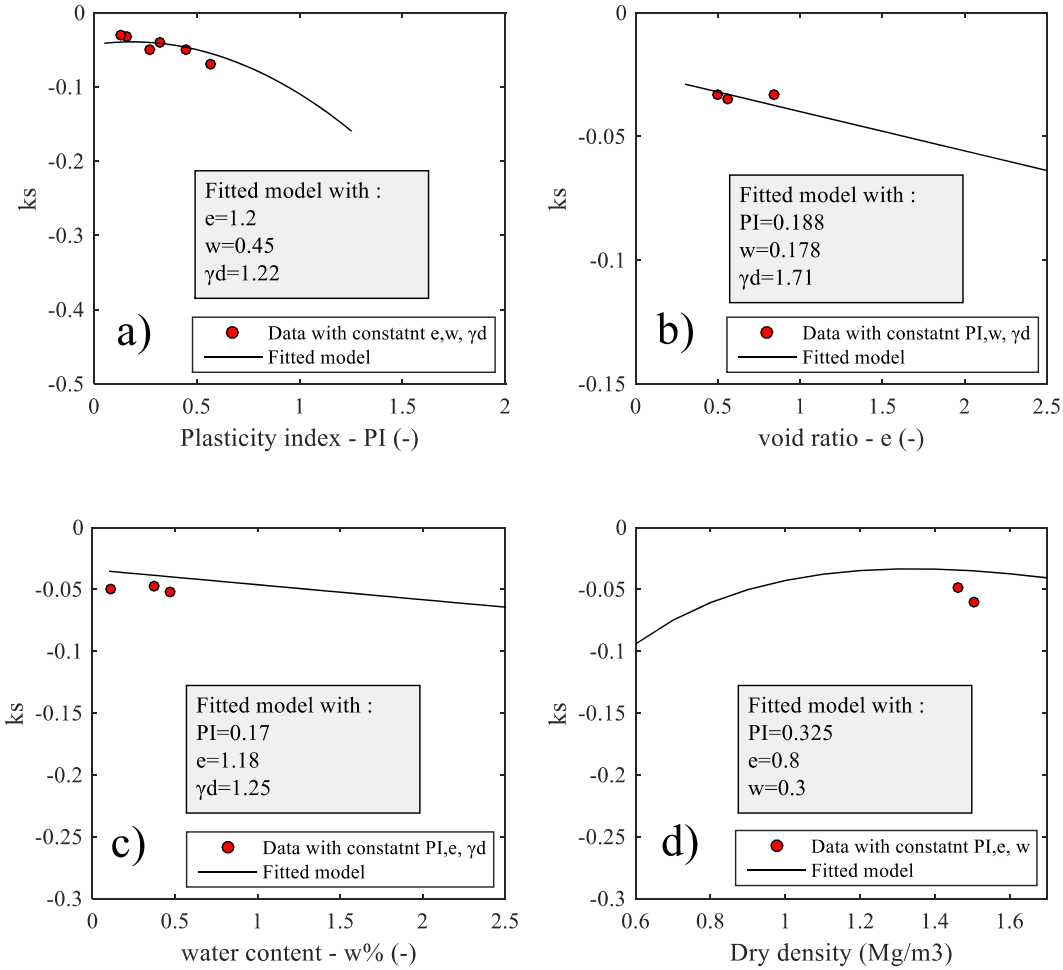

Figure 2.28 - Comparison of the proposed equation for k_s with each geotechnical parameter; a) for PI by maintaining e, w and γ_d constant; b) for e by maintaining PI, w and γ_d constant; c) for w% by maintaining PI, e and γ_d constant; d) for γ_d by maintaining PI, e and w% constant

On the other hand, the same procedure is adapted for λ_s as shown in Figure 2.29. The variations of λ_s with the plasticity index by maintaining the other parameters constant are shown in Figure 2.29 a). Four soils data were used for this comparison with varying plasticity indexes and almost constant e, w and γ_d. The fitted model with the varying plasticity index shows good agreement with the provided data. Figure 2.29 b) shows the variations of the void ratio with a negligible under estimation of the fitted model. The variation of λ_s with the soil water content is presented in Figure 2.29 c). Two soil data were used for the comparison. The fitted model shows a good agreement with the data, however, the variation of λ_s within the range of small water content variations (0 - 50%) could be negligible. Nevertheless, the influence of the water content is taken into account in further analysis. Finally, the variation of λ_s with the soil dry density is shown in Figure 2.29 d) by maintaining other parameters constant. Only two studied materials were chosen from Table 2.6 for the comparison. It can be deduced that the model predicts with a good accuracy the changes in λ_s. It should be mentioned that the variation of λ_s within the large range of dry density values are almost constant.

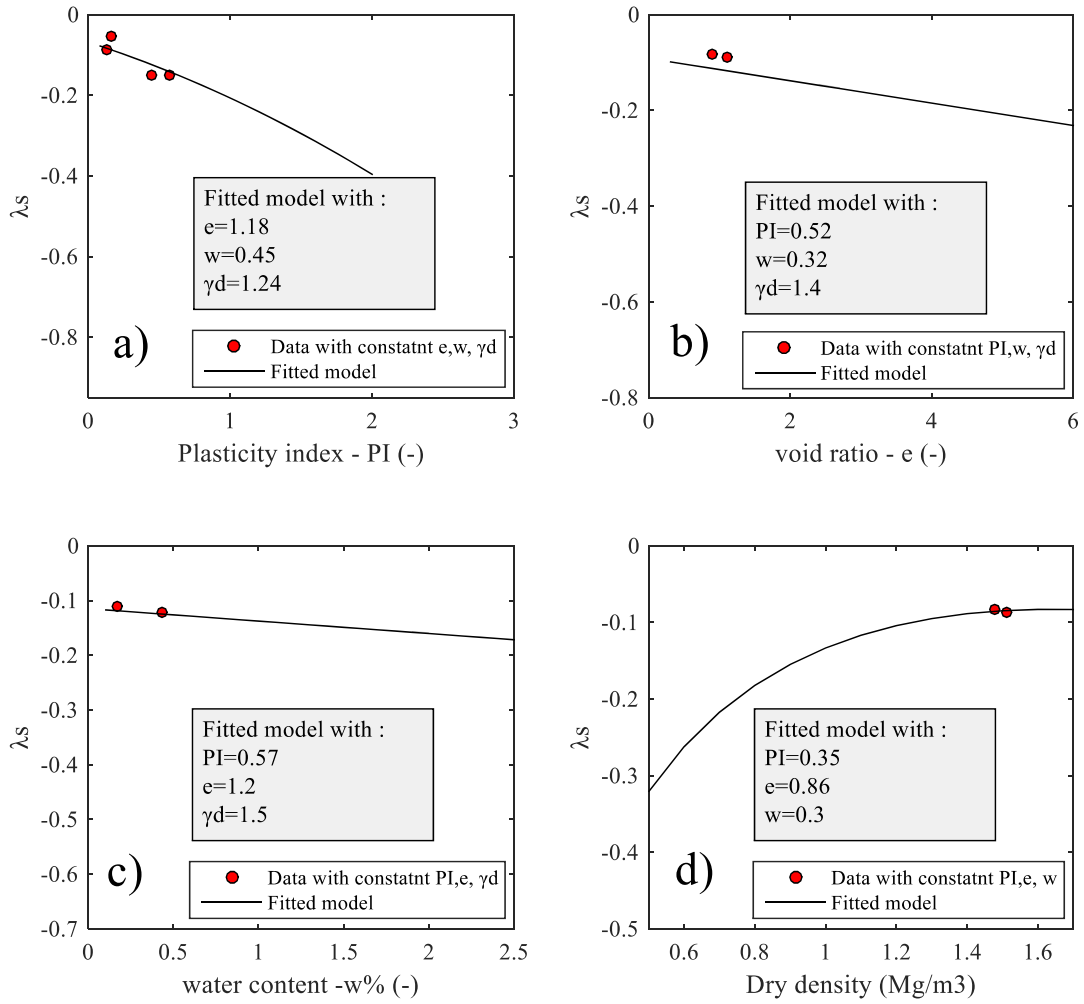

Figure 2.29 - Comparison of the proposed equation for λ_s with each geotechnical parameter; a) for PI by maintaining e, w and γ_d constant; b) for e by maintaining PI, w and γ_d constant; c) for w% by maintaining PI, e and γ_d constant; d) for γ_d by maintaining PI, e and w% constant

2.6 Complementary parameters and validation

2.6.1 Correlation of model's suction parameters with basic geotechnical parameters

To determine the volumetric deformations by knowing the volumetric indices, the transition suction (S_{tr}) between the two indices and the shrinkage limit suction (S_{shrink}) should be known. Data presented in Table 2.6 was used to correlate these two suction parameters with the basic geotechnical properties of different soils. It can be observed in Figure 2.30 a) that the soil dry density is related to the transition suction by an exponential type equation. It should be mentioned that not all the data presented in Table 2.6 was used in this correlation process however, most of the data follows the exponential path with a determination coefficient of 0.84 which shows an acceptable agreement of the fitted equation with the data. Figure 2.30 b) shows the correlation of the shrinkage limit suction with the shrinkage limit (SL) of each soil. It can be observed that the best fit equation for this set of data is a power law type equation which has a determination coefficient of 0.72 showing an acceptable coherence with the data. The equations are expressed as follows:

$$S_{tr} = 0.214 \exp(4.54\ \gamma_d) \tag{2.38}$$

$$S_{shrink} = 7.64\ SL^{-3.264} \tag{2.39}$$

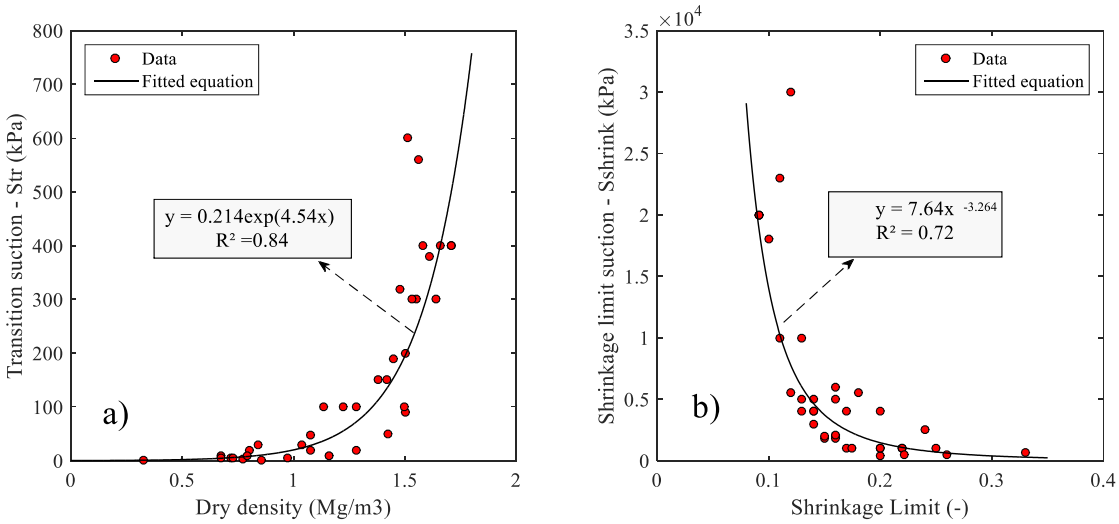

Figure 2.30 - a) the variation of the transition suction with the dry density b) the variation of the shrinkage limit suction with the shrinkage limit.

It should be highlighted that these suction parameters are determined graphically on the results of the experiments in the literature in most cases, thus the associated error should also be considered which could lead to smaller determination coefficients and less precision in predicting S_{tr} and S_{shrink}. By having the 5 basic geotechnical properties (PI, SL, e, w and γ_d) the shrink swell model of the soil can be established under zero stress condition.

Since SL is not always part of the geotechnical testing programs, thus the relationship between the shrinkage index (SI=LL - SL) and the plasticity index of the soils presented in Table 2.6 is investigated. Figure 2.31 shows the correlation statistic where the coefficient of determination is 0.94 with an acceptable accuracy of the fitted model with the data. The following expression is proposed to estimate SL based on the most frequently tested parameters in geotechnical laboratory tests (the plastic limit - PL and the liquid limit - LL):

$$SL = LL - 1.22\ PI + 3.4 = 1.22\ PL - 0.22\ LL + 3.4 \tag{2.40}$$

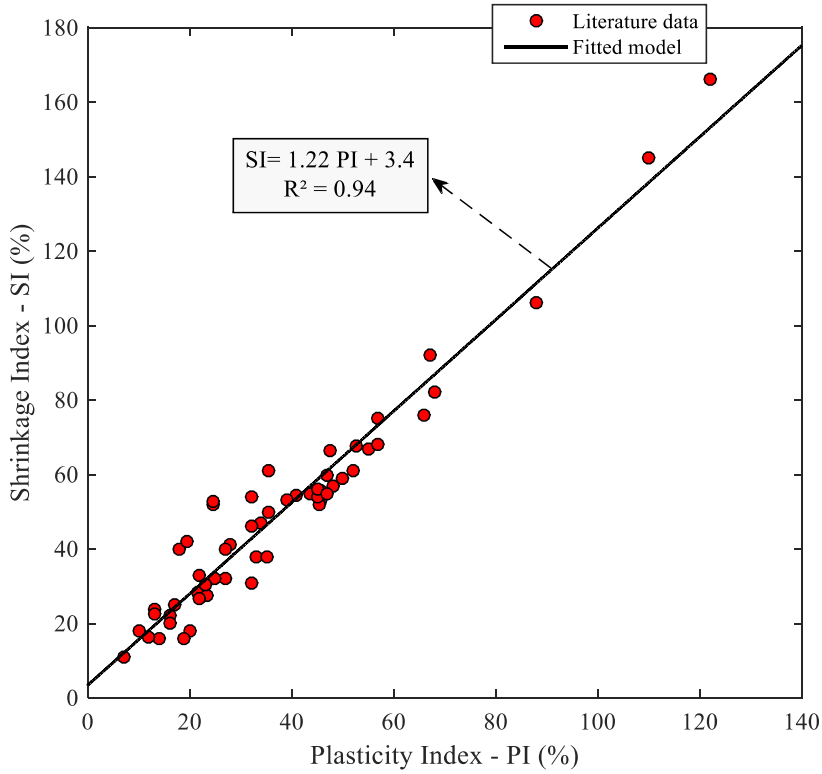

Figure 2.31 - Relationship between measured shrinkage index SI and plasticity index PI based on the presented data.

It should be mentioned that the data provided in Table 2.6 presents the volumetric indices under no loading conditions or very small (negligible) applied loads. As the volumetric behavior of an unsaturated soil is also dependent on the loading condition, it is crucial to study its effect on the volume change behavior.

2.6.2 The effect of the applied stress on the volumetric indices

The state surface of an unsaturated soil is mainly controlled by the changes in the void ratio due to the simultaneous effect of the soil suction and the net mechanical stress throughout a coupled hydro-mechanical process. The complexity of the coupled approaches does not make it easy for engineering practice due to the numerous parameters that should be measured for lunching the calculation process. In this section, the volumetric indices of some soils are investigated for different loading conditions under drying wetting cycles. Measurements carried out in the literature (Table 2.8) show that the influence of the loading conditions on the transition suction and the shrinkage limit suction are negligible thus, S_{tr} and S_{shrink} are considered to stay constant under applied stresses. However, the volumetric indices are influenced by the applied stress on the soil during drying wetting cycles. Table 2.8 presents the studied soils in this section.

The volumetric indices are calculated for each loading conditions under drying wetting cycles. Figure 2.32 shows the variation of these volumetric indices with the applied stress for the Al Qatif clay. It can be observed that the changes in the volumetric indices follow a logarithmic curve which is plotted on the figure. The same observations can be made in Figure 2.33 to Figure 2.37 for different soils.

Table 2.8 - Literature data of the volumetric indices at different loading condition under drying wetting cycles.

References	Material	k_s	λ_s	Applied stress P (kPa)
Elkady et al. (2013)	Al Qatif clay	-0.03689	-0.1909	7
		-0.027125	-0.16275	100
		-0.01519	-0.10416	600
Zhou and Xu (2016)	Macau silty sand	-0.003609	-0.03663	25
		-0.002519	-0.03539	50
		-0.00165	-0.03445	100
		-0.000627	-0.033	200
Estabragh et al. (2015)	Clay	-0.03051	-0.11068	1
		-0.02404	-0.096	6.25
		-0.023	-0.093	10
Ng et al. (2016)	Low plasticity clay	-0.0135	-0.05	0
		-0.002523	-0.003782	50
		-0.002075	-0.002521	110
Sabbagh (1997)	Madrid clay	-0.00818	-0.00967	10
		-0.001128	-0.003671	150
		-0.000582	-0.0006671	500
Monroy (2005)	London clay	-0.009888	-0.0231	7
		-0.001563	-0.01173	65
		-0.0000091	-0.0058	220
Nowamooz (2007)	Deffend clay	-0.006769	-0.02465	20
		-0.00491	-0.02234	40
		-0.004286	-0.01946	60

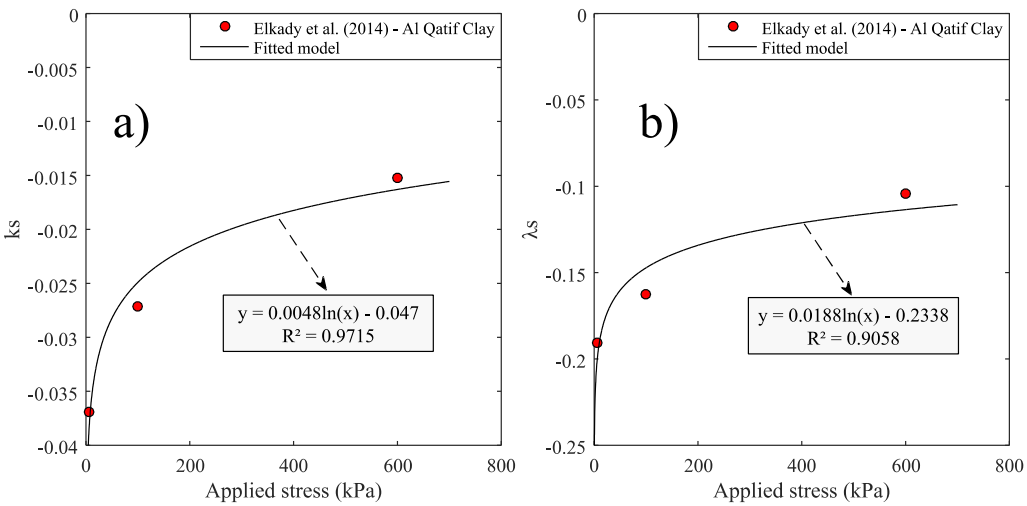

Figure 2.32 - Variation of the volumetric indices; a) k_s and b) λ_s with the applied stress for the Al Qatif clay.

The data provided in Table 2.8, follow all a logarithmic curve in a form of the following equation:

$$k_s \ or \ \lambda_s = A \ln (P) + B \tag{2.41}$$

where A and B are the curve fitting parameters, P represents the applied stress in kPa. It can be observed from Figure 2.32 to Figure 2.37 that the variation of A is different for each soil type thus it is possible to relate this parameter to the soil geotechnical properties. Table 2.9 shows the variation of the curve fitting parameters and the associated geotechnical data for each soil. The volumetric indices at zero or very low stress condition are also presented in Table 2.9. It should be mentioned that the intercept (B) in Eq. (2.41) does not represent the volumetric index at zero stress condition due to the fact that the natural logarithm of a zero stress tends to infinity. To fix this problem, the variation of the intercept B is related to the calculated k_{s0} and λ_{s0} which are the volumetric indices at zero or negligible stress condition (described in the previous section).

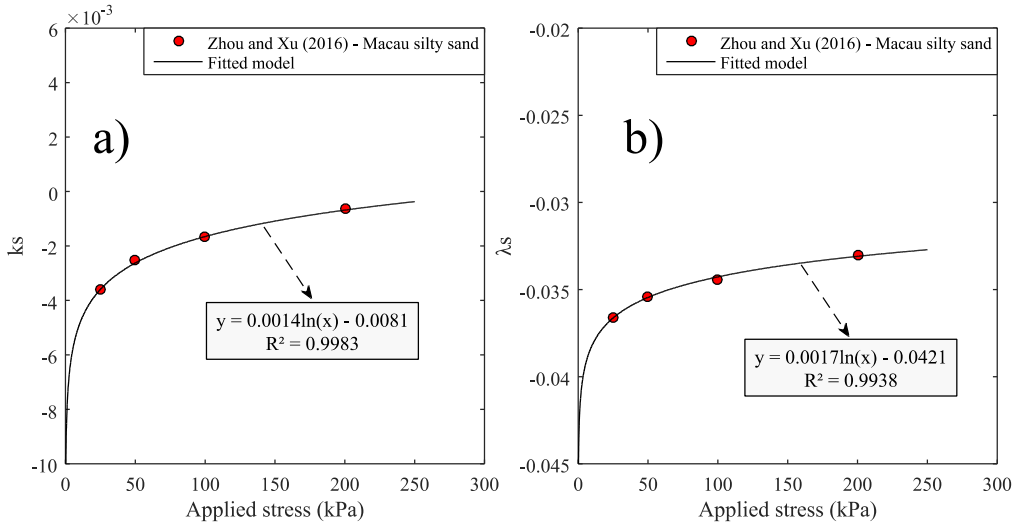

Figure 2.33 - Variation of the volumetric indices; a) k_s and b) λ_s with the applied stress for the Macau silty sand.

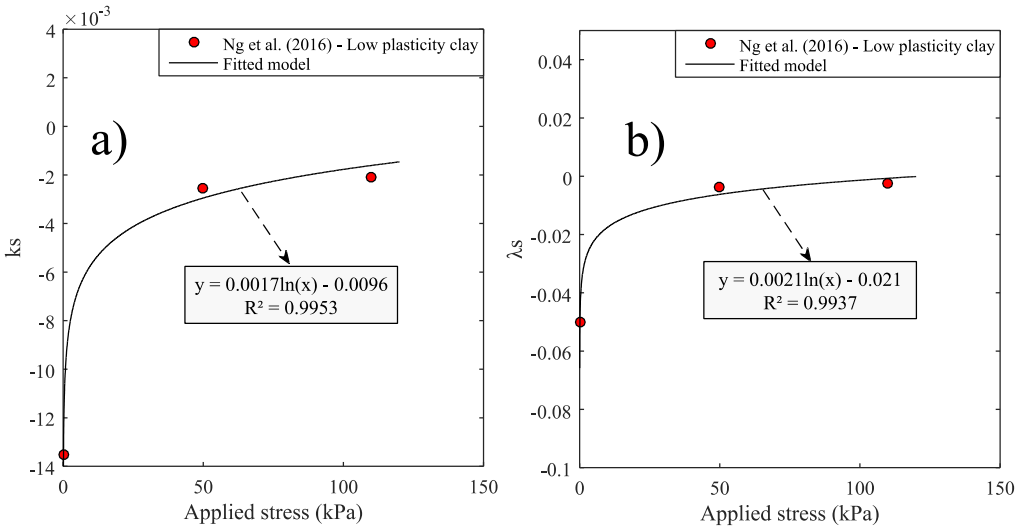

Figure 2.34 - Variation of the volumetric indices; a) k_s and b) λ_s with the applied stress for the low plasticity clay.

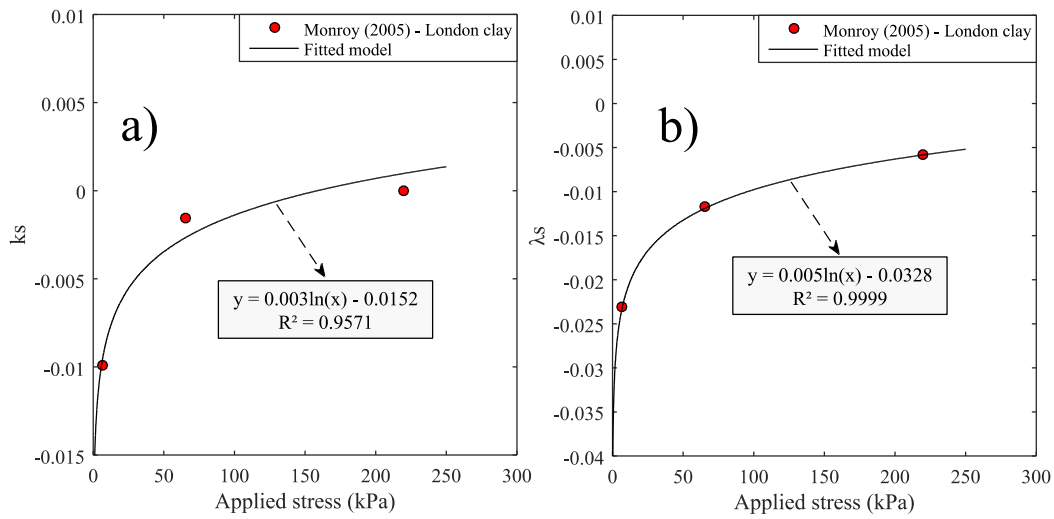

Figure 2.35 - Variation of the volumetric indices; a) k_s and b) λ_s with the applied stress for the London clay.

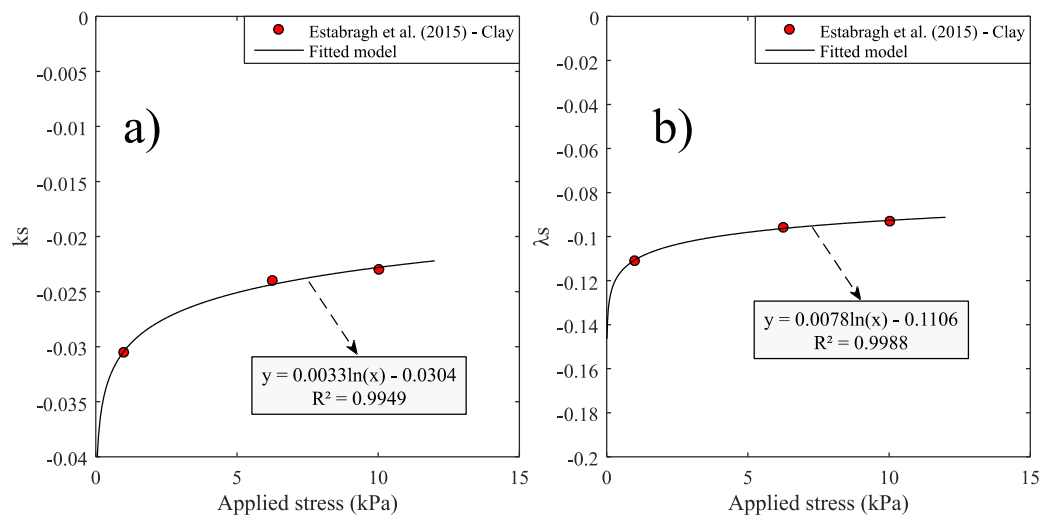

Figure 2.36 - Variation of the volumetric indices; a) k_s and b) λ_s with the applied stress for the clayey soil.

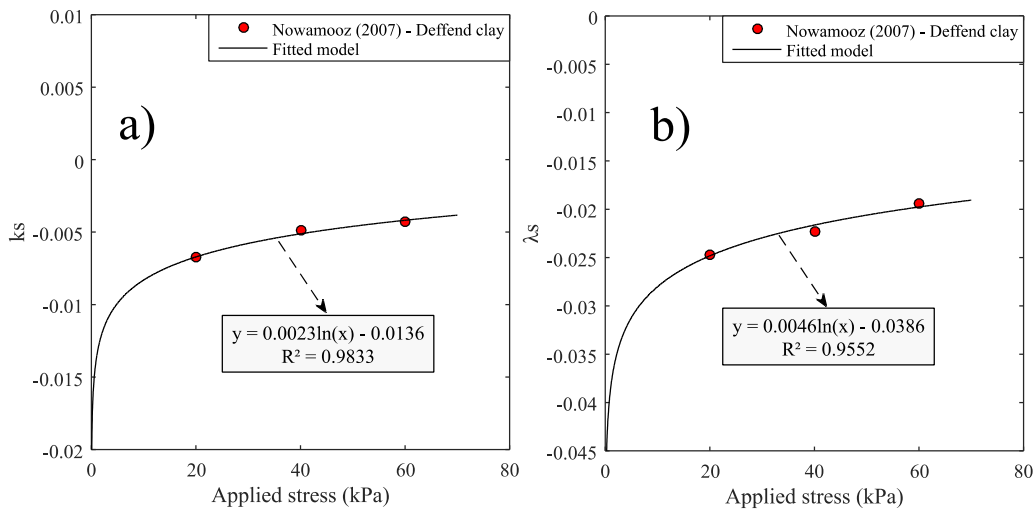

Figure 2.37 - Variation of the volumetric indices; a) k_s and b) λ_s with the applied stress for the Deffend clay.

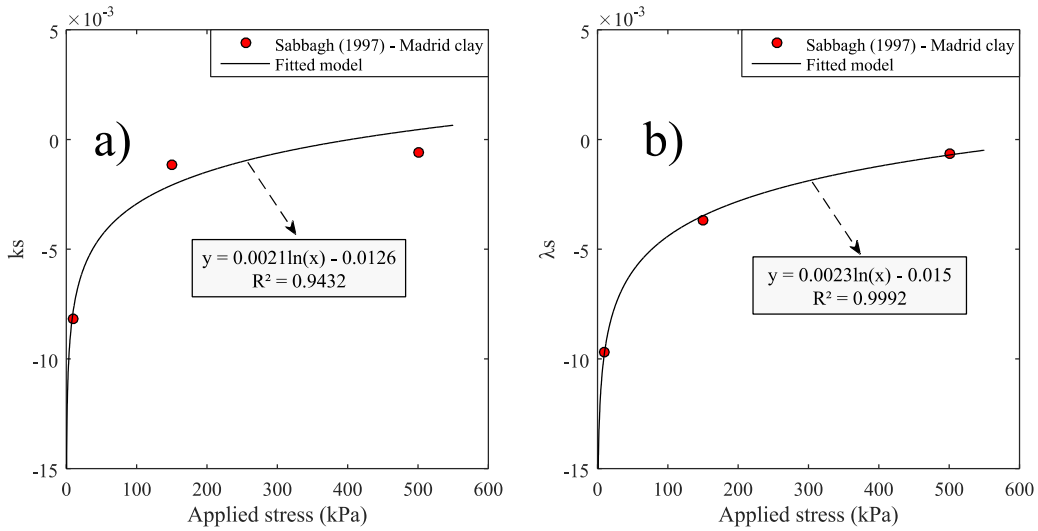

Figure 2.38 - Variation of the volumetric indices; a) k_s and b) λ_s with the applied stress for the Madrid clay.

Following the provided data, the fitting parameter A is related to the plasticity index (PI) or the liquid limit (LL) of the soil. Figure 2.39 (a) and (b) show the variation of A with the plasticity index and the liquid limit respectively. It can be observed that the correlation of the fitting parameter A with the plasticity index show a greater coefficient of determination compared to the correlation of A with the liquid limit (0.88>0.85 and 0.91>0.9), however, both equations could be used in the calculation process. The plasticity index is used in this study and is expressed as follow for each volumetric index:

$$A = \begin{cases} 3 \times 10^{-5} \exp(0.069\ PI)\,, & for\ k_s \\ 0.0011 \exp(0.0344\ PI)\ , & for\ \lambda_s \end{cases} \tag{2.42}$$

Table 2.9 - Fitted A and B parameters for k_s and λ_s along with the plasticity index, the liquid limit and the volumetric indices at zero stress conditions.

References	k_s		λ_s		**LL**	**PI**	k_{s0}	λ_{s0}
	A	B	A	B				
Elkady et al. (2013)	0.0048	-0.047	0.0188	-0.2338	137	77	-0.0368	-0.1909
Zhou and Xu (2016)	0.0014	-0.0081	0.0017	-0.0421	38	10	-0.0036	-0.0366
Estabragh et al. (2015)	0.0033	-0.0304	0.0078	-0.1106	88	57	-0.03051	-0.1106
Ng et al. (2016)	0.0017	-0.0096	0.0021	-0.012	36	19	-0.0135	-0.05
Sabbagh (1997)	0.0021	-0.0126	0.0023	-0.015	70	31	-0.00818	-0.0096
Monroy (2005)	0.003	-0.0152	0.005	-0.0328	83	54	-0.009888	-0.0231
Nowamooz (2007)	0.0023	-0.0136	0.0046	-0.0517	85.6	31.92	-0.00676	-0.0246

On the other hand, the fitting parameter B is the intercept of the logarithmic equation which is expected to be equal to the volumetric indices under zero stress conditions. The variation of B is shown with k_s and λ_s volumetric indices under negligible stress conditions by linear regression. It can be observed that there is an acceptable coherence between B and the provided data.

It should be mentioned that the error can be related to the fact that the calculated volumetric indices are not completely under zero stress conditions which is the result of the deviations from B. It can be shown that the soils which were tested under 0 and 1 kPa are in great coherence with B thus, the following expressions are used to estimate the fitting parameter B:

$$B = \begin{cases} k_{s0} \ , & for\ k_s \\ \lambda_{s0} \ , & for\ \lambda_s \end{cases} \tag{2.43}$$

where k_{s0} and λ_{s0} are calculated based on the procedure described in the previous section using the four basic geotechnical parameters (PI, e, w and γ_d) under no applied pressure. Substituting A and B into the general logarithmic Eq. (2.41) will lead to the determination of the volumetric indices at any given applied stress (P). The shrink swell model is now established and the volumetric deformations due the changes in the soil suction through SVA interaction and loading conditions could be evaluated. A validation example with laboratory test is presented in Appendix 3.

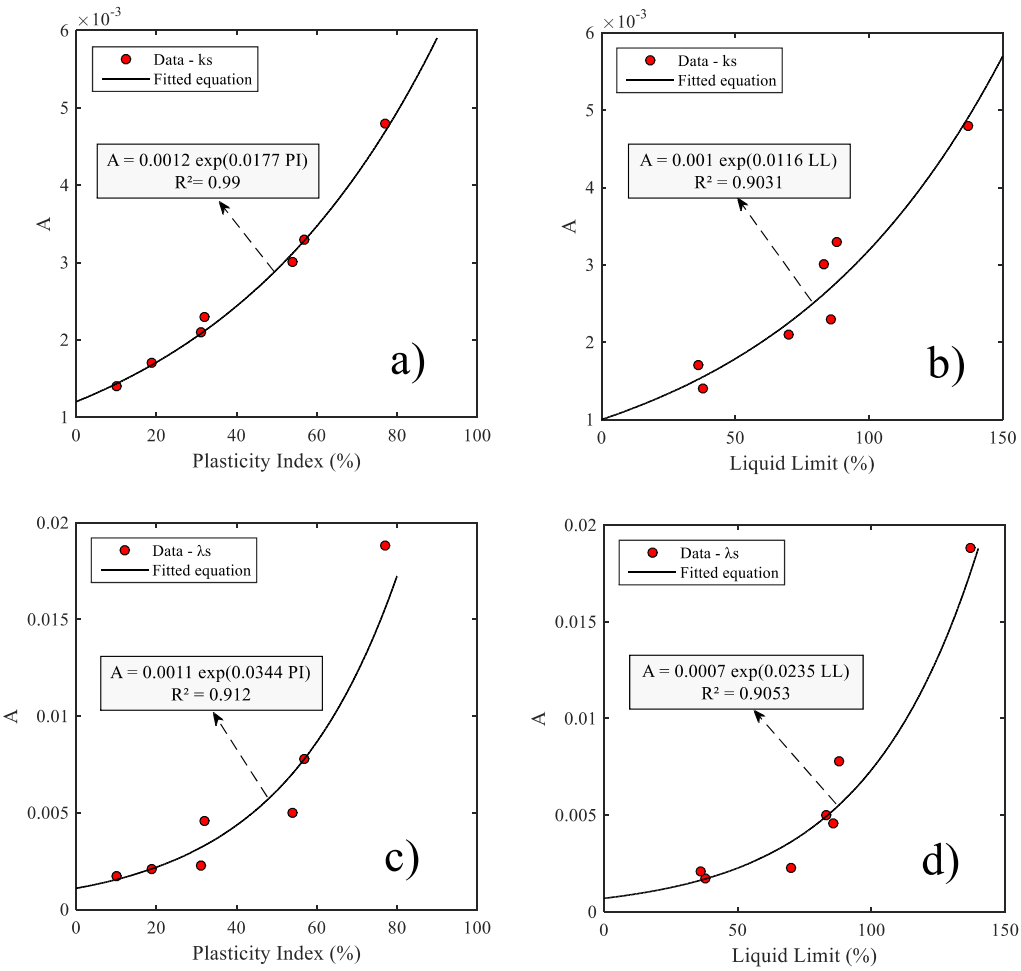

Figure 2.39 - Variation of fitting parameter A a) for k_s with the plasticity index; b) for k_s with the Liquid limit; c) for λ_s with the plasticity index and d) for λ_s with the liquid limit.

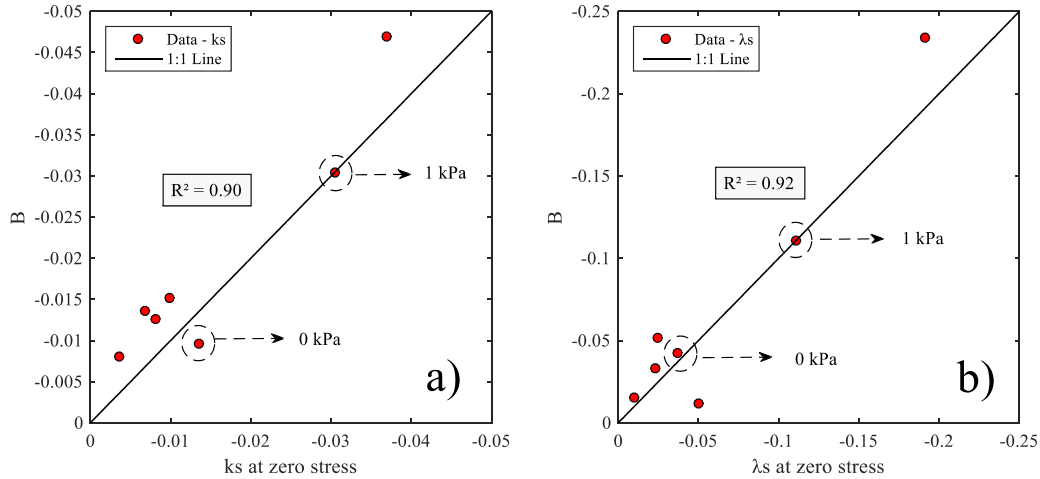

Figure 2.40 - Variation of fitting parameter B a) with k_s under zero stress condition; b) with λ_s under zero stress condition.

2.7 Conclusion

In this chapter, the modelling approach was presented. The approach was established based on the soil's physical parameters which allowed the calculation of the volumetric deformations in the soil medium. Based on the provided information in chapter 2 regarding the soil-vegetation-atmosphere interaction analysis and the use of the soil suction as an initial input condition in this chapter, the following flowchart can be determined for the adapted modelling approach. It can be observed in Figure 2.41 that a set of input climatic parameters is required for the soil-atmosphere interaction analysis and the time variable boundary conditions. Thereafter, the spatial - temporal variations of the soil temperature and water content are determined using a hydro-thermal soil model, where the influence of the vegetation on the soil can also be taken into account. The soil retention curve as well as the hydraulic and thermal parameters are used in this step. Finally, the temporal variations of the soil suction are used to calculate the soil volumetric deformations based on the shrink-swell model. The volumetric indices and the model parameters along with the influence of the loading conditions on the volumetric indices are determined in this step which allows the determination of the soil movements in time.

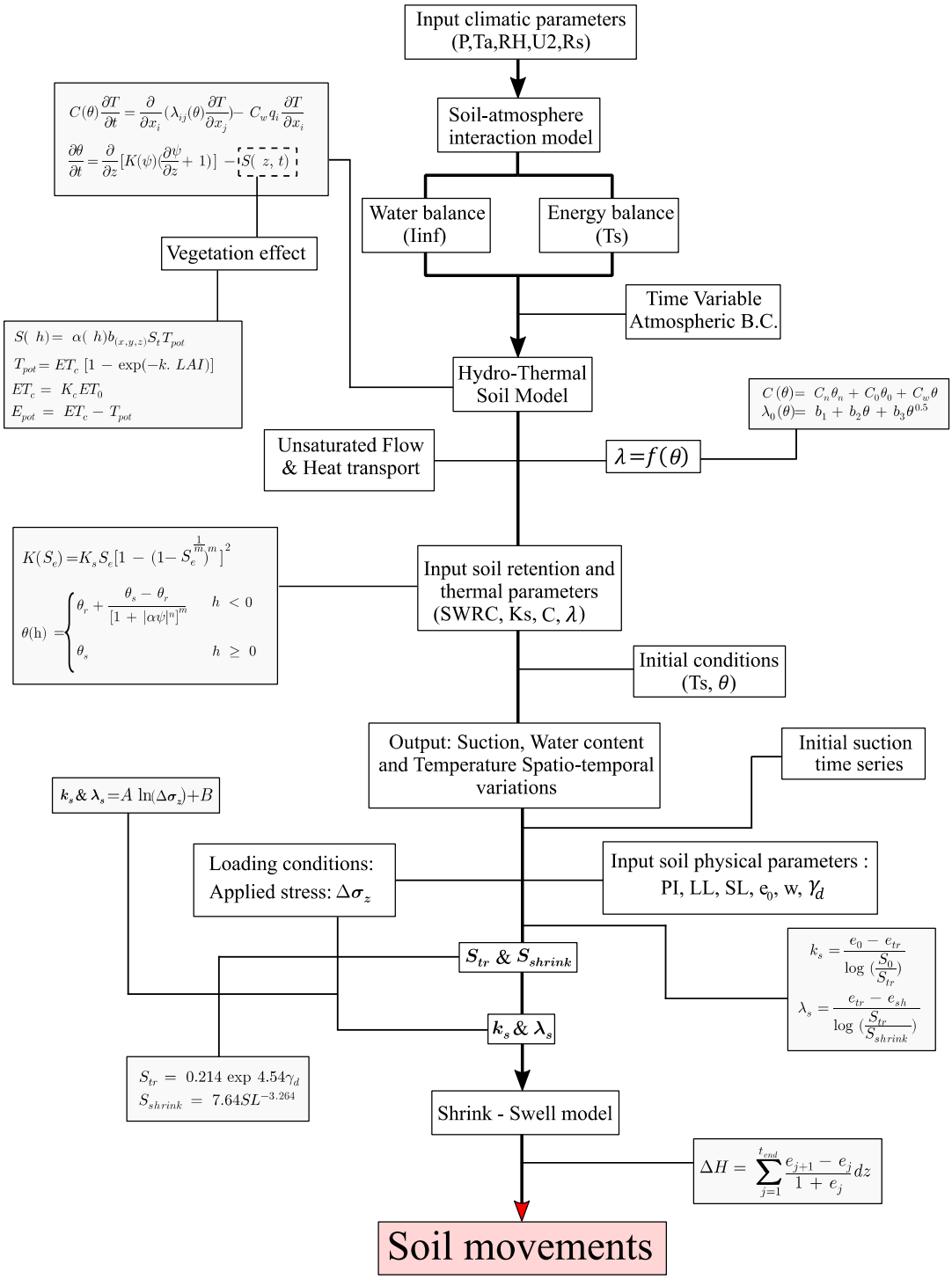

Figure 2.41. Flowchart of the adapted modelling approach

Chapter 3. Application and validation

3.1 Application to Roaillan experimental site

The site consists of a residential building which is located in the south west of France close to the Bordeaux city in Roaillan-Langon. The building is constructed in 2004/2005 and is a one floor residential L shaped construction with slab on ground floor and shallow footings which have a depth of 50 to 80 cm with a 50*30 cm section. The building was damaged due to differential settlements probably caused by environmental factors such as the presence of trees in the vicinity of the building and the climatic conditions during the monitoring period. Figure 3.1 shows the location and the satellite image of the building with the associated shrink-swell hazard map provided by the French Geological Survey (BRGM).

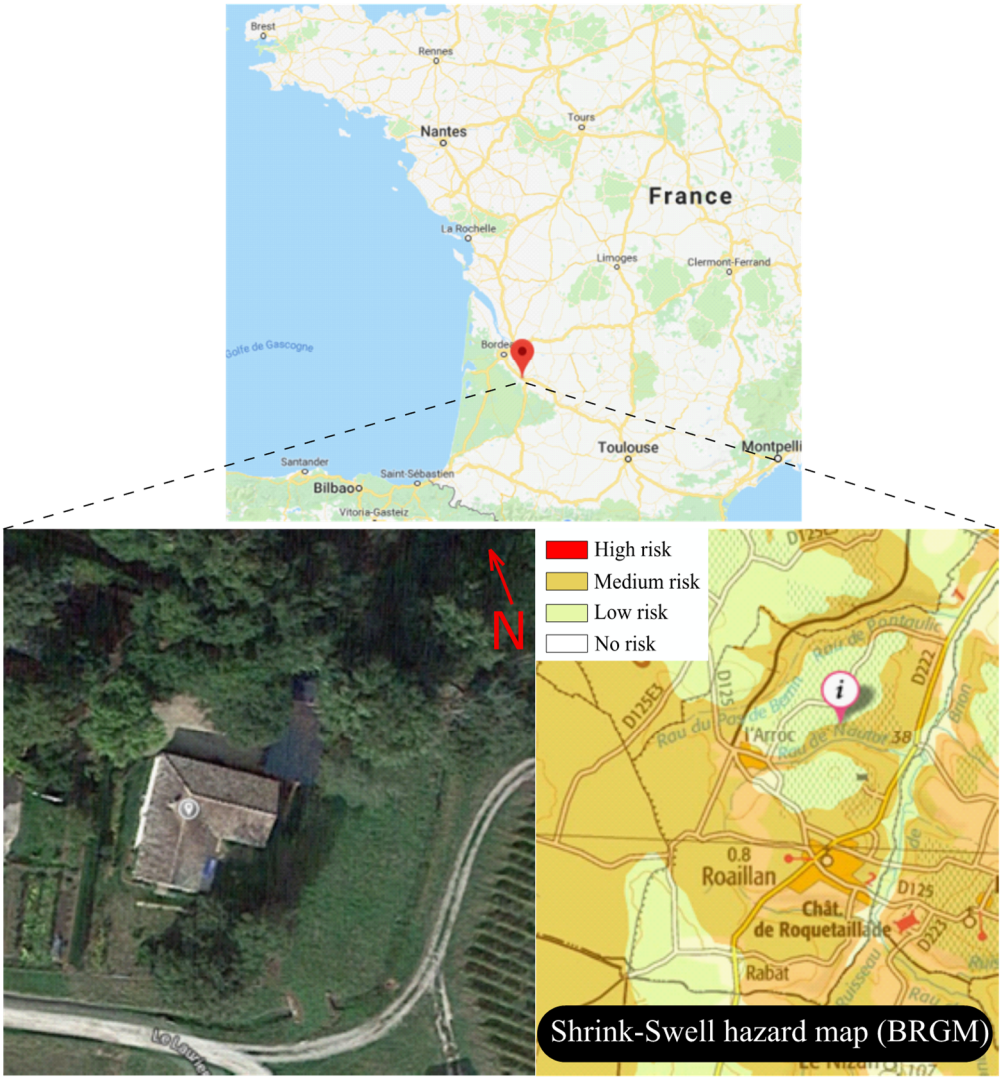

Figure 3.1 - Studied site location with the associated shrink-swell hazard map.

The geological formation of the site is characterized as a medium risk of shrink swell hazard based on the shrink-swell hazard map which makes the environmental factors a highly probable

cause of the observed damages. The first damages observed in 2009 on the building were mainly characterized by horizontal and vertical cracks, both in and outside the building. These damages evolved during the next years generating larger cracks on the walls, which put in danger the stability of the building. The area is mainly surrounded by tall oak trees so that in one angle of the building (south) a tree is located 2m away from it. However, in the north angle of the building the trees are at least 5 to 6 meters away from the building. It is generally deduced that the cause of the observed damages were differential settlements caused by the presence of tree (root water uptake) and the variation of climatic parameters over time.

3.2 Monitoring of the Roaillan site

The monitoring program of this site began in September 2011 in order to evaluate the changes of the soil physical parameters (mostly expansive clays) close to the building and to the trees (Mathon and Godefroy 2015). The crack openings on the building were also monitored during this period. In addition to meteorological conditions, the building was also exposed to the root water uptake by trees in its vicinity. Figure 3.2 shows the schematic representation of the building with the position of the closest trees to the building. The tree located in the north angle of the building (0.8m diameter and 14.8m height) is approximately 5m away, however, the trees in the south angle of the building are located 2 and 6m away and have a diameter of 0.65 and 1m respectively. The building seems to be damaged mainly on the west and the south side walls which are mainly the walls being exposed to the root water uptake (Assadollahi and Nowamooz, 2018b, 2018c, 2018d, 2018e).

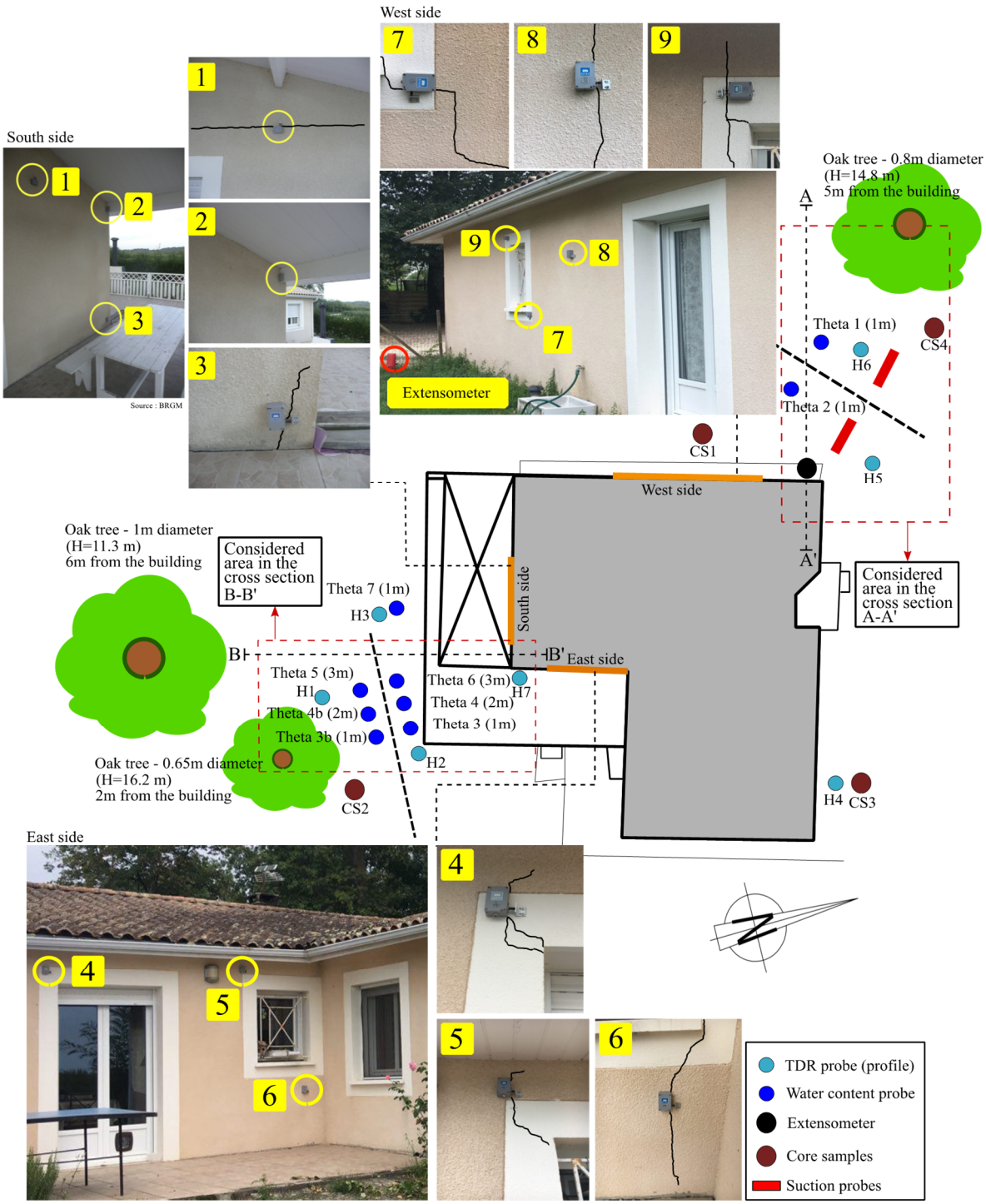

Figure 3.2 - The schematic representation of the monitored building with probes and the cracked monitored walls.

3.2.1 Geotechnical Investigations

Core sampling (CS) was carried out as shown in Figure 3.3 at four different angles of the building to investigate the present soil state at the site in depth. Laboratory investigations on samples collected from 0.4 to 7 m depth showed that almost all soils are characterized as fine-grained and plastic. Table 3.1 summarizes the measured parameters based on the French soil classification system (NFP 11-300). Furthermore, these tests showed that these samples are

characterized as very plastic and plastic clays. As shown in Figure 3.4, the plasticity range of the samples at different angles of the building varies from intermediate to very high plasticity. Generally, the swelling potential of these samples are also characterized as highly potential using the Vijayvergiya and Ghazzaly (1973) classification which is based on the Casagrande chart. These investigations confirmed that the construction site contains mainly high plasticity expansive clays which are very sensitive to environmental conditions.

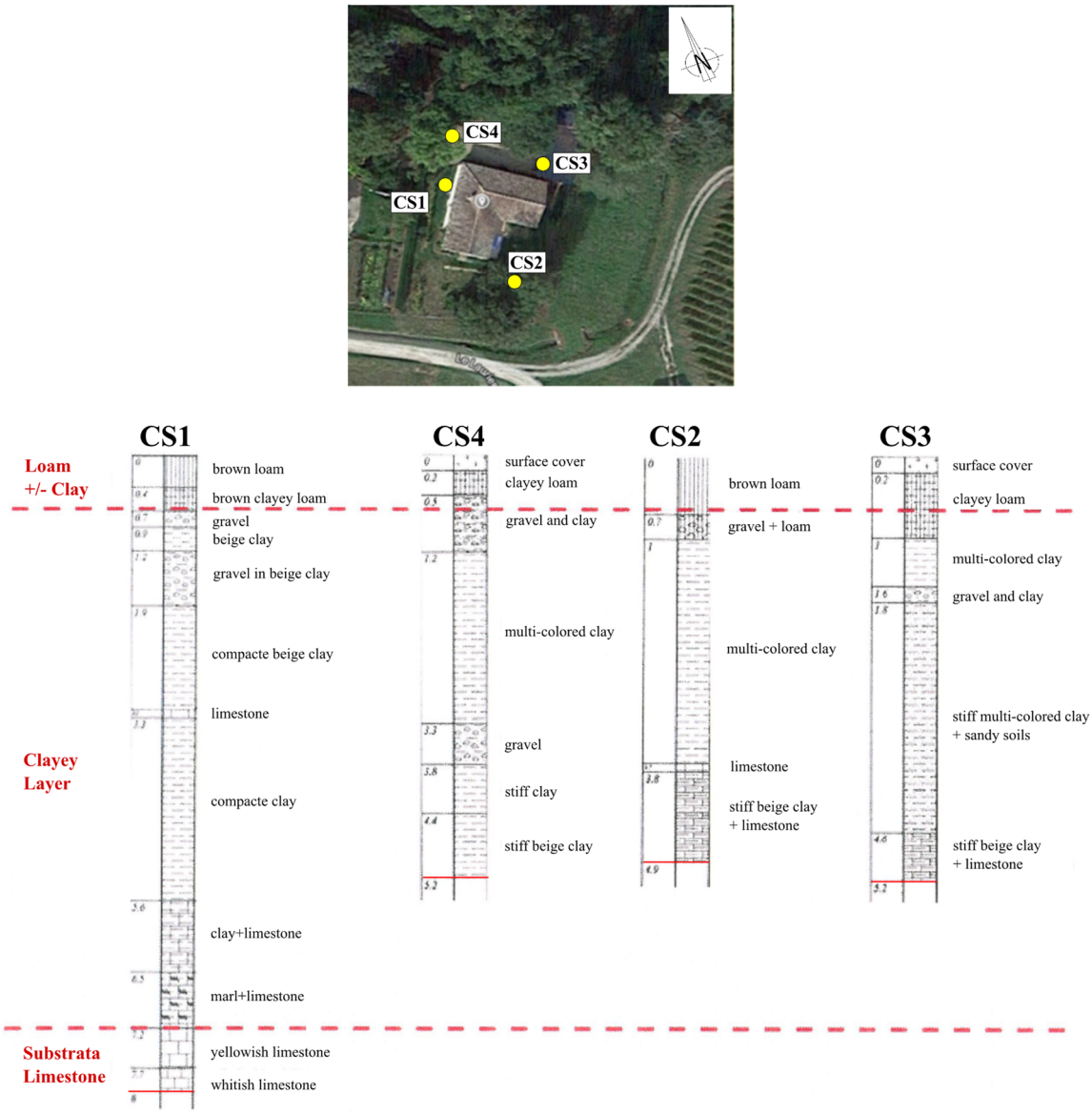

Figure 3.3 - Core samples at different locations surrounding the building (CEREMA).

Table 3.1 - Soil identification parameters of the Roaillan experimental site (Mathon and Godefroy, 2015)

Depth (m)	**Core samples**	**Geological formation**	$\emptyset < 80\,\mu m$ (%)	**Clay particles content (%)**	**Liquid Limit (LL)**	**Plastic Limit (PL)**	**Plasticity index (PI)**	**Methylene blue value VBS**	**Activity (%)**	**GTR classification**	**USCS classification**
0.4-0.8 m	CS1	Clayey silt	66.8	29	35	17	18	-	62.07	A2	CL
0.9-1m	CS1	Clay	98.6	70	71	35	36	9.09	51.42	A4	MH
1.2-1.6 m	CS2	Colored clay	95.3	73	85	33	52	9.58	71.23	A4	CH
1.2-2m	CS4	Colored clay	99.6	76	70	27	43	9.63	56.57	A4	CH
1.3-1.6m	CS3	Colored clay	69.8	49	47	18	29	3.5	59.18	A3	CL
2.3-2.6m	CS1	Compacted clay	99.4	-	69	30	39	7.55	-	A3	CH
2.4-2.8m	CS3	Stiff clay + sand	93.1	75	70	29	41	9.01	54.66	A4	CH
3.1-3.2m	CS2	Colored clay	99.8	-	68	27	41	7.95	-	A4	CH
3.6-3.8m	CS1	Compacted clay	99.2	80	65	29	36	8.11	45	A4	CH
3.8-4.4m	CS4	Stiff Ocher clay	99.9	79	60	26	34	9.8	43.04	A4	CH
4.2-4.3m	CS2	Stiff clay + limestone	87.6	-	49	24	25	6.71	-	A2	CL
4.4-5.2m	CS4	Stiff beige clay	99.1	62	47	18	29	5.51	46.77	A2	CL
5.2-5.6m	CS1	Compacted clay	96.5	63	45	22	23	5.14	36.5	A2	CL

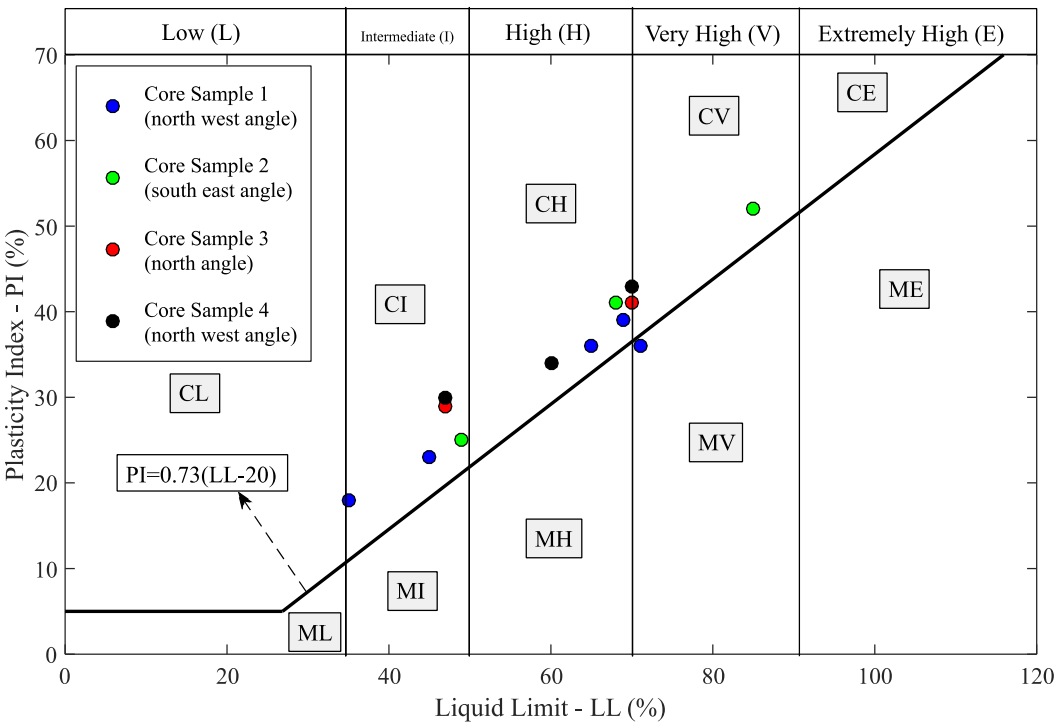

Figure 3.4 - Plasticity range of studied samples by the Casagrande plasticity chart.

3.2.2 Structural and Geotechnical monitoring sensors

3.2.2.1 Crack displacement sensor

In order to monitor the structural stability and the movements of the cracks, tree sides of the building were monitored since 2011 using displacement sensors installed on the observable cracks generated in 2009 (BRGM). Three sensors were primarily installed in 2011 on the south side of the building where the cracks were mostly horizontal. The measurements resolution is 0.003mm with a precision of 0.01mm and a ±5mm of measurement range followed by a data storage frequency of 8 hours (i.e. 3 measurements per day). The Fissuro-Thermo-Loggers (F10TN) are able to determine if the crack is moving (closing-opening) and are also able to monitor its amplitude in a precise way (Figure 3.6 a)). The configuration of these three sensors was changed in 2014 and were installed on the west side of the building where the largest crack was observed (45°) and finally, three other sensors were installed at the same time in 2014 on the east side of the building (south east angle) where vertical and 45° staircases like cracks could be observed.

3.2.2.2 Soil movement sensor - extensometer

In addition to these displacement sensors, a multi-point rod extensometer was installed in a borehole to monitor displacements at various depths (from 1 to 5m) using rods of different material and lengths. The rods are fixed to the adjacent soil and the relative movements between the anchors and the reference head are measured manually with caliper or linear transducers, assembled on the reference head for remote monitoring. It is generally supposed that the north angle of the building is in a more critical state compared to the south angle because of the presence of larger cracks on this side.

3.2.2.3 Soil matrix potential sensor

As indicated in Figure 3.2, water content probes were installed both in the north and south angle of the building at different depth. The north side of the building contains suction probes at different depth (from 0.8m to 3m) which were installed by the CEREMA and were reported in Mathon and Godefroy (2015) covering the period of 2011 until early 2014. These probes were installed with an initial span of 0.75m from the building and 0.25m for others. The monitoring of the soil suction continued until late 2015 and is reported here. Furthermore, new suction probes were installed in 2013 starting form a depth of 2.5m to 5m, both close to the tree and close to the building in the north angle for monitoring the root water uptake and its effect on the soil in the building's vicinity.

The sensor was calibrated to obtain a relationship between the measured matrix potential (suction) and the soil water content. These measurements were carried out on 3 samples at three different depths (2.3m and 4.3m on core sample 1 – CS1 and at 1.8m on core sample 3 – CS3). The following steps were adapted in the calibration process: The samples were first saturated, then the probes were installed on the samples, the samples were dried and the matrix suction was measured each 15 minutes. Figure 3.5 shows the calibrated retention curves of these three samples. These curves allow the deduction of the volumetric soil water content corresponding to the measured soil matrix suction in site. Note that the mathematical relationship can be both obtained by fitting a polynomial equation on the data or retention models in the literature.

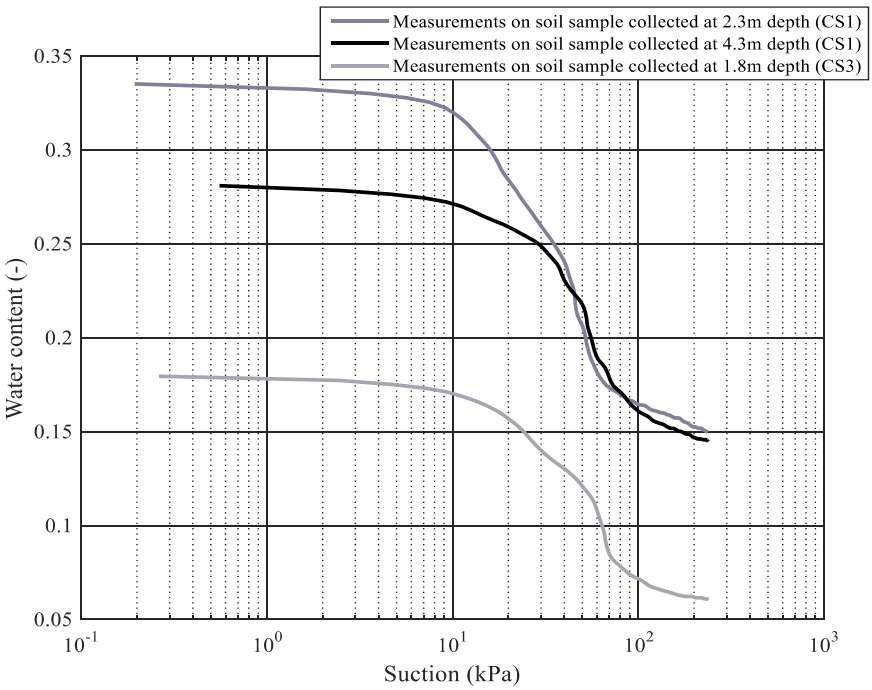

Figure 3.5 - Calibration of the soil matrix suction sensors with the water content for three collected samples (CEREMA, 2015)

3.2.2.4 Soil moisture sensor

On the other hand, seven water content probes (Theta probe) are installed in the south angle of the building in 1, 2 and 3m depth as shown in Figure 3.2. Two water content probes are installed in the north angle of the building (close to the tree and close to the building) in 1m

depth. The results of the water content monitoring for the period of 2011 until late 2013 are reported by the BRGM. However, the monitoring continued until march 2014. Therefore, the additional results of the water content probes are also reported here. The mentioned periods cover the displacement monitoring period of cracks which started in early 2014.

Theta Probe type sensors (Figure 3.6 c)) were used to measure volumetric soil moisture content, θ_v, by the well-established method of responding to changes in the apparent dielectric constant. These changes are converted into a DC voltage, virtually proportional to soil moisture content over a wide working range. These sensors measure soil parameters by applying a 100 MHz signal via a specially designed transmission line whose impedance is changed as the impedance of the soil changes. The difference between the voltage is used by the sensor to measure the apparent dielectric constant of the soil.

Both of these sensors (Watermark and ThetaProbe) were installed by digging separate access holes for each depth which ensures that each probe is installed into undisturbed soil at the bottom of its own hole. It should be mentioned that there was no water flow into the refilled holes, however, even a failure on a single hole doesn't jeopardize all the data, as it would if all the measurements were made in a single hole. The main drawback to this method is that a hole must be dug for each depth in the profile.

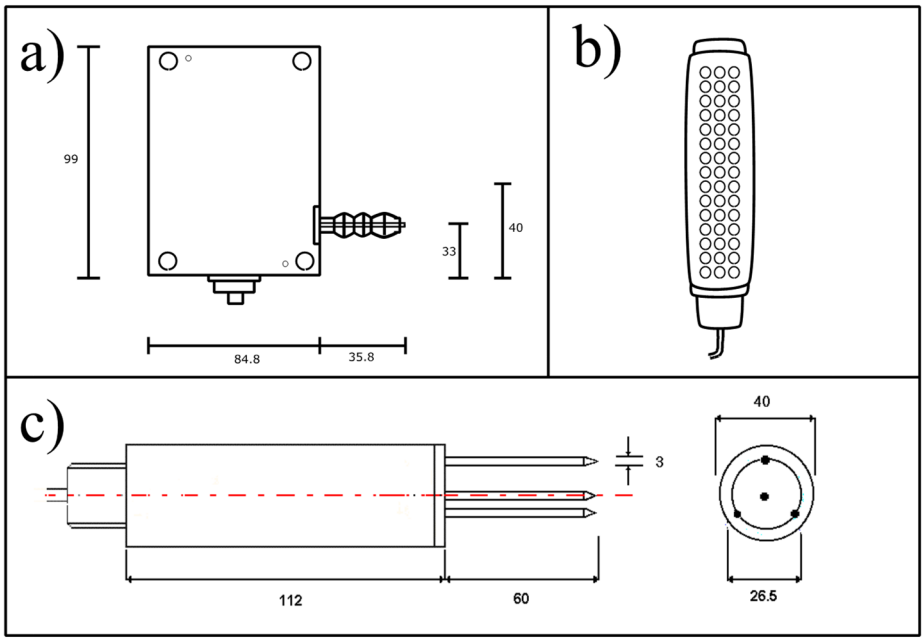

Figure 3.6 - Some instruments used in for monitoring: a) displacement sensor, measuring crack closing/openings (F10TN); b) Soil matrix suction sensor (Watermark); c) Soil volumetric water content/moisture sensor (Theta Probe)

3.2.2.5 Soil temperature sensor

These sensors are TDR type sensors which were installed primarily in 2011 at 1.5m and 4m depths. The installation was carried out by digging access boreholes.

3.2.2.6 TDR profiling probe

In order to measure the variation of the soil temperature and water content profiles on the site, 7 different points were considered as shown in Figure 3.2. Sensors used for this purpose are TRIME-PICO type sensors which are measurement devices for continuous and non-destructive determination of volumetric soil moisture and soil temperature at the same time using an integrated temperature sensor. This sensor is designed for mobile field use and can be connected to a data logger or a PC for monitoring and data logging purposes.

The measurement is carried out by a TDR tube access probe especially designed for water content and temperature profiling which makes routine and non-destructive measurements. The tube probe consists of a cylindrical PVC-body, which has four spring-mounted aluminum plates as TDR wave guides on opposite sides. It should be mentioned that these operations were carried out by the I2M laboratory of Bordeaux. Seven access boreholes (H1 to H7) were executed in order to install the PVC tubes into the soil and to a depth of 2.95m. The H1, H2 and H7 probes were considered in the south angle of the building and the H5 and H6 probes were designated for the north angle.

3.2.2.7 Data Loggers

Finally, all of the sensors are connected to data loggers which allows continuous monitoring of the variations over time. As indicated in Figure 3.7, WaterMark type data loggers are used to store data provided by the matrix potential, temperature and soil moisture sensors. On the other hand, the data provided by the Theta probes (humidity probes) are stored in another data logger installed by the BRGM (French Geological Survey). The data provided by the Fissuro-Thermo-Loggers and the extensometers as well as the TDR profiling probes are stored by separate data loggers.

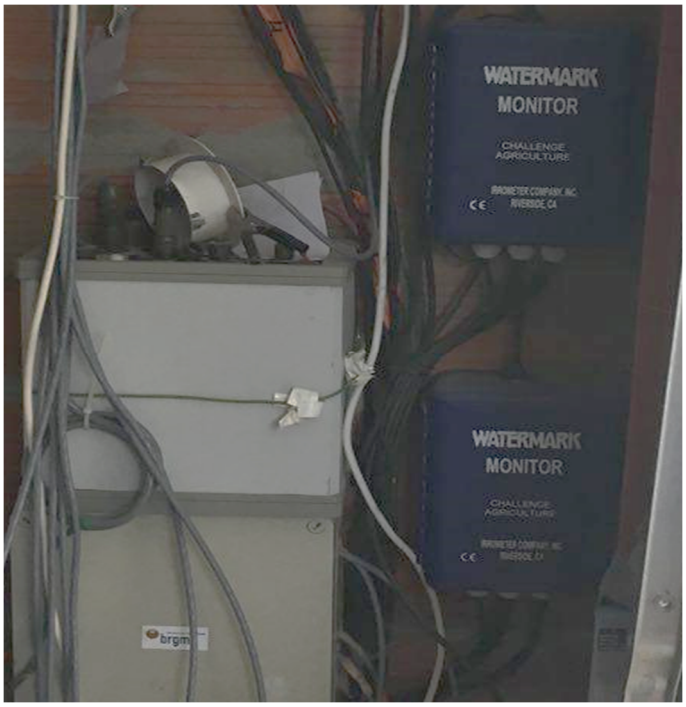

Figure 3.7 - Different data loggers used in the monitoring operations

3.3 Model setup for simulating the site

3.3.1 Model dimensions and adapted profiles

Figure 3.8 shows the 2D vertical profile (A-A' cross section) of the north angle with the tree which is located 5 meters away from the building. The foundation of the building is a shallow type of footing which has a 0.8m depth. As shown in Figure 3.8 different probes are installed both near the building and near the tree. The red points show the primary soil matrix potential sensors which were installed close to the tree and the building. The blue points show the soil moisture sensors installed close to the surface. The yellow points show the temperature probes and the green points indicate the location of additional soil matrix potential sensors which were installed in 2013. H5 and H6 are the profiling probes in which the water content and the temperature are measured up to a depth of 2.95m.

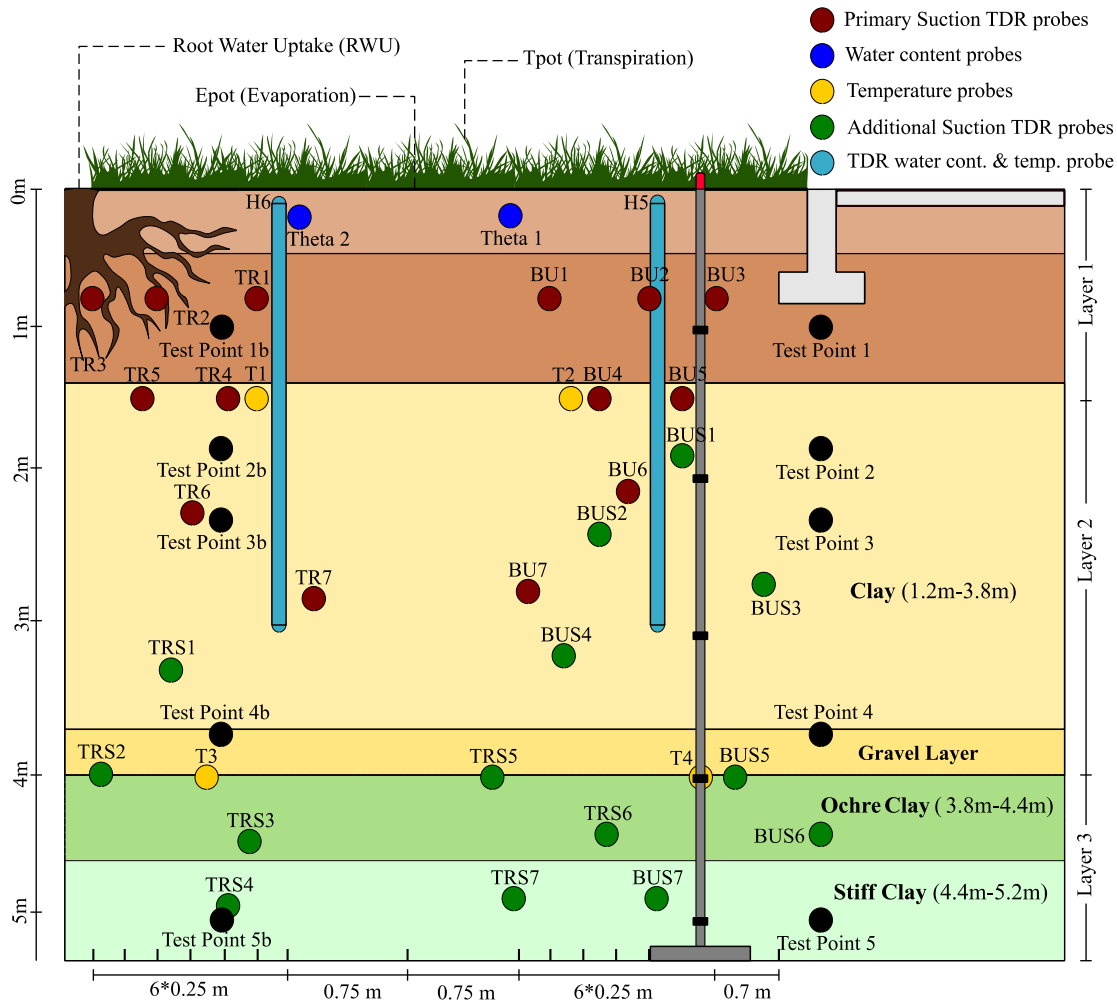

Figure 3.8 - 2D profile of the geological formation at the north angle (A-A' cross section).

Based on the measurements of the retention properties at three depths in this vertical profile, three soil layers were considered with different hydraulic and thermal properties for the Soil-Atmosphere-Vegetation analysis and the transient hydro-thermal simulation.

On the other hand, Figure 3.9 shows the vertical profile of the B-B' cross section indicated in Figure 3.2 for the south angle where the tree is located 2.5m from the terrace. The blue points show the soil moisture sensors close to the tree and the building. H1 H2 and H7 are the boreholes for the measurement of water content and temperature profiles up to a depth of 3m. The black points show the different test points which will be discussed in the results section. Based on the geotechnical investigations, the vertical profile is divided in four different layers with each having different hydro-thermal properties.

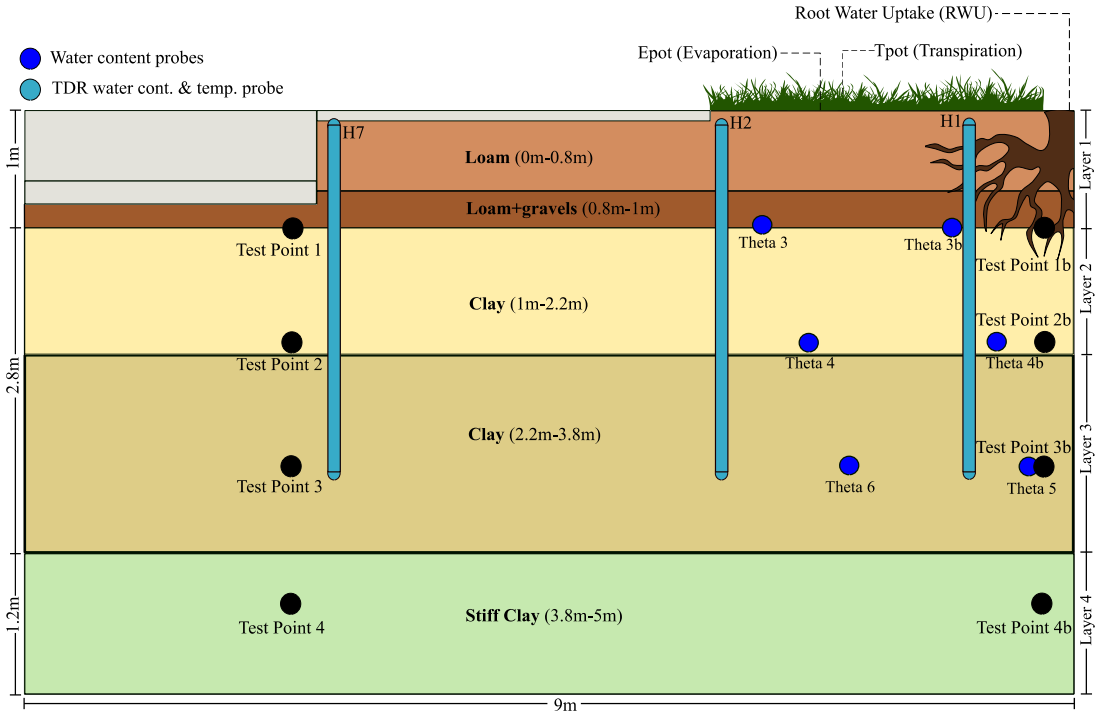

Figure 3.9 - 2D profile of the geological formation at the south angle (B-B' cross section).

Figure 3.10 shows the results of the monitoring at the north angle of the building. Figure 3.10 a) shows the water content variations at surface (1m) close to the tree and the building. Both probes show similar results and follow the imposed climatic conditions. The tree does not seem to affect the soil water content at the depth of 1m.

Figure 3.10 b) shows the soil suction variations near the tree. Many sensors were installed at different depths to investigate the suction induced by root water uptake. It can be observed that the soil suction at 0.8m for TR1, TR2 and TR3 probes shows approximately the same pattern. The soil suction seems to drop to almost zero at 1.5m showing a saturated state however it shows higher values up to 250 kPa (which is the maximum capacity of the suction measurments) at 2.3m. The additional sensors installed in late 2013 at 4m, 4.5m and 5m depth show stable values of suction around 40 kPa. It can be deduced that the desiccation front generated by root water uptake is located from 0 to 0.8m depth and from 2.3m to 4m depth. The soil stays in an almost saturated state between these limits (from 1 to 2m depth approximately) and is not influenced by the root water uptake. On the other hand, Figure 3.10 c) shows soil suction variations at different depth near the building. It can be observed that the soil suction follows the climatic conditions imposed on the site and shows a complete saturated state when the infiltration rate is positive. The soil suction in BU1, BU2 and BU3 measured at 0.8m, shows the

same pattern and almost the same values. Furthermore, the BU4, BU5 and BU6 probes showed zero suction values during the monitoring (at 1.5m and 2.3m) indicating the presence of a saturated soil. The BU7 probe at 3m depth shows the same results as the previous sensors until 03/2014 but it shows a sudden increase in suction values in 03/2015 (started from 03/2014) which could be related to the desiccation front generated by root water uptake or maybe the result of cracking in a clayey soil, as shown in Figure 3.10 c). It is worth mentioning that the additional sensors installed in 2013 at higher depth showed a complete saturated state of the soil with zero suction values.

Figure 3.10 d) shows the crack openings on the west side wall (north angle). Sensors were installed on the largest cracks observed on the building. All three sensors show cyclic movements of the crack. Sensor 7 (crack 7) with an initial opening of 0.9mm shows larger variations than the other ones. It follows not only the climatic conditions imposed on the site, but also the root water uptake generated near the building at 3m depth. The crack tends to open when the soil near the building shows a dry state from 06/2014 to 10/2014 and from 06/2015 to 10/2015. However, the crack tends to close in wet periods which could be observed from the data beginning from 10/2015 until 02/2016. Furthermore, the provided data from the extensometer installed in 2014 confirmed the shrink swell characteristic of the soil and consequently the crack openings.

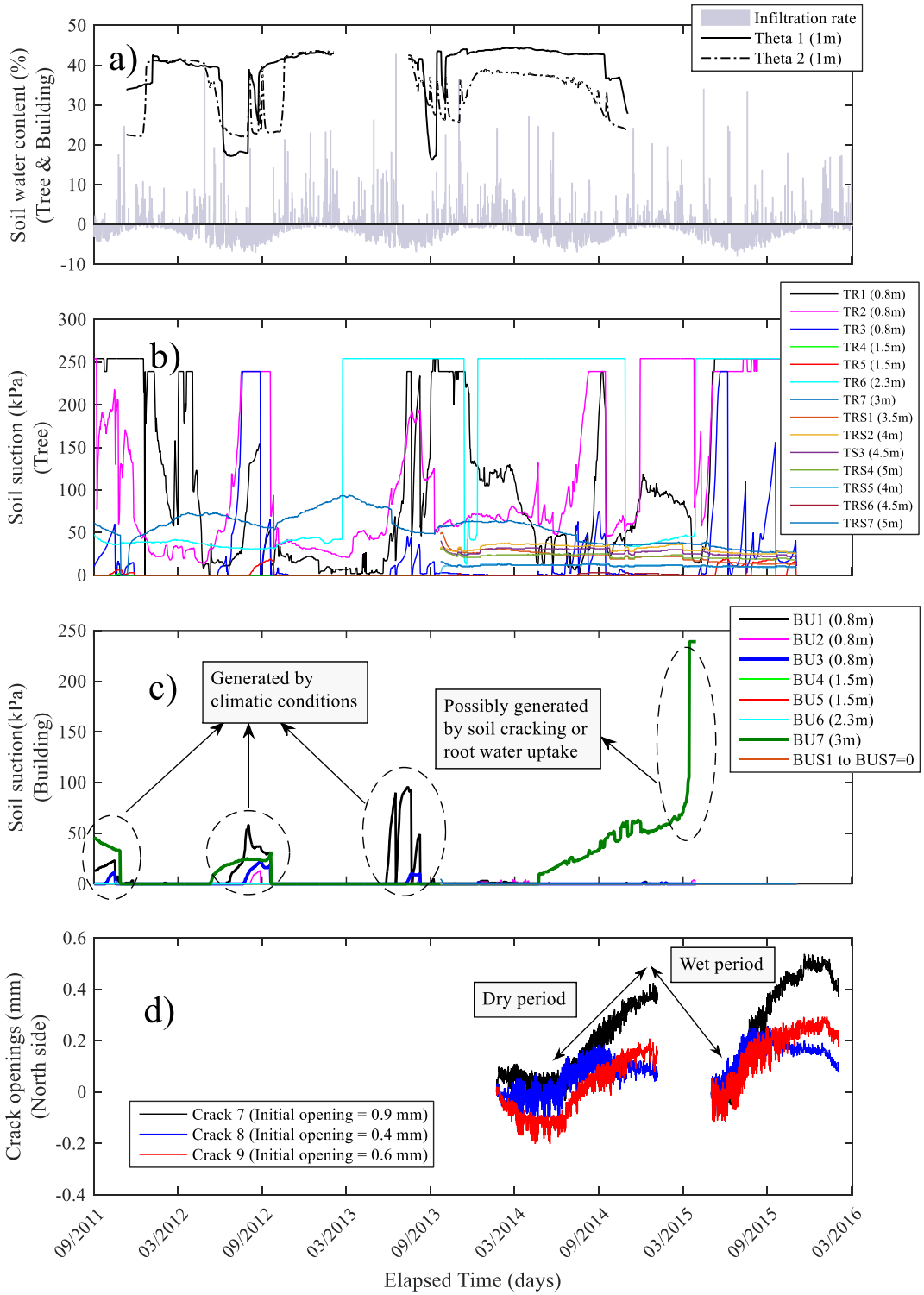

Figure 3.10 - Results of the monitoring at the north angle of the building: a) water content variations near the building vs variations near the tree; b) soil suction variation at different depth near the tree – sensors installed in the same depth have a 0.25 to 0.5

Figure 3.11 shows the obtained results from the monitoring at the south angle of the building. Figure 3.11 a) shows the water content variation near the building at 1, 2 and 3m depth. It is observed that the water content variations follow the climatic conditions imposed at the site

mostly at 1 and 2m depths. On the other hand, Figure 3.11 b) shows the variations of water content near the tree at 1, 2 and 3m depth. It is observed that the variations of the water content are lower than the ones near the building and the soil near the tree shows generally higher saturated state which could be related to the root distribution pattern.

Figure 3.11 c) shows the crack openings at the south side of the building (09/2011-08/2013). It can be observed that the sensor 1 (crack 1) located on a horizontal crack shows a stable behavior and does not move during the monitored period. The same behavior is observed for sensor 3 (crack 3) which was located on a 45° crack at the base of the wall. The sensor 2 (crack 2) located on the beam shows cyclic movements during the monitoring, however, the range of variation is negligible. Following the stable behavior of the south side, sensors were installed on the south east wall in 01/2014 where major cracks were observed.

Figure 3.11 d) shows crack movements results on the south east side. Sensors 6 (crack 6) located on a crack show a complete stable state without any movement during the monitoring (01/2014 - 01/2015 and 08/2015 – 02/2016). Sensor 5 (crack 5) installed on a micro crack shows a negligible cyclic movement by a range of lower than 0.1 mm. However, sensor 4 (crack 4) installed on the top right-hand side of the window on the east side wall show a cyclic movement which is in coherence with the dry and wet periods. It can be observed that the crack tends to open during the dry period (negative infiltration rate) and tends to close during the wet periods (positive infiltration rate) which follows the climatic conditions imposed at the site from 01/2014 until 01/2015. For the next period starting from 08/2015 and ending at 02/2016, the same cyclic movement is observed. The crack tends to open until the infiltration rate is negative (dry period) which continues until 10/2015 and it tends to close after this specific time by starting positive infiltration rate. The maximum range of movements on this crack is about 0.4mm.

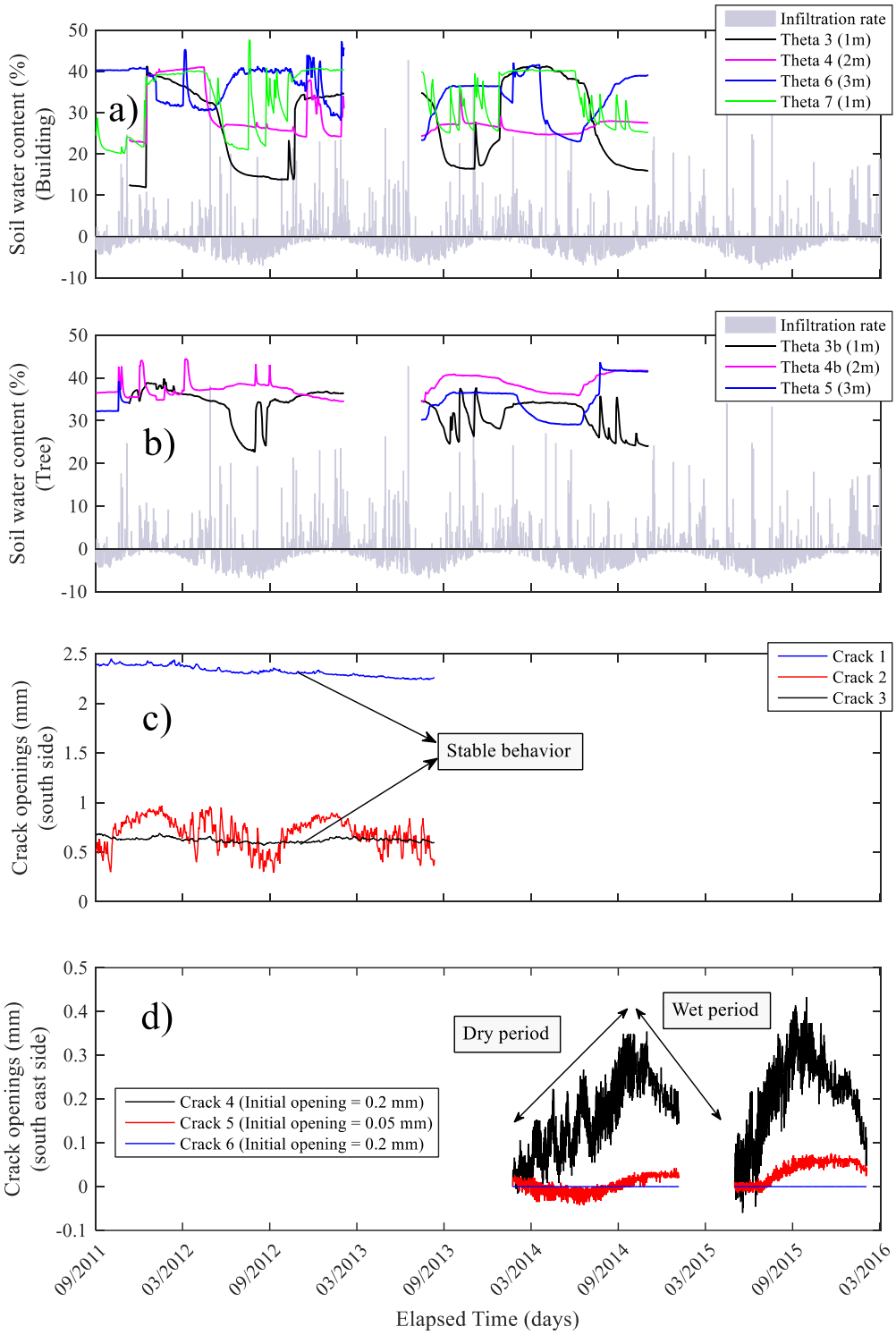

Figure 3.11 - Results of the monitoring at the south angle of the building: a) water content variations near the building; b) water content variations near the tree at three different depths; c) crack closing/openings on the south side of the building; d) crack clos

3.3.2 Soil input parameters

In this section the soil input parameters of the experimental site are presented primarily for the hydro-thermal simulation phase and secondly for the calculation of the soil shrinkage and swelling based on the proposed approach.

3.3.2.1 Soil-Water retention curves (SWRC)

Figure 3.12 a) shows the water retention curves of the three studied samples on the north angle of the building. The obtained retention curves from experimentation were fitted by using the Van Genhutchen model. The associated parameters are listed in Table 3.2. It should be mentioned that no measurement was carried out on the first layer (0-1.5m), therefore its retention properties are estimated based on the nature of the soil in the top layer and values suggested by Hydrus 2D.

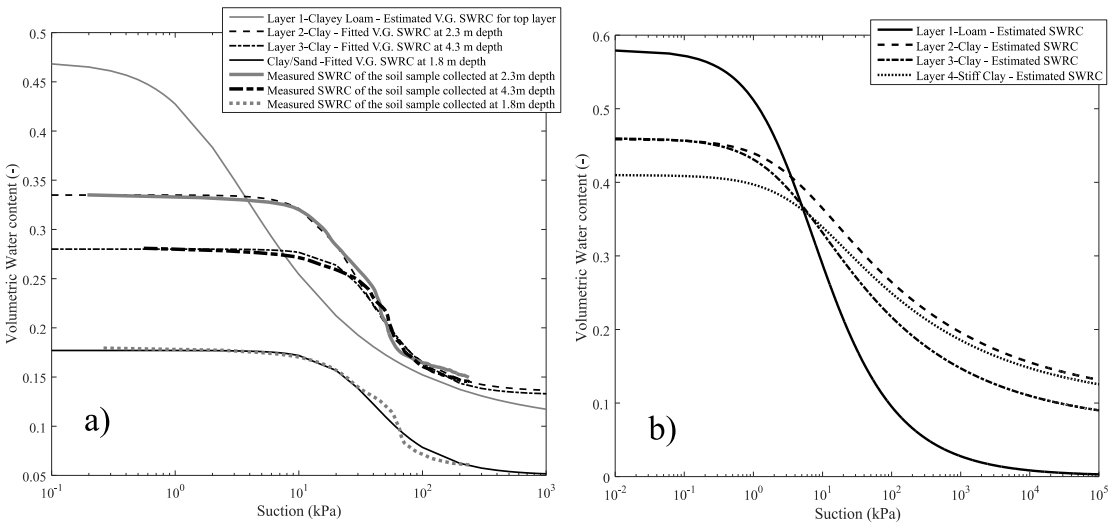

Figure 3.12 - SWRC of the soil layers in a) the north angle and b) the south angle of the building.

On the other hand, Figure 3.12 b) shows the soil water retention curves at the south angle of the building, where no measurements were carried out. The retention curves were estimated by the retention parameters optimization. During the process typical retention parameters were primarily associated to each soil type, representing generally the retention behavior of these kind of soils. Secondly the unsaturated flow simulation was performed for the south angle and the results were compared to the measurements of volumetric water content at different depths (Theta 3, Theta 3b, Theta 4, Theta 4b, Theta 5 and Theta 6). Finally, the error between the simulated water contents and the observed ones were reduced by optimizing the retention parameters. It should also be mentioned that these procedures could also be carried out by adapted algorithms or inverse modelling techniques which could be time consuming based on the number of parameters interacting in the modelling process.

However, the following retention curves are finally proposed for modelling the unsaturated behavior of the geological formation of the south angle of the building. The retention curve of the first layer represents the behavior of a loamy soil and the other three layers are associated to clayey soils which behave approximately in the same manner. The retention parameters are listed in Table 3.2.

3.3.2.2 Unsaturated Hydraulic Conductivity functions

Based on the Van Genhutchen model, the hydraulic conductivity can be plotted against suction variations. Figure 3.13 a) shows the hydraulic conductivity functions for each layer at the north angle of the building. A saturated hydraulic conductivity of 650 mm/day was associated to the first layer due to the fact that it also contains gravel. The other two clayey layers are also presented in this figure which have much smaller saturated hydraulic conductivities. A saturated hydraulic conductivity value of 5 mm/day is attributed to the last layer because it only covers last 0.5m of the soil profile of the model (4.5-5m).

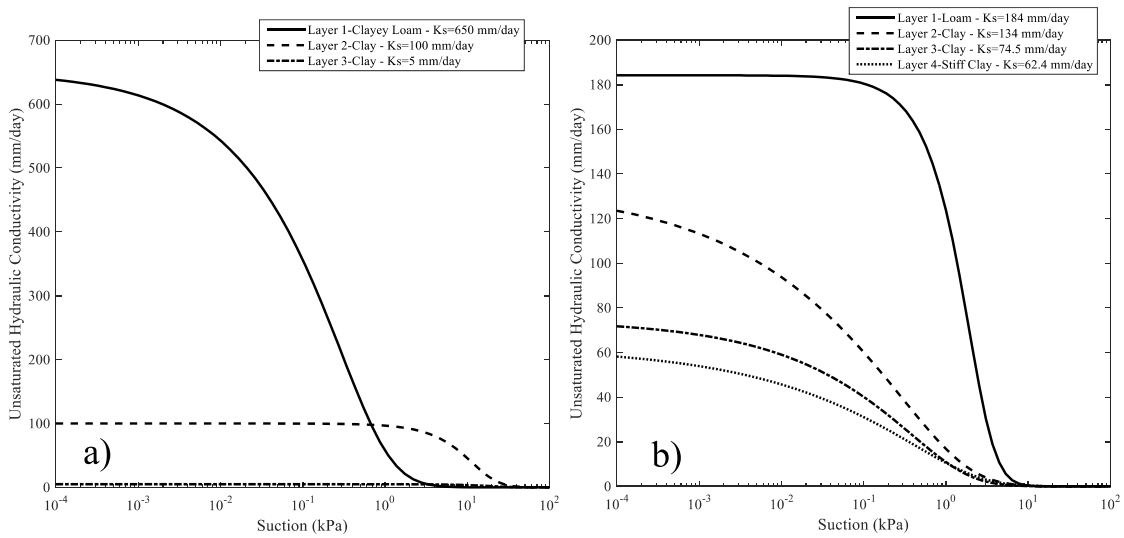

Figure 3.13 - Unsaturated Hydraulic Conductivity functions of the soils in a) the north angle and b) the south angle of the building.

The hydraulic conductivity functions of the south angle of the building are presented in Figure 3.13 b). It can be observed that a larger saturated hydraulic conductivity is attributed to the first layer which is constituted mostly by loamy soil. The following three layers have smaller saturated hydraulic conductivities and are associated to clayey soils. These saturated hydraulic conductivity functions were chosen based on the soil data base provided in Hydrus 2D software. It should be mentioned that the adjustment of the saturated hydraulic conductivities (along with other retention parameters) was carried out in the north angle in order to fit the observed data and to provide a more realistic behavior of the water flow parameters.

3.3.2.3 Thermal Conductivity functions (TCF)

No direct thermal measurements were carried out on the soil samples of this site. Thus, typical TCF functions were considered based on measured thermal conductivities of typical soils. Figure 3.14 shows the thermal conductivity functions adapted for each soil type. Two thermal conductivity functions were presented for the sake of simplicity. For a typical clay and clayey loam soil, the thermal conductivity behaves as shown in Figure 3.14 in function of the soil water content. The adapted function for a clayey loam was generated by fitting it to typical measurements on a clayey loam sample analyzed in Lu (2007). The first function is associated to the first layer of each of the soil profiles at the north and the south angle of the building. The second TCF function represents a clayey soil's thermal behavior which is also fitted to typical experimental

data of a clayey soil sample presented in Lu (2015) and is associated to the second and third soil layer in the north angle of the building and to the second, third and fourth soil layer in the south angle of the building. The fitted empirical parameters for the generation of the TCF functions are presented in Table 3.2.

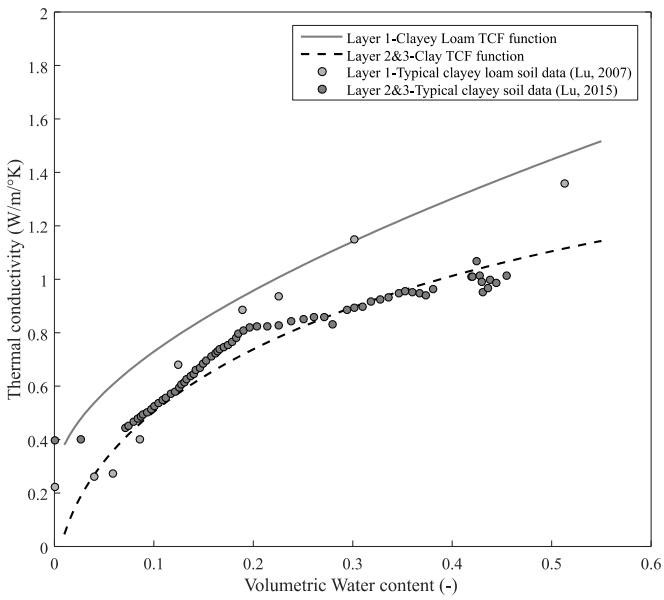

Figure 3.14 - Thermal conductivity functions fitted to typical soils data.

The soil volumetric heat capacity (which depends on the solid and liquid phase heat capacities) is also determined for the simulation purpose. It should be mentioned that the liquid phase volumetric heat capacity is taken equal to 3.12 $MJ\ m^{-3}\ °C^{-1}$ and the volumetric heat capacity of the solid phase is adapted by introducing different volumetric fractions to each soil layer.

Table 3.2 - Hydro thermal input soil parameters

Building Angle	**Layer**	**Depth (m)**	$\varepsilon\ \left(\frac{1}{mm}\right)$	n	θ_s	θ_r	l	$K_s\left(\frac{mm}{day}\right)$	b_1	b_2	b_3	C_n $(MJ\ m^{-3}\ {}^{\circ}C^{-1})$
North	1	0-1.5 m	0.0059	1.48	0.47	0.1	0.5	650	0.243	0.393	1.534	1.4
	2	1.5-4 m	0.00042	2.3	0.335	0.135	0.5	100	-0.197	-0.962	2.531	1.43
	3	4-5.5 m	0.00027	2.5	0.28	0.132	0.5	5	-0.197	-0.962	2.531	1.43
South	1	0-1 m	0.00248	2.25	0.58	0.001	0.5	184.2	0.243	0.393	1.534	1.4
	2	1-2 m	0.0026	1.305	0.458	0.0982	0.5	134.1	-0.197	-0.962	2.531	1.43
	3	2-3.8 m	0.00312	1.384	0.46	0.068	0.5	74.5	-0.197	-0.962	2.531	1.43
	4	3.8-5m	0.0019	1.31	0.41	0.095	0.5	62.4	-0.197	-0.962	2.531	1.43

3.3.2.4 Soil volume change parameters

The input volume change parameters for each soil layer at the north angle of the building are presented in Table 3.3. It should be mentioned that only the north angle volumetric parameters are considered for the validation purpose because the shrink-swell measurement by the extensometer is only carried out in the north angle. Since the measurements of the soil movements were carried out at 3 different points, the assigned parameters are also considered for these 3 points (1m, 2m and 3m depth).

As mentioned in Table 3.3, PI, w%, e_0 and γ_d are the key input parameters for the determination of the volumetric indices k_s and λ_s. On the other hand, LL and SL are used to determine the model suction-based parameters (S_{tr} and S_{shrink}) and the infulence of the loading conditions on the volumetric indices by calculating the fitting parameters A and B. It should be mentioned that in this section the influence of the building's load on the volumetric indices are not taken into account in the modelling process since the extensometer is not installed right under the foundation soil of the building but in its left vicinity. In this case, the in-situ applied stress due to the building's load on the soil in the left vicinity is negligible.

Table 3.3 - Volume change parameters of the soil at 1, 2 and 3m depth (North angle)

Depth (m)	**PI (%)**	**LL (%)**	**SL (%)**	**w% Sat.**	e_0	γ_d **(Mg/m³)**	k_s	λ_s	S_{tr} **(kPa)**	S_{shrink} **(kPa)**
1	36	71	27	0.46	0.95	1.38	-0.0381	-0.0596	112.55	548.43
2	39	69	14	0.33	0.89	1.42	-0.0371	-0.0541	134.96	4678.76
3	36	65	22	0.33	0.89	1.42	-0.0359	-0.0532	134.96	1070.1

The plasticity index and the soil liquid limit are experimentally investigated at different depths in the previous sections. The soil water content at saturation is adapted based on the retention curves of the soils. The shrinkage limit and the soil void ratio at saturation could be determined by a shrink-swell test. The dry density of the soil could be calculated using existing physical parameters. Same comments could be made for the calculation of the shrinkage limit. In this case SL was calculated using the proposed Eq. (2.40) and was measured for the second and third points based on a shrink-swell test.

Figure 3.15 shows the shrink swell curve of the three studied samples in the water content and void ratio plan [w, e] at 3 different depths. As a measure of volume change, the soil's void ratio is plotted against water content. On the drying curve, the soil first follows the saturation line (expressed by $e = (\gamma_s/\gamma_w)\ w$). Following the continuous decrease of the soil water content, the void ratio tends towards a constant value. As shown in the figure, the shrinkage limits are defined and indicated on the curve as the intersection between the saturation line and the horizontal asymptote of the curve when the water content tends to zero.

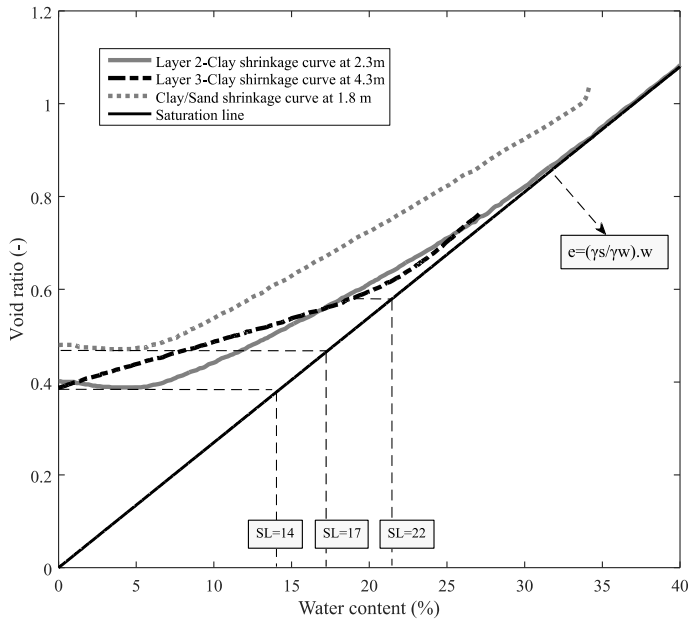

Figure 3.15 - Shrink-Swell curve [w,e] of three soil samples collected from the Roaillan experimental site.

3.3.3 Climatic parameters

The meteorological data of the experimental site are presented in Figure 3.16 and was collected from the MERRA dataset tool (Gelaro et al. 2017) which is less than 50 Km away from the site. The considered period starts from September 2011 and continues until late 2017. These climatic parameters are used to construct the time variable atmospheric boundary conditions of the site which will be discussed in following sections. Figure 3.16 a) shows the amount of rainfall during the adapted period. It can be seen that daily rainfall achieves maximum values of about 30 and 40 mm/day until late 2016 but it reaches more than 60 mm/day in late 2017. Air temperature variations follow almost a sinusoidal path during the considered period as shown in Figure 3.16 b). The same comment could be made for the relative humidity variations. Wind speed is measured at 10m above the surface (Figure 3.16 d)) which is corrected and brought to 2m above the ground surface for the calculation of the evapotranspiration rate using Eq. (2.10). Finally, the global solar radiation data follows also a sinusoidal path with a maximum value of 320 (W/m^2) during the considered period (Figure 3.16 e)). These climatic parameters lead to the calculation of the reference evapotranspiration.

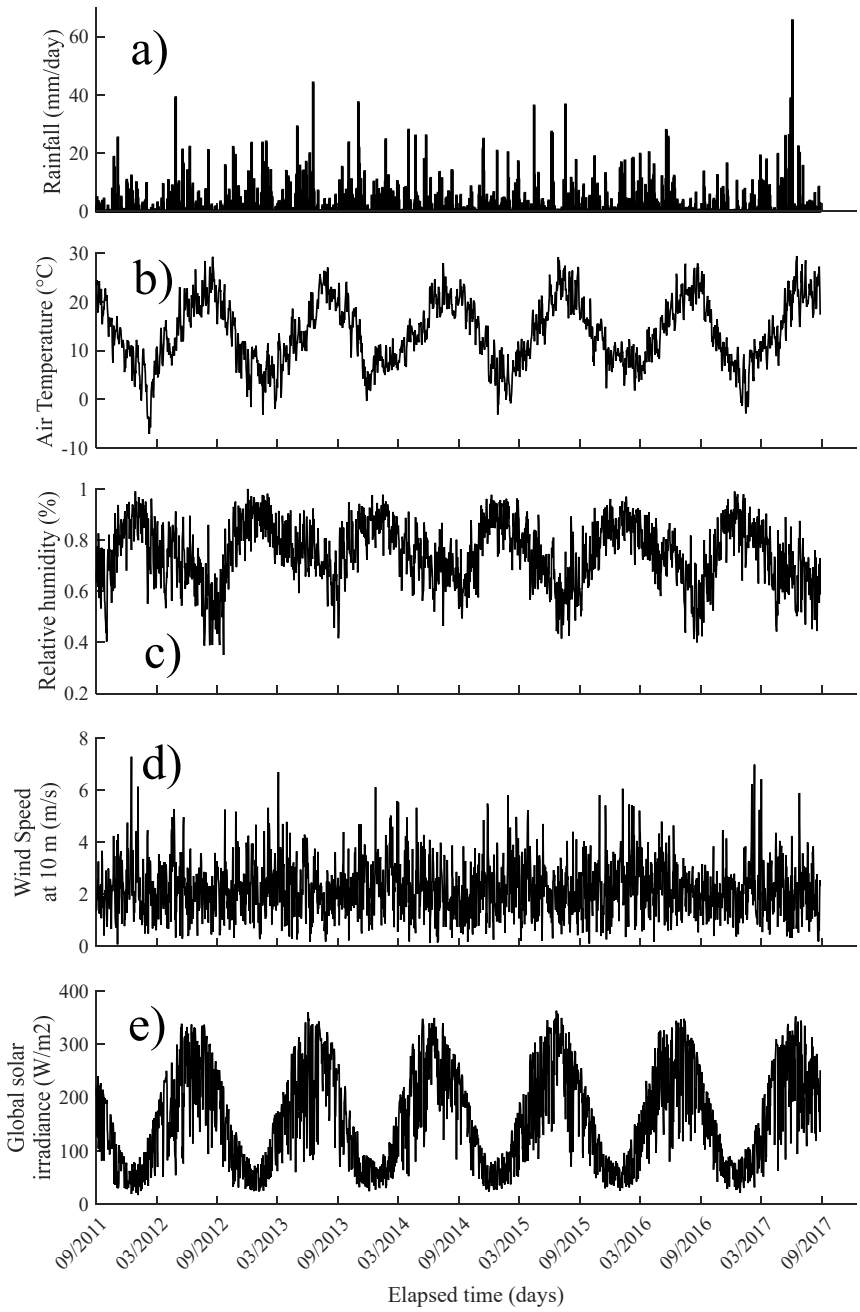

Figure 3.16 - Climatic parameters of the Roaillan experimental site: a) Rainfall (mm/day) b) Air temperature (°C) c) Relative humidity (-) d) Wind speed at 10 m height (m/s) e) Global solar radiation (W/m2)

3.3.4 Vegetation parameters

3.3.4.1 Crop coefficient of the site

In order to differentiate between the amount of plant transpiration and the potential soil evaporation, vegetation parameters should be adapted. These parameters will allow the determination of time variable atmospheric boundary conditions. For partitioning $\mathbf{ET_0}$, the crop coefficient should be first determined. Thus, the suggested method by FAO 56 (Allen et al. 1998) is used by considering a single type crop coefficient. Figure 3.17 shows the variations of the crop coefficient (pasture grass and oak tree) for a typical period of the year which also shows the

different stages of the crop development. It should be mentioned that a single crop coefficient was adapted to this experimental site considering both the grass and the tree. An initial Kc_{ini} value of 0.6 was chosen based on the suggestions available in Allen et al. (1998). The mid-season coefficient Kc_{mid} and the late season coefficient Kc_{late} are calculated by numerical approximations based on the climatic data at that specific time (Allen et al. 1998). The length of the crop development stage is also suggested in the FAO 56 guide. A yearly distribution of the crop coefficient is adapted for this specific site due to the fact that the trees play a more important role on the vegetation parameters (25 days for initial stage, 40 days for the development stage, 240 days for the mid-season stage and 60 days for the late season stage).

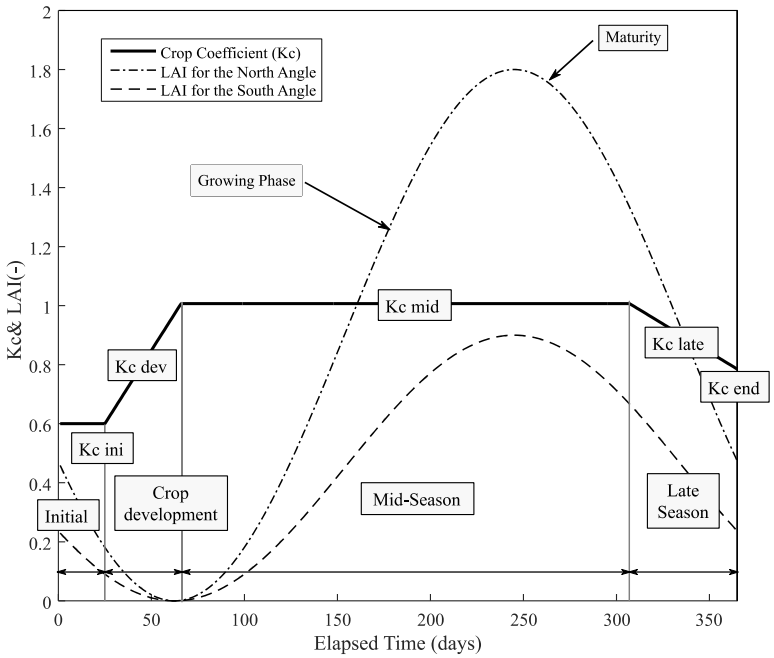

Figure 3.17 - Vegetation parameters of the experimental site.

3.3.4.2 Leaf Area Index of the site

The Leaf Area Index is generally measured directly on site. However, there is no direct measurements of LAI for this specific site. Thus, a sinusoidal function was adapted to the LAI variations in time (a year) for each angle of the building which reaches a maximum value of 1.8 and 0.9 for the north and the south angle respectively and a minimum value of zero for both angles (Figure 3.17). These limits are determined based on the suggestion in Asner et al. (2003) for a pasture grass and oak tree type vegetation. It should be mentioned that the reason for taking a different LAI index for each angle of the building is because the grass cover on the south angle appear to be very poor compared to the grass on the north angle. In addition to the grass cover, the size of the trees in the two angles are different. The tree in the north side has a diameter almost two times greater than the tree in the south angle. The crop coefficient and the LAI index are calculated from 2011 to 2017 period in which the LAI index is the same for each considered season however, the crop coefficient could vary due to the different climatic parameters during this period.

3.3.5 Boundary condition and FE Mesh geometry

The main boundary conditions of the model are the infiltration rate (P-ET_0), the potential transpiration (T_{pot}), the potential evaporation (E_{pot}) and the soil surface temperature (T_s). Figure 3.18 a) shows the calculated reference evapotranspiration based on the climatic parameters of the site. The potential crop evapotranspiration is shown in Figure 3.18 b) which is calculated by applying the crop coefficient.

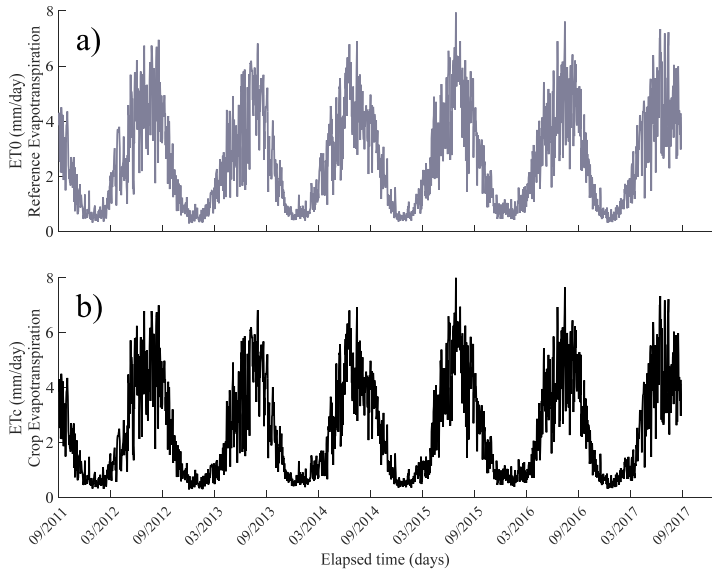

Figure 3.18 - Calculated evapotranspiration of the experimental site: a) Reference evapotranspiration (ET0) b) Crop evapotranspiration (ETc)

The partitioning of the potential transpiration and the potential soil evaporation for the north and the south angle of the building is shown in Figure 3.19 a) and b) respectively. It can be observed that the rate of transpiration in the north angle of the building is higher than the rate of transpiration in the south angle due to the difference between the LAI indexes. On the other hand, the soil evaporation in the south angle is greater than the north angle due to the fact that most of the evapotranspiration rate is taken by the potential transpiration in the north angle.

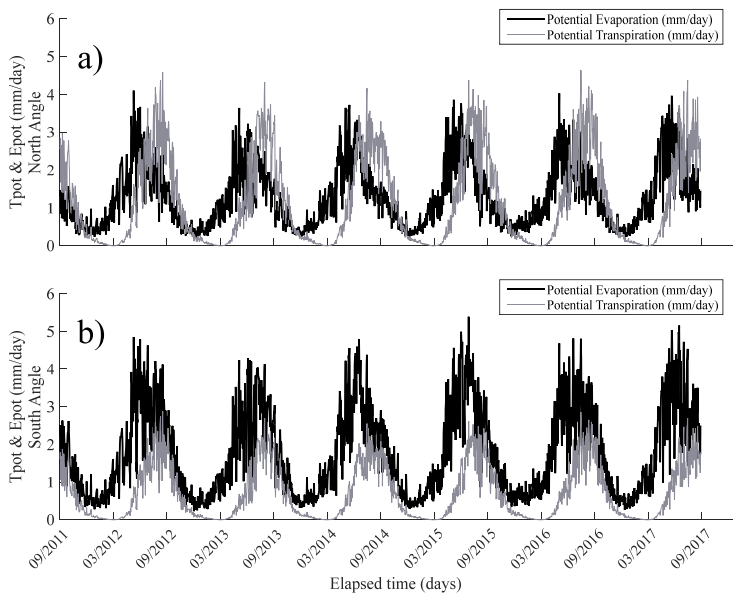

Figure 3.19 - Partitioning of the evapotranspiration rate into potential transpiration (Tpot) and potential evaporation (Epot): a) For the north angle b) For the south angle

The infiltration rate and the soil surface temperature are also determined (Figure 3.20) using the amount of precipitation and the reference evapotranspiration based on the simplified mass balance and thermal based energy balance approach described in previous sections.

The determined boundary conditions of the simulation can now be applied as atmospheric time variable boundary to the surface of the soil as shown in the Finite Element mesh geometry in Figure 3.21 a) and b) for the north and the south angle of the building respectively. Additionally, a free drainage type boundary condition is applied to the bottom of the geometry and closed flux conditions on the side and on the upper boundaries of the footing and the terrace (for the south angle).

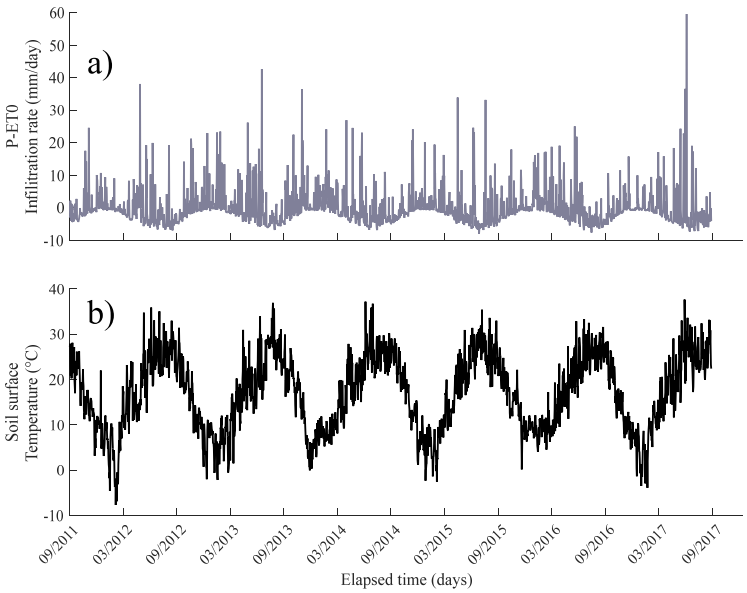

Figure 3.20 - Calculated time variable boundary condition of the experimental site for the hydro-thermal simulation: a) Infiltration rate (P-ET0) b) Soil surface temperature

The mesh of the north angle geometry is composed of 1795 triangular elements with varying mesh sizes. There are 970 nodes in this mesh. A refinement of the mesh was carried out close to the foundation of the building and at the soil surface were the atmospheric conditions are applied.

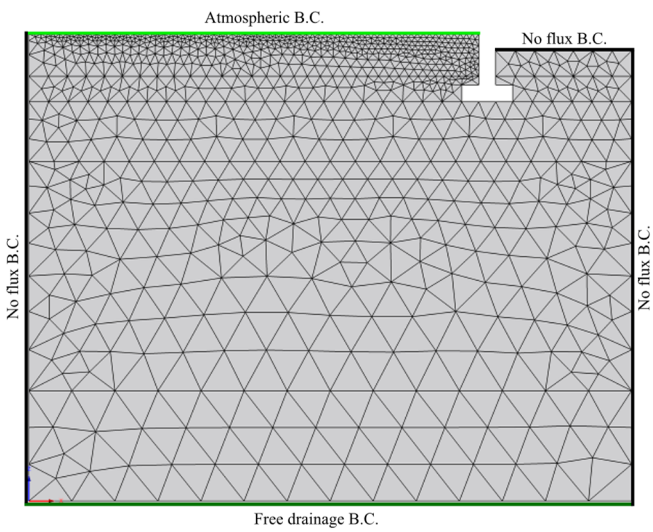

Figure 3.21 - The adapted geometry and triangular meshing of the north angle geological formation of the site along with the applied boundary conditions

Figure 3.22 shows the meshed geometry of the south angle of the building. The mesh is composed of 2045 triangular elements with varying mesh sizes. There are 1095 nodes in this mesh. The mesh refinement was carried out where the atmospheric boundary condition was applied.

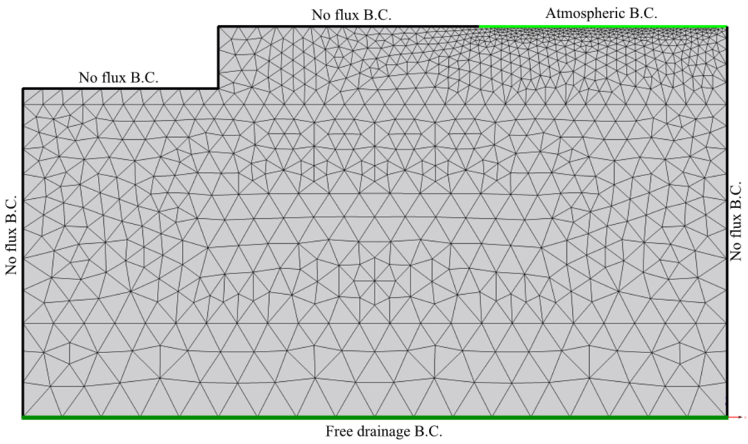

Figure 3.22 - The adapted geometry and triangular meshing of the south angle geological formation of the site along with the boundary conditions.

3.3.6 Initial Conditions

The initial conditions of the model are set based on the measured water content, soil suction and soil temperature at different depth. Figure 3.23 a) and b) shows the initial water content and temperature distribution in the north angle of the building. The water content distribution is based on the water content measurements close to the surface and takes the following form. However, a linear distribution of the soil temperature is adapted for initial temperature conditions starting from 25 °C at the top and finishing at 13 °C at the bottom. This distribution in the soil profile is in coherence with the first observed value of the temperature sensor in 09/2011, which shows a value of 20 °C at 1.5m depth. Figure 3.23 c) and d) shows the adapted initial water content and temperature in the south angle of the building, respectively. It can be observed that the water content distribution was adapted based on the first measurements by H1, H2 and H7 at three different parts of the profile (close to the tree, close to the building and under the foundation). On the other hand, a linear distribution was applied for initial temperature profile. The same conditions as the north angle profile (25 °C at the top and 13 °C at the bottom) are applied in this case as there is no measurements of temperature changes in 09/2011 in the south angle.

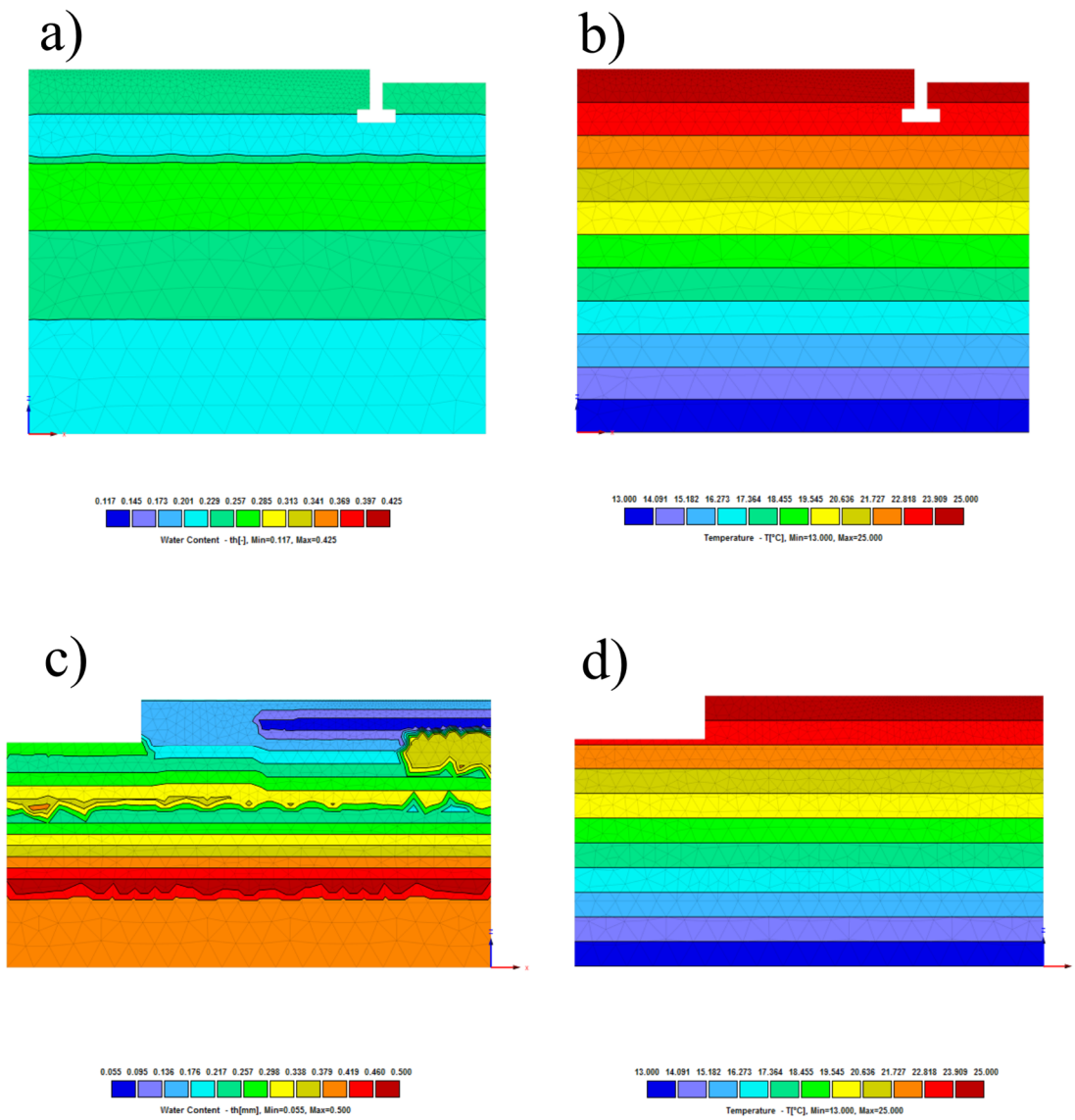

Figure 3.23 - Initial condition plots of water content and temperature: a) and b) at the north angle respectively c) and d) at the south angle respectively.

In addition to water content and temperature initial conditions, the vegetation parameters or the initial root distribution pattern should be applied to the geometry. Figure 3.24 a) shows the root water uptake distribution in the geological formation at the north angle of the building. It should be mentioned that this manual root distribution was adapted based on the soil suction measurements in the north angle profile which revealed approximately the following form for the root distribution into the soil. One part of the roots is distributed in the first 1m depth and the other part is mostly distributed between 2 and 3m depth. On the other hand, since there are no suction measurements in the south angle of the building a typical root distribution pattern was applied into the soil as shown in Figure 3.24 b). The rooting depth and length are both fixed to 3.5m into the soil.

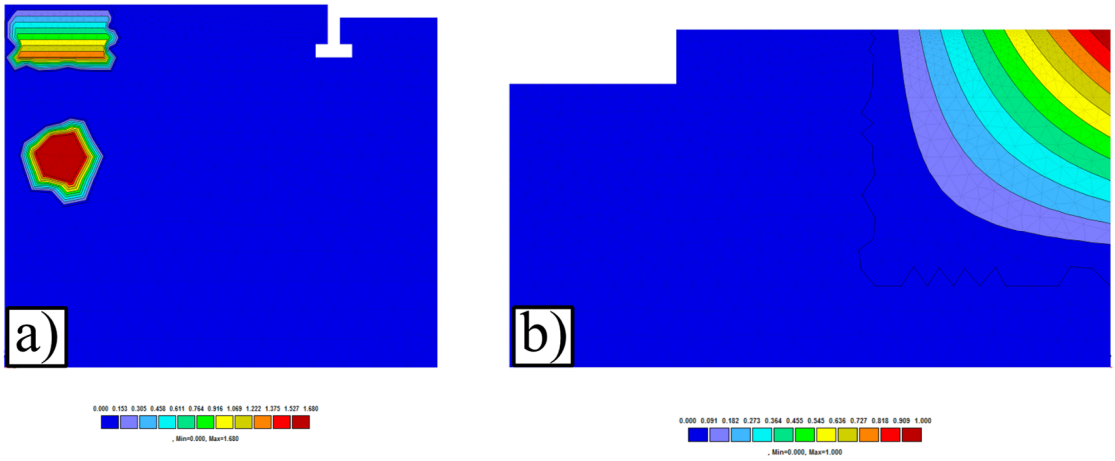

Figure 3.24 - Initial root distribution pattern at: a) the north angle and b) the south angle

3.4 Comparison and Validation with field measurements

3.4.1 North angle measurements

3.4.1.1 Comparison of the simulated suction with field data

This section presents the obtained results of the simulation and the comparison to the field measurements for validating the discussed approach. 32 observation points were assigned in the simulation of the north angle at the exact same position of the probes.

Figure 3.25 shows the results of the comparison of the simulated soil suction close to the tree. It can be observed that the simulations are generally in coherence with the observations. Figure 3.25 a), b) and c) which corresponds to the same position of the sensors TR1, TR2 and TR3 (0.8m depth), shows higher suction values compared to the other plots close to the tree side. Sudden peak values are observed both in the simulation and the measurements which correspond to the root water uptake effect. Two probes at 1.5m (TR5 and TR4) show almost a saturated state with maximum generated suction of 20 kPa, however the simulation suggests slightly higher suction values (Figure 3.25 d)). This could be related to the fact that the considered retention properties for the layer do not represent the real retention properties of the soil. It should also be mentioned that the overestimation of the peak values of suction is because the maximum recording capacity of the soil suction by the sensors are limited to 250 kPa. This can be observed in Figure 3.25 a), b) and c) where the maximum suction value reaches 250 kPa however the exact value could potentially be greater than 250 kPa.

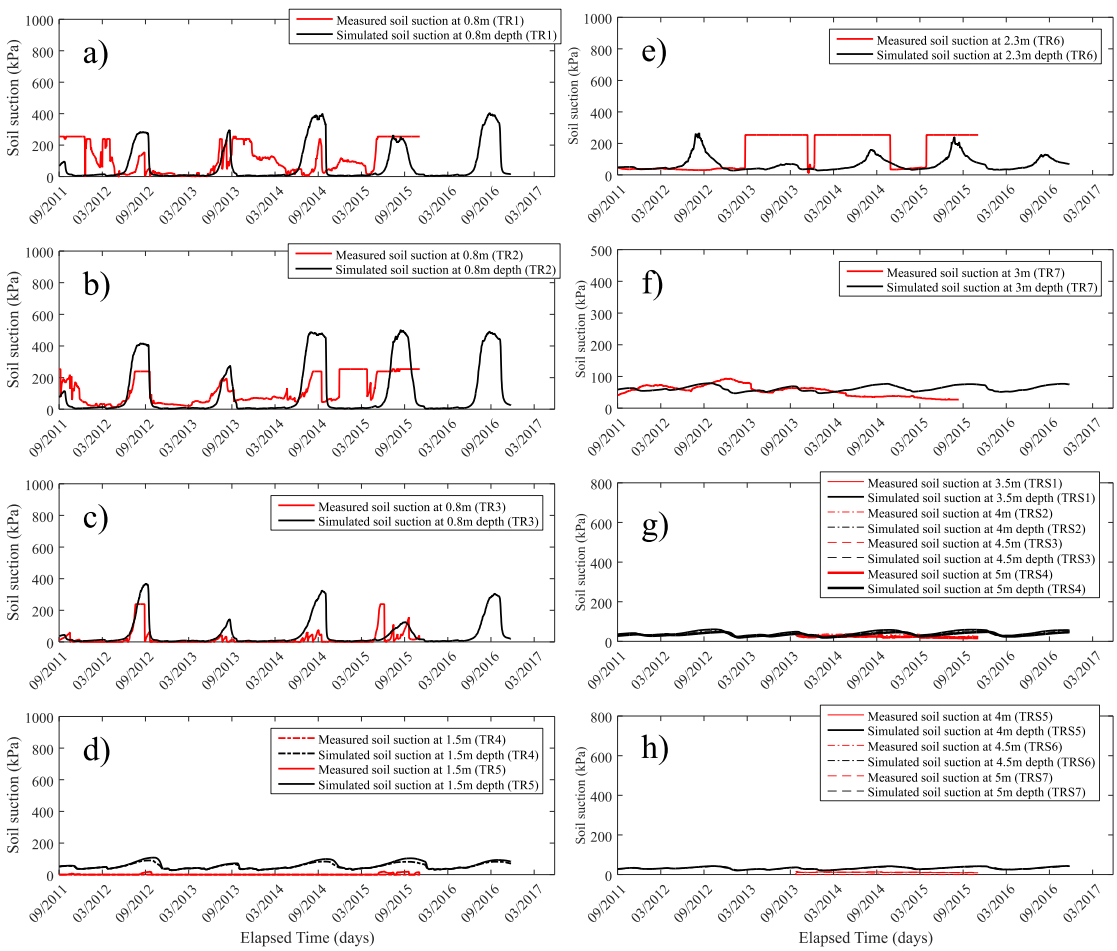

Figure 3.25 - Comparison of the measured and the simulated soil suction in the north angle of the building - close to the tree (TR1 to TR7)

The simulated suction at 2.3m (TR6) in Figure 3.25 e) is in coherence with the observations until 04/2012. From this date on, the peak value determined by the simulation is not observed in the measurements. However, the following two peaks starting at 01/2014 are in an acceptable coherence with measurements where there is a sudden change in the suction value that reaches 250 kPa. Figure 3.25 f) shows that there is a great coherence between the measured and the simulated soil suction at 3m depth. The same discussion could be made for the additional probes (installed in late 2013). Figure 3.25 g) shows an acceptable comparison of the simulation with the observed results which shows values around 20 to 30 kPa during the monitoring period. Figure 3.25 h) shows the comparisons from 4m to 5m depth where suction values are lower than the latest plots and are comparable to the simulation.

On the other hand, Figure 3.26 shows the results of the comparison between the simulation and the measurements close to the building side in the north angle. Figure 3.26 a), b) and c) show the simulated and measured soil suction (BU1, BU2 and BU3) at 0.8m depth. It can be observed that the simulation does not match the measurements from 08/2013 to 09/2013 where a suction peak of 100 kPa is observed. This could be related to the fact that the arbitrary root distribution in the simulation does not represents the real root distribution in the field. However, the other two plots (Figure 3.26 b) and c)) shows good agreement with the measurements, mostly when the peak values are observed. The last plot in Figure 3.26 indicates a complete saturated state

at 1.5m based on the measurements carried out by BU4 and BU5 probes. The simulation results at 1.5m depth does not show a complete saturated state but the variation ranges are acceptable.

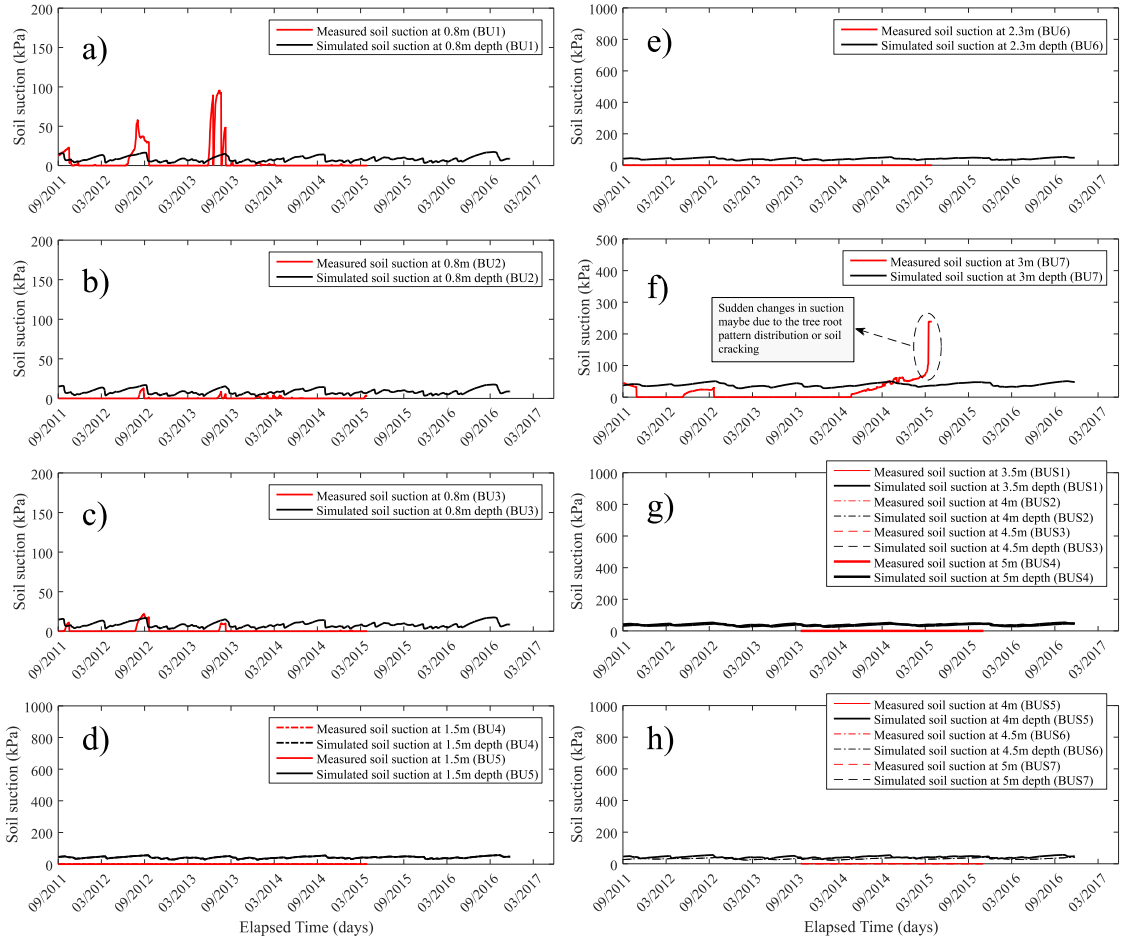

Figure 3.26 - Comparison of the measured and the simulated soil suction in the north angle of the building - close to the building (BU1 to BUS7)

Figure 3.26 e) also shows a complete saturated state based on the measurements data collected by BU6 probe installed at 2.3m depth. The simulation also shows very small suction variations close to zero at 2.3m depth. Figure 3.26 f) sows the results of the comparison at 3m depth in the same exact position of the BU7 probe. It can be observed that the simulation results are in coherence with the observation until 03/2015 where a suction peak is observed. This sudden change in suction could simply be because of soil cracking or root distribution pattern that changed over time and begin to generate suction at this time which could have not been known in the initial conditions of the simulation. Finally, Figure 3.26 g) and h) show the results of the additional probes installed in late 2013 from 3.5m to 5m depth. It can be observed that the simulation shows almost a saturated state as shown by the measurements. However, the they are comparable to the observations as they show low suction values.

3.4.1.2 Comparison of the simulated water content with field data

Figure 3.27 shows the results of the comparison between the soil volumetric water content measurements and simulations near the surface. Figure 3.27 a) shows the comparison of the volumetric water content close to the tree and Figure 3.27 b) shows the comparison of the

volumetric water content close to the building. It can be first noticed that the two plots show approximately the same values both for the simulation and the observations expect in some periods were the soil becomes saturated. This could be related to the fact that the chosen meteorological data from the nearest station does not exactly represent the actual mass balance at the soil surface. Also, the hydraulic properties in the first layer are estimated which is also another reason that shows the underestimation of the simulation. Generally, there is an acceptable agreement between the simulation and in situ field data during hot periods (lower water content).

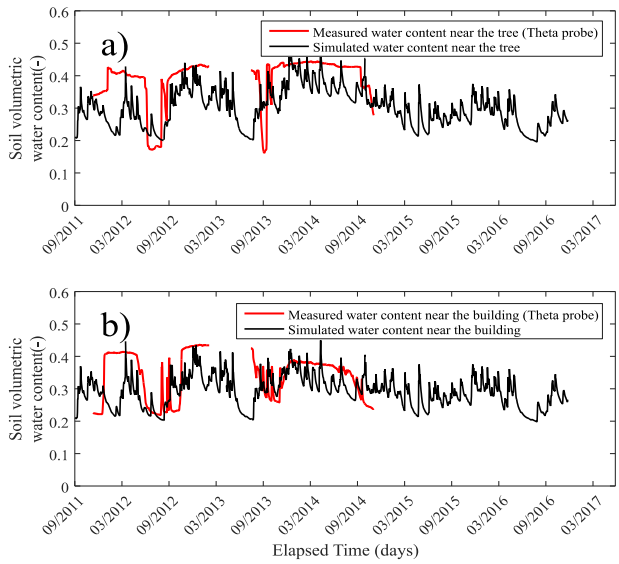

Figure 3.27 - Comparison of the simulated volumetric water content with field measurements at the north angle

3.4.1.3 Comparison of the simulated temperature with field data

Four temperature probes were installed on the site. Two of them close to the building (T2 and T4) and two others close to the tree (T1 and T3). Figure 3.28 a) shows the comparison at 1.5m depth close to the tree, it is observed that the simulated soil temperature values follow the measured temperature variations for the first year however, from early 2013 to early 2014, the coherence cannot be observed between simulation and measurements. Furthermore, the simulation result agrees well with the observations from 08/2014 to 10/2015. Generally, a sinusoidal variation is expected from the measurements which is not observed in none of these plots. This could be related to the fact that some additional probes installed in 2013 would have disturbed the probes and their measurements accuracy. Figure 3.28 b) shows the comparison at 1.5m close to the building. It can be seen that the measured temperatures are approximately the same as the measured temperatures in Figure 3.28 a) which confirms that the unusual temperature changes are not related to the root water uptake. However, there is still good agreement like Figure 3.28 a) in the first and last years of the monitoring period. Figure 3.28 c) shows the comparison at 4m depth close to the tree. It can be observed that measurements at 4m show higher temperature values compared to the measurements at 1.5m (T1) which should normally be lower. The simulation results do not match the measurements from 09/2013 to 09/2014. However, the results are more coherent with the measured temperatures from this date on. In Figure 3.28 d) the measured temperatures at 4m depth are smaller than the measured temperature at 1.5m which is normal, but the fluctuations during the period of 09/2013 and 09/2014 do

not match the simulation results however, the results are more coherent after 02/2015. It should also be mentioned that the error could be related to the fact that the soil thermal parameters were not directly measured on the site and were supposed as typical parameters for different soil types. Additionally, the model doesn't consider the flow in total gas phase. The flow is defined by Richards' equation which assumes that the total gas pressure is equal to the atmospheric pressure. Another reason could be the fact that the sensors begin to malfunction after installing additional ones in early 2013. Based on the comparison of the first-year results from 09/2011 to 09/2012 in Figure 3.28 a) and b) it can be justified that the error from the simulation is almost negligible. Considering the unusual changes after this time, the error could most certainly be related to sensors disturbance. This justifies that the simulation was performed correctly.

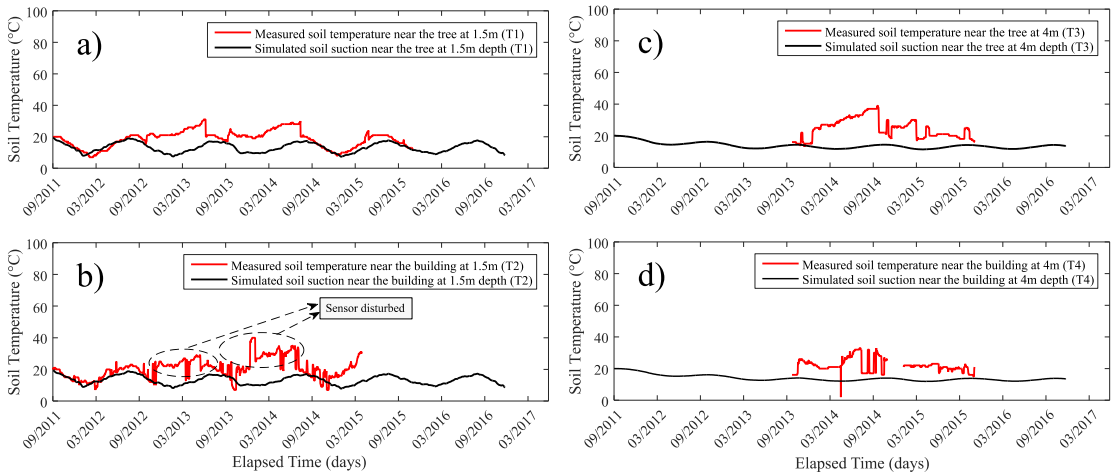

Figure 3.28 - Comparison of the simulated soil temperature with field measurements.

3.4.1.4 Comparison of the simulated water content and temperature profiles with H5 and H6 data

Profile variation of the soil water content and temperature in the north angle of the building are analyzed in this section. Based on the two TDR profiling probes H5 and H6, the water content and temperature profiles are plotted at different times. The water content measurements began in 10/2011 and temperature measurements began in 06/2013. Figure 3.29 a) shows the variation of the volumetric water content profiles at four different times measured by H5 profiling probe to a depth of 2.95m. Simulation results of the water content changes in depth show good agreement with the measurements. Based on the simulation results most of the changes in water content profile appears in the first 1.5m depth.

Temperature profiles also measured by H5 are presented in Figure 3.29 b). It can be observed that the temperature changes in depth are not very significant. However, the changes at each time are considerable. It is generally observed that the simulation results follow the measured path by the probe except in 04/09/2013 where the deviation from the measurements is approximately 4 °C. The difference in some results is due to the applied thermal parameters. However, there is generally an acceptable agreement with the measurements.

Figure 3.29 c) shows the profile variation of water content at different times measured by H6 profiling probe. It is observed that the there is an acceptable agreement between the simulation results and the measured water content in most cases. The comparison at 12/03/2012 is not

satisfying, because of the difference between simulated and measured water content. This could also be due to an error in the measurement process. On the other hand, it is also worth mentioning that the influence of the root water uptake by the tree could be seen in the plots between 0.8m and 1.5m depth where the water content drops to almost 10%. However, these water content drops are not observed at 12/03/2012 which indicates that the measured water content and temperature by H5 are nor influenced by root water uptake.

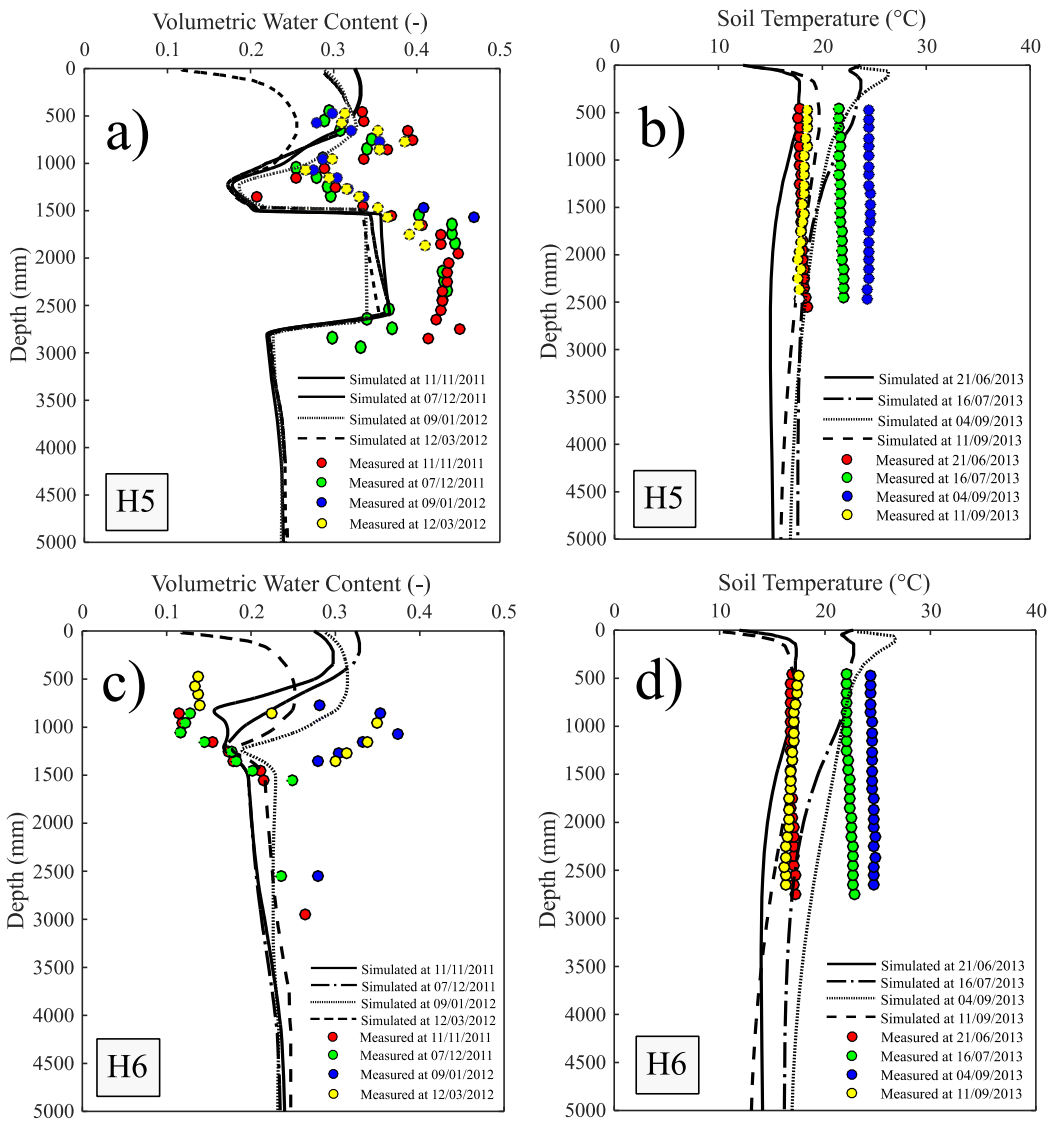

Figure 3.29 - Comparison of the simulated water content and temperature profiles with field measurements by H5 and H6 probe.

Temperature profiles presented in Figure 3.29 d) show also acceptable agreement between the measured temperature profiles by H6 and the simulation results at different times. The difference observed between the data and the simulation results in some cases are not significant and stays in the range of 3 °C. It should be mentioned that in most cases, the measured temperature profiles are almost constant in the profile which indicates that the surface temperature can directly affect temperature changes in depth and that the root water uptake does not influence significantly the changes in temperature.

3.4.1.5 Comparison of the simulated shrink-swell with field data

This section tends to validate the modelling approach of the shrinkage and swelling in time, described in previous sections. Figure 3.30 shows the comparison between the simulated and the measured soil movements at three different depth (1, 2 and 3m) by the extensometer installed in the north angle of the building. The simulation was carried out using the parameters listed in Table 3.3 and the initial condition of the simulation was fixed to 09/2011 even though the measurements of the soil movements started at 02/2014. It can be generally observed that there is an acceptable agreement between the simulation results and the data. Figure 3.30 a) shows the variations of the soil movements in time at 1m depth. Based on the data, the maximum range of soil movement is about 0.5 mm and tends to swell during the monitoring period, which is also confirmed by the simulation results. Figure 3.30 b) shows the soil movements at 2m depth. It can be observed that the range of the movements are slightly smaller than the movements in 1m depth. The simulation results are in good coherence with the data and the movements seem to stabilize at the end of the monitoring period. Same comments could be made for the soil movements at 3m depth (Figure 3.30 c)). It can be observed that the movements range are slightly smaller than the movements at 1m depth and the movements tends to stabilize at the end of the monitoring period. This could be related to the fact that in cold periods, the changes in soil suction are not significant enough to trigger a considerable soil movement. However, most of the soil movements are observed during warm periods of the year and when there is a quick transition between warm and cold periods (rainfall and evapotranspiration).

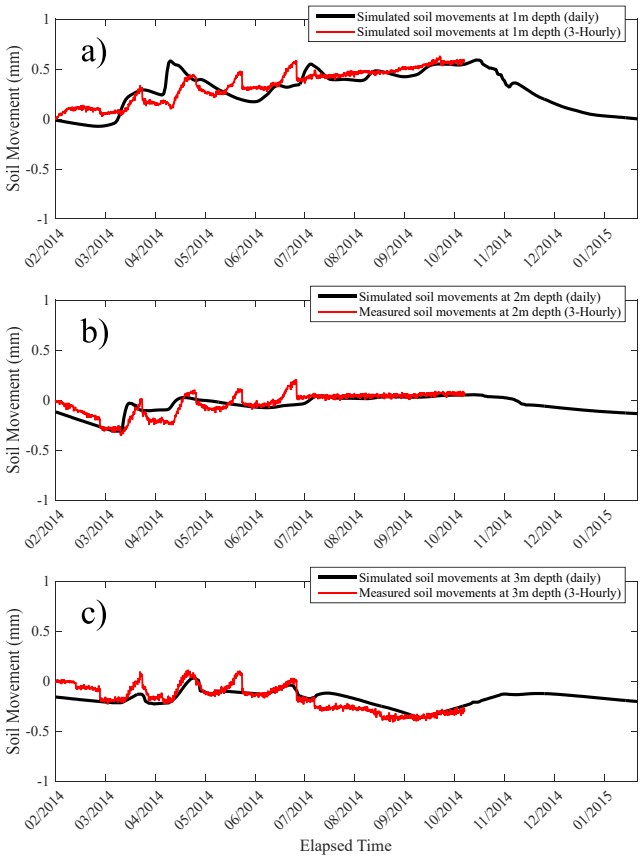

Figure 3.30 - Comparison of the simulated soil movements with field measurements, a) 1m; b) at 2m; c) at 3m depth.

3.4.2 South angle measurements

3.4.2.1 Comparison of the simulated water content with field data

Figure 3.31 a), b) and c) shows the comparison of the measured and the simulated soil water contents at 3 different depths in the south angle close to the tree. It can be noticed that the simulated water contents match reasonably well the in-situ observations. Some errors are observed at 2 and 3m depth in late 2014. However, a general agreement is observed during drought and humidification cycles and mostly close to the surface. It can be drawn from these measurements that the tree's roots are not able to influence the volumetric water contents at these specific points which could possibly be due to root distribution pattern.

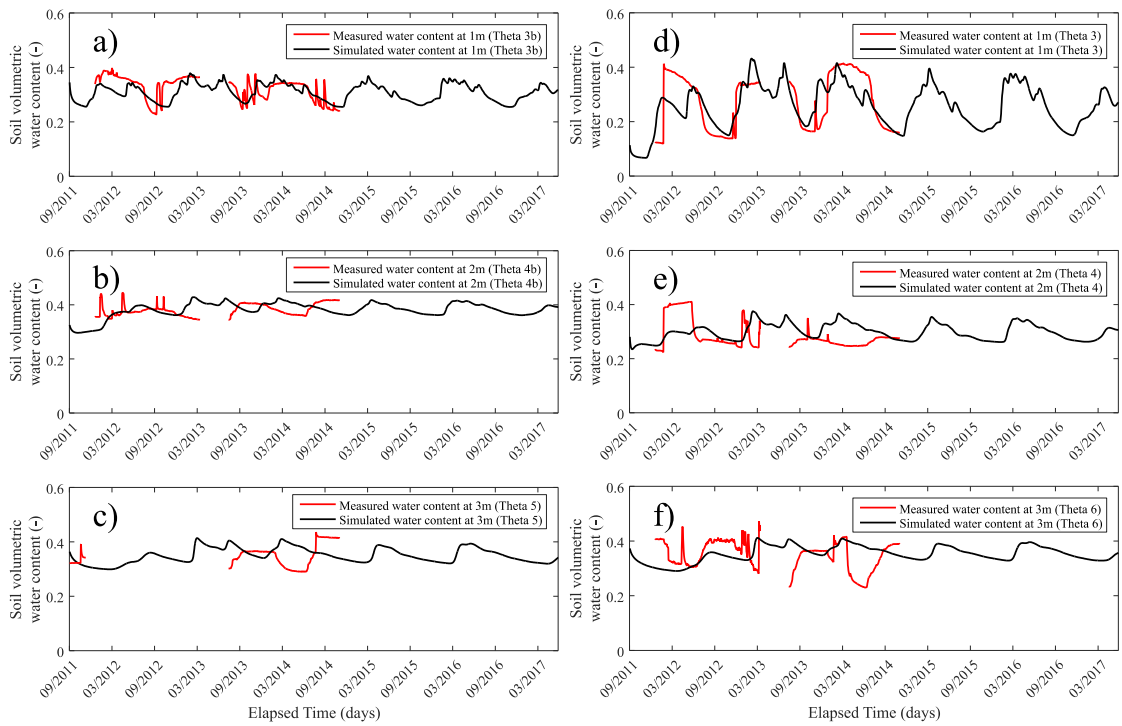

Figure 3.31 - Comparison of the measured and the simulated water content at 1, 2 and 3m depth in the south angle.

Figure 3.31 d), e) and f) shows the comparison of the measured and the simulated soil water contents at 3 different depths in the south angle close to the building. It can be observed that the simulation is generally in good agreement with the in-situ measurements. The observation of some errors at 2 and 3 m depth in late 2014 can be related to the fact that the retention properties of the corresponding layer does not exactly match the retention properties of that specific point due to heterogeneities in the soil medium. It should also be mentioned that there is no sign of sudden changes in soil water content in this monitored area, which points out that the measurements are not influenced by the presence of the tree.

3.4.2.2 Comparison of the simulated water content and temperature profiles with H1, H2 and H7 data

Figure 3.32 a) shows the comparison between the simulated and the measured water content by H1 profiling probe at four different times starting from 09/2011. As shown in the 2D cross section of the south angle, the H1 probe is installed close to the tree. It can be seen in most cases

that the water content drops close to 10% in the first meters showing a dry state of the soil. It can be observed that the measurements are in good agreement with the simulation results and follow almost correctly the changes in water content.

Figure 3.32 b) shows the comparison of the simulation results and the temperature measurements by H1 profiling probe. It can be seen that there is a good and acceptable agreement between the simulation and the carried-out measurements. However, the changes in temperature profiles stay constant in the first 2m depth according to the measurements but there is a slight temperature gradient in the simulation results which shows that temperature varies with depth. Additional measurements in deeper regions of the soil could confirm the simulation results and add more credit to its performance.

Figure 3.32 c) shows the comparison of the simulated and the measured volumetric water content close to the building by the H2 profiling probe. It can be observed quickly that there is a great coherence between the simulation results and the measured water contents in depth at these four different times. Changes in the water content at each layer are also in great coherence with the simulation results. It should be mentioned that most of the considerable changes of the water content appears in the first 1m depth of the soil profile. Water content changes deeper than 1m are not significant.

Same comment can be made for the temperature profiles. It can be observed in Figure 3.32 d) that the simulated soil temperatures and the measured soil temperatures by H2 profiling probe are in good agreement. The profiling of the temperature was carried out to a depth of 2.95m. In this case some changes in depth are observed both in the measurements and the simulation. This comparison confirms the capability of the model to predict soil temperature changes in space and time.

Figure 3.32 e) shows the comparison of the simulated water content and the measured one by the H7 profiling probe which is installed under the foundation of the building. It can be observed that there is generally good agreement between the data and the simulation results. It should also be mentioned that the water content profiles do not change significantly at different times. This is due to the fact that the climatic boundary condition is far away from the foundation soil, thus it does not influence the state of the water content into the soil profile.

This is also observed in the measured water contents which does not have a considerable change at each different time. It is also worth mentioning that the soil under the foundation is in an almost dry state (5% of water content) meaning that it is not influenced by climatic conditions or any other factor during the monitoring period.

Figure 3.32 f) shows the simulated and the measured temperature profiles by the H7 temperature profiling probe under the foundation of the building. It can be observed that there is generally a good agreement between the data and the simulation results. It should be mentioned that the changes in temperature profiles are eventually more considerable than the changes of the water content profiles. It is observed that the temperature profiles changes at different times. However, the variation in depth is almost constant which is also confirmed by the measurements.

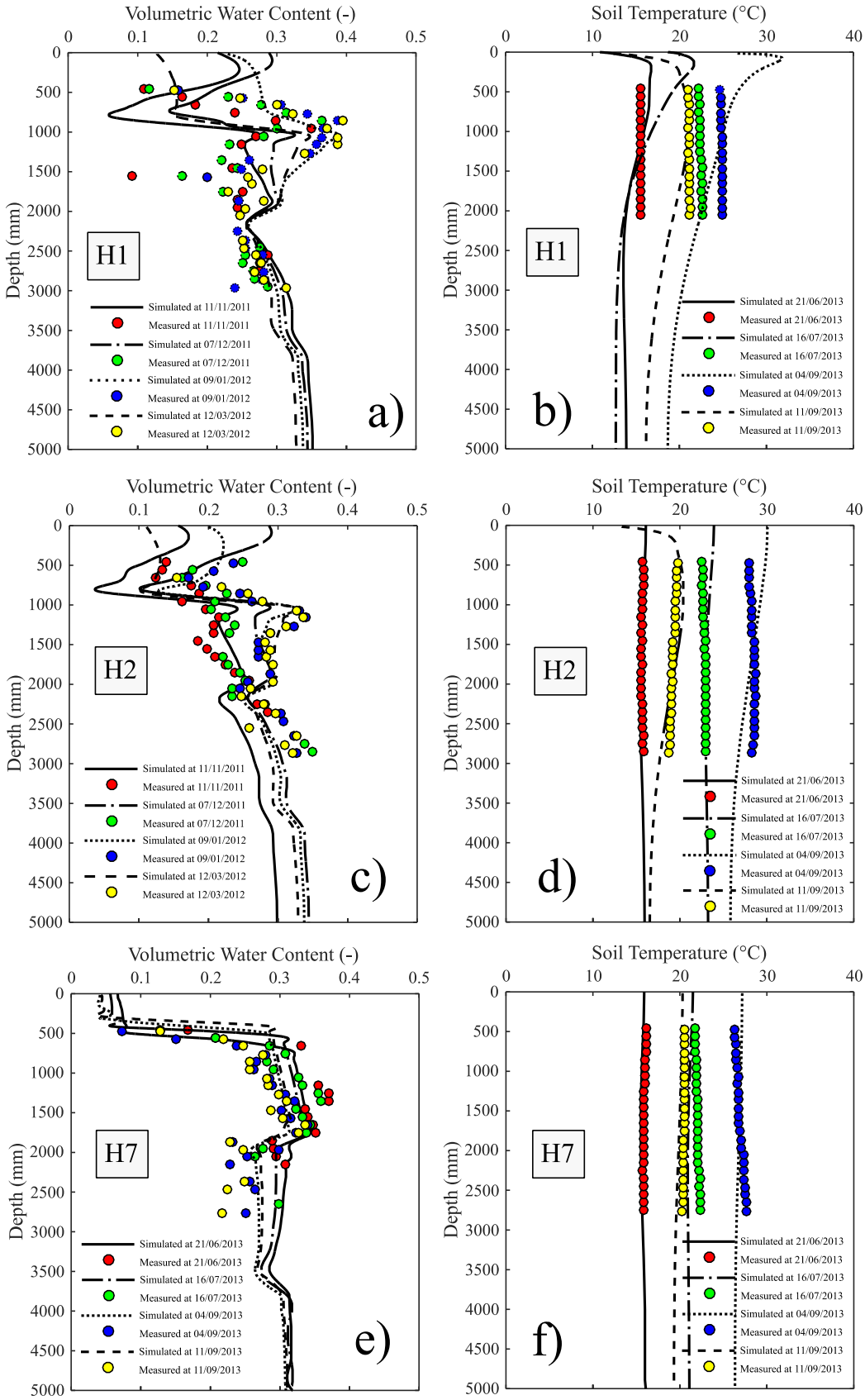

Figure 3.32 - Comparison of the simulated water content profiles with field measurements by H1 probe close to the tree.

3.5 Conclusion

In this chapter the proposed approach was compared to filed measurements in an experimental building in the south west of France which was mainly influenced by tree root water uptake and climatic conditions. The SVA interaction method showed an acceptable accuracy to simulate the soil water content, temperature and suction. Both profile variations and time series showed great coherence with the measured variables at the site. Using the proposed shrink-swell approach, the variations of the soil movements in time were deduced at different depth and were compared to field measurements which showed acceptable coherence.

Chapter 4. Further investigations on soil movements

4.1 Differential movements at Roaillan experimental site

Following the validation of the modelling approach, the model was extended to study the influence of environmental interactions in order to evaluate the soil movements at each angle and consequently the differential movements. Short term and long-term predictions of soil movements were carried out based on the projected climatic parameters of three different climate change scenarios.

4.1.1 Loading conditions at each angle

In order to evaluate the soil movements both close to the building and the trees, a number of test points were chosen at different depths. Some test points were specified right under the foundation of the building at both angles (Figure 3.8 and Figure 3.9) thus the influence of the loading conditions must be taken into account. The fundamental equation for the vertical stress increase at a point in a soil mass as the result of a line load can be used to determine the vertical stress at a point caused by a flexible strip load of width B. The calculation method and associated equations are provided in Appendix 4.

Figure 4.1 presents the detailed map of the building with the considered spans in red for the calculation of the applied load on the foundations at each angle. A detailed cross section is also presented in Figure 4.2 which shows the characteristics and the detailed geometry of different structural elements. From now on, the calculation of the applied loads is based on these indicated material type.

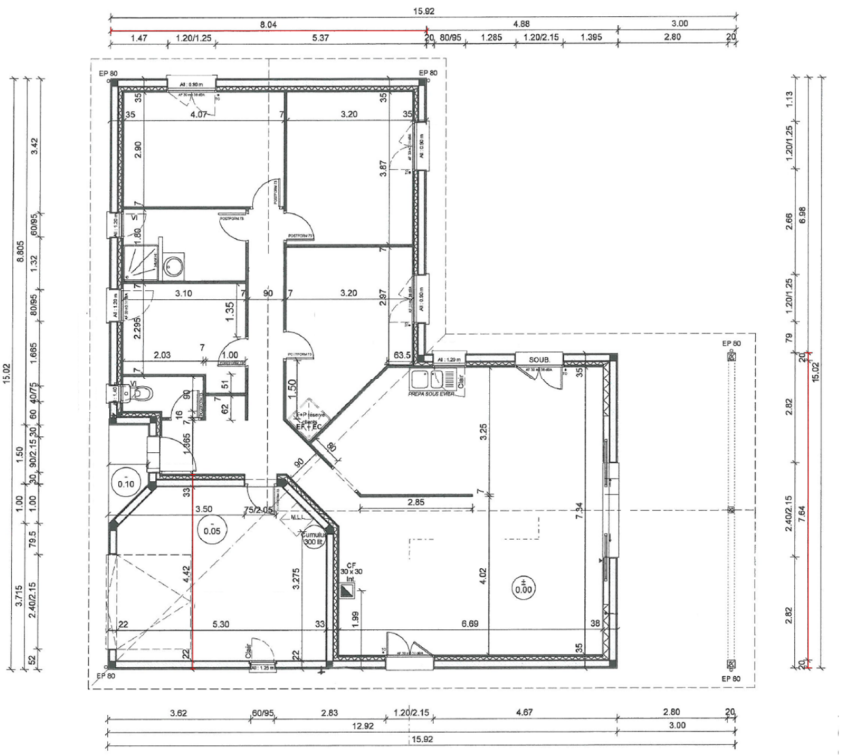

Figure 4.1 - Detailed floor plan of the building

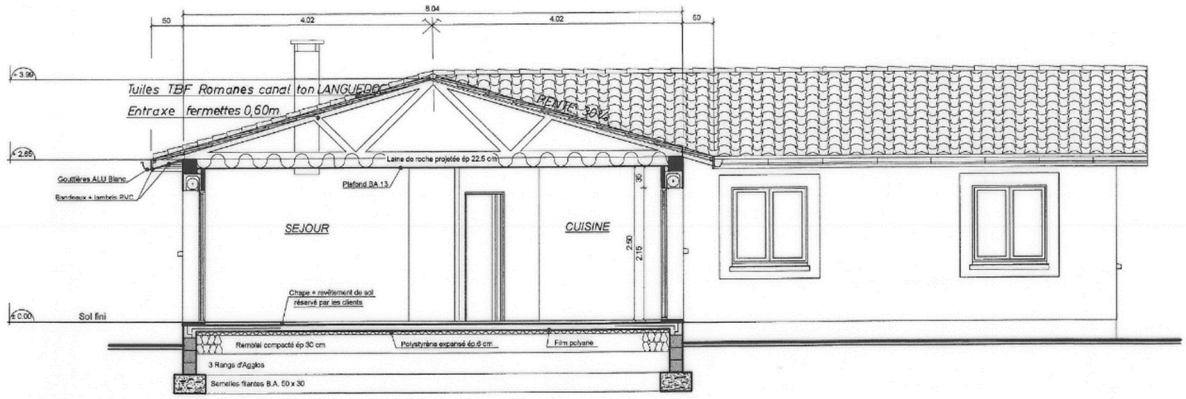

Figure 4.2 - Cross section at the right side of the plan

In this section, the applied loads on the strip footing of the building on the north and the south angle are determined. Figure 4.3 and Figure 4.4 shows the north and south side elevation of the building respectively (front side). Each structural element's load is calculated primarily by the associated unit weight or density if needed. The following procedure was adapted for the determination of the applied load on the foundation soil. It should be mentioned that the live loads applied by snow and wind are neglected in this study. The total serviceability limit state load (SLS) can be calculated using the simple load combination as shown in Table 4.1. The applied load per unit area at the base of the foundation of the building is calculated by dividing the linearly distributed load by the length of the foundation (B).

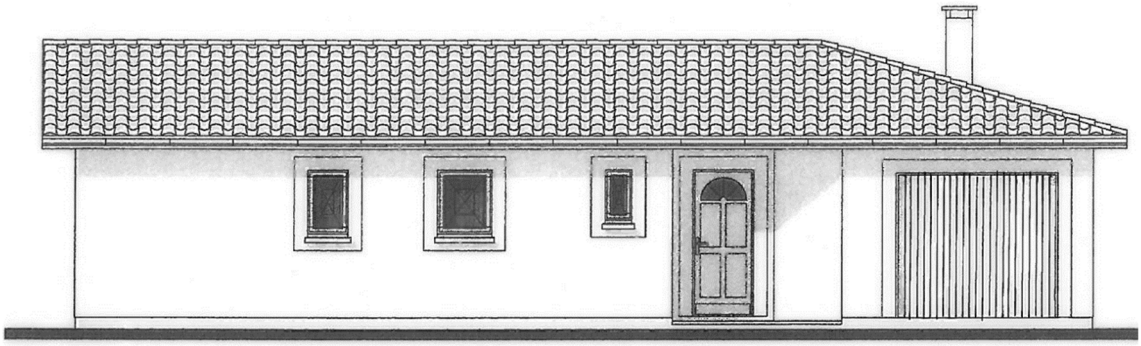

Figure 4.3 - North side elevation of the building

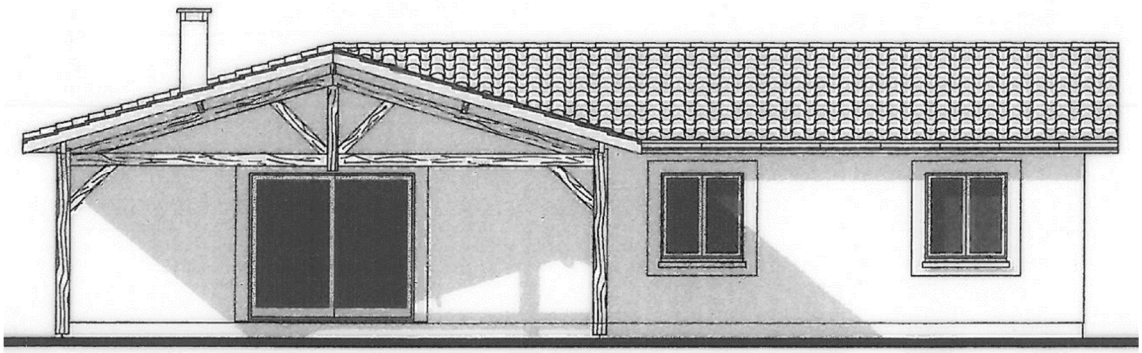

Figure 4.4 - South side elevation of the building

Table 4.1 - Loading actions on each angle of the building

Dead load calculation ($\boldsymbol{D_L}$)	**North angle**	**South angle**
Roof load:	$150\ \left(\frac{kg}{m^2}\right) \times 8.04\ (m) = 1206\frac{kg}{ml}$	$150\ \left(\frac{kg}{m^2}\right) \times \frac{7.64}{2\ Sin\ 30°}\ (m) = 1146\frac{kg}{ml}$
Wall load:	$1450\ \left(\frac{kg}{m^3}\right) \times 0.2\ (m) \times 2.5\ (m) = 725\frac{kg}{ml}$	$1450\ \left(\frac{kg}{m^3}\right) \times 0.2\ (m) \times 2.5\ (m) = 725\frac{kg}{ml}$
Isolation load:	$10\ \left(\frac{kg}{m^2}\right) \times 2.5\ (m) = 25\frac{kg}{ml}$	$10\ \left(\frac{kg}{m^2}\right) \times 2.5\ (m) = 25\frac{kg}{ml}$
Floor load:	$350\ \left(\frac{kg}{m^2}\right) \times \frac{4.64}{2}(m) = 812\frac{kg}{ml}$	$350\ \left(\frac{kg}{m^2}\right) \times \frac{7.64}{2}(m) = 1337\frac{kg}{ml}$
Cover, siding, bulkhead load:	$100\ \left(\frac{kg}{m^2}\right) \times \frac{4.64}{2}(m) = 232\frac{kg}{ml}$	$150\ \left(\frac{kg}{m^2}\right) \times \frac{7.64}{2}(m) = 573\frac{kg}{ml}$
Substructure wall load:	$1800\ \left(\frac{kg}{m^3}\right) \times 0.2\ (m) \times 0.6\ (m) = 216\frac{kg}{ml}$	$1800\ \left(\frac{kg}{m^3}\right) \times 0.2\ (m) \times 0.6\ (m) = 216\frac{kg}{ml}$
Foundation load:	$2500\ \left(\frac{kg}{m^3}\right) \times 0.5\ (m) \times 0.3\ (m) = 375\frac{kg}{ml}$	$2500\ \left(\frac{kg}{m^3}\right) \times 0.5\ (m) \times 0.3\ (m) = 375\frac{kg}{ml}$
Total dead Load=$\sum \boldsymbol{D_L}$	$3591\frac{kg}{ml}$	$4397\frac{kg}{ml}$
Live load calculations ($\boldsymbol{L_L}$)	$250\ \left(\frac{kg}{m^2}\right) \times \frac{4.64}{2}\ (m) = 557.5\frac{kg}{ml}\ \ (L_L)$	$150\ \left(\frac{kg}{m^2}\right) \times \frac{7.64}{2}\ (m) = 573\frac{kg}{ml}$
Serviceability limit state load: $\boldsymbol{Q_{SLS} = D_L + L_L}$	$4148.5\ \frac{kg}{ml}$	$4970\ \frac{kg}{ml}$
Applied load per unit area: $\boldsymbol{q = \frac{Q_{SLS}}{B}}$	$\frac{4148.5}{0.5} = 81.36\ kPa$	$\frac{4970}{0.5} = 97.47\ kPa$

4.1.2 Soil movements at each angle

Following the determination of the applied loads on the foundation soil of the two angles of the building, the loading conditions at each considered test point (from 1 to 5m depth) under the foundation can now be determined. Table 4.2 summarizes the soil shrink-swell parameters at the north angle of the building. Since the test points close to the tree (1b to 5b) are considered not to be influenced by the building's load, a zero stress was applied. It should also be mentioned that the Atterberg's limits were attributed to each point, based on the core sampling results and the volumetric indices were calculated afterwards.

Table 4.2 - Shrink-Swell parameters at the north angle of the building.

Test point	**z (m)**	**$\Delta\sigma_z$ (kPa)**	**PI (%)**	**LL (%)**	**SL (%)**	**w% Sat.**	**e_0**	**γ_d (Mg /m^3)**	**k_s**	**λ_s**	**S_{tr} (kPa)**	**S_{shrink} (kPa)**
1	1	71.67	36	71	27	46	0.95	1.38	-0.0284	-0.0434	112.55	548.43
2	1.7	27.39	43	70	14	33	0.89	1.42	-0.0305	-0.0394	134.96	4678.76
3	2.3	16.95	39	69	22	33	0.89	1.42	-0.0304	-0.0422	134.96	1070.1
4	3.75	8.73	36	65	22	25	0.6	1.68	-0.0316	-0.0317	439.4	1070.1
5	5	6.15	23	45	17	22	0.6	1.68	-0.0299	-0.0314	439.4	2482.6
1b	1	0	36	71	27	46	0.95	1.38	-0.0381	-0.0596	112.55	548.43
2b	1.7	0	43	70	18	33	0.89	1.42	-0.039	-0.0554	134.96	2060.07
3b	2.3	0	39	69	21	33	0.89	1.42	-0.0371	-0.0541	134.96	1245.57
4b	3.75	0	34	60	18	25	0.6	1.68	-0.0359	-0.0394	439.4	2060.07
5b	5	0	29	47	12	22	0.6	1.68	-0.0341	-0.0373	439.4	7738.3

Based on the number of considered test points in the analysis (10 test points), five different comparisons were carried out. The first comparison shows the variation of the soil physical parameters at test point 1 and 1b (1m depth). Figure 4.5 a) shows the comparison of the variation of the soil suction close to the building and the tree. It can be observed that there is

eventually a significant difference between these two values due to the root water uptake. Figure 4.5 b) shows the soil water content at these two points, a larger variation of the soil water content is observed at point 1b as expected were the soil is influenced by root water uptake. Figure 4.5 c) shows the comparison of the soil temperature at these two points. It can be observed that the range of variation of the temperature close to the tree is slightly larger to the soil temperature changes close to the building. This is eventually because of the changes of the thermal conductivity function due to the changes in water content (considered in the hydro-thermal soil model). However, the difference is smaller in comparison to the soil suction and water content. In Figure 4.5 d) the variation of the soil void ratio is presented. It can be observed that as the suction cycles are larger, the amount of total decrease of the soil volume is larger and consequently the void ratio is smaller. In this comparison, the variation of the void ratio close to the tree are greater than the changes close to the building due to the applied suction. Figure 4.5 e) shows the daily variation of the soil movements calculated using the proposed modelling approach. It can be easily observed that the speed of deformation is also greater close to tree due to the larger suction variations. Finally, Figure 4.5 f) shows the variation of the cumulative soil movements close to the tree and the building which indicates a maximum shrink-swell of 4mm close to tree and less than 1mm close to the building.

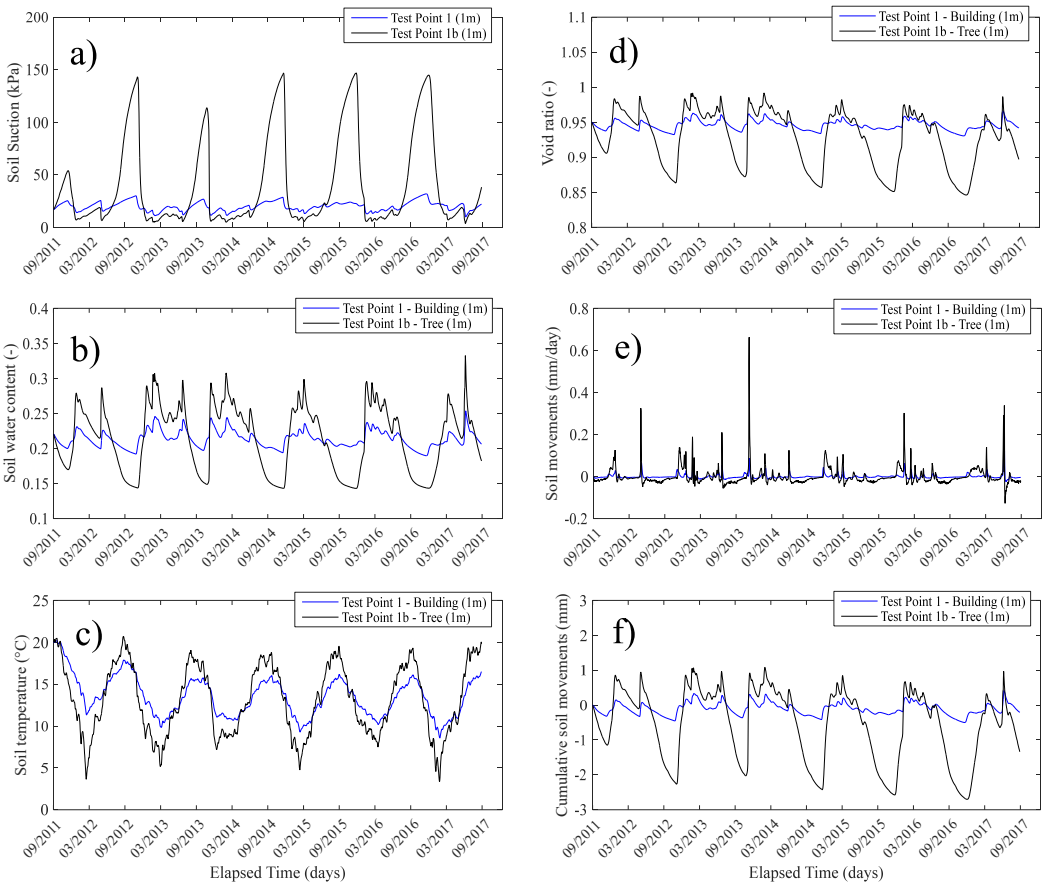

Figure 4.5 - Comparison of the soil physical variables close to the tree and the building at 1m depth (point 1 and 1b).

Same sets of comparisons are carried out at 1.7m depth in Figure 4.6 where suction values are smaller which means that the tree roots influence less the soil at 1.7m compared to 1m. As expected, larger water content and void ratio variations are observed close to the tree which lead

to larger cumulative soil movements. However, the variations of the soil movements are smaller compared to the calculations carried out at 1m depth due to the fact that the suction changes were larger than 1.7m. Additionally, the maximum shrink-swell is about 1.5mm close to tree and less than 0.5mm close to the building.

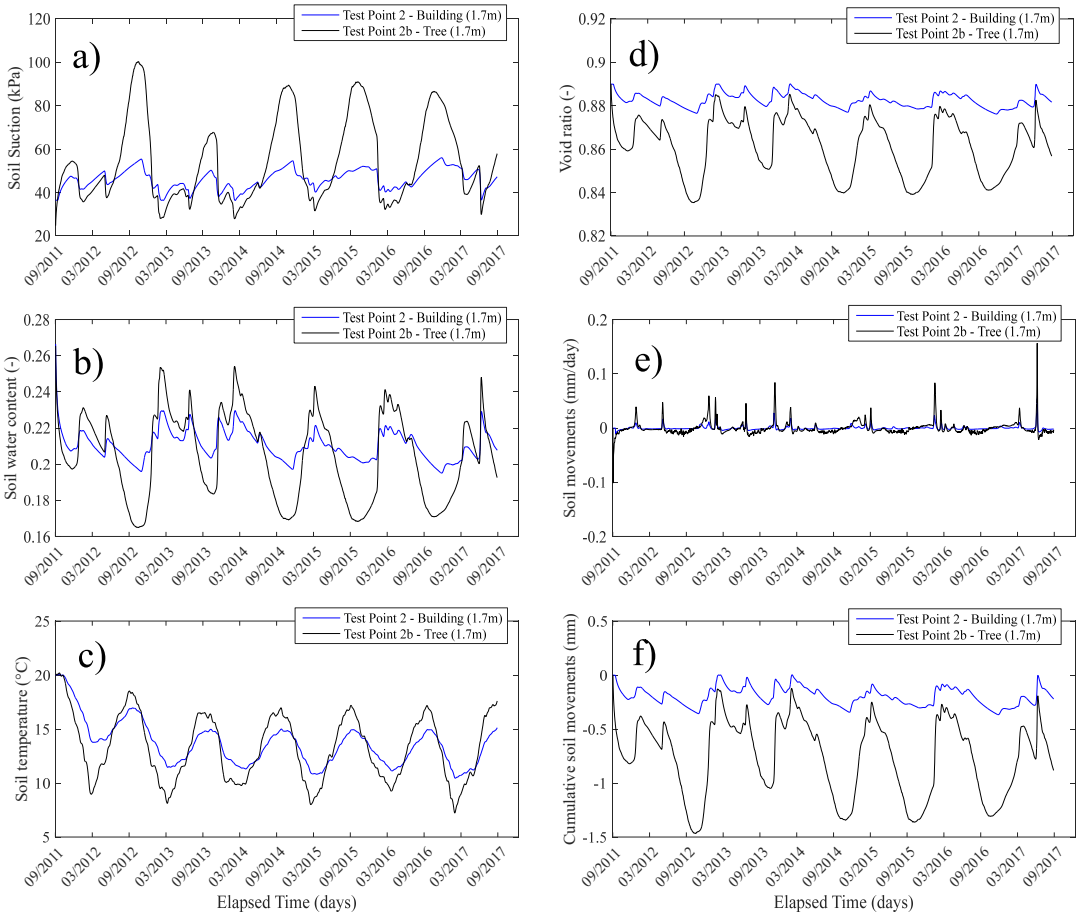

Figure 4.6 - Comparison of the soil physical variables close to the tree and the building at 1.7m depth (point 2 and 2b).

The comparison at point 3 and 3b (2.3 m depth) presented in Figure 4.7, shows larger suction variations close to the tree compared to the variations close to the building. These suction values close to the tree are even larger than the two last points analyzed indicating the presence of tree roots at this depth as expected. These large suction cycles cause an important void ratio decrease into the soil which consequently generates large cumulative soil movements with a tendency to shrinkage during the simulated period. The shrinkage caused in time is because the soil reaches the transition suction stage (S_{tr}) at some point and possibly at peak values. The transition suction is equal to 134.96 kPa in the model and the suction plot shows clearly larger peak values which means that not only k_s is used in the calculation of the volume change behavior but also λ_s interferes in the model. Since λ_s has a greater value compared to k_s, it generates additional volume change and consequently additional cumulative soil movements which in this case is followed by shrinkage. It should also be mentioned that the transition dry density between loose and dense soil state is considered 1.5 Mg/m^3. It is also observed that the daily soil movements are also greater than the last two points and the maximum soil movement appear in 09/2015 when the maximum cumulative shrinkage is also observed.

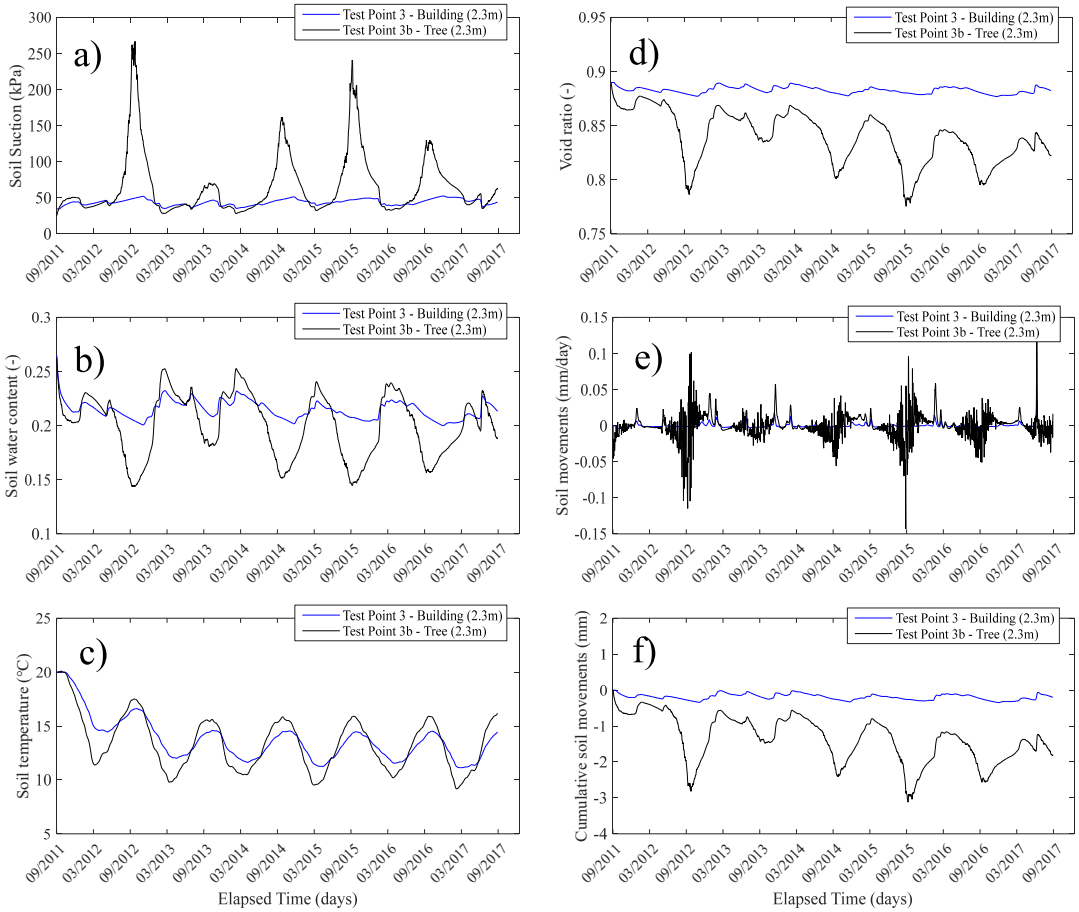

Figure 4.7 - Comparison of the soil physical variables close to the tree and the building at 2.3m depth (point 3 and 3b).

Figure 4.8 shows the comparison of the soil physical variables at 3.75m depth (point 4 and 4b). It can be observed from the suction plot (Figure 4.8 a)) that the soil suction is less influenced by the tree root at point 4b. This can also be observed in other plots such as the water content and the soil temperature. The void ratio does not show a significant difference as expected and the daily soil movements are approximately the same. The cumulative soil movements are limited to maximum 1mm and the difference between the two cases could be negligible. It can be deduced from this comparison that the root water uptake does not influence significantly the soil movements even close to the tree which is because of the root distribution pattern adapted in the north angle.

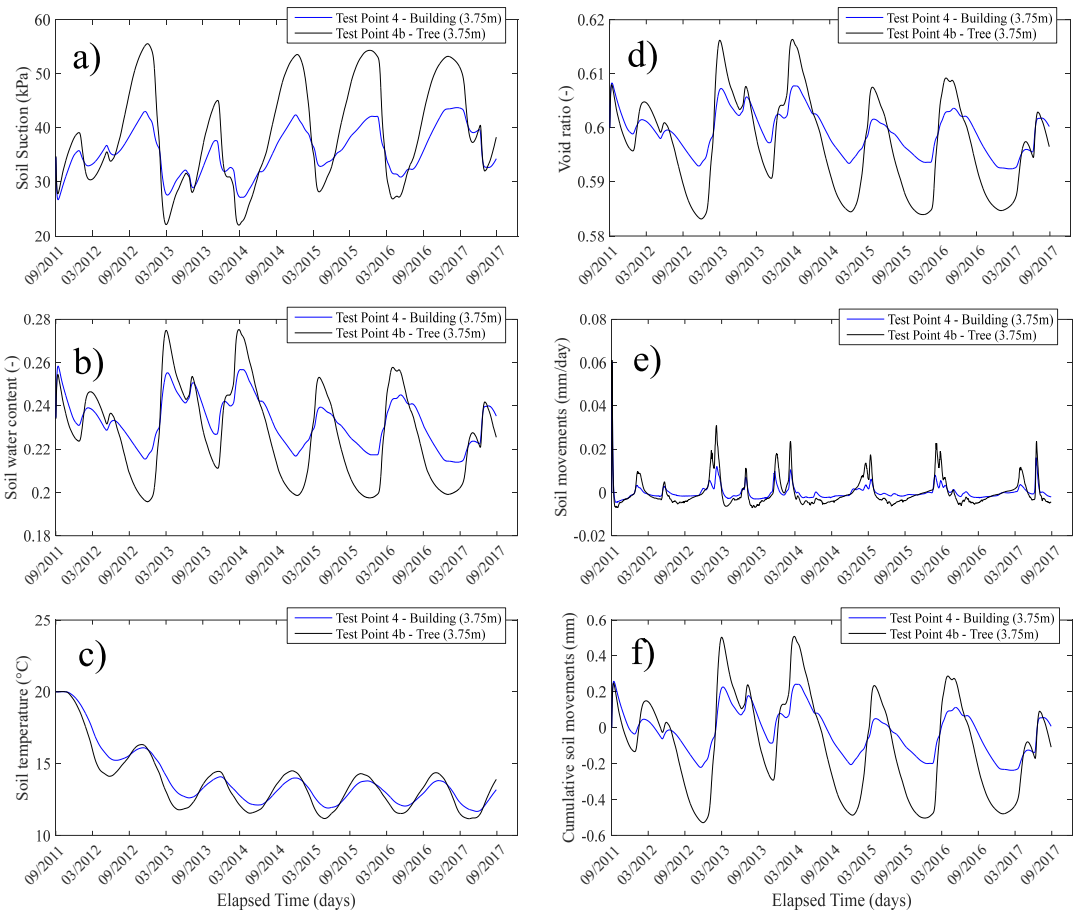

Figure 4.8 - Comparison of the soil physical variables close to the tree and the building at 3.75m depth (point 4 and 4b).

Figure 4.9 shows the comparison of the soil's physical variables at 5m depth (point 5 and 5b). It can be observed that the soil suction variations are much smaller and that the two curves (tree and building) are almost the same as expected. This can be seen in other plots such as the water content and void ratio. The cumulative soil movements in this case stay at the positive side due to the initial drop in the soil suction which is followed by a primary swelling phase. However, the range of variations are about 0.4 to 0.8mm which is smaller compared to the other points analyzed previously in this section.

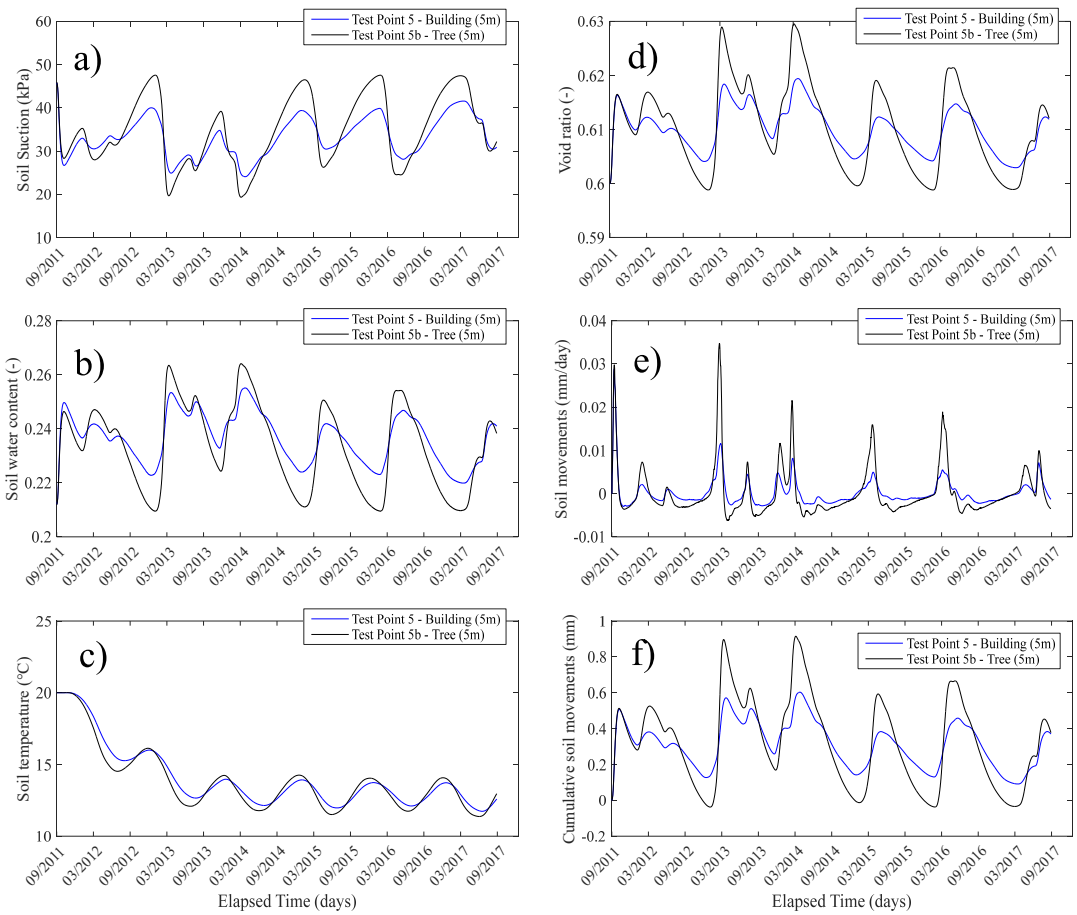

Figure 4.9 - Comparison of the soil physical variables close to the tree and the building at 5m depth (point 5 and 5b).

Based on the comparisons and analysis carried out at 5 different depths, it can be deduced that the root water uptake does not influence directly the soil movements under the foundation soil. Also, the tree roots do not influence significantly the soil movements after 3m depth thus the geotechnical influence zone is limited to 3m depth. This is shown in Figure 4.10 where four plots of the soil water content are presented at different times. Since the largest soil suction values appear at the end of summer based on the comparative analysis, two times were chosen to illustrate the influence of root water uptake. On the other hand, two other times were chosen to illustrate the soil water content at lower suctions or when the root water uptake does not influence the soil. It can be confirmed by this graphical representation that the tree roots do not influence significantly the soil conditions under the foundation and the influence depth of the roots are limited to about 3m as shown previously in the comparative analysis.

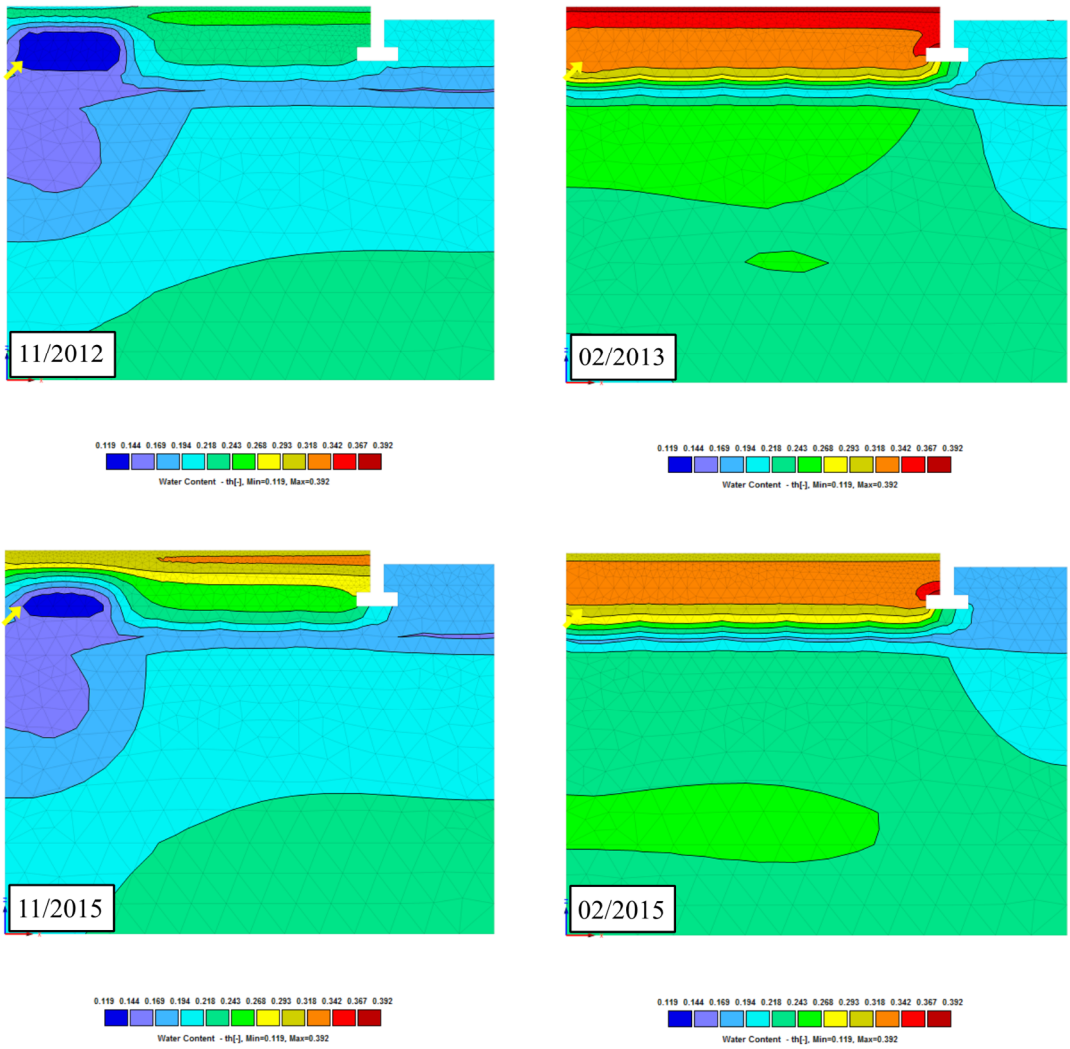

Figure 4.10 - Water content plots at four different times illustrating the influence of root water uptake at the north angle of the building.

The same comparative analysis is carried out for the south angle of the building. The shrink-swell parameters are presented in Table 4.3. The applied stress on the soil at the considered test points is then calculated. It is worth mentioning that the reference depth considered in the calculation of the applied stress in the soil mass is set to the base of the foundation (i.e. 80 cm). 8 points were considered in this analysis in which four are close to the tree and four are under the foundation. The Atterberg's limits are attributed to each depth based on the core samples and the shrink-swell test. As mentioned in the previous section, the influence of the building's load on the soil mass close to the tree is considered negligible because of the distance of the tree from the building. Thus, a zero-stress increase is attributed to the points close to the tree as shown in Table 4.3. It should be mentioned that the water content at saturation is attributed to each depth based on the retention properties of each soil layer. The initial void ratio is attributed to each depth based on the shrink swell tests. However, a larger void ratio is attributed to the first point and a smaller one to the last point (4.2m). The soil dry density is calculated based on the initial void ratio (if not measured).

Table 4.3 - Shrink-Swell parameters at the south angle of the building.

Test point	z (m)	$\Delta\sigma_z$ (kPa)	PI (%)	LL (%)	SL (%)	w% Sat.	e_0	γ_d (Mg /m³)	k_s	λ_s	S_{tr} (kPa)	S_{shrink} (kPa)
1	1	85.87	52	85	21.5	45	0.95	1.38	-0.0332	-0.0354	112.55	1153.5
2	2	25.13	41	70	20	45	0.89	1.42	-0.0315	-0.0429	134.96	1460.6
3	3	13.98	41	68	18	42	0.89	1.42	-0.0326	-0.0449	134.96	2060.07
4	4.2	7.73	25	49	18.5	42	0.6	1.68	-0.0320	-0.0355	439.4	1883.8
1b	1	0	52	85	21.5	45	0.95	1.38	-0.0467	-0.0647	112.55	1153.5
2b	2	0	41	70	20	45	0.89	1.42	-0.0395	-0.0575	134.96	1460.6
3b	3	0	41	68	18	42	0.89	1.42	-0.0391	-0.0568	134.96	2060.07
4b	4.2	0	25	49	18.5	42	0.6	1.68	-0.0358	-0.0409	439.4	1883.8

Figure 4.11 shows the comparison between the soil physical variables at 1m depth in the south angle (points 1 and 1b). It can be observed in Figure 4.11 a) that the soil suction plot under the foundation (in blue) is less influenced by the climatic conditions of the site. This can be due to the presence of the perimeter cover in this side of the building.

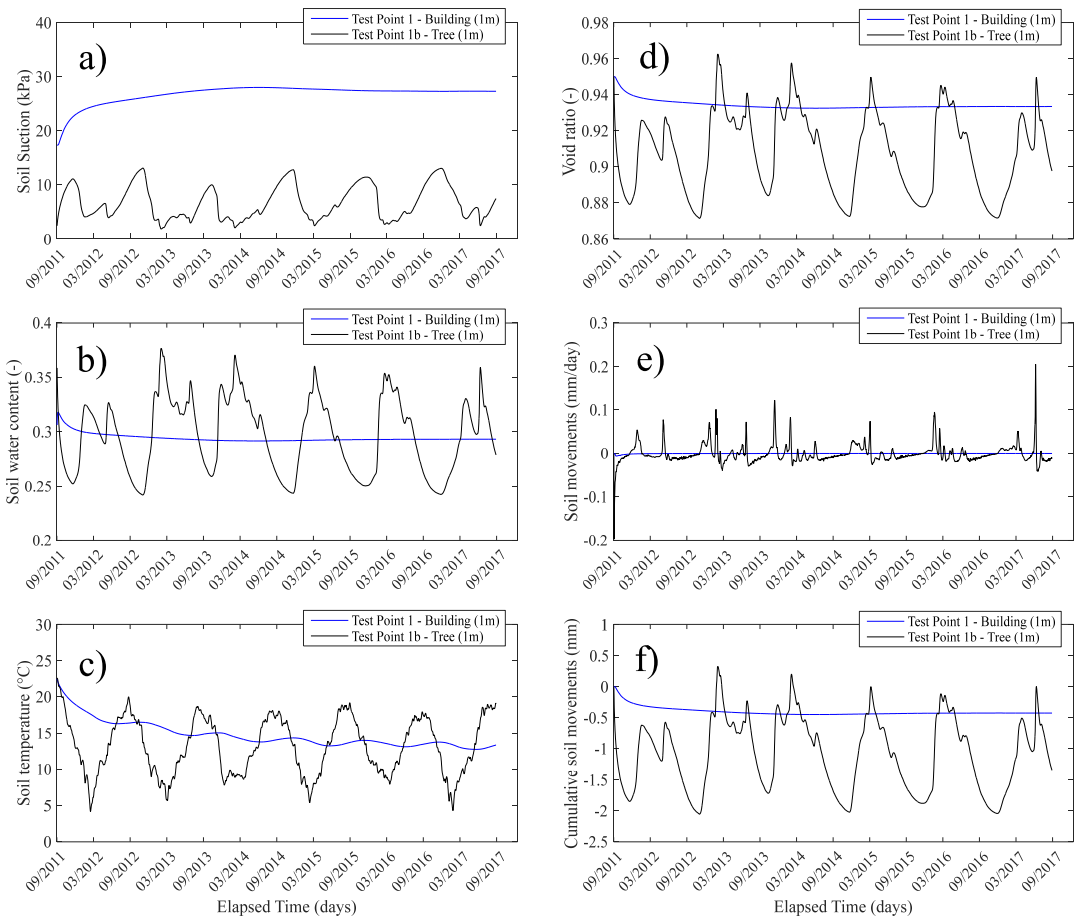

Figure 4.11 - Comparison of the soil physical variables close to the tree and the building at 1m depth (point 1 and 1b).

On the other hand, the suction plot close to the tree side follows the imposed climatic conditions as expected but the generated suction is smaller than the one in the north angle of the building due to the difference in the root distribution pattern and the attributed parameters.

Figure 4.11 b) and c) show also a considerable difference between the simulation results close to the tree and the building as expected. Figure 4.11 d) shows the variation of the soil void ratio. It can be observed that most of the changes in the void ratio under the foundation soil happens at the beginning where there is a slight desaturation of the soil. However, the void ratio changes close to tree follow the soil suction variations as expected. In Figure 4.11 e) the daily soil movements are presented and it can be seen that the movements under the foundation are almost zero compared to the movements close to the tree. Finally, the cumulative soil movements are presented in Figure 4.11 f) where a maximum initial shrinkage of 0.5mm is observed under the foundation soil and a maximum shrink-swell of about 2mm is observed close to the tree. This highlights that the soil is not influenced by the climatic conditions and the tree under the foundation soil. A stable behavior is observed after less than 3 months which is also not a considerable amount of soil movement.

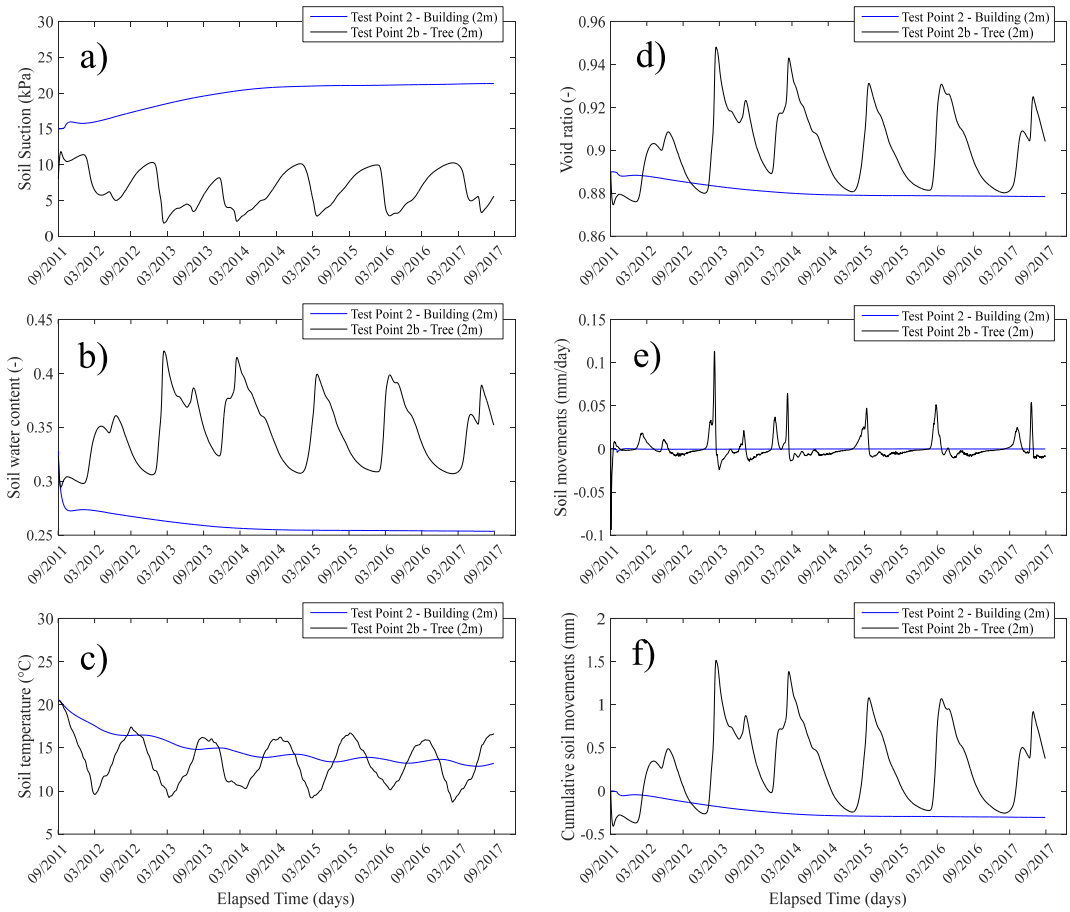

Figure 4.12 - Comparison of the soil physical variables close to the tree and the building at 2m depth (point 2 and 2b).

Figure 4.12 shows the comparison of the soil physical variables at 2m depth (points 2 and 2b) at the south angle of the building. It can be observed that the suction plots are different and again, the soil conditions under the foundation is stable compared to the movements close to the tree. Same comments could be made for the water content and the temperature variations. The changes in the void ratio are almost stable under the foundation soil as expected (Figure 4.12 d)). However, the variation of the void ratio is considerable due to the fact that they follow the soil suction changes over time. The daily soil movements and the cumulative soil movements both reveal that the soil is in a stable state under the foundation of the building. However, the

cumulative soil movements close to the tree reach a maximum shrink-swell value of 1.8mm during the simulated period.

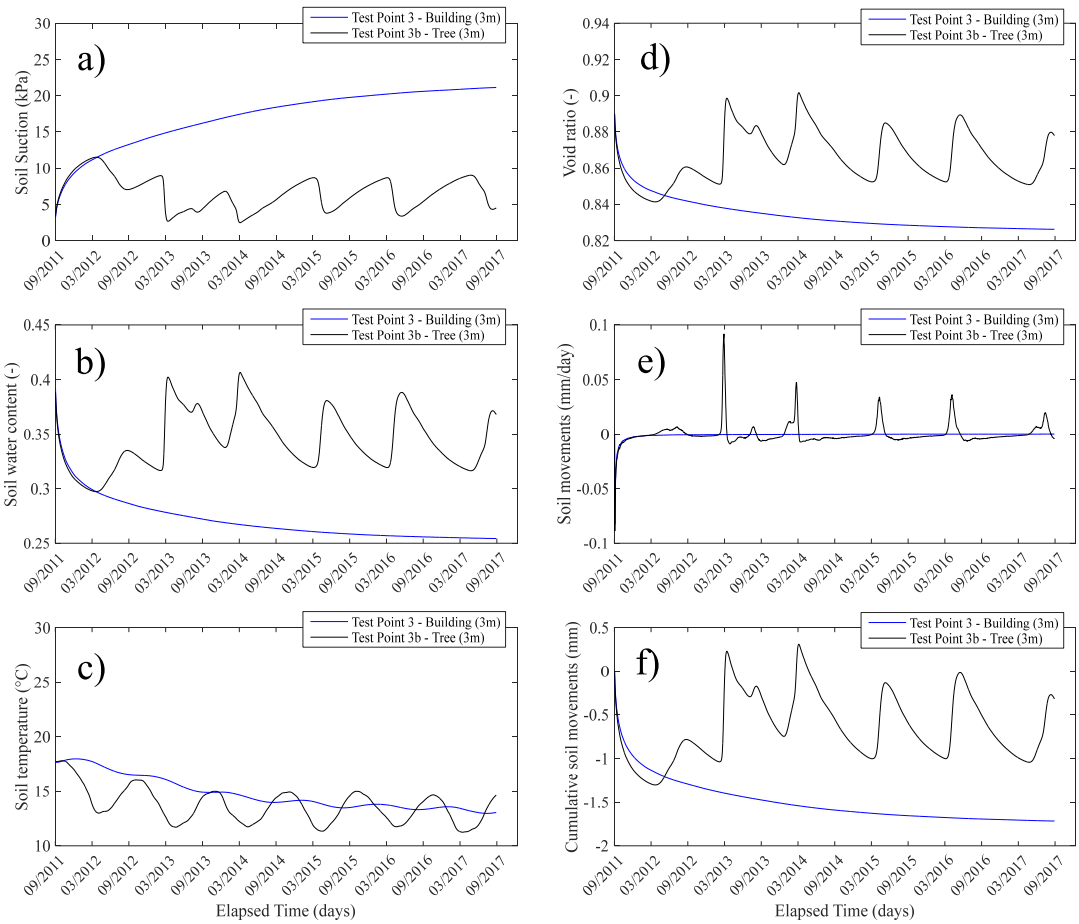

Figure 4.13 - Comparison of the soil physical variables close to the tree and the building at 3m depth (point 3 and 3b).

Figure 4.13 shows the comparative analysis of the soil physical variables at 3m depth (point 3 and 3b). The soil suction plots in Figure 4.13 a) shows that the soil under the foundation tends to desaturate by increasing gradually the suction value. This could be related to the initial conditions and the associated retention properties of the soil. This is also observed in Figure 4.13 b) where the water content gradually drops as the soil suction increases under the foundation soil. On the other hand, the variation of the soil suction and water content close to tree at 3m depth are followed by the imposed climatic conditions. This is also shown in the void ratio plot in Figure 4.13 d) where the void ratio varies between 0.9 and 0.84 during the considered period. However, this is observed only in the first 3 months of the calculation under the foundation soil and the variation becomes stable afterward. The daily soil movements and cumulative soil movements both shows that the movements caused by gradual desaturation under the foundation mostly takes place at the first months of the simulated period. The soil movements close to the tree at 3m depth have a maximum shrink-swell value of 1.5mm which is smaller than the two higher points (1b and 2b). The maximum value of shrink-swell under the foundation at 3m depth is also about 1.5mm which is mostly a shrinkage (settlement) behavior as expected.

Based on the last three comparative analyses, it can be deduced that in the south angle of the building, the tree does not influence the soil under the foundation soil because of two main reasons:

- The perimeter covers at the top of the soil which surround this side of the building are limiting the imposed climatic conditions close to the building.
- The vegetative cover and the tree in the south angle are different from the one in the north angle in a way that less transpiration is attributed to this side of the building.

Therefore, a stable soil movement is observed in most of the points under the foundation soil unlike the movements close to the tree where they are directly influenced by the climatic conditions and the root water uptake. This could also be verified by the graphical plots of the soil water content at different times in Figure 4.14. It can be observed that the volumetric water content becomes stable after the first plot at 10/2011 under the foundation and the variations are negligible in depth. The water content generated by root water uptake at the warm periods (10/2011 and 09/2014) does not seem to influence the water content state under the foundation. The difference between the water content distribution in some parts of the geometry is related to the fact that three different initial condition profiles were adapted to this geometry based on the H1, H2 and H7 profiling probes measurements. It should be mentioned that the last point at 4.2m depth was not considered in the comparative analysis because of the root distribution pattern which stops at 2m depth. The influence depth of the tree is about 3m in this side of the building like the north angle. The next section deals with the differential soil movements at these two angles which may have caused the observed structural damages to the building.

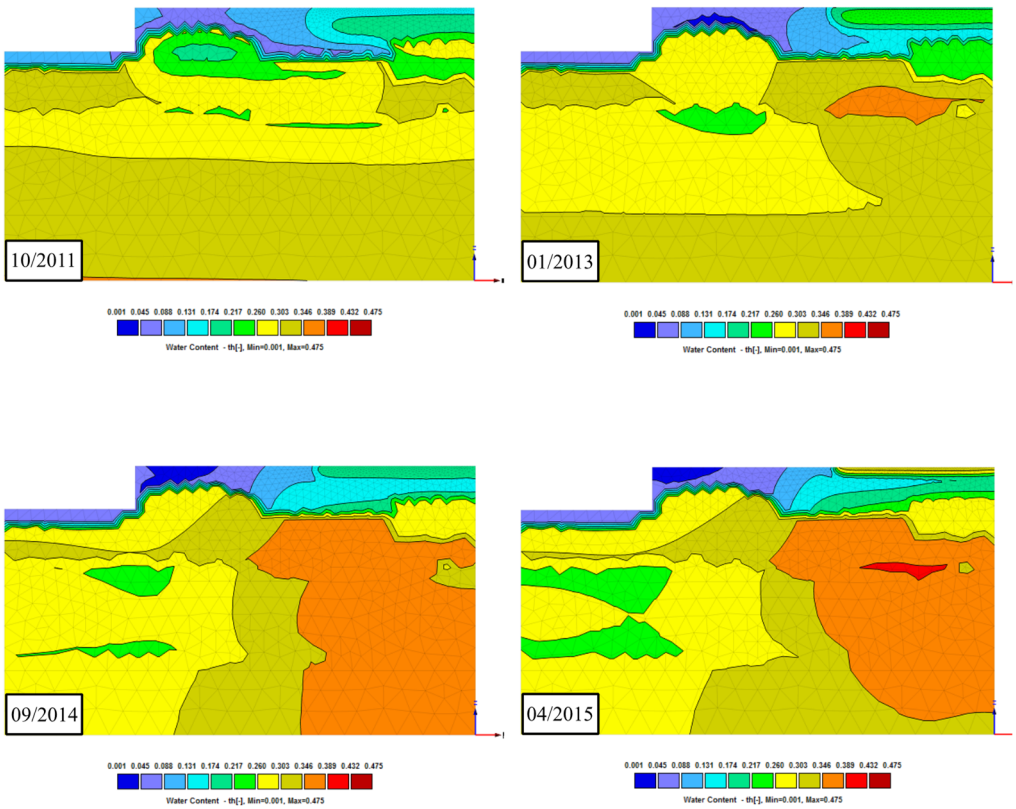

Figure 4.14 - Water content plots at four different times illustrating the influence of root water uptake at the south angle of the building.

4.1.3 Differential soil movements

The analysis of the differential soil movements is of paramount importance for evaluating the potential damages on lightweight constructions. Based on the soil surface suction plots at these two angles of the building, the soil movements can be determined using the listed parameters for the top layer of each angle in Table 4.2 and Table 4.3 (by considering a free heave of the site, i.e. $\Delta\sigma_z = 0$). Figure 4.15 shows the daily variation and the 3 months moving average of the soil surface movements at the two angles of the building. It can be observed that the surface movements in the north angle reaches 12mm unlike the surface movements at the south angle that reaches approximately 4mm at the end of the simulated period. The difference could be related to the attributed retention properties and the generated suction values at the surface. The maximum differential settlement in this case is about 8mm which could be a considerable value. It should also be mentioned that a cumulative shrinkage (settlement) is observed in both cases which is related to the fact that the soil in the top has a lower density and based on the modelling approach a volume loss is observed after several drying wetting cycles.

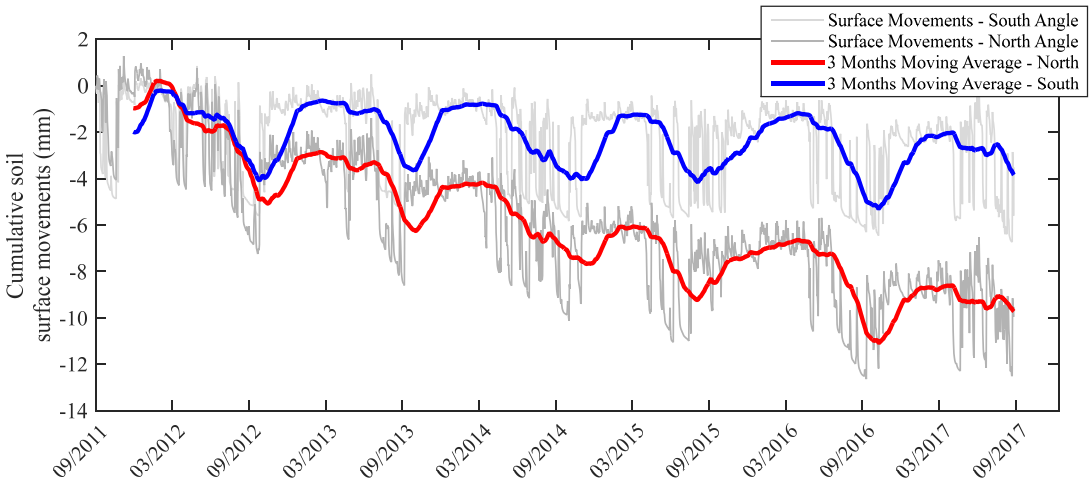

Figure 4.15 - Differential soil surface movements at the north and the south angle.

Based on the comparative analysis carried out in the last section, the suction plots under the foundation of the two angles (1m) could be used to determine and analyze the differential soil movements. Figure 4.16 shows the cumulative and the daily soil movements in the two angles of the building. The cumulative movements plot show that at some points in time, a considerable differential soil movement is observed. The maximum differential movement is about 1mm which is generated in 05/2017 due to a significant amount of rainfall (Figure 3.16). Since the foundation soil in the north angle is directly influenced by climatic conditions unlike the south angle, thus this differential movement could be expected. It should also be mentioned that the soil and the vegetation parameters are both different in these two angles. Figure 4.16 b) also shows considerable daily differential movements since there is almost zero movements in the south angle. The daily soil movement at 05/2017 also shows the maximum differential movement as expected.
It is worth mentioning that the differential movements which occur repeatedly during the considered period could act like a dynamic load under the building and could lead to structural damages. Even though the movements are in the acceptable range of differential settlement for a typical residential building (3-6mm) but it should be mentioned that in this case, the shrinkage and swelling of the soil is calculated (not the settlement) which is like a prescribed displacement.

Additionally, by comparing the crack monitoring sensors results on the north angle (Figure 3.10) with the cumulative soil movements in Figure 4.16 a), it can be deduced that the cracks tend to close from 02/2014 to 04/2014 due to the swelling of the soil (and the increase of the differential movement) as simulated in the same period. An opening of the cracks is observed after this period (04/2014) due to the shrinkage of the soil as shown in the simulated soil movements for the same period. Same comments could be made for the next year of the crack measurements (2015). On the other hand, the monitoring data of the cracks in the south angle of the building show almost a stable movement in most of the sensors as shown in Figure 3.11 which is in coherence with the simulated soil movements at this side of the building.
The differential soil movements are also investigated close to the trees in both sides of the building. The tested points with larger suction values were chosen in this analysis. Point 2b in the south angle and 3b at the north angle. It can be observed that in Figure 4.16 c) the differential soil movement primarily reaches 2.7mm in 09/2012 and secondly the maximum value reaches 3.1mm at 09/2015. Daily differential soil movements in Figure 4.16 d) show also that the maximum differential movement is observed at 09/2015. The range of variation is greater than the movements under the foundation soil due to the root water uptake.

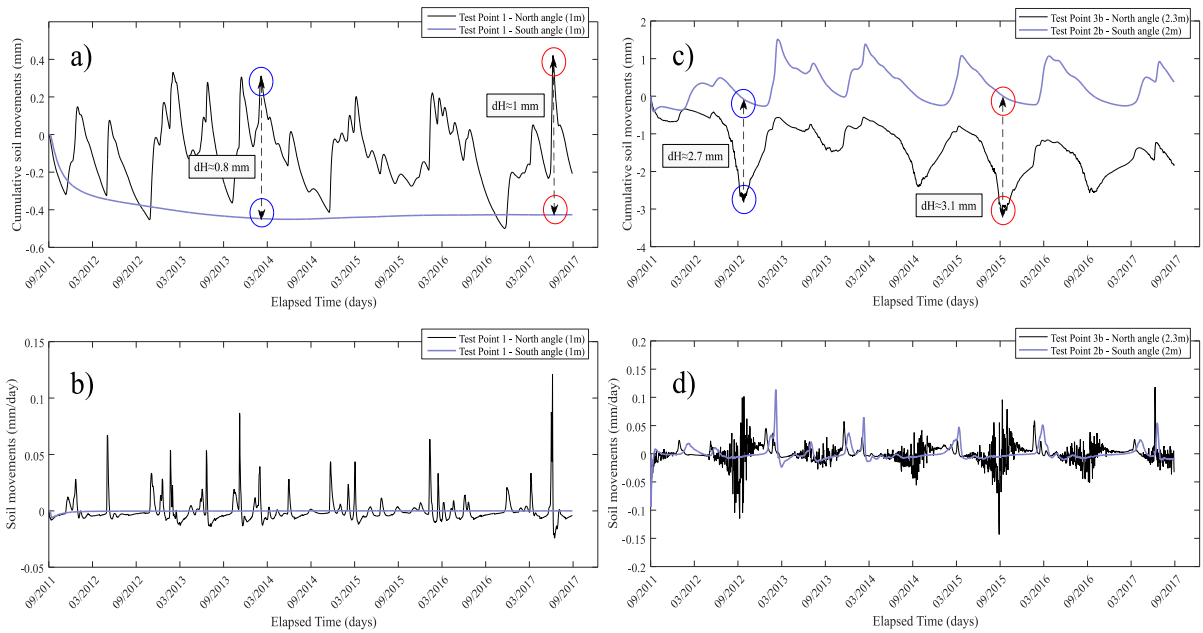

Figure 4.16 - Differential soil movements under the foundation in the north and south angle a) of the building b) close to the trees

4.2 Climate change impact on soil movements

In this section, three RCP climate change scenarios (RCP 2.6, 4.5 and 8.5) are used for the projection of the climatic parameters and for evaluating the soil physical variables at the experimental site. The projected climatic parameters until 2050 are used in this analysis. The difference between some parameters is obvious in each different scenario. For example, the amount of rainfall, temperature and wind speed are among the parameters that have a significant difference in each scenario. However, the projected relative humidity and the global solar radiation are not significantly different from each other in each of these three scenarios. It should be mentioned

that the combined effect of the climatic parameters should be taken into account in the analysis. The calculation was carried out using daily projected data.

Considering the same vegetation parameters and the sinusoidal leaf area index function with the crop coefficient adjusted to climatic parameters as described in section 3.3.4, the reference evapotranspiration and the crop evapotranspiration can be determined for each of these three scenarios. Figure 4.17 a) and b) show the calculated evapotranspiration rate. There is a slight difference in the results however the maximum rate of evapotranspiration is observed in the worst-case scenario (RCP 8.5) as expected.

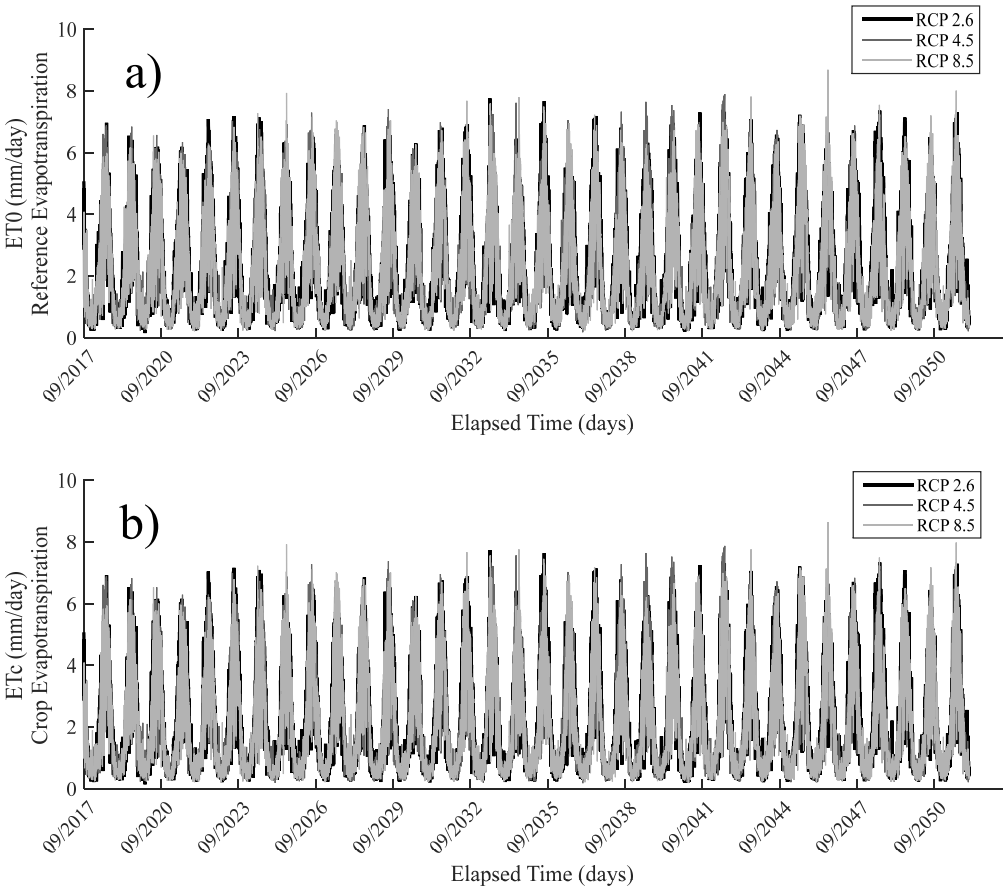

Figure 4.17 - Calculated evapotranspiration of the experimental site with the projected climatic parameters: a) Reference evapotranspiration (ET0) b) Crop evapotranspiration (ETc)

The partitioning of the evapotranspiration into potential transpiration and evaporation is carried out using the same method described in section 2.4.3. Here, the same procedure is repeated three times for each of the sides of the building. Figure 4.18 shows the portioning of each of the three scenarios for the north angle of the building. Figure 4.18 a) and b) show the partitioning with the RCP 2.6 and RCP 4.5 models respectively, where there is an almost equal partitioning of the potential transpiration and evaporation unlike the RCP 8.5 model in which the transpiration rate is slightly higher than the potential soil evaporation. It should be mentioned that the partitioning is highly dependent of the leaf area index (LAI) function which in this case is considered as a sinusoidal function like the previous section.

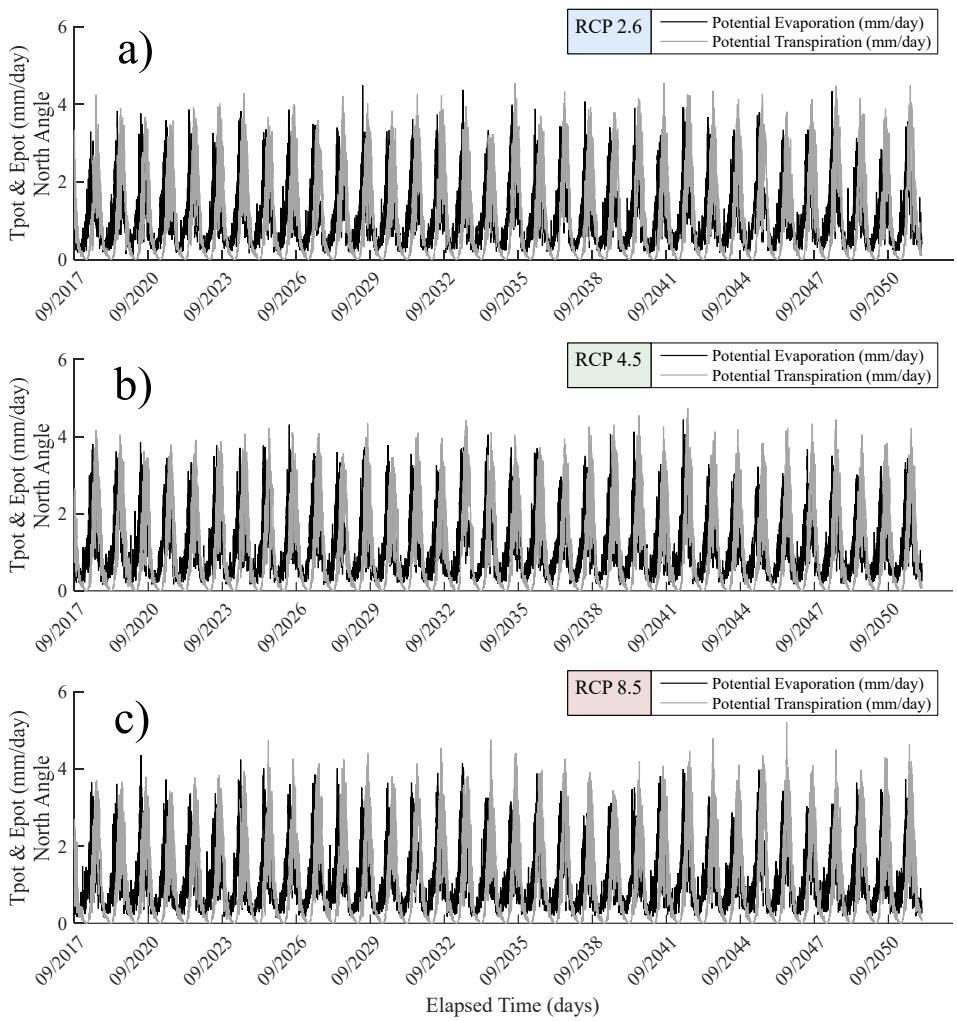

Figure 4.18 - Partitioning of the evapotranspiration rate into potential transpiration (Tpot) and potential evaporation (Epot) in the north side of the building: a) with RCP 2.6 model b) with RCP 4.5 model and c) with RCP 8.5 model.

The same procedure is adapted for the south side of the building in which the LAI is considered to be 2 times smaller than the LAI at the north side of the building due to the tree size and the vegetative cover of the ground.

Figure 4.19 shows the partitioning of the evapotranspiration in the south angle of the building into potential transpiration and evaporation for the three RCP models. It is generally observed that the rate of transpiration is smaller than the rate of potential evaporation in all of the three scenarios as expected. However, there is a considerable difference between the time series of the potential transpiration and evaporation in each scenario. The maximum rate of T_{pot} and E_{pot} is observed in the RCP 8.5 model projection in Figure 4.19 c) as expected. It is worth mentioning that some maximum peak values are also observed in the RCP 4.5 projection model as shown in Figure 4.19 b).

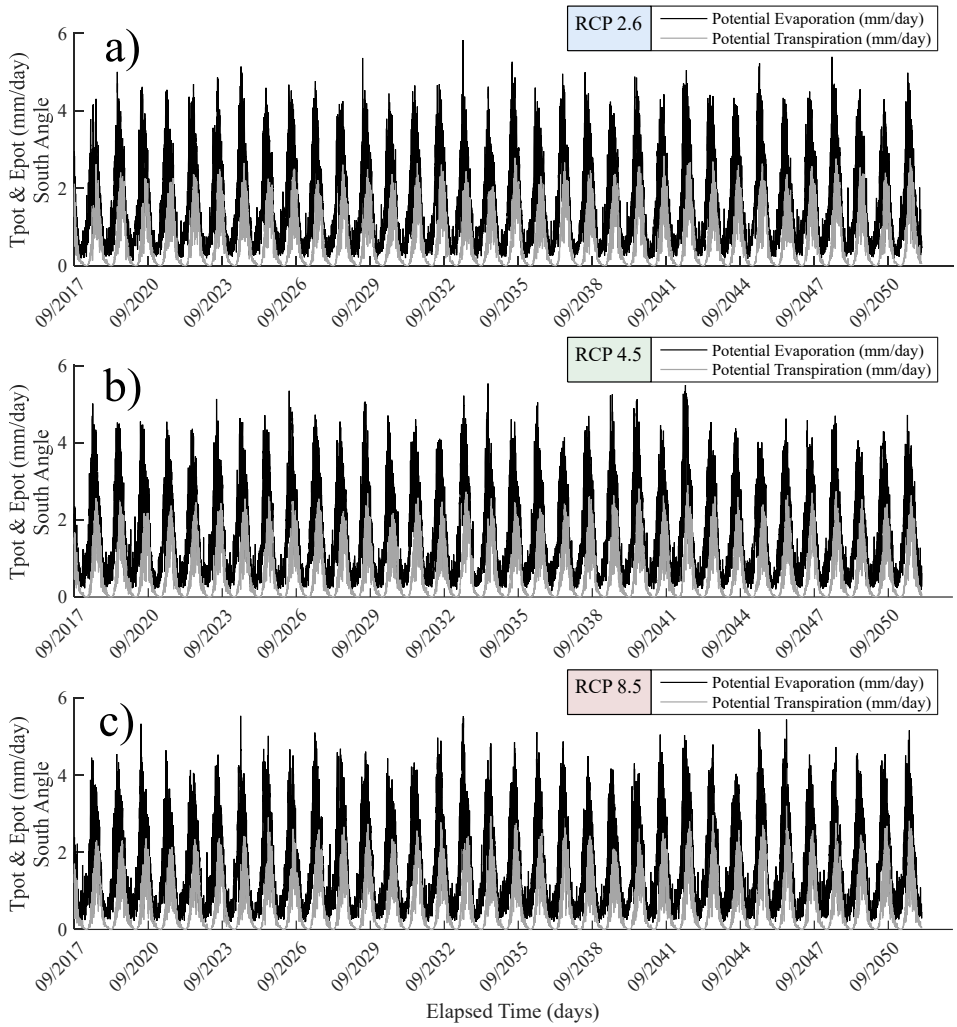

Figure 4.19 - Partitioning of the evapotranspiration rate into potential transpiration (Tpot) and potential evaporation (Epot) in the south side of the building: a) with RCP 2.6 model b) with RCP 4.5 model and c) with RCP 8.5 model.

Following the partitioning of the evapotranspiration rate in the atmospheric conditions, the hydro-thermal boundary conditions can now be determined for each of these three projected scenarios. Figure 4.20 shows the projected time variable atmospheric boundary conditions for the hydro-thermal analysis. The projected infiltration rate is presented in Figure 4.20 a) where the difference between each scenario is not negligible. The calculations were made using the water balance approach. On the other hand, the thermal based energy balance approach was used to determine the soil surface temperature for each projected scenario as shown in Figure 4.20 b). The surface temperature changes approximately between -10 and 30°C in all three RCP models. However, there is a slight difference in the variation of surface temperature in each scenario which will be considered in the simulation phase. It should be mentioned that each RCP model can provide different soil movement result based on the combined influence of the climatic parameters.

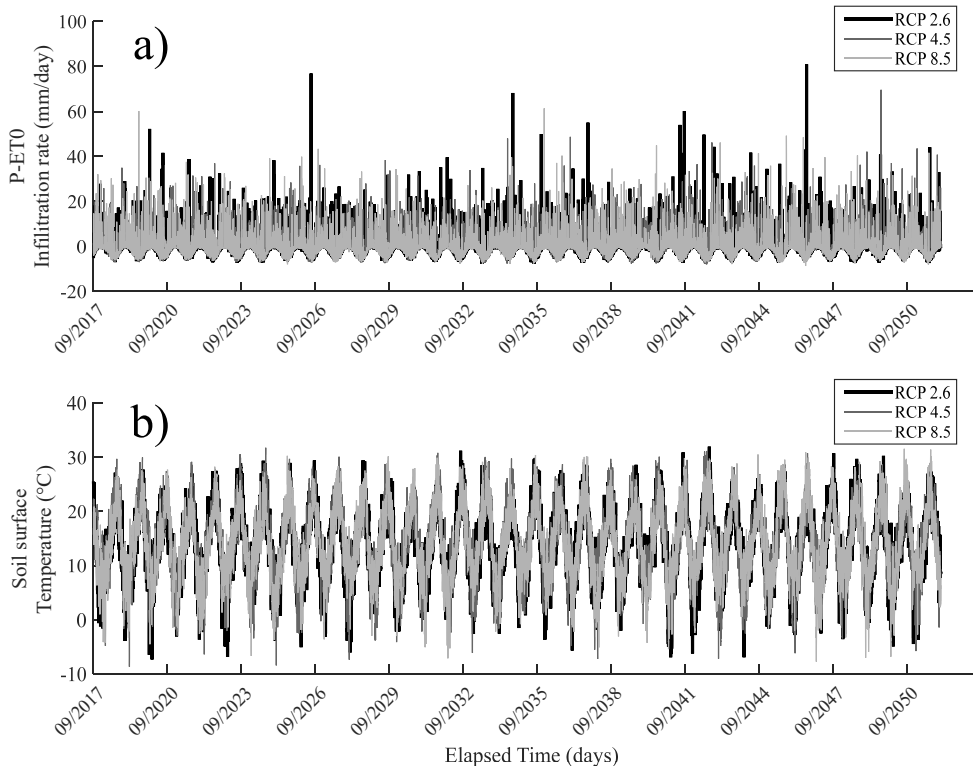

Figure 4.20 - Calculated time variable boundary condition of the experimental site for the hydro-thermal simulation with the RCP models: a) Infiltration rate (P-ET0) b) Soil surface temperature

4.2.1 Short term soil movements

Soil movements are evaluated primarily by considering the short-term projections of climatic parameters. The calculations are carried out until late 2021 which allows the evaluation of the time series of the soil physical variables. Figure 4.21 shows the cumulative soil surface movements at both sides of the building using each RCP scenario. The calculated soil movements at the north side are presented in Figure 4.21 a) where the calculations by the RCP 4.5 model show the maximum amount of shrinkage (16mm). All three scenarios show a cumulative shrinkage behavior with higher intensities in RCP 4.5 and RCP 8.5. On the other hand, Figure 4.21 b) shows the times series of the cumulative soil surface movements in the south side of the building. It can be observed that there is not a significant difference between the three projected scenarios at the end of the simulation period. Based on the historical records and calculations until 09/2017, there was a slight tendency for a cumulative shrinkage of the soil. However, the projections show that the shrinkage and swelling of the soil becomes stable in the south side of the building. The maximum shrinkage of the soil based on the initial condition is about 6mm which is the same value shown in the historical records (09/2011-09/2017). It should also be mentioned that the graphs in grey represent the cumulative movements in a daily time scale and the colored graphs represent the 3 months moving average of the calculations in order to compare each scenario easier.

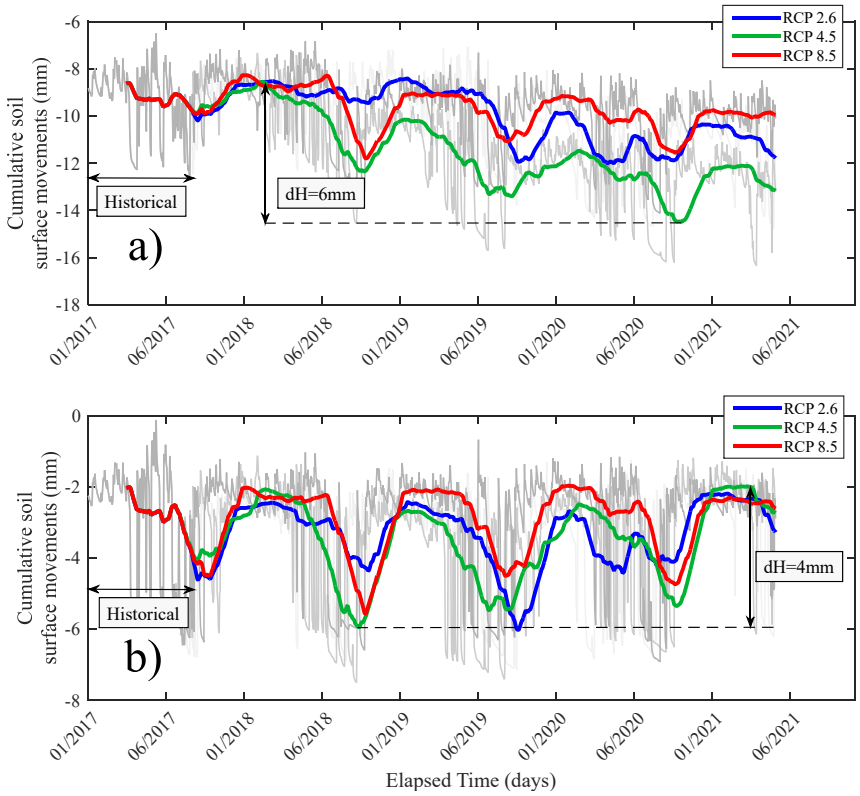

Figure 4.21 - Cumulative soil surface movements using the RCP models (short term) at a) the north side and b) at the south side of the building.

The projected models are also used to evaluate the test points in both sides of the building which were analyzed in previous sections. Figure 4.22 shows the predicted soil physical variables calculated with the hydro-thermal soil model at 1m depth under the foundation in the north angle of the building. The historical variables are plotted along with the predicted variables on the graph. It can be observed in Figure 4.22 a) that the soil suction reaches its maximum value in RCP 4.5 scenario in late 2018. The RCP 2.6 scenario shows smaller suction variations at the beginning until 01/2019 and larger ones which reaches 29 kPa afterward. The RCP 8.5 scenario generates almost the same values as the RCP 4.5 scenario with a slight difference in the maximum peak values. The variations of the soil temperature under the foundation are presented in Figure 4.22 b). The RCP 4.5 scenario shows slightly larger temperature changes compared to the two other scenarios. The water content time series are plotted in Figure 4.22 c) and shows that the minimum water content is reached in RCP 4.5 scenario.

The physical variables of the shrink-swell model are presented in Figure 4.22. The void ratio time series are presented in Figure 4.22 d) where the minimum value is observed in RCP 4.5 scenario because of the generated soil suction. The daily soil movements are presented in Figure 4.22 e). The maximum daily soil movement is observed in the RCP 8.5 scenario in late 2018. It can be observed that the peak daily movements of the RCP 8.5 scenario are larger than the RCP 4.5 scenario in most cases. However, the cumulative movements shown in Figure 4.22 f) indicates that the RCP 4.5 model, generates the maximum soil settlement. The fluctuations in the soil movements of the RCP 8.5 model take place more often during the simulation period which could be due to the daily soil movements.

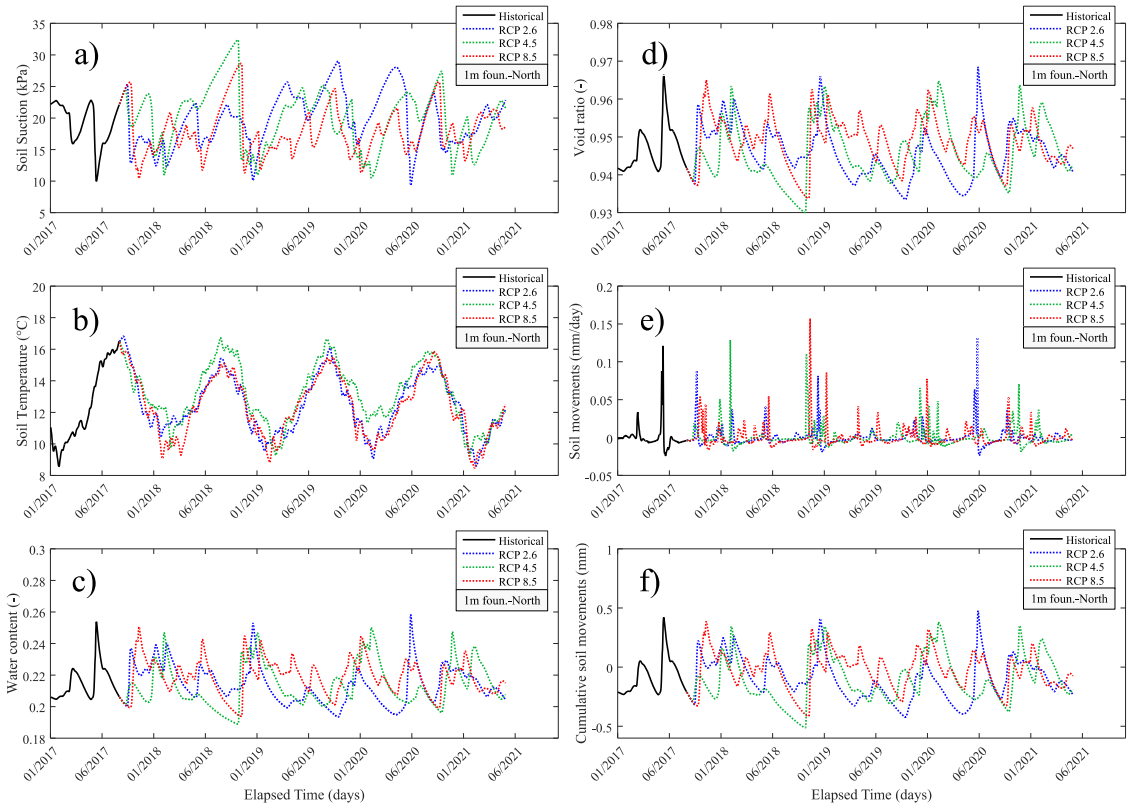

Figure 4.22 - Calculated variables using RCP models (short term) at 1m depth, under the foundation (1m depth) at the north angle of the building, a) soil suction; b) soil temperature; c) soil water content; d) void ratio; e) daily soil movements; f) cumulative soil

The physical variables are also investigated close to tree in the south angle of the building. For this purpose, the test point 3b at 2.3m depth in the north angle is considered. Figure 4.23 shows the times series of the soil physical variables calculated with the hydro thermal soil model. The soil suction short term variations using RCP 4.5 model shows larger peak values compared to the other two scenarios due to the root water uptake effect on the soil. The RCP 8.5 model shows generally the same suction variations as the historical records. The time series of the soil temperature at 2.3m depth are presented in Figure 4.23 b) where a slight difference in the calculated temperature by RCP 4.5 is observed with the two other scenarios (as for 1m depth). The water content time series are presented in Figure 4.23 c) and the variations are as expected. The physical variables of the shrink-swell model at 2.3m depth close to the tree are presented in Figure 4.23. The void ratio times series in Figure 4.23 d) shows that in the short term, the soil modeled with the RCP 4.5 model, loses the most void volume compared to the other two scenarios. This can also be observed in Figure 4.23 e) where the times series of the daily soil movements are plotted. Additionally, the cumulative soil movements calculated by the RCP 4.5 model confirm that the RCP 4.5 scenario generates larger soil movement values close to the tree.

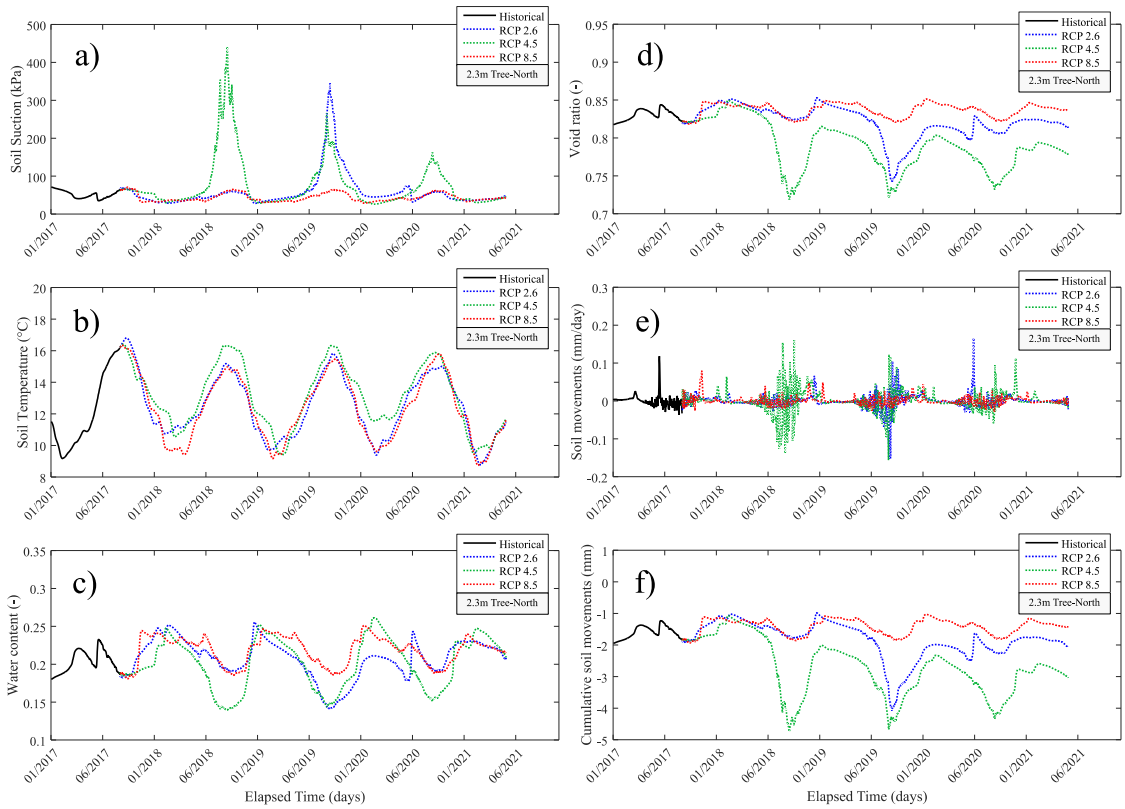

Figure 4.23 - Calculated variables using RCP models (short term) at 2.3m depth, close to the tree at the north angle, a) soil suction; b) soil temperature; c) soil water content; d) void ratio; e) daily soil movements; f) cumulative soil movement

The calculations were also carried out at the south angle of the building. Figure 4.24 shows the soil hydro-thermal variables at 1m depth in the south angle of the building. The soil suction time series presented in Figure 4.24 a) shows that the changes of the soil suction are less than 1 kPa in each scenario which could be negligible. This can be confirmed in the water content time series in Figure 4.24 c) where there is a slight tendency to a wet state in RCP 8.5 and the changes in the other two scenarios are negligible. The soil temperature changes under the foundation soil are slightly higher with the RCP 4.5 model.

The calculated times series of the shrink-swell model variables under the foundation in the south angle at 1m depth are presented in Figure 4.24. As expected, the void ratio changes are negligible in each of these scenarios as shown in Figure 4.24 d). This could be confirmed by the daily soil movements plot in Figure 4.24 e) where the values are in the 10^{-4} mm of orders of magnitude. And finally, the cumulative soil movements presented in Figure 4.24 f) show that a negligible swelling of the soil is observed in RCP 8.5 unlike the two other scenarios in which a negligible cyclic movement is observed in the short term.

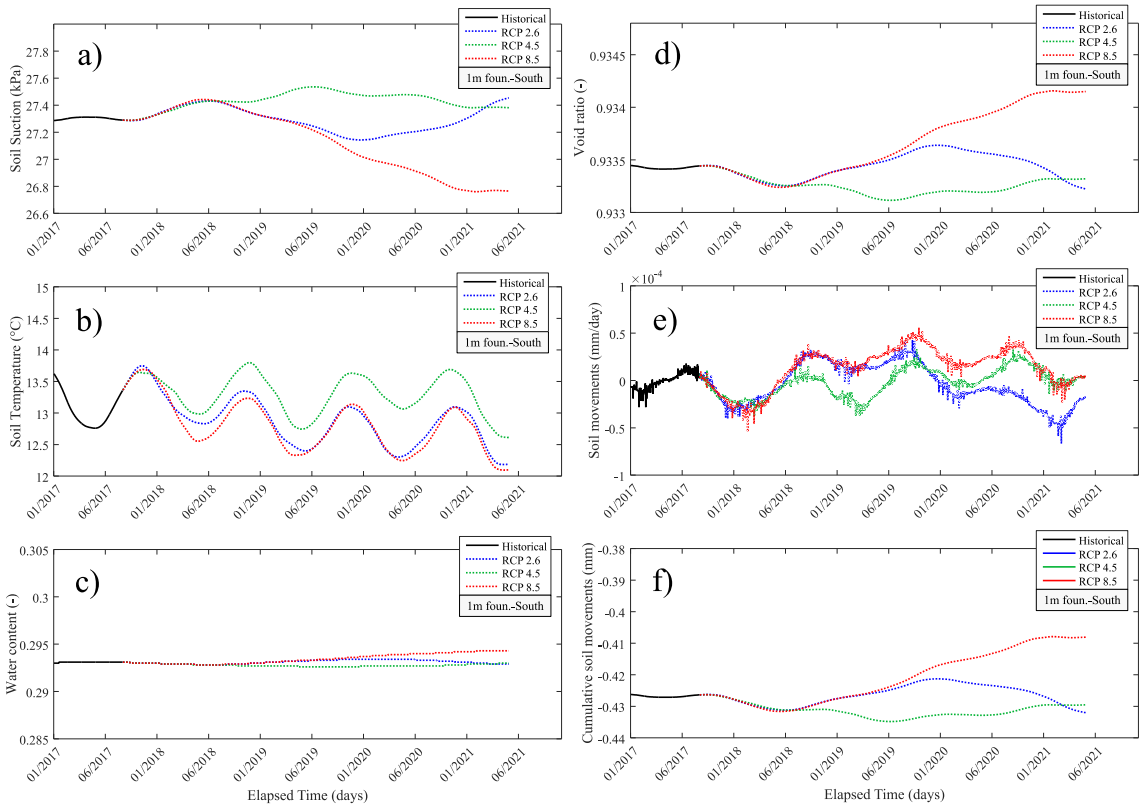

Figure 4.24 - Calculated variables using RCP models (short term) at 1m depth, under the foundation at the south angle of the building, a) soil suction; b) soil temperature; c) soil water content; d) void ratio; e) daily soil movements; f) cumulative soil movements

The same procedure for the north angle is employed here for the south angle by considering a test point (2b) at 2 m depth close to the tree. The hydro-thermal variables using the three scenarios are presented in Figure 4.25. The suction time series (Figure 4.25 a)) shows that the RCP 4.5 model generates the maximum suction as well as in the north side. However, the range of variation is limited to 8 kPa. The soil temperature time series indicate that the RCP 4.5 model generates slightly higher temperature values during the simulation period (Figure 4.25 b)). The time series of the soil water content are presented in Figure 4.25 c) where the maximum range of variation is observed in the RCP 4.5 model as expected.

Figure 4.25 shows the time series of the shrink-swell model variables for the short-term calculation at 2m depth close to the tree. It can be observed in Figure 4.25 d) that more volume change is generated in the RCP 4.5 scenario. However, the daily soil movements show that there are more fluctuations in the RCP 8.5 scenario but larger peaks values which corresponds to the swelling of the soil are observed in the RCP 4.5 scenario. The cumulative soil movements presented in figure jsdjs c) shows also that the RCP 4.5 scenario is dominant in terms of shrinkage and swelling during the simulated period.

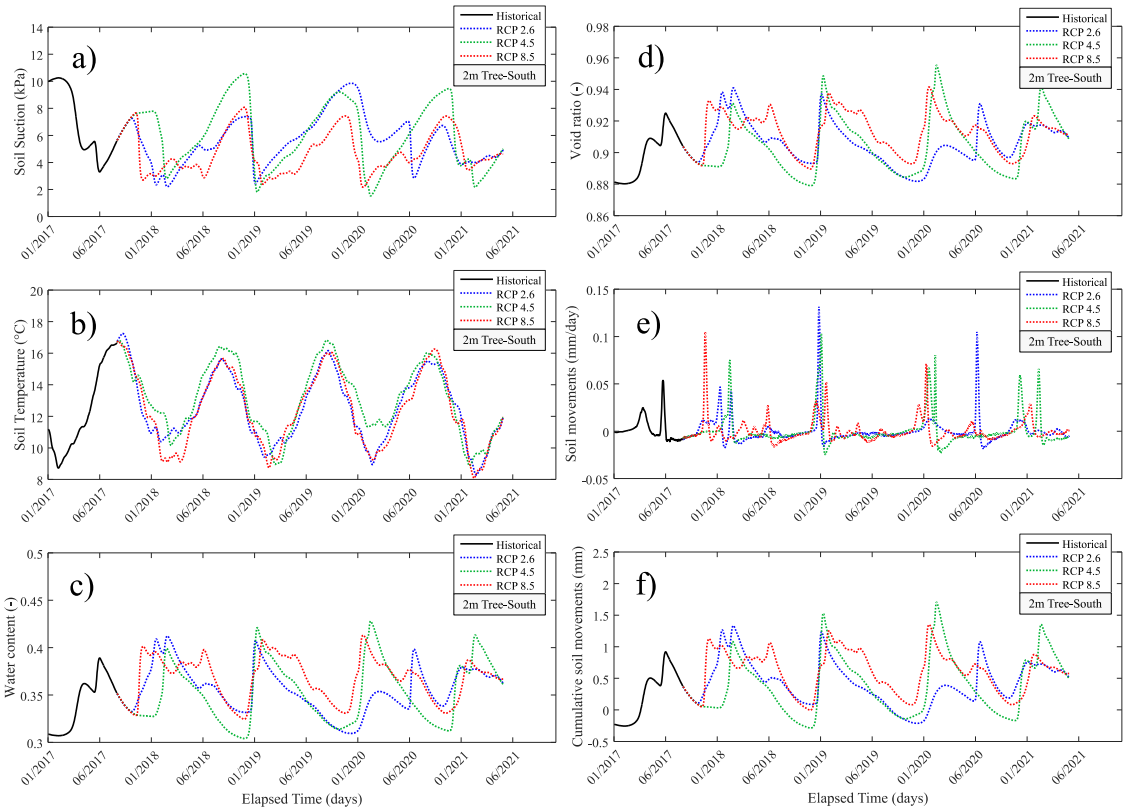

Figure 4.25 - Calculated variables using RCP models (short term) at 2m depth, close to the tree at the south angle of the building, a) soil suction; b) soil temperature; c) soil water content; d) void ratio; e) daily soil movements; f) cumulative soil movements

Althought the times series of the physical variables under the foundation and close to trees in both sides of the building are mostly influenced by the RCP 4.5 scenario, but the differential soil movements in the short term projections should also be evaluated. Figure 4.26 shows the compariosn of the cumulative soil movements under the foundation of the building in each considered scenario. It can be observed in Figure 4.26 a) that the maximumm differential movement in the RCP 2.6 scenario occurs at 06/2020 were the movements in the north angle are followed by a considerable swelling of the soil. This is related to the amount of rainfall in this scenario. The maximum differential movement is about 0.9mm which is approximately the same as the historical records calculations (09/2011-09/2017). The maximum diffierential movement in the RCP 4.5 scenario take place at 02/2020 which is earlier compared to the RCP 2.6 scenario as shown in Figure 4.26 b). The maximum value is about the same as RCP 2.6 (0.8mm). Figure 4.26 c) shows the calculated soil movements with the RCP 8.5 scenario. The calculations indicate that the maxmimum differential movement occurs at 11/2017 following a swelling of the soil under the foundation of the north angle. It occurs also earlier than the two other scenarios with a maximum value of 0.8mm which is the same as RCP 2.6 and 4.5. Therefore, it can be deduced that even thought the RCP 4.5 scenario showed larger influence on the physical variables but the maximum differential soil movements in each scenario is approximately the same however, the RCP 8.5 scenario indicates that the maximum differential movement will occure earlier than the other two.

The comparison of the differntial soil movements are also carried out close to the trees at 2 and 2.3m depth in both sides of the building. It can be shown in Figure 4.26 d) that the maximum

diffeential movement in the RCP 2.6 scenario is about 4mm and occures at 09/2019. This is due to the soil suction generated by the root water uptake and eventually the associated evapotranspiration. As shown in Figure 4.26 e) the maximum differential movement in the RCP 4.5 scenario is about 4.4mm which is larger than the RCP 2.6 scenario and it occures earlier at 09/2018. The same amount of differential movement is genetared in the next years during the summer time. Figure 4.26 f) indicates that the maximum differential movement in the RCP 8.5 scneario is about 2.2mm that occurs at 01/2020. It should be mentioned that there is a constant differential movement of about 2mm during the short term period which is due to the fact that the imposed climatic conditions do not generate the same amount of transpiration rate as the RCP 2.6 and RCP 4.5 scenarios.

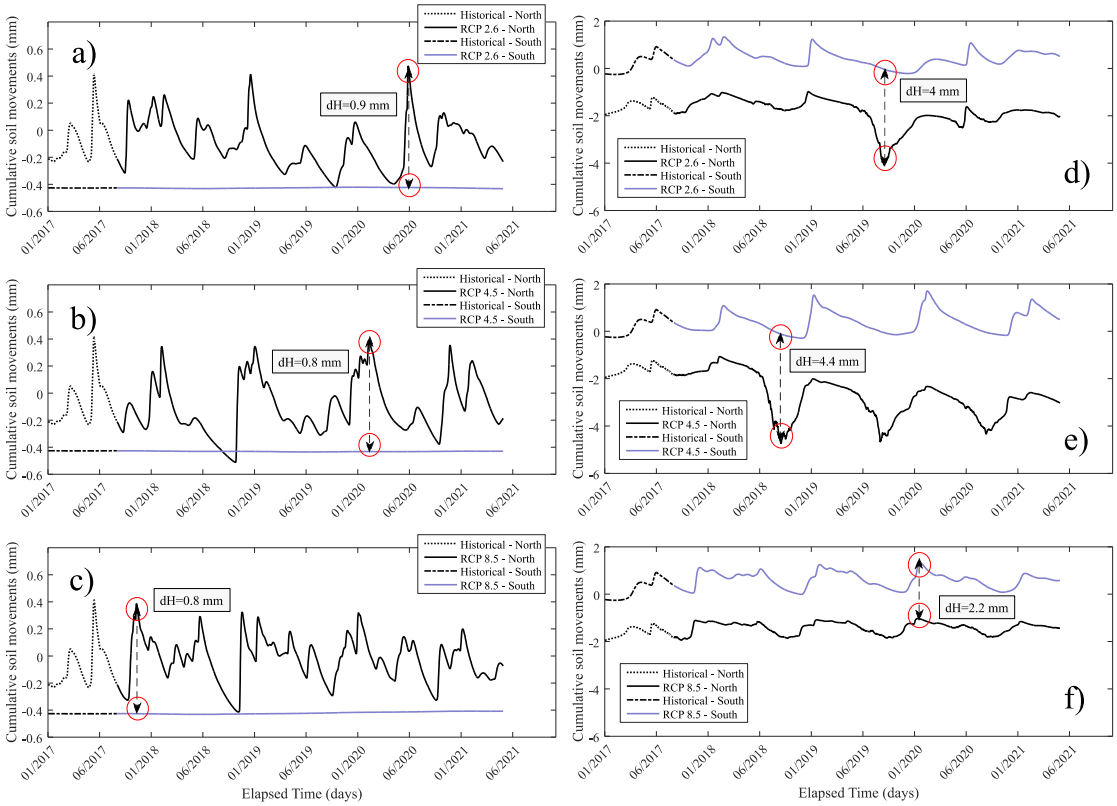

Figure 4.26 - Short term differential soil movements under the foundation (1m depth) and close to the tree (2 and 2.3m depth) using the a) RCP 2.6 scenario; b) RCP 4.5 scenario; and c) RCP 8.5 scenario

It can be deduced form this comparison that the RCP 4.5 scenario will generate larger differential movements in the short term compared to the RCP 2.6 and 8.5 scenarios in the presence of an external environmental stress like the trees in this case. However, considering the differential soil movements under the foundations of the building, it can be deduced that RCP 8.5 could be the worst-case scenario in the short term due to the numerous fluctuations and the maximum movement that occurs earlier than the two scenarios during the simulation period. The analysis of the soil physical variables with the long-term climatic projections could also be useful for the evaluation of each scenario and its impact on the long-term soil movements.

4.2.2 Long term soil movements

In this section the long-term behavior of the soil's physical variables is analyzed. Figure 4.27 shows the soil surface movements calculated with the long-term projections of the three RCP scenarios. The cumulative surface movements in a daily scale are presented in grey and the colored curves corresponds to the 12-month moving average of the surface movements. Figure 4.27 a) shows the long-term surface movements at the north side of the building. A general shrinkage or settlement of the ground is observed during the simulation period. The RCP 4.5 scenario generates almost 60mm of settlement in late 2050 which is larger compared to the other two scenarios (50mm). The RCP 8.5 scenario begins with a slight swelling phase and then shrinks until late 2050. However, the RCP 2.6 and 4.5 start by a shrinkage phase from the beginning of the simulation.

On the other hand, Figure 4.27 b) shows the long-term surface movements at the south side of the building. There is a slight swelling phase at the beginning of the projected models. However, a maximum shrinkage of about 14mm is observed in the RCP 2.6 and 4.5 scenarios in late 2050 unlike the RCP 8.5 scenario which shows a maximum shrinkage of about 10mm. It should be mentioned that this scenario is repeatedly changing movement phases during the simulation period.

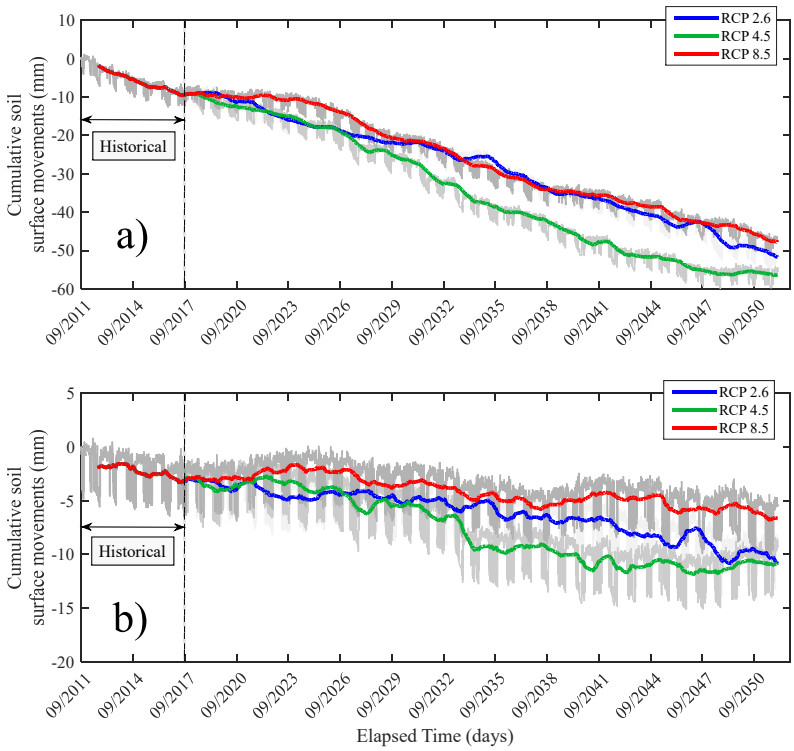

Figure 4.27 - Cumulative soil surface movements using the RCP models (long term) at a) the north side and b) at the south side of the building.

In addition to the long-term surface movements, the soil physical variables in both sides of the building are analyzed. Figure 4.28 shows the long-term behavior of the soil's hydro-thermal variables under the foundation of the building (1m) in the north angle. It can be observed in Figure 4.28 a) that the soil suction follows the same path as the short-term soil suction however, an unusual increase of the soil suction is observed in late 2048 in the RCP 2.6 scenario. Soil temperatures follow the same sinusoidal path with a slight increase in the RCP 8.5 scenario as

shown in Figure 4.28 b). The soil water content time series are presented in Figure 4.28 c) where the changes in the long term are similar to the changes in the short term.
The void ratio time series show a similar trend to the short-term calculations as expected (Figure 4.28 d)). The maximum daily soil movement presented in Figure 4.28 e) take place at 2026 in the RCP 8.5 scenario which is probably followed by a rainfall event. Finally, the cumulative soil movements presented in Figure 4.28 f) vary approximately between -0.5 and 0.5mm range both in short term and long-term calculations. The 12-month moving average of the daily calculations in the RCP 8.5 model show that there is a slight swelling phase at the beginning which is followed by a shrinkage phase in 2027-2032 and a slight swelling phase again that begins at 2032. However, the RCP 2.6 and 4.5 scenarios are generally similar to the short-term projections except for a shrinkage phase in the RCP 2.6 scenario at 2048.

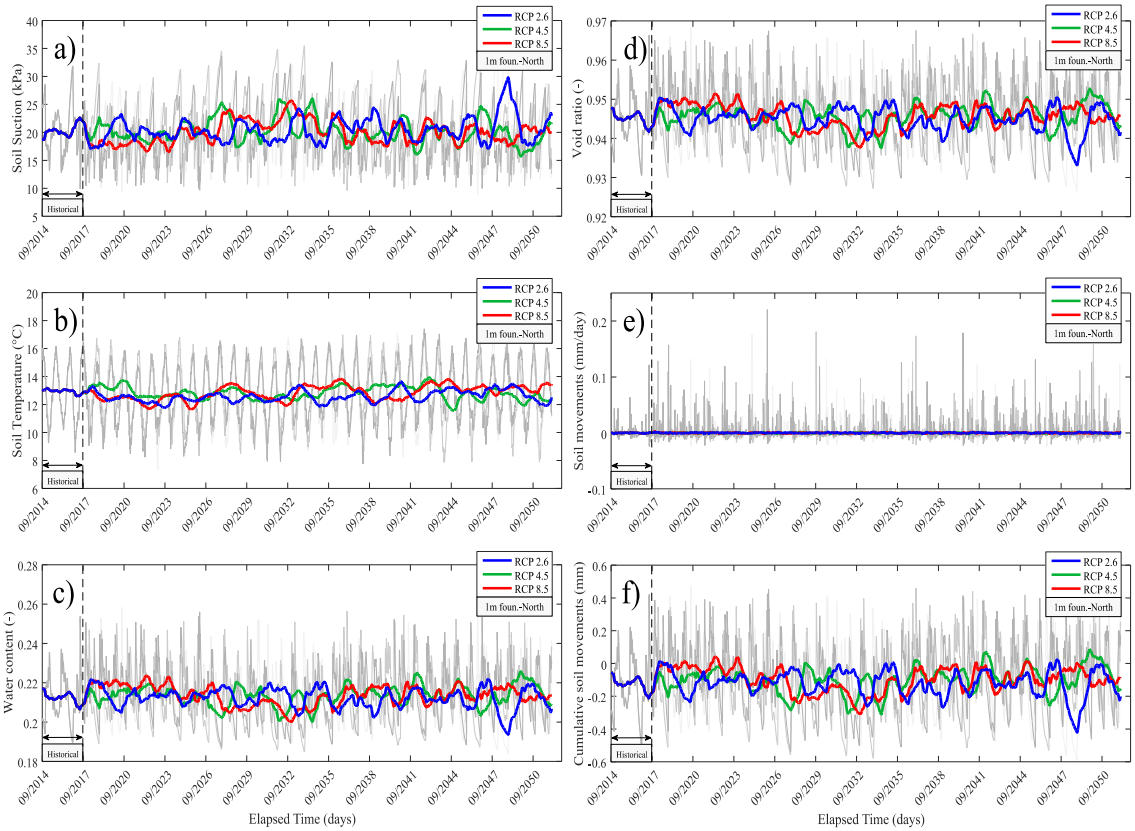

Figure 4.28 - Calculated variables using RCP models (long term) at 1m depth, under the foundation at the north angle of the building, a) soil suction; b) soil temperature; c) soil water content; d) void ratio; e) daily soil movements; f) cumulative soil movements

The long-term soil's hydro-thermal variables are also analyzed close to the tree at the north side of the building (2.3m) as shown in Figure 4.29. The soil suction times series plotted in Figure 4.29 a) show that there is an increase in the peak values after late 2026 where the maximum value takes place in late 2048 in the RCP 2.6 scenario, at 2027 in RCP 4.5 scenario and in late 2032 in RCP 8.5 scenario. The soil temperature time series follow the same sinusoidal path as expected with a slight increase in the RCP 8.5 model's temperature. Water content changes follow the soil suction time series. A desaturation phase is observed during late 2032 where the peak values of suction took place for all scenarios. The minimum water content is observed in late 2048 in the RCP 2.6 model due to the maximum peak suction value at that time.

The soil void ratio plots presented in Figure 4.29 d) shows that the considerable decrease of the void ratio is observed after the peak suction values in each scenario. Daily soil movements presented in Figure 4.29 e) show maximum values in late 2032 due to the desaturation phase as shown in the suction and water content plot. Finally Figure 4.29 f) shows the long-term cumulative soil movements close to the tree. A long-term shrinkage phase is observed for all scenarios as expected. The RCP 4.5 scenario shows the maximum cumulative soil movement at the end of the simulation period (20mm). Changes in the RCP 8.5 model are similar to RCP 4.5 model with a maximum settlement of 17mm. However, the RCP 2.6 scenario changes gradually over time but reaches the maximum value of 17mm.

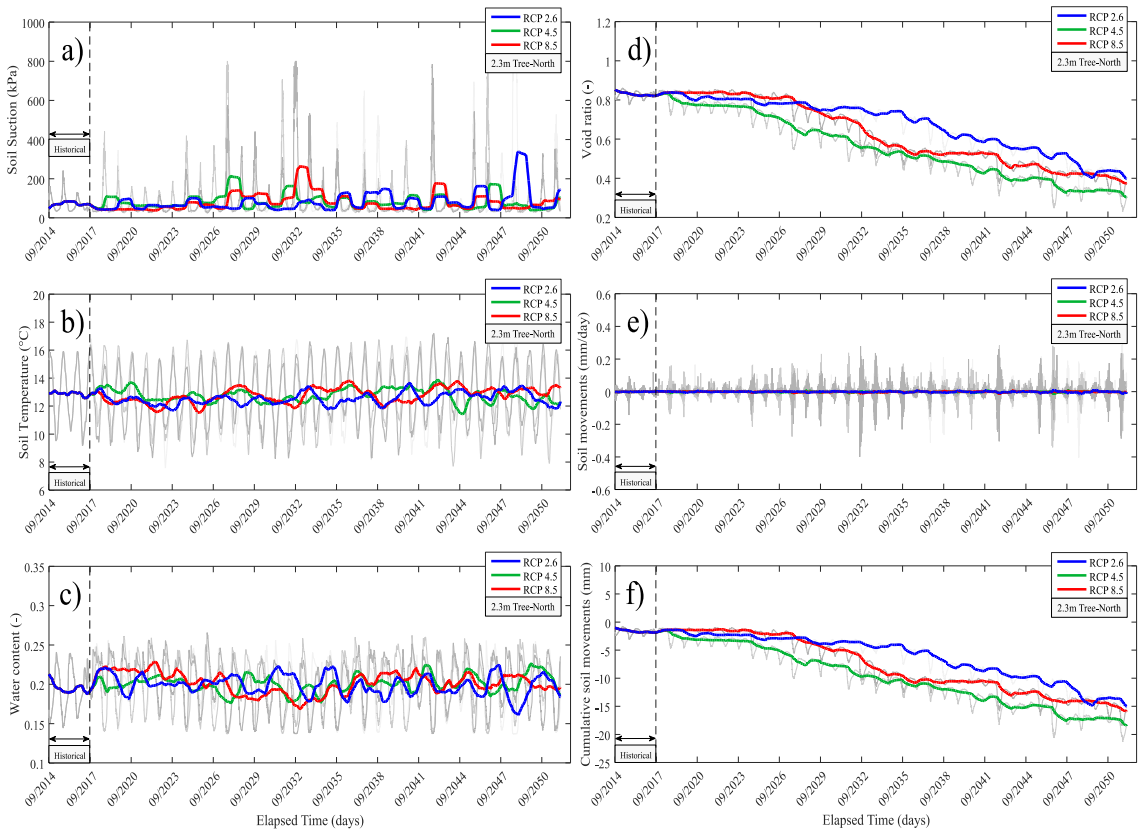

Figure 4.29 - Calculated variables using RCP models (long term) at 2.3m depth, close to the tree at the north angle of the building, a) soil suction; b) soil temperature; c) soil water content; d) void ratio; e) daily soil movements; f) cumulative soil movements

The same procedure is adapted for the south side of the building. The long-term time series of the hydro-thermal variables are presented in Figure 4.30. The soil suction times series under the foundation at the south angle are presented in Figure 4.30 a). The RCP 4.5 and 8.5 scenarios begin with a slight saturation phase and start to desaturate from 2024 until late 2035 and are followed by a saturation phase. However, the RCP 2.6 model begin with a gradual desaturation phase until the end of the simulated period. It should be mentioned that the maximum range of suction variation are about 3kPa which is a negligible value. Figure 4.30 b) shows the sinusoidal variations of the soil temperature with a slight increase in the RCP 8.5 scenario. The soil water content presented in Figure 4.30 c) follows the soil suction times series as expected and confirms the slight saturation and desaturation phases.

The shrink-swell variables can now be determined using the soil suction time series. The range of void ratio changes are limited to 0.1 which is a negligible value, however, the trends follow the soil suction time series as expected. Even though the RCP 8.5 scenario shows larger daily soil movement values in the long-term simulation but the range of variation of these movements are negligible as presented in Figure 4.30 e). The cumulative soil movements presented in Figure 4.30 f) indicates that the RCP 8.5 model generates larger soil movements compared to the other scenarios. The movements in RCP 8.5 begins with a swelling phase and is followed by a shrinkage phase and ends with a swelling phase as shown in the suction time series. The same comments could be made for the RCP 4.5 scenario as well. However, a cumulative settlement is observed in the RCP 2.6 model.

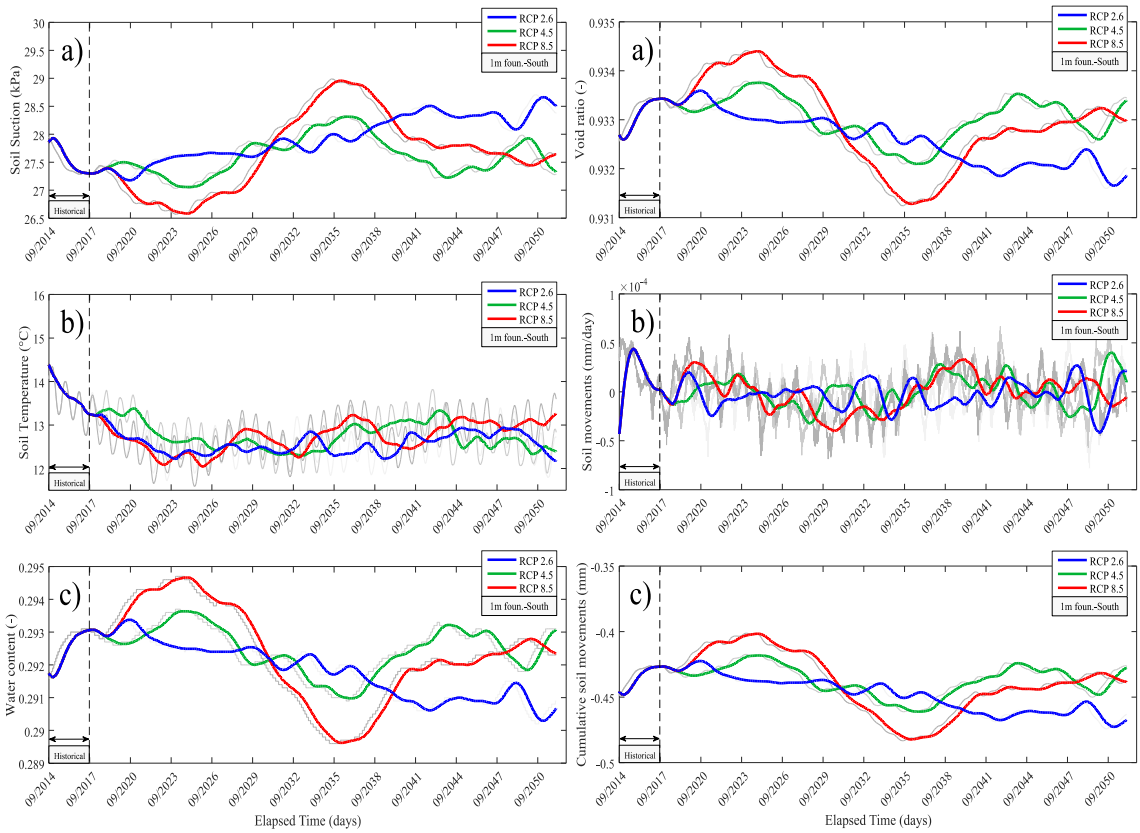

Figure 4.30 - Calculated variables using RCP models (long term) at 1m depth, under the foundation at the south angle of the building, a) soil suction; b) soil temperature; c) soil water content; d) void ratio; e) daily soil movements; f) cumulative soil movements

The variables are also investigated close to the tree at the south side of the building. Figure 4.31 shows the long-term behavior of the hydro-thermal soil variables at 2m depth close to the tree in the south side of the building. It can be observed form Figure 4.31 a) that the soil suction time series are approximately similar to each other. A sudden increase in the soil suction is observed in late 2048 in the RCP 2.6 model which is also the maximum suction value. Soil temperature time series shown in Figure 4.31 b) follow a sinusoidal path as expected with a slight larger temperature values in the RCP 8.5 scenario. Figure 4.31 c) shows the long-term water content time series where the plots are globally similar to each other.

The void ratio time series are shown in Figure 4.31 d). All three scenarios show approximately the same void ratio variation range. A considerable decrease in the void ratio is observed in late 2048 which is related to the rate of evapotranspiration and the associated soil suction. The daily

soil movements time series close to the tree are plotted in Figure 4.31 e) and the variations are almost in the same range during the long-term calculations. Finally, the cumulative soil movement times series are plotted in Figure 4.31 f) where the soil movements vary between 0 and 1.5mm. It can be observed that the trends in the cumulative movement are similar and a complete shrinkage phase is not observed unlike the north side calculations. This is due to the retention properties and consequently the soil suction values that do not reach the transition suction.

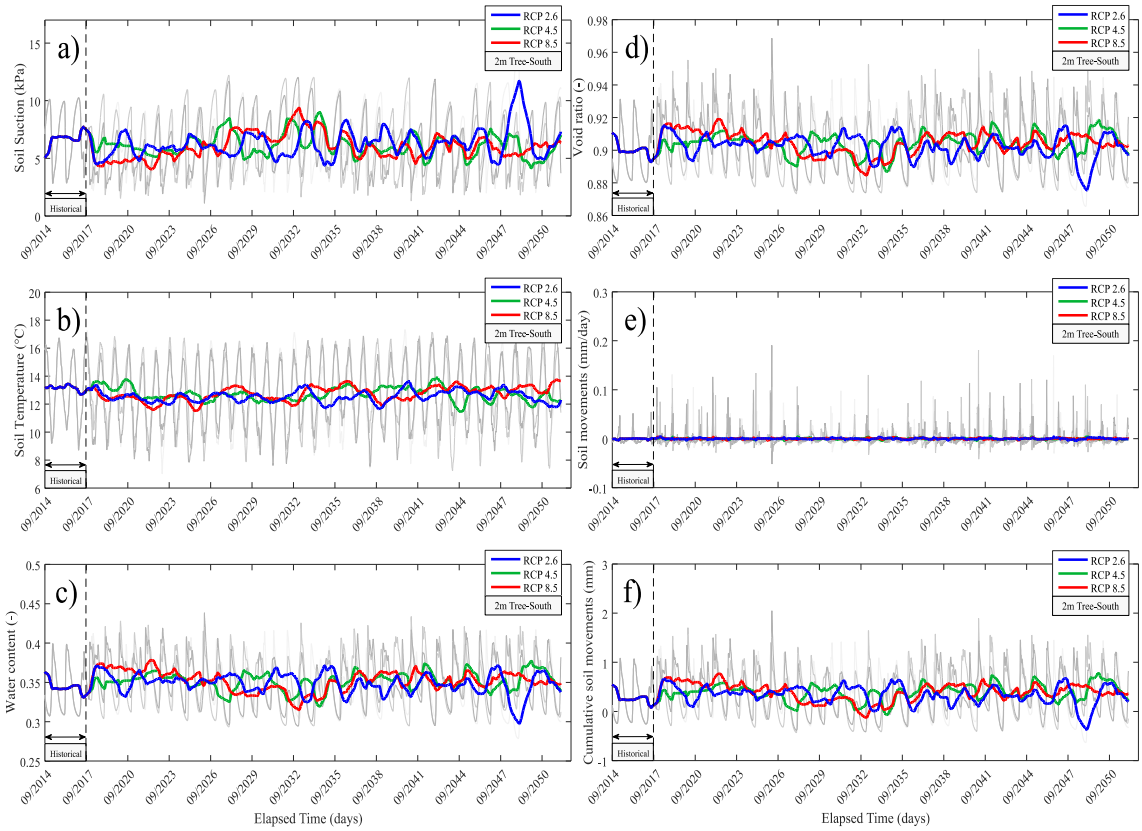

Figure 4.31 - Calculated variables using RCP models (long term) at 2m depth, close to the tree at the south angle of the building, a) soil suction; b) soil temperature; c) soil water content; d) void ratio; e) daily soil movements; f) cumulative soil movements

Similar to the short-term evaluation of the soil movements, the long-term differential movements are also evaluated. Figure 4.32 shows the long-term differential soil movements under the foundation of the building using the three RCP scenarios. It can be observed that the maximum differential movement is approximately the same for each scenario (1mm). However, the time that the maximum differential movement takes place is different in each scenario. The RCP 8.5 scenario shows the earliest maximum differential movement and the soil is generally followed by shrinkage and swelling phases during the simulation period as shown in Figure 4.32 c). In the RCP 2.6 scenario, the maximum differential movement takes place close to the end of the simulation period as shown in Figure 4.32 a). It should be mentioned that the long-term movements are in the same range of the short-term differential movements due to the normal suction changes over time.

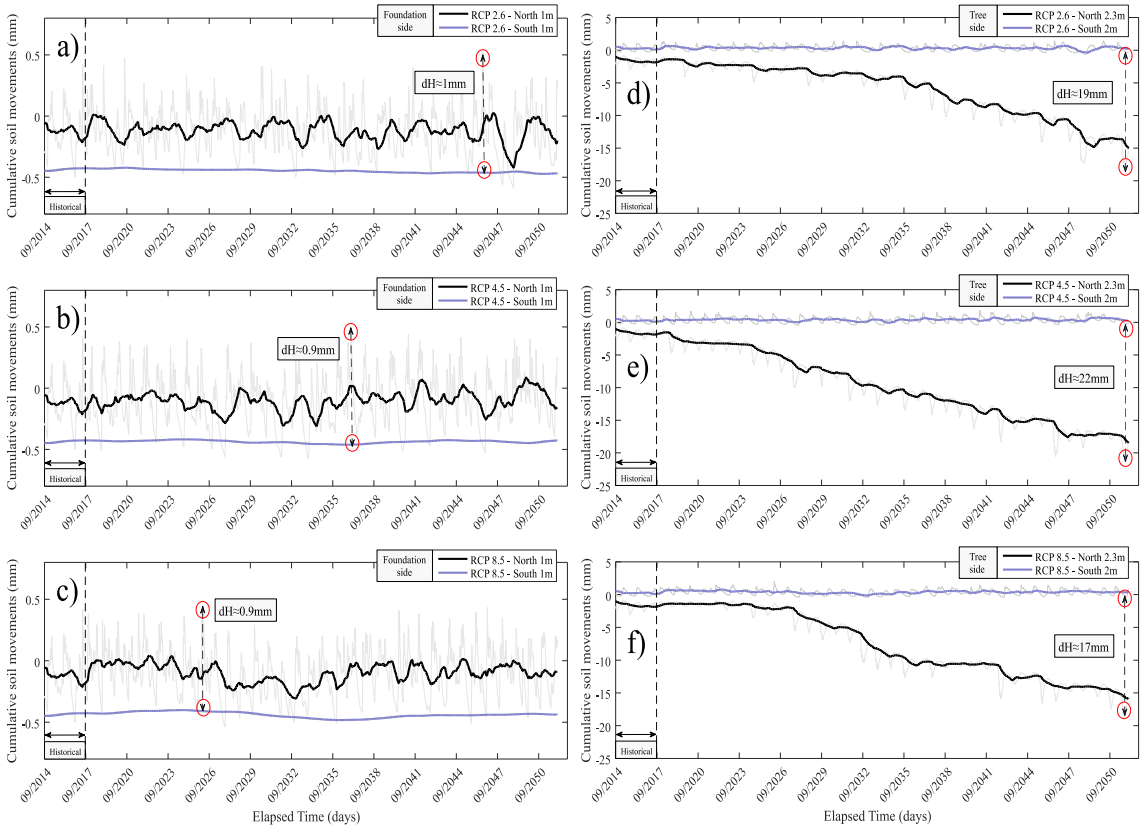

Figure 4.32 - Long term differential soil movements under the foundation (1m depth) and close to the tree (2m and 2.3m depth) using the a) RCP 2.6 scenario; b) RCP 4.5 scenario; and c) RCP 8.5 scenario

The evaluation is also carried out using the two test points (2b and 3b) for the soil movements close to the trees. The results indicate that the long-term differential soil movements are clearly different from the short-term results. The differential soil movements have a negative trend during the simulation process. The maximum differential movement takes place in the RCP 4.5 scenario (22mm) as shown in Figure 4.32 e). The RCP 2.6 scenario shows a maximum differential movement of about 19mm as shown in Figure 4.32 d) and the RCP 8.5 scenario generates 17mm of differential movement at the end of the simulation period. It should also be mentioned that the beginning time of the shrinkage phase is different in each scenario which takes place earlier in the RCP 4.5 scenario compared to the other two scenarios.

It can be deduced from the long-term analysis, that the differential soil movements under the foundation soil are similar to the short-term analysis based on the variation range during the simulation period. Additionally, the shrinkage and swelling trends are mostly observed in the RCP 8.5 scenario and the maximum differential movement is observed earlier as well as the short-term analysis. Therefore, the RCP 8.5 scenario is considered to be the worst-case scenario. However, considering the differential soil movements influenced by the trees, the long-term analysis is not comparable to the short-term analysis due to the considerable shrinkage phases in each scenario. In addition to that, based on the maximum differential movement, the RCP 4.5 scenario could potentially be the worst-case scenario in the presence of external environmental stress.

4.3 Applicable approach towards France

4.3.1 Introduction

The objective of this chapter is to apply the developed approach to France in regional scales. For this purpose, France is divided into six regional climate zones based on different existing climate types. A soil type is attributed to each of these climate zones based on the available maps provided for the distribution of soils in France. These soils (cited as reference soils) are defined using typical input parameters (PI, w%, e_0 and γ_d). The reference condition also comprises the vegetation and the foundation parameters. The reference condition in each region is used to provide the soil suction times series under the considered building's foundation using the SVA interaction analysis which thereafter leads to the calculation of the soil movements. A parametric study is carried out to investigate the influence of these factors on the resulting soil movements.

Figure 4.33 shows six main climate types in France. The central region is mostly dominated by a modified oceanic climate. The east and the west of France are characterized as oceanic and semi continental climate types respectively. The south west is dominated by oceanic Aquitaine climate, however the central south and south west of France are characterized as mountainous climate. Finally, the south cost of France is generally dominated by a Mediterranean climate. In order to attribute coherent climatic parameters for these six regions, five different points in each region were analyzed. The employed data in this section, covers the period of 2016 until late 2018 (this period was chosen based on the geotechnical data base of the company). Thereafter, the input climatic parameters for the SVA interaction analysis are defined for each regional climate zone.

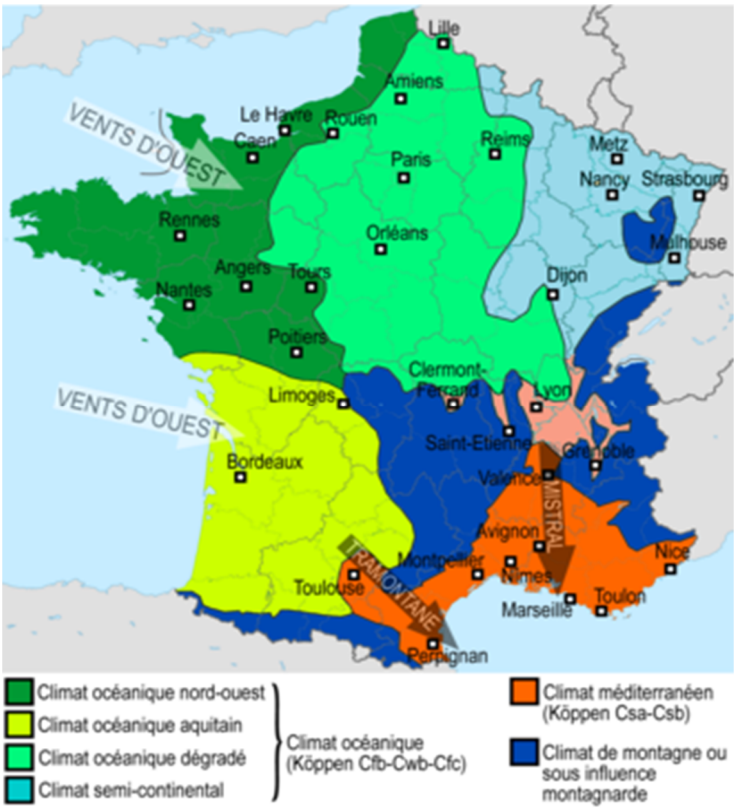

Figure 4.33 - Six climate regions in France

4.3.2 Reference condition and soil parameters

The reference condition consists of a one floor residential building with shallow strip footing of a depth of 0.8m and a width of 0.5m constructed on a non-vegetated soil. It should be mentioned that a typical vertical stress of 60 kPa is considered on the soil at the bottom of the foundation. Different soil types were attributed to each climate regions based on the provided maps of the BRGM for the distribution of soils in France. Based on these maps, it was deduced that the top soil layers in the central region and the north west of France are mostly dominated by loams. On the other hand, the Eastern region and the south west region are mostly dominated by clayey soils. The south cost of France is characterized as clays and clayey loams. Finally, the central south and the south east are dominated by sandy soils in the top layers. This distribution allows to determine the soil movements in each region based on the previously defined climatic parameters for each region.

The performed simulations in this section are based on a homogeneous soil formation hypothesis and single retention properties for each case. Based on the divided regions and the attributed soil type, six reference state can be defined for France in a regional scale. Table 4.4 shows the reference parameters for this six regions. Simulations are primarily performed for each region. Figure 4.34 shows the soil movements calculated for each six regions having different soil properties and different climatic conditions.

Table 4.4 - Reference condition parameters in the divided regions

		Region 1	**Region 2**	**Region 3**	**Region 4**	**Region 5**	**Region 6**
Soil	Texture	Loam	Loam	Clay	Clay	Sand	Clayey loam
	PI (%)	25	25	50	50	10	35
	LL (%)	60	60	80	80	30	70
	w (%)	37	37	30	30	45	33
	e_0	1	1	0.8	0.8	1.2	0.9
	γ_d (Mg/m^3)	1.35	1.35	1.5	1.5	1.2	1.4
	θ_r	0.078	0.078	0.098	0.098	0.065	0.095
	θ_s	0.43	0.43	0.46	0.46	0.55	0.41
	α (1/mm)	0.0036	0.0036	0.0015	0.0015	0.0075	0.0019
	n	1.56	1.56	1.25	1.25	1.89	1.31
	K_s (mm/days)	250	250	147.5	147.5	1061	62.4
Climate	Type	Modified Oceanic	Oceanic	Semi continental	Oceanic Aquitaine	Mountainous climate	Mediterranean
	Location	Center	North West	East	South West	Central south and South East	South
Vegetation	Tree/Grass	N.A.	N.A.	N.A.	N.A.	N.A.	N.A.
	Distance	N.A.	N.A.	N.A.	N.A.	N.A.	N.A.
Structure	Foundation depth (m)	0.8	0.8	0.8	0.8	0.8	0.8
	Foundation width (m)	0.5	0.5	0.5	0.5	0.5	0.5
	Number of floors - Load (kPa)	R+1 60 kPa	R+1 60 kPa	R+1 60 kPa	R+1 60 kPa	R+1 60 kPa	R+1 60 kPa

It can be observed that the maximum swelling under the reference conditions occurs in the south west of France having an oceanic Aquitaine climate type with clayey soils. On the other

hand, the minimum shrinkage occurs in a mountainous climate with sandy soils. Other soils fluctuate in between these two regions. These curves give a general estimation of the soil movements in different regions of France during a specific time frame. It is assumed that the soil hydraulic and mechanical properties are constant in these regions.

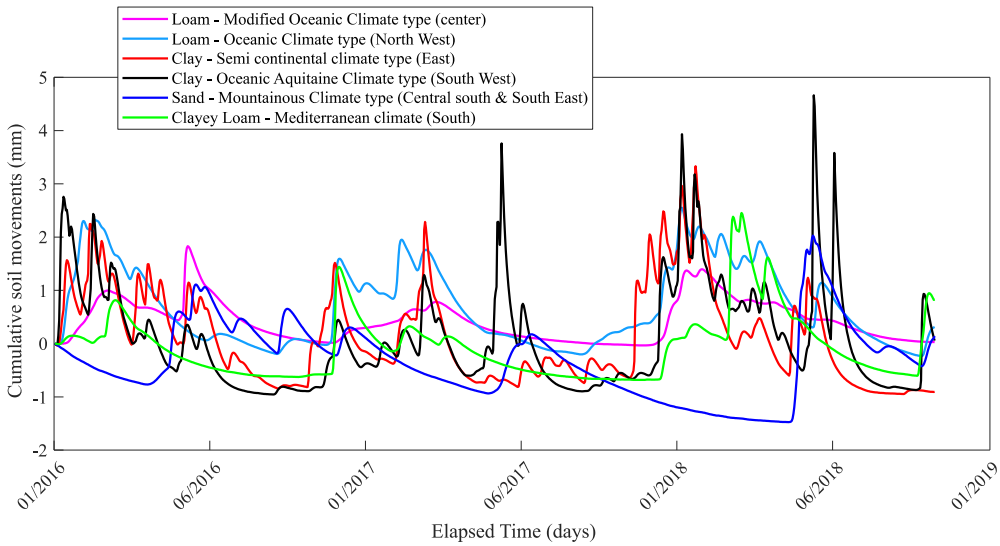

Figure 4.34 - Reference soil movements in six different regions in France

In the following sections a parametric study is performed on some influencing factors on the soil movements in each region. Figure 4.35 shows these different factors along with the reference condition of the structural elements of the building foundation and vegetation conditions.

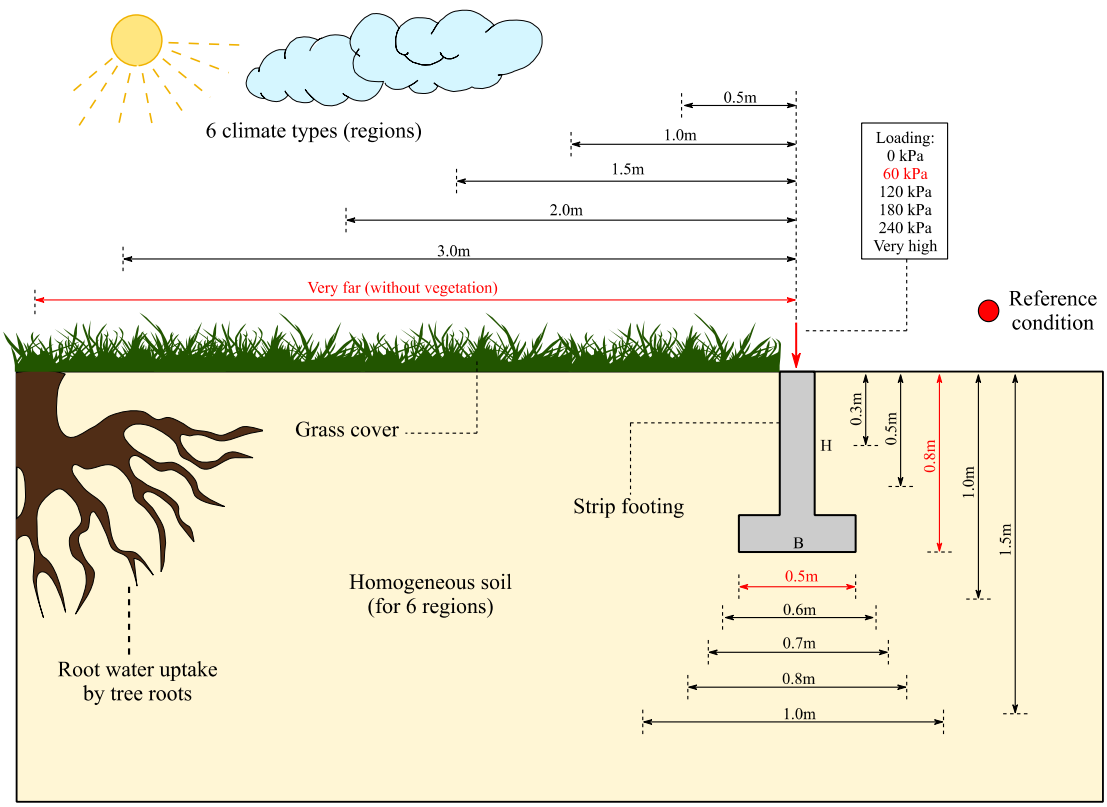

Figure 4.35 - Influencing parameters along with the reference condition calculated for six regions.

4.3.3 Parametric analysis

In this section the influence of the grass cover and the presence of a tree on the soil shrinkage and swelling is investigated in the six considered regions of France. For this purpose, the worst case scenario is considered in which a fruity tree is located close to the building with a vegetated soil cover surrounding the building. The associated parameters are defined using the climatic data in each six regions as described in chapter 2 and 3 for the crop coefficients and the leaf area index which lead to the determination of the transpiration. The root distribution function is supposed to be distributed evenly in the width and the depth of the soil profile (Z_m & $X_m = 2m$, z^* & $x^* = 3m$, p_z & $p_x = 0.4$). The pressure head reduction function of the root water uptake based on the Feddes model is defined by applying the following parameters: ($h_1 = 1\ kPa$, $h_2 = 2.5\ kPa,\ h_{3h} = 20\ kPa,\ h_{3l} = 100\ kPa,\ h_4 = 5000\ kPa$).

The methodology in this section is to investigate the influence of the tree's distance from the building on the soil movements under the footing. Five distances are considered in the analysis as shown in Figure 4.35 along with the reference condition which is simulated without the presence of the tree or the grass cover. Figure 4.36 shows the results of the simulations obtained in each six regions using different reference soil properties and climatic parameters. The simulation results in the first region with a loamy soil type and the modified oceanic climate are presented in Figure 4.36 a). It can be observed that the soil movements reach 40mm when the tree is located 0.5m from the foundation. A slight difference is observed when the tree is located 1.0m from the foundation. Considerable movements are observed when the tree is located 1.5m from the building however, the soil movements are approximately the same as the reference condition (without vegetation) at 2m and 3m from the building. It can be deduced that the influence zone is located 2m from the foundation. Same comments could be made for Figure 4.36 b) to Figure 4.36 f) for the other regions. It can be observed that in Figure 4.36 b) the movements under the foundation reach maximum settlement of 50mm and are greater compared to region 1 which has the same soil type but the difference is due to the climate type i.e. climatic parameters. Maximum settlements observed in the third region are around 15mm as shown in Figure 4.36 c) when the tree is located 0.5m from the foundation. The settlement values are smaller compared to the first and the second region which is because of the soil hydraulic conductivity and retention properties. The drying front in the root zone is dispersed quicker in regions 1, 2, 5 and 6 compared to regions 3 and 4 which are based on clayey soils.

Similar results to region 3 are observed in region 4 as shown in Figure 4.36 d) with slightly lower values compared to region 3 due to the difference in climatic parameters of the regions. Based on the simulation results, larger soil movements are triggered when the tree is closer than 2m from the foundation.

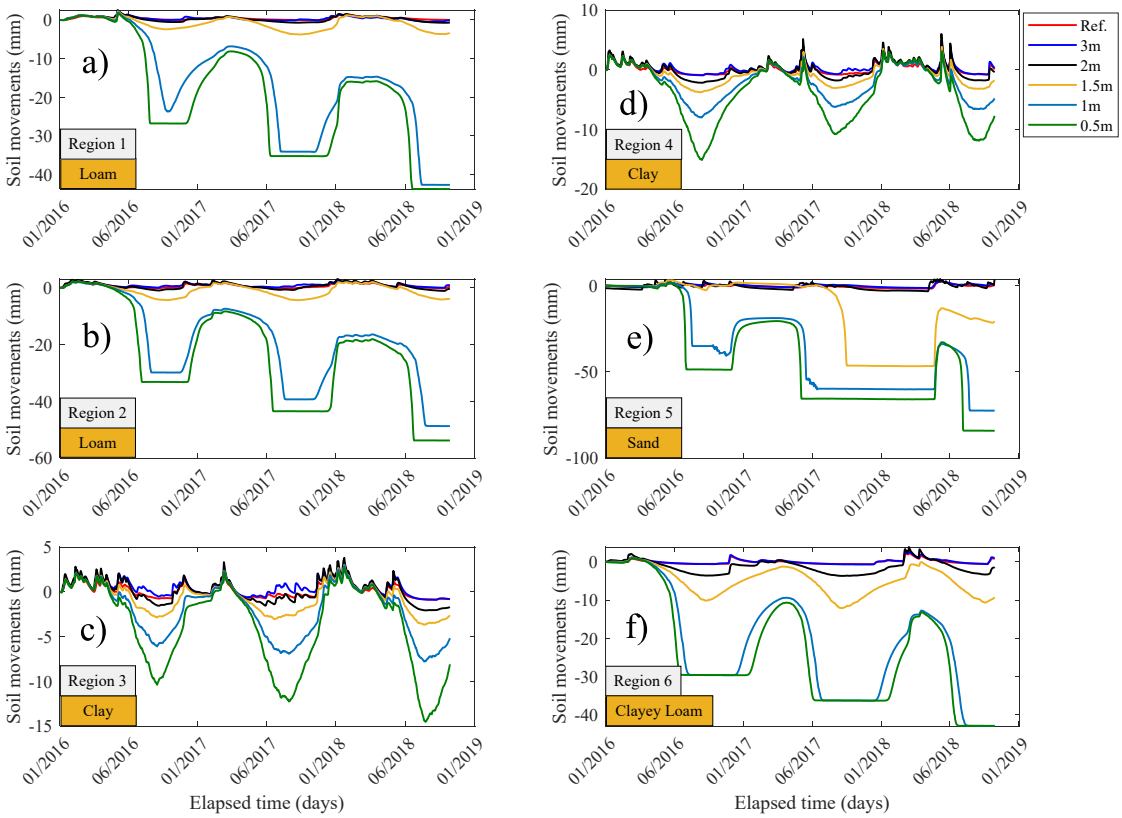

Figure 4.36 - Calculated soil movements at different vegetation (tree) distances from the foundation in six different regions in France.

Thereafter, the influence of the foundation depth and width are investigated on the soil movements under the foundation. The foundation depth is primarily investigated by changing the reference depth (0.8m) to 0.3m, 0.5m, 1m and 1.5m. These changes are made in each six regions. Results are shown in Figure 4.37 for these 6 regions. Figure 4.37 a) shows the soil movements at different foundation depths in the first region. It can be observed that the amplitude of the movements decreases as the depth of the foundation increases. At 1.5m the soil movements are almost negligible. Similar results are obtained for other regions indicating a continuous decrease of the amplitude of the soil movements by increasing the foundation depth. Even though soil movements at 1.5m depth in some regions like 3, 4 and 6 are not completely stabilized, but they stay under the 1mm range as shown in Figure 4.37 c), d) and f). Thus it can be deduced the influence depth of climatic conditions are limited to less than 1.5m by supposing a homogeneous soil layer.

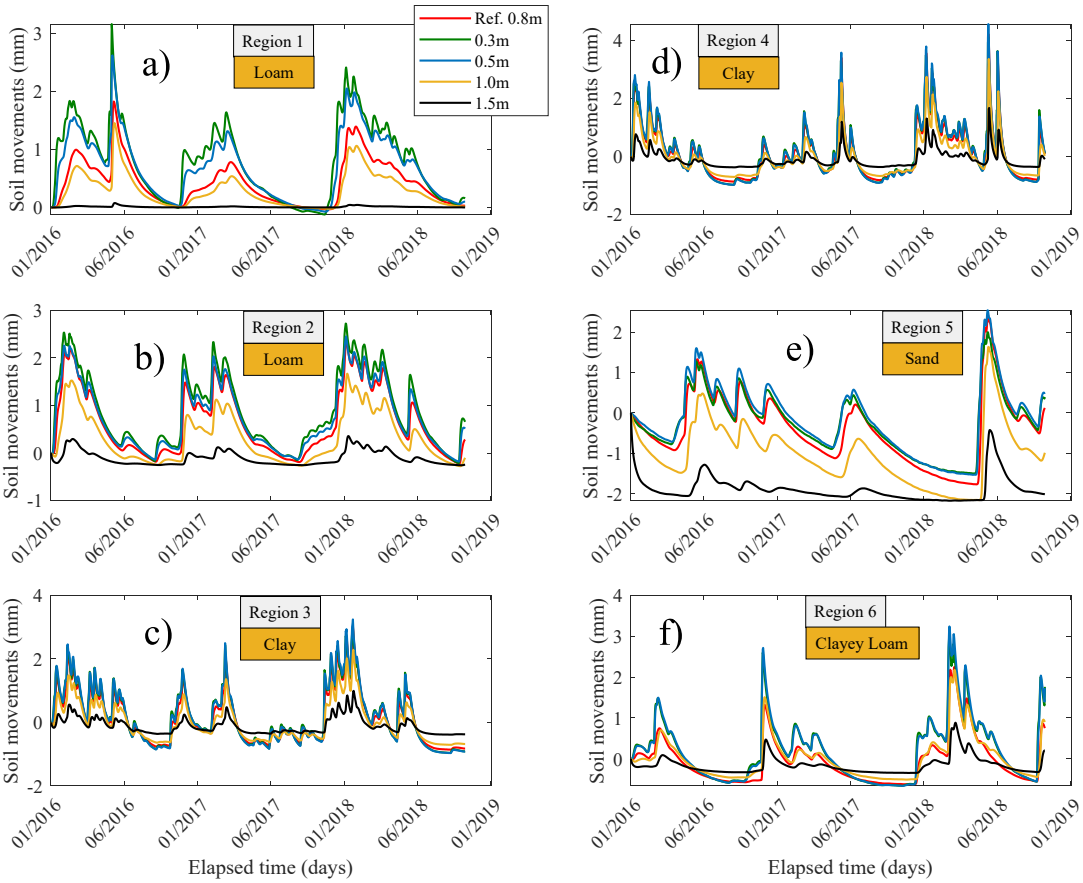

Figure 4.37 - Calculated soil movements at different foundation depth in six regions of France.

The second part concerns the influence of the foundation width on the soil movements. It should be mentioned that this parameter in not only a geometric parameter in the simulation process but also plays a role in the loading conditions of the foundation. The analysis is carried out by increasing the width of the foundation and supposing the same reference structure (one floor building) which have a typical loading condition of 60 kPa. In this conditions, increasing the width of the foundation means a decrease of the loading or the pressure on the soil under the foundation. Each foundation depth represents an applied stress on the soil. Figure 4.38 shows the obtained results for the 6 different regions. The foundation depth is changed from 0.5m to 0.6m, 0.7m, 0.8m, 1m and finally a condition with no foundation (i.e. no loading) on the soil. It can be observed from the results that the difference in the soil movements are negligible and show approximately the same results of the reference conditions. However, the amplitude of the soil movements during zero loading conditions (no foundation) are slightly greater that the reference condition. This could be related to the fact that a one floor building is a lightweight structure and the range of the applied load on the soil does not influence the generated movements by climatic conditions.

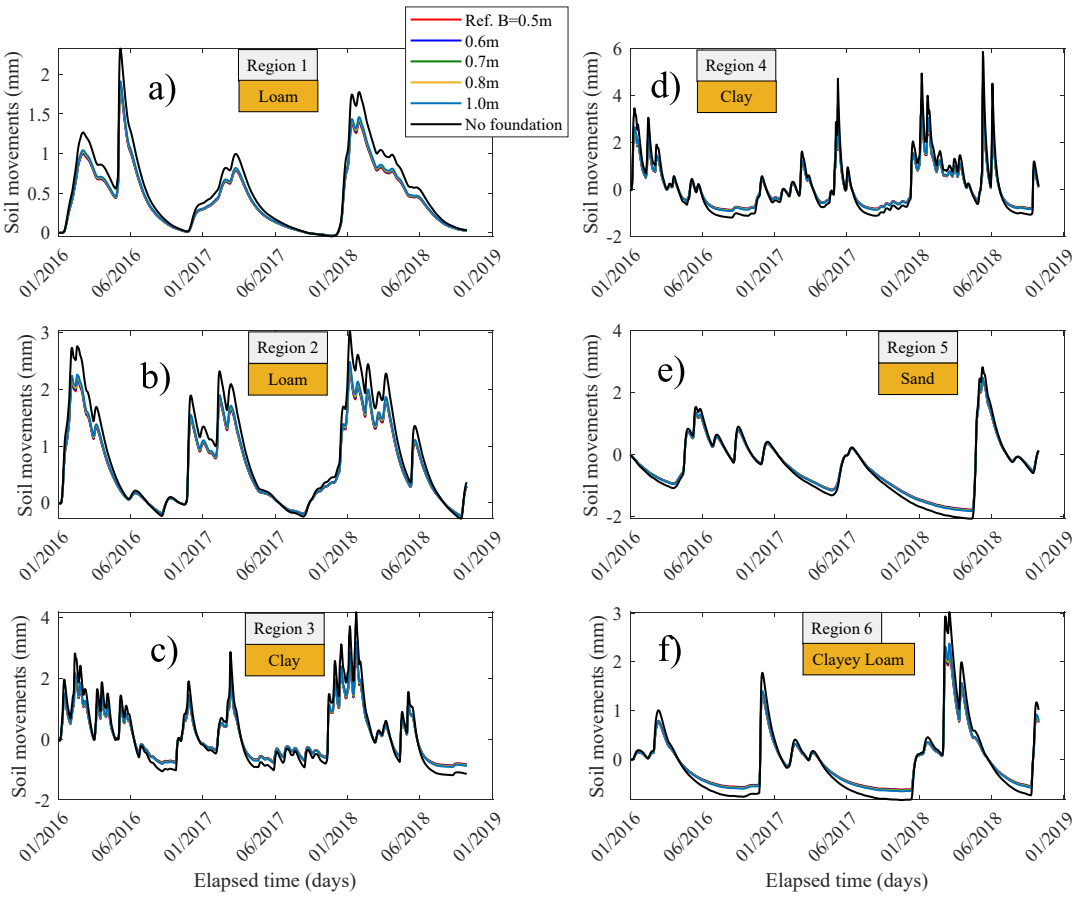

Figure 4.38 - Calculated soil movements for different foundation width in six regions of France.

The influence of the applied stress under the foundation, on the soil movements is also investigated in the six regions of France. The applied reference load is changed to 0 kPa, 120 kPa, 180 kPa, 240 kPa and finally 10 MPa for considering a large loading condition of the soil. Figure 4.39 shows the obtained results in the six considered regions. It can be generally deduced that by increasing the applied stress, the amplitude of the soil movements decrease. However, the range of the applied stresses between 120 kPa and 240 kPa does not seem to have a considerable effect on the soil movements. On the other hand, by increasing roughly the applied stress to more than 10 MPa, the amplitude of the soil movements seems to considerably decrease. This changes are observed in all the regions regardless of the soil type and climatic conditions. It can be deduced from this analysis that for lightweight constructions, the soil movements can be limited by the loading conditions and are dominated by climatic conditions i.e. the soil suction changes over time.

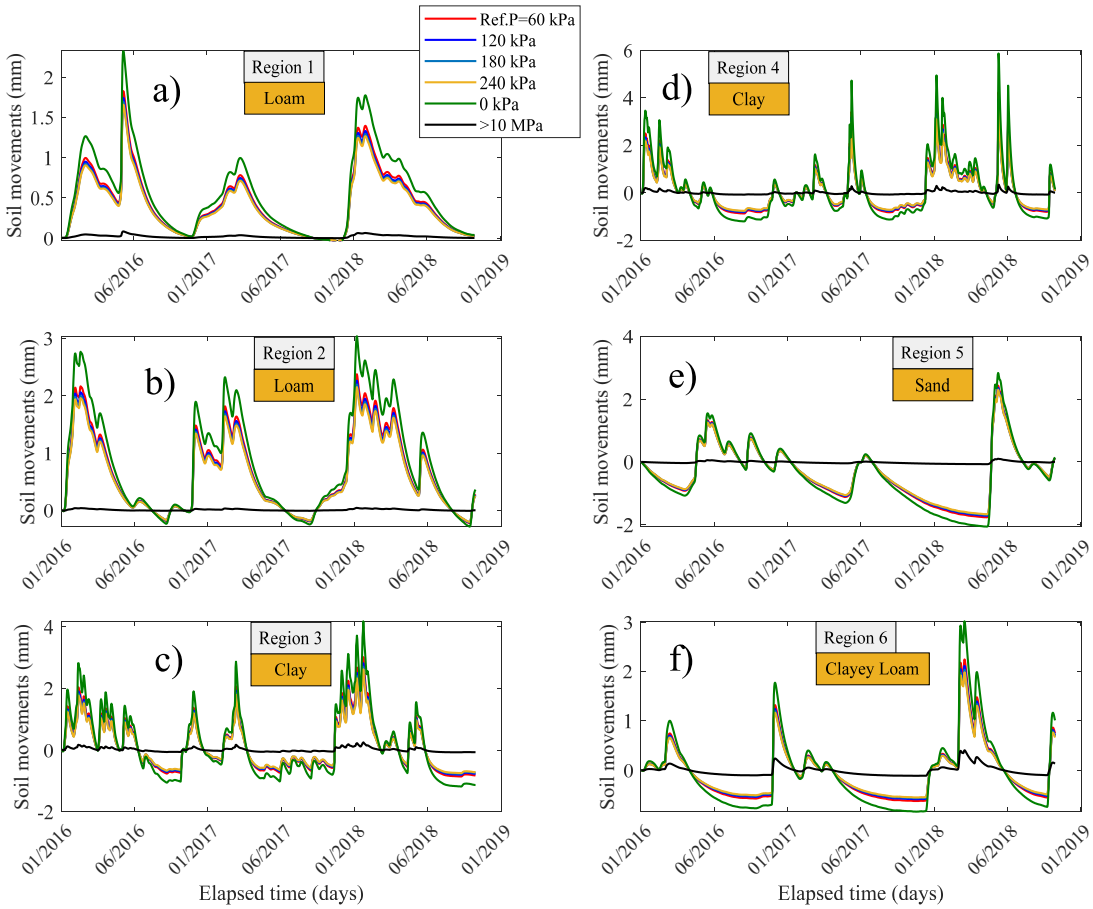

Figure 4.39 - Calculated soil movements at different applied stresses, in six regions of France.

4.4 Conclusion

The proposed modelling approach was extended to explore primarily the shrink-swell behavior of the soil in both (north and south) angles of the building. The results indicate that the solicitations are greater in the north angle of the building due to the impact of both climatic conditions and vegetation effect. To predict the behavior of the soil in the future, the numerical approach was extended to explore the hydro-thermal soil variables along with the soil movements, under three RCP climate change scenarios. The results indicate that the soil suction and consequently the soil movements shows larger values in the north angle of the building which will lead to considerable differential settlement in the future.

The simulation results of the parametric study in this section showed that root water uptake by vegetation influences considerably the soil movements in each six regions if the vegetation species is located less than 2m from the building foundation. It should also be mentioned that the root distribution pattern in a specific case could be different than the employed one in this simulation process.

On the other hand, it was shown that the depth of the foundation plays a considerable role in decreasing the amplitude of the shrinkage and swelling of the soils. It should be mentioned that the calculations were performed by assuming a homogeneous soil layer where the soil physical parameters do not change in depth. A foundation depth of greater than 1.5m can prevent the climatic conditions from influencing the soil movements. However, the analysis performed

on the width of the foundation showed that there is a negligible influence on the soil shrinkage and swelling range in all the considered regions.

Finally, loading conditions in the considered range for lightweight structures showed that the influence on the soil movements are negligible and the amplitude of the shrinkage and swelling is limited by applying higher pressure to the soil.

General conclusion

To answer the needs for the development of simple approaches for evaluating the shrinkage and swelling phenomenon, this research work presented a comprehensive approach for modelling the in-situ soil movements under Soil-Vegetation-Atmosphere interaction conditions using numerical tools. As primarily input parameters, the meteorological data are used to construct the time variable boundary conditions of the hydro-thermal soil model, using the soil-atmosphere interaction concept. In this stage, the mass balance and energy balance equations are used to incorporate the climatic parameters in the coupled model using a simple approach. This approach was validated using actual surface temperature and usual climatic parameters in an experimental site which confirmed the coherence and the applicability of the approach. The approach was then used to determine the natural surface conditions in terms of soil infiltration rate and surface temperature which allowed the determination of the spatial-temporal variations of the hydro-thermal variables using unsaturated heat and moisture flow theory. This includes the variations of the soil suction, water content and temperature in the unsaturated soil medium which are obtained using hydraulic and thermal parameters. A complementary approach was then suggested to determine the soil retention properties using basic geotechnical parameters based on some examined soils in the company. Using the plasticity index and the measured clay content of the soil, the associated retention curves can be deduced with an acceptable accuracy for different swelling range. This method can be used when there is no information on the retention properties of the soils. Comparisons with another previously developed method showed that there is an acceptable agreement in the generated retention curves. In terms of thermal parameters, a water content dependent thermal conductivity function was employed in the hydro-thermal analysis with the adequate soil volumetric heat capacity. In addition to the hydro-thermal parameters, the source term in the unsaturated flow equation was used to incorporate the water uptake by vegetation roots in the analysis. An existing model in the literature (Feddes) was used to model the root water uptake effect on the hydro-thermal variables using adequate parameters of the vegetation crops such as the crop coefficient curve, the root distribution function and the LAI index which led to the determination of the transpiration rate from the soil surface. This allowed the decomposition of the evapotranspiration into soil evaporation and transpiration using the crop coefficient curve. It was deduced from the performed analysis that the root water uptake has a considerable amount of influence on the soil water content and suction and should be taken into account in the simulation process if present on site.

Thereafter, the attention was given to the volume change behavior of unsaturated soils under environmental solicitations. The linear model was used to relate the soil suction time series to the soil void ratio based on the results of experimental tests carried out in the literature. The volume change behavior of a soil was determined using the slopes of the linear model which represents the soil volumetric indices and led to the calculation of the deformations in the soil. These indices were correlated with the basic geotechnical properties by analyzing numerous tested soils in the literature. The parametric study of the developed correlations showed that the prediction range of the soil's volumetric indices are in an acceptable range and can be employed in further analysis for the determination of the soil movements over time. This can reduce the

time and the cost of laboratory tests to determine the volumetric indices. Complementary correlations were also suggested to account for the model's parameters.

The established methodology was then tested by comparing the simulation results with provided data from an instrumented site. The comparison with the hydro-thermal variables showed an acceptable agreement both in the south and the north angle of the building. The simulated soil movements were also in agreement with the field measurements which confirmed the applicability of the proposed method. Changes in the profile variation of the soil water content and temperature during the monitored period, were also observed in the simulation results. Generally, acceptable agreement was observed between the simulated results and the in-situ measurements. The method was then extended in order to explore the influence of the trees on the differential soil movements of the building. Results indicated that the larger soil movements are generated close to the trees in both sides of the building. However, the amplitude of the movements is larger in the north angle of the building which is probably the cause of the observed structural damages. It should also be mentioned that the foundation soil of the building in the south angle is less affected by the climatic conditions than the north angle due to the perimeter cover of the building in the south angle. It is suggested to use perimeter covers in buildings in order to limit the influence depth of the climatic conditions.

In order to have an idea of the future evolution of the simulation variables, i.e. soil water content, suction, temperature, void ratio and the soil movements, the climatic parameters were projected until the year 2050 using three RCP scenarios. The short term and the long-term behavior of the soil were investigated in the considered site. Results indicated that in the short term the RCP scenarios did not show considerable changes expect in the north angle with the RCP 4.5 scenario. However, in the long term, the RCP 8.5 scenario showed to behave in a cyclic manner which could potentially have more impact on the soil in both angles of the building. The differential soil movements close to trees reached considerable values in all three scenarios and the differential soil movements under the foundation soil were mostly important in the RCP 4.5 and 8.5 scenarios. It can be concluded that this kind of analysis could be helpful in order to prevent damages on lightweight constructions. In this specific case, the differential movements close to the trees could potentially affect the building's stability. One of the preventive solutions could be the installation of root barrier systems between the building foundation and the tree (which was employed in this case). The efficiency of this kind of solution can also be verified by modelling approaches and adequate monitoring systems. On the other hand, for limiting the influence zone of the foundation soil due to climate change in the future, perimeter covers could be constructed around the buildings as mentioned previously.

The last section of this thesis dealt with the application of the methodology to the national scale as well as a parametric study. Six reference conditions were defined for France based on the climate type and the associated soil properties to each region. Each reference condition gave the variation of the soil movements over time and were then analyzed by changing the vegetation conditions, the foundation geometry and the loading actions on the foundation soil. Results showed that a distance of at least 2m is required for not being located in the influence distance of the typical vegetation. Otherwise, considerable soil movements and mostly cumulative settlement will be observed under the foundation. On the other hand, it is suggested to build the foundations of the buildings to a depth of at least 1.5m since the influence of the climatic conditions could decrease significantly. However, the width of the foundation soil does not play a

crucial role on the generated soil movements. Finally, the applied stresses to the soil in the range of lightweight constructions do not restrict considerably the soil movements over time.

Some points could be mentioned as recommendations for future research. Regarding the Soil-Vegetation-Atmosphere interaction analysis, simple root water uptake models could be developed to reduce the number of input parameters. Concerning the volume change behavior, the correlations could be improved by adding tested soil data in order to reduce the soil movements estimation errors. Simple correlations could also be made between the soil thermal parameters and the basic geotechnical properties in order to reduce the number of parameters. Another interesting subject to evaluate could potentially be the influence of soil and foundation reinforcement in residential buildings (such as resin injection and micro pile systems) on the soil movement and its possible amount of reduction. This will also require adequate in-situ monitoring and reliable numerical modelling approaches.

The resolution of the national scale analysis can be improved by attributing a climate type and a soil type for each commune of France which will of course require numerous amounts of computing time. Another interesting topic could possibly be the application of the methodology to the French territory using different climate change projection models. This could allow the construction of the future soil movements maps based on different climate change scenarios. In this research work some tested soils by DETERMINANT group were used, however, the number of geotechnical reports in the context of shrink-swell claim management are about 700 reports per year. Therefore, there is the need for evaluating such a huge data base in the French territory. This data base, which is still under construction, could potentially be used to evaluate and improve the methodology in this work. Calculated soil movements throughout the presented methodology can be employed for effective design purposes in residential buildings. This would allow to propose adequate designing methods for different regions of France.

References

Adem, H.H., and Vanapalli, S.K. (2013). Constitutive modeling approach for estimating 1-D heave with respect to time for expansive soils. International Journal of Geotechnical Engineering, 7(2): 199-204.

Adem, H.H., and Vanapalli, S.K. (2014). Soil–environment interactions modelling for expansive soils. Environmental Geotechnics, 3(3): 178-187. doi:10.1680/envgeo.13.00089

Adem, H.H., and Vanapalli, S.K. (2015). Review of methods for predicting in situ volume change movement of expansive soil over time. Journal of Rock Mechanics and Geotechnical Engineering, 7(1): 73-86. doi:10.1016/j.jrmge.2014.11.002.

AFA - L'Association française de l'assurance, 2015.

Airò Farulla, C., Ferrari, A., and Romero, E. (2007). Mechanical behaviour of compacted scaly clay during cyclic controlled-suction testing. Experimental Unsaturated Soil Mechanics, 345-354. Springer, Berlin, Heidelberg.

Airò Farulla, C., Ferrari, A., and Romero, E. (2010). Volume change behaviour of a compacted scaly clay during cyclic suction changes. Canadian Geotechnical Journal, 47(6): 688-703.

Al-Homoud, A.S., Basma, A.A., Husein Malkawi, A.I., and Al Bashabsheh, M.A. (1995). Cyclic swelling behavior of clays. Journal of geotechnical engineering, 121(7): 562-565.

Allen, R.G., Pereira, L.S., Raes, D., and Smith, M. (1998). Crop evapotranspiration-Guidelines for computing crop water requirements-FAO Irrigation and drainage paper 56, 300(9). Fao, Rome.

Alonso, E.E., Gens, A., Josa, A. (1990). A constitutive model for partially saturated soils. Géotechnique, 40(3): 405-30.

Alonso, E.E., Vaunat, J., and Gens, A. (1999). Modelling the mechanical behaviour of expansive clays. Engineering geology, 54(1-2): 173-183. doi:10.1016/S0013-7952(99)00079-4.

Alonso, E.E., Romero, E., Hoffmann, C., and García-Escudero, E. (2005). Expansive bentonite–sand mixtures in cyclic controlled-suction drying and wetting. Engineering geology, 81(3): 213-226. doi:10.1016/j.enggeo.2005.06.009.

Aluwihare, S., and Watanabe, K. (2003). Measurement of evaporation on bare soil and estimating surface resistance. Journal of Environmental Engineering, 129(12): 1157-1168.

An, N., (2017) Numerical Investigation of Soil-Atmosphere Interaction: Application to Embankments of Treated Soils. PhD thesis, Université Paris-Est, Paris.

An, N., Hemmati, S., and Cui, Y.J. (2017a) Numerical analysis of soil volumetric water content and temperature variations in an embankment due to soil-atmosphere interaction. Computers and Geotechnics, 83: 40-51.

An N., Hemmati S., and Cui Y.-J. (2017b) Assessment of the methods for determining net radiation at different time-scales of meteorological variables. Journal of Rock mechanics and Geotechnical Engineering n°9, pp. 239-246. doi:10.1016/j.jrmge.2016.10.004.

An N, Hemmati S, Cui Y-J, Tang C-S. (2018a) Numerical investigation of water evaporation from Fontainebleau sand in an environmental chamber. Engineering Geology, 234: 55–64.

An N. et al. (2018b) Numerical analysis of hydro-thermal behaviour of Rouen embankment under climate effect. Computers and Geotechnics, 99: 137-148. doi:10.1016/j.compgeo.2018.03.008.

Andrieux, C., Chrétien, M., Denis, A., Fabre, R., and Lataste, J.F. (2011). Shrinkage and swelling of clay soil: Comparison between laboratory and in situ measurements. European Journal of Environmental and Civil Engineering, 15(5): 819-838. doi:10.1080/19648189.2011.9693367.

Asner, G.P., Scurlock, J.M., and A. Hicke, J. (2003). Global synthesis of leaf area index observations: implications for ecological and remote sensing studies. Global Ecology and Biogeography, 12(3): 191-205. doi:10.1046/j.1466-822X.2003.00026.x.

Assadollahi H., Nowamooz, H. (2017). Clay-Atmosphere Interaction in a high risk of shrinkage and swelling zone. Scientific research abstracts, XVI International Clay Conference / ICC 2017 Vol. 7, p. 46.

Assadollahi, H., and Nowamooz, H. (2018a). Predicting Swelling Potential and Soil-Water Retention Curves of Some Characterized Expansive Clays Based on Geotechnical Properties. In International Congress and Exhibition" Sustainable Civil Infrastructures: Innovative Infrastructure Geotechnology", 21-36. Springer, Cham. doi:10.1007/978-3-030-01935-8_3.

Assadollahi H., Nowamooz, H. (2018b). The effect of environmental factors on the stability of residential buildings built on expansive clays. In: Hoyos L., McCartney J. (eds) Recent advancements on expansive soils. GeoMEast 2018. Sustainable Civil Infrastructures. Springer, Cham

Assadollahi H., Nowamooz, H. (2018c). Modeling Root Water Uptake, Climate and Unsaturated Vegetated Clays Interactions in the Context of Shallow Foundation Soils. In: Hoyos L., McCartney J. (eds) Novel Issues on Unsaturated Soil Mechanics and Rock Engineering. GeoMEast 2018. Sustainable Civil Infrastructures. Springer, Cham

Assadollahi H., Nowamooz, H. (2018d). Using a Complementary Evapotranspiration Relationship to Estimate Surface Suction for Soil-Atmosphere Interaction Analysis: Wu W., Yu HS. (eds) Proceedings of China-Europe Conference on Geotechnical Engineering.

Assadollahi H., Nowamooz, H. (2018e). In-situ shrinkage and swelling in expansive clays induced by climatic conditions. Proceedings of the 7th international conference on unsaturated soils. Hong Kong, Vol. 2, p. 1043-1048.

Assadollahi H., Nowamooz, H. (2018f). Characterizing drought in the south of France using the standardized precipitation-evapotranspiration index SPEI. Proceedings of the 7th international conference on unsaturated soils. Hong Kong, Vol. 2, p. 1237-1242.

Assadollahi H., Sharma L.K., Dinh A.Q., Tharaud B. (2018a) A New in Situ Measurement Technique for Monitoring the Efficiency of Expansive Polyurethane Resin Injection Under

Shallow Foundations on Clayey Soils. In: Wu W., Yu HS. (eds) Proceedings of China-Europe Conference on Geotechnical Engineering. Springer Series in Geomechanics and Geoengineering. Springer, Cham

Assadollahi, H., Sharma, L.K., Dinh, A.Q., and Tharaud, B. (2018b). Monitoring the Efficiency of Polyurethane Resin Injection for Foundation Remediation in Damaged Residential Buildings Exposed to Expansive Clays. In International Congress and Exhibition" Sustainable Civil Infrastructures: Innovative Infrastructure Geotechnology", pp. 148-157. Springer, Cham.

Aydin, M., Yano, T., Evrendilek, F., and Uygur, V. (2008). Implications of climate change for evaporation from bare soils in a Mediterranean environment. Environmental Monitoring and Assessment, 140: 123-130.

Aydin, M., Yang, S.L., Kurt, N., and Yano, T. (2005). Test of a simple model for estimating evaporation from bare soils in different environments. Ecological Modelling, 182(1): 91-105.

Baille, W., Tripathy, S., and Schanz, T. (2014). Effective stress in clays of various mineralogy. Vadose Zone Journal, 13(5).

Basma, A.A., Al-Homoud, A.S., Malkawi, A.I.H., and Al-Bashabsheh, M.A. (1996). Swelling-shrinkage behavior of natural expansive clays. Applied Clay Science, 11(2-4): 211-227. doi:10.1016/S0169-1317(96)00009-9.

Béchade, A-F., Fabre, R., Mathon, D. (2015). Vegetation, clays and constructions. Symposium International SEC. Marne la Vallée, France.

Benchouk, A., Derfouf, M., Abou-Bekr, N., and Taibi, S. (2013). Behavior of some clays on drying and wetting paths. Arabian Journal of Geosciences, 6(12): 4565-4573. doi:10.1007/s12517-012-0777-1.

Biarez, J., Fleureau, J.M., Zerhouni, M.I., and Soepandji, B.S. (1987). Variations de volume des sols argileux lors de cycles de drainage-humidification. Revue Française de géotechnique, (41): 63-71. doi:10.1051/geotech/1987041063.

Blight, G.E. (1997). Interactions between the atmosphere and the earth. Géotechnique, 47(4): 715-767. doi: 10.1680/geot.1997.47.4.713.

Bowen, I.S. (1926). The ratio of heat losses by conduction and by evaporation from any water surface. Physical Review. 27: 779–787. doi:10.1103/PhysRev.27.779.

Briaud, J.L., Zhang, X., and Moon, S. (2003). Shrink test–water content method for shrink and swell predictions. Journal of geotechnical and geoenvironmental engineering, 129(7): 590-600.

Brutsaert, W. (1982). Evaporation into the atmosphere: Theory. History, and Applications, 1.

Brutsaert, W. (1988). The parameterization of regional evaporation—Some directions and strategies. Journal of Hydrology, 102(1-4): 409-426. doi:10.1016/0022-1694(88)90109-6.

Burt, C.M., Mutziger, A.J., Allen, R.G., and Howell, T.A. (2005). Evaporation research: review and interpretation. Journal of Irrigation and Drainage Engineering, 131(1): 37-58.

Buzzi, O., Fityus, S., Sasaki, Y., and Sloan, S. (2008). Structure and properties of expanding polyurethane foam in the context of foundation remediation in expansive soil. Mechanics of Materials, 40(12): 1012-1021. doi:10.1016/j.mechmat.2008.07.002.

Buzzi, O., Fityus, S., and Sloan, S.W. (2010). Use of expanding polyurethane resin to remediate expansive soil foundations. Canadian Geotechnical Journal, 47(6): 623-634. doi:10.1139/T09-132.

Campbell, G.S. (1985). Soil physics with BASIC: transport models for soil-plant systems, 14. Elsevier, Amsterdam.

Chassagneux, D., Stieljes, L., Mouroux, P., Ménilliet, F., and Ducreux, G.H. (1996). Cartographie de l'aléa retrait-gonflement des sols (sécheresse-pluie) à l'échelle départementale. Approche méthodologique dans les Alpes de Haute-Provence. Rapport BRGM n° R39218, 6.

Chehbouni, A., Seen, D.L., Njoku, E.G., Lhomme, J.P., Monteny, B., and Kerr, Y.H. (1997). Estimation of sensible heat flux over sparsely vegetated surfaces. Journal of Hydrology, 188: 855-868. doi:10.1016/S0022-1694(96)03174-5.

Chen, F.H. (2012). Foundations on expansive soils (Vol. 12). Elsevier.

Chojnicki, B.H., Strzelinski, P., Danielewska, A., and Baran, M. (2010). Tree canopy leaf area index (LAI) measurements with the hemispherical photography at a Tuczno forest. Acta Agrophysica, 179: 89-101.

Chrétien, M. (2010). Compréhension des mécanismes de retrait-gonflement des sols argileux : approche sur site expérimental et analyse de sinistres sur constructions individuelles. PhD These, Université Bordeaux 1.

Chrétien, M., Lataste, J.F., Fabre, R., and Denis, A. (2014). Electrical resistivity tomography to understand clay behavior during seasonal water content variations. Engineering geology, 169: 112-123. doi:10.1016/j.enggeo.2013.11.019.

Chung, S.O., and Horton, R. (1987). Soil heat and water flow with a partial surface mulch. Water Resources Research, 23(12): 2175-2186. doi:10.1029/WR023i012p02175.

Cui, Y.J., and Zornberg, J.G. (2008). Water balance and evapotranspiration monitoring in geotechnical and geoenvironmental engineering. Laboratory and Field Testing of Unsaturated Soils, 171-186. Springer, Dordrecht. doi:10.1007/s10706-008-9198-z.

Cui, Y.J., Gao, Y.B., and Ferber, V. (2010). Simulating the water content and temperature changes in an experimental embankment using meteorological data. Engineering Geology, 114(3-4): 456-471.

Cutler, D.F., and Richardson, I.B. (1989). Tree roots and buildings, Second edition. Longman, Harlow.

Daamen, C.C., and Simmonds, L.P. (1994). Soil, water, energy and transpiration, a numerical model of water and energy fluxes in soil profiles and sparse canopies. Department of Soil Science, 15. University of Reading, Reading.

Dakshanamurthy, V., and Raman, V. (1973). A simple method of identifying an expansive soil. Soils and foundations, 13(1): 97-104. doi:10.3208/sandf1972.13.97.

Dalton, J. (1802). Experimental essays on the constitution of mixed gases; on the force of steam or vapor from water and other liquids in different temperatures, both in a Torricellian vacuum and in air; on evaporation and on the expansion of gases by heat. Memoirs of the Literary and Philosophical Society of Manchester, 5(2): 535-602.

Das, B.M., and Sobhan, K. (2013). Principles of geotechnical engineering. Cengage learning.

De Vries, D.A. (1963). Thermal properties of soils. Physics of plant environment. Amsterdam: 693 North-Holland p. 210-35.

Dei Svaldi, A., Favaretti, M., Pasquetto, A., and Vinco, G. (2005). Analytical modelling of the soil improvement by injections of high expansion pressure resin. Bulletin für angewandte Geologie, 10(2): 71-81.

Delage, P., Suraj De Silva, G.P.R., and Vicol, T. (1992). Suction controlled testing of non saturated soils with an osmotic consolidometer. In 7th International Conference of Expansive Soils, pp. 206-211.

Delage, P., Howat, M.D., and Cui, Y.J. (1998). The relationship between suction and swelling properties in a heavily compacted unsaturated clay. Engineering geology, 50(1-2): 31-48. doi:10.1016/S0013-7952(97)00083-5.

Derriche, Z., and Kebaili, M. (1998). Prévision du gonflement des argiles d'In-Aménas. Bulletin des Laboratoires des ponts et Chaussées, 218: 15-23.

Dif, A.E., and Bluemel, W.F. (1991). Expansive soils under cyclic drying and wetting. Geotechnical Testing Journal, 14(1): 96-102. doi:10.1520/GTJ10196J.

Dobos, E. (2003). Albedo, Encyclopedia of Soil Science, pp. 1-3. doi:10.1081/EESS 120014334.

Elkady, T.Y., Al-Mahbashi, A.M., and Al-Refeai, T.O. (2013). Stress-dependent soil-water characteristic curves of lime-treated expansive clay. Journal of Materials in Civil Engineering, 27(3): 04014127.

Estabragh, A.R., Parsaei, B., and Javadi, A.A. (2015). Laboratory investigation of the effect of cyclic wetting and drying on the behaviour of an expansive soil. Soils and foundations, 55(2): 304-314. doi:10.1016/j.sandf.2015.02.007.

Evett, S.R., and Lascano, R.J. (1993). ENWATBAL. BAS: A mechanistic evapotranspiration model written in compiled BASIC. Agronomy Journal, 85(3): 763-772.

Feddes, R.A., Bresler, E., and Neuman, S.P. (1974). Field test of a modified numerical model for water uptake by root systems. Water Resources Research, 10(6): 1199-1206. doi:10.1029/WR010i006p01199.

Feddes, R.A., Kowalik, P., Kolinska-Malinka, K., and Zaradny, H. (1976). Simulation of field water uptake by plants using a soil water dependent root extraction function. Journal of Hydrology, 31(1-2): 13-26. doi:10.1016/0022-1694(76)90017-2.

Feddes, R.A., Kowalik, P.J., and Zaradny, H. (1978). Water uptake by plant roots. Simulation of field water use and crop yield, pp.16-30.

Feddes, R.A., and Raats, P.A.C. (2004). Parameterizing the soil–water–plant root system. Unsaturated-zone Modeling: Progress, Challenges, Applications, 6: 95-141.

Fernandes, M., Denis, A., Fabre, R., Lataste, J.F., and Chrétien, M. (2015). In situ study of the shrinkage-swelling of a clay soil over several cycles of drought-rewetting. Engineering geology, 192: 63-75. doi:10.1016/j.enggeo.2015.03.017.

Fleureau, J.M., Kheirbek-Saoud, S., Soemitro, R., and Taibi, S. (1993). Behavior of clayey soils on drying–wetting paths. Canadian geotechnical journal, 30(2): 287-296. doi:10.1139/t93-024.

Fleureau, J.M., Verbrugge, J.C., Huergo, P.J., Correia, A.G., and Kheirbek-Saoud, S. (2002). Aspects of the behaviour of compacted clayey soils on drying and wetting paths. Canadian geotechnical journal, 39(6): 1341-1357. doi:10.1139/t02-100.

Fredlund, D.G., and Morgenstern, N.R. (1976). Constitutive relations for volume change in unsaturated soils. Canadian Geotechnical Journal, 13(3): 261-276. doi:10.1139/t76-029.

Fredlund, D.G., and Hasan, J.U. (1979). One-dimensional consolidation theory: unsaturated soils. Canadian Geotechnical Journal, 16(3): 521-531. doi:10.1139/t79-058.

Fredlund, D.G., Rahardjo, H. (1993). Soil mechanics for unsaturated soils. John Wiley and Sons.

Freeze, R.A. (1969). The mechanism of natural ground-water recharge and discharge: 1. One-dimensional, vertical, unsteady, unsaturated flow above a recharging or discharging ground-water flow system. Water Resources Research, 5(1): 153-171.

Frelin, M. (1998). Caractéristiques des fluids. Techniques de l'Ingénieur.

Ganjian, N., Pisheh, Y.P., and Hosseini, S.M.M.M. (2007). Prediction of soil–water characteristic curve based on soil index properties. In Experimental Unsaturated Soil Mechanics, pp. 355-367. Springer, Berlin, Heidelberg. doi:10.1007/3-540-69873-6_36.

Gardner, W. R. (1960). Dynamic aspects of water availability to plants. Soil science, 89(2): 63-73.

Gardner, W.R. (1964). Relation of Root Distribution to Water Uptake and Availability 1. Agronomy Journal, 56(1): 41-45. doi:10.2134/agronj1964.00021962005600010013x.

Gatmiri, B., and Arson, C. (2008). θ-STOCK, a powerful tool of thermohydromechanical behaviour and damage modelling of unsaturated porous media. Computers and Geotechnics, 35(6): 890-915. doi:10.1016/j.compgeo.2008.08.008.

Gelaro, R. et al. (2017). The modern-era retrospective analysis for research and applications, version 2 (MERRA-2). Journal of Climate, 30(14): 5419-5454.

Gens, A., and Alonso, E.E. (1992). A framework for the behaviour of unsaturated expansive clays. Canadian Geotechnical Journal, 29(6): 1013-1032. doi:10.1139/t92-120.

Geo-Slope. (2005). GEO-STUDIO VADOSE/W software package for seepage analysis, Version 6.16. Calgary, Alberta, Canada: Geo-Slope International Ltd.

Gourdier, S., and Plat, E. (2018). Impact du changement climatique sur la sinistralité due au retrait-gonflement des argiles. Journées Nationales de Géotechnique et Géologie de l'Ingénieur (JNGG) 2018.

Hemmati, S. (2009). Etude de l'interaction Sol-Végétation-Atmosphère avec une approche couplée Thermo-Hydro-Mécanique. PhD Thesis, Université Paris-Est.

Hemmati, S., Gatmiri, B., Cui, Y.J., and Vincent, M. (2012). Thermo-hydro-mechanical modelling of soil settlements induced by soil-vegetation-atmosphere interactions. Engineering Geology, 139: 1-16. doi:10.1016/j.enggeo.2012.04.003.

Hillel, D., Beek, V., and Talpaz, H. (1975). A microscopic-scale model of soil water uptake and salt movement to plant roots. Soil Science, 120(5): 385-399.

Hillel, D., and Talpaz, H. (1976). Note Simulation of Root Growth and its Effect on the Pattern of Soil Water Uptake by a Nonuniform Root System. Soil Science, 121(5): 307-312.

Hillel, D. (2004). Introduction to Environmental Soil Physics. Elsevier Academic Press, Amsterdam.

Ho, D.Y.F., Fredlund, D.G., and Rahardjo, H. (1992). Volume change indices during loading and unloading of an unsaturated soil. Canadian Geotechnical Journal, 29(2): 195-207. doi:10.1139/t92-023.

Holmes, R.M. (1961). Estimation of soil moisture content using evaporation data. Proceedings of Hydrology Symposium, 2: 184-196. Canadian National Research Council.

Idso, S.B. (1981). A set of equations for full spectrum and 8 to 14 micron and 10.5 to 12.5 micron thermal radiation from cloudless skies. Water Resources Research, 17(2): 295–304. doi:10.1029/WR017i002p00295.

IPCC - Intergovernmental Panel on Climate Change. Retrieved 22 February 2019.

Irmak, S., Irmak, A., Allen, R.G., and Jones, J.W. (2003). Solar and net radiation-based equations to estimate reference evapotranspiration in humid climates. Journal of Irrigation and Drainage Engineering, pp. 336–347. doi:10.1061/(ASCE)07339437 (2003)129:5(336).

Ito, M., Hu, Y. (2011). Prediction of the behavior of expansive soils. In Proceedings of the 2011 Pan-Am CGS conference, pp. 1-8. Toronto, Ontario.

Ito, M., and Azam, S. (2013). Engineering properties of a vertisolic expansive soil deposit. Engineering Geology, 152(1): 10-16. doi:10.1016/j.enggeo.2012.10.004.

Jahangir, E. (2011). Phénomènes d'interaction sol-structure vis-à-vis de l'aléa retrait-gonflement pour l'évaluation de la vulnérabilité des ouvrages. PhD Thèse, Institut National Polytechnique de Lorraine-INPL.

Jahangir, E., Deck, O., and Masrouri, F. (2013). An analytical model of soil–structure interaction with swelling soils during droughts. Computers and Geotechnics, 54: 16-32. doi:10.1016/j.compgeo.2013.05.009.

Jones Jr, D.E., and Holtz, W.G. (1973). Expansive soils-the hidden disaster. Civil Engineering, 43(8): 49-51.

Karunarathne, A.M.A.N., et al. (2018). Modelling of climate induced moisture variations and subsequent ground movements in expansive soils. Geotechnical and Geological Engineering, 36(4): 2455-2477.

Kassiff, G., and Shalom, A.B. (1971). Experimental relationship between swell pressure and suction. Géotechnique, 21(3): 245-255.

Kodikara, J.K., and Choi, X. (2006). A simplified analytical model for desiccation cracking of clay layers in laboratory tests. Geotechnical special publication, 147(2): 2558.

Kondo, J., Saigusa, N., and Sato, T. (1990). A parameterization of evaporation from bare soil surfaces. Journal of Applied Meteorology, 29(5): 385-389.

Kramer, P.J. (1933). The intake of water through dead root systems and its relation to the problem of absorption by transpiring plants. American Journal of Botany, 20(7): 481-492. doi:10.1002/j.1537-2197.1933.tb08905.x.

Krisdani, H., Rahardjo, H., and Leong, E.C. (2008). Effects of different drying rates on shrinkage characteristics of a residual soil and soil mixtures. Engineering Geology, 102(1-2): 31-37. doi:10.1016/j.enggeo.2008.07.003.

Lal, R., Shukla, M.R. (2004). Principles of Soil Physics. Marcel Dekker, CRC Press., New York.

Li, Z.S. et al. (2017). Global representation of the drying–wetting curves of four engineering soils: experiments and correlations. Acta Geotechnica, 13(1): 51-71. doi:10.1007/s11440-017-0527-3.

Li, Z.S. et al. (2018). Volume change behavior of two compacted clayey soils under hydraulic and mechanical loadings. Journal of Geotechnical and Geoenvironmental Engineering, 144(4): 04018013.

Li, K.Y., Boisvert, J.B., and Jong, R.D. (1999). An exponential root-water-uptake model. Canadian Journal of soil science, 79(2): 333-343. doi:10.4141/S98-032.

Li, J.H., and Zhang, L.M. (2011). Study of desiccation crack initiation and development at ground surface. Engineering Geology, 123(4): 347-358. doi:10.1016/j.enggeo.2011.09.015.

Linacre, E.T. (1992). Climate data and resources: A reference and guide, Routledge Press, London, 149–185.

Linacre, E.T. (1993). Data-sparse estimation of lake evaporation, using a simplified Penman equation. Agricultural and Forest Meteorology, 64(3-4): 237-256.

Liu, X., Buzzi, O., Yuan, S., Mendes, J., and Fityus, S. (2015). Multi-scale characterization of retention and shrinkage behaviour of four Australian clayey soils. Canadian Geotechnical Journal, 53(5): 854-870. doi:10.1139/cgj-2015-0145.

Lloret, A., and Alonso, E.E. (1980). Consolidation of unsaturated soils including swelling and collapse behaviour. Géotechnique, 30(4): 449-477. doi:10.1680/geot.1980.30.4.449.

Lloret, A., Gens, A., Batlle, F., and Alonso, EE. (1987). Flow and deformation analysis of partially saturated soils. Hanrahan ET, Orr TLL, Widdis TF, editors. Proceedings of the 9th European conference on soil mechanics and foundation engineering, pp. 565-8, Dublin. Rotterdam, the Netherlands: A.A. Balkema.

Lu, N., and Dong, Y. (2015). Closed-form equation for thermal conductivity of unsaturated soils at room temperature. Journal of Geotechnical and Geoenvironmental Engineering. doi:10.1061/(ASCE)GT.1943-5606.0001295, 04015016.

Lu, S., Ren, T.S., Gong, Y.S., and Horton, R. (2007). An improved model for predicting soil thermal conductivity from water content. Soil Science Society of America Journal, 71: 8-14. doi:10.2136/sssaj2006.0041.

Luo, Y., Ouyang, Z., Yuan, G., Tang, D., and Xie, X. (2003). Evaluation of macroscopic root water uptake models using lysimeter data. Transactions of the ASAE, 46(3): 625. doi:10.13031/2013.13598.

Mahfouf, J. F., and Noilhan, J. (1991). Comparative study of various formulations of evaporations from bare soil using in situ data. Journal of Applied Meteorology, 30(9): 1354-1365.

Marinho, F.A.M. (1994). Shrinkage behaviour of some plastic soils. PhD These, University of London.

Mathon, D., and Godefroy, A. (2015). Monitoring of an instrumented house damaged by drought. In Symposium International SEC, Marne la Vallée.

Mathur, S. (1999). Settlement of soil due to water uptake by plant roots. International journal for numerical and analytical methods in geomechanics, 23(12): 1349-1357.

Mbonimpa, M., Aubertin, M., Maqsoud, A., and Bussière, B. (2006). Predictive model for the water retention curve of deformable clayey soils. Journal of Geotechnical and Geoenvironmental Engineering, 132(9): 1121-1132.

McKee, T.B. (1995). Drought monitoring with multiple time scales. Proceedings of 9th Conference on Applied Climatology, Boston.

McKee, T.B., Doesken, N.J., and Kleist, J. (1993). The relationship of drought frequency and duration to time scales. Proceedings of the 8th Conference on Applied Climatology, 17(22): 179-183. MA: American Meteorological Society, Boston.

Molz, F.J., and Remson, I. (1970). Extraction term models of soil moisture use by transpiring plants. Water Resources Research, 6(5): 1346-1356. doi:10.1029/WR006i005p01346.

Molz, F.J., and Remson, I. (1971). Application of an Extraction-Term Model to the Study of Moisture Flow to Plant Roots 1. Agronomy Journal, 63(1): 72-77. doi:10.2134/agronj1971.00021962006300010023x.

Molz, F.J., and Remson, I. (1981). Models of water transport in the soil–plant system: A review. Water Resources Research, 17(5): 1245–1260.

Monteith, J. L. (1973). Principles of environmental physics, Edward Arnold, London, 241.

Monteith, J.L., and Szeicz, G. (1961). The radiation balance of bare soil and vegetation. Quarterly Journal of the Royal Meteorological Society, 87(372): 159-170. doi:10.1002/qj.49708737205.

Mrad, M. (2005). Modélisation du comportement hydromécanique des sols gonflants non saturés. PhD These, Institut National Polytechnique de Lorraine-INPL.

Mualem, Y. (1976). A new model for predicting the hydraulic conductivity of unsaturated porous media. Water resources research, 12(3): 513-522. doi:10.1029/WR012i003p00513.

Musy, A., and Higy, C. (2004). Hydrologie: Tome 1, Une science de la nature. Presses Polytechniques et Universitaires Romandes (PPUR).

Nelson, J.D., Chao, K.C., and Overton, D.D. (2007). Definition of expansion potential for expansive soil. In Proceedings of the Third Asian Conference on Unsaturated Soils.

Nelson, J.D., and Miller, D.J. (1997). Expansive soils: problems and practice in foundation and pavement engineering. John Wiley & Sons.

Nelson, J.D., Reichler, D.K., and Cumbers, J.M. (2006). Parameters for heave prediction by oedometer tests. In Proceedings of the Fourth International Conference on Unsaturated Soils 2006, pp. 951-961.

Ng, C.W.W., Sadeghi, H., Hossen, S.B., Chiu, C.F., Alonso, E.E., and Baghbanrezvan, S. (2016). Water retention and volumetric characteristics of intact and re-compacted loess. Canadian Geotechnical Journal, 53(8): 1258-1269. doi:10.1139/cgj-2015-0364.

Notton, G., Cristofari, C., and Poggi, P. (2006). Performance evaluation of various hourly slope irradiation models using Mediterranean experimental data of Ajaccio. Energy Conversion and Management, 47(2): 147-173. doi: 10.1016/j.enconman.2005.03.022.

Nowamooz, H. (2007). Swelling/shrinkage of compacted and natural clayey soils. PhD These, Institut National Polytechnique de Lorraine-INPL.

Nowamooz, H. (2016). Resin injection in clays with high plasticity. Comptes Rendus Mécanique, 344(11-12): 797-806. doi: 10.1016/j.crme.2016.09.001.

Nowamooz, H., Jahangir, E., and Masrouri, F. (2013). Volume change behaviour of a swelling soil compacted at different initial states. Engineering Geology, 153: 25-34. doi: 10.1016/j.enggeo.2012.11.010.

Nowamooz, H., Jahangir, E., Masrouri, F., and Tisot, J.P. (2016). Effective stress in swelling soils during wetting drying cycles. Engineering geology, 210: 33-44. doi:10.1016/j.enggeo.2016.05.021.

Nowamooz, H., and Masrouri, F. (2009). Density-dependent hydromechanical behaviour of a compacted expansive soil. Engineering Geology, 106(3-4): 105-115. doi: 10.1016/j.enggeo.2009.03.010.

Nowamooz, H., and Masrouri, F. (2010). Relationships between soil fabric and suction cycles in compacted swelling soils. Engineering geology, 114(3-4): 444-455. doi: 10.1016/j.enggeo.2010.06.005.

Nowamooz, H., Mrad, M., Abdallah, A., and Masrouri, F. (2009). Experimental and numerical studies of the hydromechanical behaviour of a natural unsaturated swelling soil. Canadian Geotechnical Journal, 46(4): 393-410. doi:10.1139/T08-127.

Nyambayo, V.P., and Potts, D.M. (2010). Numerical simulation of evapotranspiration using a root water uptake model. Computers and Geotechnics, 37(1-2): 175-186. doi: 10.1016/j.compgeo.2009.08.008.

Overton, D.D., Chao, K.C., and Nelson, J.D. (2006). Time rate of heave prediction for expansive soils. In GeoCongress 2006: Geotechnical Engineering in the Information Technology Age, pp. 1-6.

Penman, H.L. (1948). Natural evaporation from open water, bare soil and grass. Proceedings of the Royal Society of London. Series A. Mathematical and Physical Sciences, 193(1032): 120-145.

Piran, J.P., Donsimoni, M., Vincent, M. (2000). Cartographie de l'aléa retrait-gonflement des argiles dans le dépatement de l'Essonne. Rapport BRGM n° RP-50376-FR, p. 269.

Prasad, R. (1984). Influence of time step in the simulation modelling of evapotranspiration. Sadhana, 7(2): 91-118.

Prasad, R. (1988). A linear root water uptake model. Journal of Hydrology, 99(3-4): 297-306.

Priestley, C.H.B., and Taylor, R.J. (1972). On the assessment of surface heat flux and evaporation using large-scale parameters. Monthly weather review, 100(2): 81-92.

Qu, W., et al. (2016). The integrated water balance and soil data set of the Rollesbroich hydrological observatory. Earth System Science Data, 8(2): 517-529.

Rajeev, P., Chan, D., and Kodikara, J. (2012). Ground–atmosphere interaction modelling for long-term prediction of soil moisture and temperature. Canadian Geotechnical Journal, 49(9): 1059-1073. doi:10.1139/t2012-068.

Richards, L. A. (1931). Capillary conduction of liquids through porous mediums. Physics, 1(5), 318-333. doi:10.1063/1.1745010.

Richards, B.G. (1974). Behavior of unsaturated soils. In Lee IK, editor. Soil mechanics - new horizons, 112-57. Elsevier, New York, USA.

Richards, B.G., Peter, P., and Emerson, W.W. (1983). The effects of vegetation on the swelling and shrinking of soils in Australia. Geotechnique, 33(2): 127-139. doi: 10.1680/geot.1983.33.2.127.

Robinet, J.C., Pasquiou, A., Jullien, A., Belanteur, N., and Plas, F. (1997). Expériences de laboratoire sur le comportement thermo-hydro-mécanique de matériaux argileux remaniés gonflants et non gonflants. Revue française de géotechnique, (81): 53-80. doi:10.1051/geotech/1997081053.

Rohwer, C. (1931). Evaporation from free water surfaces, Technical Bulletin 271.

Romanenko, V.A. (1961). Computation of the autumn soil moisture using a universal relationship for a large area. Proc. of Ukrainian Hydrometeorological Research Institute, 3: 12-25.

Sabbagh, A. (1997). Stress and suction in the volume change of unsaturated expansive soils. In Proceedings of the International Conference on Soil Mechanics and Foundation Engineering-International Society for Soil Mechanics and Foundation Engineering, 1: 395-398. AA BALKEMA.

Santanello Jr, J.A., and Friedl, M.A. (2003). Diurnal covariation in soil heat flux and net radiation. Journal of Applied Meteorology, 42(6): 851-862.

Santarato, G., Ranieri, G., Occhi, M., Morelli, G., Fischanger, F., and Gualerzi, D. (2011). Three-dimensional Electrical Resistivity Tomography to control the injection of expanding resins for the treatment and stabilization of foundation soils. Engineering Geology, 119(1-2): 18-30. doi: 10.1016/j.enggeo.2011.01.009.

Sedighi, M., Hepburn B.D.P., Thomas, H.R. and Vardon P.J. (2018) Energy balance at the soil atmospheric interface. Environmental Geotechnics, 5(3): 146-157.

Seed, H.B., and Lundgren, R. (1962). Prediction of swelling potential for compacted clays. Journal of the soil mechanics and foundations division, 88(3): 53-88.

Šejna, M., and Šimůnek, J. (2007). HYDRUS (2D/3D): Graphical user interface for the HYDRUS software package simulating two-and three-dimensional movement of water, heat, and multiple solutes in variably-saturated media. Available at www.pc-progress.cz (verified 20 Feb. 2008). PC-Progress, Prague, Czech Republic.

Shams, M.A., Shahin, M.A., and Ismail, M.A. (2018). Simulating the behavior of reactive soils and slab foundations using hydro-mechanical finite element modelling incorporating soil suction and moisture changes. Computers and Geotechnics, 98: 17-34. doi: 10.1016/j.compgeo.2018.01.013.

Simunek, J., Huang, K., and Van Genuchten, M.T. (1995). The SWMS_3D code for simulating water flow and solute transport in three-dimensional variably-saturated media. US Salinity Laboratory Agricultural Research Service, (139).

Šimůnek, J., Van Genuchten, M.T., and Sejna, M. (2006). The HYDRUS software package for simulating the two-and three-dimensional movement of water, heat, and multiple solutes in variably-saturated media. Technical manual, 1. PC Progress, Prague, Czech 539 Republic, pp. 241.

Singh, V.P. (1988). Hydrologic systems: watershed modeling, 2. Prentice Hall.

Song, W. (2014). Experimental investigation of water evaporation from sand and clay using an environmental chamber. PhD Thesis, Université Paris-Est.

Sophocleous, M. (1979). Analysis of water and heat flow in unsaturated-saturated porous media. Water Resources Research, 15(5): 1195-1206. doi:10.1029/WR015i005p01195.

Soubeyroux, J.M., Vidal, J.P., Najac, J., Kitova, N., Blanchard, M., Dandin, P., Martin, E., Pagé, C., and Habets, F. (2011). Projet ClimSec: Impact du changement climatique en France sur la sécheresse et l'eau du sol. Météo-France, Toulouse, France.

Staniec, M., and Nowak, H. (2016). The application of energy balance at the bare soil surface to predict annual soil temperature distribution. Energy and Buildings, 127: 56-65. doi:10.1016/j.enbuild.2016.05.047.

Sun, D.A., Sheng, D.C., Cui, H.B., and Sloan, S.W. (2007). A density-dependent elastoplastic hydro-mechanical model for unsaturated compacted soils. International journal for numerical and analytical methods in geomechanics, 31(11): 1257-1279.

Ta, A.N. (2009). Etude de l'interaction sol-atmosphère en chambre environnementale. PhD Thesis, Ecole des Ponts ParisTech.

Tanner, C.B. (1968). Evaporation of water from plants and soil. Kozlowski, T.T. ed. Water deficits and plant growth, 1. Academic press, New York.

Terzaghi, K.V. (1936). The shearing resistance of saturated soils and the angle between the planes of shear. In First international conference on soil Mechanics, 1: 54-59.

Thornthwaite, C.W. (1948). An approach toward a rational classification of climate. Geographical review, 38: 55-94.

Tripathy, S., and Rao, K.S.S. (2009). Cyclic swell–shrink behaviour of a compacted expansive soil. Geotechnical and Geological Engineering, 27(1): 89-103.

Tripathy, S., Rao, K.S.S., and Fredlund, D.G. (2002). Water content-void ratio swell-shrink paths of compacted expansive soils. Canadian geotechnical journal, 39(4): 938-959. doi:10.1139/t02-022.

Turc, L. (1954). Le bilan d'eau des sols. Relation entre les précipitations, l'évaporation et l'écoulement. Annales Agronomique, 5: 491-596.

Turc, L. (1955). Le bilan d'eau des sols. Relation entre les précipitations, l'évaporation et l'écoulement. Annales Agronomique, 6: 5-131.

Valentino, R., Romeo, E., and Stevanoni, D. (2014). An experimental study on the mechanical behaviour of two polyurethane resins used for geotechnical applications. Mechanics of Materials, 71: 101-113. doi:10.1016/j.mechmat.2014.01.007.

Van Bavel, C.H.M., and Hillel, D.I. (1976). Calculating potential and actual evaporation from a bare soil surface by simulation of concurrent flow of water and heat. Agricultural Meteorology, 17(6): 453-476. doi:10.1016/0002-1571(76)90022-4.

Van Genuchten, M.T. (1980). A closed-form equation for predicting the hydraulic conductivity of unsaturated soils 1. Soil science society of America journal, 44(5): 892-898.

Van Genuchten, M.T. (1987). A numerical model for water and solute movement in and below the root zone. United States Department of Agriculture Agricultural Research Service US Salinity Laboratory.

Vanapalli, S.K., and Fredlund, D.G. (2000). Comparison of different procedures to predict unsaturated soil shear strength. Geotechnical Special Publication, 195-209.

Verhoff, A., Allen, S.J., and Lloyd, C.R. (1999). Seasonal variation of surface energy balance over two sahelian surface. International Journal of Climatology, 19(11): 1267–1277.

Vijayvergiya, V.N., and Ghazzaly, O.I. (1973). Prediction of swelling potential for natural clays. In Proceedings of the 3rd International Conference on Expansive Soils, 1: 227-236.

Vincent, M., et al. (2009). Rapport de synthèse final du projet ARGIC (Analyse du retrait/gonflement et de ses incidences sur les constructions). Projet ANR-05-PRGCU-005. Rapport BRGM/RP-57011-FR en partenariat entre le Centre de géosciences, le BRGM, le LMSSMat, le CERMES, Fondasol, l'INERIS, le LAEGO, l'INRA, le LGCIE, le LCPC, Météo-France, le GHYMAC et l'université de Poitiers, 29.

Vicente-Serrano, S.M., Beguería, S., and López-Moreno, J.I. (2010). A multiscalar drought index sensitive to global warming: the standardized precipitation evapotranspiration index. Journal of climate, 23(7): 1696-1718.

Vidal, J.P., Marin, E., Franchisteguy, L., Baillon, M., Soubeyroux, J.M., (2010). A 50-year high-resolution atmospheric reanalysis over France with the Safran system. International Journal of Climatology, 30: 1627–1644.

Vogel, T. (1987). SWMII - Numerical model of two-dimensional flow in a variably saturated porous medium, Research Report No. 87, Department of Hydraulics and Catchment Hydrology, Agricultural University, Wageningen.

Vrugt, J.A., Bouten, W., Gupta, H.V., and Sorooshian, S. (2002). Toward improved identifiability of hydrologic model parameters: The information content of experimental data. Water Resources Research, 38(12): 48-1. doi:10.1029/2001WR001118.

Vrugt, J.A., Bouten, W., and Weerts, A.H. (2001a). Information content of data for identifying soil hydraulic parameters from outflow experiments. Soil Science Society of America Journal, 65: 19–27.

Vrugt, J.A., Hopmans, J.W., and Šimůnek, J. (2001b). Calibration of a twodimensional root water uptake model for a sprinkler-irrigated almond tree. Soil Science Society of America Journal, in press.

Vrugt, J.A., Van Wijk, M.T., Hopmans, J.W., and Šimůnek, J. (2001). One-, two-, and three-dimensional root water uptake functions for transient modeling. Water Resources Research, 37(10): 2457-2470. doi:10.1029/2000WR000027.

Vu, H.Q., and Fredlund, D.G. (2004). The prediction of one-, two-, and three-dimensional heave in expansive soils. Canadian Geotechnical Journal, 41(4): 713-737. doi:10.1139/t04-023.

Vu, H.Q., and Fredlund, D.G. (2006). Challenges to modelling heave in expansive soils. Canadian Geotechnical Journal, 43(12): 1249-1272. doi:10.1139/t06-073.

Wilson, G.W. (1990). Soil evaporative fluxes for geotechnical engineering problems. PhD Thesis, University of Saskatchewan, Saskatoon, Saskatchewan, Canada.

Wilson, G.W., Fredlund, D.G., and Barbour, S.L. (1994). Coupled soil-atmosphere modelling for soil evaporation. Canadian Geotechnical Journal, 31(2): 151-161. doi:10.1139/t94-021.

Wilson, G.W., Fredlund, D.G., and Barbour, S.L. (1997). The effect of soil suction on evaporative fluxes from soil surfaces. Canadian Geotechnical Journal, 34(1): 145-155.

Wray, W.K. (1997). Using soil suction to estimate differential soil shrink or heave. In Unsaturated Soil Engineering Practice, 66-87. ASCE.

Wray, W.K., El-Garhy, B.M., and Youssef, A.A. (2005). Three-dimensional model for moisture and volume changes prediction in expansive soils. Journal of Geotechnical and Geoenvironmental Engineering, 131(3): 311-324.

Wright, J. L. (1982). New evapotranspiration crop coefficients. Journal of the Irrigation and Drainage Division, 108(IR2): 57–74.

Wu, J., Zhang, R., and Gui, S. (1999). Modeling soil water movement with water uptake by roots. Plant and soil, 215(1): 7-17.

Yahia-Aïssa, M. (1999). Comportement hydromécanique d'une argile gonflante fortement compactée. PhD These. Ecole nationale des ponts et chaussees, spécialité : geotechnique.

Yigzaw, Z. (2009). Analyse des processus de retrait-gonflement de sols argileux en réponse à des sollicitations hydriques cycliques : rôle de la microstructure. PhD Thesis, ENMP, Paris.

Zemenu, G., Martine, A., and Roger, C. (2009). Analysis of the behaviour of a natural expansive soil under cyclic drying and wetting. Bulletin of Engineering Geology and the Environment.

Zhang, J., Sun, D.A., Zhou, A., and Jiang, T. (2015). Hydromechanical behaviour of expansive soils with different suctions and suction histories. Canadian Geotechnical Journal, 53(1): 1-13. doi:10.1139/cgj-2014-0366.

Zhang X. (2004). Consolidation theories for saturated-unsaturated soils and numerical simulations of residential buildings on expansive soils. PhD Thesis, USA: Texas A&M University, College Station, Texas.

Zhang, X., and Briaud, J.L. (2015). Three dimensional numerical simulation of residential building on shrink–swell soils in response to climatic conditions. International Journal for Numerical and Analytical Methods in Geomechanics, 39(13): 1369-1409. doi:10.1002/nag.2360.

Zhao, N.F., Ye, W.M., Chen, Y.G., Chen, B., and Cui, Y.J. (2019). Investigation on swelling-shrinkage behavior of unsaturated compacted GMZ bentonite on wetting-drying cycles. Bulletin of Engineering Geology and the Environment, 78(1): 617-627.

Zhou, W.H., and Xu, X. (2016). Shear strength of unsaturated completely decomposed granite soil under different stress state conditions. Japanese Geotechnical Society Special Publication, 2(4): 230-235. doi:10.3208/jgssp.HKG-16.

A. Appendix

Appendix 1: Resin injection for controlling expansive soils

A1.1 Introduction

Few traditional methods for repairing and controlling damaged constructions due to expansive soils were discussed in chapter 1. Although these methods are reliable for geotechnical engineers, but they are not always cost effective and can be very expensive in some cases and the way they are executed on the site is sometimes complicated and time consuming. The alternative method recently adapted and developed for repairing damaged and cracked buildings, is the injection of expansive polyurethane resin into the supporting soil. The injected resin, densifies the soil by expanding itself and increases the soil density and bearing capacity. Although this method is much more cost effective and is not time consuming but the evaluation of its efficiency stays a big challenge. Many authors showed that it could be very efficient in laboratory scale by studying its physical and mechanical characteristics (Buzzi et al., 2008; Buzzi et al., 2010 Valentino et al. 2014, Svaldi et al. 2005). Santarato et al. (2011) investigated its expansion into the soil by using 3D electrical tomography technique. Nowamooz (2016) investigated its expansion using numerical methods.

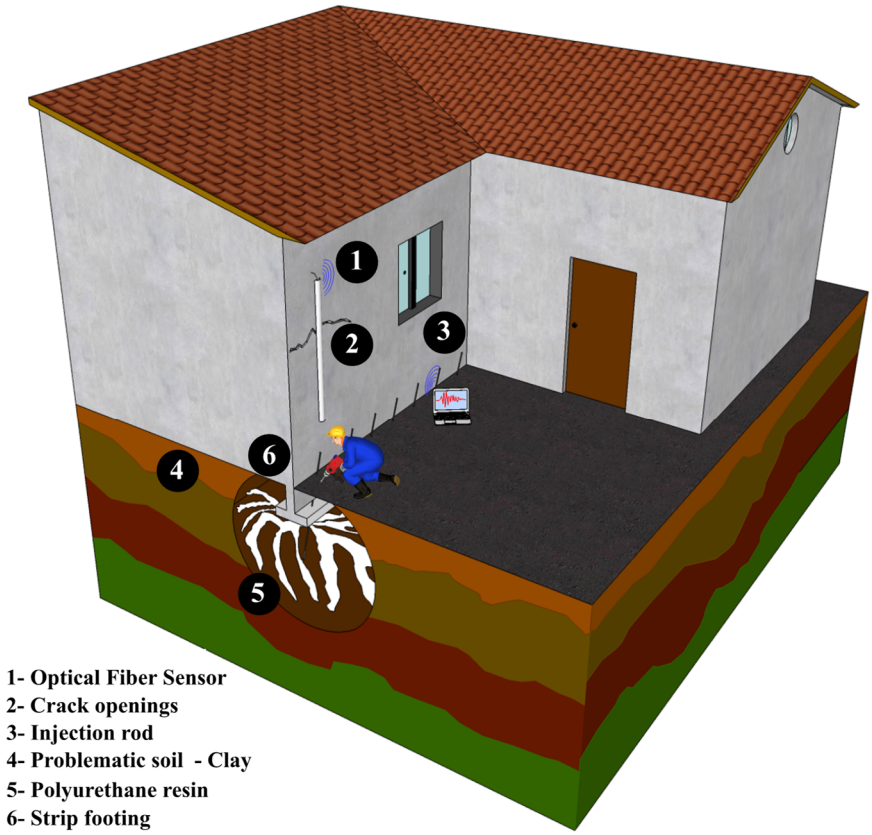

Figure A.1 - The general monitoring process and foundation soil treatment of damaged buildings by polyurethane injection repair technique (Assadollahi et al. 2018a).

Lightweight constructions like residential buildings are very sensitive to the injection pressure, so that a higher amount of injection can cause irreversible damage on the structure by lifting it

upward. To avoid such problems, in situ monitoring is proposed to be executed on the structure. The schematic representation of the procedure is shown in Figure A.1 indicating that the effect of the injection process on the structure's cracks is monitored by fiber optic sensors, while the soil is densifying in order to create an alerting system to avoid additional displacements of the building. In addition to that, it is crucial to investigate the obtained improvements in the soil's in situ mechanical characteristics. Therefore, some results from in situ measurements and monitoring of a damaged residential building, repaired by the polyurethane resin injection technique are presented in this section.

A1.2 Site investigation

The studied site concerns a one floor residential building constructed with strip footing which is damaged by 45° and vertical cracks on its walls. The building is located in the west side of the Castelnau d'Estretefond region. The geological data provided by the French Geological Survey (BRGM) map, classify the site to be composed of modern Alluviums, constituted by silts and gravels. To monitor the improvements of the soil characteristics, Geotechnical investigations were carried out before and after the injection process both at laboratory and field scale. In addition to the soil laboratory investigation, in situ PANDA tests were carried out in order to determine the dynamic tip resistance of the soil in depth at different points around the building allowing to have a general idea of the mechanical characteristics of the geological formation before and after treatment. The concept of a PANDA test is to drive a cone fixed at the end of a set of rods into the soil using a hammer. The depth of rod penetration and the tip dynamic resistance q_d are recorded automatically after each hammer hit. The dynamic tip resistance is expressed as $q_d = \frac{M_g H}{(1+a)e}$ where M is the hammer mass, H is its falling height, a is the ratio of masses (a=P/M, the rod-system penetrated mass, P, over the hammer mass, M), e is the penetration of the rod after impact and g=9.8 m/s2.

A1.3 Monitoring procedure

In addition to the monitoring of the soil characteristic, it is of great importance to monitor also the displacements of the building in real time. It is important to identify the damaged areas on the building, especially cracks openings before any monitoring procedure. The expansive polyurethane resin was injected under the foundations and some parts of the floor slabs mainly on the north side of the building as a repairing solution. The important point in the process is to be as efficient as possible in order to avoid any secondary damage on the structure. This could be done by monitoring the upper structure displacements. In order to monitor the injection process in real time, optical fiber sensors were used. Four optical fiber sensors were installed on four different angles of the building which were used in dynamic mode with measurement time steps at each 20 milliseconds with a resolution of 20 µm. Each strain measurement was made when the injection was taking place at that specific point. Three sensors were installed on the building's walls on very small cracks however, one of the sensors was installed on the largest crack of the building. Each of these measurements points were followed by a complementary PANDA test to evaluate the dynamic resistance profile after the treatment phase (Assadollahi et al., 2018a; Assadollahi et al., 2018b).

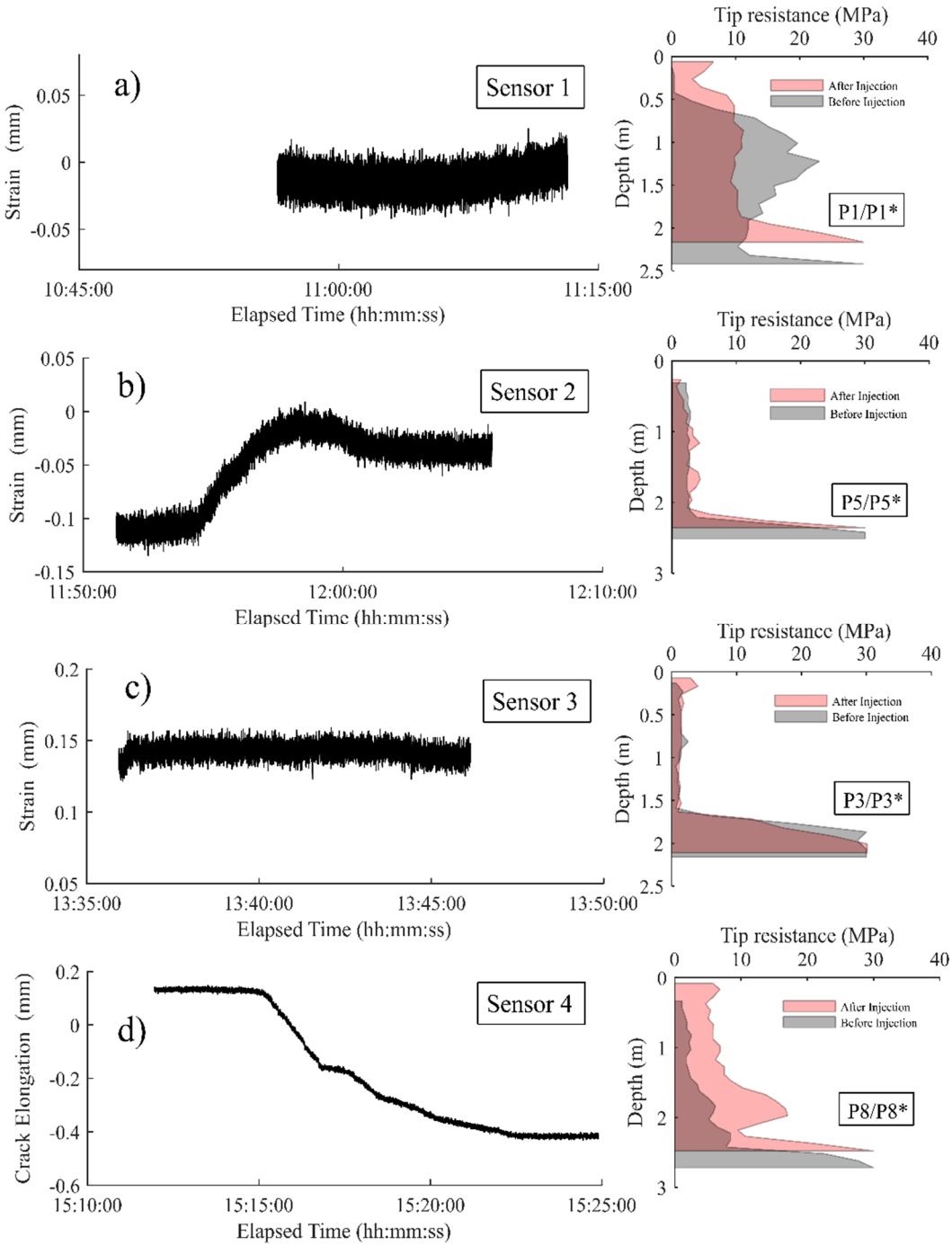

Figure A.2 - Results obtained from the optical fiber sensors at 4 different position of the building along with the results of in-situ PANDA tests before and after the injection process (Assadollahi et al., 2018a).

A1.4 Results and discussion

It should be noted that the soil heterogeneity and the resin distribution in the material is not always homogenous and samples may not be affected by the injection at all. Furthermore, results of the in-situ monitoring by fiber optics along with the dynamic resistance of the soil are presented in Figure A.2 Each of these four measurements results are analyzed here:

- Figure A.2 a) shows that the injection under the monitored wall with sensor 1, has caused a slight tension of the optical sensor after injecting 25 kg of resin. It showed a stable behavior of the structure during the injection. The wall was slightly compressed (0.02 mm) during the injection and when the injection was completed, it went back to its initial state (generating a tension of 0.01 mm which seems linked to the evolution of the temperature during the monitoring process). The results of the PANDA test at this point (P1/P1*) show a significant improvement of the dynamic resistance in the first 60cm of the soil profile but a decrease from 60cm to 2m depth. The test after the injection has stopped quickly than the one carried out before the injection. It is generally concluded that the wall at this point was rising up stably and the soil has been improved in the first meter.
- Figure A.2 b) shows mainly a tension of the optical fiber from the beginning of the injection. 35 kg of resin was injected at this point but the results of the optical fiber measurements did not show any compression at the beginning meaning that the resin was not being distributed at the considered spot under the footings. It was then observed that the resin was diffused under the slab instead. However, a compression phase and a rising up of the wall is captured by the sensor 2 at the end of the monitoring period. The injection was stopped right after the compression phase was observed. The results of the PANDA test at this point (P5/P5*) did not show any changes in the soil profile as expected because the resin was not distributed in the considered spot.
- Figure A.2 c) shows that the injection under the footing at this point has led to an overall rise in the structure resulting in a stable response of the optical fiber sensor. 25 Kg of resin were injected under this wall without causing any damage. Results of the PANDA test in the vicinity of this point (P3/P3*) show a slight improvement in the top layer of the profile and almost no change in the dynamic resistance after the injection phase. It can be derived that the complementary PANDA test after the injection (P3*) was not able to capture the effects of the injection but the stability of the structure in rising up the wall was confirmed with the optical fiber sensor.
- Figure A.2 d) shows the results of the crack openings observed by the 4th optical fiber sensor installed on the largest external crack and potentially the most damaged part of the building. This unique curve shows that the resin injection under the foundation soil resulted in a closure of the crack in a range of 0.5 mm. It should be noted that the closing of the largest crack was observable with the naked eye during the injection phase. 27 kg of resin were injected at this point and the results from the PANDA test carried out before and after the injection phase (P8/P8*) show significant improvements in the whole soil profile by at least two times higher. The first stage corresponds to the resin filling phase and a stable state which means that the soil is densifying. The second stage corresponds to the primarily sealing of the cracks in which the resin is taking effect and a compression of the crack is observed. The third stage shows the secondary sealing of the cracks along with a stable rising up of the structure meaning that the building tends to move upward after the crack is sealed. The last stage shows the stabilized phase in which the crack is completely sealed and the structure does not move anymore, therefore the injection phase could be stopped at this point. Without the help of monitoring, the right moment for stopping the injection process wouldn't be known which could have led to additional damage on the building.

A1.5 Conclusions

A case of a damaged building due to the presence of shrink-swell soil was investigated and repaired by the resin injection technique. The soil laboratory investigations before and after the injection phase on a sample showed that the swelling potential of the sample decreased after the injection while the water content profile couldn't give a reasonable argument of the injection effect on the samples' physical characteristics. It should be noted that this may also be because of the heterogeneities in the in situ geological formation. The in-situ improvements could not be completely verified by laboratory investigations however, the in-situ geotechnical investigation showed much more coherent results. The use of optical fiber sensors and the in situ mechanical test of the soil dynamic tip resistance together is a combined monitoring technique that can give an idea of the strain and the movement of the structure, along the improvements of the soil mechanical parameters. For this case, sensors 1 and 3 showed a stable rising of the structures and the wall along with acceptable improvements of the soil dynamic resistance with the PANDA test mostly in the top layer. For the case of the sensor 2, the resin wasn't exactly distributed at the considered spot, so the PANDA test couldn't show the improvement at that specific point, furthermore the use of the sensor allowed the monitoring of the downward movement of the wall and was adapted as an alerting system. The sensor 4 is a unique example of a re-pairing technique in which the crack is being monitored and is being closed as the injection is taking place.

It can be concluded that the injection can continue on until the sensors are showing stable strain values and until a tension has not taken place (meaning a downward movement). If sensors are installed on cracks, the injection should be stopped after a complete compression and a stabilization phase is shown on the sensor results. This technique could be used in further geotechnical monitoring projects in order to guarantee the safety of the structures. It should also be noted that the uncertainty in the distribution of the resin into the soil medium does not make the monitoring procedure easy and pose serious problems if the right tools are not adapted. For this case the use of optical fiber sensors is recommended however classical extensometers could also be used to measure the amount of soil movements. Further geotechnical study both in laboratory and field scale could give better understanding of this uncertainty.

Appendix 2: HYDRUS 2D/3D

A2.1 Introduction

HYDRUS is a suite of Windows-based modeling software that can be used for analysis of water flow, heat and solute transport in variably saturated porous media especially in soils. HYDRUS suite of software is supported by an interactive graphics-based interface for data-preprocessing, discretization of the soil profile, and graphic presentation of the results. While HYDRUS-1D simulates water flow, solute and heat transport in one-dimension, and is a public domain software, HYDRUS 2D/3D extends the simulation capabilities to the second and third dimensions, and is distributed commercially (Wkipedia). The HYDRUS (2D/3D) (version 1) software package (Šimůnek et al., 2006; Šejna and Šimůnek, 2007) is an extension and replacement of HYDRUS-2D (version 2.0) and SWMS_3D (Šimůnek et al., 1995). This software package is a complete rewrite of HYDRUS-2D and its extensions for two- and three-dimensional geometries. In addition to features and processes available in HYDRUS-2D and SWMS_3D, the new computational modules of HYDRUS (2D/3D) consider (a) water flow and solute transport in a dual-porosity system, (b) root water uptake with compensation, (c) the spatial root distribution functions, (d) additional soil hydraulic property models and other options which are not considered in this thesis.

A2.2 Simulation process

Both HYDRUS models may be used to simulate movement of water, heat, and multiple solutes in variably saturated media. Both programs use linear finite elements to numerically solve the Richards equation for saturated-unsaturated water flow. The flow equation also includes a sink term to account for water uptake by plant roots as a function of both water and salinity stress. The unsaturated soil hydraulic properties can be described using van Genuchten, Brooks and Corey, modified van Genuchten, Kosugi, and Durner type analytical functions. The heat transport equation considers conduction as well as advection with flowing water. The HYDRUS packages use a Microsoft Windows based graphical user interface (GUI) to manage the input data required to run the program, as well as for nodal discretization and editing, parameter allocation, problem execution, and visualization of results. All spatially distributed parameters, such as those for various soil horizons, the root water uptake distribution, and the initial conditions for water, heat and solute movement, are specified in a graphical environment. The program offers graphs of the distributions of the pressure head, water content, water and solute fluxes, root water uptake, temperature and solute concentrations in the subsurface at pre-selected times.

Appendix 3: Validation of the shrink-swell approach with a laboratory cyclic suction-controlled test

A3.1 Studied material

A cyclic suction-controlled test performed by Nowamooz et al. (2009) on a natural clayey soil from the Deffend experimental site is considered in this section for validation purposes of the proposed approach. The studied site is located in the Mignaloux-Beauvoir region close to Le Deffend, about 4 km southeast of Poitiers, in France. An in-situ core sampling was performed to a depth of 7 m for the geological and geotechnical investigations in November 2005 within the framework of the ANR–ARGIC project (Vincent et al. 2009). The studied soil was selected in a homogeneous clayey layer between 6 and 6.80 m because of its high swelling potential. The geotechnical characteristics of the clayey material are presented in Table A.1.

Table A.1 - Geotechnical properties of the studied material in Le Deffend experimental site.

Properties	Value
Liquid limit (%)	85.6
Plasticity index (%)	31.9
Specific gravity, Gs	2.60
Passing 80 mm sieve (%)	99
Clay content, <2 mm (%)	72
Dry density (Mg/m^3)	1.1

The hydro-mechanical tests on the natural soil was performed in an osmotic oedometer. A schematic representation of an osmotic oedometer proposed by Kassif and Ben Shalom (1971) and modified by Delage et al. (1992) is presented in Figure A.3. In order to study the mechanical behavior of the sample, a minimum number of drying-wetting cycles should be performed. The considered soil was subjected to 4 successive drying wetting cycles in the range of 0 to 2 MPa which lasted three months. The initial suction of the studied material was measured by the filter paper technique and was about 0.5 MPa. Thus, an initial wetting was performed to reach the saturation state.

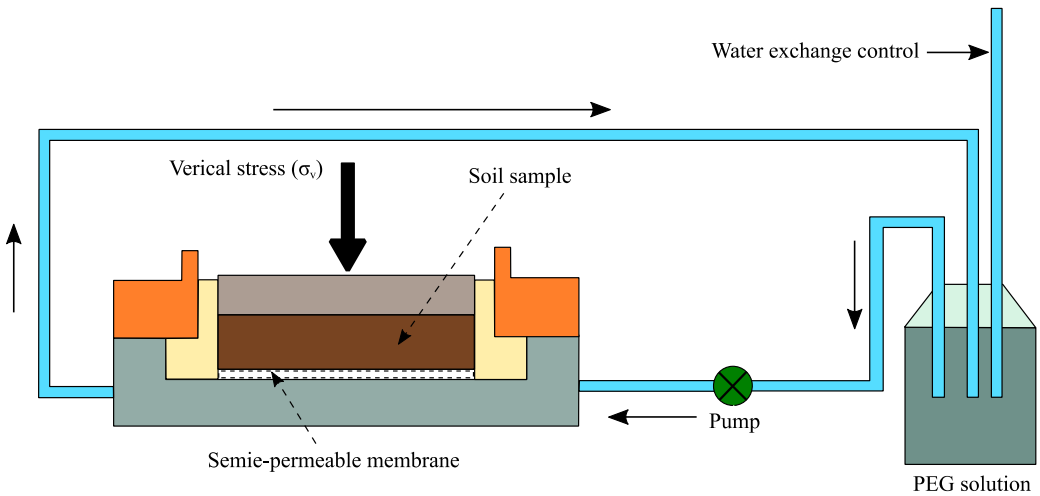

Figure A.3 - Schematic of the suction-controlled odometer device using osmotic solutions reported in Nowamooz et al. (2009).

Figure A.5 a) shows the applied suctions in each considered cycle under a constant 20 kPa vertical stress. The experimental volumetric strain of the sample is shown in Figure A.5 b) where the swelling strains are considered positive. The sample showed a cumulative swelling as a result of the successive drying-wetting cycles, and the volumetric strains converged towards an equilibrium stage. The total volumetric strain or deformation can be decomposed to two different components; the reversible volumetric deformation and the irreversible volumetric deformation. The reversible volumetric deformation is simply the rate of deformation at each drying-wetting cycle. Based on the measurements of the cumulative deformations, the reversible deformations can be deduced.

A3.2 Methodology

The model parameters are determined to carry out the simulation. Table A.2 shows the main parameters of the model for the calculation of the volumetric indices. The applied suctions exceed the transition suction (S_{tr}), thus the volumetric deformations are calculated based on both k_s and λ_s .

Table A.2 - Input and output parameters of the shrink-swell model for the Deffend clayey soil.

Input parameters							**Output parameters**			
$\Delta\sigma_z$ **(kPa)**	PI (%)	LL (%)	SL (%)	w% Sat.	e_0	γ_d (Mg/m³)	k_s	λ_s	S_{tr} (kPa)	S_{shrink} (MPa)
20	31.9	85.6	12	41	1.3	1.1	-0.0420	-0.0904	25.19	7.7

The volumetric deformation is defined as the ratio of the changes in void ratio of the specimen in each cycle (Δe) to the initial volume of the specimen ($1 + e_0$), where e_0 is the initial void ratio taken equal to 1.3. The initial height of the studied sample was 11.6 mm based on the provided information in Nowamooz et al. (2009).

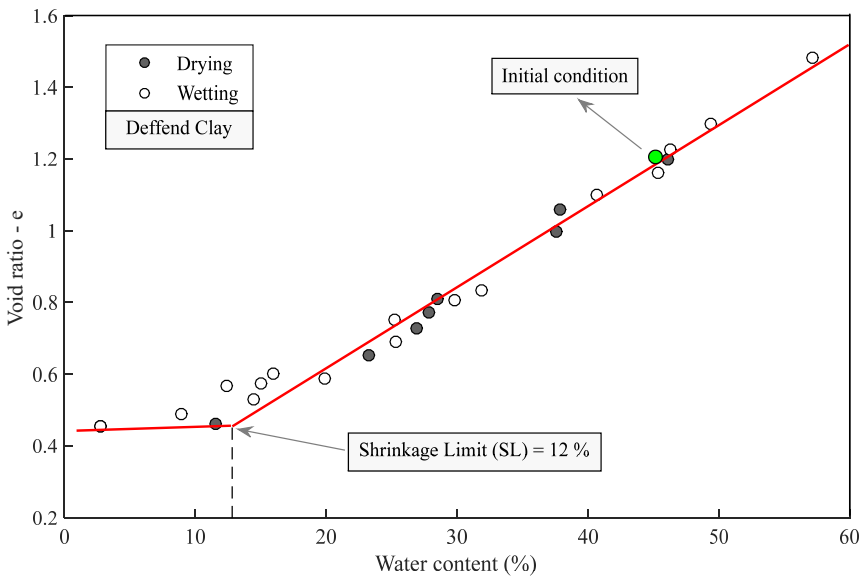

Figure A.4 - Shrinkage curve of the studied material in the Deffend site (6.44 - 6.48m) determined by Nowamooz (2007)

In addition to that, the soil shrinkage limit is also required for the calculation of the shrinkage limit suction. A shrinkage test was performed by Nowamooz (2007) on the studied material as

shown in Figure A.4. The test results suggest that the shrinkage limit is equal to 12% as indicated in Figure A.4. There is almost no volume change due to the change in the soil water content for lower water contents than the shrinkage limit. It should be mentioned that SL can be determined based on the developed equations if measurements are not available.

A3.3 Results

The simulated volumetric deformations are presented in Figure A.5 b). The comparison between the measured volumetric deformations and the simulated ones are in an acceptable agreement. The simulations also confirm that the soil shows a cumulative swelling behavior and the volumetric deformation reaches the same value as the measured one at the end of the drying-wetting cycles. The simulated volumetric deformations at each cycle are also presented in Figure A.5 b) where it can be observed that there is also a good agreement with the measured deformations.

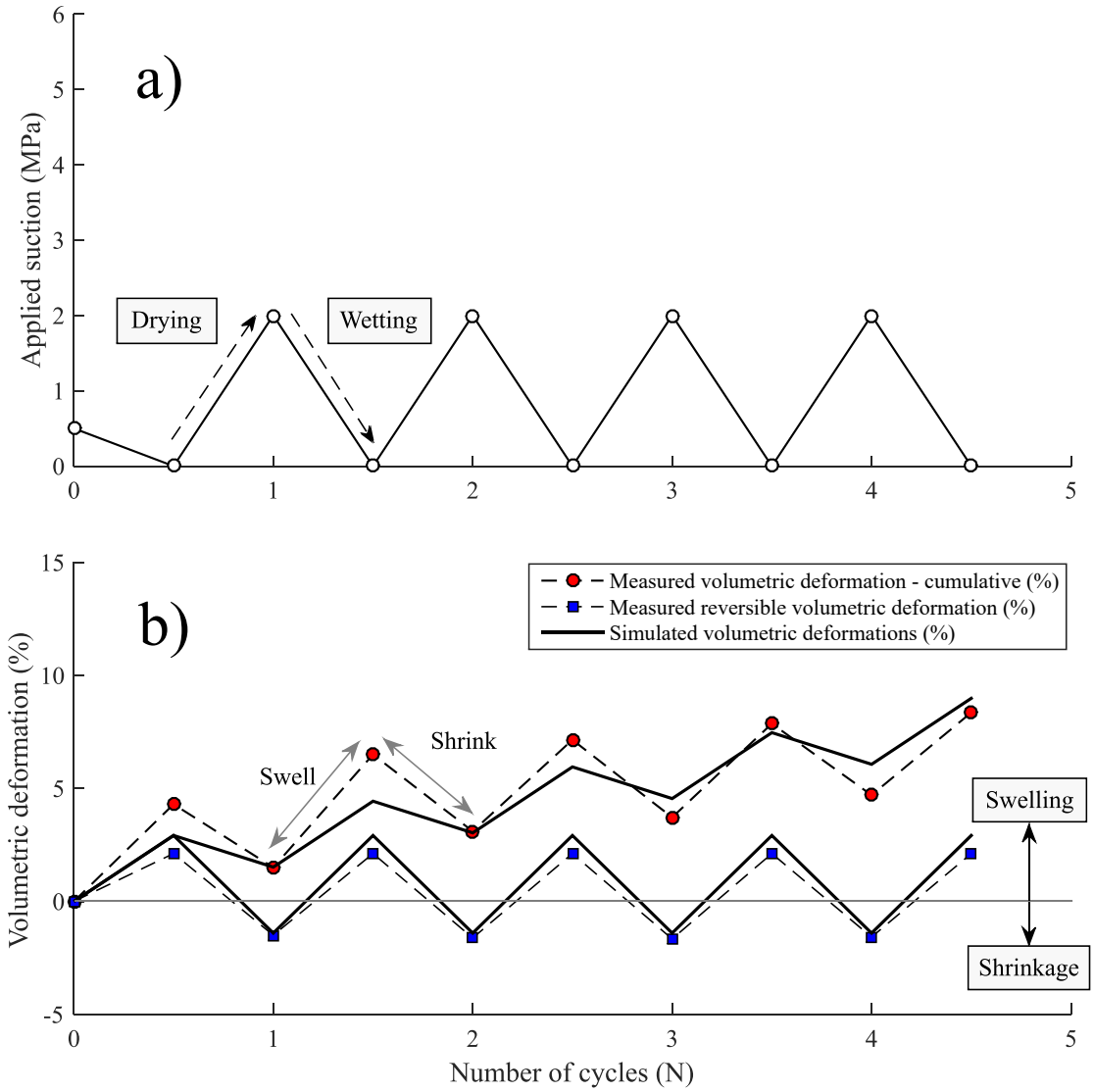

Figure A.5 - Comparison between the simulated and the measured volumetric deformations under 20 kPa vertical stress in a cyclic suction control test: a) applied suction b) volumetric deformations

Appendix 4: Stress distribution in a soil mass

A4.1 Theory:

If we consider an elemental strip of width dr, the load per unit length of this strip is equal to q.dr (Figure A.6). This elemental strip can be treated as a line load. The vertical stress increase is defined as shown in Eq. (A.1).

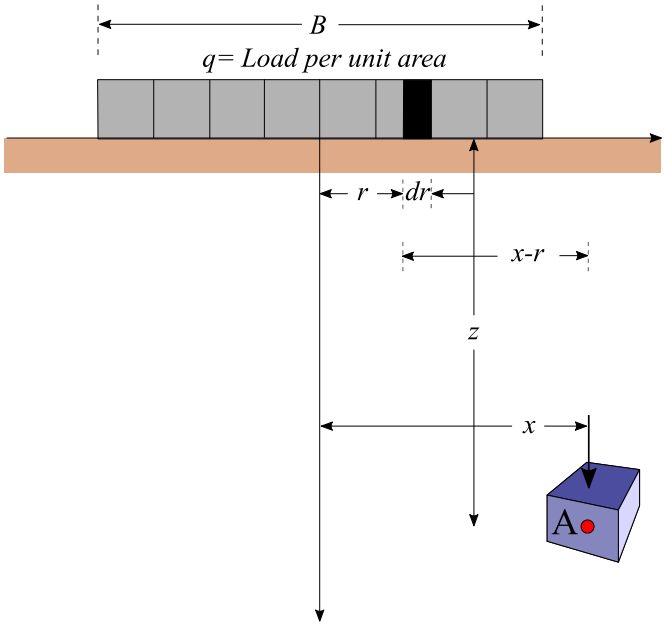

Figure A.6 - Vertical stress caused by a flexible strip load (M. Das and Sobhan, 2012)

$$d\sigma_z = \frac{2\ (q\ dr)z^3}{\pi[(x-r)^2+z^2]^2} \tag{A.1}$$

The total increase in the vertical stress ($\Delta\sigma_z$) at point A caused by the entire strip load of width B can be determined by integration of Eq. (A.1) with limits of r from -B/2 to +B/2, as shown below:

$$\begin{aligned}\Delta\sigma_z = \int d\sigma_z &= \int_{-B/2}^{+B/2}\left(\frac{2q}{\pi}\right)\left(\frac{z^3}{[(x-r)^2+z^2]^2}\right)dr \\ &= \frac{q}{\pi}(tan^{-1}\left[\frac{z}{x-\left(\frac{B}{2}\right)}\right] - tan^{-1}\left[\frac{z}{x+\left(\frac{B}{2}\right)}\right] \\ &- \frac{Bz\left[x^2-z^2-\left(\frac{B^2}{4}\right)\right]}{\left[x^2+z^2-\left(\frac{B^2}{4}\right)\right]^2+B^2z^2})\end{aligned} \tag{A.2}$$

With respect to Eq. (A.2), the following should be kept in mind:
The terms with $\tan^{-1}$ are in radius.
The magnitude of $\Delta\sigma_z$ is the same value of x/z (±).

Eq. (A.2) is valid as shown in Figure A.6 for point A, (x ≥B/2). However, for x=0 to x< B/2, the magnitude of the $tan^{-1}\left[\frac{z}{x-(\frac{B}{2})}\right]$ becomes negative. For this case, that should be replaced by $\pi + tan^{-1}\left[\frac{z}{x-(\frac{B}{2})}\right]$.

A4.2 Determination of the soil stress

It should be mentioned that a table can be established to determine the variation of $\Delta\sigma_z$/q with 2z/B and 2x/B based on the equation dhejd. This table can be used conveniently for the calculation of vertical stress at a point caused by a flexible strip load. Tables are provided in M. Das and Sobhan (2012). Figure A.7 show the contours of $\Delta\sigma_z$/q from 0.05 to 0.9.

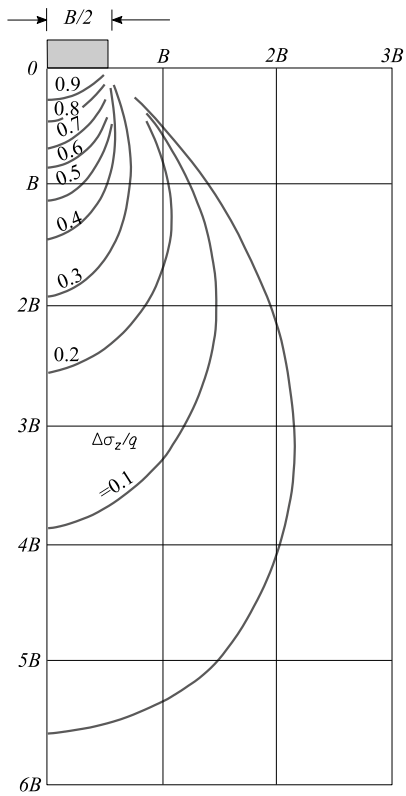

Figure A.7 - Contours of $\Delta\sigma_z$/q below a strip load (M. Das and Sobhan, 2012)

Résumé étendu

1. Introduction

Les préoccupations continuent de croître dans le monde entier sur l'impact des événements climatiques qui causent d'énormes pertes économiques et humaines à la société. Les projections actuellement disponibles montrent que la France connaîtra des hivers plus humides avec des précipitations plus intenses, en particulier dans le nord, et des étés plus secs associés à des températures plus élevées à la fin du 21e siècle. En France, le réchauffement climatique et les facteurs environnementaux ont provoqué de nombreux dégâts, en particulier sur les constructions légères (bâtiments résidentiels, bâtiments industriels, structures de chaussée, réseaux de canalisation, etc.) construites sur des sols gonflants, à cause des changements importants dans les propriétés physiques et mécaniques du sol étant associées à des mouvements différentiels dus au phénomène de retrait et de gonflement. Ce phénomène appelé aussi "sécheresse géotechnique" est à l'origine de nombreux dommages sur ces types de constructions. Les dommages causés sur ces types de construction reposant sur des sols gonflants ont été largement déclarés dans de nombreux pays tels que l'Australie, la Chine, l'Inde, Israël, l'Afrique du Sud, le Royaume-Uni et les États-Unis. Rien qu'aux États-Unis, l'ensemble des dégâts causés par des sols ont couté 15 milliards USD par an, soit deux fois plus que les dégâts causés par les inondations, les ouragans, les tornades et les tremblements de terre. La Société américaine des ingénieurs civils (ASCE) estime qu'un foyer sur quatre subit des dommages causés par des sols gonflants. Le coût annuel des dégâts importants causés par des sols en Chine est estimé à environ 15 milliards de dollars. L'Association des assureurs britanniques a estimé le coût moyen par un des dommages causés par les sols gonflants à plus de 400 millions de pondes, ce qui est le risque géologique le plus important au Royaume-Uni à ce jour.

En France, ce type de catastrophe naturelle est considéré comme le deuxième aléa naturel le plus coûteux après les inondations (5 milliards d'euros entre 1988 et 2007) et devrait être pris en compte dans les plans d'adaptation au changement climatique (projets ARGIC ANR). À ce jour, il n'existe pas de base de données fiable associée à une méthode prédictive capable d'informer les parties concernées : sociétés d'assurance, secteurs publics et secteurs privés. Dans ce contexte, il est nécessaire de mettre en place une méthodologie en tenant compte de tous les facteurs qui contribuent à déclencher et à aggraver ce phénomène.

La survenue de ce phénomène nécessite deux types de facteurs, les facteurs de prédisposition (nature du sol, contexte hydrogéologique, végétation environnante) et les facteurs de déclenchements (évaporation, précipitations). Les cycles d'humidification et de séchage entraînent des variations importantes de la succion du sol, à la fois en surface et en profondeur et, par conséquence, une variation importante du volume des vides, ce qui entraîne des mouvements différentiels dans le sol. Il est donc primordial d'étudier l'impact de ces facteurs sur le comportement couplé des sols à l'aide des outils numériques permettant de prédire l'intensité du retrait-gonflement dans le temps. Plusieurs modèles existent dans la littérature pour décrire le comportement hydromécanique des matériaux argileux gonflants non saturés. La combinaison de ces modèles avec le comportement in situ tout en prenant en compte l'interaction sol-végétation-atmosphère (SVA) est une tâche complexe. Dans le premier chapitre de cette thèse, un état de l'art des

différentes méthodes de détermination des mouvements du sol dans un contexte SVA a été présenté.

Le deuxième chapitre de cette thèse est consacré au développement d'une méthode numérique pour l'interaction sol-végétation-atmosphère (SVA) afin de déterminer les conditions aux limites temporelles naturelles en se basent sur des données météorologiques. Un modèle couplé hydro-thermique de sol est utilisé à l'aide du logiciel HYDRUS pour déterminer les variations spatio-temporelles de la succion du sol, de la teneur en eau et de la température. L'influence des contraintes environnementales telles que la présence de la végétation est également prise en compte à travers des modèles d'absorption d'eau par les racines. L'analyse des interactions SVA repose sur la théorie de l'écoulement d'eau et du transfert de chaleur dans les sols non saturés. Afin de déterminer le comportement volumique du sol ou plus précisément le retrait-gonflement dans le temps, les variations temporelles de la succion du sol sont liées à l'indice des vides du sol en proposant un modèle linéaire basé sur les résultats des essais expérimentaux réalisés dans la littérature. Une approche simple a été proposée pour déterminer les indices volumétriques des sols soumis à des cycles de séchage et d'humidification. Ces indices correspondent aux pentes du modèle linéaire dans le plan indice des vide-log succion et sont corrélés aux paramètres géotechniques de base tels que l'indice de plasticité, la densité sèche, la teneur en eau de saturation et l'indice des vides.

Dans le troisième chapitre de cette thèse, la validation de l'approche proposée a été réalisée en comparant les résultats de la modélisation numérique avec les mesures effectuées sur un site instrumenté au sud-ouest de la France. Le site est consisté d'un bâtiment sinistré par des facteurs environnementaux, notamment les conditions climatiques et la présence des arbres à proximité. Les dommages observés sont composés de fissuration structurelles sur les façades dues au tassement différentiel des fondations (semelle filante). L'investigation géotechnique a confirmé la présence des couches d'argile sensibles, jusqu'à 5 m de profondeur. Une campagne d'instrumentation a été programmée pour surveiller les variations des propriétés physiques de ces sols argileux à différentes profondeurs. Des capteurs de teneur en eau du sol, de température et de succion ont été installés dans les deux angles les plus sinistrés du bâtiment. Des fissuromètres ont été installés sur toutes les fissures afin de surveiller leurs ouvertures/fermetures pendant la période d'instrumentation. Un extensomètre multipoints a été installé sur un angle du bâtiment (nord) pour surveiller le retrait-gonflement des argiles à différentes profondeurs. La comparaison entre les simulations numériques et les mesures expérimentales a montré une cohérence acceptable qui a permis d'étudier l'influence des arbres sur le retrait-gonflement du sol, dans leur zone d'influence. Cette analyse a révélé l'influence de l'absorption d'eau par les racines des arbres sur le comportement du sol en terme de changement de volume et, par conséquence, sur ses mouvements différentiels sous les deux angles du bâtiment.

Dans le quatrième chapitre de cette thèse, la méthode a ensuite été étendue pour étudier l'impact de différents scénarios de changement climatique sur le retrait et le gonflement des argiles à court terme et à long terme. Trois scénarios RCP ont été pris en compte dans cette analyse : un scénario d'atténuation (RCP 2.6), un deuxième scénario de stabilisation (RCP 4.5) et un dernier scénario sévère (RCP 8.5). Les données météorologiques ont été projetées jusqu'à 2050 pour chacun de ces scénarios, en tenant compte de l'influence de la végétation dans le calcul de l'évapotranspiration. Les résultats de la simulation ont montré une augmentation des mouvements différentiels dans le sol, particulièrement à proximité des arbres. Les scénarios RCP 4.5

et 8.5 ont été identifiés comme des scénarios cycliques dans lesquels les variables hydro-thermiques et, par conséquence, le retrait-gonflement du sol, varient de manière régulièrement cyclique dans le temps et engendre des mouvements différentiels plus importants.

Dans la dernière partie de cette thèse, l'approche développée a été appliquée à l'échelle nationale. Pour ce faire, la France est divisée en six régions climatiques. Un type de sol spécifique est attribué à chacune de ces régions climatiques sur la base des cartes disponibles pour la répartition des sols en France. Ces sols (sols de référence) sont définis à l'aide des paramètres d'entrée de la méthode (PI, w%, e_0 et γ_d). La condition de référence inclut également les paramètres de végétation et de structure (fondation). Cette condition de référence dans chaque région est utilisée pour fournir les variations temporelles de la succion du sol sous les fondations du bâtiment, obtenues à l'aide de l'analyse d'interaction SVA. Ces variations temporelles sont ensuite utilisées dans les calculs des mouvements du sol sur la période 2016 - 2018. Une étude paramétrique est également menée pour étudier l'influence de ces facteurs sur les mouvements du sol. Les résultats sont potentiellement utiles pour les acteurs concernés du domaine, notamment les assureurs et les réassureurs, en termes de gravité et d'amplitude du phénomène de retrait-gonflement sur l'ensemble du territoire français.

La survenue du retrait-gonflement dans la nature nécessite deux types de facteurs :

- facteurs de prédisposition (nature du sol, contexte hydrogéologique, végétation) ;
- Facteurs de déclanchement (évapotranspiration, précipitations et changement climatique).

Les facteurs de prédisposition sont caractérisés comme les facteurs qu'induisent le phénomène de retrait-gonflement, mais ne suffisent pas pour le déclencher. Certains facteurs internes sont liés à la nature du sol et des facteurs environnementaux qui caractérisent le site (E. Jahangir, 2011). Les principaux facteurs de prédisposition sont :

- La nature du sol : La nature du sol, sa microstructure, sa teneur en eau et toutes ses propriétés mécaniques jouent un rôle très important dans le déclenchement du phénomène de retrait-gonflement.
- L'hydrogéologie du site : La présence d'une nappe phréatique à faible profondeur peut éventuellement affecter les propriétés physiques et mécaniques des sols superficiels. Ceci met en évidence l'importance des formations géologiques et de leurs influences sur la surface du sol.
- Végétation : La végétation joue un rôle assez important dans le comportement volumique des sols argileux. Les racines des arbres et les couvertures végétales peuvent appliquer une forte succion pendant les périodes de sécheresse contrairement aux périodes humides dont des valeurs de succion plus faibles sont générées. La végétation est une cause fréquente des sinistres de deuxième génération. Lorsqu'une construction endommagée a été correctement réparée et que de nouveaux dommages réapparaissent après un certain temps, un sinistre de deuxième génération est déclaré. Les nouveaux dommages de la construction s'expliquent souvent par des facteurs incidents non identifiés et traités. L'influence de la végétation et de la succion générée par les racines est l'un des facteurs d'incidence les plus coûteux parmi les sinistres de deuxième génération.

D'autre part, les facteurs de déclanchement sont caractérisés comme les facteurs qui causent un phénomène de retrait-gonflement qui n'a un effet significatif que s'il existe des facteurs de prédisposition (Vincent et al., 2009). Ces facteurs peuvent être classés en deux catégories générales :

- Phénomènes climatiques : les sols argileux ne se comportent pas de la même manière dans un climat aride, que dans un climat semi-aride et tempéré. Ainsi, ils risquent de connaître d'importants changements de volume. C'est pendant la période de sécheresse que le sol peut montrer une diminution significative du volume (retrait). Les phénomènes météorologiques sont la principale cause du retrait-gonflement des argiles, car ils impactent directement la teneur en eau du sol (changement climatique, évaporation, précipitations, etc.). Lorsque le taux d'évaporation est supérieur aux précipitations, le sol peut être en déficit hydrique, ce qui entraîne un retrait du sol.

- Facteurs anthropiques : D'autre part, les facteurs anthropiques affectent l'évolution hydrologique naturelle du sol, en modifiant la distribution des écoulements superficiels et souterrains. En général, ils sont engendrés par des travaux de réparation/construction tels que le drainage à proximité immédiate de la structure considérée ou la rupture d'une canalisation enterrée.

En résumé, le phénomène de retrait-gonflement se produit en présence d'un sol gonflant en tant que facteur de prédisposition et d'une variation de la teneur en eau du sol en tant que facteur de déclenchement.

Comme présenté sur la Figure 1, lors des cycles d'humidification et de séchage, le sol de support des constructions légères (dans ce cas, des une maison individuelle) est soumis à des phases de retrait et de gonflement, respectivement. Les mouvements différentiels du sol peuvent entraîner des dommages structurels généralement caractérisés par des fissures. Ces fissures sont principalement classées comme des fissures en forme d'escalier, des fissures horizontales et des fissures verticales dans certains cas.

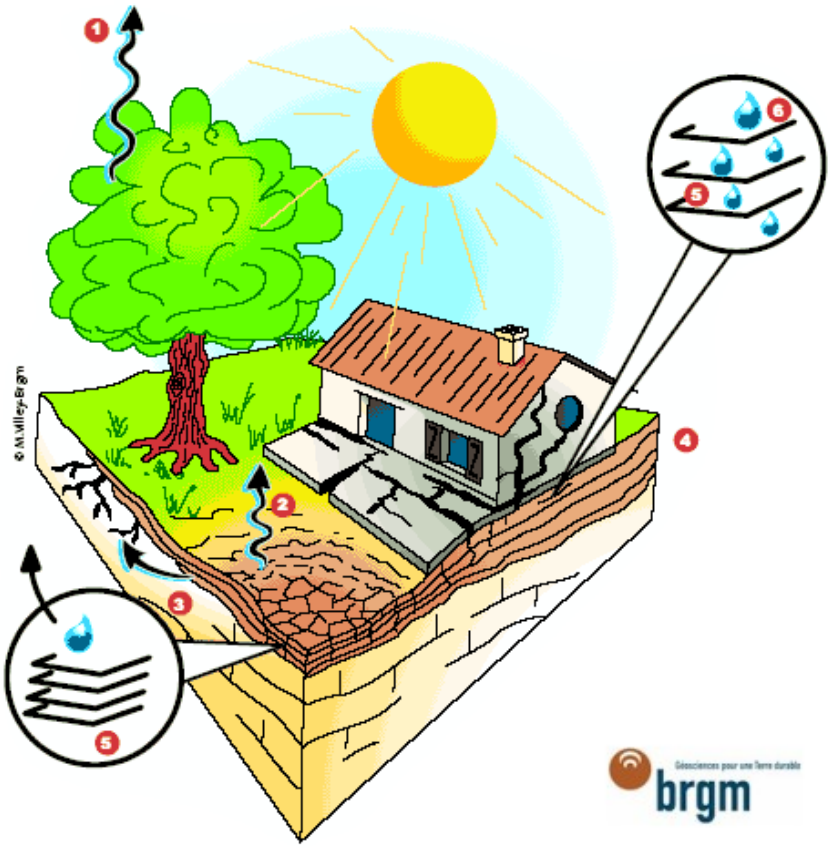

Figure 1 - Le phénomène de retrait-gonflement (BRGM)

2. Modélisation du retrait-gonflement des sols dans le contexte d'interaction Sol-Végétation-Atmosphère

Dans ce chapitre, l'approche de modélisation adaptée à l'analyse d'interaction SVA est brièvement présentée. Une méthode d'interaction sol-atmosphère simplifiée est utilisée pour déterminer les conditions aux limites atmosphériques dans le temps à l'aide des données météorologiques. Deuxièmement, un modèle hydro-thermique de sol est utilisé pour déterminer les variations spatio-temporelles de la teneur en eau, de la succion et de la température du sol dans le profil de sol considéré, en utilisant les propriétés thermiques et de rétention du sol. La détermination des propriétés de rétention est basée sur des paramètres géotechniques de base qui conduisent à l'estimation de la courbe de rétention d'eau du sol. Par la suite, l'effet de l'absorption d'eau par la végétation est intégré dans le modèle de sol hydro-thermique en utilisant le terme source dans l'équation d'écoulement non saturé. Enfin, les séries temporelles de succion du sol sont utilisées comme conditions aux limites pour déterminer le retrait et le gonflement du sol dans le temps à l'aide d'une approche simple, basée sur les résultats des essais de séchage et d'humification réalisés sur différents sols. Un modèle linéaire est adapté dans cette phase pour intégrer le comportement volumique sous les variations de succion dans le plan indice des vides-succion. Les paramètres essentiels du modèle, à savoir les indices volumétriques (les pentes du modèle linéaire), sont estimés à l'aide de la corrélation et de l'analyse de régression multiple sur des paramètres géotechniques de base.

Les sollicitations engendrées par le climat sont modélisées à l'aide d'une méthode d'interaction sol-atmosphère basée sur les équations de bilan de masse et d'énergie. Des modèles hydro-thermiques de sol sont utilisés pour analyser l'état hydraulique et thermique du sol en profondeur.

L'effet de la racine végétale sur l'état hydrique du sol peut être étudié dans le cadre d'une analyse SVA. Le comportement de la zone racinaire non saturée étant imprévisible, les chercheurs soulignent la nécessité de développer des modèles numériques pour simuler ce comportement. L'absorption d'eau par les racines dépend en grande partie de la distribution du système racinaire, des propriétés hydrauliques du sol et des conditions climatiques au fil du temps. L'objectif principal des modèles de simulation de l'absorption d'eau est de suivre les différents composants du bilan hydrique et de simuler la répartition de la teneur en eau ou de la succion dans le profil du sol à différents moments. Depuis 1960, l'écoulement de l'eau dans un milieu non saturé est calculé à l'aide de la solution analytique de l'équation de Richards. Les modèles d'absorption d'eau par les racines se divisent en deux groupes (les modèles microscopiques et macroscopiques). Les modèles microscopiques prennent en compte les informations détaillées et la dynamique du système racinaire, ce qui est très complexe à déterminer. D'autre part, les modèles macroscopiques sont basés sur une profondeur de racine statique ou sur un terme d'extraction d'eau simplifié (constant, uniforme, linéaire et exponentiel) dans la zone racinaire. Dans cette étude, l'absorption d'eau dans les racines (RWU) est exprimée à l'aide du modèle de Feddes (Feddes et al. 1978) qui utilise un terme de distribution d'extraction de l'eau constant.

Les essais expérimentaux menées par Nowamooz et al. (2013, 2016) ont souligné qu'un sol lâche a tendance à diminuer en volume et qu'un sol dense a tendance à augmenter en volume après plusieurs cycles de séchage et d'humidification. La modélisation physique est basée sur

les tests de séchage-humidification sur le plan (e-log S) de différents sols. Le concept général de l'approche de modélisation est illustré sur la Figure 2.

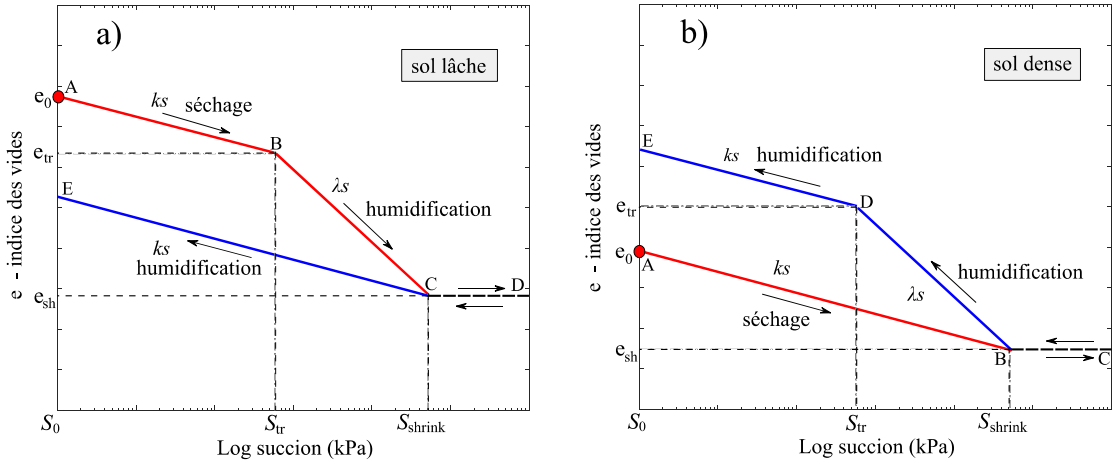

Figure 2 - Approche de modélisation physique du comportement volumique d'un sol non saturé soumis à des cycles de séchage et d'humidification à a) à l'état lâche et b) à l'état dense

Les chemins d'humidification et de séchage sont contrôlés par deux indices volumétriques notés k_s et λ_s. Pour le sol lâche, le chemin de séchage A-B correspond à une faible variation de l'indice des vides et est par conséquence caractérisé par un comportement élastique sur consolidé. Le chemin de séchage B-C correspond à une plus grande variation de l'indice des vides par rapport à la succion qui définit un domaine plastique normalement consolidé. La transition entre ces deux chemins se produit à un état de succion (point B) appelé succion de transition (S_{tr}) avec son indice des vides associé (e_{tr}). Sur le chemin de séchage ultime (C-D), on observe une très petite variation presque négligeable de l'indice des vides qui correspond à un comportement élastique. Les variations volumétriques sont considérées comme négligeables au-delà du point C, représenté par la succion au point de retrait (S_{Shrink}) et l'indice des vides associé (e_{sh}). D'autre part, la pente du chemin d'humidification (D-E-C) correspond approximativement à celle de (A-B) ayant un comportement élastique. Les mêmes remarques peuvent être effectuées sur le sol dense avec le point D pour la succion de transition et le point B pour la succion au point de retrait.

Pour établir une relation entre les indices volumétriques et les paramètres géotechniques de base, quelques essais de séchage/humidification réalisés dans la littérature ont été analysés. L'établissement de ces relations a été proposé par différents auteurs (Ho et al. 1992, Fleureau et al. 2002, Li et al. 2017, Li et al. 2018). Cependant, la base de données utilisée dans ces études était limitée à quelques dizaines de sols. Il faut également mentionner que toutes les corrélations ont été effectuées uniquement avec la limite de liquidité du sol, qui est un paramètre simple à obtenir. Cependant, ces indices pourraient également être impactés par d'autres paramètres de base. Plus de 55 sols ont été analysés dans cette étude.

Les Figures 3 et 4 montrent respectivement la corrélation de k_s et λ_s avec l'indice de plasticité, l'indice des vides, la teneur en eau de saturation et la densité sèche du sol. Il faut mentionner que la limite de retrait et la limite de liquidité ont montré une moindre corrélation avec k_s et λ_s

et n'ont donc pas été prises en compte dans l'analyse de régression multivariée. Comme représenté sur la Figure 3 a), l'indice volumétrique k_s est une fonction polynomiale de l'indice de plasticité du sol. En augmentant l'indice de plasticité, la valeur absolue de k_s augmente. La même remarque pourrait être effectuée pour les Figures 3 b) 3 c) où k_s est une fonction linéaire du l'indice des vides et de la teneur en eau saturée, respectivement. Cependant, comme représenté sur la Figure 3 d), k_s est une fonction logarithmique de la densité sèche du sol.

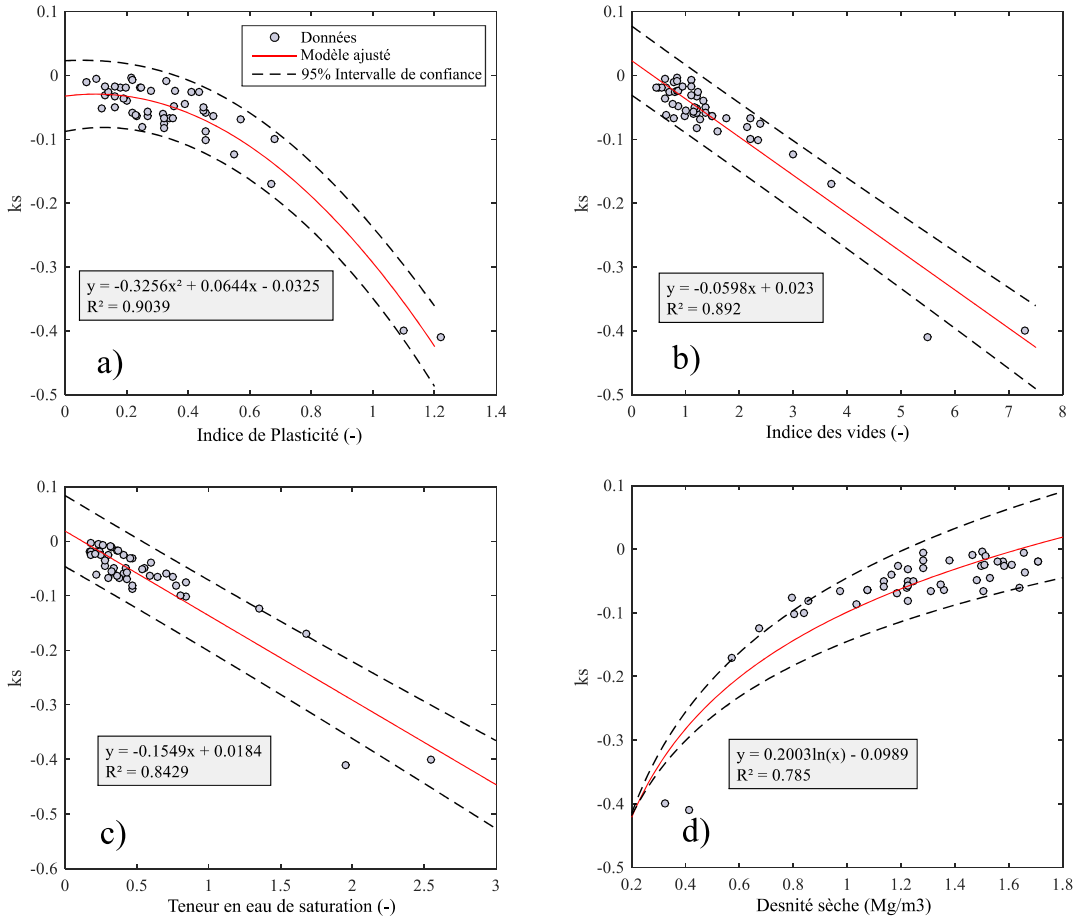

Figure 3 - Corrélation de k_s avec les paramètres géotechniques de base : a) indice de plasticité ; b) indice des vides ; c) teneur en eau de saturation ; d) densité sèche.

D'autre part, la Figure 4 a) montre la variation de λ_s avec l'indice de plasticité. La valeur absolue de l'indice augmente en même temps que l'indice de plasticité. Pour les deux Figures 4 b) et c), λ_s augmente linéairement avec l'augmentation de l'indice des vide et de la teneur en eau de saturation. Enfin, une courbe logarithmique relie les modifications de λ_s à la densité sèche du sol. Comme indiqué sur la Figure 4 d) λ_s diminue quand la densité sèche augmente.
Les modèles proposés sont en accord avec les données et la plupart des données dispersées restent entre les intervalles de confiance supérieur et inférieur à 95% des modèles linéaires et non linéaires ajustés.

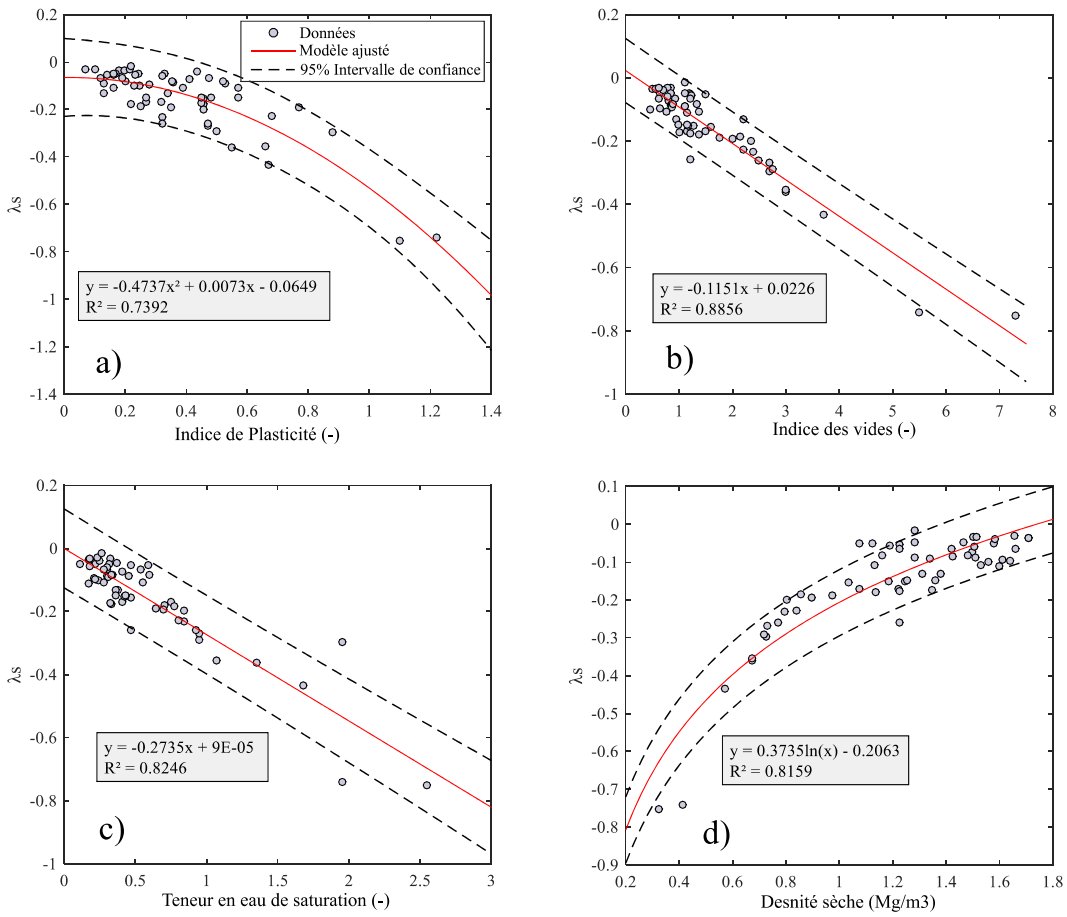

Figure 4 - Corrélation de λ_s avec les paramètres géotechniques de base : a) indice de plasticité ; b) indice des vides ; c) teneur en eau de saturation ; d) densité sèche.

Les indices volumétriques de certains sols sont étudiés pour différentes conditions de chargement lors des cycles de séchage et d'humidification. Les mesures effectuées dans la littérature montrent que l'influence des conditions de chargement sur la succion de transition et l'succion au point de retrait sont négligeables ; ainsi, S_{tr} et S_{shrink} sont considérés constants. Cependant, les indices volumétriques sont impactés par la contrainte appliquée au sol pendant les cycles de séchage et d'humidification et montrent une relation logarithmique avec le chargement appliqué.

Dans ce chapitre, l'approche de modélisation a été présentée. L'approche a été établie sur la base des paramètres physiques du sol, ce qui a permis de calculer les déformations volumétriques dans le sol comme présenté sur l'organigramme ci-dessous (Figure 5). Ensuite, les variations spatio-temporelles de la température du sol et de la teneur en eau sont déterminées à l'aide d'un modèle hydro-thermique du sol, dans lequel l'influence de la végétation sur le sol peut également être prise en compte. La courbe de rétention du sol ainsi que les paramètres hydrauliques et thermiques sont utilisées dans cette étape. Enfin, les variations temporelles de la succion du sol sont utilisées pour calculer les déformations volumétriques du sol en se basent sur le modèle linéaire de retrait-gonflement. Les indices volumétriques et les paramètres du modèle, ainsi que l'influence des conditions de chargements sur les indices volumétriques, sont déterminés lors de cette étape, ce qui permet de déterminer les mouvements du sol dans le temps.

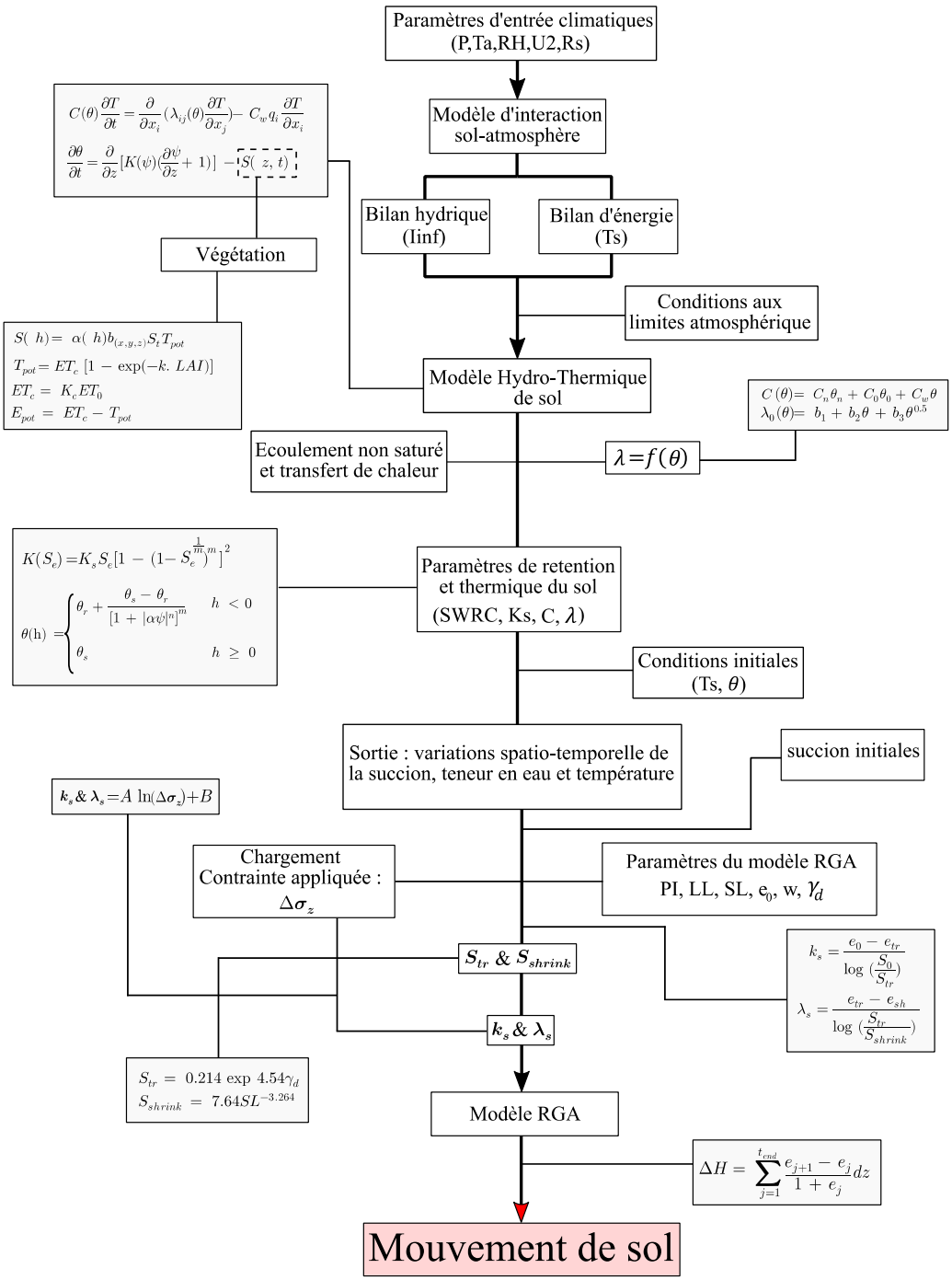

Figure 5 - Organigramme de l'approche de modélisation adaptée

3. Application sur le site de Roaillan

Le site consiste d'un bâtiment résidentiel situé dans le sud-ouest de la France, près de la ville de Bordeaux, à Roaillan-Langon. Construit en 2004/2005, le bâtiment est une construction résidentielle en L sur terre-plein avec des semelles ancrées entre 50 et 80 cm de profondeur ayant une section de 50 * 30 cm. Le bâtiment a été sinistré à cause des tassements différentiels probablement causés par des facteurs environnementaux tels que la présence des arbres à proximité du bâtiment et les conditions climatiques pendent de la période de surveillance.

La formation géologique du site est caractérisée par un risque moyen de retrait-gonflement, selon la carte des risque RGA du BRGM. Les premiers dommages observés en 2009 sur le bâtiment étaient principalement caractérisés par des fissures horizontales et verticales, à la fois à l'intérieur et à l'extérieur du bâtiment. Ces dommages ont évolué au cours des prochaines années. La zone est principalement entourée des chênes, de sorte que dans un angle du bâtiment (sud), un chêne se trouve à 2 mètres de celui-ci. Cependant, dans l'angle nord du bâtiment, les arbres se trouvent à au moins 5 à 6 mètres du bâtiment. On en déduit généralement que les dommages observés étaient dus à des tassements différentiels dus à la présence d'arbres (absorption d'eau de racines) et à la variation des paramètres climatiques au fil du temps.

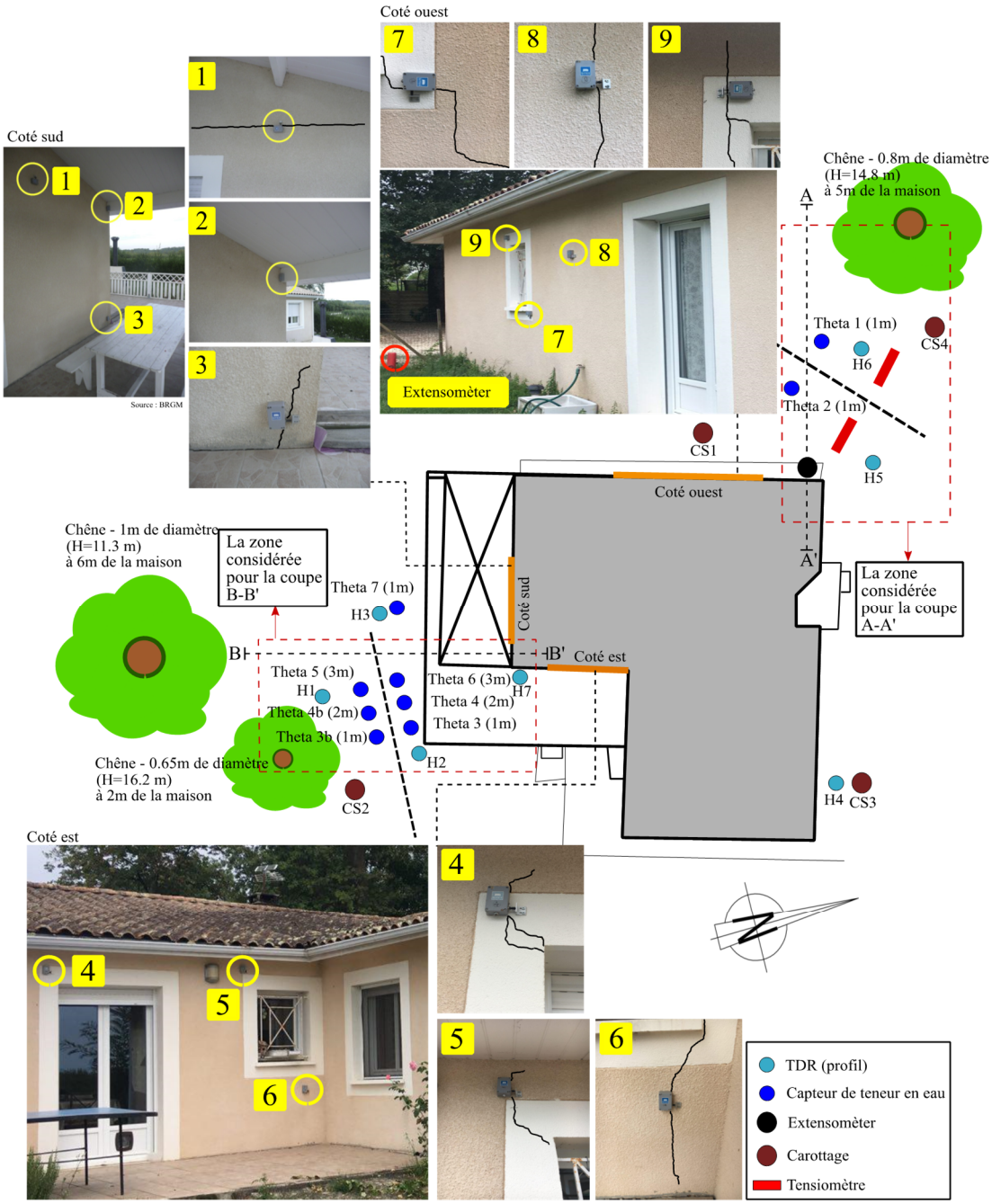

Figure 6 - Représentation schématique du bâtiment instrumenté

Le programme de surveillance de ce site a débuté en septembre 2011 afin d'évaluer les modifications des paramètres physiques du sol (principalement des argiles gonflantes) à proximité du bâtiment et des arbres (Mathon et Godefroy 2015). Les ouvertures de fissures dans le bâtiment ont également été surveillées pendant cette période. La Figure 6 montre la représentation schématique du bâtiment avec la position des arbres à proximité du bâtiment. L'arbre situé dans l'angle nord du bâtiment (0,8 m de diamètre et 14,8 m de hauteur) se trouve à environ 5 m. Cependant, les arbres situés dans l'angle sud du bâtiment sont situés à 2 et 6 m et ont un diamètre de 0,65 et 1 m respectivement. Le bâtiment semble avoir été endommagé principalement sur les façades ouest et sud, qui sont principalement exposés à l'absorption d'eau par les racines (Assadollahi et Nowamooz, 2018b, 2018c, 2018d, 2018e).

Des carottages ont été réalisés comme indiqué sur la Figure 6 à quatre angles du bâtiment pour étudier l'état actuel du sol en profondeur sur le site. Les analyses effectuées au laboratoire sur des échantillons prélevés entre 0,4 et 7 m de profondeur ont montré que presque tous les sols sont caractérisés comme étant fins et plastiques. De plus, ces essais ont montré que ces échantillons sont caractérisés comme moyennement plastiques et très plastiques. La Figure 7 montre le profil vertical 2D (section transversale A-A ') de l'angle nord avec l'arbre situé à 5 mètres du bâtiment. Comme illustré sur la Figure 7, différentes sondes sont installées à la fois coté bâtiment et coté arbre. Les points rouges représentent les tensiomètres principaux qui ont été installés à proximité de l'arbre et du bâtiment. Les points bleus indiquent les capteurs d'humidité du sol installés proche de la surface. Les points jaunes indiquent les sondes de température et les points verts indiquent l'emplacement des tensiomètres supplémentaires installés en 2013. H5 et H6 sont les sondes de profil dans lesquelles la teneur en eau et la température sont mesurées jusqu'à 2,95 m de profondeur.

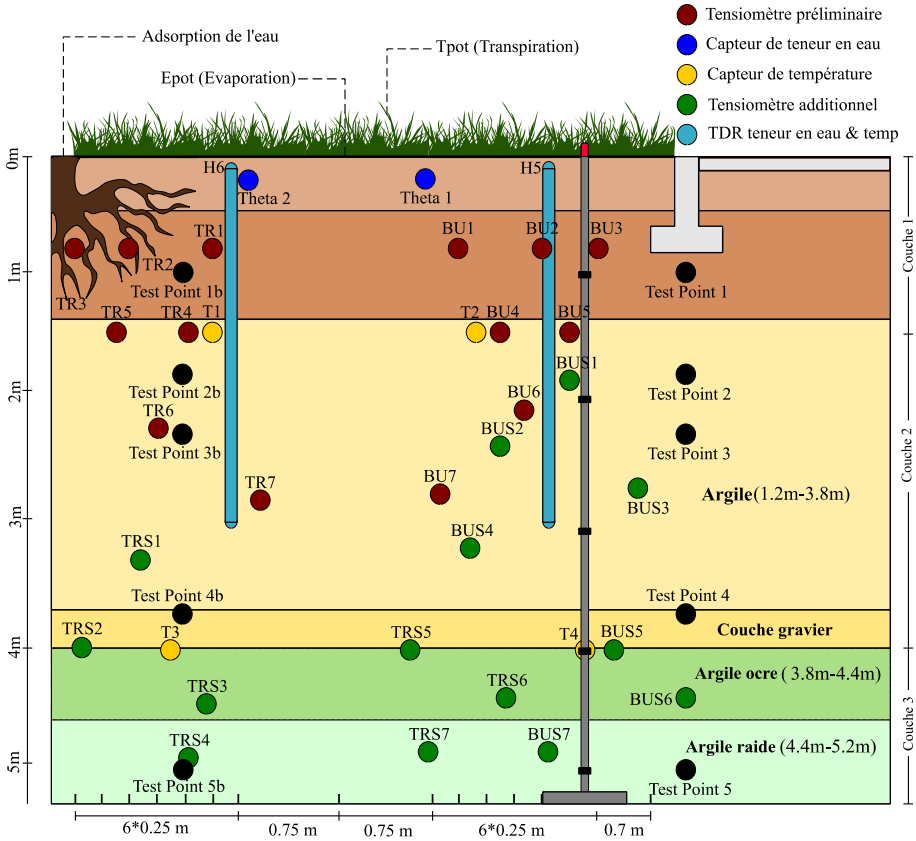

Figure 7 - Profil 2D de la formation géologique à l'angle nord (coupe A-A ').

En se basent sur les mesures des propriétés de rétention à trois profondeurs dans ce profil vertical, trois couches de sol ont été considérées avec des propriétés hydrauliques et thermiques différentes pour l'analyse sol-atmosphère-végétation et la simulation hydro-thermique.

La Figure 8 montre en revanche le profil vertical de la coupe transversale B-B indiquée sur la Figure 6 pour l'angle sud où l'arbre est situé à 2,5 m de la terrasse. Les points bleus représentent les capteurs d'humidité du sol à proximité de l'arbre et du bâtiment. H1 H2 et H7 sont les sondes de forage pour la mesure des profils de teneur en eau et de température jusqu'à 2,95 m de profondeur. Les points noirs indiquent les différents points de test. Suivant les investigations géotechniques, le profil vertical est divisé en quatre couches ayant chacune des propriétés hydro-thermiques différentes.

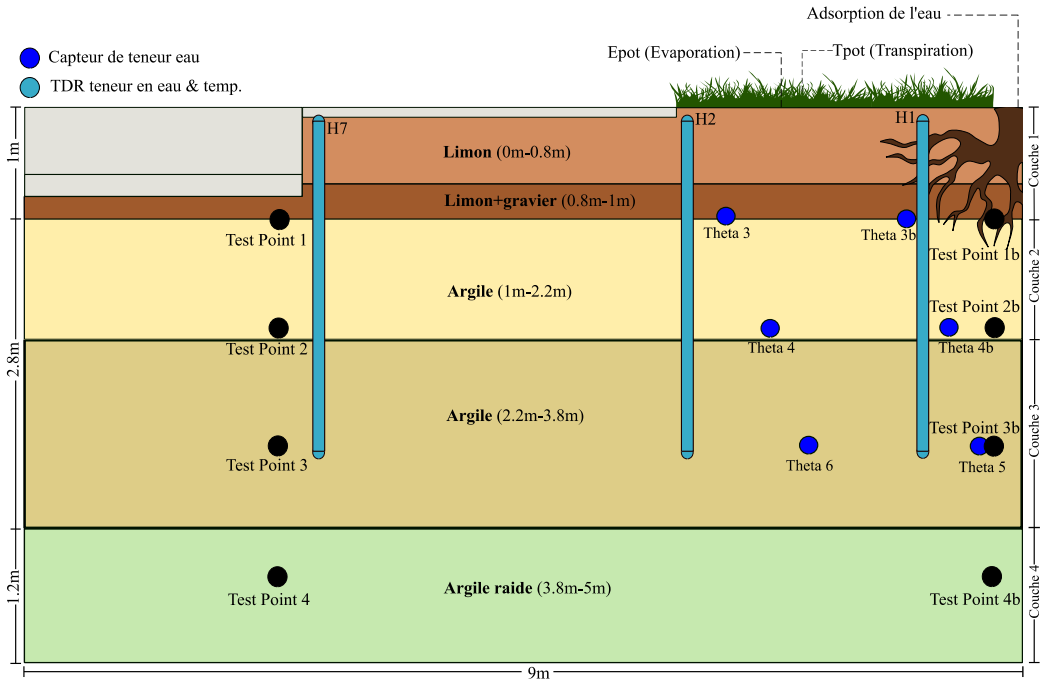

Figure 8 - Profil 2D de la formation géologique à l'angle sud (coupe transversale B-B).

3.1 Paramètre du sol :

Les paramètres hydro-thermiques sont présentés dans le Tableau 1. Les paramètres de changement de volume pour chaque couche de sol à l'angle nord du bâtiment sont présentés dans le Tableau 2. Il faut mentionner que seuls les paramètres volumétriques de l'angle nord sont pris en compte pour la validation, car la mesure de retrait-gonflement par l'extensomètre n'est effectuée que dans l'angle nord. Les mesures des mouvements du sol ayant été effectuées en 3 points différents, les paramètres attribués sont également pris en compte pour ces 3 points (profondeur 1m, 2m et 3m).

Comme indiqué dans le Tableau 2, PI, w%, e_0 et γ_d sont les paramètres d'entrée pour la détermination des indices volumétriques k_s et λ_s. Par ailleurs, LL et SL sont utilisés pour déterminer les paramètres du modèle basés sur la succion (S_{tr} et S_{shrink}). L'influence de la charge du bâtiment sur les indices volumétriques n'est pas été prise en compte dans le processus de modélisation car l'extensomètre se situe dans le voisinage de la fondation du bâtiment.

Tableau 1 - Paramètre hydro-thermiques

Angle du bâtiment	**Couche**	**Prof. (m)**	$\boldsymbol{\varepsilon}\ \left(\frac{\mathbf{1}}{\boldsymbol{mm}}\right)$	$\boldsymbol{n}$	$\boldsymbol{\theta_s}$	$\boldsymbol{\theta_r}$	$\boldsymbol{l}$	$\boldsymbol{K_s}\left(\frac{\boldsymbol{mm}}{\boldsymbol{day}}\right)$	$\boldsymbol{b_1}$	$\boldsymbol{b_2}$	$\boldsymbol{b_3}$	$\boldsymbol{C_n}$ $(\boldsymbol{MJ\ m^{-3}\ {}^{\circ}C^{-1}})$
Nord	1	0-1.5 m	0.0059	1.48	0.47	0.1	0.5	650	0.243	0.393	1.534	1.4
	2	1.5-4 m	0.00042	2.3	0.335	0.135	0.5	100	-0.197	-0.962	2.531	1.43
	3	4-5.5 m	0.00027	2.5	0.28	0.132	0.5	5	-0.197	-0.962	2.531	1.43
Sud	1	0-1 m	0.00248	2.25	0.58	0.001	0.5	184.2	0.243	0.393	1.534	1.4
	2	1-2 m	0.0026	1.305	0.458	0.0982	0.5	134.1	-0.197	-0.962	2.531	1.43
	3	2-3.8 m	0.00312	1.384	0.46	0.068	0.5	74.5	-0.197	-0.962	2.531	1.43
	4	3.8-5m	0.0019	1.31	0.41	0.095	0.5	62.4	-0.197	-0.962	2.531	1.43

Tableau 2 - Paramètres du modèle de retrait-gonflement (angle nord)

Prof. (m)	**PI (%)**	**LL (%)**	**SL (%)**	**w% Sat.**	e_0	γ_d **(Mg/m³)**	k_s	λ_s	S_{tr} **(kPa)**	S_{shrink} **(kPa)**
1	36	71	27	0.46	0.95	1.38	-0.0381	-0.0596	112.55	
2	39	69	14	0.33	0.89	1.42	-0.0371	-0.0541	134.96	4678.76
3	36	65	22	0.33	0.89	1.42	-0.0359	-0.0532	134.96	1070.1

L'indice de plasticité et la limite de liquidité du sol ont été étudiés expérimentalement à différentes profondeurs dans les sections précédentes. La teneur en eau du sol à l'état de saturation est adaptée en fonction des courbes de rétention des sols. La limite de retrait et l'indice des vides du sol à l'état de saturation pourraient être déterminés par un essai de retrait-gonflement. La densité sèche du sol pourrait être calculée à l'aide de paramètres physiques existants. Les mêmes commentaires sont valables pour le calcul de la limite de retrait.

Des essais de retrait gonflement ont été effectués sur trois échantillons étudiés dans le plan de teneur en eau et de l'indice des vides [w, e] à trois profondeurs différentes. Pour mesurer le changement de volume, l'indice des vides du sol est comparé à sa teneur en eau. Sur la courbe de drainage, le sol suit d'abord la droite de saturation (exprimée par $e = (\gamma_s/\gamma_w)\ w$). Suite à la diminution continue de la teneur en eau du sol, l'indice des vides tend vers une valeur constante. Cet essai permet de définir la limite de retrait par l'intersection de la ligne de saturation et de l'asymptote horizontale de la courbe lorsque la teneur en eau tend vers zéro.

3.2 Paramètres climatiques :

Les données météorologiques du site expérimental ont été recueillies à partir de la base de données MERRA (Gelaro et al. 2017). La période considérée commence en septembre 2011 et se termine en fin 2017. Ces paramètres climatiques permettront de définir les conditions limites atmosphériques du site, qui seront examinées dans les sections suivantes. Ces paramètres climatiques permettront aussi de calculer l'évapotranspiration de référence.

3.3 Paramètres de végétation :

Afin de différencier la quantité de transpiration et de l'évaporation potentielle du sol, il convient d'adapter les paramètres de la végétation. Ces paramètres permettront de déterminer les conditions aux limites atmosphériques variables dans le temps. Pour décomposer ET0, le coefficient de culture doit d'abord être déterminé. Ainsi, la méthode proposée par FAO 56 (Allen et al. 1998) est utilisée en considérant un coefficient de culture de type unique. Un seul coefficient de culture a été adapté à ce site expérimental pour la surface et pour l'arbre. Une valeur initiale de Kc_{ini} de 0,6 a été choisie sur la base des suggestions disponibles dans Allen et al. (1998). Le coefficient Kc_{mid} et le coefficient de fin de saison Kc_{late} sont calculés à l'aide d'approximations numériques basées sur les données climatiques de cette période (Allen et al., 1998). Une distribution annuelle du coefficient de culture est adaptée pour ce site spécifique en raison du rôle plus important des arbres dans les paramètres de végétation (25 jours pour la période initiale, 40 jours pour la période de développement, 240 jours pour le milieu de la saison et 60 jours pour la période finale).

L'indice de surface foliaire est généralement mesuré directement sur place. Cependant, il n'y a pas de mesures directes de LAI pour ce site spécifique. Donc une fonction sinusoïdale a été adaptée aux variations temporelles du LAI (une année) pour chaque angle du bâtiment, qui atteint respectivement les valeurs maximales de 1,8 et 0,9 pour les angles nord et sud et une valeur minimale de zéro pour les deux angles. Ces limites sont déterminées en suivant les recommandations de Asner et al. (2003). Le coefficient de culture et l'indice LAI sont calculés de 2011 à 2017, période pendant laquelle l'indice LAI reste identique pour chaque saison considérée. Toutefois, le coefficient de culture pourrait varier en raison des différents paramètres climatiques au cours de cette période.

3.4 Conditions aux limites :

Les principales conditions aux limites du modèle sont le taux d'infiltration (P-ET0), le potentiel de transpiration (Tpot), l'évaporation potentielle (Epot) et la température à la surface du sol (Ts). Les Figures 9 a) et b) montrent la répartition de la transpiration potentielle et de l'évaporation potentielle du sol pour les angles nord et sud du bâtiment. On peut observer que le taux de transpiration dans l'angle nord du bâtiment est supérieur au taux de transpiration dans l'angle sud en raison de la différence entre les indices LAI. D'autre part, l'évaporation du sol dans l'angle sud est supérieure à l'angle nord du fait qu'une partie du taux d'évapotranspiration est prise par la transpiration potentielle dans l'angle nord.

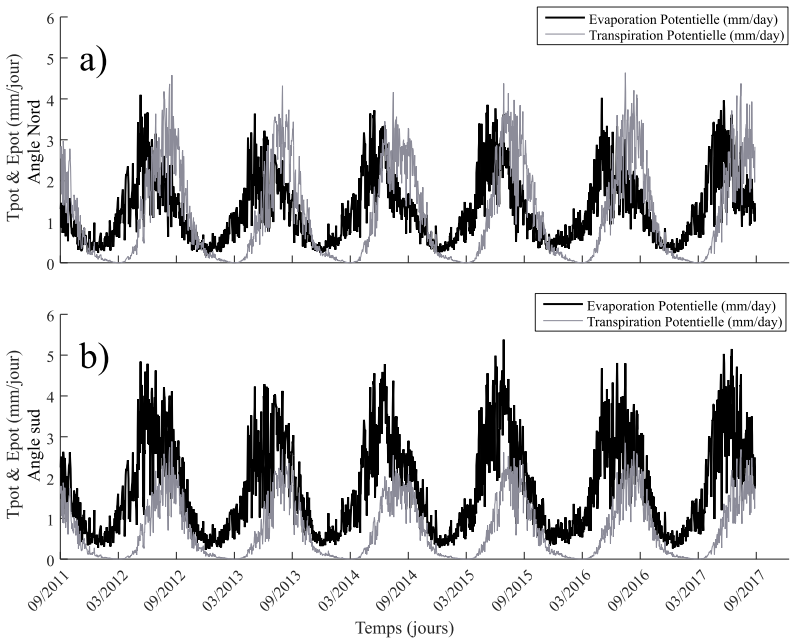

Figure 9 - Décomposition du taux d'évapotranspiration en transpiration potentielle (Tpot) et évaporation potentielle (Epot) : a) pour l'angle nord b) pour l'angle sud

Le taux d'infiltration et la température à la surface du sol sont également déterminés (Figure 10) à l'aide de la quantité de précipitation et de l'évapotranspiration de référence sur la base de l'approche simplifiée du bilan de masse et du bilan énergétique.

Les conditions aux limites déterminées peuvent maintenant être appliquées en tant que conditions aux limites atmosphériques variables dans le temps à la surface du sol, dans le maillage

aux éléments finis. De plus, une condition au limite de type drainage libre est appliquée en bas de la géométrie.

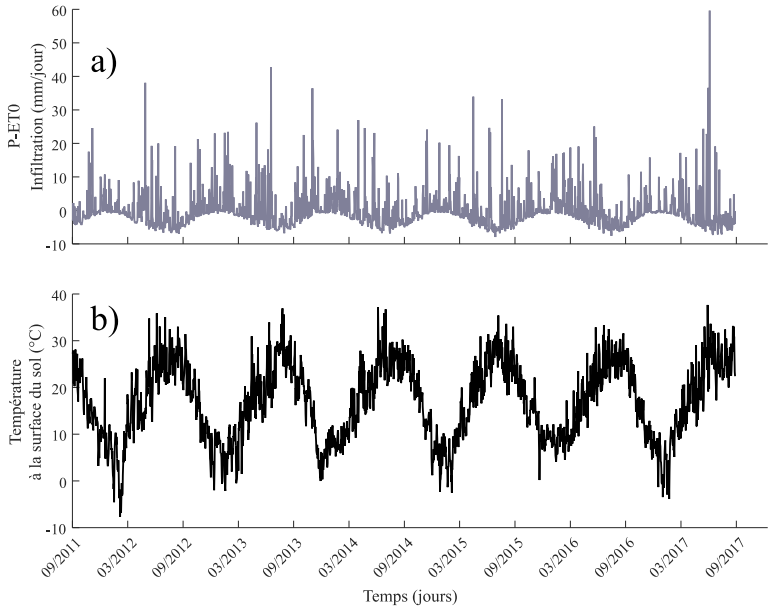

Figure 10 - Condition limite variable dans le temps du site expérimental pour la simulation hydrothermique : a) Taux d'infiltration (P-ET0) b) Température de la surface du sol.

3.5 Conditions initiales :

Les conditions initiales du modèle sont définies en fonction de la teneur en eau mesurée, de la succion du sol et de la température du sol à différentes profondeurs. La distribution de la teneur en eau à l'angle nord est basée sur les mesures de la teneur en eau mesurée à la surface et prend une forme quasi linéaire. Cependant, une distribution linéaire de la température du sol est adaptée pour les conditions de température initiales. Cette répartition dans le profil de sol est en cohérence avec la première valeur observée du capteur de température en 09/2011, qui indique une valeur de 20 ° C à 1,5 m de profondeur. La distribution de la teneur en eau a été adaptée sur la base des premières mesures effectuées par H1, H2 et H7 sur trois zones différentes du profil (proche de l'arbre, proche du bâtiment et sous la fondation). D'autre part, une distribution linéaire a été appliquée pour le profil de température initial. Les mêmes conditions que le profil de l'angle nord (25 ° C en haut et 13 ° C en bas) sont appliquées dans ce cas car il n'y a pas de mesures des variations de température en 09/2011 à l'angle sud.

Outre les conditions initiales de teneur en eau et de température, les paramètres de végétation ou la forme de distribution initial des racines doivent être appliqués à la géométrie. Il faut mentionner qu'une distribution manuelle des racines a été adaptée en fonction des mesures de la succion du sol dans le profil à l'angle nord. Une partie des racines est répartie dans les premiers mètres et l'autre partie entre 2 et 3 m de profondeur. D'autre part, étant donné qu'il n'y a pas de mesure de succion à l'angle sud du bâtiment, une distribution typique a été appliquée dans le sol. La profondeur et la longueur des racines sont tous les deux fixées à 3,5 m dans le sol.

3.6 Comparaison du retrait-gonflement du sol :

La Figure 11 montre la comparaison entre les mouvements du sol modélisés et mesurés à trois profondeurs (1, 2 et 3 m) par l'extensomètre installé dans l'angle nord du bâtiment. Une cohérence acceptable entre les résultats de la simulation et les données peuvent être observée. La Figure 11 a) montre les variations dans le temps des mouvements du sol à 1 m de profondeur. D'après les données, l'amplitude maximale de mouvement du sol est d'environ 0,5 mm, ce qui confirme également les résultats de la simulation. La Figure 11 b) montre les mouvements du sol à 2 m de profondeur. On peut constater que l'amplitude des mouvements est légèrement inférieure à celle des mouvements à 1 m de profondeur. Les résultats de la simulation sont en bonne cohérence avec les données et les mouvements semblent se stabiliser à la fin de la période de surveillance. Les mêmes commentaires sont valables pour les mouvements du sol à 3 m de profondeur (Figure 11 c)). On peut observer que la plage de mouvements est légèrement inférieure aux mouvements à 1 m de profondeur et que les mouvements ont tendance à se stabiliser à la fin de la période de surveillance. Cela pourrait être lié au fait que pendant les périodes d'humidification, les changements de succion du sol ne sont pas assez importants pour déclencher un mouvement considérable du sol. Cependant, la plupart des mouvements du sol sont observés pendant les périodes chaudes de l'année et lorsqu'il y a une transition rapide entre les périodes de sécheresse et d'humidification (précipitations et évapotranspiration).

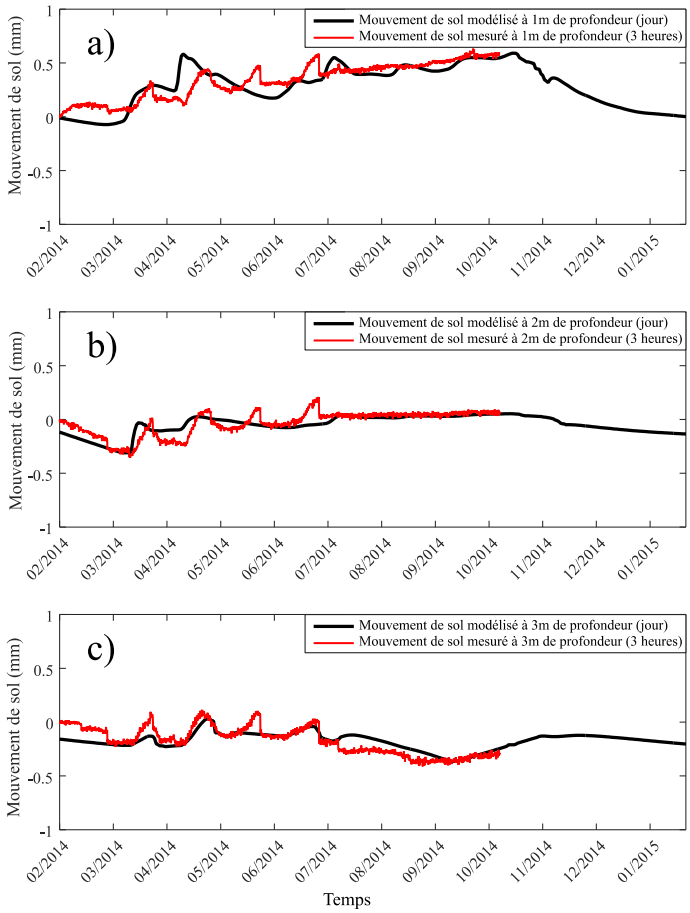

Figure 11 - Comparaison des mouvements de sol modélisés avec des mesures effectuées sur site, a) 1m ; b) à 2 m ; c) à 3m de profondeur.

4. Analyse des mouvements différentiels dans le contexte du changement climatique

L'analyse des mouvements différentiels du sol est essentielle pour évaluer les dommages potentiels sur les constructions légères. En se basent sur les séries temporelles de la succion à la surface du sol dans les deux angles du bâtiment, les mouvements du sol peuvent être déterminés. La Figure 12 montre la variation journalière et la moyenne mobile sur 3 mois des mouvements de sol en surface aux deux angles du bâtiment. On peut observer que les mouvements de sol en surface dans l'angle nord atteignent 12 mm, contrairement aux mouvements dans l'angle sud qui atteint environ 4 mm à la fin de la période modélisée. La différence pourrait être liée aux propriétés de rétention attribuées et aux valeurs de succion générées à la surface. Le tassement différentiel maximal dans ce cas est d'environ 8 mm, ce qui pourrait représenter une valeur considérable. Il convient également de mentionner qu'un retrait cumulatif (tassement) est observé dans les deux cas, ce qui est lié au fait que le sol en surface a une faible densité et que, selon l'approche de modélisation, une perte de volume est observée après plusieurs cycles de séchage et d'humidification.

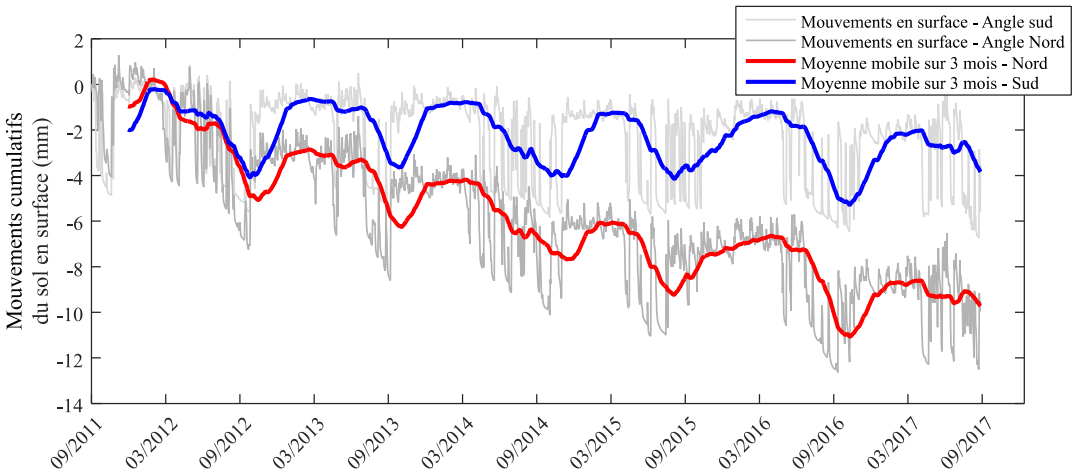

Figure 12 - Mouvements différentiels de la surface du sol aux angles nord et sud.

En se basent sur l'analyse comparative réalisée dans la dernière section, les variations de succion sous la fondation des deux angles (1m) pourraient être utilisées pour déterminer et analyser les mouvements différentiels du sol. La Figure 13 montre les mouvements cumulés et journaliers du sol dans les deux angles du bâtiment. Le mouvement différentiel maximal est d'environ 1mm. Il est généré en 05/2017 en raison des précipitations importantes. Étant donné que le sol sous fondation dans l'angle nord est directement impacté par les conditions climatiques, contrairement à l'angle sud, ce mouvement différentiel est donc prévisible. La Figure 13 b) montre également des mouvements différentiels journaliers considérables puisqu'il n'y a presque aucun mouvement dans l'angle sud.

Les mouvements différentiels du sol sont également étudiés à proximité des arbres des deux côtés du bâtiment. Les points de test avec des valeurs de succion plus élevées ont été choisis dans cette analyse (Le point 2b dans l'angle sud et 3b dans l'angle nord). On peut constater que sur la Figure 13 c), le mouvement différentiel du sol atteint principalement 2,7 mm en 09/2012 et que la valeur maximale atteint 3,1 mm en 09/2015. Les mouvements différentiels journaliers

du sol (Figure 13 d) montrent également que le mouvement différentiel maximal est observé à 09/2015. La gamme de variation est plus importante que les mouvements sous fondation en raison de l'absorption de l'eau par les racines.

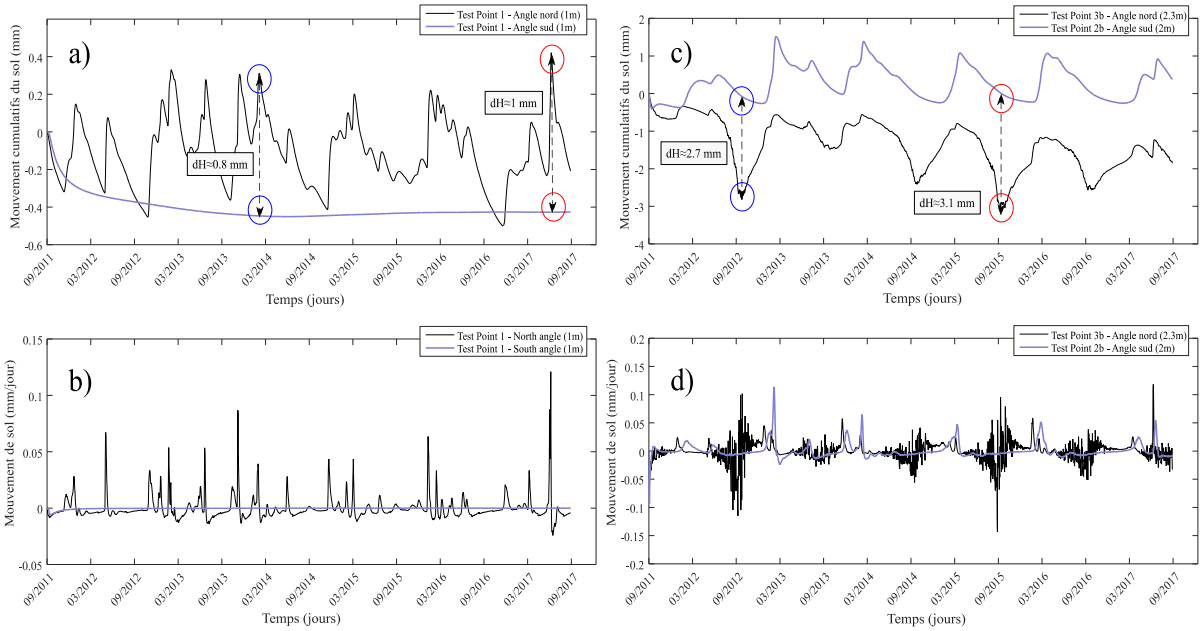

Figure 13 - Mouvements différentiels du sol sous les fondations dans les angles nord et sud a) du bâtiment b) à proximité des arbres

Dans cette section, trois scénarios de changement climatique du RCP (RCP 2.6, 4.5 et 8.5) sont utilisés pour la projection des paramètres climatiques et l'évaluation des variables physiques du sol sur le site expérimental. Les paramètres climatiques projetés jusqu'à 2050 sont utilisés dans cette analyse.

Les mouvements de sol sont évalués premièrement en prenant en compte les projections à court terme des paramètres climatiques. Les calculs sont effectués jusqu'à la fin de 2021, ce qui permet d'évaluer la série chronologique des variables physiques du sol.

La Figure 14 montre la composition des mouvements de sol cumulés sous les fondations du bâtiment dans chaque scénario considéré. Il peut être déduit que le scénario RCP 4.5 a une influence plus importante sur les variables physiques, mais que les mouvements différentiels maximaux dans le sol sont similaires. Toutefois, le scénario RCP 8.5 montre que le mouvement différentiel maximal se produira plus tôt par rapport aux deux autres scénarios.

La comparaison des mouvements différentiels du sol est également effectuée à proximité des arbres à 2 et 2,3 m de profondeur des deux côtés du bâtiment. Cette comparaison a mis en évidence que le scénario RCP 4.5 est capable de générer des mouvements différentiels plus importants à court terme par rapport aux scénarios RCP 2.6 et 8.5 en présence d'une contrainte environnementale externe comme les arbres dans ce cas. Toutefois, compte tenu des mouvements différentiels de sol sous fondations, le RCP 8.5 pourrait être le scénario le plus problématique à court terme en raison des nombreuses fluctuations et aussi du mouvement maximal qui se produit plus tôt que les deux scénarios lors de la période de simulation.

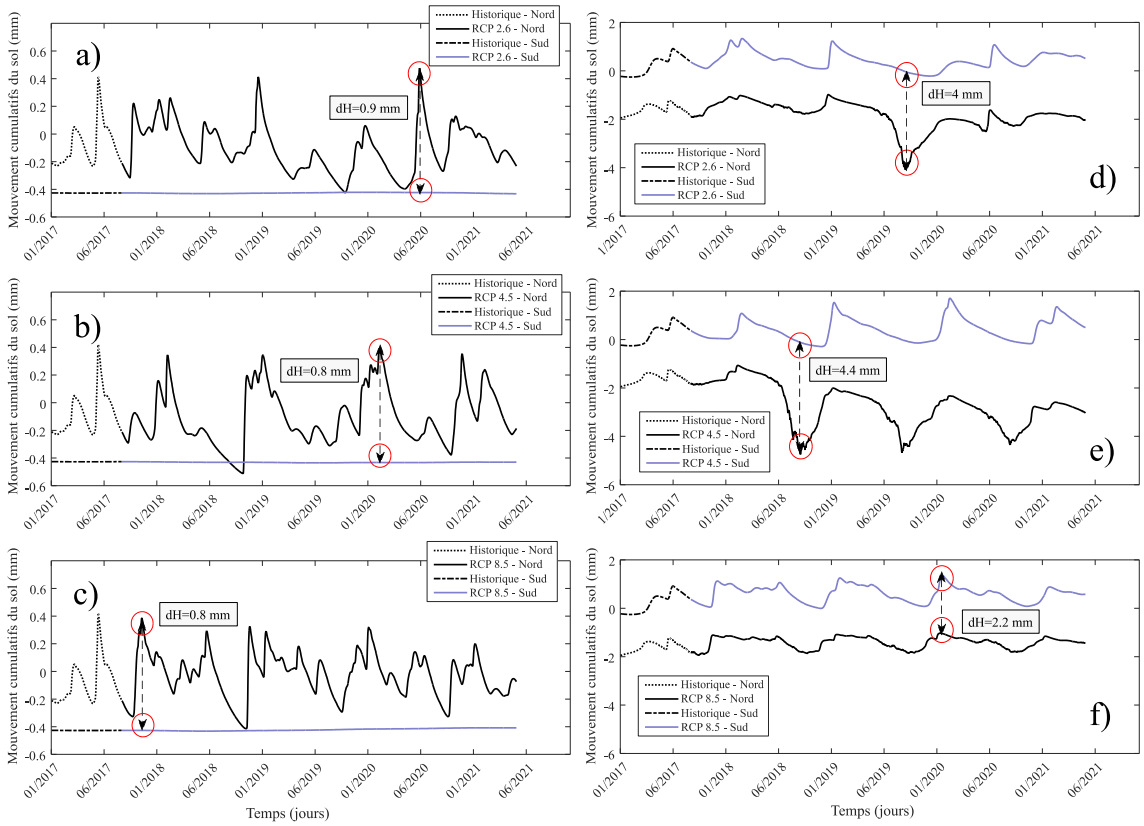

Figure 14 - Mouvements différentiels du sol à court terme sous les fondations (profondeur de 1 m) et proches de l'arbre (profondeur de 2 et 2,3 m) selon le scénario a) RCP 2.6; b) scénario RCP 4.5; et c) scénario RCP 8.5

Comme l'évaluation à court terme des mouvements du sol, les mouvements différentiels à long terme sont également évalués. La Figure 15 montre les mouvements différentiels du sol à long terme sous les fondations du bâtiment à l'aide des trois scénarios RCP. Il peut être observé que le mouvement différentiel maximal est approximativement le même pour chaque scénario (1 mm). Cependant, le moment correspondant au mouvement différentiel maximum est différent dans chaque scénario. Il faut mentionner que les mouvements à long terme se situent dans la même gamme de variation que les mouvements différentiels à court terme en raison des variations de succion dans le temps.

Cette évaluation est également effectuée en utilisant les deux points de test (2b et 3b) pour les mouvements du sol à proximité des arbres. Les résultats indiquent que les mouvements différentiels du sol à long terme sont clairement différents des résultats à court terme. Les mouvements différentiels du sol ont tendance à l'accumulation du retrait. L'analyse à long terme a montré que les mouvements différentiels du sol sous fondation sont similaires à l'analyse à court terme. De plus, les tendances au retrait gonflement sont principalement observées dans le scénario RCP 8.5 et le mouvement différentiel maximal est observé plus rapidement comme l'analyse à court terme. Par conséquence, le scénario RCP 8.5 est considéré comme le pire des cas. Cependant, compte tenu des mouvements différentiels du sol à proximité des arbres, l'analyse à long terme n'est pas comparable à l'analyse à court terme en raison des phases de retrait progressives dans chaque scénario. De plus, en se basent sur le mouvement différentiel maximal, le scénario RCP 4.5 pourrait potentiellement être le pire des scénarios en présence de contraintes environnementales externes.

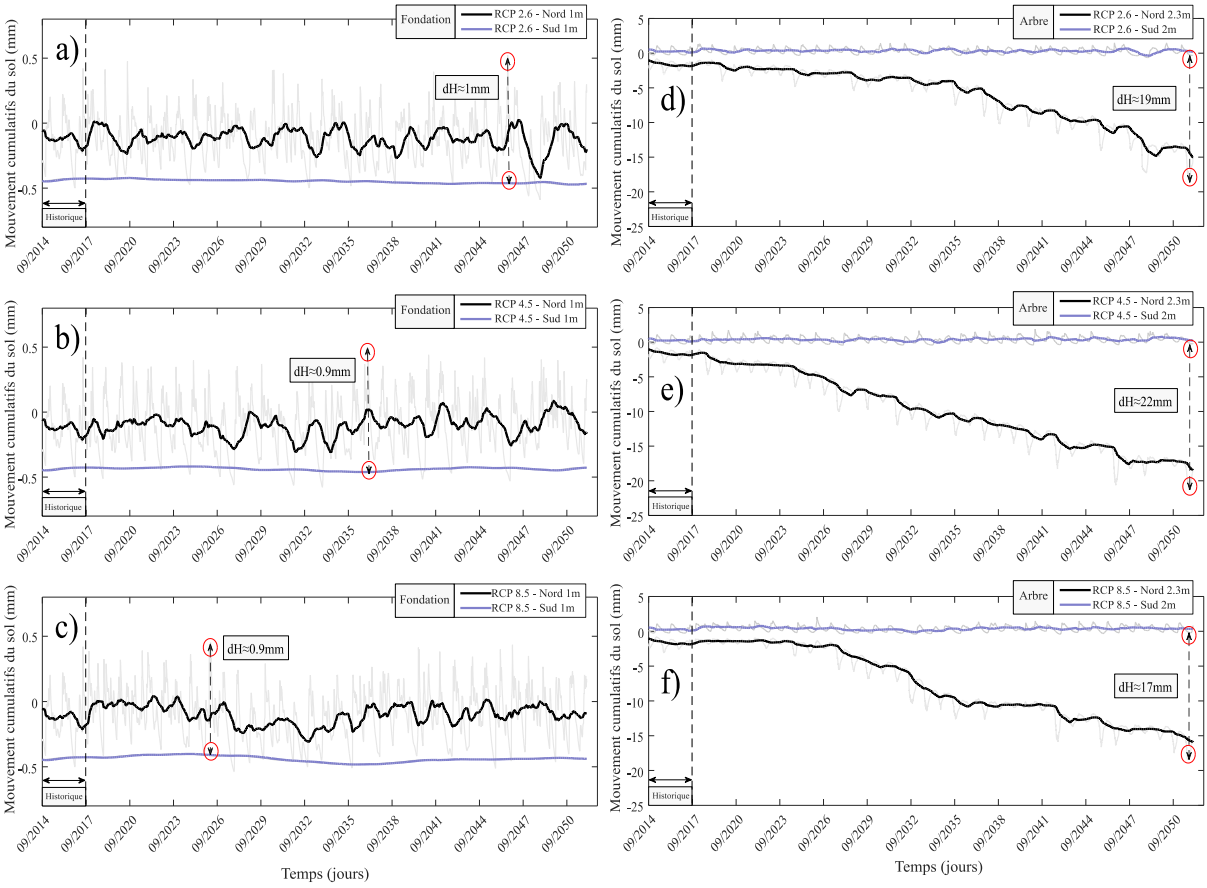

Figure 15 - Mouvements différentiels du sol à long terme sous fondations (profondeur de 1 m) et à proximité de l'arbre (profondeur de 2 m et de 2,3 m) en utilisant le scénario a) RCP 2.6; b) scénario RCP 4.5; et c) scénario RCP 8.5

5. Application sur le territoire français :

L'objectif de ce chapitre est d'appliquer l'approche développée à l'échelle nationale. À cette effet, la France est divisée en six zones climatiques basées sur différents types de climat existants. Un type de sol est attribué à chacune de ces zones climatiques sur la base des cartes disponibles pour la répartition des sols en France. Ces sols (cités en tant que sols de référence) sont définis à l'aide de paramètres d'entrée du modèle. La condition de référence comprend également les paramètres de végétation et de structure. La condition de référence dans chaque région est utilisée pour fournir les séries temporelles de succion du sol sous fondation du bâtiment, qui conduit ensuite au calcul des mouvements du sol. Une étude paramétrique est menée pour étudier l'influence de ces facteurs sur les mouvements de sol résultants.

La Figure 16 montre les six principaux types de climat en France. La région centrale est principalement dominée par un climat océanique dégradé. L'est et l'ouest de la France sont caractérisés respectivement par des types de climat océanique et semi-continental. Le sud-ouest est dominé par le climat océanique Aquitaine, mais le massif central et le sud-ouest de la France se caractérisent par un climat montagneux. Enfin, le sud de la France est généralement dominé par un climat méditerranéen. Afin d'attribuer des paramètres climatiques cohérents pour ces six régions, cinq points différents dans chaque région ont été analysés. Les données utilisées dans cette section couvrent la période de 2016 jusqu'à la fin de 2018 (cette période a été choisie suivant

la base de données géotechniques de DETERMINANT). Par la suite, les paramètres climatiques d'entrées pour l'analyse des interactions SVA sont définis pour chaque zone climatique.

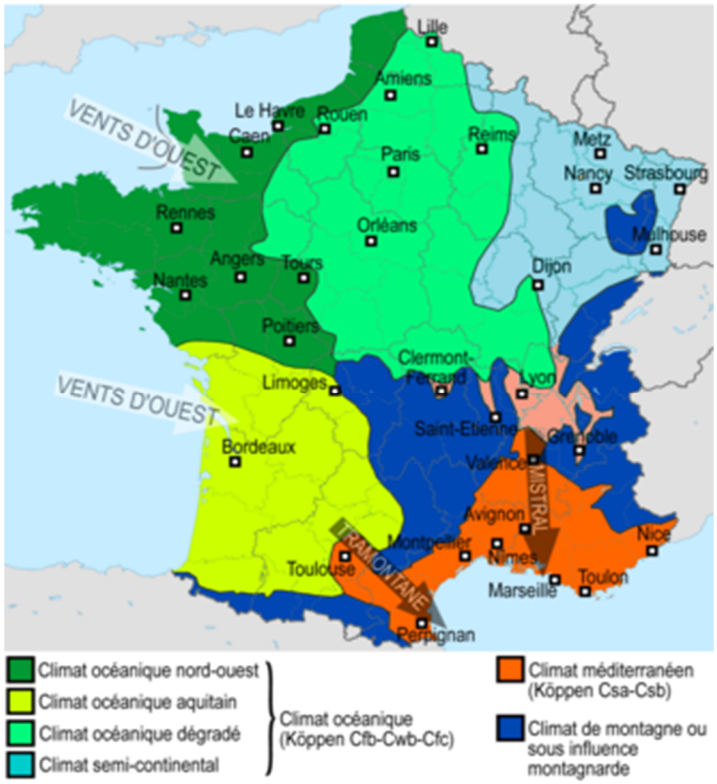

Figure 16 - Six types de climat en France

La condition de référence est définie en supposant un bâtiment résidentiel sur terre-plein avec une semelle filante d'une profondeur de 0,8 m et d'une largeur de 0,5 m, construit sur un sol sans végétation. Il faut mentionner qu'une contrainte verticale de 60 kPa est considérée sur le sol. Différents types de sol ont été attribués à chaque région climatique sur la base des cartes fournies par le BRGM pour la répartition des sols en France. Sur la base de ces cartes, il a été déduit que les couches superficielles des sols du massif central et du nord-ouest de la France sont principalement caractérisées par des limons. D'autre part, les régions est et sud-ouest sont principalement caractérisées par des sols argileux. Le sud de la France est caractérisé par des argiles et des limons argileux. Enfin, le centre et le sud-est sont dominés par des sols sableux dans les couches supérieures. Cette distribution permet de déterminer les mouvements du sol dans chaque région en fonction des paramètres climatiques définis au préalable pour chaque région.

Les simulations effectuées dans cette section sont basées sur une hypothèse de formation géologique homogène et des propriétés de rétention uniques pour chaque cas. Le Tableau 3 présente les paramètres de référence pour ces six régions. La Figure 17 montre les mouvements de sol calculés pour chacune des six régions ayant des propriétés de sol et des conditions climatiques différentes.

Tableau 3 - Paramètres de condition de référence dans les 6 régions considérées

		Region 1	**Region 2**	**Region 3**	**Region 4**	**Region 5**	**Region 6**
Sol	Texture	Limon	Limon	Argile	Argile	Sable	Limon argileux
	PI (%)	25	25	50	50	10	35
	LL (%)	60	60	80	80	30	70
	w (%)	37	37	30	30	45	33
	e_0	1	1	0.8	0.8	1.2	0.9
	γ_d (Mg/m^3)	1.35	1.35	1.5	1.5	1.2	1.4
	θ_r	0.078	0.078	0.098	0.098	0.065	0.095
	θ_s	0.43	0.43	0.46	0.46	0.55	0.41
	α (1/mm)	0.0036	0.0036	0.0015	0.0015	0.0075	0.0019
	n	1.56	1.56	1.25	1.25	1.89	1.31
	K_s (mm/days)	250	250	147.5	147.5	1061	62.4
Climat	Type	Océanique dégradé	Océanique	Semi continental	Océanique Aquitaine	Montagne	Méditerranéen
	Localisation	Center	Nord-Ouest	Est	Sud-Ouest	Central sud et Sud Est	Sud
Végétation	Arbre	N.A.	N.A.	N.A.	N.A.	N.A.	N.A.
	Distance	N.A.	N.A.	N.A.	N.A.	N.A.	N.A.
Structure	Fondation Prof. (m)	0.8	0.8	0.8	0.8	0.8	0.8
	Fondation Largeur (m)	0.5	0.5	0.5	0.5	0.5	0.5
	Chargement (kPa)	R+1 60 kPa	R+1 60 kPa	R+1 60 kPa	R+1 60 kPa	R+1 60 kPa	R+1 60 kPa

On peut observer que le gonflement maximal dans les conditions de référence se produit dans le sud-ouest de la France, ayant un climat océanique Aquitaine et des sols argileux. D'autre part, le retrait minimum se produit dans un climat montagneux avec des sols sableux. Les autres types de sols varient entre ces deux régions.

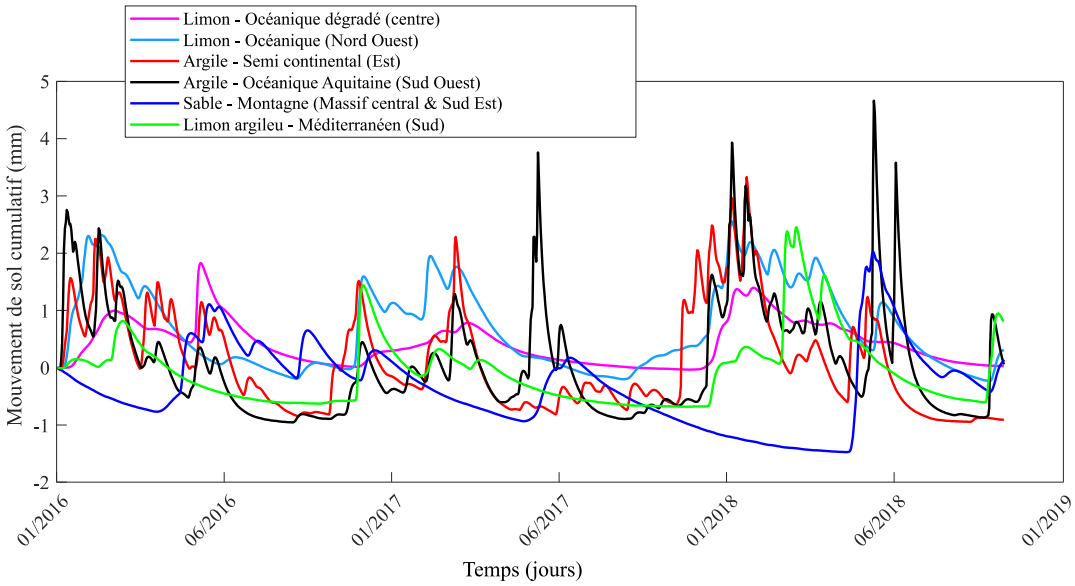

Figure 17 - Mouvements de sol de référence dans six régions différentes en France

Une étude paramétrique est réalisée sur certains facteurs (comme la distance de la végétation-arbre, la profondeur de la fondation, la largeur de la fondation et le chargement du sol) qui ont un impact sur les mouvements du sol dans chaque région. La Figure 18 montre ces différents facteurs ainsi que l'état de référence des éléments structurels de la fondation du bâtiment et les conditions de la végétation.

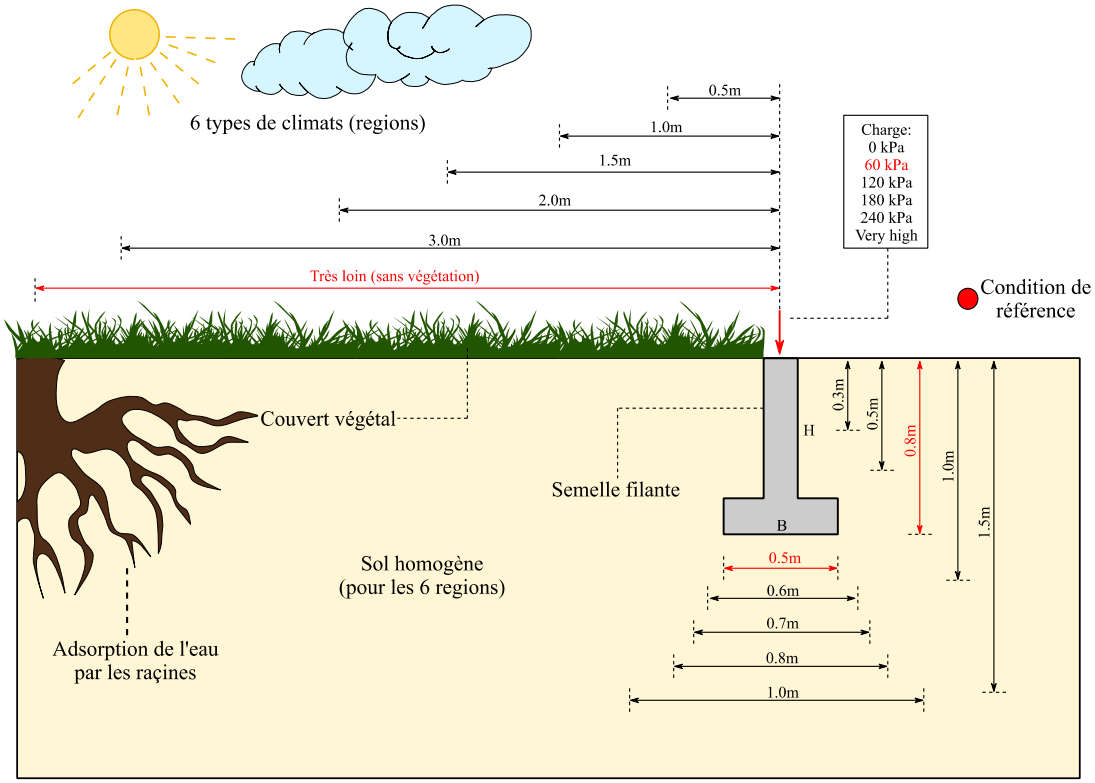

Figure 18 - Paramètres d'influence ainsi que la condition de référence calculée pour six régions.

Les résultats de l'étude paramétrique ont montré que l'absorption de l'eau par les racines peut avoir une influence considérable sur les mouvements du sol dans chacune des six régions si l'arbre était situé à moins de 2 m des fondations du bâtiment. Il faut également mentionner que le schéma de distribution des racines dans un cas spécifique pourrait être différent de celui utilisé dans ce processus de simulation.

D'autre part, il a été démontré que la profondeur de la fondation joue un rôle considérable dans la réduction de l'amplitude du retrait et du gonflement des sols. Il faut mentionner que les calculs ont été effectués en supposant une couche de sol homogène où les paramètres physiques du sol ne changent pas en profondeur. Une profondeur de fondation supérieure à 1,5 m peut empêcher les conditions climatiques d'impacter les mouvements du sol. Cependant, l'analyse réalisée sur la largeur de la fondation a montré que l'influence est négligeable sur le retrait gonflement du sol dans toutes les régions considérées.

Enfin, les conditions de chargement de sol dans la gamme considérée pour les constructions légères ont montré que l'influence sur les mouvements du sol est négligeable et que l'amplitude du retrait et du gonflement est limitée en appliquant un chargement supérieur sur le sol.

6. Conclusion générale

Afin de répondre aux besoins de développement d'approches simples permettant d'évaluer le phénomène de retrait gonflement, ces travaux de recherche ont présenté une approche globale pour modéliser les mouvements de sol in situ dans des conditions d'interaction sol-végétation-atmosphère à l'aide des outils numériques. Les données météorologiques servent principalement de paramètres d'entrée pour la définition des conditions aux limites atmosphérique du modèle hydro-thermique, en utilisant le principe d'interaction sol-atmosphère. À cette étape, les équations du bilan de masse et du bilan énergétique permettent d'intégrer les paramètres climatiques dans le modèle couplé selon une approche simple. En plus des paramètres hydro-thermiques, le terme source de l'équation de Richards a été utilisé pour intégrer l'absorption d'eau par les racines de la végétation dans l'analyse. Un modèle existant dans la littérature (Feddes) a été utilisé pour modéliser l'effet de l'absorption d'eau par les racines sur les variables hydro-thermiques en utilisant certains paramètres de végétation, telles que la courbe du coefficient de culture, la fonction de distribution des racines et l'indice foliaire de surface (LAI) qui permet de déterminer le taux de transpiration à la surface du sol. Cela a permis la décomposition de l'évapotranspiration en évaporation et transpiration du sol en utilisant la courbe du coefficient de culture. L'analyse effectuée a permis de déduire que l'absorption d'eau par les racines avait une influence considérable sur la teneur en eau et la succion du sol et devait être donc prise en compte dans le processus de simulation, le cas échéant.

Par la suite, l'attention a été portée sur le comportement de changement de volume des sols non saturés soumis à des sollicitations environnementales. Le modèle linéaire a été utilisé pour relier les variations temporelles de succion du sol à l'indice des vides, en se basent sur les résultats des essais expérimentaux menés dans la littérature. Le comportement volumique d'un sol a été déterminé à l'aide des pentes du modèle linéaire qui représentent les indices volumétriques du sol qui permet de calculer les déformations du sol. Ces indices ont été corrélés avec les propriétés géotechniques de base en analysant de nombreux sols testés dans la littérature. L'étude paramétrique des corrélations développées a montré que l'intervalle de confiance des indices volumétriques du sol se situe dans un intervalle acceptable et peut être utilisé pour des analyses plus poussées permettant de déterminer les mouvements du sol dans le temps.

La méthodologie établie a ensuite été testée en comparant les résultats de la simulation avec les données fournies d'un site instrumenté. La comparaison avec les variables hydro-thermiques a montré une cohérence acceptable à la fois dans les angles sud et nord du bâtiment. Les mouvements de sol simulés étaient également en accord avec les mesures sur le terrain.

Afin d'avoir une idée de l'évolution future des variables d'état de la simulation, à savoir la teneur en eau du sol, la succion, la température, l'indice des vides et les mouvements du sol, les paramètres climatiques ont été projetés jusqu'à 2050 à l'aide de trois scénarios RCP. Le comportement à court terme et à long terme du sol a été étudié sur le site considéré. Les résultats ont montré qu'à court terme, les scénarios RCP ne montraient pas de changements considérables dans l'angle nord avec le scénario RCP 4.5. Cependant, à long terme, le scénario RCP 8.5 a montré un comportement cyclique qui pourrait potentiellement avoir plus d'impact sur le sol dans les deux angles du bâtiment. Les mouvements différentiels de sol à proximité des arbres ont atteint des valeurs considérables dans les trois scénarios et les mouvements sous fondation

étaient principalement importants dans les scénarios RCP 4.5 et 8.5. On peut en conclure que ce type d'analyse pourrait être utile pour éviter des dommages sur les constructions légères. L'une des solutions préventives pourrait être l'installation de systèmes de barrière anti-racines entre la fondation du bâtiment et l'arbre (utilisé dans ce cas). L'efficacité de ce type de solution peut également être vérifiée par des approches de modélisation et des systèmes de surveillance adaptés. D'autre part, pour limiter la zone d'influence du sol sous fondation due aux changements climatiques, des couvertures périmétriques pourraient être construites autour des bâtiments, comme indiqué précédemment.

La dernière partie de cette thèse portait sur l'application de la méthodologie à l'échelle nationale ainsi que sur une étude paramétrique. Chaque condition de référence dans les 6 régions considérées a déterminé la variation des mouvements du sol au fil du temps et a ensuite été analysée en modifiant les conditions de la végétation, la géométrie de la fondation et les actions de chargement sur le sol. Les résultats ont montré qu'une distance d'au moins 2 m est nécessaire pour ne pas être situé dans la distance d'influence de la végétation. Sinon, des mouvements de sol considérables et un tassement essentiellement cumulatif seront observés sous les fondations. D'autre part, il est suggéré d'ancrer les fondations des bâtiments à une profondeur d'au moins 1,5 m, car l'influence des conditions climatiques pourrait diminuer considérablement. Cependant, la largeur du sol de fondation ne joue pas un rôle crucial sur les mouvements de sol calculés. Enfin, les contraintes appliquées au sol dans la gamme des constructions légères ne limitent pas considérablement les mouvements du sol dans le temps.

پایان!